Universitat Politècnica de Catalunya

Departament d'Enginyeria Química

Ph.D. Thesis in

ELECTRON TRANSFER PROCESSES IN BIOMIMETIC MEMBRANES INCORPORATING PRENYLQUINONES

Javier Hoyo Pérez

Supervisors

Prof. Joan Torrent Burgués
Ph.D. Ester Guaus Guerrero

Barcelona, 5 de setembre de 2014

INDEX

STRUCTURE

This Ph. D. Thesis studies the electron transfer process that takes place in photosynthesis using biomimetic membranes. The complexity of this biomimetic membrane increases according to the lipids and quinones that compose it, beginning from model lipids and ending with the use of a lipid mixture that represents the 70% of the natural lipid content. So that, this Ph. D. Thesis presents studies of several biomimetic systems, which have a similar State of the Art and also a similar discussion, so that, I have decided to present the Ph. D. Thesis as a large scientific journal in which the State of the Art and the Materials and Methods chapters involve all the studied systems and techniques. On the other hand, the Results and Discussion chapter is divided in sections, and each of them presents the results and their corresponding discussion of each system. Finally, the conclusions obtained from each system are summarized in the Conclusions Chapter.

Chapter 1 defines the objectives and motivation of this Ph. D. Thesis.

Chapter 2 explains the techniques used in this Ph. D. Thesis for biomimetic membrane preparation and characterization, in order to understand the basis of them and their applications to the systems studied, without exposing the full mathematical background of the different techniques. Moreover, the mathematical expressions for the experimental results treatment are also exposed.

Chapter 3 explains the State of the Art. It exposes briefly the photosynthesis process, which takes place in the thylakoid membrane. Moreover, it presents the substrates used in the literature to support biomimetic membranes. On the other hand, it also explains the model membrane characteristics, physical state and the factors that influence both of them. Finally, it is presented the ternary interactions between the model membrane, the electrolyte solution and the substrate, and also the effects of the addition of ions and molecules on the model membrane. Finally, an extended description of the molecules studied in this Ph. D. Thesis is presented, explaining also the different studies done that can be related with our results.

Chapter 4 exposes the chemicals and the instruments that we have used.

Chapter 5 presents the results and discussion divided in three blocks. The first involves the two quinones that we use in our studies. The second block corresponds to the pure lipids used and the third block explains the lipid-quinone systems. The last section gives a global sight of the galactolipid and galactolipid:quinone systems.

Chapter 6 exposes the conclusions obtained from the different systems studied achieving a general vision of the quinone position in the lipid matrix and the redox processes that influence it.

The relevance of the photosynthetic process makes it subject of multidisciplinary study, so we use terms and knowledge coming from biology, surface science, chemical equilibrium, microscopic techniques, electrochemistry … The out discipline concepts are treated in a non-expert vocabulary to help the reader to understand the main objective of this Ph. D. Thesis.

Chapter 1

Motivation and Objectives

Most of the actions we perform in our way of life require energy. Since we stand up we use electricity for clock alarm, for heating the shower water, for bread toasting... We use fuel for work travelling and electricity for the computer and other electronic devices we use in our work time. We use electricity for leisure, lighting and heating. The energy we consume is present in different forms electricity, gas or fuel. Electricity is the most used and its sources can be fossil like: gas, fuel, coal and nuclear, or renewal, like: solar, wind, geothermic… Fossil sources have several inconvenients, specially that they are finite and the pollution they produce. On the other hand, renewal sources have the inconvenience that energy must be used at the time it is produced.

The world population has increased 17 % in the last ten years. On the contrary, the energy global consumption has increased 23 % in the same period of time. The reasons for this increase are out of the scope of this introduction, but the tendency is clear and it seems that this consumption will increase over the coming years. In response of that, improvements have been implemented in renewal energy sources, but their efficiency is still far to be optimum. Consequently, the increasing World energy necessity makes essential the research on new and efficient energy sources. One of the most promising ways is mimicking the processes of natural photosynthetic organisms for energy obtaining. These processes involve several complex steps and the deep knowledge of each step allows optimizing the global process efficiency.

The photosynthesis in higher plants takes place in the thylakoid membrane that is a lipid bilayer composed mainly by galactolipids, being the most important monogalactosyl diacylglycerol, MGDG (≈ 50%), and digalactosyldiacylglicerol DGDG (≈ 25%). Plastoquinone (PQ) molecules are placed between both leaflets of the bilayer acting PQ as the electron and proton shuttle from the Photosystem II (PSII) to the cytochrome *b6f*.

Artificial photosynthesis comprises the different attempts that humans perform to mimic the natural photosynthetic process. The knowledge of photosynthesis started when Aristotle (ca. 350 B.C.) theorized that the substance of plants came from the soil. In 1450, Nicholas of Cusa proposed (but seems that never perform) an experiment in which a plant is weighted and then planted in a weighted amount of soil. After a period of growth, the final weights of the plant, the soil and the water applied are compared with the initial values. He speculated that the mass increment of the plant was derived from the water rather than the soil. In 1648, Jean Baptiste van Helmont performed the experiment proposed by Nicholas of Cusa, concluding that the mass of the plant came from the water and ignoring the very slight decrease in the soil weight. Edmé Mariotte in 1679 provided the first theory of metabolism by proposing that all plants are made up of basic substances, which are taken up from the soil and transformed into metabolites thanks to the atmosphere. In 1727, Hales performed experiments with sunflowers and described the leaves as organs of transpiration, and postulated that plant exchange gases with the atmosphere and the sunlight might be involved. In 1771, Priestley performed experiments on a jar placing a sprig of mint and a candle on it, the candle was burned until the oxygen went out. After some days, he used a mirror to burn the candle and it burned, so he demonstrated the restoring of gas done by the plant. In the following 25 years, it was demonstated that green plants take carbon dioxide from the air and they only release oxygen when they are illuminated, suggesting that it was provoked by the sunlight. In addition the basic photosynthetic equation was established.

Since the ending of the 18th century till the detailed determination of the photosynthetic reaction center structure in 1984 by the Nobel Prizes Deisenhofer, Michel and Huber, scientists have obtained several advances in the Photosynthesis knowledge. After this milestone, the knowledge of this process has increasingly been focused on applying this knowledge to obtain human benefits. Probably, the first study in which photosynthesis is carried out using artificial light is done by Dastur and Samant in 1933. Since this year,

scientists have performed several experiments on the photosynthetic process changing artificially some variables to evaluate its response. The first time that the concept artificial photosynthesis appears, is in 1962 in a NASA document titled *Applied research concerning artificial photosynthesis*. The artificial phostoynthesis remains with low interest until 1978. After the 1973 oil crisis, scientists saw the opportunity that artificial photosynthesis represents. The science interest on this field grew till the Great Recession of 2007 when the interest increased exponentially until nowadays.

The photosynthetic process involves three main steps: light absorption, electron transfer and energy production. Each step is complex and implies several variables, so the access to the complex functioning of biological photosynthetic membranes is a real challenge, in consequence, researchers have focused their efforts in studying only one of these steps.

1.1 Motivation

My Ph.D. career began in 2007 when I finished my Degree Project in Chemical Engineering in the Technische Universität Berlin (TUB). There, I was offered to study my Ph. D. Thesis in a biotechnological field, but Prof. Fausto Sanz in collaboration with Prof. Joan Torrent offered me the possibility of studying the photosynthesis and I enrolled. Prof. Fausto Sanz is the group leader of the nanoprobes and nanoswitches group in the Institute for Bioengineering of Catalonia (IBEC) and he is also Professor of electrochemistry at the University of Barcelona. On the other hand, Prof. Joan Torrent and Ph. D. Ester Guaus are group leaders of the Laboratory of Molecular Electrochemistry, Interfaces and Nanometric Films (LEIPN) group at Universitat Politècnica de Catalunya, where both leaders teach nanometric techniques.

The bibliographic research confirmed the little information related with the electron transfer process within the membranes, so we must begin using model molecules. Our first attempts consisted on preparing SPB of Dipalmitoylphosphatidylcholine (DPPC) and benzoquinone (BQ) studying their topography and electrochemical response using several substrates and buffer compositions. DPPC is a model membrane lipid that is widely studied and BQ is the simplest quinone. After studying the DPPC:BQ system, we studied DPPC SPBs inserting

duroquinone (DQ), that is a more hydrophobic redox molecule than BQ, in order to avoid the solubilization of quinone in the aqueous electrolyte solution. These results were presented in the Master Thesis of Chemical Processes studied at the UPC and part of them was also published in the first volume of *Avances de la electroquímica en Iberoamérica, Portugal y España.* The use of DPPC and quinones, which are not present in natural photosynthetic membranes, is explained thanks to the widely knowledge of these molecules and the low economical cost of them. These reasons allow us to perform many experiments to adapt the several techniques used in this Ph. D. Thesis to work with more complex molecules. We also designed a new glass cell and the architecture of its supports, to adapt them to both the low concentrations that we would use and also the rectangular shape of the ITO working electrode.

The Ph. D. Thesis content began studying SPBs and LB films of DPPC inserting ubiquinone (UQ) that is a molecule similar in shape and size to PQ, having the former ten times lower economical cost. These experiments worth to realize that the reproducibility of the SPBs when using this kind of systems is lower than the obtained with the LB films transferred on hydrophilic substrates, so from this point, we only worked using the LB technique. Next step was studying UQ with the lipid most present in natural photosynthetic membranes (MGDG). The initial idea of working with UQ was using it as a prior step to work with the natural present PQ, but its results were of great relevance, so finally we spent a couple of years working with UQ. After that, we prepared MGDG films inserting the PQ and we continued studying DGDG films inserting PQ. The last step has been increasing the difficulty and the reliability of the model preparing a mixture of MGDG and DGDG (MD) inserting also PQ, which represents ca. 70% of the lipidic content of natural cell membranes and implies a leap on the study of these systems. Part of the results of this Ph.D. Thesis have been already published in prestigious indexed international scientific journals of this field.

1.2 Objectives

The main target of this Ph.D. Thesis is the knowledge of the electrochemical processes that take place in a biomimetic membrane and the position of the quinone molecules in the galactolipid matrix simulating several conditions that can be applied to artificial photosynthesis. We were aware of the ambitious objective of preparing biomimetic membranes using the natural present components, so that, we prepared a timeline according to that. Obviously, an accurate preliminary electrochemical characterization of simple quinone (BQ or DQ) in solution using several working electrodes was required to check our results with the little literature that there is on this field. Therefore, choosing the best experimental conditions and adapting the experimental set up to work with these systems using, as substrate, indium tin oxide glass slides (ITO), which has good electrical and optical features.

Once the techniques were adapted, the next step was working with natural present components, increasing at each step the work difficulty, achieving to mimic conditions close to that of a natural membrane at the end of this Ph. D. Thesis. The final results of these experiments show that the MD monolayer establishes a correct environment to embed the PQ molecule and permits its redox activity using ITO.

The objectives of these Ph. D. Thesis involve:

- The formation of mono- and bilayers of DPPC and DPPC:UQ mixtures on solid substrates using, respectively, the LB and vesicle fusion technique. The characterization of these films will permit the evaluation of the film reproducibility depending on the preparation technique.
- The formation of DPPC and DPPC:UQ bilayers on ITO using the vesicle fusion technique will permit their topographic and nanomechanical characterization. The combination of these results with the electrochemical response should light the quinone position in the bilayer.

- The formation of monolayers using the Langmuir technique of pure quinones (UQ and PQ), pure lipids (DPPC, MGDG, DGDG and MD) and the selected lipid: quinone mixtures at the air-water interface. The study of these monolayers will indicate the physical state and the mixing behaviour in the mixtures case.
- The monolayers described will be transferred on mica and, using AFM, the topography and the height of the transferred monolayers will be characterized. This characterization permits obtaining both the compactness and the physical state of the monolayer on a solid substrate.
- The described monolayers will also be transferred on ITO, and using cyclic voltammetry, their successful transfer on this conductive and hydrophilic substrate and their electrochemical response will be evaluated.
- The combination of the results of the techniques exposed should light the position of the quinones in the monolayer.

Chapter 2

Fundamental techniques

As it has been stated in the Objectives section, the main target of this Ph.D. Thesis is the understanding of the redox processes in biomimetic membranes for a further use in artificial photosynthesis. This target can be classified as part of the nanobioengineering due to requires controlled elaboration of nanoscale systems and, so that, request the use of nanoscale resolution techniques. Natural photosynthesis takes place in the cell membrane that is a selectively permeable lipid bilayer. It is composed of a variety of biological molecules being the most important lipids and proteins. Both are primarily responsible for membrane function, as well as structure, and interact between them. So that, the techniques for studying biomimetic membranes (membranes that mimic the biological ones) must consider the structure formed and the interaction between the different components.

In this chapter, I will present the techniques that we have used in this Ph.D. Thesis to prepare and characterize biomimetic membranes. The techniques are exposed and explained to understand the basis of them and their applications to the systems studied, without exposing the full mathematical background of the different techniques.

Firstly, I present the main techniques used to prepare the biomimetic membranes (Section 2.1). Starting with monolayers, we have employed the Langmuir film technique to record π-A isotherms and decide at which film stage is interesting to transfer Langmuir-Blodgett (LB) monolayers. In addition, the phase and miscibility behaviour of the Langmuir monolayer at several surfaces pressures have been studied.

The use of LB technique offers an accurate control of the transferred monolayer, resulting in a higher reproducibility, especially in substrates with nanometric roughness like indium tin oxide (ITO). We have also used the vesicle fusion technique to prepare supported planar bilayers (SPB). This technique has been improved by us to achieve a good reproducibility in nanometric roughness substrates, but the precise film stage deposition achieved with the LB technique made us to prepare the major part of the biomimetic membranes using this technique.

The second section (Section 2.2) exposes the molecules and the substrates used, and the third section (Section 2.3) explains the different techniques used for the characterization of the biomimetic membranes. The cyclic voltammetric (CV) technique is presented in a separated section (Section 2.4) due to it has not been only used to characterize the quality of the biomimetic membrane. In this Ph. D. Thesis, CV is mainly performed to study the electron transfer processes.

2.1. Methods for preparing supported biomimetic membranes

Supported biomimetic membranes can be prepared using several procedures. The most used are vesicle fusion and Langmuir-Blodgett (LB) or a combination of LB+Langmuir-Schaefer (LS) transfer. The vesicle fusion and LB technique are explained in depth in the following sections due to they are used in this Ph. D. Thesis.

The LB-LS permits forming asymmetric bilayers, whereas the vesicle fusion method is only capable of forming symmetric bilayers. However, there are more methods for mono- or bilayer formation. A simple technique for preparing phospholipids bilayers consists on freshly cut surface of metals like Au, Pt or a freshly made Hg drop, dipped to a volatile solvent phospholipid solution followed by soaking the cut surface in an electrolyte solution. More recent techniques are self-assembled monolayer (SAM) and tethered bilayer membranes (t-BLM). SAM involves the modification of the substrate surface with a monolayer of thiols and depositing a phospholipid monolayer on it. Depending on the application, the monolayer of thiols has a hydrophilic or hydrophobic end group, so influencing the second mono- or bilayer deposition. SAMs have satisfactory barrier

properties but they have the inconvenience of not having a water layer between the monolayer and the substrate, so the fluidity of the biomimetic membrane is reduced [1[2[3]. t-BLM is similar to SAM using the former a thiolipid instead of a thiol to form the first leaflet, and preparing a mono- or bilayer on this first leaflet [4]. Recently, Mach et al. [5] have developed a potential driven formation of SPB achieving a SPB more stable against electrical and mechanical perturbations than using other SPB preparation techniques. In this section we explain only the used techniques.

Compared with other techniques for preparing biomimetic membranes, the techniques that use solid supports (in this Ph. D. Thesis SPB and LB) have an important advantage with the increase in robustness and stability. Moreover, the formation on this support permits using analytical techniques like AFM, quartz crystal microbalance, surface plasmon resonance, ellipsometry…On the other hand, the main disadvantage is that transmembrane proteins can not be placed in the formed SPB or LB due to the interaction with the substrate. As a result, some authors have proposed SAMs to establish a height difference between the substrate and the SPB with transmembrane protein inserted.

2.1.1 Langmuir and Langmuir-Blodgett techniques

LB technique allows building up lamellar lipid stacking by transferring onto a solid support a monolayer (Langmuir film) previously formed at the air|water interface. Langmuir films of lipid molecules have been extensively used as models to understand the role and the organization of biological membranes and to improve the knowledge about the molecular recognition process [6]. LB films present multiple applications ranging from signal transducer and nanobiocatalysis in biomimetic situation to its use in bioelectronics and nanobiosensors. Moreover, LB technique has shown its increasing relevance in drug vectorisation and drug delivery [7].

This section will focus on the fundamental principles and practical aspects of the elaboration of biomimetic lipid layers through LB deposition. Moreover, at the end of this section are exposed the basic expressions for the mathematical treatment of the results obtained using this technique.

2.1.1.1 Langmuir monolayer formation

Langmuir films are based on the properties of certain organic molecules like lipids to orient themselves at the air|water interface between the gaseous and the liquid phase. The Langmuir monolayer is considered an extreme case of adsorption to interfaces with all the spread molecules concentrated at the interface [7]. Most of the molecules capable to form Langmuir films are insoluble amphiphilic molecules, also known as amphiphiles, composed of two main regions being a hydrophilic headgroup (head) and a hydrophobic tailgroup (tail).

The first step for obtaining a Langmuir film is preparing a solution of the amphiphilic molecules in a solvent with the following characteristics: non-polar, volatile, water-immiscible and chemically stable. The second step involves pouring the subphase in the trough. The trough is a PTFE container with a swimming pool shape, so having a very large 2D surface and short depth. This container has also one or two PTFE movable barriers controlled by a computer (Figure 2.1A). The third step consists on placing drops of the previously prepared solution onto the subphase (Figure 2.1B). It results in molecules spreading over the entire available area due to the intermolecular forces. After some minutes for solvent evaporation, thanks to the self assembly nature of the molecules, a monolayer has been formed (Figure 2.1C) at the interface with the headgroups immersed in the subphase and the tails remaining outside, pointing towards the gas phase. This orientation is achieved to minimise their free energy. Then, the movable controlled barriers compress the film achieving the different phase stages (Figures 2.1D-F) that will be explained in the following sections.

2.1.1.2 Basics of the Langmuir films technique

The thermodynamic properties of the air|liquid interface drive the formation of an amphiphilic molecules monolayer. There is an excess of free energy in the liquid surface compared with the liquid bulk due to the different environment.

At the interface, a molecule is surrounded by fewer molecules than one in the bulk so the equilibrium of forces is disrupted. The surface molecules experience an imbalance of forces due to unbalanced molecular attraction. In this situation, a molecule at the air|water

interface has a larger attraction towards the liquid than the gas phase, obtaining an attractive force towards the bulk so minimizing the air|water interface area. The interaction between water surface molecules and the polar group of the amphiphile implies a reduction of the free energy of the system and, in consequence, the expansion of the air|water interface. In this situation, a force arises between the liquid molecules (cohesion), which depends on the substance properties.

The line force acting on the surface molecules is the surface tension γ (Figure 2.2). In the case of water its value is high (72.8 $mN \cdot m^{-1}$ at 20˚C) owing to the strong intermolecular forces. The surface tension of a flat interface can be described by the Expression 2.1 [9,10] where S is the area of the subphase surface and F and G are respectively the Helmholtz and the Gibbs free energies of the system. Keeping constant the temperature T, volume V or pressure P and amounts of all components n_i.

$$\gamma = \left(\frac{\delta F}{\delta S}\right)_{T,V,ni} = \left(\frac{\delta G}{\delta S}\right)_{T,P,ni} \qquad \text{Expression 2.1}$$

In the case of a pure liquid that is in equilibrium with its saturated vapour at the flat interface, Expression 2.1 can be simplified in Expression 2.2 where F^S refers to the surface excess free energy.

$$\gamma = \frac{F^S}{S} \qquad \text{Expression 2.2}$$

2.1.1.3 Surface Pressure measurements

The attractive interactions of the water molecules at the interface are lowered when the amphiphilic molecules accumulate at the air|liquid interface. So that, some authors has classified the surface tension as a negative pressure [7]. The surface tension remains invariable while the amphiphile concentration per area unit is low. Increasing the amphiphile concentration per unit area (closing the barriers), a reduction of the intermolecular distances occurs, thus lowering the surface tension. Surface pressure is the difference between the surface tension of pure subphase (γ_0) and the surface tension of the subphase with the presence of amphiphile (γ_1). This is a force per length unit, although it is called pressure (Expression 2.3) in analogy with a force in a two dimensions model.

$$\pi = \gamma_0 - \gamma_1 \qquad \text{Expression 2.3}$$

The Wilhelmy plate is the most used method for experimentally measuring the surface pressure during the monolayer compression because of its simplicity and its uses for experimentally surface tension measurement.

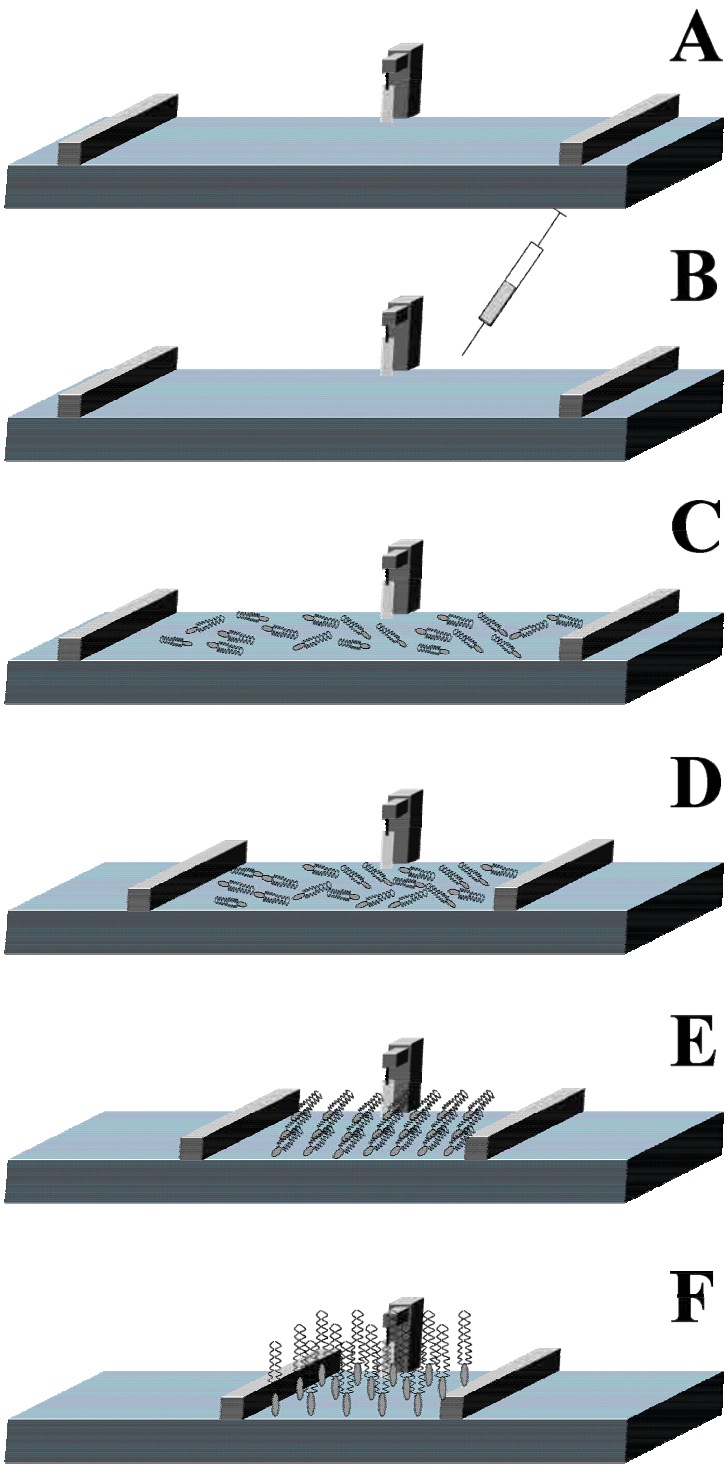

Figure 2.1. Langmuir film formation scheme. Experimental through (A). Amphiphile addition (B). After solvent evaporation and compression, the different film phase stages are presented (C-F).

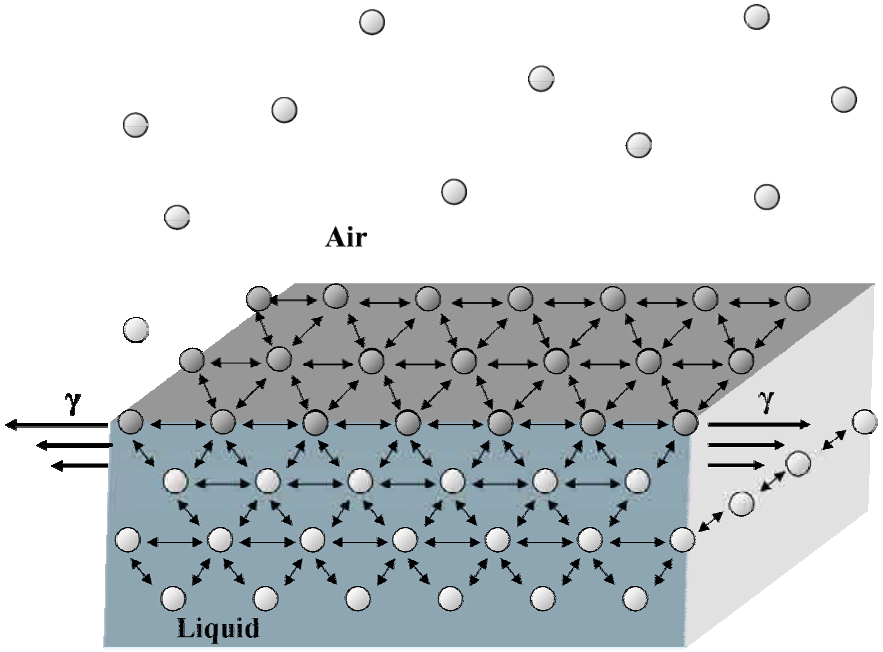

Figure 2.2. Surface tension scheme at the air|water interface.

The Wilhelmy plate method quantifies the absolute force exerted on a platinum sheet or a chromatography filter paper plate partially immersed in the subphase (Figure 2.3). The surface tension is measured in the pure subphase before the amphiphile is added and after this addition. The difference between both surface tensions is then converted to surface pressure.

Expression 2.4 correlates the F_0 (net downward force) with the surface tension of the subphase, being L the plate length, w the width and t the thickness. ρ_p is the material density and h is the height of the plate immersed in a liquid of density ρ_L, g the gravitational constant, θ_0 the contact angle of the liquid with the solid plate [6].

$$F_0 = \rho_p gLwt + 2\gamma_0(t+w)\cos\theta_0 - \rho_L gtwh \qquad \text{Expression 2.4}$$

Similar equation (Expression 2.5) is obtained for the monolayer when it has been spread on the subphase, being θ_m the contact angle of the liquid covered by the monolayer on the solid plate and F_m the force exerted on the plate.

$$F_m = \rho_p gLwt + 2\gamma_1(t+w)\cos\theta_m - \rho_L gtwh \qquad \text{Expression 2.5}$$

The Wilhelmy plate measures the change of the force exerted in the presence of the monolayer maintaining h constant, following the Expression 2.6.

$$\Delta F = F_m - F_0 = 2(t + w)(\gamma_1 \cos\theta_m - \gamma_0 \cos\theta_0) \qquad \text{Expression 2.6}$$

As we can affirm that t<<w and considering the plate completely wetted, then, the contact angle becomes zero, the change in force can be expressed as in Expression 2.7. The perfect wetting is only achieved when the plate is freshly cleaned prior to being immersed. This is the principal limitation of the Wilhelmy method.

$$\Delta F = 2w(\gamma_1 - \gamma_0) = 2w\Delta\gamma \qquad \text{Expression 2.7}$$

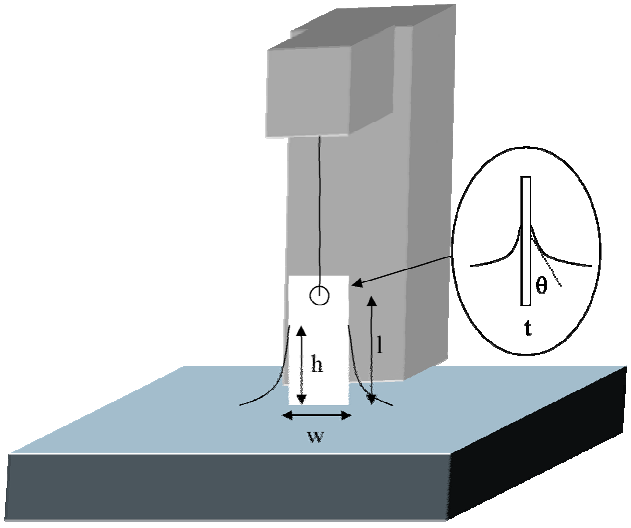

Figure 2.3. Surface pressure measurement scheme using the Wilhelmy Balance.

Introducing the surface pressure concept, the Expression 2.7 can be also expressed as follows:

$$\pi = -\Delta\gamma = -\frac{\Delta F}{2w} \qquad \text{Expression 2.8}$$

2.1.1.4 Surface Pressure – Area Isotherms

The surface pressure (π)-Area (A) isotherm is the plot of the surface pressure change as a function of the area available for each molecule on the subphase surface at constant temperature (Figure 2.4). This π-A isotherm represents a fingerprint of the monolayer in the subphase conditions used.

The π-A isotherm quantify the surface pressure while the barriers are continuously compressing, so changing the total covered area. When compressing, the hydrophilic and hydrophobic parts of the molecule drives the whole molecule orientation. In this process, the number of molecules in the subphase surface is maintained and the area is reduced (closing barriers), then the area per molecule is reduced. The forces that origin the different physical state (phases) are the interaction forces between the molecules of the film and between the film and the subphase. The interactions between molecules of the film depend on the van de Waals forces between the hydrocarbon chains and the forces between the headgroups, whereas the interactions between the film molecules and the subphase depend on the attraction-repulsion forces between them.

The first appearing phase is gas phase (G) and appears at low concentration of amphiphiles per unit area, causing a very low surface pressure ($\pi < 0.5$ $mN \cdot m^{-1}$). Increasing the compression, three phases can be observed (not all always present), liquid expanded (LE), liquid condensed (LC) and solid (S). These phases correspond to different molecular organization in which the molecules have different degrees of freedom.

The phase change can be identified in the π-A isotherm as discontinuities of the isotherm whereas the plateaus are associated with enthalpy changes in the monolayer [6]. The initial phase (G) is characterized by large distance between molecules, so the intermolecular forces are small and have no lateral adhesion. So that, having little effect on the free energy of the aqueous subphase. As the gaseous phase is compressed, the hydrocarbon chains start to lift away from the air|water interface (Lift-off point) due to the weakness of interactions between the tailgroups and the subphase.

LE appears when reducing the surface area of the monolayer. The molecules in this phase are characterized by having their polar groups in contact with the subphase and the

hydrocarbon chains randomly oriented and presenting gauche conformations. The area per molecule obtained in this phase has no relation with any of the dimensions of the constituent molecules.

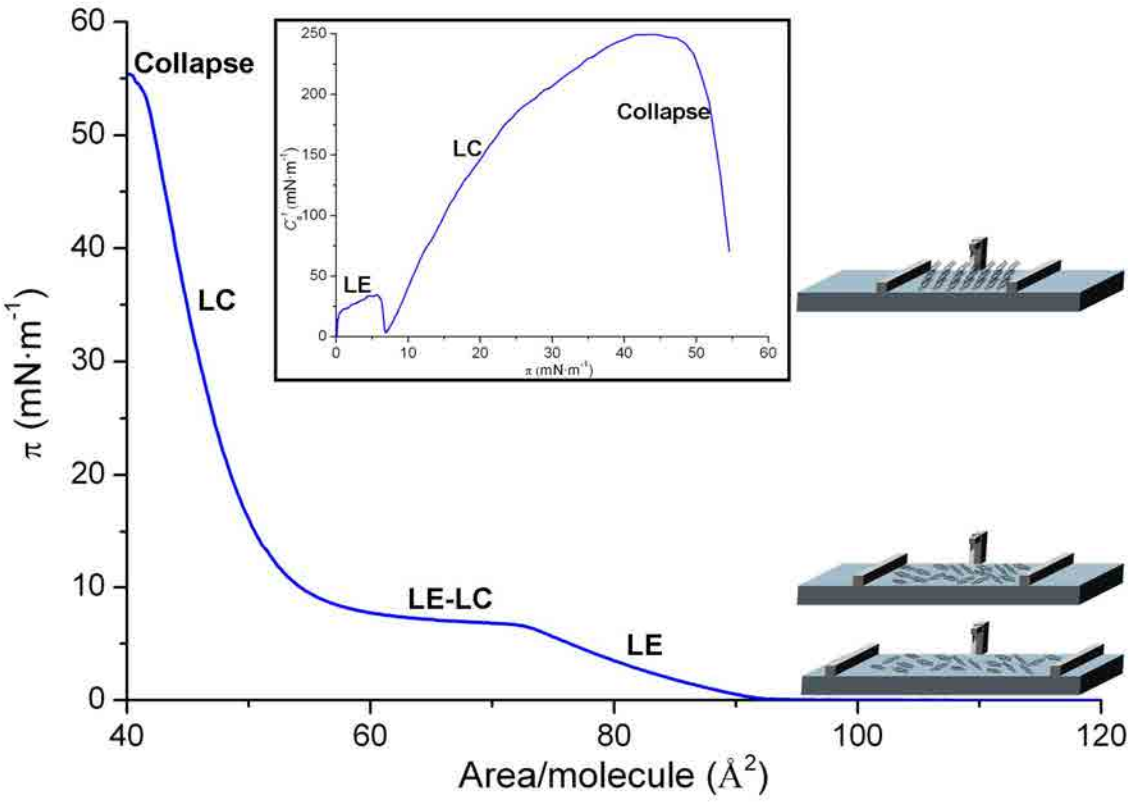

Figure 2.4. Model π -A isotherm with its corresponding representation of the inverse of the compressibility modulus (C_s^{-1}) vs. the surface pressure (Inset). Both representations present the physical state at each zone of the isotherm or the C_s^{-1} curve. In addition, the scheme of the molecules orientation at each physical state is presented.

Further compression implies the emergence of condensed domains in the expanded phase forming a second and more extended plateau in the π-A isotherm. Condensed phases include LC and S and can appear one or both. The monolayer in a condensed phase has a strong molecule cohesion, which produces a close packing presenting all the hydrocarbon chain uniformly oriented. The various states of the condensed phases are caused by the different interactions and arrangements between hydrophobic and hydrophilic parts of the molecule. The area per molecule in a condensed phase is close to the molecular cross-section area.

In further compressing of the condensed phases, the molecules are forced out of the interfacial film and the monolayer collapses. The collapse situation can produce several effects on the interface film; being the formation of disordered multilayers over the interface film the most common. Other possible effects are the formation of micelles if the amphiphile posses a strong polar head group relatively to the non-polar part of the molecule. On the other hand, if the polarity of the headgroup of the molecule is not strong compared with the hydrophobic part, the molecules can form vesicles. This last situation applies mainly to long-chain molecules that possess two hydrocarbon chains for each polar headgroup.

The collapse region appearance is defined by the equilibrium spreading pressure which corresponds to the equilibrium pressure between the monolayer (2D state) and the solid (3D state). Over the equilibrium spreading pressure, the monolayer has the tendency to aggregate into crystals by nucleation and crystalline growth processes [8].

The phase behaviour of the monolayer is mainly determined by the physical and chemical properties of the amphiphilic molecule. On the other hand, the isotherm shape of a compound depends on the temperature, the subphase composition and pH, so at given conditions, a determined phase of the film can not be observed. This is the case of reducing the temperature in a given lipid monolayer, so the intermolecular (chain to chain) interactions increase producing an extension of the LC phase reducing the LE-LC transition, being in some cases no visible the LE-LC transition. The LE-LC transition also varies within a compound family. When having compounds with the same polar head but having different hydrocarbon chain length or different number of unsaturations, the increase of the hydrocarbon chain length or the reduction of the number of unsaturations, increases the chain to chain interactions occurring an extension of the LC phase and a consequent reduction of the LE-LC transition. When comparing same number of unsaturations, the cis form provokes larger area per molecule than the trans form producing the latter a LE-LC transition reduction. One particular case of a phase absence in the isotherm occurs when working with molecules with a very long hydrocarbon chain in which the van der Waals forces are so strong that may not exist the LE phase. A temperature increase facilitates the observation of the LE phase although the plateau’s

length of the isotherm is considerably reduced. Another factor to obtain more condensed phases is favouring complexes of metal ions with the acid headgroup of the fatty acids.

The monolayer is always in a metastable state rather than in an absolutely stable equilibrium state, so the monolayer integrity can be lost. There are several factors that can enhance the monolayer integrity. The most important is the pH and the presence of multivalent ions in the aqueous subphase. In a general view, divalent metal ions interact with the acid headgroup of fatty acids depending on their electronegativity. At high electronegativity they interact covalently, whereas at low electronegativity they interact electrostatically being this behaviour a contribution for the alkyl chains packing [11].

Besides the temperature and the subphase conditions, the experimental part for recording a π-A isotherm must be performed with a extreme cleanness and a precise control of several variables. These requirements are important due to the phase changes and especially the collapse region depend on the compression rate and the ageing time of the monolayer so a precise control of both variables is indispensable for a good reproducibility.

2.1.1.5 Langmuir π-A isotherms experimental information

The thermodynamic analysis of the Langmuir π-A isotherms offers a wide range of possibilities to study the film behaviour. Probably, the most used because of its high relevance for identification of states and phase transitions in the monolayers [12,13] is the inverse of the compressibility modulus. Others studies that can be performed investigate the ideality of a two-component mixture and the interaction forces between them. Finally, the phase rule can be applied to reveal the number of phases present at a given surface pressure.

Inverse of the compressibility modulus

The parameter used for phase identification is the inverse of the compressibility modulus, which is defined by Expression 2.9 where A is the mean area per molecule ($Å^2 \cdot molecule^{-1}$), π the surface pressure ($mN \cdot m^{-1}$) and T is the absolute temperature.

$$C_s^{-1} = -A\left(\frac{d\pi}{dA}\right)_T \qquad \text{Expression 2.9}$$

As it has been stated by previous authors [13], an inverse of the compressibility modulus between 0 to 12.5 $mN \cdot m^{-1}$ indicates that this π-A isotherm zone corresponds to gas phase. LE phase is accorded to be present between 12.5 to 50 $mN \cdot m^{-1}$, a LE-LC coexistance zone between 50 to 100 $mN \cdot m^{-1}$ and LC between 100 to 250 $mN \cdot m^{-1}$. Above 250 $mN \cdot m^{-1}$ is widely assumed to be in solid phase. In accordance to that, plotting the inverse of the compressibility modulus, the inflexion points (kink points) can be identified. The kink points can be caused by two film internal processes of the film: phase change or component separation in case of a mixed film.

The inset of Figure 2.4 presents the LE state at very low surface pressure and presents an inflexion point that indicates the beginning of the phase change from LE to LC. In the example case, although the curve achieves C_s^{-1} values close to 250 $mN \cdot m^{-1}$, solid phase is not observed. Further compression of the LC state implies the collapse of the monolayer.

Mixture ideality and interactions between its components

The representation of the mean area per molecule versus the molar fraction at a selected pressure gives valuable information about the ideality of the mixture at this surface pressure. The area per molecule of both pure components are connected, and it is set as the ideal mixture limit line, so that, any deviation from the ideal line indicates miscibility although non-ideality [14] (Figure 2.5). Negative deviations of the mean area per molecule of the mixtures (red line) referred to the ideal mixture line (dashed line) means that the balance between attractive and repulsive interactions between the monolayer components molecules is shifted to the monolayer components molecules attraction, at these composition and pressure conditions. Opposite behaviour is observed in the case of positive deviations (Blue line referred to dashed line), in which the attraction between molecules of the same component are larger than the interaction between molecules of different components [15,16].

The ideality of a mixture can also be studied through the free energy of mixing (ΔG_{mix}). In the case of a mixed monolayer of two components, ΔG_{mix} can be expressed as [16-18]:

$$\Delta G_{mix} = \Delta G_{id} + G^E \qquad \text{Expression 2.10}$$

$$\Delta G_{id} = RT(X_1 \ln X_1 + X_2 \ln X_2) \qquad \text{Expression 2.11}$$

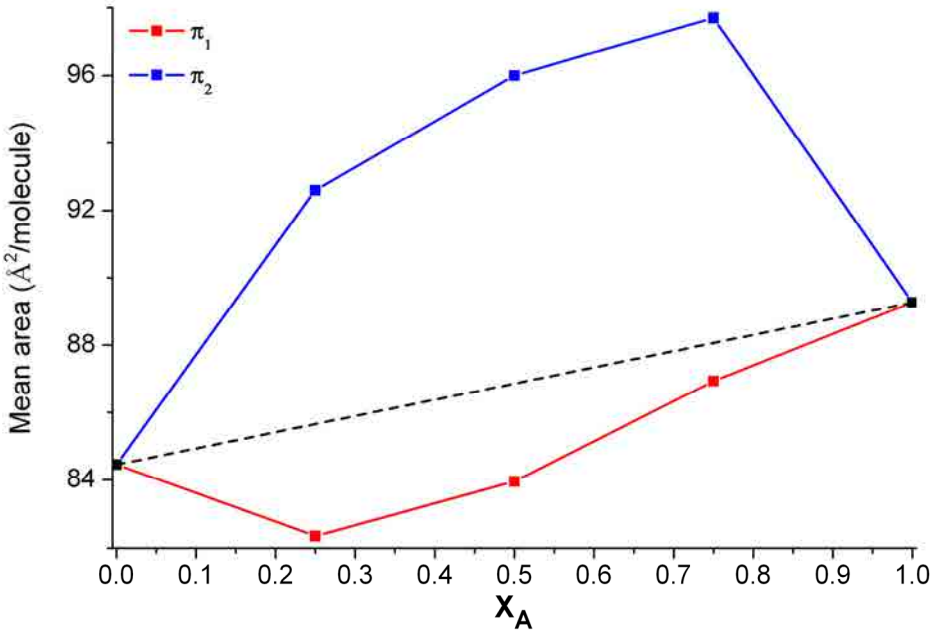

Figure 2.5. Plot of the Mean area per molecule vs. the molar fraction representation for a mixture of components A and B. Dashed line represents the ideal behaviour for the selected surface pressure.

ΔG_{id} is the ideal free energy of mixing, which can be evaluated from Expression 2.11, being R the gas constant and T the absolute temperature, and G^E the excess free energy of mixing. G^E is a representation of the free energy deviation of a real mixed system from an ideal mixed one. The G^E at a specific surface pressure can be calculated from the π-A isotherm data through Expressions 2.12 and 2.13 for a system of two components, being N_A the Avogadro's number and A^E the excess area, A_{12} the mean area per molecule for the mixture and, A_1 and A_2 the area per molecule for the individual components.

$$A^E = A_{12} - (x_1 A_1 + x_2 A_2) \qquad \text{Expression 2.12}$$

$$G^E = N_A \int_0^{\pi} A^E d\pi \qquad \text{Expression 2.13}$$

The illustration of G^E vs. one component molar fraction gives information about the interactions between components. The case of positive G^E values (Figure 2.6) indicates that

interactions between both components are not favoured compared with an ideal mixture suggesting that at least one component could form aggregates or enriched domains [16,19]. Therefore, negative G^E values indicate attractive intermolecular interaction between different components molecules. The presence of a minimum value at a given composition and surface pressure can be a sign of two different processes: First, at these conditions, the mixture presents the largest thermodynamic stability in comparison with the pure components. Second, it indicates the formation of a complex between molecules of different species.

The representation of ΔG_{mix} vs. one component molar fraction gives also information about the mixing behaviour. ΔG_{mix} negative values (Figure 2.7) indicate that the mixed monolayers are more stable compared with non-mixed because of the entropic contribution. On the other hand, ΔG_{mix} positive values indicate phase separation in the mixture. G^E and ΔG_{mix} give different information, ΔG_{mix} indicates whether the components are mixed or not and G^E gives idea about the favouring interactions between components.

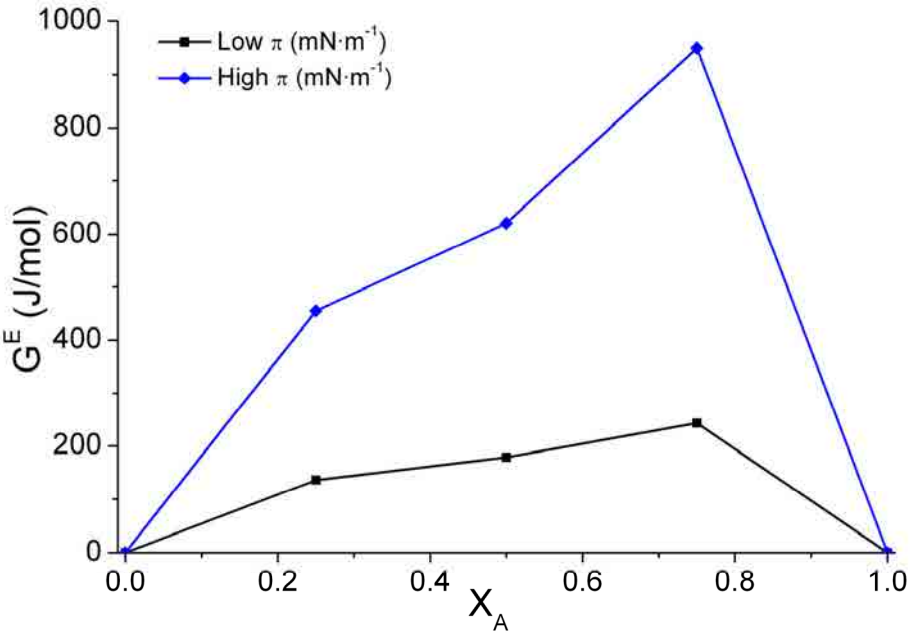

Figure 2.6. Plot of the excess energy vs. the molar fraction for a mixture of components A and B.

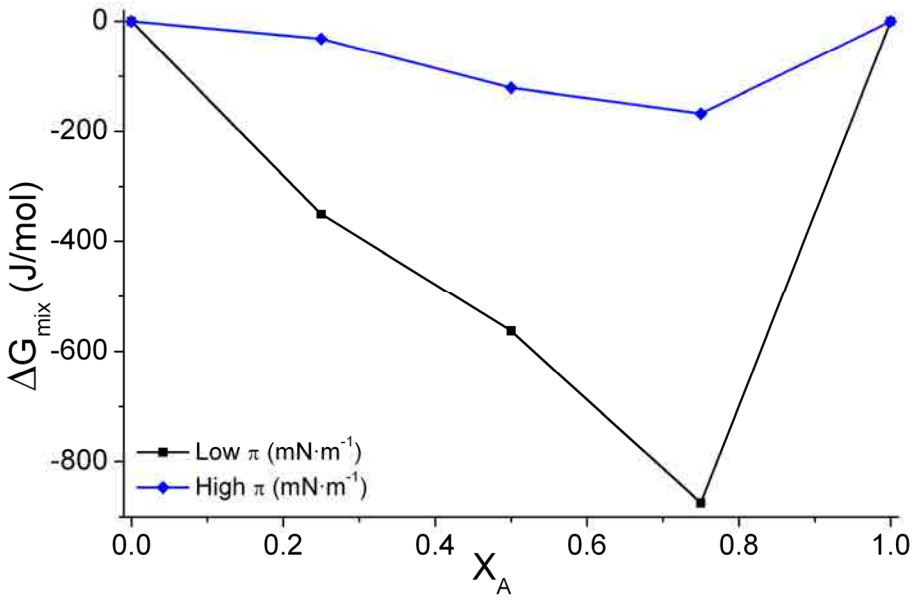

Figure 2.7. Plot of the mixing energy vs. the molar fraction of components A and B.

Phase rule applied at Langmuir films

The thermodynamic study allows also to apply the phase rule to a selected zone of the π-A isotherm. It is commonly used in phase changes or just prior the collapse region. In the case of a two completely immiscible component mixture, it is frequent that one of the components collapse at lower surface pressures than the other. The presence of similar collapse pressures for the mixture and one of the components usually indicates that the component that collapses at a lower surface pressure has been expulsed and this fact can be confirmed with the phase rule.

Maintaining temperature and external pressure constant, the number of degrees of freedom F of the monolayer system is given by the Expression 2.14 [15]:

$$F = C_B + C_S - P_B - P_S + 1 \qquad \text{Expression 2.14}$$

Where C_B is the number of components in the bulk, C_S is the number of components confined to the surface, P_B is the number of bulk phases, and P_S is the number of monolayer phases in equilibrium with each other. In a π-A isotherm case, at the air|water interface, C_B = 2 (air and water), C_S = 2 (Component A and B), and P_B = 2 (gas and liquid), thus $F=3-P_S$. According to that, homogenous mixed films achieve the collapse equilibrium with P_S = 2

(condensed and collapsed state) so the system will have one degree of freedom. In the case of one of the pure components and the mixture have very similar collapse pressure (Figure 2.8), this indicates zero degrees of freedom, which is according with $P_S = 3$. So that, at the collapse (Zone 1 in Figure 2.8) coexist component A condensed, component B condensed and collapse of component B. One clear example of this application is presented in Section 5.7.1.

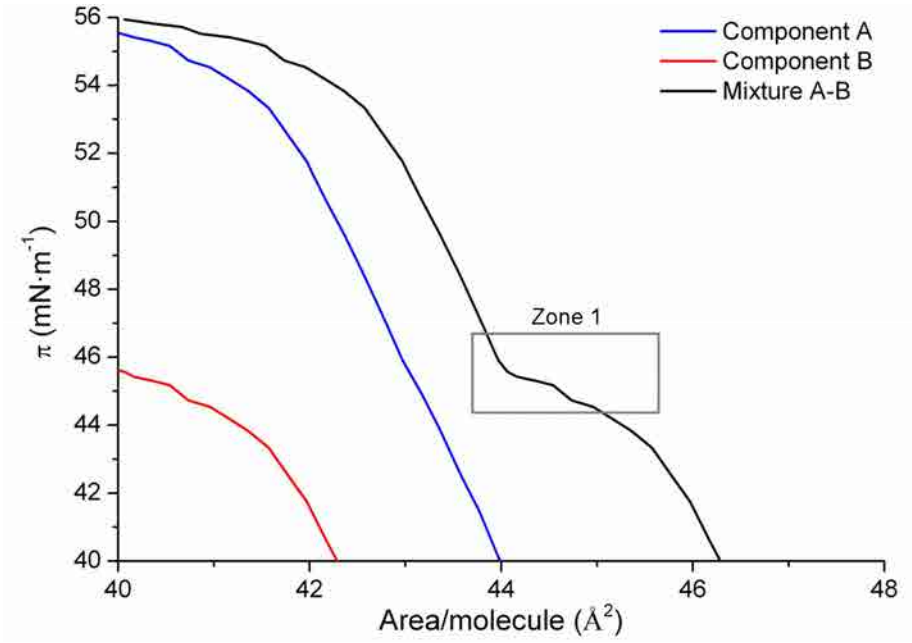

Figure 2.8. Collapse region of the isotherms of an A-B mixture and its pure components.

2.1.1.6 Langmuir-Blodgett Technique

The Langmuir-Blodgett technique (LB) was introduced by Irving Langmuir and Katharine Blodgett in 1934 and it consists on transferring a part of the interfacial film (monolayer) like a carpet onto a solid plate (substrate) at a selected surface pressure. The relaxation time is the time waited since the target surface pressure is reached till the monolayer is stable after the compression. The stability of the monolayer can be checked observing no variations in the area or surface pressure during a period of time.

The monolayer can be transferred as the substrate is lowered (immersion, or downstroke) or raised (emersion, or upstroke) through the interfacial film. Emersion (Figure 2.9A) is usually used for hydrophilic substrates and consist on that the substrate is immersed into the subphase before the amphiphile addition. The deposition of the first monolayer converts the substrate surface in hydrophobic, so the next monolayer will be deposited by an immersion process (Figure 2.9B). Conversely, a hydrophobic substrate becomes hydrophilic after the first monolayer deposition, so the second monolayer must be transferred by emersion. When building up multilayers the current hydrophilic character of the substrate surface after each monolayer deposition must be considered.

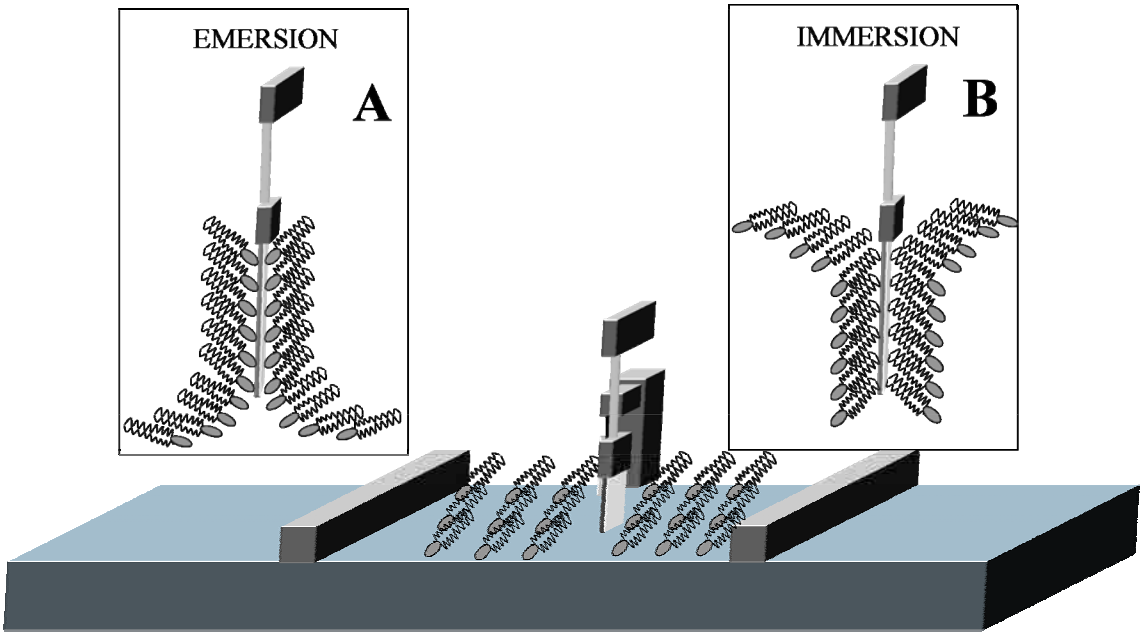

Figure 2.9. Langmuir-Blodgett film deposition.

Pure Types of building up multilayers using the LB technique

There are several types of building up multilayers (Figure 2.10), which depends on the amphiphilic balance of the molecules, the hydrophilic character of the substrate and the dipping conditions. These dipping conditions include the surface pressure, deposition speed, pH, temperature and composition of the subphase [7]. Sometimes a non-unique type is produced. The most used type (Y-type) consists on the deposition by immersion-emersion sequence or vice-versa. The Y-type is the most similar to the natural cell membranes. X-type deposition occurs when the monolayer have been only transferred by immersion and Z-type only by emersion. Z-type occurs commonly when performing multilayers of aromatic molecules with short or no hydrocarbon chains that do not form true monolayers at the air|water interface. A XY-type refers to the monolayer formed only by immersion but part of the monolayer is also transferred when raising the substrate out of the subphase.

In a Y-Type LB film, the X-ray d spacing represents the distance between the polar planes, which means the thickness of two molecular layers. A X-ray d spacing less than twice the molecular length may indicate some tilting or interdigitation, or both.

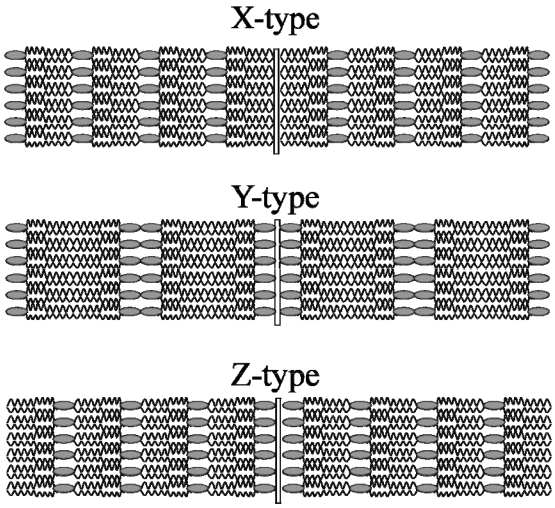

Figure 2.10. Pure types of building up multilayers using LB technique.

There are two different deposition modes, the reactive and the non-reactive. In the reactive deposition the molecules adsorbs spontaneously onto the substrate at the same speed as new substrate surface is available during the substrate emersion. These monolayers films quickly drain the subphase and tightly bind to the substrate surface. The dynamic contact

angle formed in emersion by the water meniscus against the solid substrate is around 50˚–60˚ [20]. The non-reactive deposition occurs in emersion process when the substrate surface available area is higher than the molecular adsorption so part of the subphase remains at the air/substrate monolayer. In this case, the monolayer is poorly adhered and requires a waiting time for draining the subphase; otherwise this monolayer can be re-spread in the subphase when trying to build up one more layers.

In order to obtain reactive deposition, the transfer rate (speed at which the substrate is immersed or emerged) must be moderated according to the drainage speed, which depends on the crystallised state and the viscoelasticity properties of the monolayer [21]. Surface viscosity must be low enough to do not obtain a rigid and brittle film. Otherwise the meniscus between the substrate and the air|liquid interface is not good, resulting in a bad monolayer transfer.

In natural cell membranes it is often found that the upper lipid layer composition differs from the lower layer. The LB technique allows depositing films containing more than one type of monomolecular layer. This is possible by performing the LB using the compound A molecules by emersion and then, performing a LB using the compound B molecules by immersion. In this way, an alternate multilayer structure ABABAB is prepared. Asymmetric membranes by LB deposition are used for lipid phase-separation and lipid domain formation in mixed bilayers [7, 22, 23].

Asymmetric bilayers formed by zwitterionic phospholipids in the bottom layer and, in the top one, by anionic phospholipids favours the protein incorporation since many of them associate with membranes using interactions with anionic phospholipids. On the other hand, the asymmetric bilayer has lower defects density when the first layer is composed of phosphatidylethanolamine (PE) compared with phosphatidylcholine (PC) due to the different hydration shell [24, 25].

The multilayers formed on solid substrates can commonly be removed by simple wiping with a tissue, but the first monolayer of this multilayer is very hard to remove. This is because the multilayers are kept together thanks to van der Waals forces, whereas the first

layer is attached to the substrate surface through stronger forces which could be a combination of electrostatic, hydrogen bond or chemical bond.

Transfer Ratio

Transfer ratio of a monolayer is the relation between the decrease of the monolayer area S_m and the total substrate area (S_s) available for depositing the LB (Expression. 2.15). S_m is the decrease of the interface monolayer area after the LB deposition maintaining constant the surface pressure. It must be highlighted that S_s includes all the sides of the substrate, the face where we want to deposit the LB and the other substrate faces that are also immersed. Moreover it should be considered that sometimes the substrate faces are not all made of the same material, so having different hydrophilic behaviour and roughness, so that the monolayer affinity will be different for one face than the others. In this situation S_m will be described by Expression 2.16 where f is the total number of substrate faces.

$$TR = \frac{S_m}{S_s} \qquad \text{Expression 2.15}$$

$$S_s = \sum_{1}^{f} S_{sf} \qquad \text{Expression 2.16}$$

A transfer ratio close to one is an indicator of a good deposition and that the molecules orientation on the substrate is very similar to their orientation on the water surface. An ideal Y-type film is a multilayer system with transfer ratio of one for both up and down directions [7]. There is a 20% acceptable tolerance for a good TR acceptance depending on the microscopic heterogeneities of the substrate surface or small molecular orientation changes during the deposition process. More than this tolerance, it is considered an unsatisfactory film deposition.

The obtaining of a good transfer ratio depends basically on the transfer surface pressure and the molecular interaction between the substrate and the layers. The transfer surface pressure implies a determined phase, lateral cohesion, homogeneity and alkyl chains tilting. However, some amphiphiles can change some of these parameters when changing the air|subphase interface to the air|solid interface.

A good control of the transfer rate can also be important to obtain a good transfer ratio. When building up multilayers, the transfer rate can be different for immersion than

emersion, and can also be different for the first monolayer than the subsequent. In the case of emersion, the transfer rate must be controlled according to the dynamic properties of the interface monolayer and the rate at which the subphase drains from the monolayer|solid interface [7]. This monolayer drainage depends on the adhesion of the monolayer onto the solid and the headgroup dehydration.

2.1.1.7 LB films special features

It is usual that LB films are prepared in condensed phases because the monolayer is close-packed with strong lateral cohesion and that permits a good deposition. The optimal pressure for LB formation is the pressure where the solid phase begins. This pressure combines a good lateral cohesion with low density of condensed domain defects. The decrease of surface tension when compressing the monolayer reduces the affinity of the polar group of the amphiphile for the water interface so increasing the importance of the polar group|substrate interactions and, in consequence, favouring the adsorption onto hydrophilic substrate. Despite the optimal pressure, LB of some amphiphiles has been also successfully transferred at the LE phase and also close to the collapse zone, where the monolayer is brittle [15].

The presence of defects in the film is usual and commonly represents an advantage like patterned surfaces or biomimetic membranes. The most frequent defects are disclinations, in-homogeneous crystalline domains, pinholes, local collapses, vacancies, transbilayer and lateral heterogeneities. The major part of the defects appears prior the LB transfer, during the monolayer ageing time or during the change from the air|subphase interface to the air|solid interface. In the last situation, the stronger attractive interaction between the molecules and the hydrophilic substrate may modify the molecular packaging obtaining more condensed phases than at the air|subphase interface [6]. This behaviour also causes some differences between the expected and the experimental formed LB, especially when depositing in the LE phase close to the LE-LC transition. Another difference occurs with given fatty acids, which forms LC islands on the substrate when they are transferred at the LE phase. All these changes in the molecular arrangement may generate defects, which will grow up when building up multilayer structures.

The presence of subnanometer holes in phospholipid LB bilayers is explained by the lipids desorption of the first monolayer when transferring the second one [24]. The incoming phospholipids, thus cover only the hydrophobic surface of the first monolayer, maintain the substrate surface where the holes were. The presence of transbilayer holes are also due to desorption process, which is probably common in any supported bilayer system.
The monolayer is usually deposited preserving the surface variations of the underlying substrate, spanning the voids and other defects in the substrate. In the case of very irregular substrates, it is possible that the LB film can resemble the undulations of it. On the other hand, for surface roughness at the nanometric scale, at the moment of the deposition, the monolayer will bridge over the voids supported by a layer of water. When the water layer is drained or dried, the film will collapse [10].

Generally speaking, the adhesion of the first layer to the underlying substrate determines the quality of subsequent layers and this adhesion depends on the substrate surface, its chemical composition and the interaction forces between the substrate and the lipid. Several pre-treatments can be performed on the substrate to improve the first monolayer quality like lipid precoating, silanization, vacuum metal deposition, etc. This pre-treatment induces changes in the chemical and physical structure of the first monolayer but these changes does not apply to the next built up monolayers [6].

The highlights of this section are that a higher transfer surface pressure results in more uniform and tightly packed phospholipid bilayers with fewer pinhole defects [7], the first deposited monolayer highly determines the quality of the subsequent deposited monolayers. The most hydrophilic the substrate is, the better adsorption is achieved so more layers can be stacked.

Some suggestions can be followed to enhance the quality of the deposited LB. The first is that monolayer compression speed must be low enough to avoid local overcompressions, where solid condensed domain defects can be formed [26]. Moreover, after the LB deposition, some cares must be considered to preserve the integrity of the multilayer structure and to avoid any molecular desorption. Besides maintaining cleanness and a constant temperature, the most important for biological applications is to keep the supported mono- or bilayer always wet using the working solution.

2.1.2 SPB technique by vesicle fusion

2.1.2.1 Vesicles preparation

The exposition of given amphiphilic lipids with high hydrophobic tails to an aqueous environment form closed spherical structures called vesicles or liposomes. They are the most energetically stable form in water hiding the hydrophobic tail from the water contact forming a hydrophobic region and exposing their hydrophilic head to the aqueous solution, so obtaining a hydrophilic environment at both sides of the vesicle and a hydrophobic part between layers. The first study with vesicles was performed by Bangham [27] who concluded that ions cross these vesicles in a similar manner that it is observed in biological membranes. Therefore, it was the beginning of using vesicles as biomimetic membranes.

One of the most important features of vesicles is lamellarity, which indicates the number of bilayers contained within a single vesicle. It can be distinguished two different lamellar organizations. A unilamellar vesicle (sphere of one bilayer) is the less stable, but is the most used in biomimetic membranes. The second organization is multilamellar vesicles (MLVs) ranging from 0.1 to 10 μm in diameter. Unilamellar can also be divided into three groups, small unilamellar vesicles (SUVs) with less than 100 nm of diameter, large unilamellar vesicles (LUVs) with a diameter ranging between 100 to 500 nm and Giant unilamellar vesicles (GUV) with a diameter larger than 1μm.

The structural properties of the vesicles depend on several factors being the most influents the composition and concentration of the constituent lipids. Moreover, the time of hydration and the ionic strength of the medium affect the liposomal size and fluidity.

The preparation method will lead to the formation of vesicles with a given diameter, although it can be modified with a post-treatment. The general preparation method for multilamellar vesicles of a lipid mixture consist on dissolving each desired lipid in organic solvent (chloroform or chloroform-methanol mixture) in different test tubes, and then, the appropriated quantity of each test tube is mixed in a new one. Then the mixture is dried under a stream of nitrogen to form a uniform film on the walls of the test tube. The dry residue is reconstituted by adding the electrolyte solution. Finally, the reconstituted mixture

is gently agitated for rehydration. It is relevant to consider that long time is required when performing the rehydration step for encapsulating external molecules in lipid vesicles.

The vesicles formation includes the organic solvent evaporation and electrolyte addition. These steps swell the bilayer thanks to the increased water content. Then, the bilayer formed in the flask walls is fragmented into small patches, which have the hydrophobic chains of the edges exposed to water. Beyond a critical radius these patches close and form vesicles.

Post-treatments can be applied to obtain the desired vesicle size. The most used methods are sonication during the rehydration step, so obtaining SUVs, and vesicle extrusion through polycarbonate filters of known pore size after the rehydration step. Other procedures can be used like freeze – thawing, ethanol injection and detergent adding method, but all of them have, in general, more disadvantages than the sonication or extrusion method, and they are basically used for a specific objective.

2.1.2.2 Vesicle fusion method for SPB formation

The vesicle fusion method for SPB preparation is the most used method for bilayer formation, and it consists on placing a drop of the reconstituted vesicle solution on the substrate surface and then, incubates it at temperature above the phase transition temperature (T_m) from the gel phase to liquid crystalline phase (L_α) of the lipid, in order to maintain the lipid membrane fluidity. The process implies the interaction vesicle-substrate (adsorption), the vesicles aperture (rupture) forming SPB patches and finally the spreading and fusion of these patches to form microscopically large zones of SPB. The SPB formation traps a water layer of 10-20 Å that separates the substrate and the SPB and permits it to maintain its fluidity.

The last step in SPB formation is the washing process, it consist on rinsing the SPB, which may content unopened vesicle, using water or electrolyte solution. Depending on this choice it may be caused an osmotic pressure change in the surface adhered vesicles, which added to the mechanical stress exerted, help the multilysis of the vesicles [30].

The vesicle fusion mechanism is presented in Figure 2.11. Vesicles arrive to the working substrate surface, adsorb, flatten and open forming a high density phase patch. The destabilization of this high density phase and the amphiphilic nature of lipids lead the lipid propagation over the surface forming a low-density phase [28]. Bilayers usually have zero spontaneous curvature, so Gibbs energy is requested for bending them, in consequence, the SPB propagation on a nanometric rough substrate surface implies the bending of the bilayer around contoured regions without increasing the membrane's distance from the surface [29].

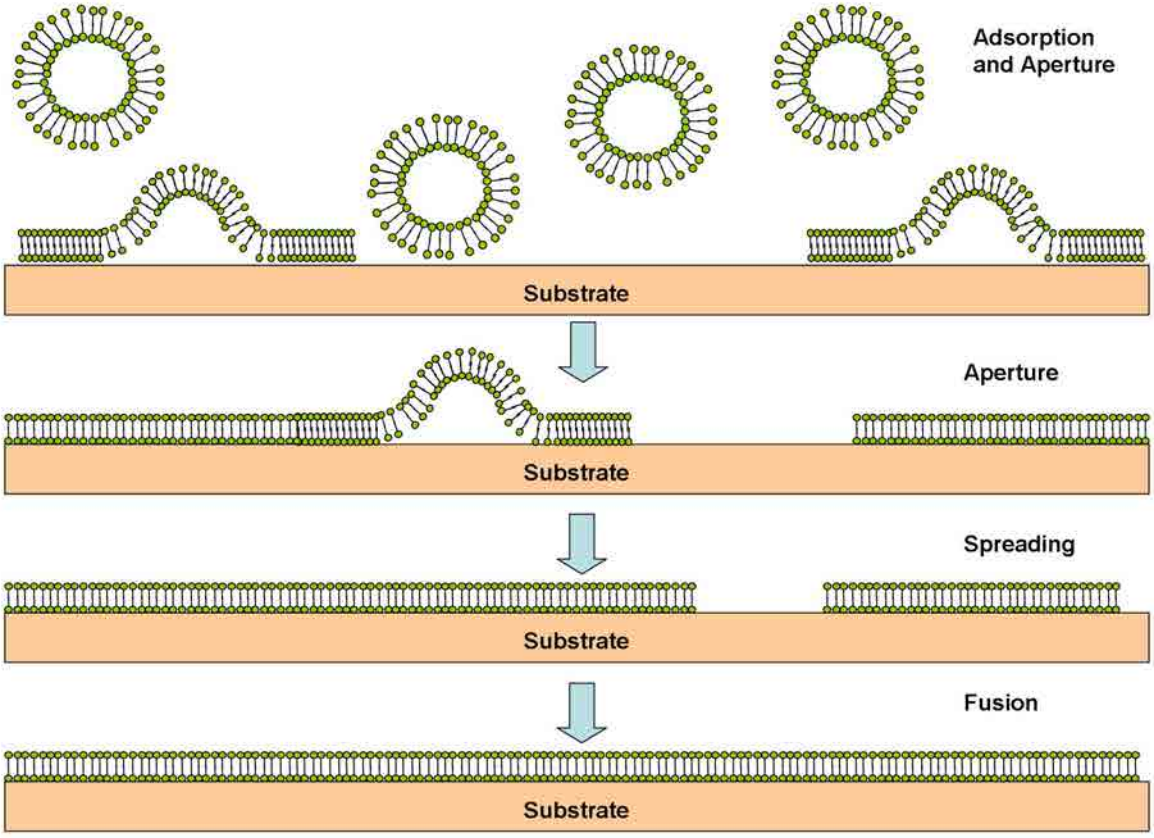

Figure 2.11. SPB formation scheme.

The flattening is not always observed. The driving force for this step depends on the nature of the substrate surface. In fact, the rate of the vesicle adsorption and flattening step is a good indicator of the lipid-substrate affinity [30].

The reduction of the free energy of the alkylchain/water leads the fusion and spreading on hydrophilic substrates [31]. In the case of hydrophobic substrates, the driving forces are weaker, so the mechanism involves adhesion, rupture and lateral fusion [32]. The addition

of certain molecules to the lipid vesicles maintains the mechanism but may slow down one of the steps favouring the vesicle deposition. The balance between the hydrophobic energy of the disk edge and the bending energy leads the vesicles aperture or the remaining in flat disk shape. The height of these disks is double to that of the SPB so it can be easily recognized in AFM images. Vesicles may aggregate and return to the equilibrium lamellar phase in excess of solvent. It has been observed that the minimum radius for bilayer retransforming in vesicles is 3-5 times the bilayer thickness [33].

Seifert and Lipowsky [34] proposed that the bilayer is comparable with a 2D sheet embedded in a 3D space and the adsorption, rupture and spreading depends on the balance between the gain in adhesion energy and the vesicles curvature energy. However, recent studies propose that more factors are involved in the SPB formation like the distribution of different lipids in a multispecie vesicle and the interaction between vesicles. This interaction is called critical vesicular coverage (CVC) and it refers to the minimum adsorbed vesicles quantity required for vesicle aperture thanks to the interaction between neighbouring vesicles [35].

The aperture of vesicles implies that the patches expose an edge to the solution. These edges, are thermodynamically unstable so the spreading and fusion with other patches is favoured to decrease the edge length exposed to the solution [36,37]. After the SPB is formed, it must be always kept wet and warm to maintain its characteristics. However, some researchers have developed several techniques to prepare air-stable lipid SPB [38] but they have some disadvantages, especially in fluidity.

External influences to the SPB formation

There is a large list of factors affecting the adsorption and fusion of SUV to form SPB. It can be classified into three groups. The first refers to the vesicle composition, size, lipid charge, preparation method and osmotic pressure, the second refers to the buffer solution composition, temperature, pH and ionic strength, and the third group refers to the substrate that it is important its charge, roughness and cleanliness [39-42]. This third group is explained in Section 2.2 due to the similar effect on the several techniques proposed for biomimetic membranes forming.

The vesicle size is an important factor due to it influences the kinetics of vesicle aperture and fusion, being slower the vesicle fusion rate as smaller the vesicle are. This is the rate-limiting step due to small vesicles are stable in vesicle form on the substrate [43], according to the Raviakine and Brisson observations [41] that vesicle fuse when their radius is larger than the critical radius. Once opened, curved membrane areas are more hydrophobic and they have a higher surface energy than the less curved zones, so curved areas are more prone to membrane fusion [44]. In the case of large or giant vesicles, each lipid molecule experiences a flat curvature similar to that observed in the planar lamellar phase [33], so the deposition is favoured.

Temperature is an important influence in vesicle fusion due to the vesicle aperture is enhanced when increasing the temperature of the system, especially when working above the melting temperature (T_m) [39,45]. On the other hand, after the SPB has been formed, a reduction of the temperature has non-desired effects like shrink and cracking depending on the lipid phase [46-48].

At low pH and high ionic strength, negatively charged vesicles adsorb and fuse rapidly on nanometric roughness glass due to the favourable van der Waals forces [29]. Increasing the pH or reducing the ionic strength, provokes electrostatic repulsions between the surface and the vesicles, which may overwhelms the van der Waals attraction. Once the SPB has been adhered, it is difficult to reverse the process using variations of pH or ionic strength [29]. On the other hand, the creeping rate of the SPB on the substrate surface, which in natural mimicking conditions is $\approx$ 15 $\mu m \cdot min^{-1}$ [29], or the holes healing rate can be tunned modifying the pH and ionic strength conditions. On the other hand, the adsorption process can be enhanced adding divalent cations (Ca^{2+}, Mg^{2+}) or adding fusigenic agents (i.e. polyethylene glycol) but its effects on the system must be previously considered.

On smooth surfaces, the spreading of the bilayer takes place at low pH, regardless of the ionic strength and the membrane charge. The driving force is the van der Waals attraction explained for the vesicle fusion. At high pH, spreading is inhibited regardless of the ionic strength and the membrane charge, probably, due to the changes of the surface hydration under high basic conditions [29].

Partial bilayer asymmetry can be obtained adding Ca^{2+} [47,49] or using chemical methods like pH changes or osmotic pressure alterations, which acts preferently on the outer layer [50]. On the other hand, the modification of the substrate charge can also favour the spreading [51].

2.1.3 Differences between the biomimetic membranes formed using each method

The method used for biomimetic membrane deposition influences several features of the resulting membrane. Probably, the most relevant is the thickness since to the bilayer formed using the LB-LS method is thicker than the same bilayer formed using vesicle fusion method [52,53], which is explained by the differences in the tilt angle (Figure 2.12).

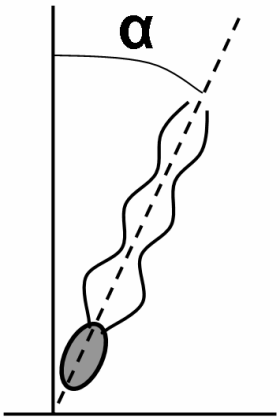

Figure 2.12. Scheme of the lipid tilt angle (α)

The Expression 2.17 relates the tilt angle (α) and the thickness (d) of a bilayer, considering that the bilayer thickness is ≈ 5.4 nm when the tilt angle is 0º.

$$\cos\alpha = \frac{d}{5.4} \qquad \text{Expression 2.17}$$

The tilt angle obtained for vesicle fusion SPB is close to 54,4º which is the tilt angle for randomly oriented chains [54,55]. In the case of SPB formed by LB-LS method, the angle is ≈ 32º for lamellar gel phase and ≈ 20º for the lamellar crystalline state, which indicates that LB-LS method produces a higher ordered bilayer and a more precise control of the film structure [43]. The tilt angle can be modified in conductive substrates changing the electrode potential. In the case of SPB formed using vesicle fusion technique, the tilt angle is more dependent of the potential than for SPBs formed using LB-LS technique [5].

The tilt angle of each leaflet of a SPB can be obtained separately using isotopically labelled phospholipids, and the results for DMPC indicate that in the adsorbed state on gold, the top layer is ≈ 35º whereas the bottom layer is ≈ 25º indicating that the different environment of each leaflet (aqueous solution vs. substrate surface) leads to a different tilting angle [56]. The top leaflet has a tilting angle similar to that of the monolayer at the air|solution interface thanks to the low interaction with lower leaflet, whereas the lower leaflet has a different tilting angle due to the stronger interactions with the substrate [117]. Therefore, the application of potential in the adsorbed state induces more tilting change in the top leaflet [55]. In the detached state, after potential application, the lipid sawtooth fashion induces changes in the compactness of the upper layer, so reducing the tilt angle [118].

It is worth to explain the differences between the techniques used to measure the thickness. The diffraction method involves an interpretation of the electron density or electron scattering length density profiles, whereas AFM may involve an error due to the substrate roughness or the absence of layer defects. The use of force curves involves an error caused by the tip-sample interactions that leads to smaller thicknesses compared with other techniques [54].

SPB formed by vesicle fusion should have a similar shape capacitance curve than the LB-LS if the vesicles have been correctly opened and fused. Otherwise, the dissimilar shape of the capacitance curves indicates that vesicles may be adhered but not fused on the substrate surface [43].

The thermotropic behaviour of the bilayer of unilamellar vesicles in solution and the same composition bilayer formed on a gold substrate using LB-LS is similar indicating similar characteristics of both bilayers [55]. On the other hand, it could be thought that in phospholipid bilayers formed by vesicle fusion, the leaflet in direct contact (bottom leaflet) with the solid surface should have similar thermotropic behaviour than the same phospholipid monolayer prepared using LB on the same substrate and the same aqueous conditions. In addition to the explained differences in order and tilting, the differences in the surrounding medium, being the alkyl chains of the top leaflet in the former case, and aqueous solution in the LB case, induce important changes, especially, in its melting temperature and in its breakthrough force. A clear example is the case of DPPC bilayers,

whose breakthrough force is two hundred-fold the monolayer value [57]. The interactions between water molecules are ten times stronger than the water-alkyl chains, so reducing the stability of the monolayer [58]. In the case of phospholipid bilayers, the van der Waals interactions between the alkyl chains of both leaflets stabilize the bottom leaflet obtaining a higher temperature of phase transition [57].

The monolayer formed using LB can be stabilized thanks to the elimination of the aqueous medium, so obtaining the LB monolayer in air. Air is more hydrophobic than the aqueous solution so the alkyl chains of the LB in air suffers less repulsion, and in consequence, the melting temperature is increased. However, the air-stabilization in LB is lower than the alkyl-stabilization between both leaflets in a SPB [57].

2.1.4 Limitations of biomimetic membranes

There are some differences between the natural cell bilayer and the artificially formed supported bilayers. One of the most relevant is the strong interaction between the first layer and the hydrophilic substrate, which may modify some characteristics of the biomimetic membrane. The most important of them is the fluidity, which is essential for biomembranes natural functions, and it is constrained in supported bilayers. Another limitation is the tethering effect. This phenomenon refers the interaction between the biomolecules that will be associated with the bilayer and the substrate. The tethering becomes a major problem when associating transmembrane proteins than associating peripheral proteins. Some authors have deposited two double bilayers using the LB-LS method to overcome this problem. This method permits the existence of a hydration layer between both bilayers reducing the influence of the substrate so giving more fluidity to the upper bilayer. The upper bilayer is called free bilayer and is floating at 2 to 3 nm above the lower bilayer (Figure 2.13A) [59]. Another solution applied to form free-bilayers is preparing a hybrid (SAM)/bilayer system. In this method, a SAM of octadecyltrichlorosilane (OTS) is prepared on the substrate prior to the desired bilayer LB or SPB deposition. The SAM increases the quality of the transferred bilayer, so obtaining a hydrated and fluid free bilayer at 2 to 3 nm above the existing SAM.

One particular case of biomimetic membrane is referred to the lipid layers formed underwater which can bridge small holes. A bilayer formed in that way is called black lipid membrane (BLM) and it is used for ion transport studies. A BLM is a bilayer formed on a small aperture with a diameter less than 1 mm. The hole is formed on a hydrophobic material wall which separates two compartments that can be filled with different aqueous solutions. Then, BLM are suspended in solution so there are no interferences with the support as happens with SPB and also permits the presence of transmembrane proteins without denaturalizing it. This BLM is more mobile and active than SPB, but its stability and robustness is very low, and it can not be widely characterized. The main application of BLM is the study of ion channels in phospholipids bilayers, so it will not be used in this Ph.D. Thesis.

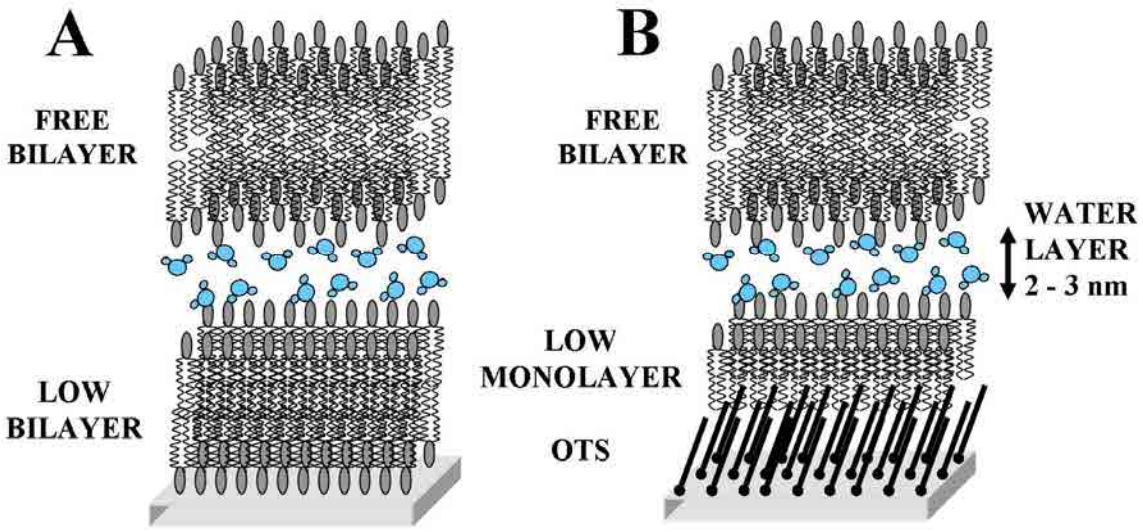

Figure 2.13. Free standing bilayer schemes. A) double bilayer deposition and B) SAM with single bilayer.

2.2 Molecules and substrates used for biomimetic membranes preparation

2.2.1 Amphiphilic molecules in biomimetic membranes

The membrane amphiphilic molecules major present in natural cells have a highly hydrophilic part due to the polar headgroup in glycolipids, or the zwitterionic or anionic headgroup in other lipid families. In most of the cases, the presence in the molecule of two hydrocarbon chains confers a high hydrophobic character to the tail, which balances the strongly hydrophilic character of the headgroup [7].

There is a large range of amphiphilic molecules that are able to form biomimetic membranes being fatty acids, phospholipids and glycolipids the most important for preparing biomimetic membrane. Cholesterol, a type of steroid, is also important because its large presence in cell membranes [7].

The amphiphile affinity for the air|water interface is consequence of the physico-chemical properties of the hydrophilic part (polarity, size, charge and hydration capacity) and the hydrophobic part (alkyl chain length). When the balance between the hydrophobic and the hydrophilic forces is disrupted, the amphiphile could not form a stable monolayer. In the case of the dominant hydrophilic part, like amphiphiles with only an alkyl chain, this chain should be at least of 12 hydrocarbons long. Otherwise, this compound will be partially solved in the subphase and the molecules remaining in the interface will form micelles. On the other hand, if the hydrophobic part is dominant, the amphiphile may crystallize on the subphase surface.

2.2.2 Substrate relevance for preparing biomimetic membranes

The formation of a SPB is strongly affected by the physicochemical properties of the substrate surface. These properties can be summarized in the hydrophilicity of the substrate surface. The interaction between SPB and the substrate surface is a balance between the van der Waals attraction and hydration repulsion [41,60]. This hydration repulsion appears

when the water layer present close to the lipid heads and the water layer on the substrate surface overlap, hindering the adsorption from a thermodynamic or a kinetic point of view. Mica, which is the main model for substrates, has a water contact angle less than 10º [61]. The contact angle for ITO is ≈ 35º [62] whereas for smooth gold is 70º [63] and for the most hydrophobic metal (Hg) is above 100º [64]. The Electro-wetting on dielectric (EWOD) method permits changing the wettability of a dielectric surface by applying voltage across the dielectric layer. This feature permits changing the contact angle of the droplet on the selected surface [65].

Nevertheless, hydrophilicity is a general requirement but not always sufficient for a correct spreading, so the experimental conditions and pre-treatments can help to extend large zones of SPB of a certain lipid in unfavoured conditions. This is the case of low hydrophilic substrates that can be used when enhancing its hydrophilicity or preparing SAMs (See Section 2.14) prior the SPB deposition.

In addition to the correct bilayer spreading, SPB substrates must show other features depending on the applications, for instance, when a conductive substrate is requested. In this line, several attempts of SPBs have been performed on gold, silver, platinum and indium tin oxide (ITO) [59]. Although an atomically surface roughness is the best option, high quality SPB have been prepared in nanometric roughness [72] and the result is that the bilayer resembles the substrate surface topography.

The bilayer formation mechanism is hydrophobic substrates is different than the explained for hydrophilic and negatively substrates [66], which is electrostatically governed. In hydrophobic substrates, a high ionic strength solution produces large planar patches, whereas under distilled water small islands are observed [67]. On hydrophobic substrates, the molecules released by vesicle rupture are self-assembled at the metal surface into well ordered monolayers of flat lying molecules thanks to the acyl chain-metal surface interaction. The accumulation of the molecules at the surface favours the transformation into a bilayer. In consequence, the SPB formation on gold is a time dynamic process in which the monolayer formation is fast but the bilayer transformation is very slow [54,55].

The presence of the lipid layer in a hydrophobic substrate may facilitate the redox activity of a molecule compared with the same substrate without the lipid layer. Some procedures permits to convert a hydrophobic substrate in a hydrophilic one, although the resulting substrates may not behave ideally [68]. In hydrophilic substrates, the presence of SPB slow down the electron transfer achieving, in some cases, two orders of magnitude [69]. On the other hand, the protons requested for the reduction of trapped redox couple are provided from the solution side [51,70], although in some buffer cases, water molecules act as electron donor. The addition of an electron donor (like EDTA) to the solution enhances the electron transfer towards the electrode. Viceversa occurs with an electron acceptor (like $Fe(CN)_6^{3-}$) [69].

Other substrate properties like surface chemistry, charge and morphology affect the deposited bilayer properties such as fluidity, permeability and thermotropic behaviour. Moreover, they can favour the formation of domains and asymmetric molecular distribution across leaflets in mixed lipid bilayers [71]. The substrates selected for forming a high quality SPB with little defect density and high lipid mobility should be hydrophilic, smooth and clean. The most common case is the extension of vesicles with positively charged head lipids spread on negative hydrophilic surfaces like mica.

2.2.2.1 Substrates used in this Ph. D. Thesis

Mica

Muscovite mica is composed by several negatively charged layers that are maintained together by K^+ interlayer cations. Each stratum has two hexagonal layers of SiO_4 crosslinked by the Aluminium atoms with incorporated OH^- groups [30]. The cleavage of mica breaks the electrostatic bond between the K^+ and the oxygen atoms. In aqueous neutral buffered solution mica has a negative charge due to the mismatch between the sublayer of OH^- (complexed to Al^{3+}) and the surface bound K^+ ions. This phenomenon favours the deposition of the zwitterionic lipid headgroups. Mica surface can be modified to achieve a net positive charge using aminopropyltriethoxysilane (APTES) [73]. In mica, oxygen groups are shielded by the potassium ions whereas in oxide surfaces, oxygens are not shielded. The presence of a higher density of available surface oxygens favours the bilayer compactness [74]

The superhydrophillic character of mica, its low surface roughness (≈ 0.08 nm) [74] and its negative surface charge makes mica the model substrate for mono- or bilayer deposition.

ITO

The substrate consisting on a glass slide with an indium tin oxide deposition on its surface is called ITO. Its optical and electrical properties make ITO a perfect candidate for studying artificial photosynthesis and other energy producing devices. ITO has been used for many applications, including solar cells, heat-reflecting mirrors, antireflective coating, gas sensors, flat panel and optoelectronic devices like organic light-emitting diodes [75].

ITO can be studied using several surface analytical techniques that are not applicable to metal substrates. These techniques include surface plasmon resonance (SPR), optical waveguide spectroscopy (OWS) and fluorescence [76].

The conditions and method of indium tin oxide deposition establish the ITO properties specially, resistivity, transmitivity and surface roughness. These parameters are very important for mono- or bilayer deposition and reproducibility on the ITO surface [77,78]. The high ITO roughness influences the multilayer deposition. In the case of lipid mono- or bilayer formation, the ITO roughness is resembled, but in an attenuated way, by the lipid membrane. Some techniques have been used to reduce this influence, the most important is placing a polymer cushion onto ITO prior the layer formation [68,79]. Depending on the initial roughness of ITO, the height of this polymer cushion must be larger to avoid the effect of ITO roughness [79]. The commercial ITO roughness is between 1.4 and 2 nm [80], although different pre-treatments can vary the hydrophilicity and the roughness of the ITO electrodes [81]. ITO has a sheet resistance (Rs) of 25-40 Ω sq^{-1} [78, 81,82]. The electron transfer is more efficient in the ITO polycrystalline state rather than the amorphous [83].

Several methods have been proposed for preparing lipid mono- or multilayers on ITO. One of the most used consists on a drop casting of the lipid solution on ITO, then, after the solvent evaporation, a multilayer is formed [5,84,85]. The main inconvenient of this method is the uncertainty in the number of layers deposited, so the reproducibility is low. To overcome this problem, vesicle fusion technique for bilayers [78] and LB for

monolayers have been used [15,68]. Other methods involves the encapsulation of the lipids in a kind of chamber, and the bilayer formation may be favoured thanks to voltage application [82].

Bare ITO is hydrophilic so it deposits the headgroups in direct contact with the ITO surface. However, Yang and Kleijn [68] hydrophobized ITO and observed that it deposits the tails in direct contact with the ITO surface, as it was expected.

ITO with a solution buffered at pH 7.5 behaves as a polarizable electrode, so no faradaic current is observed in the working potential window -0.8V to 1.2 V [77,79,86]. It has been demonstrated that in acidic medium the irreversible reduction of In_2O_3 to In occurs at potentials close to -0.6V [87] and it occurs at more negative potentials when increasing the pH value [79]. On the other hand, ITO has the point of zero charge in aqueous solution at pH ≈ 3 [68].

The Lipkowski [55] observations for quartz suggest that ITO, like other oxide substrates, has an electrolyte cushion between the lipid mono- or bilayer and the ITO surface. Gritsch et al. [88] proposed that ITO has dissociable surface groups that are in equilibrium with the protons of the electrolyte solution, being the ITO surface with a pH = 7.5 solution negatively charged. The application of negative potential can produce an increase of the surface pH of 4-5 pH units toward the basic state thanks to a change of the proton distribution at the surface, and in consequence, modifying the ITO capacitance.

ITO is a highly degenerated n-type semiconductor with relatively high conductivity which is correlated with the close position between Fermi level and conduction band edge being the band gap ≈ 3.8 eV [89-91]. The n-type doping has two donors, the double charged oxygen vacancies and substitutional four valent tin in the indium sublattice [92]. The nonstoichiometric nature of ITO provokes a high disorder of the material surface so provoking a high density of electronic states and therefore, enhancing the electron transfer rate [83].

The deposition of lipid mono- or bilayer onto the ITO substrate slightly reduces the redox probe peaks intensity and it decreases the reversibility of the system compared with the

bare ITO, being this effect more intense for the bilayers rather than for the monolayers [68]. The observation of this slight reduction indicates that the lipid deposition is not tightly packed, it has surface defects and/or the ITO surface has large uncovered areas [69,93].

2.3 Characterization techniques

In this section, the characterization techniques that have been used in this Ph.D. Thesis will be presented. The first explained is Brewster Angle Microscopy (BAM), which permits studying in situ the Langmuir films. The information provided by this technique is qualitative and permits observing the monolayer state at the time of recording the π-A isotherm. The following explained technique is atomic force microscopy and its related modes. They permit obtaining qualitative and quantitative information of LB and SPB on substrate surfaces, which allows studying the film state and the presence of defects in similar samples than those that it will be studied using cyclic voltammetry.

2.3.1 Brewster Angle Microscopy

The Brewster Angle Microscopy (BAM) is a non-invasive technique emerged in 1991 [94,95] to study the micrometric morphology of Langmuir monolayers in situ. This technique is based on the change of refractive index that occurs at the interface when the monolayer is formed, as it will be explained in the next section. According to optical laws, a p-polarized laser beam that arrives to the air|water interface at the value of the Brewster angle, do not present reflected beam. This condition is not fulfilled when a Langmuir monolayer is formed, and a reflected beam appears (Figure 2.14). The reflected light when the monolayer is present, although it is very small compared with the refractive light, permits recording the present structure at the micrometer scale. BAM can be applied at Langmuir films of a large variety of amphiphilic molecules, obtaining better images when using molecules with larger refractive index compared with the subphase used [96,97].

2.3.1.1 Principles of the BAM microscope

The reflectivity of an interface between two media of different refractive index, being n_0 and n_1 that depends on the polarization α_p of the incident light and the angle of incidence θ. If the refractive index roughly changes from n_0 to n_1 for z = 0 (called Fresnel interface) and the p polarization is considered, the reflectivity becomes zero at the Brewster angle θ_B

according with Expression 2.18 where n_0 is the air refractive index and n_1 is the subphase refractive index.

$$\tan[\theta_B] = \frac{n_1}{n_0} \qquad \text{Expression 2.18}$$

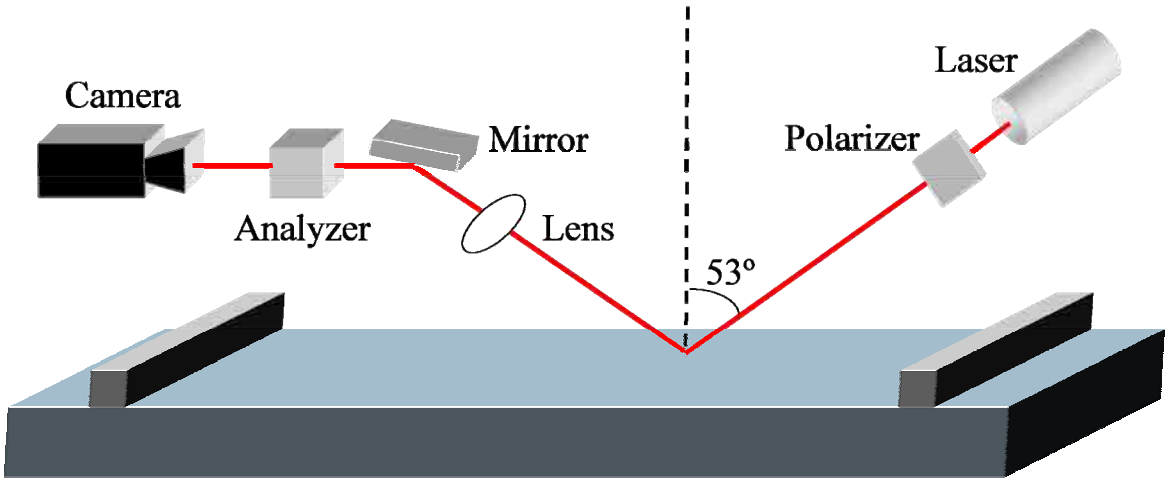

Figure 2.14. Typical BAM microscope scheme.

In real situation, the reflective intensity is largely decreased in the Brewster angle but never becomes zero due to three reasons: the thickness and roughness of the interface and the anisotropy of the monolayer. The thickness induces a new refractive index n_i which is different from the n_0 and n_1 and it depends on the interface thickness. The roughness caused by thermal fluctuations can produce variations in the thickness and, in consequence, in n_i. Finally, the optical film anisotropy may increase the reflected intensity, moving from the theoretical Brewster angle [94]. At the air|water interface case, the Brewster angle is ≈ 53º.

The intensity at each point of a BAM image depends on the local monolayer thickness and its optical properties. The reflected intensity strongly depends on the laser wavelength and power, so the laser characteristics must be chosen according to the samples that will be observed.

2.3.1.2 Main BAM applications

BAM is basically used for imaging the phase transitions in a Langmuir monolayer, where the different coexisting domains can be distinguished. The presence of inner textures within the domains indicates the existence of a high molecular order in the Langmuir film [96]. It

is extensively believed that the light reflected by a Langmuir film of amphiphilic molecules corresponds to the rearrangement of their alkyl chains; although some studies show the importance of the headgroup, especially its hydration shell in the light reflected. When the headgroup hydration is high, the refractive index is closer to that of the pure air|water interface.

2.3.2 AFM and related techniques

Atomic force Microscopy (AFM) forms part of the Scanning Probe Microscopy (SPM) family and it permits obtaining images of the samples' topography and its nanomechanical properties. The variety of samples that can be observed with AFM is wide ranging from solid materials to cells, tissues and other soft materials. Moreover, liquid-AFM permits observing these soft materials in their natural liquid environment, which represent an important difference compared with other characterization techniques.

The AFM technique consists on a thin cantilever with a sharp tip that approaches the sample. The cantilever senses the interaction forces between the tip and the sample. These forces include the van der Waals and electrostatic interactions and the electronic repulsion [98]. At the repulsive region, when the tip stronger interacts with the sample, the cantilever bends upwards during the vertical force (F_v) is being applied. This bending, which depends on the spring constant of the cantilever (k_v), produces a reflection in the laser diode beam, which is collected by a photodiode and transduced into an electric signal, which after processing, is converted into local topographic information (Figure 2.15). The scan of the selected zone provides information of each local point so providing the topographic image of the scanned zone.

AFM cantilevers have a sharp tip, which apex has an initial radius between 5 to 30 nm. Cantilevers can exist with rectangular geometry that is the most used for working in air conditions and, triangular geometry that have a wider back-plated zone for easier laser focussing and are mainly used in liquid environment.

The piezoelectric part permits the scanning movement in the surface plane and it also moves the sample in the Z axis accordingly with the sample topography. A piezoelectric material produces a small electric signal when it is compressed and vice-versa, so that, the

piezoelectric piece is useful for adjusting the tip-sample distance when scanning the topography. The feedback expands or compress accurately the piezoelectric to maintain a constant F_v [99,100].

There are one nanomechanical working mode and two AFM topographic modes, contact and amplitude modulation (AM-AFM), that can be performed with a conventional AFM instrument without supplementary modules, and they will be explained in the following sections.

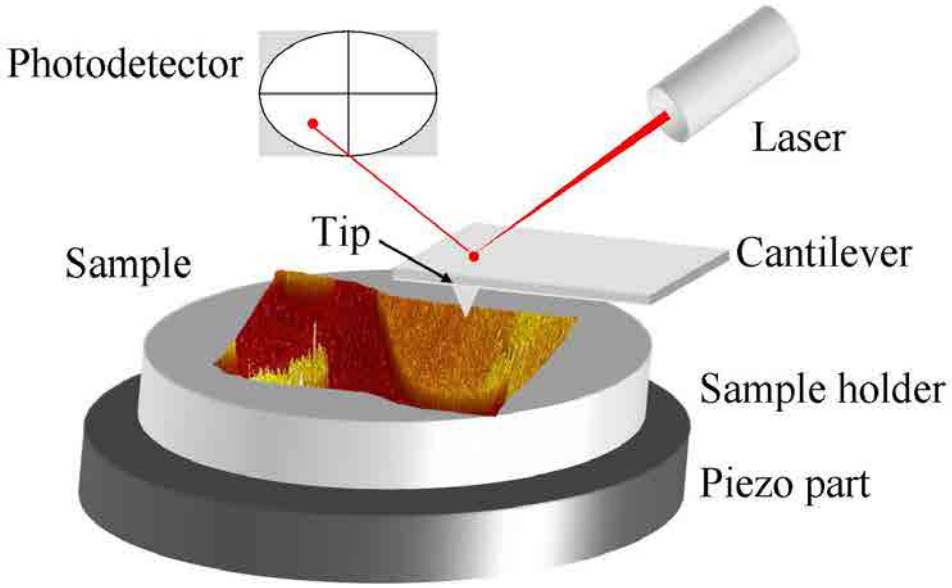

Figure 2.15. AFM operation scheme.

2.3.2.1 Topographic modes

The contact mode implies that tip and sample are in contact during scanning, so the feedback governs the piezoelectric component to maintain a constant Δx and F_v value (Figure 2.16 Contact-AFM). This mode presents the best topographic resolution, but it use with soft materials is not recommended because the tip, which is close to real contact, can modify the sample surface topography and its properties. In case of performing this method in soft materials, cantilevers with very low k_v is mandatory to minimize the tip effects on the sample.

The AM-AFM mode, also called tapping mode, is based on forcing the tip to vibrate in its own resonance frequency thanks to a small piezoelectric situated on the cantilever holder. The operation consists on approaching the tip to the sample, so the vibration amplitude is reduced due to the interactions between the tip and the sample surface (Figure 2.16 AM-AFM). The feedback loop controls a constant tip-sample distance thanks to the control of the vibration amplitude. The resolution is lower than the contact mode, but the AM-AFM produces no damages even in the case of very soft surfaces.

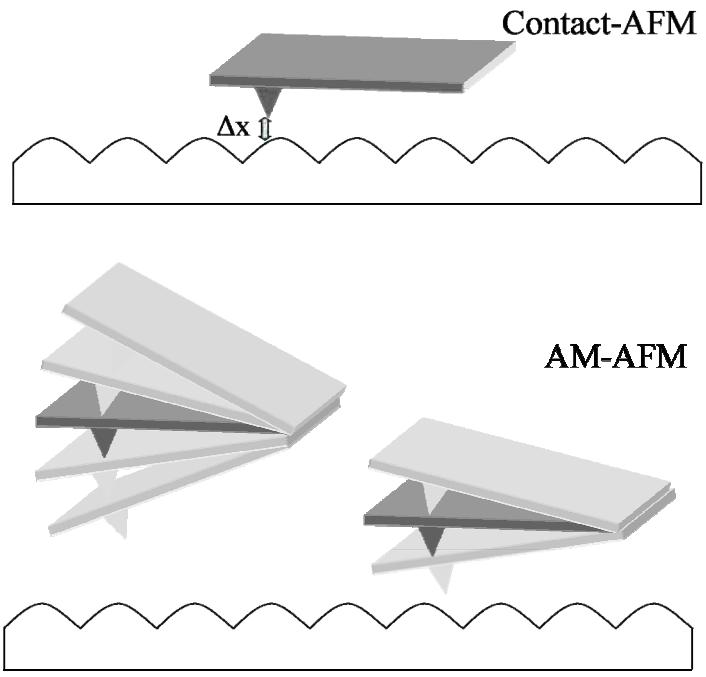

Figure 2.16. Scheme of topographic AFM modes.

2.3.2.2 Force Spectroscopy

Nanoidentation is another mode that can be performed using AFM. The technique is schematically explained in Figure 2.17, where the curve of the cantilever deflection vs. piezo component displacement (Δx vs Δz) for a lipid bilayer is depicted. The curve consists on measuring the vertical displacement of the cantilever towards the sample surface. At the beginning, the tip is far from the surface producing no interaction between them. Then the tip approaches the substrate surface producing interactions tip-sample like van der Waals, electrostatic and capillarity forces. When the tip contacts the surface, the cantilever bends suddenly, situation called jump-to-contact [101,102]. When applying a higher F_v (Figure 2.17), the cantilever continues bending upwards due to the electronic repulsion between the

atoms of the tip and the sample. Increasing the F_v applied, the bilayer is punctured and the tip reaches the substrate surface.

The threshold force (F_y) is the force at which the film (mono- or bilayer) locally collapses due to the vertical force exerted by the AFM tip. In fact, it can be regarded as a fingerprint of a given sample, as it was demonstrated in a previous work [74]. Conceptually, F_y marks the transition between the elastic regime and the plastic deformation or fragile rupture. Therefore, F_y gives an accurate idea of both the intermolecular interaction forces that arise inside the film and also the possible electrostatic interactions that bind the film to the substrate.

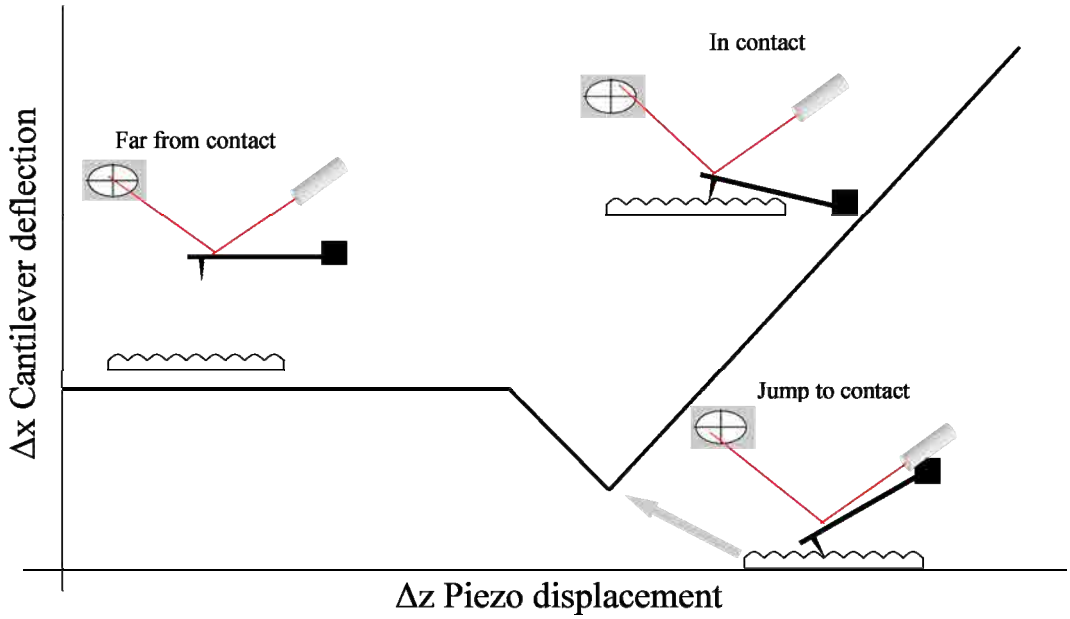

Figure 2.17. Δx vs. Δz ideal representation. At each zone, the scheme of the different contact regimes is depicted.

The nanoidentation mode permits applying F_v ranging from mN to pN depending on the AFM tip so it can be applied to all kind of samples [103, 104] to study their elastic and plastic properties. The F_v exerted to puncture the bilayer can be obtained from the Δx vs Δz plot (Figure 2.18) following the Expression 2.19, where P_d is the puncture deformation, Δx is the photodetector signal variation (V) when the cantilever bends and S_v ($V \cdot nm^{-1}$) is the vertical sensitivity (relationship between the signal variation in the photodetector and the corresponding cantilever deflection).

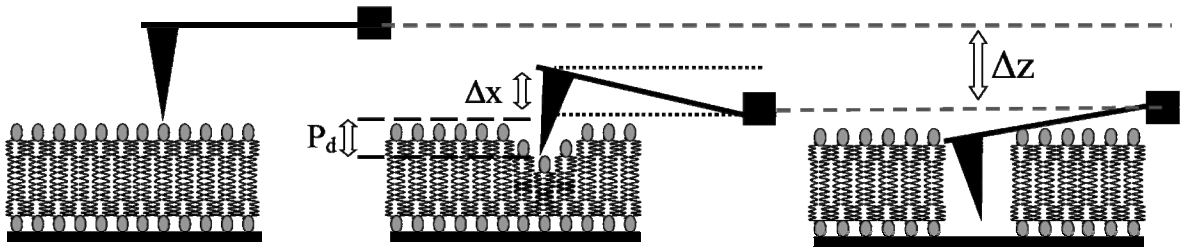

Figure 2.18. Scheme of a SPB being punctured by an AFM tip.

$$\Delta z = P_d + \frac{\Delta x}{S_v} \qquad \text{Expression 2.19}$$

In the case that the sample is immensely harder than the cantilever, such as when using mica Pd ≈ 0, so the Expression 2.20 can be written as follows.

$$\Delta z = \frac{\Delta x}{S_v} \qquad \text{Expression 2.20}$$

Δz is also defined by Expression 2.21.

$$\Delta z = \frac{F_v}{k_v} \qquad \text{Expression 2.21}$$

Combining Expression 2.20 and 2.21 the F_v can be obtained.

$$F_v = \frac{\Delta x}{S_v} k_v \qquad \text{Expression 2.22}$$

When performing mechanical studies, the cantilever is modelled as a spring, so it is characterized by an elastic vertical constant (k_v) which depends on the cantilever geometry and material. The k_v knowledge is very important for high quality experiments of nanoidentation, so k_v must be calculated for each tip regardless the manufacturing value. There are various methods to measure experimentally the cantilever k_v value, being chosen in function of the cantilever geometry and material. We have used in our experiments the thermal noise [105,106], which records the thermal spectrum of the cantilever and approximates it to a simple harmonic oscillator. The resulting amplitude follows the Expression 2.23 so the k_v of triangular probes can be obtained.

$$\frac{\partial F_z}{\partial z} = \frac{1}{A_{rms}} \sqrt{\frac{4 k_b T B k_c}{\omega_0 Q_f}} \qquad \text{Expression 2.23}$$

Where F_z is the minimum detectable interaction force due to thermal noise, A_{rms} is the rms-amplitude of the driven cantilever, k_b is the Boltzmann constant, T is the absolute temperature (K), B is the measurement bandwidth, k_c is the cantilever constant, ω_0 is the free cantilever resonance frequency and Q_f is the quality factor.

Nanoidentation experimental procedure and mathematical treatment

Force extension curves are performed on several zones of the samples, being more restricted in SPB where the force-extensions curves must be performed on the central regions to avoid rim effects. At each force curve, the cantilever deflection, which is proportional to the vertical force exerted on the sample, is 0 before the tip-sample contact (Point 1, Figure 2.19). Increasing the tip compression on the SPB, the vertical force increases until the layer breaks due to the pressure exerted on it. This breakthrough appears as a sudden jump in the force curve (Point 2, Figure 2.19), being this value the F_y measurement. As the vertical force keeps on increasing, the tip is in contact with the sample substrate. A more handy representation of the force curve (Vertical piezo displacement (Δz) vs. Vertical force (F_v) is the penetration curve (FvP)) [78]. Inset of Figure 2.19 shows this kind of representation, where two characteristic regions can be easily recognized; from point 1 to 2 the curve shows the elastic compression of the sample. At higher forces (after the breakthrough event), the plastic compression of the substrate is represented. Interestingly, the elastic region of the FvP comprises two different interactions. First of all, electrostatic forces between tip and sample, which arise when the electrical double layer induced by the lipid zwitterionic headgroups meet the slightly negative charge of the AFM tip. This force was measured to be extremely small for SPB prepared in usual conditions of pH $\approx$ 7 and 0.150 M KCl for ionic strength [107]. The second contribution is the mechanical deformation of the sample, which will be considered to account for the totality of the measured interaction.

The representation of the F_y values obtained from individual FvP curves is commonly depicted in histograms graphs. They have been fitted in this Ph. D. Thesis using a Gaussian model, although the continuum nucleation model proposed by Butt et al. [105,106] could also be used but the mathematical treatment difficulty is increased.

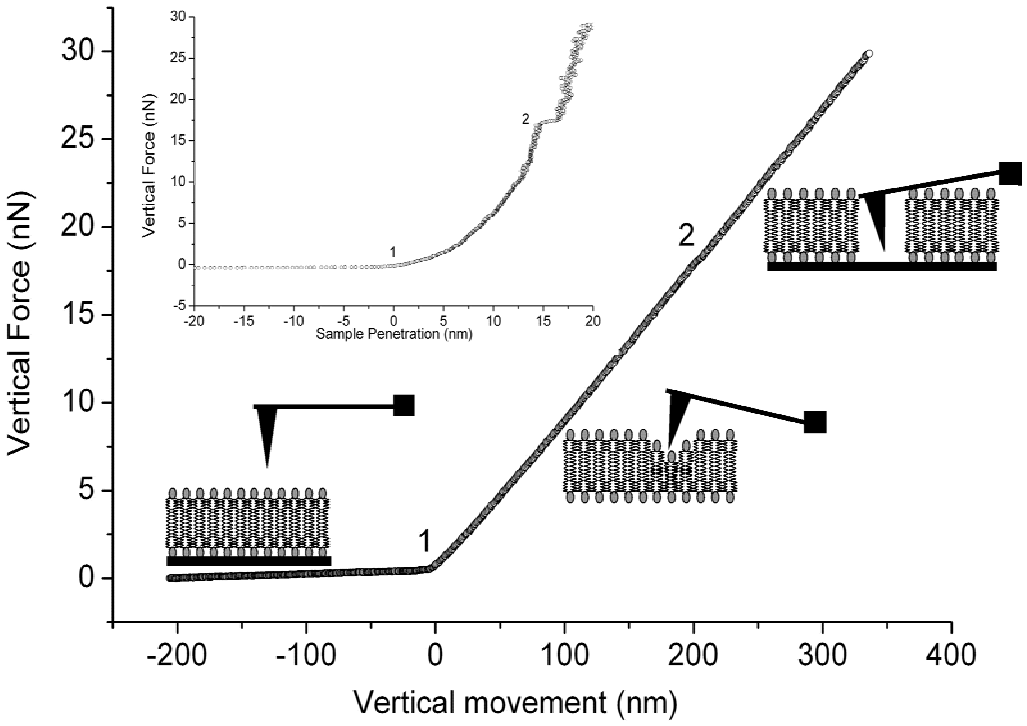

Figure 2.19. Characteristic lipid force curve including the scheme of the cantilever position in each zone (inset: FvP of a characteristic lipid force curve).

2.4. Voltammetric technique

I will consciously explain the voltammetric technique in a separate section than the characterization techniques. Although voltammetric studies are usually performed on biomimetic membranes to characterize the quality of the deposited film, in my Ph.D. Thesis, voltammetry is mainly performed to study the electron transfer in a biomimetic membrane; the objective is to relate the structure of the performed biomimetic membrane with the electron transfer.

Voltammetry is a dynamic electrochemical technique for studying reduction-oxidation reactions (redox) through current-voltage relationships. The current is measured when applying the desired voltage to the electrochemical cell. The most important techniques are linear sweep voltammetry (LSV), also known as linear potential sweep chrono-amperometry, and cyclic voltammetry (CV), cyclic potential sweep chronoamperometry. Both techniques will be explained in this section, especially CV that is widely employed due to its simplicity and the relevant information that can provide. CV is extensively used for the study of multielectron transfer reactions, especially for organic and organometallic systems, adsorbed species on the electrode surface, catalysis…

2.4.1 Electrode processes

The voltammetric technique applied to a given system implies three main electrode processes being: electron transfer, charging of the double-layer and mass transfer dynamics [108,109]. The electron transfer is consequence of the redox reaction, faradaic current (i_f), and it must be the main source of total current in the cell. There is also an omnipresent capacitor current, charging current (i_c), on the electrode corresponding to the charging and discharging of the double layer due to the voltage excitation demands some current flow. This current arises when a potential is established on a working electrode, where the metal side will be charged and therefore, the other side (the side in contact with the solution) acquire the opposite charge. This current flows across the capacitor when the potential is changed. Considering the interface electrode|aqueous solution, the charging current is caused by the compact inner layer of the water dipole. This dipole acts as the dielectric medium, separating the outer charged layer. Most of working electrodes act like a capacitor

at the electrode|solution interface and the typical value of this double layer capacitance is 10-100 $\mu F \cdot cm^{-2}$. The third electrode process is mass transfer dynamics in which it can be distinguished three kind of analyte transportation to the working electrode surface: diffusion, convection and migration. Diffusion takes place when there is a concentration gradient created by the electron transfer reaction. Convection occurs when an external fluid movement is applied like stirring, pumped flow, ultrasounds… Finally, migration is produced when charged species move under an electric field.

The limit current is established when the oxidized molecule is reduced as fast as the oxidized molecule arrives to the electrode surface, so the mass transfer rate reaches its maximum value. It is frequently used a supporting electrolyte such as KCl or $KClO_4$ to minimize the migration current. In that way, the supporting electrolyte carries all the charges through ion transport in the electric field. Therefore, the electroactive specie present in small concentrations (mM or less) is not affected by migration effects [108,109].

2.4.2 Voltammetry set up

The electrochemical reactions take place in a cell controlled with electrodes connected to a voltage or current source (potentiostat/galvanostat) that can be programmed and monitored. The cell is composed commonly by three electrodes (Figure 2.20): working electrode (W), counter electrode (C), and the reference electrode (R), which has usually a Luggin capillary to minimize iR loss [109,77]. The working electrode is the substrate where the reaction is carried out. The W can be metallic (gold, platinum…), containing carbon (HOPG, Glassy carbon…) or a glass slide with deposited films like ITO. Working electrode can be presented in many shapes, but the main common ones are flat discs, sheets or cylindrical structures.

One of the most important criterion for selecting the substrate is its potential working window where substrate-solvent interactions must be insignificant and electrolyte must remain electrochemically inert. The aqueous and organic solvents contain supporting electrolyte to avoid migration effects. The redox processes of the electrolyte components, the electrode material itself or the impurities present define the limits of the working

potential window and all the observable reactions must be placed inside this window to avoid interferences.

The reference electrode is placed near the working electrode to measure the W potential referred to the reference electrode. The common reference electrodes are NHE (Normal hydrogen electrode), SSC (Silver-silver chloride) and SCE (saturated calomel electrode containing mercury). Reference electrodes contain saturated solution of KCl (sometimes NaCl) as the inner electrolyte to maintain constant composition. The counter electrode is the current carrying electrode and it must be inert and have large area. Usually, the materials used for counter electrode are platinum foil or platinum wire [109,111].

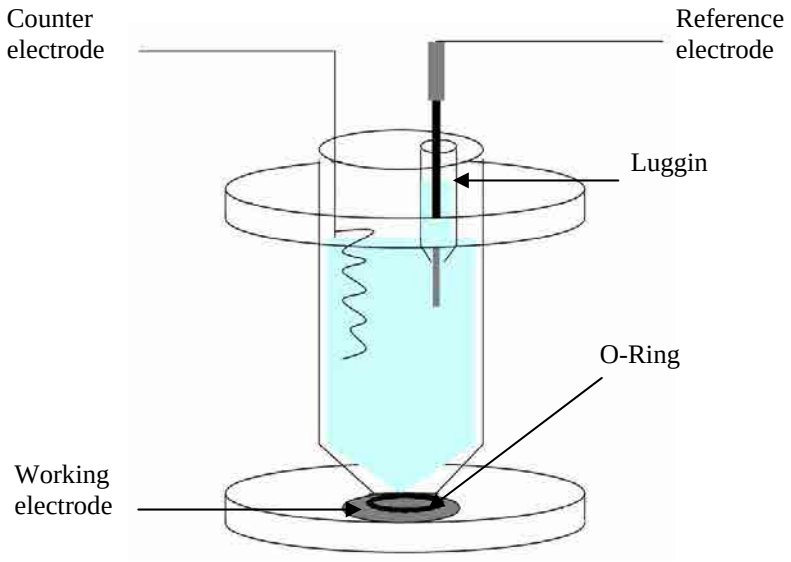

Figure 2.20. Voltammetry operation scheme.

2.4.3 Linear and cyclic voltammetry

The voltammetric techniques record the current *i* through a working electrode as a function of potential *E*, whereas the potential applied to this electrode is controlled as a linear function of t.

The electrode potential in LSV is changing linearly at a fixed scan rate from the initial potential (E_1), where no faradaic reaction takes place, to a selected potential (E_2). In CV, the potential is scanned back to a final potential (E_f), which normally coincides with E_1 (Figure 2.21). The scan is done in small voltage steps, being commonly the scan rate set ten times the voltage step. E_2 is called inversion potential due to the scanning direction is reversed. The scanning direction is very important in CV, so it must be specified when

scanning first to the cathodic potentials and finishing in anodic potentials (cathodic-anodic scan) or vice-versa (anodic-cathodic scan).

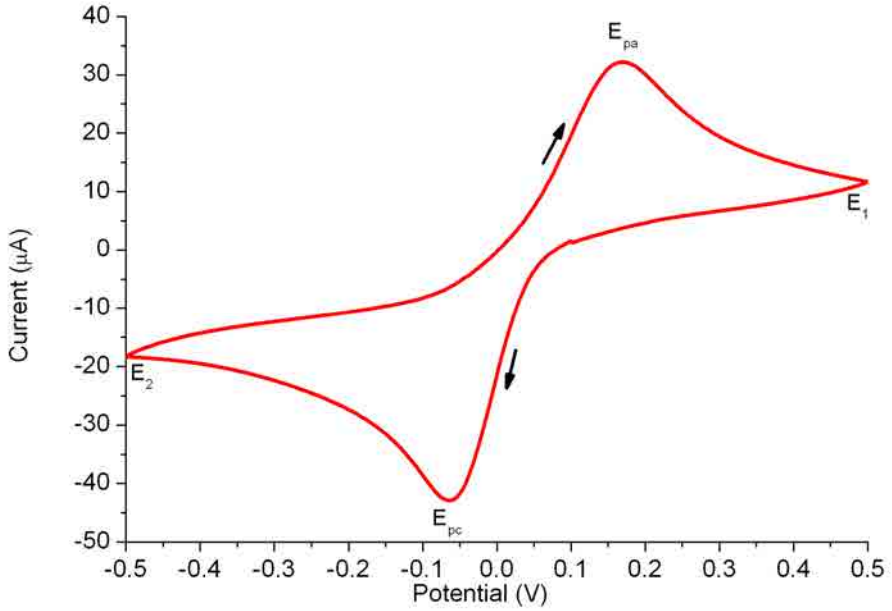

Figure 2.21. Cyclic voltammogram of a substance A.

The CV shape can be explained having a look at the reduction reaction. When the voltage reaches more negative values, the reduction process takes place, so the surface concentration of the oxidized form decreases, increasing the concentration gradient and the current starts to rise. When the surface concentration arrives to zero, and diffusion cannot replace the oxidized molecule, the current decreases creating a current peak (E_{pc}). Then, the concentration gradient remains low and unchanged making a flat shape at the end of the reduction zone. When the scan is reversed, the same processes take place but the most present specie is the reduced form and it gets oxidized drawing a peak (E_{pa}). It is frequent that the system requires some cycles to reach the steady state because the concentration at E_1 shifts between the first cycles.

Voltammetry mathematical treatment

The mathematical formalism to describe the voltammetric response depends on the considered experimental redox system.

In the case of systems with a simple redox process ($O + ne^- \rightleftharpoons R$), it can be considered two extreme situations, being the oxidized (O) and the reduced form (R) solved in the bulk of

the electrochemical solution, or both adsorbed or confined on the surface of the working electrode. In the first case, the Randles-Sevcik equation (Expression 2.24) defines the peak current for a reversible couple [110,111].

$$i_p = 0.4463nFA_w c_0^* \sqrt{\frac{nF}{RT} vD_O} \qquad \text{Expression 2.24}$$

Where n is the number of electrons, F the Faraday constant, A_w is the electrode area (cm^2), c_0^* is the concentration of the specie O in the bulk ($mol \cdot cm^{-3}$), R is the ideal gas constant ($J \cdot mol^{-1} \cdot K^{-1}$), T is the absolute temperature (K), v is the scan rate ($V \cdot s^{-1}$), n is the number of electrons involved in the charge transfer step and D_O is the diffusion coefficient ($cm^2 \cdot s^{-1}$) of O.

The peak (mV) potential at 25ºC is given by the Expression 2.25:

$$E_p = \frac{28.5}{n} \qquad \text{Expression 2.25}$$

Thus, for the reversible simple redox process in solution, E_p is independent of the scan rate and i_p is proportional to $v^{1/2}$. The later property indicates diffusion control for the redox process.

In the irreversible system case for both species O and R in the bulk electrochemical solution, the peak current is given by the Expression 2.26 where α_t is the transfer coefficient [111].

$$i_p = (2.99 \cdot 10^5) nA_w c_0^* \sqrt{\alpha_t nD_O v} \qquad \text{Expression 2.26}$$

In the case of a simple redox system in which only the adsorbed or confined species on the electrode surface are electroactive, the general expression of the linear sweep voltammograms was developed by Laviron [112]. The expression of the peak current for a totally reversible charge transfer is defined by Expression 2.27 where Γ is the surface concentration of the electroactive species ($mol \cdot cm^{-2}$).

$$i_p = \frac{F^2}{4RT} n^2 A_w \Gamma v \qquad \text{Expression 2.27}$$

The general expression is deduced assuming that no adsorption or desorption occurs during the scan, and for this reason, it is valid either for the case of adsorbed or confined electroactive species. In this kind of system the faradaic charge transfer is correlated with the total surface concentration of the electroactive species by the equation:

$$Q = nFA_w \Gamma \qquad \text{Expression 2.28}$$

The peak potential for this systems occurs at $E = E^{0'}$, where $E^{0'}$ is the formal redox potential of the redox couple [108] and $E_{pa} = E_{pc}$. This condition means that both peaks are completely symmetrical and they have the same shape. In the real systems this last condition is only accomplished in systems with the standard rate constant of the redox reaction (k^0) very high. In general, in real systems the peaks are asymmetric and a difference $|E_{pc}-E_{pa}|$ is obtained. This difference is higher as k^0 decreases or the scan rate increases. It is usual to consider the experimental criterion [112] that when $|E_{pc}-E_{pa}| >$ 200/n mV, the systems behaves as completely irreversible and, in this case, the expressions of the peak current and peak potentials are given by expressions 2.29-2.32.

$$i_{pc} = \frac{\alpha_t F^2 A_w v \Gamma}{2.718 RT} \qquad \text{Expression 2.29}$$

$$E_{pc} = E^{0'} + \frac{RT}{\alpha_t F} \ln\left(\frac{RTk^0}{\alpha_t F v}\right) \qquad \text{Expression 2.30}$$

$$i_{pa} = \frac{(1-\alpha_t) F^2 A_w v \Gamma}{2.718 RT} \qquad \text{Expression 2.31}$$

$$E_{pa} = E^{0'} + \frac{RT}{(1-\alpha_t) F} \ln\left(\frac{RTk^0}{(1-\alpha_t) F v}\right) \qquad \text{Expression 2.32}$$

It is observed that for a simple redox system in which only the adsorbed or confined species on the electrode surface are electroactive, i_p is proportional to v, either in the case of reversible or irreversible behaviour. Importantly, the previous Expressions 2.26-2.32 are applied for monolayers adsorbed or confined on the electrode surface without interaction forces between the electroactive species. In other cases (electrodes modified with multilayers of electroactive species, not homogeneous layer thickness, interactions between the electroactive species, electroactive species not evenly distributed inside the layer, charge transfer controlled by the diffusion of the electrons from the electrode surface or the counter ions from the electrochemical solution) the shape of the voltammogrames departs from the ideal reversible behaviour [113-116].

Since the potential is continuously changing in a potential sweep experiment, a charging capacitor current always flows, and the capacitance of the double layer (C_d) at a given potential can be obtained in absence of electroactive species by the Expression 2.33.

$$C_d = \frac{(i_a - i_c)}{2vA_w}$$ Expression 2.33

Where i_a and i_c are the capacitive current for the anodic and cathodic scan respectively. In presence of electroactive specie, the experimental current measured includes both, the faradaic and the charging current. Thus, the faradaic current must always be measured from the baseline of charging current.

As summary of this section, CV permits defining which of the previous cases suits better to the system in study. Commonly, the experimental behaviour has part of each ideal case, but one of them is predominant. The experimental procedure consists on performing CVs at wide range of scan rates. The peak intensity relation with the scan rate will determine where the redox specie is mainly placed: in the bulk having the relation $i_p = f(\sqrt{v})$ or adsorbed, having the relation $i_p = f(v)$ [77, 110].

2.5. References of Chapter 2

[1] Buoninsegni, F.T.; Herrero, R.; Moncelli, M.R. Alkanethiol monolayers and alkanethiol|phospholipid bilayers supported by mercury: an electrochemical characterization. J. Electroanal. Chem, 1998, 452, 33-42.

[2] Woodward, J.T.; Meuse, C.W. Mechanism of formation of vesicle fused phospholipid monolayers on alkanethiol self-assembled monolayer supports. J Colloid Interface Sci. 2009, 334, 139-145.

[3] Bilewicz, R.; Sek S.; Zawisza, I. Electron transport through composite monolayers. Russ. J. Electrochem. 2002, 38, 29-38.

[4] Naumann,R.; Schiller S.M.; Giess, F.; Grohe, B.; Hartman K.B.; Kärcher, I.; Köper, I.; Lübben, J.; Krasimir, V.; Knoll, W. Tethered Lipid Bilayers on Ultraflat Gold Surfaces. Langmuir, 2003, 19, 5435–5443.

[5] Mach, T.; Chimerel, C.; Fritz, J.; Fertig, N.; Winterhalter, M.; Fütterer, C. Miniaturized planar lipid bilayer: increased stability, low electric noise and fast fluid perfusion. Anal Bioanal Chem. 2008, 390, 841, 846.

[6] Petty, M.C. Langmuir-Blodgett films, An introduction. Cambridge: Cambridge University Press, 1996, 12-93.

[7] Girard-Egrot A.P.; Marquette, C.A.; Blum, L.J. Biomimetic membranes and biomolecule immobilisation strategies for nanobiotechnology applications. Int. J. Nanotechnol. 2010, 7, 753-807.

[8] Girard-Egrot A.P.; Blum, L.J. Langmuir-Blodgett Technique for Synthesis of Biomimetic Lipid Membranes. Nanobiotechnology of Biomimetic Membranes. New York: Springer Science, 2007, 23-74.

[9] Birdi, K.S. Lipid and Biopolymer Monolayers at Liquid Interfaces. New York: Plenum Press, 1989.

[10] Gaines, G.L. Insoluble monolayers at Liquid-Gas interfaces, New York, Wiley-Interscience, 1966.

[11] Schwartz D.K.; Viswanathan R.; Zasadzinski J.A.N. Commensurate defect superstructures in a Langmuir-Blodgett film. Phys. Rev. Lett. 1993, 70, 1267–1270.

[12] Davies, J.T.; Rideal, E.K.; Interfacial Phenomena, Academic Press Inc. NewYork, 1963, p.265.

[13] Vitovič, P.; Nikolelis, D.P.; Hianik, T. Study of calix [4] resorcinarene–dopamine complexation in mixed phospholipid monolayers formed at the air–water interface Biochim. Biophys. Acta 2006, 1758, 1852-1861.

[14] Mansourian, A.R.; Brain, A.P.R.; Quinn, P.J. Intermolecular mixing of saturated and unsaturated galactolipids. Biochem. Soc. Transactions 1986, 14, 738–739.

[15] Hoyo, J.; Guaus, E.; Torrent-Burgues, J. Biomimetic monolayer films of monogalactosyl-diacylglycerol incorporating ubiquinone. J. Colloid Interface Sci. 2012, 384, 189 − 197.

[16] Gong, K.; Feng, S-S.; Go, M.L.; Soew, P.H. Effects of pH on the stability and compressibility of DPPC/cholesterol monolayers at the air–water interface. Colloids Surf. A 2002, 207, 113-125.

[17] Domenech, O.; Torrent-Burgués, J.; Merino, S.; Sanz, F.; Montero, M.T.; Hernandez-Borrell, J. Surface thermodynamics study of monolayers formed with heteroacid phospholipids of biological interest. J. Colloids Surf. B 2005, 41, 233-238.

[18] Chou, T.-H.; Chu, I.-M.; Chang, C.-H. Interaction of paclitaxel with DSPC in monolayers at the air/water interface at different temperatures. Colloids Surf. B 2002, 25, 147-155.

[19] Gzyl-Malcher, B.; Filek, M.; Makyła, K.; Paluch, M. Differences in surface behaviour of galactolipoids originating from different kind of wheat tissue cultivated in vitro. Chem. Phys. Lipids, 2008, 155, 24-30.

[20] Buhaenko M.R.; Goodwin J.W.; Richardson R.M.; Daniel M.F. The influence of shear viscosity of spread monolayers on the Langmuir-Blodgett process. Thin Solid Films 1985, 134, 217–226.

[21] Buhaenko M.R.; Richardson R.M. Measurements of the forces of emersion and immersion and contact angles during Langmuir-Blodgett deposition. Thin Solid Films 1988, 159, 231–238.

[22] Gennis R.B. Biomembranes. Molecular structure and function. New York: Springer-Verlag, 1989.

[23] Girard-Egrot A.P.; Morélis R.M.; Coulet P.R. Direct influence of the interaction between the first layer and a hydrophilic substrate on the transition from Y- to Z-type transfer during deposition of phospholipid Langmuir-Blodgett films. Langmuir 1996, 12, 778–783.

[24] Rinia H.A.; Demel R.A.; van der Eerden P.J.M.; de Kruijff, B. Blistering of Langmuir-Blodgett bilayers containing anionic phospholipids as observed by atomic force microscopy. Biophys. J, 1999, 77, 1683–1693.

[25] Bassereau P.; Pincet F. Quantitative análisis of holes in supported bilayers providing the adsorption energy of surfactants on solid substrate. Langmuir 1997, 13, 7003–7007.

[26] Morélis R.M.; Girard-Egrot A.P.; Coulet P.R. Dependence of Langmuir-Blodgett film quality on fatty acid monolayer integrity. 1. Nucleation crystal growth avoidance in the monolayer through the optimized compression procedure. Langmuir 1993, 9, 3101–3106.

[27] Bangham, A.D.; Standish, M.M.; Watkins, J.C. Diffusion of univalent ions across the lamellae of swollen phospholipids. J. Mol. Biol. 1965, 13, 238–252.

[28] Lasic, D.D. The mechanism of vesicle formation. Biochem J. 1988, 256, 1–11.

[29] Cremer, P. S. and Boxer S. G. Formation and Spreading of Lipid Bilayers on Planar Glass Supports. Biochemistry 1996, 35, 14773-14781.

[30] Leonenko, Z.V.; Carnini, A.; Cramb, D.T. Supported planar bilayer formation by vesicle fusion: the interaction of phospholipid vesicles with surfaces and the effect of gramicidin on bilayer properties using atomic force microscopy. Biochim. Biophys. Acta 2000, 1509, 131-147.

[31] Kalb, E.; Frey,S.; Tamm, L.K. Formation of supported planar bilayers by fusion of vesicles to supported phospholipid monolayers. Biochim Biophys Acta 1992, 1103, 307-316.

[32] Raedler, J.; Strey, H.; Sackmann, E. Phenomenology and Kinetics of Lipid Bilayer Spreading on Hydrophilic Surfaces. Langmuir 1995, 11, 4539–4548.

[33] Berti, D.; Caminatia, G.; Baglioni, P. Functional liposomes and supported lipid bilayers: towards the complexity of biological archetypes. Phys. Chem. Chem. Phys. 2011, 13, 8769–8782.

[34] Seifert, U.; Lipowsky, R. Adhesion of vesicles. Phys. Rev. A 1990, 42, 4768-4771.

[35] Zhdanov, V. P.; Kasemo, B. Van der Waals interaction during protein adsorption on a solid covered by a thin film. Langmuir 2001, 17, 3518-3521.

[36] Richter, R. P.; Mukhopadhyay, A.; Brisson, A. Pathways of lipid vesicle deposition on solid surfaces: a combined QCM-D and AFM study. Biophys. J. 2003, 85, 3035-3047.

[37] Richter, R. P.; Brisson, A. Following the formation of supported lipid bilayers on mica: a study combining AFM, QCM-D, and ellipsometry. Biophys. J. 2005, 88, 3422-3433.

[38] Wittek, M.; Möbius, D.; Majda, M. Charge transport in two-component monolayers of lipid matrix and adsorbed electro-active component. Colloid Surf. A,2006, 284-285, 20-28.

[39] Reimhult, E.; Hook, F.; Kasemo, B. Intact vesicle adsorption and supported biomembrane formation from vesicles in solution: Influence of surface chemistry, vesicle size, temperature, and osmotic pressure. Langmuir 2003, 19, 1681-1691.

[40] Johnson, J.M.; Ha, T.; Chu, S.; Boxer, S.G. Early steps of supported bilayer formation probed by single vesicle fluorescence assays. Biophys. J. 2002, 83, 3371-3379.

[41] Reviakine, I.; Brisson, A. Formation of supported phospholipid bilayers from unilamellar vesicles investigated by atomic force microscopy. Langmuir 2000, 16, 1806-1815.

[42] Lipowski, R.; Seifert, U. Adhesion of Vesicles and Membranes Mol. Cryst. Liq. Cryst. 1991, 202, 17-25.

[43] Li, M.; Chen, M.; Sheepwash, E.; Brosseau, C.L.; Li, H.; Pettinger, B.; Gruler, H.; Lipkowski, J. AFM studies of solid-supported lipid bilayers formed at a Au(111) electrode surface using vesicle fusion and a combination of Langmuir-Blodgett and Langmuir-Schaefer techniques. Langmuir 2008, 24, 10313-10323.

[44] Ohki, S.; Arnold, K. Experimental evidence to support a theory of lipid membrane fusion. Colloids Surf B 2008, 63, 276-281.

[45] Seantier, B.; Breffa, C.; Félix, O.; Decher, G. Dissipation-enhanced quartz crystal microbalance studies on the experimental parameters controlling the formation of supported lipid bilayers. J Phys Chem B 2005, 109, 21755-21765.

[46] Charrier, A.; Thibaudau, F. Main phase transitions in supported lipid single-bilayer. Biophys J. 2005, 89, 1094-1101.

[47] Garcia-Manyes, S.; Oncins, G.; Sanz, F. Effect of temperature on the nanomechanics of lipid bilayers studied by force spectroscopy. Biophys J. 2005, 89, 4261-4274.

[48] Leonenko, Z.V.; Finot, E.; Ma, H.; Dahms, T.E.S.; Cramb, D.T. Investigation of Temperature-Induced Phase Transitions in DOPC and DPPC Phospholipid Bilayers Using Temperature-Controlled Scanning Force Microscopy. Biophys J. 2004, 86, 3783–3793.

[49] Richter, R.P.; Maury, N.; Brisson, A.R. On the effect of the solid support on the interleaflet distribution of lipids in supported lipid bilayers. Langmuir 2005, 21, 299-304.

[50] Hope, M.J.; Redelmeier, T.E.; Wong, K.F.; Rodriguez, W.; Cullis, P.R. Phospholipid asymmetry in large unilamellar vesicles induced by transmembrane pH gradients. Biochemistry 1989, 28, 4181-4187.

[51] Hauser, H.; Pascher, I.; Pearson, R.H.; Sundell, S. Preferred conformation and molecular packing of phosphatidylethanolamine and phosphatidylcholine. Biochim Biophys Acta 1981, 650, 21-51.

[52] Bin, X.; Zawisza, I.; Goddard, J.D.; Lipkowski, J. Electrochemical and PM-IRRAS studies of the effect of the static electric field on the structure of the DMPC bilayer supported at a Au(111) electrode surface. Langmuir 2005, 21, 330-347.

[53] Brosseau, C.L.; Bin, X.; Roscoe, S.G.; Lipkowski, J. Electrochemical and PM-IRRAS characterization of DMPC + cholesterol bilayers prepared using Langmuir–Blodgett/Langmuir–Schaefer deposition. J. Electroanal. Chem. 2008, 621, 222-228.

[54] Chen, M.; Li, M.; Brosseau, C.L.; Lipkowski, J. AFM studies of the effect of temperature and electric field on the structure of a DMPC-cholesterol bilayer supported on a Au(111) electrode surface. Langmuir 2009, 25, 1028-1037.

[55] Lipkowski, J. Building biomimetic membrane at a gold electrode surface. Phys. Chem. Chem. Phys. 2010, 12, 13874-13887.

[56] Garcia-Araez, N.; Brosseau, C. L.; Rodriguez, P.; Lipkowski, J. Layer-by-Layer PM-IRRAS Characterization of DMPC Bilayers Deposited on a Au(111) Electrode Surface. Langmuir 2006, 22, 10365–10371.

[57] Oncins, G.; Picas, L.; Hernández-Borrell, J.; Garcia-Manyes, S.; Sanz, F. Thermal Response of Langmuir-Blodgett Films of Dipalmitoylphosphatidylcholine Studied by Atomic Force Microscopy and Force Spectroscopy. Biophys J. 2007, 93, 2713–2725.

[58] Günster, J.; Souda, R. On the wettability of lipid DPPC films. Langmuir. 2006 22, 6939-6943.

[59] Castellana, E. T.; Cremer, P. S. Solid supported lipid bilayers: from biophysical studies to sensor design. Surf. Sci. Rep. 2006, 61, 429−444.

[60] Tero, R. Substrate effects on the formation process, structure and physicochemical properties of supported lipid bilayers. Materials 2012, 5, 2658-2680.

[61] Falini, G.; Fermani, S.; Conforti, G.; Ripamonti, A; Protein crystallisation on chemically modified mica surfaces. Acta Crystallogr D Biol Crystallogr. 2002, 58, 1649-1652.

[62] So, S.K.; Choi, W.K.; Cheng, C.H.; Leung, L.M.; Kwong, C.F. Surface preparation and characterization of indium tin oxide substrates for organic electroluminescent devices Appl. Phys. A 1999, 68, 447–450.

[63] Abdelsalam, M.E.; Bartlett, P.N.; Kelf, T.; Baumberg, J. Wetting of regularly structured gold surfaces. Langmuir 2005, 21, 1753-1757.

[64] Aït-Mokhtar, A.; Amiri, O.; Dumargue, P.; Bouguerra, A. On the applicability of Washburn law: study of mercury and water flow properties in cement-based materials. Materials and Structures 2004, 37, 107-113.

[65] Nelson, W.C.; Kim, C.J. Droplet Actuation by Electrowetting-on-Dielectric (EWOD): A Review. J. Adhes. Sci. Technol. 2012, 26, 1747–1771.

[66] Xu, S.; Szymanski, G.; Lipkowski, J. Self-assembly of phospholipid molecules at a Au(111) electrode surface. J Am Chem Soc. 2004, 126, 12276-12277.

[67] Garcia-Manyes, S.; Oncins, G.; Sanz, F. Effect of ion-binding and chemical phospholipid structure on the nanomechanics of lipid bilayers studied by force spectroscopy. Biophys J. 2005, 89, 1812-1826.

[68] Yang, J.; Kleijn J. M. Order in phospholipid Langmuir-Blodgett layers and the effect of the electrical potential of the substrate. Biophys J. 1999, 76, 323–332.

[69] Gao, H.; Luo, G.A.; Feng, J.; Ottova, A.L.; Tien, H.T. Fabrication and photoelectric properties of self-assembled bilayer lipid membranes on conducting glass. J Photochem Photobiol B 2000, 59, 87-91.

[70] Moncelli, M.R.; Becucci, L.; Nelson, A.; Guidelli R. Electrochemical modeling of electron and proton transfer to ubiquinone-10 in a self-assembled phospholipid monolayer. Biophys J. 1996, 70, 2716-2726.

[71] Oleson, T.A.; Sahai, N., Pedersen, J.A. Electrostatic effects on deposition of multiple phospholipid bilayers at oxide surfaces. J Colloid Interface Sci. 2010, 352, 327-336.

[72] Mornet, S.; Lambert, O.; Duguet, E.; Brisson, A. The formation of supported lipid bilayers on silica nanoparticles revealed by cryoelectron microscopy. Nano. Lett. 2005, 5, 281-285.

[73] Lindsay, S.M.; Lyubchenko, Y.L.; Tao, N.J.; Li, Y.Q; Oden, P.I.; DeRose, J.A.; Pan, J. Scanning tunneling microscopy and atomic force microscopy studies of biomaterials at a liquid–solid interface. J. Vac. Sci. Technol. A 1993, 11, 808-813.

[74] Nussio, M. R.; Oncins, G.; Ridelis, I.; Szili, E.; Shapter, J. G.; Sanz, F.; Voelcker, N. H. Nanomechanical Characterization of Phospholipid Bilayer Islands on Flat and Porous Substrates: a Force Spectroscopy Study. J. Phys. Chem. B 2009, 113, 10339−10347.

[75]Kim, H.; Horwitz, J. S.; Kushto, G.; Piqué, A.; Kafafi, Z.H.; Gilmore, C.M.; Chrisey, D .B. Effect of film thickness on the properties of indium tin oxide thin films. J. Appl. Phys. 2000, 88, 6021-6025.

[76] Kibrom, A.; Roskamp, R.F.; Jonas, U.; Menges, B.; Knoll, W.; Paulsen, H.; Naumann, R.L.C. Hydrogel-supported protein-tethered bilayer lipid membranes: a new approach toward polymer-supported lipid membranes. Soft Matter 2011,7, 237-246.

[77] Hoyo, J.; Guaus, E.; Torrent-Burgues, J.; Sanz, F. Electrochemical behaviour of mixed LB films of ubiquinone−DPPC. J.Electroanal. Chem. 2012, 669, 6−13.

[78] Hoyo, J.; Guaus, E.; Oncins, G.; Torrent-Burgués, J.; Sanz, F. Incorporation of ubiquinone in supported lipid bilayers on ITO. J. Phys. Chem. B 2013, 117, 7498−7506.

[79] Hillebrandt, H.; Wiegand, G.; Tanaka, M.; Sackmann, E. High Electric Resistance Polymer/Lipid Composite Films on Indium-Tin-Oxide Electrodes. Langmuir 1999, 15, 8451-8459.

[80] Ge, C.; Orosz, K.S.; Armstrong, N.R.; Saavedra, S.S. Poly(aniline) nanowires in sol-gel coated ITO: a pH-responsive substrate for planar supported lipid bilayers. ACS Appl Mater Interfaces 2011, 7, 2677-2685.

[81] Choi, M.; Jo, K.; Yang, H. Effect of Different Pretreatments on Indium-Tin Oxide Electrodes. Bull. Korean Chem. Soc. 2013, 34, 421-425.

[82] Kreir, M.; Farre, C.; Beckler, M.; George, M.; Fertig, N. Rapid screening of membrane protein activity: electrophysiological analysis of OmpF reconstituted in proteoliposomes. Lab Chip. 2008, 8, 587-595.

[83] Popovich, N.D.; Wong, S.S.; Yen, B.K.; Yeom, H.Y.; Paine, D.C. Influence of microstructure on the electrochemical performance of tin-doped indium oxide film electrodes. Anal Chem. 2002, 74, 3127-3133.

[84] Suemori,Y.; Nagata, M.; Kondo, M.; Ishigure, S.; Dewa, T.; Ohtsuka, T.; Nango, M. Phospholipid-linked quinones-mediated electron transfer on an electrode modified with lipid bilayers. Colloids Surf B 2008, 6, 106-112.

[85] Gao, H.; Luo, G.; Feng, J.; Ottova, A.L.; Ti Tien. H. Photoelectric conversion properties of bilayer lipid membranes self-assembled on an ITO substrate. J. Electroanal. Chem. 2001, 496, 158–161.

[86] García-Esparza, S.; Blanco, L.M.; Bernès, S. Application of the Double Pulse Potential Chronoamperometry Technique to Modify the ITO Electrode Surface Portugaliae Electrochim. Acta 2008, 26, 517-525.

[87] Monk, P.M.S.; Man, C.M. Reductive ion insertion into thin-film indium tin oxide (ITO) in aqueous acidic solutions: the effect of leaching of indium from the ITO J. Mater. Sci.: Mater. Electron. 1999, 10, 101-107.

[88] Gritsch, S.; Nollert, P.; Jähnig, F.; Sackmann, E. Impedance Spectroscopy of Porin and Gramicidin Pores Reconstituted into Supported Lipid Bilayers on Indium-Tin-Oxide Electrodes. Langmuir 1998, 14, 3118-3125.

[89] Ding, K-Q. Cyclic Voltammetrically-prepared MnO2 Coated on an ITO Glass Substrate. Journal of the Chinese Chem. Soc. 2009, 56, 175-181.

[90] Balasubramanian, N.; Subrahmanyam, A. Electrical and optical properties of reactively evaporated indium tin oxide (ITO) films-dependence on substrate temperature and tin concentration, J. Phys. D: Appl. Phys. 1989, 22, 206-209.

[91] Sereno, L.; Silber, J.J. Otero, L.; del Valle Bohorquez, M.; Moore, A.L.; Moore, T.A.; Gust, D. Photoelectrochemistry of Langmuir−Blodgett Films of Carotenoid Pigments on ITO Electrodes J. Phys. Chem. 1996, 100, 814–821.

[92] Hamberg, I.; Granqvist, C.G. Evaporated Sn-doped In2O3 films: Basic optical properties and applications to energy-efficient windows J. Phys. D: Appl. Phys. 1986, 60, 123-160.

[93] Devadoss, A. Cholesterol oxidase modified microelectrodes for detection of cholesterol in the plasma membrane of single cells. Ph.D thesis, Case Western Reserve University, Cleveland, OH, 2006.

[94] Hénon S.; Meunier J. Microscope at the brewster angle: direct observation of first order phase transitions in monolayers. Rev. Sci. Instrum. 1991, 62, 936-939.

[95] Hönig, D; Möbius, D. Direct Visualization of monolayers at the air-water interface by brewster angle microscopy. J. Phys. Chem. 1991, 95, 4590-4592.

[96] Roldán-Carmona, C.; Giner-Casares, J.J.; Pérez-Morales, M.; Martín-Romero, M.T.; Camacho, L. Revisiting the brewster angle microscopy: the relevance of the polar headgroup. Adv. Colloid Interface Sci. 2012, 173, 12-22.

[97] Vollhardt D.; Fainerman V.B. Characterisation of phase transition in adsorbed monolayers at the air/water interface. Adv. Colloid Interface Sci. 2010, 154, 1-2.

[98] Oncins, G. Nanomechanics of organic layers and biomembranes. Ph.D. Thesis. University of Barcelona, Departament de Química-Física. Barcelona, 2007.

[99] Schwarz, U.D.; Zwörner, O.; Köster, P.; Weisendanger, R. Quantitative analysis of the frictional properties of carbon compounds at low loads using friction force spectroscopy. Phys. Rev. B, 1997, 56, 6987-6996.

[100] Derjaguin, B.V.; Muller, V.M.; Toporov, Y.P. Effect of contact deformations on the adhesion of particles. J. Colloid Interface Sci. 1975, 53, 314-326.

[101] Carpick, R.W.; Dai, Q.; Ogletree, D.F.; Salmeron, M. Friction force microscopy investigations of potassium halide surfaces in ultrahigh vacuum: Structure, friction and surface modification. Trib. Lett. 1998, 5, 91-102.

[102] Sader, J.E. Parallel beam approximation for v-shaped atomic-force microscope cantilevers. Review of Scientific Instruments, 1995, 66, 4583-4587.

[103] Liu, E., Blanpain, B., Celis, J.P. Calibration procedures for frictional measurements with a lateral force microscope. Wear 1996, 192, 141-150.

[104] Cain, R.G.; Page, N.W.; Biggs, S. Force calibration in lateral force microscopy, J.Colloid and Interface Sci. 2000, 227, 55-65.

[105] Butt, H. J.; Franz, V. Rupture of molecular thin films observed in atomic force microscopy. I. Theory. Phys. Rev. E: Stat., Nonlinear, Soft Matter Phys. 2002, 66, 031601-1−031601-9.

[106] Loi, S.; Sun, G.; Franz, V.; Butt, H.J. Rupture of molecular thin films observed in atomic force microscopy. II. Experiment. Phys. Rev. E: Stat., Nonlinear, Soft Matter Phys. 2002, 66, 031602-1−031602-7.

[107] Redondo-Morata, L.; Oncins, G.; Sanz, F. Force spectroscopy reveals the effect of different ions in the nanomechanical behavior of phospholipid model membranes: the case of potassium cation. Biophys. J. 2012, 102, 66−74.

[108] Compton, R.C.; Banks, C.E. Understanding Voltammetry. Singapore, 1st Ed. World Scientific Publishing, 2007, 1-151.

[109] Speiser, B. Chemistry - Encyclopedia of Electrochemistry, Instrumentation and Electroanalytical Chemistry, Wiley 2007, 3, 81-104.

[110] Wang, J. Analytical electrochemistry, New York, 2ed. Wiley, 2001, 28-60.

[111] Bard A.J.; Faulkner L.R. Electrochemical methods. Fundamentals and applications. New York, 2ed., Wiley, 2001, 226-260.

[112] Laviron, E. General Expression of the linear potential sweep voltammogram in the case of diffusionless electrochemical systems. J. Electroanal. Chem. 1979, 101, 19-28.

[113] Laviron, E. A multilayer model for the study of space distributed redox modified electrodes: Part I. Description and discussion of the model. J. Electroanal. Chem. 1980, 112, 1–9.

[114] Laviron, E.; Roullier, L.; Degrand, C. A multilayer model for the study of space distributed redox modified electrodes: Part II. Theory and application of linear potential sweep voltammetry for a simple reaction. J. Electroanal. Chem. 1980, 112, 11–23.

[115] Laviron, E. Voltammetric methods for the study of adsorbed species. Electroanalytical chemistry vol 12. Bard A.J. (ed.) New York: Marcel Dekker, 1982.

[116] Daifuku, H.; Aoki, K.; Tokuda, K.; Matsuda, H. Electrode kinetics of surfactant polypyridine osmium and ruthenium complexes confined to tin oxide electrodes in a monomolecular layer by the Langmuir-Blodgett method. J. Electroanal. Chem. 1985, 183, 1-26.

[117] Wang, X; Shindel, M.M.; Wang, S-W.; Ragan, R. A Facile Approach for Assembling Lipid Bilayer Membranes on Template-Stripped Gold. Langmuir 2010, 26, 18239-18245.

[118] Zawisza, I.; Bin, X.; Lipkowski, J. Spectroelectrochemical studies of bilayers of phospholipids in gel and liquid state on Au(111) electrode surface. Bioelectrochemistry 2004, 63, 137-147.

Chapter 3

Biomimetic membranes and its components

The first section of this chapter exposes briefly the photosynthetic process, which takes place in the thylakoid membrane. The second section explains on the one hand, the biomimetic membrane characteristics such the physical state, compactness, fluidity and defects formation and, on the other hand, the interactions between the substrate, the electrolyte and the membrane. The next sections explains the lipids and prenylquinones used in our biomimetic membranes, beginning the third section with dipalmitoyl phosphatidylcholine (DPPC) which is a model lipid widely used for biomimetic membranes. As it represents only an initial step in our investigations and it has low relevance in the photosynthetic membranes, the characteristics and physical state of DPPC are briefly explained. We focus on galactolipids, especially monogalactosyldiacylglycerol (MGDG) and digalactosyldiacylglycerol (DGDG); both represent ≈ 80% of the total lipid content of the thylakoid membrane. This subsection begins exposing the thylakoid membrane composition and a brief explanation of the lipids functions. Following this, MGDG and DGDG biosynthetisis and particular functions in the membrane are reported. The subsection concludes with the physical states of both galactolipids and the potential applications of these galactolipids for human benefits, especially their anti-cancer application.

The fourth section explains the prenylquinones UQ and PQ. PQ is present in biological photosynthetic membranes, but its isolation cost is high, so very little studies have been

performed with it. Conversely, the multiple applications of UQ has made it subject of several studies and industry obtaining. PQ and UQ are members of the quinone family; both have a quinone ring with similar substituents, a similar size and similar shape. These features permits to extrapolate, with certain restrictions, the results obtained for UQ in the literature to PQ. In this section, the natural occurrence, functions and artificial applications of UQ and PQ are exposed. Moreover, the position of UQ in the membrane, which has been subject of controversy in the literature, is extensively explained. Following this, it is explained the different environments at which quinone has been studied and the proton and electron transfer mechanism associated to them. In addition, the main techniques used in the literature for preparing confined quinones on conductive substrates and their electrochemical studies are exposed. To conclude this section, the relevant processes that experience UQ and PQ in biological membranes and that they have been mimicked in the literature are briefly explained.

3.1 Biological Photosynthesis

Photosynthesis accomplishes three important missions for life in the Earth. It is the way in which carbohydrates are obtained to produce energy for plants and animals. It is the main path of returning carbon to the biosphere and it is also the main oxygen source for the Earth atmosphere.

Photosynthetic organisms appeared 3500 million years ago. Since photosynthetic organisms emerged, practically all kind of life in the Earth obtains its energy direct or indirectly through photosynthesis.

3.1.1 Photosynthesis localization [1-3]

Photosynthesis takes place in chloroplasts for green plants and algae. Chloroplasts are organelles situated under leaf surface (in plants) and their structure consist on a fully permeable external membrane, and an inner membrane which is selective permeable. The inner membrane encloses the stroma which contains thylakoids. Thylakoids are sacklike structures stacked like coins forming units called grana. The thylakoid membrane (Figure 3.1) encloses the lumen (inner part of the thylakoid). Photosystem I (PSI) is located principally in the unstacked membranes and the photosystem II (PSII) units in the grana sacks. In addition, cytochrome b_6f complex and ATP synthase, which are fixed in the thylakoid membrane, are present. Moreover, this membrane also holds chlorophylls and some of the accessory pigments.

3.1.2 Photosynthesis process

The photosynthesis process is driven by the light energy, and its global chemical reaction is:

$$CO_2 + 2H_2O \rightarrow [CH_2O] + H_2O + O_2$$

This process takes place in several steps, which can be grouped in two subprocesses called light reactions and dark reactions. Both subprocesses require light and take place at the same time, although light does not participate directly on dark reactions. Light reactions

oxidize photochemically water using sunlight through two reactions. One reaction reduces $NADP^+$ (Nicotinamide Adenine Dinucleotide Phosphate) to NADPH producing O_2, whereas the other reaction phosphorilates ADP (adenine diphosphate) to obtain ATP (adenine triphosphate).

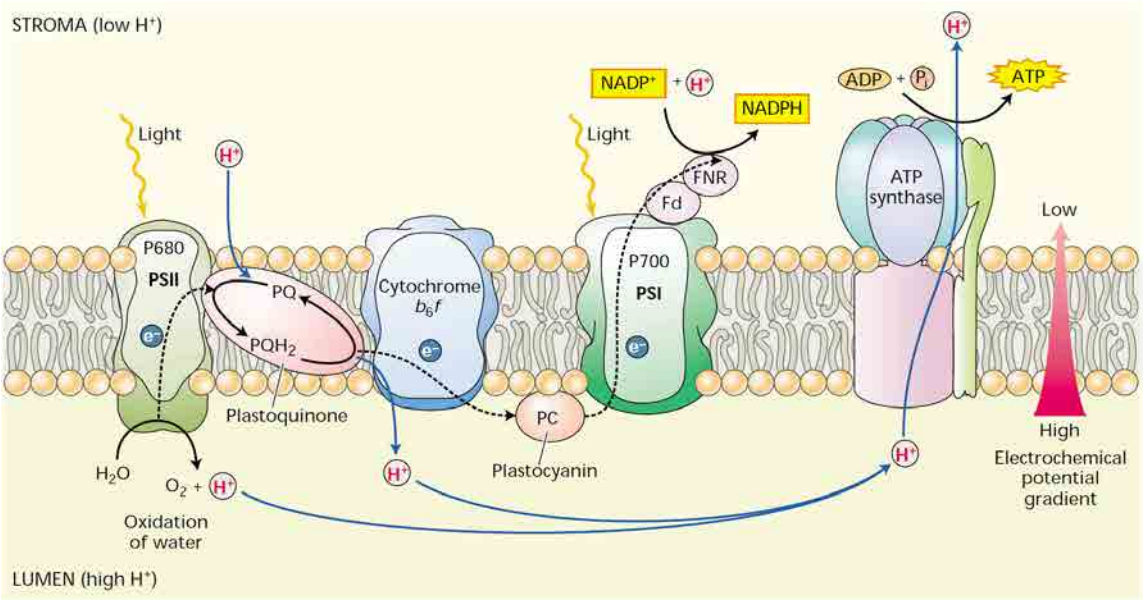

Figure 3.1 Scheme of the thylakoid membrane. Picture extracted from Taiz, L.; Zeiger, E. Plant physiology. 5th edition. EE.UU. California: Sinauer, 2010.

Light reactions take place in the lumen or in the surface of the thylakoids, and the ATP and NADPH produced in light reactions are released in the stroma where the dark reactions take place to synthesize carbohydrates using CO_2 and water. The photosynthesis starts when photosystem II (PSII) absorbs a photon and send it to its reaction centre. The excited reaction centre transfers an electron to a lower-energy electron acceptor, such as pheophytin (Ph). The electron is transferred through several redox molecules until arrives to a plastoquinone, which is bounded (PQ_A) to the PSII. Then a non-bounded plastoquinone (PQ_B) pick up two protons from the stroma reducing itself to plastoquinol (PQ_BH_2). This plastoquinol is released into the lipid portion of the thylakoid membrane and diffusses to the cytochrome b_6f. This cytochrome donates electrons to plastocyanin (PCn) and oxidise plastoquinol to plastoquinone releasing two protons in the lumen.

Plastocyanin transports electrons to PSI reaction centre through a serie of proteins until arrives to ferredoxin (F_d). F_d is solubilised in the stroma and is oxidized when transforming

$NADP^+$ to NADPH. The NADPH produced is released into the stroma to start dark reactions.

To close the photosynthesis cycle, PSI replaces the electrons lost in the transport chain with the electrons transported by plastocyanin from PSII, and PSII recovers its electrons from water. This water step takes place in an electron acceptor protein containing a cluster of four oxygen-bridged manganese atoms which split two water molecules, releasing oxygen, which diffuses out of the chloroplast. The four protons produced from the two water molecules are released into the thylakoid lumen, creating a pH gradient between the lumen and the stroma.

3.2 Biomimetic membrane models

Artificial lipid bilayers have been extensively studied as models that mimic natural membranes so they are also called biomimetic membranes. They have shown their relevance in a broad range of chemical and biological applications, being one of the most encouraging the development of artificial photoelectric devices [4-8]. On the other hand, the main characteristic of lipid membranes is that they can self-organize and they also interact with biomolecules, both within the membrane and at its surface, due to the amphiphilic character and electrostatic charge of the lipid components [4,5].

Supported planar bilayer (SPB) or monolayers onto solid surfaces are widely used as model for mimicking biological membranes (See Section 2.1). The resulting biomimetic membrane is easy to obtain, stable, robust and it has also a good reproducibility, fluidity and lateral mobility. In addition, its composition is tuneable including the insertion of proteins, nanoparticles and other species within the membrane or at its surface [9,10]. The layer-substrate compatibility is a limitation for given uses of these biomimetic membranes, being the case of transmembrane proteins one of the worst problems due to the substrate-protein interactions [9]. The characteristics of the biomimetic membranes are similar to that of the living cells, being the most important: maintaining a two-dimensional fluidity, stablishing a selective barrier between the inside and the outside of the cell, insulating inorganic ions and supporting large electrochemical potential differences across them. Biological membranes are compact, with an internal lateral surface pressure $\approx 33\ mN \cdot m^{-1}$

[11], so that, biological and biomimetic membranes should have different domains which offer a local environment to maintain their functions [12].

Biomimetic membranes have been used for several purposes like membrane structure characterization [13,14], study of the structure of membrane-associated proteins [15], and membrane-drug interaction [16-18], to probe peptide-lipid interactions [19,20] and their use in biotechnological nanodevices [21,22]. On the other hand, vesicles are also widely used for natural cell mimicking due to the structural similarity between them. Several applications has been studied, such as host model system for intrinsic membrane proteins, [23,24], nanoreactors [25,26], drug delivery [27] and sensors [28].

One of the most important features of the supported mono- or bilayers compared with other cell membrane models is that thanks to its long-term stability, they can be studied using several surface analytical techniques. These techniques include: scanning probe miscroscopy (SPM), ellipsometry, neutron reflectivity, mass spectrometry (MS), surface plasmon resonance (SPR), infrared reflection absorption spectroscopy (IRRAS), quartz crystal microbalance, vibrational sum frequency spectroscopy, polarized attenuated total reflection (ATR) spectroscopy, UV-vis spectroscopy, neutron magnetic resonance (NMR), electrochemical techniques like electrochemical impedance spectroscopy (EIS), voltammetry, coulombimetry, etc. For more details about the use of these techniques for SPB studies, the reader is addressed to the following articles and references therein [9,29, 30].

3.2.1 Biomimetic membrane characteristics

3.2.1.1 Physical states

Lipid vesicles or bilayers can adopt several physical states (Figure 3.2): the liquid-crystalline or fluid phase (L_α) and phases with ordered hydrocarbon chain arrangements, ripple phase (P_β), lamellar gel or solid phase (L_β), and subgel or lamellar crystalline or crystal phase (L_c). Bilayer physical states can be correlated with the monolayer ones, being liquid expanded (LE) related with liquid-crystalline phase (L_α), liquid condensed (LC) is linked with the lamellar gel phase (L_β) and finally, the solid phase (S) can be associated with lamellar crystal phase (L_c). Therefore, LC phase is more compact than LE, so fluidity

and permeability in LC phase is lower than in the LE state. It is generally accepted that many relevant natural processes occur in the L_α phase [34,35].

The L_α is an isotropic, loosely packed phase with high degree of lateral mobility and axial rotation of the lipid chains whereas the L_β is anisotropic and tighly packed with restricted mobility and axial rotation [36]. The phase change (L_α–L_β) implies an increase of the thickness (≈ 0.5 nm) [37]. The way that the bilayer thickness is increased through the (L_α–L_β) transition gives idea about the coupling between both leaflets of a bilayer. A sudden jump in thickness implies a high interaction between leaflets whereas a gradual increase implies that the bilayer is stressed [29].

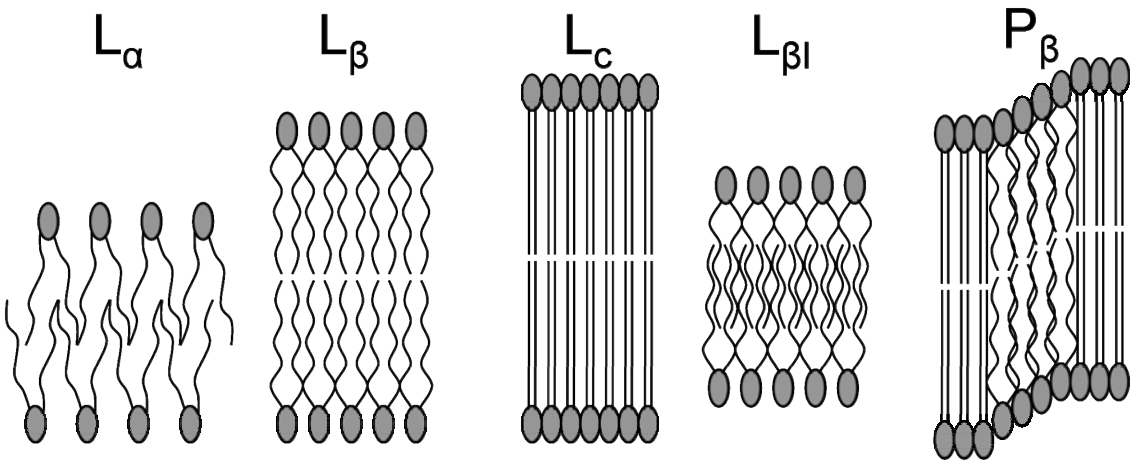

Figure 3.2. More current phases adopted by lipid vesicles or bilayers.

L_β phase becomes fully interdigitated ($L_{\beta I}$) phase by addition of ethanol and in consequence the L_β–L_α melting transition temperature of the phospholipids bilayer is modified [38]. In the L_β phase the breakthrough force decreases as the temperature is increased whereas in the L_α this magnitude tends to a plateau, according to the lipid order [14]. The steric force in a fluid phase is significantly reduced thanks to a reduction of the tail density when increasing temperature [12].

The immiscibility of two phases is based on the interactions between the acyl chains of each phase [39]. It has been concluded that phase separation in binary mixtures of saturated phospholipids with the same headgroup requires that one of them is in the L_β phase and the existence of a minimum chain length difference of four carbons [40] between both lipids.

It has been observed in vesicles [41,37] that the substrate affect to the main phase transition temperature due to the different interactions that occur at each system. Depending on the substrate hydrophilicity, the interactions substrate-lipid are stronger than interactions between leaflets, so stabilizing the system and increasing the main transition temperature. This reason also explains the observation of different transition temperature for each leaflet of the same SPB [14, 42]. In some cases, the substrate-lipid interactions are high enough to induce a phase change [5]. On the other hand, it has been observed that around the melting temperature (T_m), the membrane presents an anomalous behaviour such as the increase of the ions permeability and the conductivity, a softening of the mechanical properties, etc. This behaviour is related with the components order in the bilayer. In this situation, the headgroups order is low, so the water molecules of the bulk enter the bilayer, swelling it and achieving the bilayer maximum hydration [43]. The permeability of molecules through a bilayer depends highly on the lipid phase, being the bilayer more permeable in the L_α phase than in the L_β. The T_m can be tunned in several ways such reducing the pH [44]. In these conditions, the charged groups of the lipids are neutralised provoking an enhancement of the lipid order and, in consequence, an increase in the T_m. In contrast, high concentration of monovalent ions [44] or the presence of sterols [32] produces a mechanical stiffening of the lamellar gel phase and a reduction of the T_m.

The ripple phase is characterized by a swelling of the bilayer and the presence of undulations in a regular and large scale. The presence of this phase was suggested by Heimburg [45] who consider that the ripple phase can be classified as one-dimensional defect of the fluid lipid molecules in the lamellar gel phase matrix. However, the ripple phase observed in given systems can no be attributed to the Heimburg theory due to the characteristics of the ripple phase, which is present in a wide range of temperatures, including at temperatures above (L_β–L_α) the phase transition [46]. The explanation for that behaviour, once discarded the substrate undulations, is correlated with the relationship between the occupied area of the lipid heads and that of the lipid tails. One example for that is the experiment performed by Hauser et al. [54]. They obtained a DMPC SPB in the hydrated lamellar crystalline state using the LB-LS method. The higher size for the heads (0.47-0.54 nm^2) than the hydrocarbon chain (0.39 nm^2) leads the heads to adopt a sawtooth manner distribution to compensate this mismatch. The same bilayer deposited using vesicle fusion adopts a splay deformation to adapt to the more available space. Tilting and splays

are elements of spontaneous curvature and may be present at a wide range of temperatures even after the phase transition. However, these elements may also differ between leaflets of the same bilayer [46].

It is worth to briefly explain the hexagonal II phase (H_{II}) because it is the main phase presented by unsaturated MGDG. Although all our experiments are carried with saturated MGDG, the references to the behaviour of unsaturated MGDG are frequent. This H_{II} phase is characterized by the ordering of lipids forming closed circles with the heads in the inner part and the chains exposed to the solution. The stacking of these circles forms tubular shapes which, in turn, form hexagonal stackings.

Potential driven phase changes

Structural variations in a biomimetic membrane, including the phase transition, can be induced thanks to potential-driven changes [47]. In this line, Li et al. used DMPC bilayers to study the corrugation phase change [46]. They concluded that moving the potential to more positive values, the corrugation disappears and when the potential is swept back the corrugation is recovered. The starting potential for melting the corrugation coincides with the maximum in the differential capacitance curve being this phase transition completely reversible at the same potential when the potential is cycled back. Moving the potential to high cathodic values, the corrugation disappears and emerge a globular film, which is accompanied of a jump in the differential capacity. Scanning the potential back, the globular film disappears but it last ≈ 1h to recover the characteristics of the corrugation, so the phase reversibility in negative potentials is slow. The changes of the film thickness are correlated with changes in differential capacitance, matching the minimum film thickness with the minimum differential capacitance.

3.2.1.2 Effect of chain length, unsaturations and headgroup in the compactness of the biomimetic membrane

The deposition of a SPB implies lipid-substrate and lipid-lipid interactions. Lipid-lipid interactions are enhanced when increasing the length of the hydrocarbon chain [32], increasing the system hydrophobicity and entalphy (≈2 kJ/mol) for each extra CH_2 in the chain [3]. The alkyl-alkyl interactions enhancement produces an increase in the monolayer compactness and in the breakthrough force, but it reduces the molecular mobility [14].

The prediction of the effect of the headgroup on the membrane packing is more difficult due to they are packed thanks to electrostatic and hydrogen bonding interactions, both between headgroups and headgroups-surronding electrolyte molecules. The breakthrough force for same chain length and different headgroup in the same phase gives idea of the biomimetic membrane compactness. As a general rule for phospholipids, an increase in the compactness is produced in the following order: Phosphatidic acid (PA) < Phosphatidylethanolamine (PE) < Phosphatidylcholine (PC) < Phosphatidylserine (PS) < Phosphoglycerol (PG), being the breakthrough force range between 3 and 66 nN [32].

The introduction of unsaturations in the alkyl chain produces a molecular tilt change arising a less perfect packing, so lowering the melting temperature and changing other properties [3]. The presence of unsaturations in the lipid chains of a lipid layer reduces the temperature of the layer main phase transition (L_β-L_α) and its mechanical stability [32].

3.2.1.3 Fluidity

The bilayer fluidity depends on the lipid nature, the ionic strength and the ratio between lipid and other molecules present in the bilayer. This magnitude is the main responsible for the mobility of the membrane constituents such as small ions, molecular oxygen, proteins and other molecules. In order to mainatain their functions, higher plants cells control the number of unsaturations to maintain their fluidity [5,33].

Membrane fluidity is not simply predicted from the saturation content and the phase transition temperatures of the membrane lipids. It is also important the lipid composition and the nature of each lipid. Therefore, fluidity must be obtained studying together all these parameters, being one of the best techniques for this purpose the spin label electron

paramagnetic resonance (SL EPR) technique due to its timescale include some biologically relevant processes like acyl rotational isomerization and the rotational and translational diffusion of lipid molecules [33].

3.2.1.4 Defects formation

Mono- or bilayers have several types of defects that can be an advantage or a disadvantage depending on the objective for the supported layer formation. The most frequent defects include uncovered regions (pinholes), disordered hydrocarbon chain regions, enriched domains in multicomponent supported layer, local overcompressions, two phases coexistence and insufficient water content between the supported layer and the substrate [29,31].

The formation of defects is correlated with local and instantaneous differences in the lipid layer density leading to local differences in the lateral pressure, so establishing tensioned zones. These zones provoke surface defects when the tension is unbearable. On the other hand, the defect formation can be enhanced by lowering the supported layer temperature which favours local condensation.

Leonenko et al. [16] has been observed that the first surface defects appear immediately after the SPB formation. These defects increase in surface and depth till ≈ 90 min when the total area of defects is stabilized. After this time, defects suffer a continuous generation, fusion and annihilation process. Circular shape defects have a 100 nm diameter and adopt this structure to minimize the surface tension of the nascent boundary. The defects establish a balance between the reduction of surface tension and the instability that occurs when the lipid reorientates in the layer boundaries. When these defects grow, they adopt more elongated shapes.

3.2.2 Interactions substrate-electrolyte-membrane

3.2.2.1 Electrolyte layer

The preparation of supported layer on solid substrates generally implies the formation of a water layer which confers lubrification and fluidity to the supported layer, so that, the supported layer is able to maintain many properties of the free liposomes [9,49,50]. This

thin layer has been observed using electrodewetting techniques [51,37], fluorescence and neutron reflectivity [14] and PM-IRRAS [52,53].

There is a strong short-range force caused both by steric repulsions due to the thermal motion of the mono- or bilayers and by the hydration repulsion between adjancent solvated surfaces. The balance between the repulsive hydration force and the attractive van der Waals interactions permits the presence of a thin water layer between the surface and the mono- or bilayer (or between bilayers in a multibilayered system) [54].

Lipkowski group has studied DMPC bilayers at the gold surface and it has concluded that a compact bilayer is formed at the potential of zero charge (pzc). At more negative values than 370 mV (Ag/AgCl), the SPB starts the electroporation absorbing more water molecules, so swelling the bilayer. When the potential difference between the pzc and the applied potential is close to 1 V, the bilayer starts a process of electrodewetting maintaining the swelled thickness. The water molecules are positioned between the headgroups of the bottom leaflet and the substrate surface. At larger potential differences than 1 V, the bilayer is completely dewetted and the bilayer is detached from the substrate surface thanks to a ≈1-2 nm thick cushion of the aqueous solution. The lowest content of water and the smallest thickness are obtained at potentials where the charge density is close to zero [51,37]. The bilayer is attached to the electrode surface when the field is $< 6 \cdot 10^7$ V·m^{-1} and it is detached when the field is $> 2 \cdot 10^8$ V m^{-1}, which is correlated with the static electric fields of 10^7-10^8 V m^{-1} at which are exposed the natural membranes [53,55], although these electric fields only produce a ≈ 3º variation in the tilt angle of the SPB leaflet, being this change smaller in the bottom leaflet thanks to the surface-lipid interactions [29]. In the interval of surface charge (σ_M) of $-8 < \sigma_M < 5$ μC·cm^{-2} the bilayer is in direct contact with the gold surface. In the region of surface charge $-8 < \sigma_M < 0$ μC·cm^{-2} the thickness and the water content in the SPB increases as decreasing the charge density. At more negative surface charge values, the bilayer is detached from the gold surface at $\sigma_M < -8$ μC cm^{-2}, but it is maintained in bilayer form [29]. Conversely, Hillman et al. [56] observed that a bilayer containing a 10% of negatively charged lipids, these lipids diffuses to the bulk solution once they are detached from the surface [29].

In the detached situation of the Lipkowski group experiments, the lipids adopt a sawtooth fashion to achieve the minimum area per molecule. In the adsorbed situation, all lipid heads

interact with the surface so the area per molecule and, in consecuence, the tilt orientation respect to the surface normal is increased [29,57]. It was shown that in the adsorbed situation, carbonyl and phosphate groups are more hydrated than in the detached situation. This change is correlated with the different polar head packing. The sawtooth fashion has the smallest area per molecule. When the polar heads are in direct contact, the area per molecule is increased and water molecules fill the empty spaces [52,53].

The structure of a bilayer on gold at high negative charges ($\sigma_M < -8$ μC cm^{-2}) and a bilayer extended on natural quartz are quite similar. This behaviour is correlated with the similar charge density between the natural $\sigma_M \approx -20$ μC·cm^{-2} observed for quartz and the induced high negative charges for gold [29].

Ions addition

The presence of ions in a lipid layer increases the electrostatic interaction between the lipids headgroups due to a charge screening effect, which is translated in a higher proximity of the alkyl chains, and, in consequence, the van der Waals interactions are enhanced [58]. This effect, which occurs in negatively charged and zwitterionic phospholipids [59], induces a higher order, rigidity (less fluid), compactness and, in consecuence, a reduction in the area per molecule. Moreover, the presence of ions in a lipid layer involves a reorientation of the headgroups dipole and a charge redistribution along the system. All of these induced effects are more plausible in the gel phase rather than the liquid-crystalline phase due to the lower distance between lipids in the gel phase [39,43,49].

The addition of ions Na^+ or Ca^{2+} to a phospholipid bilayer modifies the organization and the morphology of the lamellar gel phase thanks to interactions with the carbonyl oxygen groups of the lipid heads (it has been studied that each Na^+ ion can coordinate up to three phosphate moieties [60], changing the orientation of the phospholids and their molecular packing. So that, smaller domains are obtained, being this modification reversible. It must be considered that the addition of Ca^{2+} may favour the obtaining of an asymmetric SPB and it may easy precipitate in the presence of given anions [61,37]. It is worth to remember that under pH 8 at 0.09 V vs Ag/AgCl conditions chloride ions adsorb at the gold electrode surface in chlorine atom form, involving a significant charge transfer [62]. On the other hand, the addition of other cations such as K^+ has a much lower effect due to its larger size.

Positive cations adsorbs better in the polar heads than the negative ones, although both induces more effect than pure water [49].

The addition of cations leads to a higher ionic strength which can also produce a partial or complete neutralization of the lipid negative charge and it affects the lipid hydration. These characteristics affect the membrane-substrate interactions causing both a strong adhesion and changes in the membrane structuresthat facilitates the membrane fusion [49,63].

3.2.2.2 Capacitance

The order in the hydrocarbon zone of the lipid layer is the main responsible for the capacitance that acts as a barrier for the electrolyte charged ions whereas the disordered lipids have short contribution [41]. In fact, the double layer capacitance reflects the order of the layer and therefore, its permeability to ions and other molecules [64]. An ideal biomimetic membrane should have a diferential capacitance (C_d) $\approx$ 0.8 $\mu F \cdot cm^{-2}$ and a resistance (R) $\geq$ 1 MΩ [29]. The experimental membranes are not ideal but they should have C_d and R close to the ideal values. A $C_d \geq 27$ $\mu F \cdot cm^{-2}$ indicates poor vesicle fusion and, moreover it can also indicate the presence of adsorbed ions on the substrate surface [46]. R values lower than 1 MΩ indicate that the membrane is not homogeneous [30]. On the other hand, the conductivity of a lipid layer is strong depending on the temperature, increasing one order of magnitude each 20 K [65].

3.3 Lipids used for biomimetic membrane formation

In this block the three lipids that we use in our experiments will be exposed. It starts with DPPC, which is a model lipid for biomimetic membrane preparation. In our experiments it has been utilized as a previous step to work with the thylakoid membrane occurring MGDG and DGDG. In this line, a brief explanation over DPPC will be presented, remarking only its phase state under given experimental conditions and its response against potential variations. On the other hand, MGDG and DGDG will be extensively explained including its functions in the thylakoid membrane, physical states and human applications.

3.3.1 DPPC

Dipalmitoylphosphatidylcholine (DPPC) is a phospholipid consisting of two saturated dipalmitoyl chains and a choline headgroup (Figure 3.3). The headgroup is zwitterionic so it should be uncharged at neutral pH but it is slightly negative charged in solution due to the orientation of the headgroup around the headgroup|water interface [49]. The amphiphilic nature of phospholipids allows the formation of monolayers and bilayers and also more complex structures such H_{II}, non-lamellar and cuboidal phases [66]. On the other hand, it has been observed that the stearic and palmitic acid are the major saturated fatty acid in mammalian phospholipids [67].

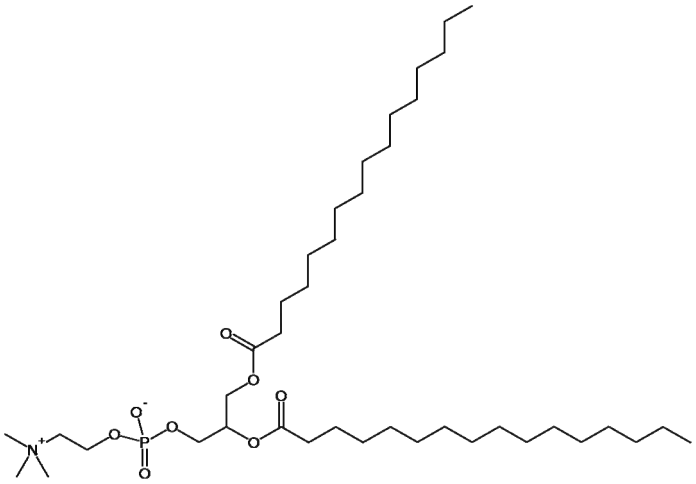

Figure 3.3. Scheme of a DPPC molecule

3.3.1.1 DPPC physical states

The π -A isotherm of DPPC at 20ºC present LE phase until $\pi \approx 6$ mN·m^{-1} where the LE-LC phase transition starts, and at $\pi > 20$ mN·m^{-1} the DPPC monolayer is in LC phase, presenting a limiting area of ≈ 54 Å^2·molec^{-1} [68-70]. On the other hand, DPPC bilayers formed by vesicle fusion present L_β phase at 22ºC on mica, and this L_β expands as the temperature is raised until the phase transition. The L_β-L_α phase transition for the top leaflet starts at 45ºC and finishes at 51ºC and the L_β-L_α phase transition for the bottom leaflet starts at 52ºC and finish at 59ºC. Cooling from the L_α phase, the L_β phase is recovered more compact than at the same temperature prior the heating, which is related with a better rearrangement of phospholipids due to the temperature effect. Moreover, in this situation, the number of holes is smaller than prior the heating but their size is larger [43]. The

presence of the mica substrate changes and broadens the L_β-L_α phase transition compared with the phase transition temperature of 41ºC [12,71] observed in liposomes.

The height of a DPPC bilayer has been widely reported in mica, presenting two different sets of values 4.7± 0.3 nm [12,72,73] and 5.6 ± 0.3 [18,74,75]. These differences may be provoked by the bilayer forming method or other factors like the size and charge of the present ions. It has also been observed that vesicle fusion forms bilayers with a thickness 0.5-1.0 nm smaller than the LB-LS technique [37]. On the other hand, the presence of positive cations, which enter in the phospholipid headgroup region, renders a z-potential closer to zero than in cation-free solutions, even achieving positive surface charged liposomes when using divalent cations as Ca^{2+}or Mg^{2+} [49].

3.3.1.2 Bilayer response to potential variations

The Lipkowski group has investigated how the polar headgroup region of dimyristoylphosphatidylcholine (DMPC) molecules reorients under the influence of the electrode potential. DMPC has the same headgroup and has the same hydrocarbon chain, with only two carbons less than DPPC, so the results obtained by Lipkowski [52] group can be extended to the DPPC molecules that we use in our experiments.

A DMPC bilayer at the gold electrode, without applying potential, is in the ripple phase (P_β). It has the acyl chains predominantly in trans conformation and it has a small fraction of the chains melted. In the potential range -1 < E < -0.4 V vs. Ag/AgCl the bilayer is detached from the gold surface and it is more ordered than when is attached. In this situation, the bilayer has a tilt angle of ≈ 35°, which is the same angle as the observed for hydrated multibilayers of DMPC in the L_α state and is somewhat higher than the angle of 28° determined for a dry film of DMPC deposited on a CaF_2 surface at room temperature [52]. Moreover, this tilt angle also agrees with the value of 29°-33° for thin hydrated films of DPPC reported by Fringeli [76]. Apparently, the disorder introduced by the adsorption of the bilayer at the substrate surface is very small in comparison to the disorder induced by the thermal melting of the chains. When E > -0.4 V, the tilt angle is ≈ 55° and the DMPC molecules are much hydrated than when the angle is ≈ 35°, accordingly with the change in

packing of the polar heads explained in Section 3.2.2.1. On the other hand, in the region between -0.4 V and 0.1 V no appreciable tilt angle change is observed [37,52].

3.3.2 MGDG and DGDG

In this section, monogalactosyldiacylglycerol (MGDG) and digalactosyldiacylglycerol (DGDG) features will be widely explained.

3.3.2.1 MGDG and DGDG occurrence in thylakoid membranes

The thylakoid membrane (See Section 3.1.1) of chloroplasts of oxygenic organisms is the site where the photochemical and electron transport reactions of photosynthesis take place. This thylakoid membrane is constituted by a lipid matrix that avoids the free diffusion of ions, maintains the fluidity of the membrane and allows an electrochemical potential difference across this membrane which is required for ATP synthase [77].

The 70% of the thylakoid membrane area is occupied by proteins and the rest is mainly constituted by lipids. The thylakoid membrane harbours the protein complexes of the oxygenic photosynthetic machinery [78]. The lipid content of the thylakoid matrix depends on the specie and the external conditions. However, it can be agreed that the typical organism is composed by the following lipids: MGDG (≈ 50%), DGDG (≈ 30%), sulfoquinovosyldiacylglycerol (SQDG) (≈ 5-10%) and phosphatidylglycerol (PG) (≈ 5-10%) [78] and small amounts of other lipids [80,81]. The main difference from one organism to another is not the lipid composition; it is the unsaturation degree in the acyl chains being higher plants polyunsaturated and microorganisms monounsaturated or fully saturated [82].

The non-photosynthetic membranes are principally composed by phosphoglycerolipids. The different composition of photosynthetic membranes compared with non-photosynthetic membranes may be correlated with the less difficult pathway to obtain the sugar for the former compared with the phosphate for the later [80].

The balance in the protein:lipid ratio permits maintaining the structure and fluidity for an effective photosynthesis. A high protein:lipid ratio, will complicate the lateral movement within the membrane, whereas a low protein:lipid ratio will destabilize the photosynthetic

machinery [83]. In consequence, thylakoid membranes of photosynthetic organisms increases the ratio of non-bilayer/bilayer forming lipids (see Section 3.3.2.3) and the unsaturation degree to adapt the fluidity and the related functions to the lower external temperature or to an increase of the protein:lipid ratio that can occur during greening [33, [84,86]. The increase of the membrane fluidity, involves an increase of the membrane permeability, which is correlated with an increase in the leakage of ions and small molecules, and finally, the loss of proton motive force for ATP synthesis and membrane transport [84]. On the other hand, the reduction of fluidity involves the reduction of the lateral mobility of the electron shuttle molecule (plastoquinone), so slowering the electron transport and enhancing the possibility of photodamage by accumulation of electrons at the acceptor side of PSII [83].

MGDG (Figure 3.4A) is a lipid which has a headgroup of 1-β-galactose linked to the diacylglycerol, whereas DGDG (Figure 3.4B) has the same structure than MGDG but the headgroup structure of DGDG has a terminal α-galactose (1→6) linked to the inner β-galactose. Both glycolipids have two acyl groups esterified at the sn−1 and sn−2 positions of the glycerol moiety and the polar headgroup at the sn−3 position [77, 80]. The molecular motion of both galactolipids depends on the number of unsaturations in the alkyl chains [78] which is determined by the fatty acid desaturase enzymes activity [85].

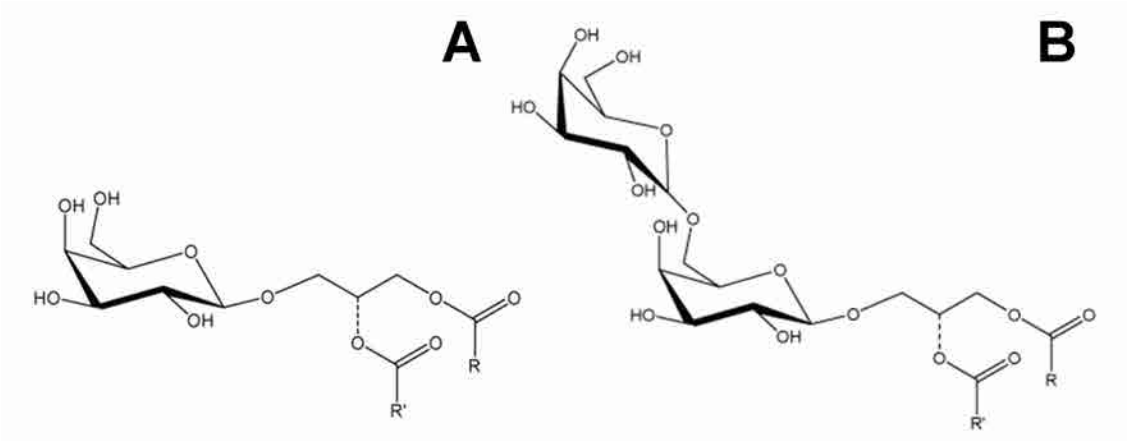

Figure 3.4. Scheme of a molecule of (A) MGDG and (B) DGDG.

3.3.2.2 MGDG and DGDG functions in thylakoid membranes

The lipids present in thylakoid membranes can be classified in three groups depending on their function on the membrane. First, lipids that forms the lipid bilayer matrix; second, lipids that surround the protein-cofactor supercomplexes and interact with the outer surface of the complexes, and finally, integral lipids that are embedded in protein-cofactor supercomplexes. Second and third group are important for the structure and function of the photosynthetic complexes [33,77,87-89]. On the other hand, it is worth to point that the 60% of the thylakoid lipids are bound to photosynthetic multi-subunit complexes [80].

MGDG and DGDG are present in all the three groups, and in addition, their content is involved in the targeting of proteins to and within the chloroplast and in the generation of lipid signaling molecules [90]. Moreover, the presence of both lipids is essenthial for the development of thylakoid membranes and the stabilization of the phostosynthetic proteins [77] although DGDG is not an essential component for the cell growth [91,92]. DGDG binds extrinsic proteins that stabilizes the oxygen evolving complex and stimulate the oxygen evolution in PSII core complex which induce changes in the protein structure [93,94]. DGDG deficiency restricts intersystem electron transport [77,81,91]. On the other hand, DGDG is also important for the function of light harvesting complex II [80,95]. More information about the role of MGDG is still not possible due to the hindrances on preparing a mutant with only lacking MGDG [77].

DGDG headgroups face the luminal side of the PSII complex being very important for its structure [77,91]. On the other hand, it has been observed that MGDG has no direct influence in the PSII activity [77]. SQDG molecule is located close to the PQ-PQH_2 exchange cavity forming a gate with MGDG and PQ to seal the cavity [77].

MGDG is assembled in the inner envelope of the membranes and is exported to the thylakoid membrane [96], whereas DGDG is naturally synthesized by dismutation of two MGDG molecules thanks to the DGDG synthase localized in the outer envelope [97]. It is interesting to point that DGDG has not been found outside of organisms with oxygenic photosynthesis [98]. For more detailed biosynthesis information of thylakoid lipids the reader is addressed to the following articles [99, 100].

3.3.2.3 MGDG and DGDG physical states

The outer envelope of chloroplast is principally composed by bilayer-forming lipids such as DGDG and phosphatidylcholines, being this zone relatively permeable [101]. On the other hand, the inner envelope is composed of non-bilayer forming lipids such as MGDG and phosphatidylethanolamine (PE). The cone shape of MGDG, with a galactose at the tip and the two fatty acyl chains oriented towards the base of the cone, leads to H_{II} regions, whereas the cylindrically shaped DGDG, SQDG, PG and PC forms convex structures in aqueous environments [81,102].

The balance between the bilayer and non-bilayer forming lipids is basic for the flexibility and stability of the photosynthetic pigment–protein complexes and therefore for the membrane function [80,103].

MGDG

In the liquid-crystalline state, unsaturated MGDG forms a mesophase in aqueous solution, in which molecules aggregate in inverted rod-like structures of infinite length in hexagonal arrays which is called hexagonal type-II (H_{II}) structure with the polar head groups facing towards the centre of micellar or tube-like structures. On the other hand, the saturated MGDG forms sheet-like (lamellar) bilayers in the same conditions [104,108]. Gounaris et al. [44] found that 0.5 double bonds per molecule of MGDG induce the conversion of lamellar phase to H_{II} structure. Moreover, increasing the unsaturations degree, the transition temperature of the lamellar phase to H_{II} is decreased [33].

In lipids like MGDG, the presence of double bonds displaces the control for the molecules order from the hydrophobic interactions between lipid chains to be leaded by the stabilization of the headgroups [82,90]. It has been observed that the introduction of the first unsaturation in a saturated lipid influences in a high extent the compact packing, but the introduction of the subsequent unsaturations does not decrease the packing in a proportionate mode [82].

L_β phase of saturated MGDG is metastable at 20ºC when formed by cooling from the L_α. The chains are arranged in hexagonal packing, but the heads present two spacings. After some minutes, the phase undergoes spontaneously to L_c in which the chains pack on orthorhombic subcell and the heads occupy a hexagonal spacing. The rearrangement of the

chains into a more closely packed subcell is produced thanks to the reorientation of the heads to reduce the steric hindrance [109]. On the other hand, the fully hydrated and unsaturated MGDG forms H_{II} phase, which after cooling undergoes liquid-crystalline state through cubic phase as intermediate. The reduction of the water content favours a direct transition from the lamellar to the H_{II} phase [110].

The transition temperature of the lipids depends on the molecule factors like the charge and hydration of the headgroup and the unsaturations and length of the acyl chains. Moreover, external factors also influence such as water content, temperature, pH, ionic strength, solutes and H-bonding between lipid molecules [110]. The saturated MGDG presents L_β to L_α at ≈ 80ºC [111]. On the other hand, unsaturated and hydrated MGDG forms nonlamellar structures such as cubic or H_{II} phase over a wide range of temperature (≈ -15°C to 80°C). The L_β to H_{II} transition for unsaturated MGDG with similar unsaturation degree has been studied in several conditions, being ≈ 32ºC in pure aqueous solution [112], ≈ 29ºC in aqueous buffered solution [113] and ≈ 84ºC in dry samples [110].

The ability of unsaturated MGDG to form non-lamellar structures like H_{II} can be neutralized when mixing it with at least 50% of bilayer forming lipids [101,103,110], although unsaturated MGDG induces regions of deformation in the lamellar structure of MGDG:bilayer forming lipid when the presence of unsaturated MGDG is between 20 and 50 mol%. Conversely, the H_{II} structure can be favoured by dehydration, either through the removal of water or the addition of electrolytes [110].

DGDG

Conversely to MGDG, DGDG forms lamellar sheets and liposomes in the liquid-crystalline state in aqueous solution regardless the saturation degree [101,104,106]. The cone shape of MGDG permits the formation of more curved zones so favouring smaller liposomes than DGDG which form larger liposomes with larger trapped volume [101]. The saturated DGDG presents L_β to L_α transition at ≈ 55ºC [111].

A fully hydrated DGDG bilayer in lamellar phase has a height of ≈ 5.5 nm which can decrease up to 4.5 nm when reducing the hydration level [90].

3.3.2.4 Glycolipids applications

Glycolipids show several biological activities and they have been proposed as anti-algal, anti-viral, anti-tumor and anti-inflamatory agents. Moreover, it has been studied their influence in immunosuppressive, inhibition or promotion activity of the cell growth and their applications as mammalian DNA polymerase inhibitor [114].

MGDG, DGDG and SQDG have potential anticancer functions due to the DNA polymerase inhibition, suppression of cancer cell proliferation, anti-angiogenesis and anti-tumor promotion properties [115,116,117]. Indeed, glycolipid fraction of spinach has been shown that has anti-tumor activity with oral administration in colon tumor in mice. Moreover, it has been observed that the hydrolized form of biological glycolipids, especially hydrolized MGDG and hydrolized SQDG, has more anti-tumor activity than the non-hydrolized form [115].

DGDG and especially MGDG have an important anti-inflamatory activity which is reduced when increasing the saturation degree [114]. On the other hand, DGDG has been proposed for controlling the appetite [118].

3.4. Biological electron and proton shuttles

3.4.1 Quinones

Quinones are components of the plasma membrane redox system and they are involved in: proton and electron shuttle, ion and metabolite transport, regulation of gene expression, transmembrane signalling, and membrane defence [119,120]. Moreover, the quinol form has an antioxidant property preventing lipid peroxidation and other effects of reactive oxygen species on membrane components [120].

Several quinones have been used as anti-tumor, anti-biotic, anti-microbial and anti-infection agents [121-123]. Additionally, quinones have been used such as dyes, as oxidizing and reducing agent in industry and as reactive for chemical synthesis [122].

Prenylquinones such UQ and PQ (Figure 3.5) are components of the biological membranes being present in a 1-5% [124] and they play an important role in bioenergetic processes, so they will be explained in the following sections.

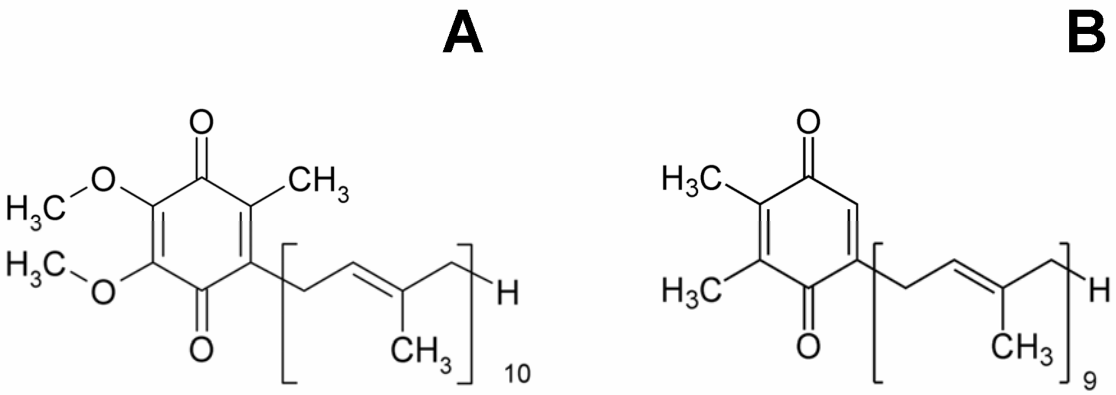

Figure 3.5. Scheme of a molecule of (A) UQ-10 and (B) PQ-9.

3.4.1.1 Ubiquinones

Ubiquinones act as a proton and electron transporter in the respiratory chain of the inner mitochondrial membranes [17,125]. It has been proposed that ubiquinones are present in biological membranes in two forms, first, associated with electron-transport complexes and the second, in a pool containing an unbound form [126]. The interaction between proteins and quinones provoke the quinones redox potential adjustment in biological membranes compared with artificial membranes [127].

In this Ph.D. Thesis, when not specified, UQ refers to ubiquinone-10 which is the most extended. The number of isoprenoid units (n) in the prenyl tail of ubiquinone homologues (UQ-n) depends on the specie. Mammals, including humans, have mainly UQ-10 and in a minor extent UQ-9, whereas invertebrates and bacteria can present UQ-8, UQ-9 and UQ-10 and finally, fungi shows a wide range from UQ-6 to UQ-10 [120]. On the other hand, the presence in higher plants mitochondria is mainly UQ-10 and UQ-9 whereas for lower plants, UQ-8 and UQ-7 is also found [120].

It is well-known the bioenergetic relevance of ubiquinone homologues, especially their function as antioxidant and free radical scavenger [128-130]. In this line, it has been concluded that ubiquinol regenerates vitamin E and C and it protects the membrane lipids against peroxidation [131,132]. An indirect antioxidant function of ubiquinones derivatives is the cytotoxic properties of certain ubiquinones that make them useful anti-cancer and anti-bacterial drugs [17]. Although UQ-10 is the human ubiquinone homologue, some short-chain analogues have a greater medical efficiency suggesting that the biological action of ubiquinone could depend on their lateral chain length and the redox properties of the quinone ring [17,133]. Ubiquinone has been proposed for treatment of several pathologies like cardiovascular diseases, myopathies, and age related degenerative diseases [133]. Conversely, ubiquinone can also act as prooxidant due to the reaction of the semiquinone radical with O_2 produces the superoxide radical [134].

Other studies shows that ubiquinone and its homologues are involved in redox homeostasis and act as a regulator of calcium cations in mitochondria [135] and as divalent cations modulator across biomimetic membrane [136]. In addition some studies point that ubiquinone and its homologues are involved in the control of cell growth and apoptosis [133,137].

UQ-10 is naturally synthesized in humans, but its effects as diet supplement and beauty product component require additional industry production. For this finality, UQ-10 is obtained using microbes that naturally produces it [138].

3.4.1.2 Plastoquinones

Plastoquinone is the main electron and proton carrier in the thylakoid membrane and it also has an antioxidant function in biological membranes [120,139]. Plastoquinone is involved in several phostosynthetic responses, such regulation of state-transition, chlorophyll biosynthesis, light-harvesting complex polypeptide accumulation, rate of photosystem protein synthesis, sensor of unbalanced electron transport and the balance of photosystem stoichiometry [139]. Additionally, plastoquinol is used as oxygen scavenger in PSII. However, the presence of excessive plastoquinol produces a regulation of the Calvin cycle and an increase of the thylakoid pH [139].

Plastoquinone pools in biological membranes may suffer a thermoinduced change of the redox state of the plastoquinone pool and a redistribution of the plastoquinone molecules between photoactive and non-photoactive pools to regulate the membrane response towards external weather conditions changes [139].

The plastoquinone tail length depends on the specie and is represented by PQ-n, being the plastoquinone-9 (PQ) the most extended. On the other hand, in the photosynthetic chain three different PQ molecules can be found. The first is PQ_A, which is fixed to PSII. PQ_A delivers electrons to the mobile PQ_B which accepts two electron-two proton and it is reduced to PQ_BH_2, then PQ_BH_2 diffuses towards cytochrome b_6f and the PQ_B is replaced by another PQ_B from the PQ pool [140]. It has been identified a third PQ molecule (PQ_C) which is not clear its function [78]. The three PQ types found are the same molecule, although the different location and environment confer each one different physico-chemical properties, like the redox potential of PQ_B which is 80 mV higher than PQ_A and allows the electron flow from PQ_A to PQ_B [141].

3.4.2 Position of UQ or PQ molecules in the biomimetic membrane

After more than thirty years of studying the position of the UQ in the lipid matrix of a bilayer, there is consensus about that UQ has two main positions in a lipid layer [142], which are called by Söderhäl and Laaksonen [143] as “diving quinone” and “swimming quinone”. The positions concluded for UQ should be also applicable, with slight differences, to PQ due to their similar size and shape. These positions are experimentally studied in Chapter 5 especially for PQ that it has been very little studied in the literature.

On the other hand, the approximated dimensions of both molecules heads are 7 Å width and 4 Å depth, having the main difference in the total length which is 37 Å for UQ and 34 Å for PQ.

DMPC and DPPC have been used for preparing SPBs inserting UQ to model the UQ positions in the bilayer. The reason is that the thickness (30 Å) of the hydrophobic midplain of the bilayer formed by these lipids corresponds to the length of the isoprenyl side chain of both prenylquinones [144].

Most of the studies performed in the literature for preparing biomimetic membranes inserting UQ involve bilayers. However, we mainly use monolayers due to the high control over the membrane structure that the LB technique confers. In addition, we consider that the positions and processes that take place in the lower leaflet of the bilayer are comparable with those that take place in the LB monolayer. Therefore, we explain in the following sections the studies of biomimetic membranes containing UQ regardless being mono- or bilayer. The reader is addressed to Section 2.1.3 where the differences that UQ can experience according to being inserted in a mono- or bilayer are presented. The Figure 3.6 represents schematically the two main positions that UQ can adopt in a biomimetic membrane. On the one hand the “diving” quinone with or without contact with substrate surface. The contact position is only favoured when using the LB technique and at low surface pressures. On the other hand, it presents the “swimming” position.

3.4.2.1 Diving quinone

Diving quinone (Figure 3.6) is characterized by an inflexion point in the hydrocarbon tail of the UQ which separates the UQ molecules in the head plus part of the tail (HPT) and the last part of the tail (LPT). HPT is placed in parallel to the lipid chains, inserted between them whereas LPT is free to move. LPT can adopt two configurations, first, perpendicular to the lipid chains, and second, inserted in parallel between the lipid chains of the opposite leaflet where the HPT is. This second position of LPT, although it may seem unfavoured, is stable due to the similar properties between the UQ tail and the lipid chains, and so that, it is soluble in this region [143].

Söderhäl and Laaksonen [143] simulations suggest that the UQ headgroup, in the lamellar state of the SPB, is placed between the 3rd and the 6th carbon atom of the lipid chain counted from the carbonyl carbon, which is consistent with the previous studies of Aranda et al. [145].

The kink point arises due to the difference between the length of the lipid chain [146] and the hydrocarbon tail of UQ. The end part of the UQ tail will not be stable in the lipid head region, so in order to accommodate it in the lipid chain region, it must form a kink point in the membrane midplane, where the atomic density is low. It is believed that this kink point causes a local distortion that may facilitate the flip-flop motion of the UQ headgroup [143].
It seems clear that at low UQ content, the major part of this UQ is in the diving quinone position [147-149], achieving in some conditions the “diving” position in direct contact with the substrate (Figure 3.6). The low content has been estimated in the range between 1-10% [150-153] and, further increase in the UQ content leads to the deposition of UQ in the midplane [150]. The quantity considered low UQ content will depend on the lipid nature, especially on its chain length, since the shorter the chain length is, the easier for UQ to place close to the lipid head [124].

The position corresponding to “diving quinone” has been proposed using several techniques. Aranda and Gomez-Fernandez using differential scanning calorimetry (DSC) [145], Katsikas and Quinn using fluorescence, DSC and wide angle X-ray diffraction analysis [154,155], Ondarroa and Quinn using difference infrared-spectroscopy [156], M. Jemiola-Rzeminska et al. [150] using fluorescence anisotropy techniques, Lenaz et al. using fluorescence quenching [142], Afri et al. using NMR chemical shift-polarity correlation [154], Stidham et al. [151] using ^{13}C NMR studies on phosphatidylcholine-UQ liposomes, Samori et al. using linear dichroism [158], Quinn and Esfahani using surface-pressure isotherms [148] and, Moncelli et al. [149] and Hoyo et al. [159] using voltammetric techniques.

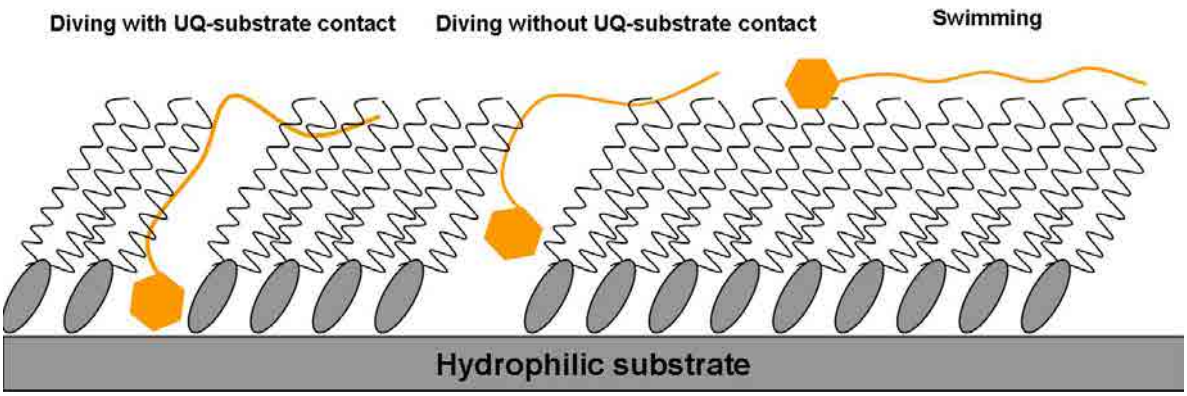

Figure 3.6. Scheme of the UQ organization in the lipid matrix of a biomimetic membrane.

UQ-UQH_2

The polarity difference between UQ and UQH_2 [160] leads the later to form more stable pure monolayers [148]. In the case of lipid-quinol monolayers, it occurs a deeper and more stable insertion in the lipid chain region placing closer to the lipid heads [144,145,147, 152,161,163], interacting with the lipid chains in a wide range of temperature, including after phase change [124]. In this situation, two interactions have been proposed. First, UQH_2 heads interact and aggregate themselves to minimize the effect of the hydrophobic environment of the chain region [161], in the same way that UQ does but with the difference that the UQ aggregates are not so much stabilized to those of UQH_2 [124]. Second, UQH_2 ring forms hydrogen bonds with the water shell of the lipid heads [153].

Although the deeper position of UQH_2 than UQ is clear, the effects of this position in the lipid order has not consensous. On the one hand, Ausili et al. [124] concluded, using DSC, infrared spectroscopy and NMR, that UQH_2 produced more disorder effect than UQ. On the other hand, Skowronek et al. [164] concluded, using fluorescence anisotropy, that the UQ disorders the lipid region in much extent than UQH_2.

3.4.2.2 Swimming quinone

“Swimming” position is characterized by the flexible hydrocarbon tail of UQ which moves randomly on the midplane and the corresponding UQ head can move a maximum of ≈ 1 nm in the lipid chains of both sides of the bilayer [143].

The “swimming” position (Figure 3.6) is more stable than the “diving” position due to, in the later, the cooperative motions between the lipid chains are disrupted by the intrusion of the UQ hydrocarbon tail. This disruption occurs especially at ordered physical states [165], at which the UQ will be more heterogeneously distributed and it will have less mobile freedom [163]. Moreover, the midplane is less molecule crowded and it has lower viscosity ($2 \cdot 10^{-3}$ Pa·s) than the polar head region (0.1-0.2 Pa·s), so being favoured the UQ position in this midplane [166,168]. The proportion of ubiquinone in the “swimmimg” position is defined by the ubiquinone content in the membrane, the length of the UQ tail and the physical state of the lipid membrane [150].

The “swimming” position has been confirmed using several techniques like fluorescence quenching, [169], voltammetric techniques [167], performing surface-pressure isotherms [142,148] NMR [142,152,170-174], differential infrared spectroscopy [156], DSC [145,155,161,175], neutron diffraction [165] and linear dicroism [158]. The “swimming” quinone position presents controversy in the membrane thickness change. Katsikas and Quinn using X-Ray diffraction [155] observed that tocopherol, which is similar to UQ, thickens the bilayer, whereas Hauss et al. [165] has not observed this effect using neutron diffraction. On the other hand, the UQ or UQH_2 in swimming position may inhibit the proton leakage according to the “water cluster” model proposed by Haines [176], although UQH_2 inhibits in a less extend [161].

3.4.2.3 UQ pools and aggregates

It is generally accepted that a large fraction of UQ segregates within the lipid biomimetic membrane forming lipid rich zones and UQ rich pools [124,145,150,151,164,170,171,177] being enhanced the purity of both enriched zones as the pressure increases in Langmuir monolayers [133]. Chazotte et al. [178] proposed that the quinone pool are located in the midplane region and has the freedom to move within it. The subject which remains unclear is at which UQ content the segregation starts. Cornell et al. [171] concluded this segregation value at 0.02 mol%. Conversely, Moncelli et al. [149] suggested this process occurs at 0.5-2 mol% which is close to the 1-2 mol% proposed by Jemiola-Rzeminska et al. [150] and the 2 mol% suggested by Bilewicz and Majda [179] but far from the 5 mol% proposed by Laval and Majda [177]. Probably, the UQ content for the segregation initialization depends on the physical state of the lipid matrix because the UQ molecules

can be accommodated better between the lipid chains in the fluid state than in the rigid phase, so being the segregation favoured in ordered phases [124,133]. On the other hand, it has been proposed [133] that UQ molecules form constant size UQ-rich microdomains so when increasing the UQ local concentration, the number of microdomains is enlarged remaining the size unchanged.

There is no consensus about the location and physical state (monomer or aggregate) of UQ in lipid membranes, which is correlated with the different lipids, experimental conditions and methods used to prepare the lipid-UQ mixtures [150]. Roche et al. [133] proposed the formation of a disordered UQ-rich phase overlying the monolayer whereas the formation of head to head aggregates has been also proposed in the literature [118,124,150,163,164]. Moreover, it has been suggested that the formation of aggregates difficult their squeezing of the monolayer [124] being the UQ fraction in aggregated state increased proportionally to its concentration [150]. On the other hand, in solvents like hexane, UQ has a very small tendency to aggregate even at relatively high UQ concentrations [160]. In addition, the self-segregation may include the deactivation of the aggregates due to orientation changes in respect to the plane of the monolayer [179] and it may be also involved in the antioxidant function of ubiquinol [124].

3.4.2.4 Ubiquinone molecules with different tail length

Ubiquinones with different tail length (UQ-n isoprenoid units) are located in different positions in the lipid membrane. Short tail ubiquinones arrange in the lipid head zone and depending on the chain length are arranged more or less parallel with the lipid chains [133,143,150], whereas long tail ubiquinones presents the two positions explained in the previous section. It is clear that the balance between the relatively polar headgroup of the ubiquinone and the isoprenoid tail hydrophobicity leads the position of the ubiquinones with different tail length. This behaviour has been concluded using fluorescene anisotropy [164], surface-pressure isotherms [133,148], NMR [152,170,173,174], infrared spectroscopy [180] and DSC [144,155,175].

The position of short chain ubiquinones in lipid-quinone mono- or bilayers has some particularities that must be explained. UQ-3 and UQ-4, which have a similar tail length than the lipid chains, are located in parallel with these lipid chains [150,164]. Moreover,

Jemiola-Rzeminska et al. [150], based on their fluorescence anisotropy studies, suggested that the UQ-4 is located deeper in the membrane than the UQ-2, which can be correlated with the ubiquinone (UQ-4) arrangement in parallel with the lipid chains. These studies also showed that UQ-5 perturbs the lipid matrix in a larger extent than UQ-10, in correlation with the larger part of UQ-5 in parallel to the lipids chains compared to UQ-10. When the lipid mono- or bilayer increases their order, the ubiquinones with three or more isoprenoid units are squeezed out of the layer. This is the case of monolayers after surface compression, in which the surface pressure at which the ubiquinone is expulsed depends on the ubiquinone chain length, presenting the UQ-3 the higher surface pressure [148].

The π-A isotherm behaviour of pure components of UQ-n and UQH_2-n is similar to that of UQ-10 being the collapse pressure increased when reducing the chain length. This observation is valid for chains between three to ten isoprenoid units, whereas UQ-2 and shorter UQ-n do not form stable monolayers because it is partially solved in aqueous subphases [148,167].

3.4.3 Quinone interactions with the lipid matrix

The insertion of UQ in the lipid matrix modifies its order. It has been observed that the presence of UQ in the DPPC matrix broads the DPPC pretransition and the main transition peak which is correlated with a reduced cooperativity between the DPPC chains [161,144]. This effect is larger for UQ-4 than for UQ-10 regardless the redox state, and it is enhanced when increasing the UQ content. These works also concluded that the quinol form influences the main phase transition in a larger extent than the quinone form in the case of UQ-4, whereas this effect is not observed for UQ-10. Additionally, UQ-10/$UQ\text{-}10H_2$ has very little effect on the pretransition peak conversely to it occurs with UQ-4. These observations are related with sterical hindrances of the ordered DPPC matrix. Other explanations like DPPC-UQ complex formation seems little plausible [144] and confirms the different position of the UQ-n homologues in the lipid matrix explained in previous sections [144,161]. On the other hand, Hauss et al. [165] observed that the incorporation of a 5% of UQ in a lipid bilayer has no influence in the bilayer height.

The polarity difference between the QH_2 and Q heads leads the former to better dipole-dipole interactions with phospholipid headgroups, which is translated in a deeper penetration in the lipid matrix. Moreover, the hydroxyl groups in the QH_2 tend to locate near the lipid|water interface where they could form hydrogen bonds with water [144]. Then, the UQH_2, which occupies a slightly smaller surface area than UQ, forms more stable monolayers than UQ thanks to the polar interaction of the quinol with the aqueous subphase [148]. Additionally, the methoxy groups present in UQ seems to establish larger interactions with the polar heads of the lipids than the methyl groups which explains the lower stability of PQ in water compared with UQ [144].

3.4.4 Quinone redox mechanisms

The UQ/UQH_2 redox process has been little studied, but the available data confirms that the similarity between UQ or other quinone derivative with quinone (Q) ring involves a similar mechanism for all quinones due to the hydrocarbon tail or other common constituents present in UQ have not electrochemical response and only produces small shifts in the peaks potentials.

Q/QH_2 process is a rather complex mechanism because the two protons and two electron transfer takes place through several routes depending on the solvent and its characteristics [181]. These routes are synthesized in the “square scheme” (Figure 3.7) proposed by Laviron [182] and extended by Flinklea [183], who proposed a mechanism which allows the electron transfer coefficients to vary with the potential.

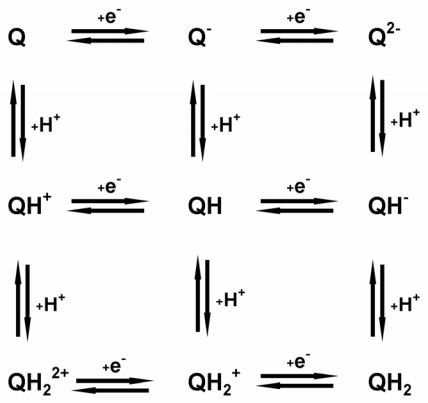

Figure 3.7. Nine-membered scheme for the overall reaction from the quinone to the hydroquinone form and vice-versa.

The reduction of quinones in solution can be classified in three mechanisms based on the nature and characteristics of the environment (Figure 3.8) [122,181] that causes different redox potentials [126], and them will be explained in this section. Moreover, the reduction mechanism of a quinone embedded in a lipid matrix will also be exposed.

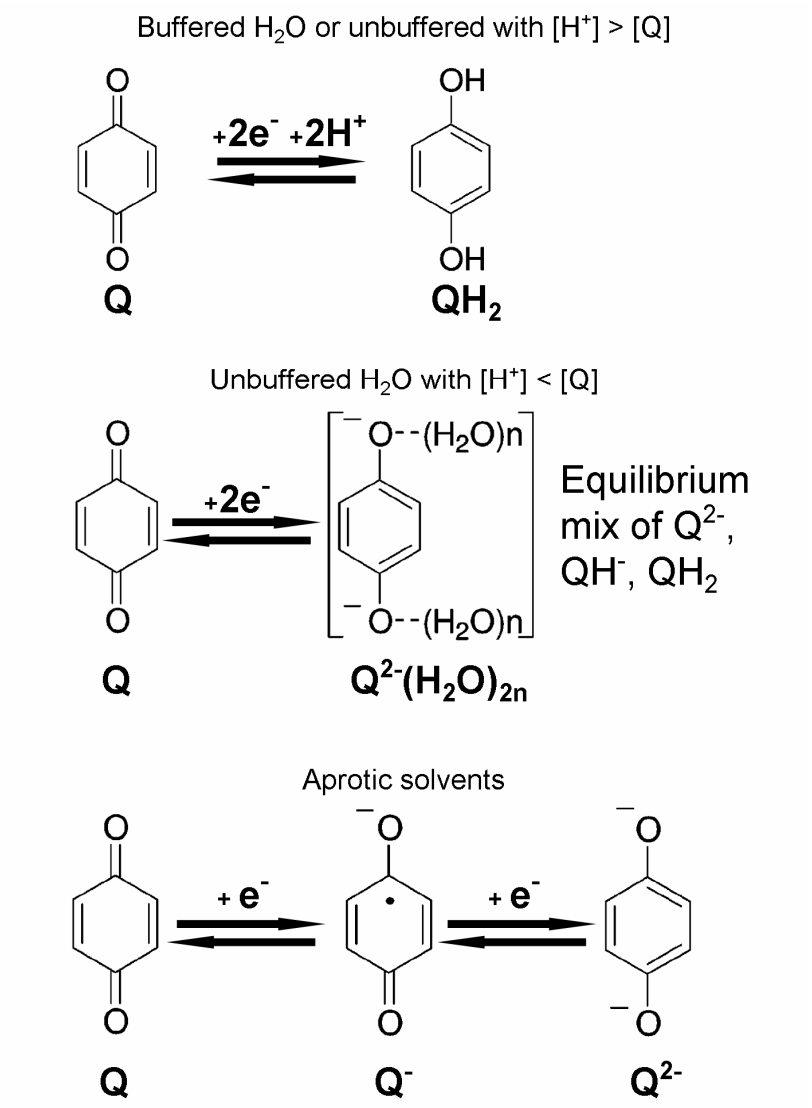

Figure 3.8. Different quinone reduction mechanisms based on the nature and the characteristics of the solvent.

3.4.4.1 Buffered aqueous solution

Q/QH_2 redox process in buffered solutions presents more irreversible character than in unbuffered solutions, increasing the peak-to-peak separation in 300 mV at the same pH conditions, so confirming that buffered and unbuffered solutions leads to a different

mechanism for the couple Q/QH_2. In buffered solution, the reduction wave is placed at more positive potentials indicating that the process is thermodynamically easier. Conversely, the increase in the peak-to-peak separation indicates that the overall process is kinetically much slower than in the unbuffered situation and this behaviour is not dependent on the chemical composition of the buffer [122].

UQ reduction in lipid environment with buffered solution involves $2e^-$ and $2\ H^+$, similar to Q directly on aqueous buffered solution [149,184]. This reduction process is pH dependent, presenting two scenarios (1 and 2) [149,185]. It is worth to expose that UQ is almost entirely uncharged at neutral pH ($pK \approx 9.45$) [148].

$$1 \qquad UQ + 2e^- + 2H^+ \rightarrow UQH_2 \qquad pH < 12$$
$$2 \qquad UQ + 2e^- \rightarrow UQ^{2-} \qquad pH > 12$$

The most common situation is the scenario 1 which has the following mechanism ($1_{a\text{-}c}$), being the process 1_b the rate limiting step [149,185,186] due to the stabilization of the intermediate product UQ·- [187,188] which is suggested to be adsorbed [188].

$$(1_a) \qquad UQ + e^- \rightarrow UQ\cdot^-$$
$$(1_b) \qquad UQ\cdot^- + H^+ \rightarrow UQH\cdot$$
$$(1_c) \qquad UQH\cdot + H^+ + e^- \rightarrow UQH_2$$

The larger widths of the reduction UQ/UQH_2 peaks compared with the expected reduction peaks is attributed to the repulsive interactions between the redox centers and the sequential two electron transfer with similar but no identical formal potentials, which is correlated with the enough stability of the $UQ\cdot^-$ in solution and lipidic environment [187,188]. The behaviour and stability of this radical and the products that can be expected from its oxidation and reduction are strongly dependent on the surrounding conditions, especially on the pH of the solution [189]. On the other hand, the stabilization of UQH· has been suggested to be due to the bonding between the donor and acceptor rings, although, as it occurs with $UQ\cdot^-$, its behaviour is strongly dependent on the experimental conditions, especially on the pH of the solution [190].

The scenario 2 involves a negative charge of mono- or dianion in the quinone, which is concentrated on the oxygens [127]. This scenario has a high degree of reversibility, indicating that the cations requested for neutralize the electric charge of the UQ^{2-} are available in the environment of the dianion [188]. The increase of the surface concentration of UQ leads to a decrease of the standard rate constant of electron transfer, which indicates the presence of intermolecular interactions in the monolayer [185].

In hydroalcoholic solution, ethanol:water (90:10), Li et al. [191] showed that UQ presents a slight shift of the formal potential towards more negative potentials than UQ-0 which is correlated with the UQ isoprenoid chain electron donating group which makes UQ more difficult to reduce. However, the overall UQ/UQH_2 process is diffusion controlled in these hydroalcoholic conditions. On the other hand, the current ratio between the cathodic and the anodic peak of UQ-n in this hydroalcoholic solution is greater than the unity which is correlated with the unstability of the UQH· [191].

3.4.4.2 Unbuffered aqueous solution

The mechanism through the UQ is reduced to UQH_2 is pH dependent, as it has been explained. In absence of buffer, the reduction of UQ produces a local increase of the pH [122,192] in the electrode surroundings. In consequence, as the protons are part of the overall redox process, the redox potential is pH dependent and it moves to more negative potentials as the pH increases.

In the situation at which the concentration of protons is larger than that of the quinone, only one wave is observed, being this process quasi-reversible and similar to the buffered solution situation. In the described situation, an increase of the pH involves that the reduction peak moves to more negative potentials whereas the oxidation peak is quite stable [122].

In the case that the concentration of protons and quinone is similar, the voltammogram in unbuffered aqueous solution shows two reduction waves. The reduction wave at more positive potential is correlated with the $2e^-$, $2H^+$ step, similar to the scenario 1 presented, although the peak potential has been displaced anodically respectively the peak potential for low pH. On the other hand, the reduction wave at more negative potentials has more

interpretations in the literature. One is that this second peak is also related with scenario 1, but in this case, the proton donors are water or UQH^- [122]. Other authors suggest that this second wave corresponds to the production of a UQ radical anion [192] or dianion [192,194] due to the high pH provide no enough protons surrounding the quinone to produce the step UQ/UQH_2 [122].

Further pH increase makes disappear the more positive reduction and oxidation peaks and only the one reduction, one oxidation wave is observed. This situation is correlated with the fact that the E$^{o'}$ of Q/Q^- and Q^-/Q^{2-} are very close in water solution, which means that the Q^{2-} is more stable than Q^-. This stabilization is based on the larger dielectric constant and larger polarity character of water compared with aprotic solvents. Moreover, the water hydrogen bonding capacity plays and important role. This stabilization is not produced in aprotic solvents where Q/Q^- and Q^-/Q^{2-} are seen in separated peaks [122].

In neutral water with unbuffered conditions, the Q/QH_2 process is similar to the process occurred in buffered solution, whereas the QH_2/Q process presents a chemically and electrochemically irreversible oxidation indicating that the QH_2 is not the product of Q at these conditions [122]. However, in buffered and unbuffered neutral conditions, the process involves $2e^-$ indicating that, at neutral pH aqueous solution, the reactant of the overall reaction is Q [122].

3.4.4.3 Aprotic solution

The electrochemical behaviour of UQ has been studied in aprotic solutions [195], although its conclusions can rarely be applied to UQ in lipidic environment due to water and its dissociation products also participate in the intermediate chemical steps [126,186].

However, based on the above idea, some authors have used organic solvents to mimic the non-polar environment of natural cell membranes, which is expected to be different than that of the aqueous solution. Ubiquinones in a dry aprotic media, like other quinones, present the scenario 2 where the process 2a $Q/Q^{\cdot -}$ is reversible and the process 2b $Q^{\cdot -}/Q^{2-}$ is quasi-reversible [196], showing each step a different peak.

$$(2a) \quad Q + e^- \rightarrow Q^{\cdot -}$$

$$(2b) \quad Q^{\cdot -} + e^- \rightarrow Q^{2-}$$

The ratio of cathodic peak current to the anodic peak current for process 2a is close to the unity, and for process 2b is ≈ 0.9, confirming the Gupta and Linschitz [196] conclusions [17]. The height of the peak of process 2b is shorter than that of the process (2a), which suggests that chemical reactions take place during process 2b [17].

The processes are diffusion controlled, but the negligible change in the voltammogram shape at high scan rates suggest that no complex mass transport involving trapped solution and linear diffusion, are present [17]. Another factor that must be considered is the access of counter-ions into the bilayer to compensate the charge of Q^{2-} [177].

3.4.4.4 Aprotic solution with water added

The addition of water to the aprotic solvent produces a cathodic shift of the $E^{o'}_{(Q-/Q2)}$ and $E^{o'}_{Q/Q-}$ being larger this shift for the process $E^{o'}_{(Q-/Q2-)}$ which is correlated with a larger effect of the hydrogen bonding [122,196]. Based on three lone pairs on each oxygen atom, the dianion can stablish at least six hydrogen bonds with a strong-to-moderate strength, whereas for Q^{-}, the number of possible hydrogen bonds is diminished. The difference in the shift extent makes both potentials to be closer than in pure aprotic medium. An additional source of Q^{2-} stabilization, only at given aprotic solvents, is the larger dielectric constant and polarity of water compared with the aprotic solvent [122].

Quan et al. [122] concluded that the main difference between the quinone electrochemical behaviour in polar-aprotic solvent and water is the hydrogen bonding, not the proton transfer.

3.4.5 Quinone electron transfer in lipid biomimetic membranes

It is generally considered that the lipid membrane features such polar head group, tail length, phase state, charge, etc., affects the electron transfer reaction for the quinone/quinol redox couple. Regarding to the lipid tail length, it has been concluded that decreasing the lipid chain length or increasing the headgroup flexibility, the electron-transfer reaction is increased [197]. In this line, Suemori et al. [198] using phospholipid-linked naphthoquinones separated by spacer methylene groups with different length, and using

buffered solution as electrolyte, showed that the electrochemistry of such system is under conditions in which diffusion of charge occurs during the voltammetric scan.

The change in the membrane resistivity with the potential evidences the establishment of a transmembrane electronic equilibrium in aqueous solution. In solvents with very low polarizability no free charges can be present, like the case of hydrocarbons chains region. In these solvents, the two-phase redox equilibrium must always involve an electroneutral ionic combination, even if the considered redox reaction involves the transfer of the proton or of any other ion to give an ion pair or an un-ionized compound in the organic phase. Bilewicz et al. discarded the participation of UQ in the reduction of $Ru(NH_3)_6^{3+}$ in a lipid-UQ monolayer due to the ≈ 200 mV anodically shift of the UQ in comparison with $Ru(NH_3)_6^{3+}$. Moreover, the UQ function as “molecular wire” in electron tunneling between $Ru(NH_3)_6^{3+}$ and the electrode surface was also discarded [179]. In consequence, Bilewicz et al. [179,199] proposed that UQ opens an access to the electrode surface by creating a channel, so UQ acts as a size selective gate molecule. This behaviour can be correlated with the channels formed by the lipids of biological membranes to allow the fast PQ/PQH_2 exchange [87,190].

Marchal et al. [181] showed that the redox behaviour of UQ and PQ is quite similar in a lipidic SAM and the redox processes for both are diffusion controlled. The reduction of both biological quinones in artificial biomimetic membrane is distorted due to the hydrogen evolution overlaps the reduction process [162].

The reproducibility of the behaviour of UQ in lipid layers is high when the UQ content is up to 2-3%, depending on the technique used to study them [149,167,186]. It has been estimated that 6% of UQ is sufficient to provide full surface coverage of each monolayer for the total lipids of the bilayer [165]. On the other hand, the maximum incorporation for UQ in liposomes was proposed at 2 mol% [152] and 5 mol% [151], Jemiota-Rzeminska et al. prepared vesicles with 12 mol% of UQ or PQ in DPPC [200].

Mechanisms

Electron transfer in a lipid layer can occur through three mechanisms that take place simultaneously although one of them should be dominant. The most common is the direct electron transfer of electroactive species. This mechanism is related with the permeability of the lipid layer and it takes place either if the electroactive specie diffuses or the ions of the electrolyte difuse. Surface layer defects and spatial fluctuations permit channels for ions, small polar molecules and water to reach the substrate surface [48,201]. This mechanism involves the ions penetration and entrapment in the hydrocarbon region thanks to short-time opened cavities produced by the hydrocarbon lateral fluctuations, which depends on the bilayer compactness. Then, the ions diffuse to the substrate, being generally the entrapment the rate-limiting process. In the case of large fluctuations, ions can enter with their hydration shell into the pores, and based on the diffusion step, this hydration shell can be maintained or reduced depending on the energy cost caused by the steric and electrostatic hindrances [65]. This mechanism emerges when the system electrons exchange kinetics is slow due to the lack of the overlap of π-electron orbitals and the delocalization of positive or negative charge added to the neutral species [202]. This mechanism is also applicable to UQ or PQ molecules that can diffuse from its stable position to the substrate surface where the redox processes takes place [150]. The second mechanism is electron tunnelling, which increases its relevance in presence of delocalized electrons along the hydrocarbon chains [64]. The rate of this mechanism decreases exponentially with the film thickness [203]. The third process is electron hopping (Figure 3.9) which consists in a successive electron exchange between the oxidized and reduced form of the redox pair, in which the product (UQH·) of the first electroreduced UQ act as reductor for the UQ beside by the proximity of electronic levels. The electron hopping mechanism is enhanced when increasing the redox molecule concentration [167].

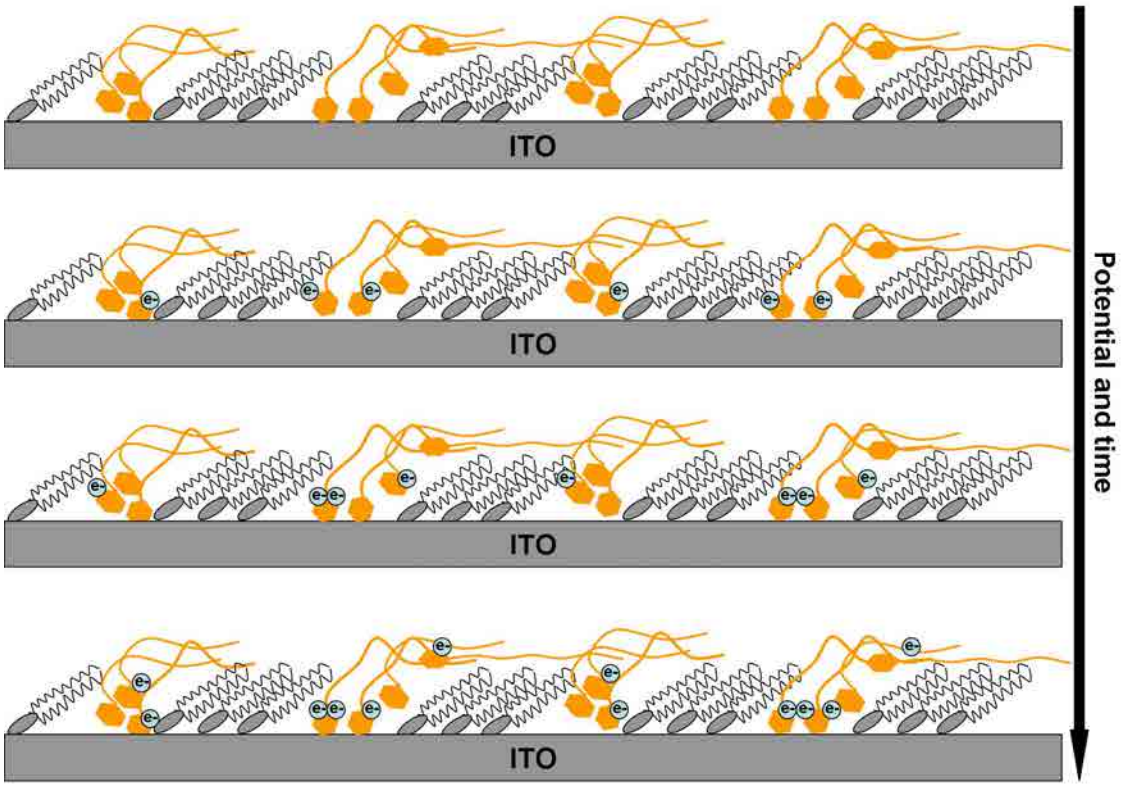

Figure 3.9. Scheme of the electron hopping effect in lipid membranes containing UQ.

3.4.6 Techniques used for preparing confined quinones on conductive substrates and their eletrochemical study.

Confined quinones have been studied using several substrates and methods. Probably, one of the most used is the preparation of SAMs on several substrates. The first approach consists on preparing an alkyl silane SAM inside the tubular microporous of an aluminium oxide substrate. These tubes are open on one side and they are in direct contact with a gold layer on the other side. Then, by vesicle fusion of lipid-UQ or lipid-PQ liposomes, a lipid monolayer is formed on the SAM and the UQ or PQ is placed between the SAM and the lipid monolayer forming a quinone pool [181,204,205]. Another important technique involves an alkanethiol SAM preparation on gold and preparing a lipid-quinone monolayer on the SAM using the LB technique [177], or using the vesicle fusion technique [206].

Other studies consist on preparing a SAM of a conductive polymer film to avoid the ITO roughness and prepare above this SAM a lipid SPB containing a quinone derivative [207]. SAMs can also be prepared to study quinone directly adsorbed to the alkanethiol layer on gold without lipid presence [188,208-212].

Nelson and Benton [213] proposed a method for preparing lipid monolayers in a hanging mercury drop. It consists on spreading a solution of the lipid in a volatile solvent on the surface of an aqueous electrolyte. After solvent evaporation, the hanging mercury drop is immersed in the solution, and a lipid layer is formed. This method was adapted by Moncelli et al. [149,186] to prepare lipid-quinone monolayers in a hanging mercury drop electrode and was also used by Gordillo and Schiffrin to prepare pure UQ monolayers on hanging mercury drop electrode. This technique leads the layer formation with the lipid or quinone chains in direct contact with the mercury surface [185]. This technique has the inconvenience that the amount of lipid and/or quinone deposited is notably in excess with respect to that required for forming a monolayer, and hence multilayers with a poorly defined structure are formed [149].

Finally, other methods employed are the drop casting method with some variants on glassy carbon and ITO [198], carbon electrodes [126] or pyrolitic graphite [214]. Spin coating was

also used by Takehara and Ide to prepare UQ films on glassy carbon [215] and a lipid-quinone vesicle fusion method directly on gold [162].

3.4.7 Relevant processes that experiences PQ and UQ in biological membranes

3.4.7.1 Electron transfer

In biological membranes, the keto-oxygens of the PQ head stablish hydrogen bonds, whose function is rather to control the PQ redox potentials than fixing the PQ orientation in the binding pocket.

The PQ suffers a two-step one-electron transfer reaction, coupled with the uptake of two protons. In the first electron transfer, the anion radical $PQ^{\bullet -}$ is formed, which is stabilized by the protonation of the adjacent amino acid side chains of the membranes proteins. This first electron transfer step is influenced by several factors such pH, temperature and dehydration. The second electron transfer step involves the first proton transfer. After the second protonation, the PQH_2 leaves the PQ_B site (buried inside the PSII, See Section 3.4.1.2) through two possible pathways called channel I and II formed by amino acid residues, phytyl chains of chlorins and fatty acid chains of lipids, building a flexible and hydrophobic environment necessary for the PQ/PQH_2 exchange [78].

3.4.7.2 Diffusion

UQ or PQ molecules in natural membranes act as electron and proton shuttle diffusing between two protein complexes. The quinone diffusion rate and the lipid one depend each other [167,204], the mobility of UQ or PQ in the lipid bilayer depends on several factors that can be classified in two groups. First, the bilayer parameters such local fluidity, physical state and protein crowding. The second group is represented by the quinone parameters like conformation, location and physical state of the quinone pool [167]. Regarding the quinone position, the swimming position presents a faster diffusion due to the lower density and viscosity of the midplain compared with the chain region [143].

The diffusion coefficients of isoprenoid quinones are difficult to measure. Using fluorescence quenching, the diffusion range was stimated in $2 \cdot 10^{-7}$ to 10^{-6} $cm^2 \cdot s^{-1}$

[142,169,216] whereas using fluorescence recovery after photobleaching (FRAP) the diffusion range was 1-5 · 10^{-8} $cm^2 \cdot s^{-1}$ [178,217], and using chronocoulometry, the diffusion coefficient range is 2.0 ± 0.5 · 10^{-8} $cm^2 \cdot s^{-1}$ (at 30°C), being the diffusion rates for UQ, UQH_2, and UQH^- very similar [167]. On the other hand, the diffusion coefficient of the lipids of the biomimetic membrane is two to threefold the observed for quinones homologues [167].

The hydrophobic midplain of the thylakoid membrane in which PQ moves is highly fluid due to the high degree of unsaturation of MGDG [218]. However, the PQ diffusion is slowed by transient binding to slow-moving or immobile quinone-binding proteins, such as PSII or the cytochrome b6f complex, or by trapping in “leaky” microdomains [83,219]. The presence of microdomains prevents long range diffusion [83,219]. Pyrene fluorescence experiments [216] revealed a diffusion coefficient of PQ in pure liposomes of (1-3.5) · 10^{-7} $cm^2 \cdot s^{-1}$ without proteins, whereas the addition of proteins reduces the diffusion coefficient (0.1–3)·10^{-9} $cm^2 \cdot s^{-1}$ [220].

UQ-n and PQ-n homologues with short tail has a diffusion coefficient ≈ 5.0 ·10^{-8} $cm^2 \cdot s^{-1}$ which is more than twofold than for long tailed quinones which is related with the low collisions occurred thanks to the lower molecule size [167]. Moreover, the longer the tail, the slower the electron transfer rate is. The reason is that increasing the hydrophobicity of the quinone, the access of the quinone head to the polar region is hindered [167].

3.5. References of Chapter 3

[1] Taiz, L.; Zeiger, E. Plant physiology. 5th edition. EEUU. California: Sinauer, 2010.

[2] Metzler D.E. et.al. Biochemistry: chemical reactions of living cells, 2nd edition. EEUU, California: Academic press inc., 2003.

[3] Berg, J. M.; Tymoczko, J. L.; Stryer, L. Biochemistry. Freeman and Company: New York, 2007.

[4] Gao, H.; Luo, G.; Feng, J.; Ottova, A.L.; Ti Tien. H. Photoelectric conversion properties of bilayer lipid membranes self-assembled on an ITO substrate. J. Electroanal. Chem. 2001, 496, 158–161.

[5] Berti, D.; Caminatia, G.; Baglioni, P. Functional liposomes and supported lipid bilayers: towards the complexity of biological archetypes. Phys. Chem. Chem. Phys. 2011, 13, 8769–8782.

[6] Ge, C.; Orosz, K.S.; Armstrong, N.R.; Saavedra, S.S. Poly(aniline) nanowires in sol-gel coated ITO: a pH-responsive substrate for planar supported lipid bilayers. ACS Appl Mater Interfaces. 2011, 7, 2677-2685.

[7] Zhan, W.; Jiang, K. A Modular Photocurrent Generation System Based on Phospholipid-Assembled Fullerenes. Langmuir 2008, 24, 13258-13261.

[8] Iglic, A. Advances in Planar Lipid Bilayers and Liposomes; Ed. Elsevier, San Diego, California. vol 13, 2011.

[9] Castellana, E.T.; Cremer P.S. Solid supported lipid bilayers: From biophysical studies to sensor design. Surface Science Reports 2006, 61, 429–444.

[10] Guidelli, R.; Aloisi, G.; Becucci, L.; Dolfi, A.; Moncelli, M.R.; Tadini Buoninsegni, F. New directions and challenges in electrochemistry. Bioelectrochemistry at metal/water interfaces. J. Electroanal. Chem, 2001, 504, 1-28.

[11] Cevc, G.; Marsh, D.. Phospholipid Bilayers. Physical Principles and Models. Wiley-Interscience, New York, 1987.

[12] Leonenko, Z.V.; Finot, E.; Ma, H.; Dahms, T. E. S.; Cramb, D. T. Investigation of Temperature-Induced Phase Transitions in DOPC and DPPC Phospholipid Bilayers Using Temperature-Controlled Scanning Force Microscopy. Biophys J. 2004, 86, 3783–3793.

[13] Schneider, J.; Dufrêne, Y.F.; Barger, W.R. Jr.; Lee G.U.; Atomic force microscope image contrast mechanisms on supported lipid bilayers. Biophys J. 2000, 79, 1107-1118.

[14] Oncins, G.; Picas, L.; Hernández-Borrell, J.; Garcia-Manyes, S.; Sanz, F. Thermal Response of Langmuir-Blodgett Films of Dipalmitoylphosphatidylcholine Studied by Atomic Force Microscopy and Force Spectroscopy. Biophys J. 2007, 93, 2713–2725.

[15] Merino-Montero, S.; Domènech,O.; Montero, M.T.; Hernández-Borrell, J. Preliminary atomic force microscopy study of two-dimensional crystals of lactose permease from Escherichia coli. Biophys. Chem. 2006, 119, 78-83.

[16] Leonenko, Z.V.; Carnini, A.; Cramb, D.T. Supported planar bilayer formation by vesicle fusion: the interaction of phospholipid vesicles with surfaces and the effect of gramicidin on bilayer properties using atomic force microscopy. Biochim. Biophys. Acta 2000, 1509, 131-147.

[17] Ma, W.; Zhou, H.; Ying, Y.L.; Li, D-W.; Chen, G-R.; Long, Y-T.; Chen, H-Y. In situ spectroeletrochemistry and cytotoxic activities of natural ubiquinone analogues. Tetrahedron, 2011, 67, 5990-6000.

[18] Leonenko, Z.V.; Cramb, D.T. Revisiting Lipid-General Anesthetic Interactions (I): Thinned Domain Formation In Supported Planar Bilayers Induced by Halothane and Ethanol. Can. J. Chem. 2004, 82, 1128–1138.

[19] Takamoto, D.Y.; Lipp, M.M.; von Nahmen, A.; Lee, K.Y.; Waring, A.J.; Zasadzinski, J.A. Interaction of lung surfactant proteins with anionic phospholipids. Biophys J. 2001, 81,153-169.

[20] Vié, V.; Van Mau, N.; Chaloin, L.; Lesniewska, E.; Le Grimellec, C.; Heitz, F. Detection of peptide-lipid interactions in mixed monolayers, using isotherms, atomic force microscopy, and fourier transform infrared analyses. Biophys J. 2000, 78, 846–856.

[21] Bally, M.; Bailey, K.; Sugihara, K.; Grieshaber, D.; Vörös, J.; Städler, B. Liposome and lipid bilayer arrays towards biosensing applications. Small. 2010, 22, 2481-2497.

[22] Yin, F; Kafi, A.K.M.; Shin, H-K.; Kwon, Y-S. Human serum albumin–octadecylamine Langmuir–Blodgett film formed by spreading human serum albumin solution directly on subphase's interface covered with a layer of octadecylamine. Thin Solid Films 488, 2005, 223–229.

[23] MirAfzali, Z; DeWitt, D.L. Liposomal reconstitution of monotopic integral membrane proteins. Methods Mol Biol. 2010; 606, 83-94.

[24] Van der Does, C.; de Keyzer, J.; van der Laan, M.; Driessen, A.J. Reconstitution of purified bacterial preprotein translocase in liposomes. Methods Enzymol. 2003, 372, 86-98.

[25] Christensen, S. M. ; Stamou, D. Surface-based lipid vesicle reactor systems: fabrication and applications. Soft Matter, 2007, 3, 828-836.

[26] Michel, M.; Winterhalter, M.; Darbois, L.; Hemmerle, J.; Voegel, J.C.; Schaaf, P.; Ball, V. Giant liposome microreactors for controlled production of calcium phosphate crystals. Langmuir. 2004, 15, 6127-6133.

[27] Tian, B.; Tao, X.; Ren, T.; Weng, Y.; Lin, X.; Zhang, Y.; Tang, X. Polypeptide-based vesicles: formation, properties and application for drug delivery. J. Mater. Chem., 2012, 22, 17404-17414.

[28] Yuan, Z.; Hanks, T.W. A reversible colorimetric and fluorescent polydiacetylene vesicle sensor platform. Polymer 2008, 49, 5023–5026.

[29] Lipkowski, J. Building biomimetic membrane at a gold electrode surface. Phys. Chem. Chem. Phys. 2010, 12, 13874-13887.

[30] Hillebrandt, H.; Wiegand, G.; Tanaka, M.; Sackmann, E. High Electric Resistance Polymer/Lipid Composite Films on Indium-Tin-Oxide Electrodes. Langmuir 1999, 15, 8451-8459.

[31] Hoyo, J.; Guaus, E.; Torrent-Burgues, J. Biomimetic monolayer films of Monogalacto-syldiacylglycerol incorporating Ubiquinone. J. Colloid Interface Sci. 2012, 384, 189–197.

[32] Garcia-Manyes, S.; Redondo-Morata, L.; Oncins, G.; Sanz, F. Nanomechanics of lipid bilayers: heads or tails? J Am Chem Soc. 2010, 132, 12874-12886.

[33] Páli, T.; Garab, G.; Horváth, L.I.; Kóta, Z. Functional significance of the lipid-protein interface in photosynthetic membranes. Cell Mol Life Sci. 2003, 60, 1591-1606.

[34] Meyer H.W.; Semmler, K.; Rettig, W.; Pohle, W.; Ulrich, A.S.; Grage, S.; Selle, C.; Quinn, P.J. Hydration of DMPC and DPPC at 4 degrees ºC produces a novel subgel phase with convex-concave bilayer curvatures. Chem Phys Lipids. 2000, 105, 149-166.

[35] Ciepichal, E.; Jemiola-Rzeminska, M.; Hertel, J.; Swiezewska, E.; Strzalka, K. Configuration of polyisoprenoids affects the permeability and thermotropic properties of phospholipid/polyisoprenoid model membranes. Chem Phys Lipids. 2011 164, 300-306.

[36] Becucci, L.; Scaletti, F.; Guidelli, R. Gel-phase microdomains and lipid rafts in monolayers affect the redox properties of ubiquinone-10. Biophys J. 101, 134-143.

[37] Chen, M.; Li, M.; Brosseau, C.L.; Lipkowski, J. AFM studies of the effect of temperature and electric field on the structure of a DMPC-cholesterol bilayer supported on a Au(111) electrode surface. Langmuir 2009, 25, 1028-1037.

[38] McIntosh, T.J.; Lin, H.; Li,S.; Huang, C. The effect of ethanol on the phase transition temperature and the phase structure of monounsaturated phosphatidylcholines. Biochim Biophys Acta. 2001, 1510, 219-230.

[39] Reviakine, I.; Simon, A.; Brisson, A. Effect of Ca2+ on the Morphology of Mixed DPPC−DOPS Supported Phospholipid Bilayers. Langmuir 2000, 16, 1473–1477.

[40] Van Dijck, P.W.; Kaper, A.J.; Oonk, H.A.; de Gier, J. Miscibility properties of binary phosphatidylcholine mixtures. A calorimetric study. Biochim Biophys Acta 1977, 470, 58-69.

[41] Woodward, J.T.; Meuse, C.W. Mechanism of formation of vesicle fused phospholipid monolayers on alkanethiol self-assembled monolayer supports. J Colloid Interface Sci. 2009, 334, 139-145.

[42] Yang, J.; Appleyard, J. The Main Phase Transition of Mica-Supported Phosphatidylcholine Membranes. J. Phys. Chem. B, 2000, 104, 8097–8100.

[43] Garcia-Manyes, S.; Oncins, G.; Sanz, F. Effect of temperature on the nanomechanics of lipid bilayers studied by force spectroscopy. Biophys J. 2005, 89, 4261-4274.

[44] Gounaris, K.; Sen, A.; Brain, A. P.R.; Quinn, P. J.; Williams, W. P. The formation of non-bilayer structures in total polar lipid extracts of chloroplast membranes. Biochim. Biophys. Acta 1983, 728, 129–139.

[45] Heimburg, T. A model for the lipid pretransition: coupling of ripple formation with the chain-melting transition. Biophys J. 2000, 78, 1154–1165.

[46] Li, M.; Chen, M.; Sheepwash, E.; Brosseau, C.L.; Li, H.; Pettinger, B.; Gruler, H.; Lipkowski, J. AFM studies of solid-supported lipid bilayers formed at a Au(111) electrode surface using vesicle fusion and a combination of Langmuir-Blodgett and Langmuir-Schaefer techniques. Langmuir 2008, 24, 10313-10323.

[47] Hauser, H.; Pascher, I.; Pearson, R.H.; Sundell, S. Preferred conformation and molecular packing of phosphatidylethanolamine and phosphatidylcholine.Biochim Biophys Acta. 1981, 650, 21-51.

[48] Yang, J.; Kleijn J. M. Order in phospholipid Langmuir-Blodgett layers and the effect of the electrical potential of the substrate. Biophys J. 1999, 76, 323–332.

[49] Redondo-Morata, L.; Oncins, G.; Sanz, F. Force spectroscopy reveals the effect of different ions in the nanomechanical behavior of phospholipid model membranes: the case of potassium cation. Biophys. J. 2012, 102, 66-74.

[50] Guidelli, R.; Becucci, L. Ion transport across biomembranes and model membranes J Solid State Electrochem. 2011, 15, 1459–1470.

[51] Burgess, I.; Li, M.; Horswell, S.L.; Szymanski, G.; Lipkowski, J.; Satija. S.; Majewski, J. Influence of the electric field on a bio-mimetic film supported on a gold electrode. Colloids Surf B 2005, 40, 117-122.

[52] Bin, X.; Zawisza, I.; Goddard, J.D.; Lipkowski, J. Electrochemical and PM-IRRAS studies of the effect of the static electric field on the structure of the DMPC bilayer supported at a Au(111) electrode surface. Langmuir 2005, 21, 330-347.

[53] Zawisza, I.; Lachenwitzer, A.; Zamlynny, V.; Horswell, S.L.; Goddard, J.D.; Lipkowski, J. Electrochemical and photon polarization modulation infrared reflection absorption spectroscopy study of the electric field driven transformations of a phospholipid bilayer supported at a gold electrode surface. Biophys J. 2003, 85, 4055-4075.

[54] Oleson, T.A.; Sahai, N.; Pedersen, J.A. Electrostatic effects on deposition of multiple phospholipid bilayers at oxide surfaces. J Colloid Interface Sci. 2010, 352, 327-336.

[55] Tsong, T.Y.; Astumian, R.D. Electroconformational Coupling: How Membrane-Bound ATPase Transduces Energy from Dynamic Electric Fields. Annual Review of Physiology, 1988, 50, 273-290.

[56] Hillman, A.R.; Ryder, K.S.; Madrid, E.; Burley, A.W. ; Wiltshire, R.J.; Merotra, J.; Grau, M.; Horswell, S.L. ; Glidle, A.; Dalgliesh, R.M.; Hughes, A.; Cubitt, R.; Wildes, A. Structure and dynamics of phospholipid bilayer films under electrochemical control. Faraday Discussions 2010, 145, 357-379.

[57] Laredo, T.; Dutcher, J.R.; Lipkowski, J. Electric Field Driven Changes of a Gramicidin Containing Lipid Bilayer Supported on a Au(111) Surface. Langmuir 2011, 27, 10072–10087.

[58] Oncins, G.; Garcia-Manyes, S.; Sanz, F. Study of frictional properties of a phospholipid bilayer in a liquid environment with lateral force microscopy as a function of NaCl concentration. Langmuir 2005, 21, 7373-7379.

[59] Pandit, S.A.; Bostick, D.; Berkowitz, M.L. Mixed Bilayer Containing Dipalmitoyl-phosphatidylcholine and Dipalmitoylphosphatidylserine: Lipid Complexation, Ion Binding, and Electrostatics. Biophys J. 2003, 85, 3120–3131.

[60] Böckmann, R.A; Hac, A.; Heimburg, T.; Grubmüller, H. Effect of Sodium Chloride on a Lipid Bilayer. Biophys. J. 2003, 85, 1647-1655.

[61] Richter, R.P.; Maury, N.; Brisson, A.R. On the effect of the solid support on the interleaflet distribution of lipids in supported lipid bilayers. Langmuir 2005, 21, 299-304.

[62] Shi, Z.; Lipkowski, J. Chloride adsorption at the Au(111) electrode surface. J. Electroanal. Chem 1996, 403, 225-239.

[63] Ohki, S.; Arnold, K. Experimental evidence to support a theory of lipid membrane fusion. Colloids Surf B 2008, 63, 276-281.

[64] Bilewicz, R.; Sek, S.; Zawisza I. Electron Transport Through Composite Monolayers. Russian Journal of Electrochemistry, 2002, 38, 29-38.

[65] Wiegand, G.; Arribas-Layton, N.; Hillebrandt, H.; Sackmann, E.; Wagner, P. Electrical Properties of Supported Lipid Bilayer Membranes. J. Phys. Chem. B 2002, 106, 4245-4254.

[66] Ridsdale, R.A.; Palaniyar, N.; Possmayer, F.; Harauz, G. Formation of folds and vesicles by dipalmitoylphosphatidylcholine monolayers spread in excess. J. Membr. Biol. 2001,180, 21-32.

[67] Demel, R.A.; van Kessel, W.S.M.; van Deenen, L.L.M. The properties of polyunsaturated lecithins in monolayers and liposomes and the interactions of these lecithins with cholesterol. Biochim Biophys Acta 1972, 266, 26-40.

[68] Toimil, P.; Prieto, G.; Miñones, J. Jr.; Sarmiento, F. A comparative study of F-DPPC/DPPC mixed monolayers. Influence of subphase temperature on F-DPPC and DPPC monolayers. Phys. Chem. Chem. Phys. 2010, 12, 13323-13332.

[69] Yun, H.; Choi, Y-W., Kim, N.J.; Sohn, D. Physicochemical Properties of Phosphatidylcholine (PC) Monolayers with Different Alkyl Chains, at the Air/Water Interface. Bull. Korean Chem. Soc. 2003, 24, 377-383.

[70] Foglia, F.; Barlow, D.J.; Szoka, F.C.; Huang, Z.; Rogers, S.E.; Lawrence, M.J. Structural studies of the monolayers and bilayers formed by a novel cholesterol-phospholipid chimera. Langmuir 2011, 27, 8275-8281.

[71] Biltonen, R. L.; Lichtenberg; D. The use of differential scanning calorimetry as a tool to characterize liposome preparation. Chem. Phys. Lipids. 1993, 64, 129–142.

[72] Hoyo, J.; Guaus, E.; Oncins, G.; Torrent-Burgués, J.; Sanz, F. Incorporation of Ubiquinone in Supported Lipid Bilayers on ITO. J. Phys. Chem. B, 2013, 117 , 7498–7506.

[73] Nussio, M.R.; Oncins, G.; Ridelis, I.; Szili, E.; Shapter, J.G.; Sanz, F.; Voelcker, N.H. Nanomechanical characterization of phospholipid bilayer islands on flat and porous substrates: a force spectroscopy study. J. Phys. Chem. B 2009, 113, 10339-10347.

[74] Mou, J.; Yang, J.; Huang, C.; Shao, Z. Alcohol induces interdigitated domains in unilamellar phosphatidylcholine bilayers. Biochemistry 1994, 33, 9981-9985.

[75] Morandat, S.; El Kirat, K. Cytochrome c provokes the weakening of zwitterionic membranes as measured by force spectroscopy. Colloids Surf. B 2011, 82, 111−117.

[76] Fringeli, U.P. The structure of lipids and proteins studied by attenuated total reflection (ATR) infrared spectroscopy. II. Oriented layers of a homologous series: phosphatidylethanolamine to phosphatidylcholine. Z. Naturforsch C. 1977, 32, 20-45.

[77] Mizusawa, N.; Wada, H. The role of lipids in photosystem II. Biochim Biophys Acta. 2012, 1817, 194-208.

[78] Glöckner, C. The donor and acceptor side of photosystem II: Structural and functional investigations. Ph.D. thesis, Technischen Universität Berlin, Berlin, 2013.

[79] Allakhverdiev, S.I.; Los, D. A.; Murata, N. in: Wada, Hajime; Murata, Norio (Eds.) Essential and Regulatory Functions, Regulatory Roles in Photosynthesis. Springer, Dordrecht, The Netherlands, 2010, 377-388.

[80] Dörmann, P.; Hölzl, G. in: Wada, Hajime; Murata, Norio (Eds.) Essential and Regulatory Functions, The Role of Glycolipids in Photosynthesis. Springer, Dordrecht, The Netherlands, 2010, 265-282.

[81] Ivanov, A.G.; Hendrickson, L.; Krol, M.; Selstam, E.; Oquist, G.; Hurry, V.; Huner, N.P. Digalactosyl-diacylglycerol deficiency impairs the capacity for photosynthetic intersystem electron transport and state transitions in Arabidopsis thaliana due to photosystem I acceptor-side limitations. Plant Cell Physiol. 2006, 47, 1146-1157.

[82] Tomoaia-Cotişel, M.; Zsakó, J.; Chifu, E.; Quinn, P.J. Influence of electrolytes on the monolayer properties of saturated galactolipids at the air-water interface. Chemistry and Physics of Lipids 1983, 34, 55–64.

[83] Mullineaux, C.W.; Kirchhoff, H. in: Wada, Hajime; Murata, Norio (Eds.) Essential and Regulatory Functions, Role of Lipids in the Dynamics, Springer, Dordrecht, The Netherlands, 2010, 283-294.

[84] Murata, N. Low-temperature effects on cyanobacterial membranes. J. Bioenerg. Biomemb. 1989, 21, 61–75.

[85] Los, D.A.; Murata, N. Structure and expression of fatty acid desaturases. Biochim Biophys Acta, 1998, 1394, 3–15.

[86] Mock, T.; Kroon, B.M. Photosynthetic energy conversion under extreme conditions-II: the significance of lipids under light limited growth in Antarctic sea ice diatoms. Phytochemistry 2002, 61, 53-60.

[87] Loll, B.; Kern, J.; Saenger, W.; Zouni, A.; Biesiadka, J. Lipids in photosystem II: interactions with protein and cofactors. Biochim Biophys Acta 2007, 1767, 509–519.

[88] Härtel, H.; Dörmann, P.; Benning, C. Galactolipids not associated with the photosynthetic apparatus in phosphate-deprived plants. J. Photochem. Photobiol. B: Biol. 2001, 61, 46–51.

[89] Boudière, L.; Michaud, M.; Petroutsos, D.; Rébeillé, F.; Falconet, D.; Bastien, O.; Roy, S.; Finazzi, G.; Rolland, N.; Jouhet, J.; Block, M.A.; Maréchal, E. Glycerolipids in photosynthesis: Composition, synthesis and trafficking. Biochim Biophys Acta 2014, 1837, 470-480.

[90] Bottier, C.; Géan, J.; Artzner, F.; Desbat, B.; Pézolet, M.; Renault, A.; Marion, D.; Vié, V. Galactosyl headgroup interactions control the molecular packing of wheat lipids in Langmuir films and in hydrated liquid-crystalline mesophases. Biochim Biophys Acta 2007, 1768, 1526-1540.

[91] Sakurai, I.; Mizusawa, N.; Wada, H.; Sato, N. Digalactosyldiacylglycerol is required for stabilization of the oxygen-evolving complex in photosystem II. Plant Physiol. 2007, 145, 1361-1370.

[92] Kelly, A.A.; Froehlich, J.E.; Dörmann, P. Disruption of the two digalactosyl-diacylglycerol synthase genes DGD1 and DGD2 in Arabidopsis reveals the existence of an additional enzyme of galactolipid synthesis. Plant Cell 2003, 15, 2694–2706.

[93] Gounaris, K., Whitford, D.; Barber, J. The effect of thylakoid lipids on an oxygen-evolving photosystem II preparation. FEBS Lett. 1983, 163, 230–234.

[94] Fragata, M.; Menikh, A.; Nénonéné, E.K. Functional and structural aspects of the thylakoid lipids in oxygen evolution in photosystem II. Trends Photochem. Photobiol. 1994, 3, 201–210.

[95] Wada, H.; Mizusawa, N. in: Wada, Hajime; Murata, Norio (Eds.) Essential and Regulatory Functions, The Role of Phosphatidylglycerol in Photosynthesis. Springer, Dordrecht, The Netherlands, 2010, 243-263.

[96] Rawyler, A.; Meylan-Bettex, M.; Siegenthaler, P.A. (Galacto) lipid export from envelope to thylakoid membranes in intact chloroplasts. II. A general process with a key

role for the envelope in the establishment of lipid asymmetry in thylakoid membranes. Biochim. Biophys. Acta 1995, 1233, 123-133.

[97] Dörmann, P. Functional diversity of tocochromanols in plants. Planta 2007, 225, 269–276.

[98] Hölzl, G.; Dörmann, P. Structure and function of glycoglycerolipids in plants and bacteria. Prog Lipid Res. 2007, 46, 225-243.

[99] Boudière, L.; Botte, C.; Saidani, N.; Lajoie, M.; Marion, J.; Bréhélin, L.; Yamaryo-Botté, Y. Satiat-Jeunemaître, B.; Breton, C.; Girard-Egrot, A.; Bastien, O.; Jouhet, J.; Falconet, D.; Block, M.A.; Maréchal, E. Galvestine-1, a novel chemical probe for the study of the glycerolipid homeostasis system in plant cells, Mol. Biosyst. 2012, 287, 22367–22376.

[100] Rolland, N.; Curien, G.; Finazzi, G.; Kuntz, M.; Marechal, E.; Matringe, M.; Ravanel, S.; Seigneurin-Berny, D. The biosynthetic capacities of the plastids and integration between cytoplasmic and chloroplast processes. Annu. Rev. Genet. 2012, 46, 233–264.

[101] Foley, A. A.; Brain, A. P.R.; Quinn, P.J.; Harwood, J.L. Permeability of liposomes composed of binary mixtures of monogalactosyldiacylglycerol and digalactosyl-diacylglycerol. Biochim. Biophys. Acta 1988, 939, 430–440.

[102] Marsh, D. Components of the lateral pressure in lipid bilayers deduced from HII phase dimensions. Biochim. Biophys. Acta 1996, 1279, 119–123.

[103] Castro, V.; Dvinskikh, S.V.; Widmalm, G.; Sandström, D.; Maliniak, A. NMR studies of membranes composed of glycolipids and phospholipids. Biochim. Biophys. Acta 2007, 1768, 2432-2437.

[104] Sen, A.; Brain, A.P.; Quinn, P.J.; Williams, W.P. Formation of inverted lipid micelles in aqueous dispersions of mixed sn-3-galactosyldiacylglycerols induced by heat and ethylene glycol. Biochim. Biophys. Acta 1982, 686, 215-224.

[105] Van den Brink-van der Laan, E.; Killian, J.A.; Kruijff, B.D. Nonbilayer lipids affect peripheral and integral membrane proteins via changes in the lateral pressure profile, Biochim. Biophys. Acta 2004, 1666, 275–288.

[106] Mansourian, A.R.; Brain, A.P.R.; Quinn, P.J. Intermolecular mixing of saturated and unsaturated galactolipids. Biochem. Soc. Transactions 1986, 14, 738–739.

[107] Hölzl, G.; Dörmann, P. Structure and function of glycoglycerolipids in plants and bacteria. Prog. Lipid Res. 2007, 46, 225–243.

[108] Gzyl-Malcher, B.; Filek, M.; Makyła, K.; Paluch, M. Differences in surface behaviour of galactolipids originating from different kind of wheat tissue cultivated in vitro. Chem Phys Lipids. 2008, 155, 24-30.

[109] Tomoaia-Cotişel, M.; Zsako, J.; Chifu, E; Quinn, P.J. Hysteresis in compression-expansion cycles of distearoylmonogalactosylglycerol monolayers. Chem. Phys. Lipids 1989, 50, 127–133.

[110] Popova, A.V.; Hincha, D.K. Thermotropic phase behavior and headgroup interactions of the nonbilayer lipids phosphatidylethanolamine and monogalactosyl-diacylglycerol in the dry state. BMC Biophysics, 2011, 4-11.

[111] Curatolo, W. The physical properties of glycolipids. Biochim. Biophys. Acta 1987, 906, 111-136.

[112] Oliver, A.E.; Hincha, D.K.; Tsvetkova, N.M.; Vigh, L.; Crowe, J.H. The effect of arbutin on membrane integrity during drying is mediated by stabilization of the lamellar phase in the presence of nonbilayer-forming lipids. Chem. Phys. Lipids 2001, 111, 37-57.

[113] Tsvetkova, N.M.; Horváth, I.; Török, Z.; Wolkers, W.F.; Balogi, Z.; Shigapova, N.; Crowe, L.M.; Tablin, F.; Vierling, E.; Crowe, J.H.; Vigh, L. Small heat-shock proteins regulate membrane lipid polymorphism. Proc. Natl. Acad. Sci. USA. 2002, 99, 13504-13509.

[114] Bruno, A.; Rossi, C.; Marcolongo, G.; Di Lena, A.; Venzo, A.; Berrie, C.P.; Corda, D. Selective in vivo anti-inflammatory action of the galactolipid monogalactosyl-diacylglycerol. Eur. J. Pharmacol. 2005, 524, 159-168.

[115] Maeda, N.; Kokai, Y.; Ohtani, S.; Sahara, H.; Kumamoto-Yonezawa, Y.; Kuriyama, I.; Hada, T.; Sato, N.; Yoshida, H.; Mizushina, Y. Anti-tumor effect of orally administered spinach glycolipid fraction on implanted cancer cells, colon-26, in mice. Lipids 2008, 43, 741-748.

[116] Maeda, N.; Kokai, Y.; Ohtani, S.; Sahara, H.; Hada, T.; Ishimaru, C.; Kuriyama, I.; Yonezawa, Y.; Iijima, H.; Yoshida, H.; Sato, N.; Mizushina, Y. Anti-tumor effects of the glycolipids fraction from spinach which inhibited DNA polymerase activity. Nutr. Cancer. 2007, 57, 216-223.

[117] Kuriyama, I.; Musumi, K.; Yonezawa, Y.; Takemura, M.; Maeda, N.; Iijima, H.; Hada, T.; Yoshida, H.; Mizushina, Y. Inhibitory effects of glycolipids fraction from spinach on mammalian DNA polymerase activity and human cancer cell proliferation. J Nutr Biochem. 2005, 10, 594-601.

[118] Chu, B.S.; Gunning, A.P.; Rich, G.T.; Ridout, M.J.; Faulks, R.M.; Wickham, M.S.; Morris V.J.; Wilde, P.J. Adsorption of bile salts and pancreatic colipase and lipase onto digalactosyldiacylglycerol and dipalmitoylphosphatidylcholine monolayers. Langmuir 2010, 26, 9782-9793.

[119] Crane, F. L. New functions for coenzyme Q. Protoplasma, 2000, 213, 127-133.

[120] Nowicka, B.; Kruk, J. Occurrence, biosynthesis and function of isoprenoid quinones. Biochim. Biophys. Acta 2010, 1797, 1587-1605.

[121] Funari, S.S.; Rebbin, V.; Marzorati, L.; di Vitta, C. Membrane morphology modifications induced by hydroquinones. Langmuir 2011, 27, 8257-8262.

[122] Quan, M.; Sanchez, D.; Wasylkiw, M.F.; Smith, D.K. Voltammetry of quinones in unbuffered aqueous solution: reassessing the roles of proton transfer and hydrogen bonding in the aqueous electrochemistry of quinones. J. Am. Chem. Soc. 2007, 129, 12847-12856.

[123] Salas, M.; Gómez, M.; González, F.J.; Gordillo, B. Electrochemical reduction of 1,4-benzoquinone. Interaction with alkylated thymine and adenine nucleobases. J. Electroanal. Chem. 2003, 543, 73–81.

[124] Ausili, A.; Torrecillas, A.; Aranda, F.; Godos, A.D.; Sánchez-Bautista, S.; Corbalán-García, S.; Gómez-Fernández, J.C. Redox state of coenzyme Q10 determines its membrane localization, J. Phys. Chem. B 2008, 112, 12696–12702.

[125] Mitchell, P. Protonmotive Q cycle. General formulation, FEBS Lett. 1975, 59, 137–139.

[126] Ksenzhek, O.S.; Petrova, S.A.; Kolodyazhny, M.V. Redox properties of ubiquinones in aqueous solutions. Bioelectrochem. Bioenerg. 1982, 9, 167-174.

[127] Ahmed, S.; Khan, A. Y.; Qureshi, R.; Subhani M. S. Hydrogen bonding association in the electroreduced intermediates of benzoquinones and naphthoquinones. Russ. J. Electrochem. 2007, 43, 811-819.

[128] Jeya, M.; Moon, H. J.; Lee, J. L.; Kim, I. W.; Lee, J. K. Current state of coenzyme Q10 production and its applications. Appl. Microbiol. Biotechnol. 2010, 85, 1653.

[129] Roura-Pérez, G.; Quiroz, B.; Aguilar-Martínez, M.; Frontana, C.; Solano, A.; González, I.; Bautista-Martínez, J. A.; Jiménez-Barbero, J.; Cuevas, G. Remote Position Substituents as Modulators of Conformational and Reactive Properties of Quinones. Relevance of the Intramolecular Interaction. J. Org. Chem. 2007, 72, 1883-1894.

[130] Turunen, M.; Olsson, J.; Dallner, G. Metabolism and function of coenzyme Q. Biochim. Biophys. Acta 2004, 1660, 171–199.

[131] Kagan, V.E.; Fabisiak, J.P.; Quinn, P.J. Coenzyme Q and vitamin E need each other as antioxidants, Protoplasma, 2000, 11–18.

[132] Ernster, L.; Dallner, G. Biochemical, physiological and medical aspects of ubiquinone function, Biochim. Biophys. Acta 1995, 1271, 195–204.

[133] Roche, Y.; Peretti, P.; Bernard, S. Influence of the chain length of ubiquinones on their interaction with DPPC in mixed monolayers. Biochim Biophys Acta 2006, 1758, 468-478.

[134] Cadenas, E.; Hochstein, P.; Ernster, L. Prooxidant and antioxidant functions of quinones and quinone reductases in mammalian-cells. Adv. Enzymol. Relat Areas Mol. Biol 1992, 65, 97–146.

[135] Bogeski, I.; Gulaboski, R.; Kappl, R.; Mirceski, V.; Stefova, M.; Petreska, J.; Hoth, M. Calcium binding and transport by coenzyme Q. J. Am. Chem. Soc. 2011, 133, 9293–9303.

[136] Mirčeski, V.; Gulaboski, R.; Bogeski, I.; Hoth, M. Redox chemistry of Ca-transporter 2-palmitoylhydroquinone in an artificial thin organic film membrane. J. Phys. Chem. C, 2007, 111, 6068–6076.

[137] Crane, F.L. New functions for coenzyme Q. Protoplasma 2000, 213, 127–133.

[138] Yoshida, H.; Kotani, Y.; Ochiai, K.; Araki, K. Production of ubiquinone-10 using bacteria, J. Gen. Appl. Microbiol. 1998, 44, 19–26.

[139] Pshybytko, N.L. Kruk, J. Kabashnikova, L.F. Strzałka, K. Function of plastoquinone in heat stress reactions of plants, Biochim. Biophys. Acta 2008, 1777, 1393–1399.

[140] Rumberg, B.; Schmidt-Mende, P.; Witt, H. T. Different Demonstrations of the Coupling of Two Light Reactions in Photosynthesis. Nature, 1964, 201, 466-468.

[141] Minagawa, J.; Narusaka, Y.; Inoue, Y.; Satoh, K. Electron transfer between QA and QB in photosystem II is thermodynamically perturbed in phototolerant mutants of Synechocystis sp. PCC 6803. Biochemistry 1999, 38, 770-775.

[142] Lenaz, G. ; Samori, B.; Fato, R.; Battino, M.; Parenti Castelli, G.; Domini, I. Localization and preferred orientations of ubiquinone homologs in model bilayers, Biochem. Cell. Biol. 1992, 70, 504–514.

[143] Söderhäll, J. A.; Laaksonen, A. Molecular Dynamics Simulations of Ubiquinone inside a Lipid Bilayer. J. Phys. Chem. B, 2001, 105, 9308-9315.

[144] Jemioła-Rzemińska, M.; Myśliwa-Kurdziel, B.; Strzałka, K. The influence of structure and redox state of prenylquinones on thermotropic phase behaviour of phospholipids in model membranes. Chem Phys Lipids 2002, 114, 169-180.

[145] Aranda, F.J.; Gomez-Fernandez, J.C. The interaction of ubiquinone-10 and ubiquinol-10 with phospholipid bilayers. A study using differential scanning calorimetry and turbidity measurements, Biochim. Biophys. Acta 1985, 820 19–26.

[146] Di Bernardo, S.; Fato, R.; Casadio, R.; Fariselli, P.; Lenaz, G. A high diffusion coefficient for coenzyme Q10 might be related to a folded structure. FEBS Lett. 1998, 426, 77-80.

[147] Kruk, J.; Strzałka, K.; Leblanc, R.M. Monolayer study of plastoquinones, alpha-tocopherol quinone, their hydroquinone forms and their interaction with monogalactosyldiacylglycerol. Charge-transfer complexes in a mixed monolayer. Biochim. Biophys. Acta 1992, 1112, 19-26.

[148] Quinn, P.J.; Esfahani, M.A. Ubiquinones have surface-active properties suited to transport electrons and protons across membranes. Biochem. J. 1980, 185, 715–722.

[149] Moncelli, M.R.; Becucci, L.; Nelson, A.; Guidelli R. Electrochemical modeling of electron and proton transfer to ubiquinone-10 in a self-assembled phospholipid monolayer. Biophys J. 1996, 70, 2716-2726.

[150] Jemiola-Rzeminska, M.; Kruk, J.; Skowronek, M.; Strzalka, K. Location of ubiquinone homologues in liposome membranes studied by fluorescence anisotropy of diphenyl-hexatriene and trimethylammonium-diphenyl-hexatriene. Chem. Phys. Lipids. 1996, 79, 55-63.

[151] Stidham, M.A.; McIntosh, T.J.; Siedow, J.N. On the localization of ubiquinone in phosphatidylcholine bilayers. Biochim. Biophys. Acta 1984, 767, 423– 431.

[152] Kingsley, P.B.; Feigenson, G.W. 1H-NMR study of the location and motion of ubiquinones in perdeuterated phosphatidylcholine bilayers. Biochim Biophys Acta 1981, 635, 602–618.

[153] Fiorini, R.; Ragni, L.; Ambrosi, S.; Littarru, G.P.; Gratton, E.; Hazlett, T. Fluorescence studies of the interactions of ubiquinol-10 with liposomes, Photochem. Photobiol. 2008, 84, 209–214.

[154] Katsikas, H.; Quinn, P.J. Fluorescence probe studies of the distribution of ubiquinone homologues in bilayers of dipalmitoylglycerophosphocholine, Eur. J. Biochem. 1983, 131, 607– 612.

[155] Katsikas, H.; Quinn, P.J. The polyisoprenoid chain length influences the interaction of ubiquinones with phospholipid bilayers, Biochim. Biophys. Acta 1982, 689, 363–369.

[156] Ondarroa, M.; Quinn, P.J. A difference infrared-spectroscopic study of the interaction of ubiquinone-10 with phospholipid bilayers, Biochem. J. 1986, 240, 325– 331.

[157] Afri, M.; Ehrenberg, B.; Talmon, Y.; Schmidt, J.; Cohen, Y.; Frimer, A.A. Active oxygen chemistry within the liposomal bilayer: Part III. Locating vitamin E, ubiquinol and ubiquinone and their derivatives in the lipid bilayer, Chem. Phys. Lipids 2004, 131, 107–121.

[158] Samori, B.; Lenaz, G.; Battino, M.; Marconi, G.; Domini, I. On coenzyme Q orientation in membranes: a linear dichroism study of ubiquinones in a model bilayer, J. Membr. Biol. 1992, 128, 193– 203.

[159] Hoyo, J.; Guaus, E.; Torrent-Burgues, J.; Sanz, F. Electrochemical behaviour of mixed LB films of ubiquinone – DPPC. J. Electroanal. Chem. 2012, 669, 6-13.

[160] Ondarroa, M.; Sharma, S.K.; Quinn, P.J. Solvation properties of ubiquinone-10 in solvents of different polarity. Biosci Rep. 1986, 9, 783-796.

[161] Roche, Y.; Peretti, P.; Bernard, S. The redox state influences the interaction of ubiquinones with phospholipid bilayers. J. Therm. Anal. Calorim. 2007, 89, 867-873.

[162] Mårtensson, C.; Agmo Hernández, V. Ubiquinone-10 in gold-immobilized lipid membrane structures acts as a sensor for acetylcholine and other tetraalkylammonium cations. Bioelectrochemistry. 2012, 88, 171-80.

[163] Aranda, F.J.; Gómez-Fernández, J.C. Influence of membrane fluidity on transport mediated by ubiquinones through phospholipid vesicles. Archives of Biochemistry and Biophysics 1982, 218, 525–530.

[164] Skowronek, M.; Jemioła-Rzemińska, M.; Kruk, J.; Strzałka, K. Influence of the redox state of ubiquinones and plastoquinones on the order of lipid bilayers studied by fluorescence anisotropy of diphenylhexatriene and trimethylammonium diphenylhexatriene. Biochim. Biophys. Acta 1996, 1280, 115-119.

[165] Hauss, T.; Dante, S.; Haines, T.H.; Dencher, N.A. Localization of coenzyme Q10 in the center of a deuterated lipid membrane by neutron diffraction. Biochim Biophys Acta 2005, 1710, 57-62.

[166] Kruk, J.; Myśliwa-Kurdziel, B.; Jemioła-Rzeminiska, M.; Strzałka, K. Fluorescence lifetimes study of alpha-tocopherol and biological prenylquinols in organic solvents and model membranes. Photochem. Photobiol. 2006, 82, 1309-1314.

[167] Marchal, D.; Boireau, W.; Laval, J.M.; Moiroux, J.; Bourdillon, C. Electrochemical measurement of lateral diffusion coefficients of ubiquinones and plastoquinones of various isoprenoid chain lengths incorporated in model bilayers. Biophys. J. 1998, 74, 1937-1948.

[168] Venable, R. M.; Zhang, Y.; Hardy, B. J.; Pastor, R. W. Molecular dynamics simulations of a lipid bilayer and of hexadecane. An investigation of membrane fluidity. Science 1993, 262, 223–226.

[169] Fato R.; Battino M.; Degli Esposti M.; Parenti Castelli G.; Lenaz G. Determination of partition and lateral diffusion coefficients of ubiquinones by fluorescence quenching of n-(9-anthroyloxy)stearic acids in phospholipid vesicles and mitochondrial membranes. Biochemistry 1986, 25, 3378—3390.

[170] Ulrich, E.L.; Girvin, M.E.; Cramer, W.A.; Markley, J.L. Location and Mobility of Ubiquinones of Different Chain Length in Artificial Membrane Vesicles. Biochemistry 1985, 24, 2501-2508.

[171] Cornell, B.A.; Keniry, M.A.; Post, A.; Robertson, R.N.; Weir, L.E.; Westerman, P.W. Location and activity of ubiquinone 10 and ubiquinone analogues in model and biological membranes, Biochemistry 1987, 26, 7702– 7707.

[172] Salgado, J.; Villalain, J.; Gomez Fernandez, J.C. Magic angle spinning 13C-NMR spin-lattice relaxion study of the location and effects of alphatocopherol, ubiquinone-10 and ubiquinol-10 in unsonicated model membranes, Eur. Biophys. J. 1993, 22, 151– 155.

[173] Metz, G.; Howard, K. P.; van Liemt, W. B. S.; Prestegard, J. H.; Lugtenburg, J.; Smith, S. O. NMR Studies of Ubiquinone Location in Oriented Model Membranes: Evidence for a Single Motionally-Averaged Population. J. Am. Chem. Soc., 1995, 117, 564–565.

[174] Ondarroa, M.; Quinn, P. J. Proton magnetic resonance spectroscopic studies of the interaction of ubiquinone-10 with phospholipid model membranes. Eur. J. Biochem. 1986, 155, 353-361.

[175] Katsikas, H.; Quinn, P.J. The distribution of ubiquinone-10 in phospholipid bilayers. A study using differential scanning calorimetry, Eur. J. Biochem. 1982, 124, 165– 169.

[176] Haines, T.H. Do sterols reduce proton and sodium leaks through lipid bilayers? Prog. Lipid Res. 2001, 40, 299–324.

[177] Laval, J.M.; Majda, M. Electrochemical investigations of the structure and electron transfer properties of phospholipid bilayers incorporating ubiquinone. Thin Solid Films. 1994, 244, 836–840.

[178] Chazotte, B.; Wu E. S.; Hackenbrock C. R. The mobility of a fluorescent ubiquinone in model lipid membranes—relevance to mitochondrial electron transport. Biochim. Biophys. Acta. 1991, 1058, 400–409.

[179] Bilewicz, R.; Majda, M. Monomolecular Langmuir-Blodgett films at electrodes. Formation of passivating monolayers and incorporation of electroactive reagents. Langmuir, 1991, 7, 2794–2802.

[180] Aranda, F.J.; Villalain, J.; Gomez-Fernandez, J.C. A fourier transform infrared spectroscopic study of the molecular interaction of ubiquinone-10 and ubiquinol-10 with bilayers of dipalmitoylphosphatidylcholine. Biochim. Biophys. Acta 1986, 861, 25–32.

[181] Marchal, D.; Boireau, W.; Laval, J.M.; Moiroux, J.; Bourdillon, C. An electrochemical approach of the redox behavior of water insoluble ubiquinones or plastoquinones incorporated in supported phospholipid layers. Biophys. J. 1997, 72, 2679-2687.

[182] Laviron, E. Electrochemical reactions with protonations at equilibrium: Part VIII. The 2 e, 2H+ reaction (nine-member square scheme) for a surface or for a heterogeneous reaction in the absence of disproportionation and dimerization reactions. J. Electroanal. Chem. 1983, 146, 15–36.

[183] Finklea, H.O. Theory of Coupled Electron−Proton Transfer with Potential-Dependent Transfer Coefficients for Redox Couples Attached to Electrodes. J. Phys. Chem. B, 2001, 105, 8685–8693.

[184] Petrova, S.A.; Kolodyazhny, M.V.; Ksenzhek, O.S. Electrochemical properties of some naturally occurring quinones. J. Electroanal.Chem. 1990, 277, 189–196.

[185] Sek, S.; Bilewicz, R. Voltammetric Probing of Molecular Assemblies of Ubiquinone-10 at the Air–Water Interfaces. J. Inclusion Phenom. Macrocyc. Chem. 1999, 35, 55-62.

[186] Moncelli, M.R.; Herrero, R.; Becucci, L.; Guidelli, R. Kinetics of electron and proton transfer to ubiquinone-10 and from ubiquinol-10 in a self-assembled phosphatidylcholine monolayer. Biochim. Biophys. Acta 1998, 1364, 373-384.

[187] Ohnishi, T.; Trumpower, B. L. Differential effects of antimycin on ubisemiquinone bound in different environments in isolated succinate-cytochrome c reductase complex. J.Biol. Chem. 1980; 255, 3278-3284.

[188] Bilewicz, R. Voltammetric Probing of Multicomponent Langmuir - Blodgett Monolayers Part I - Monolayers Containing Ubiquinone (Q10). Pol. J. Chem. 1993, 67, 9; 1695-1704.

[189] Gordillo, G.J.; Schiffrin, D.J. The electrochemistry of ubiquinone-10 in a phospholipid model membrane. Faraday Discuss. 2000, 116, 89–107.

[190] Cheng, Y.; Cunnane V.J.; Kontturi, A-K.; Kontturi, K.; Schiffrin, D.J. Potential Dependence of Transmembrane Electron Transfer across Phospholipid Bilayers Mediated by Ubiquinone 10. J. Phys. Chem., 1996, 100, 15470–15477.

[191] Li, D.; Li, D.W.; Fossey, J.S.; Long, Y.T. In situ surface-enhanced Raman scattering and X-ray photoelectron spectroscopic investigation of coenzyme Q10 on silver electrode. Phys. Chem. Chem. Phys. 2011, 13, 2259-2265.

[192] Shim, Y-B; Park, S-M. Spectroelectrochemical studies of p-benzoquinone reduction in aqueous media. J. Electroanal. Chem. 1997, 425, 201-207.

[193] Tang, Y.H; Wu, Y.R; Wang, Z.H. Spectroelectrochemistry for electroreduction of p-benzoquinone in unbuffered aqueous solution. J. Electrochem. Soc. 2001, 148, 133-138.

[194] Forster, R.J., O'Kelly, J. P. J. Protonation reactions of anthraquinone-2,7-disulphonic acid in solution and within monolayers. Electroanal. Chem. 2001, 498, 127–135.

[195] Prince, R. C.; Dutton, P. L.; Bruce, J. M. Electrochemistry of ubiquinones, menaquinones and plastoquinones in aprotic solvents. FEBS Lett. 1983, 160, 273-276.

[196] Gupta, J.; Linschitz, H. Hydrogen Bonding and Protonation Effects in Electrochemistry of Quinones in Aprotic Solvents. J. Am. Chem. Soc. 1997, 119, 6384-6391.

[197] Yoon, J.H.; Lee, K.S.; Yang, J.E.; Won, M.S.; Shim, Y.B. Electron-transfer kinetics and morphology of cytochrome c at the biomimetic phospholipid layers. J. Electroanal. Chem. 2010, 644, 36–43.

[198] Suemori,Y.; Nagata, M.; Kondo, M.; Ishigure, S.; Dewa, T.; Ohtsuka, T.; Nango, M. Phospholipid-linked quinones-mediated electron transfer on an electrode modified with lipid bilayers. Colloids Surf B 2008, 6, 106-112.

[199] Bilewicz, R.; Majda, M. Bifunctional monomolecular Langmuir-Blodgett films at electrodes. Electrochemistry at single molecule gate sites. J. Am. Chem. Soc., 1991, 113, 5464–5466.

[200] Jemiota-Rzemińska, M.; Latowski, D.; Strzałka, K. Incorporation of plastoquinone and ubiquinone into liposome membranes studied by HPLC analysis. The effect of side chain length and redox state of quinone. Chem. Phys. Lipids 2001, 110, 85-94.

[201] Clerc, S.G. and Thompson, T.E. Permeability of dimyristoylphosphatidylcholine/ dipalmitoyl phosphatidylcholine bilayer membranes with coexisting gel and liquid-crystalline phases. Biophys J. 1995, 68, 2333–2341.

[202] Shiba, H.; Maeda, K.; Ichieda, N.; Kasuno, M.; Yoshida, Y.; Shirai, O.; Kihara, S. Voltammetric study on the electron transport through a bilayer lipid membrane containing neutral or ionic redox molecules. J. Electroanal. Chem. 2003, 556, 1-11.

[203] Miller, C.; Cuendet, P.; Graetzel, M. Adsorbed omega.-hydroxy thiol monolayers on gold electrodes: evidence for electron tunneling to redox species in solution. J. Phys. Chem. 1991, 95, 877–886.

[204] Torchut, E.; Laval, J.M.; Bourdillon, C.; Majda, M. Electrochemical measurements of the lateral diffusion of electroactive amphiphiles in supported phospholipid monolayers. Biophys J. 1994, 66, 753–762.

[205] Torchut, E.; Bourdillon, C.; Laval, J.M. Reconstitution of functional electron transfer between membrane biological elements in a two-dimensional lipidic structure at the electrode interface. Biosens. Bioelectron. 1994, 9, 719-723.

[206] Ma, W.; Ying, Y.L.; Qin, L.X.; Gu, Z.; Zhou, H.; Li, D.W.; Sutherland, T.C.; Chen, H.Y.; Long, Y.T. Investigating electron-transfer processes using a biomimetic hybrid bilayer membrane system. Nat. Protoc. 2013, 8, 439-450.

[207] McBee, T.W.; Wang, L.; Ge, C.; Beam, B.M.; Moore, A.L.; Gust, D.; Moore, T.A.; Armstrong, N.R.; Saavedra, S.S. Characterization of proton transport across a waveguide-supported lipid bilayer. J Am Chem Soc. 2006, 128, 2184-2185.

[208] Takehara, K.; Takemura, H.; Ide, Y.; Okayama, S. Electrochemical behavior of ubiquinone and vitamin K incorporated into n-alkanethiol molecular assemblies on a gold electrode. J. Electroanal. Chem. 1991, 308, 345-350.

[209] Petrangolini, P.; Alessandrini, A.; Berti, L.; Facci, P. An Electrochemical Scanning Tunneling Microscopy Study of 2-(6-Mercaptoalkyl)hydroquinone Molecules on Au(111). J. Am. Chem. Soc. 2010, 132, 7445–7453.

[210] Hong, H. G.; Park, W. Electrochemical characteristics of hydroquinone-terminated self-assembled monolayers on gold. Langmuir 2001, 17, 2485–2492.

[211] Larsen, A.G.; Gothelf, K.V. Electrochemical properties of mixed self-assembled monolayers on gold electrodes containing mercaptooctylhydroquinone and alkylthiols. Langmuir, 2005 21, 1015-1021.

[212] Tsoi, S.; Griva, I.; Trammell, S.A.; Blum, A.S.; Schnur, J.M.; Lebedev, N. Electrochemically controlled conductance switching in a single molecule: quinone-modified oligo(phenylene vinylene). ACS Nano. 2008, 2, 1289-1295.

[213] Nelson, A.; Benton, A. Phospholipid monolayers at the mercury / water interface. J. Electroanal. Chem. 1986, 202, 253-270.

[214] Sanchez, S.; Arratia, A.; Cordova, R.; Gomez, H.; Schrebler, R. Electron transport in biological processes. Electrochemical behavior of Q10 immersed in a phopholipidic matrix added on a pyrolitic graphite electrode. Bioelectrochem. Bioenerg. 1995, 36, 67-71.

[215] Takehara, K.; Ide. Y. Electrochemical behavior of the ubiquinone-Q10 film coated onto a glassy carbon electrode by the spinner method. Bioelectrochem. Bioenerg. 1991, 26, 297-305.

[216] Blackwell, M. F.; Whitmarsh, J. Effect of integral membrane proteins on the lateral mobility of plastoquinone in phosphatidylcholine proteoliposomes. Biophys. J. 1990, 58, 1259 –1271.

[217] Chazotte, B.; Hackenbrock. C. R. Lateral diffusion as a rate limiting step in ubiquinone mediated mitochondrial electron transport. J. Biol. Chem. 1989, 264, 4978–4985.

[218] Kruk, J.; Strzałka, K.; Leblanc, R.M. Fourier transform infrared studies on charge-transfer interactions of plastoquinones and α-tocopherol quinone with their hydroquinone forms and MGDG. Biophys. Chem. 1993, 45, 235–244.

[219] Kirchhoff, H.; Mukherjee, U.; Galla, H.J. Molecular architecture of the thylakoid membrane: lipid diffusion space for plastoquinone. Biochemistry. 2002, 41, 4872-4882.

[220] Blackwell, M.; Gibas, C.; Gygax, S.; Roman, D.; Wagner, B. The plastoquinone diffusion coefficient in chloroplasts and its mechanistic implications. Biochim Biophys Acta, 1994, 1183, 533–543.

Chapter 4

Materials and Methods

The chemicals used in this Ph. D. Thesis and their procedence are exposed in this chapter. In addition, the different techniques used are explained in the Methods section. The fundamentals of these techniques are explained in Chapter 2, so in the present chapter only the brand and model of the instruments used and their corresponding experimental setting values are exposed.

The most of the results shown in this Ph. D. Thesis correspond to monolayers formed at the air|water interface by using the Langmuir or LB technique. However, part of the DPPC:UQ experiments have been performed using SPBs. Therefore, the Section 4.2.2 presents the vesicle and SPB formation method which consists on the general used method for preparing SPBs, but with the improvements required for inserting the redox active molecule. Our improved version of this procedure has been revealed as a successful method for inserting this kind of molecules in phospholipid SPBs deposited on substrates with nanometrical roughness.

4.1 Materials

UQ HPLC grade was provided by Sigma-Aldrich and PQ by ASM Research Chemicals. On the other hand, DPPC was purchased from Avanti Polar Lipids whereas saturated MGDG and DGDG, with acyl = stearoyl (18:0), were purchased from Matreya (USA).

KH_2PO_4, KCl and chloroform of analytical grade from Sigma-Aldrich were used in solutions preparation. Water was ultrapure MilliQ® (18.2 MΩ·cm). Mica sheets were purchased from TED PELLA Inc (CA) and ITO deposited on glass slides were purchased to SOLEMS (France).

4.2 Methods

4.2.1 Monolayer formation

Langmuir and Langmuir-Blodgett (LB) monolayer formation were carried on a trough (Nima Technology, Cambridge, UK) model 1232D1D2 equipped with two movable barriers. The surface pressure was measured using paper Whatman 1 held by a Wilhelmy balance connected to a microelectronic system registering the surface pressure (π).

The subphase used in these experiments was MilliQ® quality water. Previous to the subphase addition, the trough was cleaned twice with chloroform and once with MilliQ® quality water. Residual impurities were cleaned from the air|liquid interface by surface suctioning. The good baseline in the surface pressure-area, π–A, isotherms confirms the interface cleanliness. Solutions of lipids, prenylquinones and lipid:prenylquinone were prepared using chloroform and spread at the air|liquid interface using a high precision Hamilton microsyringe. LB monolayers were transferred to mica surface at defined surface pressures values. Barrier closing rates were fixed at 50 $cm^2 \cdot min^{-1}$ for isotherm registration and at 25 $cm^2 \cdot min^{-1}$ for LB film transfer. No noticeable influence of these compression rates was observed on the isotherm shape. Isotherm recording was carried out adding the solution to the subphase and waiting 15 minutes for perfect spreading and solvent evaporation. LB film transfer was conducted dipping the freshly cleaved mica through the air|liquid interface on the subphase before adding the solution, and five minutes were

lagged after pressure setpoint was achieved. Transfer speed was set at 5 $mm \cdot min^{-1}$ linear velocity. Experiments were conducted at 21±0.5ºC and repeated a minimum of three times for reproducibility control.

4.2.2 Vesicle and SPB formation

4.2.2.1 Vesicle Formation

3 mM pure components solutions were prepared in glass vials dissolving DPPC and UQ in chloroform. Samples were prepared mixing the appropriate volume of each pure component solutions to achieve the desired DPPC:UQ molar ratio. The solutions were dried under slow argon flow and lipids were resuspended by adding 2 mL of buffer solution (0.150 M KCl as supporting electrolyte at pH 7.4 adjusted with the KH_2PO_4/K_2HPO_4 buffer). Six cycles of 50 seconds of vortexing-heating (60ºC) followed by 30 minutes sonicating (60ºC) were performed to obtain unilamellar vesicles. These solutions were kept at 4ºC during a maximum of three weeks.

4.2.2.2 SPB formation

Vesicle solution was sonicated 30 min at 60ºC and then added inside an O-Ring placed on the ITO slide surface that had been previously cleaned once with ethanol and three times with MilliQ® grade water. After the vesicle deposition, the ITO slides were placed in an oven for 40 min using a homemade environmental cell which maintains a high moisture level, permitting to achieve 85ºC without drying the sample. After this incubation process, ITO surface was washed three times using the buffer solution. The resulting SPB was kept wet, using the buffer solution, before and during the experiments to preserve its integrity.

4.2.3 AFM characterization

The AFM topographic images of LB films were acquired in air tapping mode using a Multimode AFM controlled by Nanoscope IV electronics (Veeco, Santa Barbara, CA) under ambient conditions. Triangular AFM probes with silicon nitride cantilevers and silicon tips were used (SNL-10, Bruker) which have a nominal spring constant ≈ 0.35 $N \cdot m^{-1}$. Images were acquired at 1.5 Hz and at minimum vertical force so as to reduce sample damage. AFM images were obtained from at least two different samples, prepared on different days, and by scanning several macroscopically separated areas on each sample.

On the other hand, AFM topographic images of SPBs were acquired in liquid tapping mode at similar conditions than that exposed for LB films.

4.2.4 Force curves

The same probes were used for topographic and force measurements. Quantitative force measurements were carried out by calibrating each AFM probe individually so as to experimentally find their spring constant, k. To do that, probe sensitivity ($V \cdot nm^{-1}$) was measured by performing force curves on a hard substrate (silicon oxide), process which was immediately followed by the thermal noise calculation, which calculates k value by fitting the shape of the resonance peak obtained without external probe excitation. After this process, laser position on the cantilever surface and photodetector position remained unchanged to ensure that calibration parameters remained constant during the experiment on SPBs. Force curves were performed at a constant rate of 1 Hz and only one indentation was performed in every position so as to measure the nanomechanical properties of fresh sample regions in every individual experiment. Sets of at least 300 force curves over different places of the sample were acquired from at least two different samples with different tips to ensure reproducibility.

4.2.5 Brewster angle Microscopy (BAM)

A Brewster angle microscope, model MICROBAM NIMA-Nanofilm with lateral resolution of 8 μm and equipped with a 30 mW laser emitting p-polarised light at a wavelength λ = 659 nm, was used to visualise the structure of monolayers at the air|water interface. Each image shown in this work corresponds to an approximated area of 2.3 mm x 3.4 mm of the monolayer.

4.2.6 Electrochemical characterization

The voltammetric measurements were performed in a conventional three-electrode cell using an Autolab Potentiostat-Galvanostat PGSTAT-12 (Ecochemie, NL). Working electrodes were freshly-cleaned ITO slides (10 mm x 25 mm) cleaned once with ethanol and three times with MilliQ® grade water. Counter electrode was a platinum wire in spiral geometry and the reference electrode was an Ag/AgCl/3M KCl microelectrode (DRIREF-2SH, World Precision Instruments). This reference electrode was mounted in a Lugging

capillary containing KCl solution at the same cell concentration. All reported potentials were referred to this electrode. The electrochemical cell contained 0.150 M KCl as supporting electrolyte at pH 7.4 adjusted with the KH_2PO_4/K_2HPO_4 buffer solution. All solutions were freshly prepared with MilliQ® grade water de-aerated with a flow of Ar gas for 15 min prior to cyclic voltammetry (CV) experiments, which were conducted at 22 ± 1ºC. Voltammetric experiments were carried out at different scan rates, scanning towards cathodic potentials in a homemade glass cell with a reaction area of 33 mm^2.

Chapter 5

Results and discussion

In the first block of this chapter (Sections 5.1 and 5.2), pure prenylquinones (UQ and PQ) are studied using several techniques. The π-A isotherm gives information about the molecule stability at the air|water interface whereas the topographic images of UQ or PQ LB films transferred on mica give information about their compactness and physical state on a solid support, which represent a step forward on the characterization of these molecules. These LB films are also prepared on ITO to study their electrochemical response which will be compared in next sections with that of biomimetic systems. In the second block, the pure lipids DPPC, MGDG, DGDG and MD (Sections 5.3 to 5.6) are studied, whose specifications are presented in Section 4.1. The techniques used include π-A isotherms and AFM topographic imaging of the lipid LB films transferred on mica. The LB films are also prepared on ITO to study their electrochemical response which will be set as blank experiment for biomimetic membrane systems with electroactive molecules inserted. The third block (Sections 5.7 to 5.12) studies the lipid:prenylquinone systems where the π-A isotherms of them with a biological relevant ratio are presented. Moreover, the mathematical treatment of these isotherms permits the obtaining of the physical states and the mixing behaviour of the different ratio mixtures. In addition, the BAM images confirm in situ the physical state of the monolayer at the air|water interface. On the other hand, the study of LB films of the mixtures represents a step forward in the characterization of these biomimetic systems. The LB films transferred on mica are studied topographically using AFM, obtaining the characterization of the physical states, height and the covered area.

Finally, the transfer of LB films on a conductive substrate (ITO) permits the analysis of the electrochemical response of the lipid:prenylquinone mixtures. In Section 5.7, in addition to the explained techniques for studying the membranes prepared using the LB technique, the SPB method is used to prepare biomimetic membranes. We use AFM and Force curves in order to characterize the topography and mechanical properties of DPPC and DPPC:UQ SPB samples, so as to correlate the different behavior of SPBs on ITO referred to bare ITO. Moreover, the SPBs are also characterized using cyclic voltammetry in order to obtain the electrochemical response of the inserted UQ.

5.1 UQ system

5.1.1 π-A isotherms and physical states

The π-A isotherm of UQ and its corresponding C_s^{-1} curve (inset) calculated using the Expression 2.9 are presented in Figure 5.1.1. The isotherm shows that UQ presents the lift-off area, the area at which the isotherm starts the surface pressure increase, at 102 $Å^2 \cdot molec^{-1}$ and the limiting area, area per molecule obtained by extrapolating the highest pressure linear portion of the curve to zero surface pressure, at 88 $Å^2 \cdot molec^{-1}$ and it collapses at ≈ 11 $mN \cdot m^{-1}$.

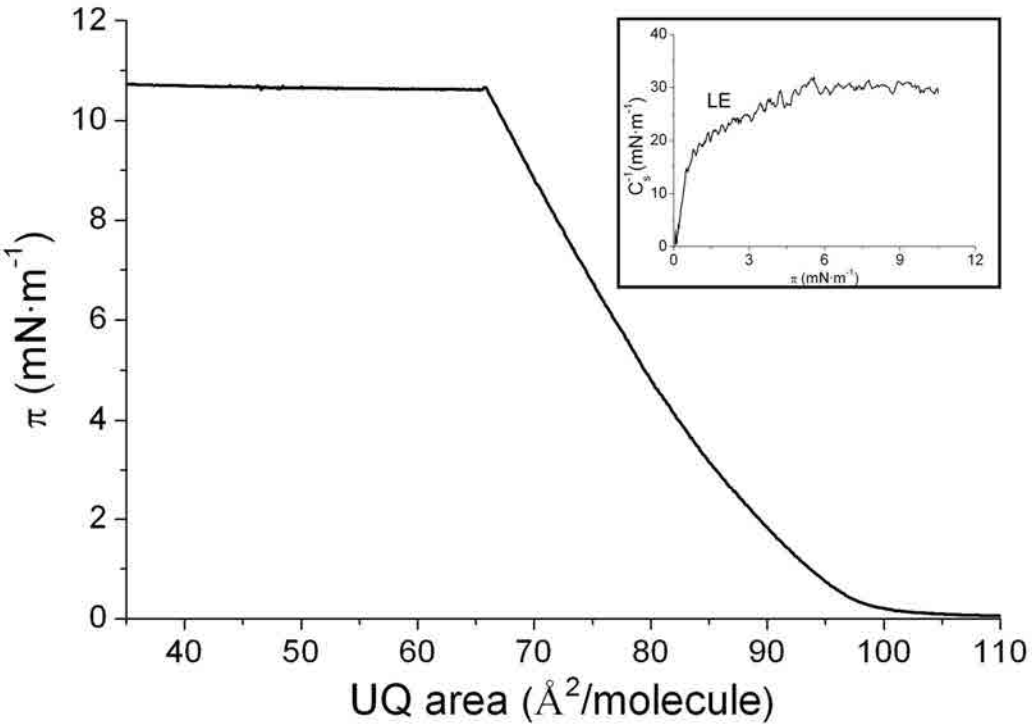

Figure 5.1.1 π-A isotherm of UQ at 21 ± 0.5 ºC on water subphase. Inset, inverse of the compressibility modulus vs. surface pressure.

The lift-off area observed is in line with the 91-94 $Å^2 \cdot molec^{-1}$ seen in part of the literature [1-4] although this area is different than the area obtained in other works which present this zone at 77-78 $Å^2 \cdot molec^{-1}$ [5,6]. Our UQ isotherm shows the limiting area value at 88 $Å^2 \cdot molec^{-1}$, in line with the 84-85 $Å^2 \cdot molec^{-1}$ observed in part of the literature [1-4] whereas other authors found this value at 71-72 $Å^2 \cdot molec^{-1}$ [5,6]. The differences observed between

both sets of values are related with the different solvent used for the UQ solution preparation, the different concentration of the UQ solution and/or the different origin of the UQ. On the other hand the collapse pressure observed in our results is in line with the 10-12 $mN \cdot m^{-1}$ observed in the literature using pure water or water with NaCl electrolyte for subphase [1-6]. Further compression of the UQ monolayer provokes the collapse of the film forming multilayers. The inset of Figure 5.1.1, in accordance with the $C_s^{-1}{}_{max}$ (maximum C_s^{-1} value) values presented by Vitovic et al. [7], shows that UQ presents LE phase till the collapse.

The high limiting area and the relatively low collapse pressure are determined by the higher hydrophobicity of the UQ tails compared with the hydrophilicity of the heads, which is low, and the large area of the tail (See Figure 3.5A). On the other hand, the literature [4] shows that UQH_2 has a higher stability than UQ presenting a collapse pressure of ≈ 14 $mN \cdot m^{-1}$ thanks to the slightly higher polarity of its head which favours the polar interactions with the subphase [1]. Moreover, the larger stability of UQH_2 is explained by the possibility of the methoxy groups of UQ to establish hydrogen bonds with aqueous solvents and the ability of the UQH_2 to establish stronger hydrogen bonds with aqueous solvents [8] than the oxidized form.

It is also interesting to point that the use of the CPK molecular model (space-filling model) gives the approximated dimensions of the UQ molecule being the total height 34 Å, corresponding 25 Å to the hydrocarbon chain and 9 Å to the head. The width of the head is 7 Å and depth is 4 Å. So that, the limiting area obtained in our experiments and in the literature for UQ is larger than the ≈ 63 $Å^2$ calculated using a CPK molecular model for UQ polar head including the hydrophobic cross section. The larger value indicates that the isoprenoid chain must adopt a conformation that increases the area per molecule occupied, as it was proposed by Bilewicz et al. [2].

5.1.2 AFM

The AFM topographic images of UQ at two surface pressures are presented to light which is the organization of these molecules once transferred to a hydrophilic and atomically flat substrate (mica), and ultimately to correlate this knowledge with the physical states proposed in the π-A isotherm section.

Figure 5.1.2 shows the AFM topographic images obtained for LB films of UQ transferred at π = 6 and 11 mN·m^{-1}. According to C_s^{-1} values (Inset of Figure 5.1.1), we deduce that both images show that UQ is in a fluid phase, most probably LE phase. Moreover, at the collapse, small yellow circles with diameter ≈ 100 nm and height ≈ 4 Å above the monolayer are seen (Figure 5.1.2B) The formation of such a fluid phase hindrances the formation of layer holes to measure the layer height so it is not possible to know whether it is a mono- or multilayer. The film transferred at π = 6 mN·m^{-1} must be a monolayer because the isotherms does not indicate other possibility and at π = 11 mN·m^{-1} the film has been transferred just after the collapse, so it may be understood that the film is also a monolayer of UQ with patches of UQ molecules (yellow circles) laying on the continue monolayer, according to the UQ molecule dimensions. The electrochemical response of the UQ film will give additional information to characterize these patches (See Section 5.1.3).

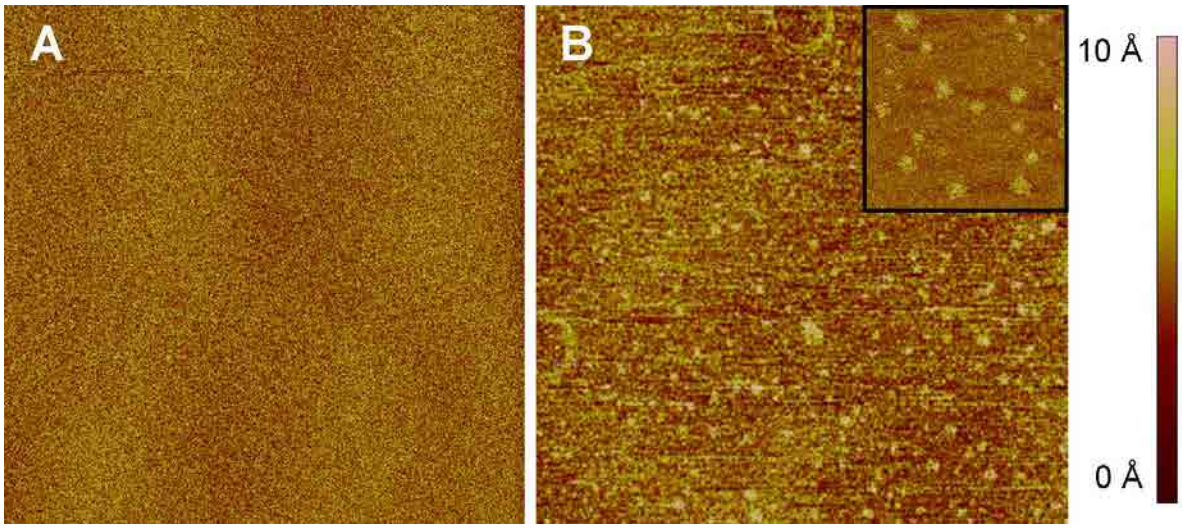

Figure 5.1.2. AFM images (5μm x 5μm) for LB films of UQ transferred on mica at 21 ºC at (A) π = 6 mN·m^{-1} and (B) π = 11 mN·m^{-1} (60 Å^2·molec^{-1}). Inset represent a (1μm x 1μm) zoom of the image B.

5.1.3 Electrochemical behaviour

Figure 5.1.3 shows the cyclic voltammogram of LB films of UQ transferred on ITO in a 0.150 M KCl cell solution buffered at pH 7.4 and at a scan rate of 10 $mV \cdot s^{-1}$. The LB films have been transferred at two different surface pressures selected according to the criterion of being one surface pressure below (π = 6 $mN \cdot m^{-1}$) and other close (π = 11 $mN \cdot m^{-1}$) to the collapse pressure. Previously, the ITO/electrolyte system has been studied to obtain the C_d from the value of the voltammetric charging current [9] and it has been observed that ITO behaves as a polarizable electrode in the experimental conditions, so no faradaic current is observed in the working potential window of -0.70 to 1.00 V (see dashed line in Figure 5.1.3) presenting a C_d around 1 $\mu F \cdot cm^{-2}$, in line with the literature [9-13].

In the experimental conditions, the cyclic volammograms (CVs) start at several positive potentials at which the UQ has the quinone ring in its oxidised form [4]. The potential is first scanned towards cathodic potentials until the final potential, which is determined by the hydrogen evolution, and then, the scan is reversed till the initial potential. The results at π = 11 $mN \cdot m^{-1}$ show two reduction and two oxidation peaks, whereas at lower surface pressures for the same system, only a reduction and an oxidation peak are present. It is also interesting to observe that the double layer capacity of the ITO/electrolyte experiments is fitted in the capacitive current of the ITO-UQ/electrolye systems at different surface pressures. The redox process comprised to the interval between -0.35 and 0.30 V and present at both surface pressures is called process I. At π = 11 $mN \cdot m^{-1}$, a second process is observed (process II), which has the reduction peak potential (II_R) at E_{pR} (II) = -0.58 ± 0.01 V and the oxidation peak potential (II_O), corresponding to the reversing scan, at E_{pO} (II) = 0.76 ± 0.02 V. Both peaks, obtained at very low scan rate, determine a formal potential for process II of E_f (II) = 0.09 ± 0.02 V. The assignment of peaks and processes has been done according to the observations for π = 11 $mN \cdot m^{-1}$ of Figure 5.1.3 and its inset, where the process I is reproduced in a narrower potential window, confirming the peaks and processes correlation. The peak and formal potentials for processes I and II are summarized in Table 5.1.1.

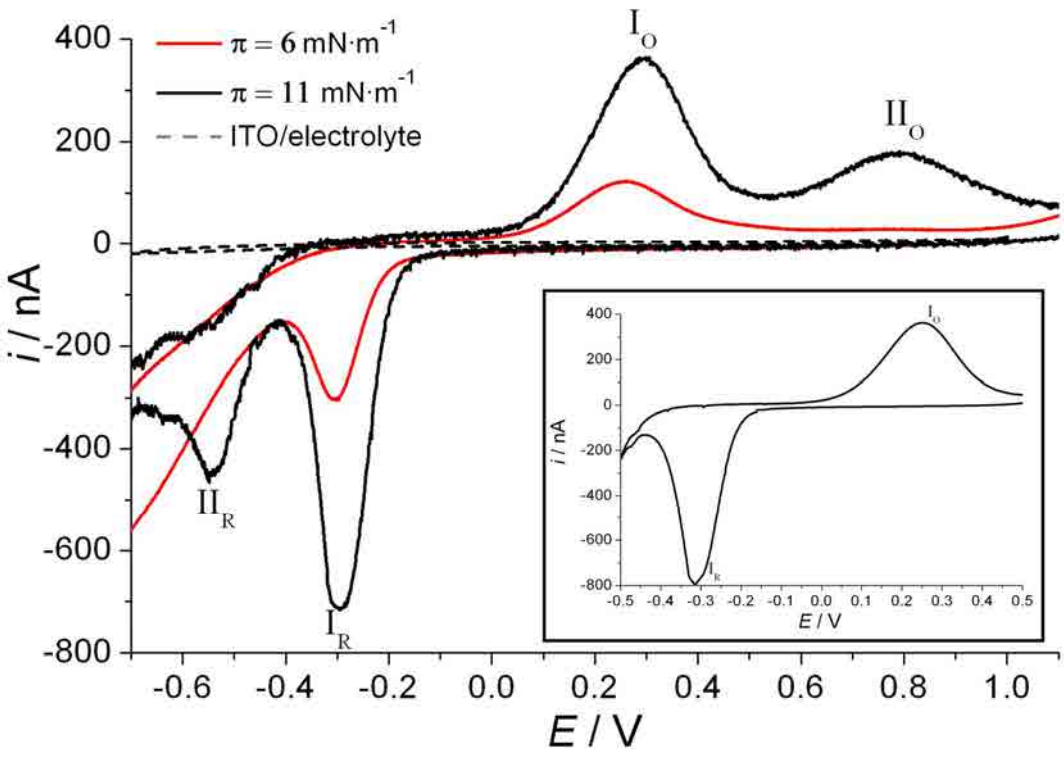

Figure 5.1.3. CVs of ITO-UQ LB films transferred at π = 6 mN·m^{-1} and 11 mN·m^{-1}. Inset, cyclic voltammogram of UQ LB film transferred at π = 11 mN·m^{-1} in a short potential window. Both carried on 0.150 M of KCl electrochemical cell using potassium phosphate buffered solution at pH 7.4 and at a scan rate of 10 mV·s^{-1}.

Table 5.1.1. Peak potentials and formal potentials for the redox processes I and II of ITO-UQ/electrolyte system.

π (mN·m^{-1})	E_{pR} (I) (V)	E_{pO} (I) (V)	E_f (I) (V)	E_{pR} (II) (V)	E_{pO} (II) (V)	E_f (II) (V)
6	-0.31 ± 0.02	0.25 ± 0.02	-0.03 ± 0.02	-	-	-
11	-0.30 ± 0.01	0.26 ± 0.01	-0.02 ± 0.02	-0.58 ± 0.01	0.76 ± 0.02	0.09 ± 0.02

Discussion of the electrochemical response of the ITO-UQ/electrolyte system

According to the literature, the global electrochemical reaction of the UQ/UQH$_2$ redox couple proposed for process I and II in our experimental conditions is the scenario (1), which is similar than that of BQ in aqueous buffered solution [14,15].

(1) $UQ + 2e^- + 2H^+ \rightarrow UQH_2$

The mechanism proposed in the literature [14-17] for confined UQ in this scenario has three main sequential reactions (1_{a-c}), being the process 1_b the rate determining step (rds) [15,18,19] due to the stabilization of the intermediate product $UQ^{\cdot -}$ [3,20]:

Reduction

(1_{ra}) $UQ + e^- \rightarrow UQ^{\cdot -}$

(1_{rb}) $UQ^{\cdot -} + H^+ \rightarrow UQH^{\cdot}$ rds

(1_{rc}) $UQH^{\cdot} + H^+ + e^- \rightarrow UQH_2$

Oxidation

(1_{oc}) $UQH_2 - e^- \rightleftharpoons UQH_2^{\cdot +}$

(1_{ob}) $UQH_2^{\cdot +} + OH^- \rightarrow UQH^{\cdot} + H_2O$ rds

(1_{oa}) $UQH^{\cdot} + OH^- - e^- \rightleftharpoons UQ + H_2O$

As it can be seen, the global redox process is pH dependent. In this Ph. D thesis the influence of the pH has not been studied and then, only the global reaction will be considered to describe the electrochemical behaviour of the UQ/UQH_2 redox couple. It is also worth to comment that the first ionization constant of UQH_2 is pKa = 12 [21,28] then at the pH 7.4 the neutral form of UQH_2 is predominant.

The shape of the voltammograms presents two important deviations respect to the theoretical models proposed in the literature to describe the cyclic voltammetric response of a surface confined reaction [29-31]. First, the peak shape, which is not symmetrical, presenting the reduction peaks a sharper shape than the oxidation ones, a similar behaviour to that seen by Märtensson and Agmo [32] and Hong and Park [22]. Second, the redox peak separation for process I or process II is larger than the expected for such systems, indicating an irreversible behaviour for the redox process. Similar deviations have been also obtained studying the surface electrochemistry of the UQ/UQH_2 system at pH < 12 [21-24].

The different shape of reduction and oxidation peaks can be explained by the different hydrophilic character of the two redox couple species UQ/UQH_2. Surface studies of UQ and UQH_2 [4] show that in the reduced form there is a shift in the balance of the hydrophobic to hydrophilic character of the molecule leading to a larger polarity. In our

system, due to the hydrophilic character of the ITO surface, the UQ molecules will be deposited with their heads oriented to the ITO surface. The larger polarity of UQH_2 compared with UQ leads the former to place in a closer position with the ITO surface, which favours the electron transfer. However, the formation of hydrogen bonds between UQH_2-ITO and UQH_2-water [4,25,26], the formation of UQH_2 aggregates [27,33-37] and the formation of UQ-UQH_2 charge-transfer complexes [21,33,39,40] overtake this effect obtaining a net oxidation hindrance.

The redox peaks separation for process II is larger than for process I indicating that process II is even more irreversible than process I. Moreover, the redox peaks separation for both processes I and II is enhanced when increasing the scan rate (see Figure 5.1.4), making the process more irreversible, which represents a similar trend to that was observed by Marchal et al. [21] and by Laval and Majda [41]. This large separation for both processes arised from the slow charge transfer rates at the ITO-monolayer|electrolyte interface [32].

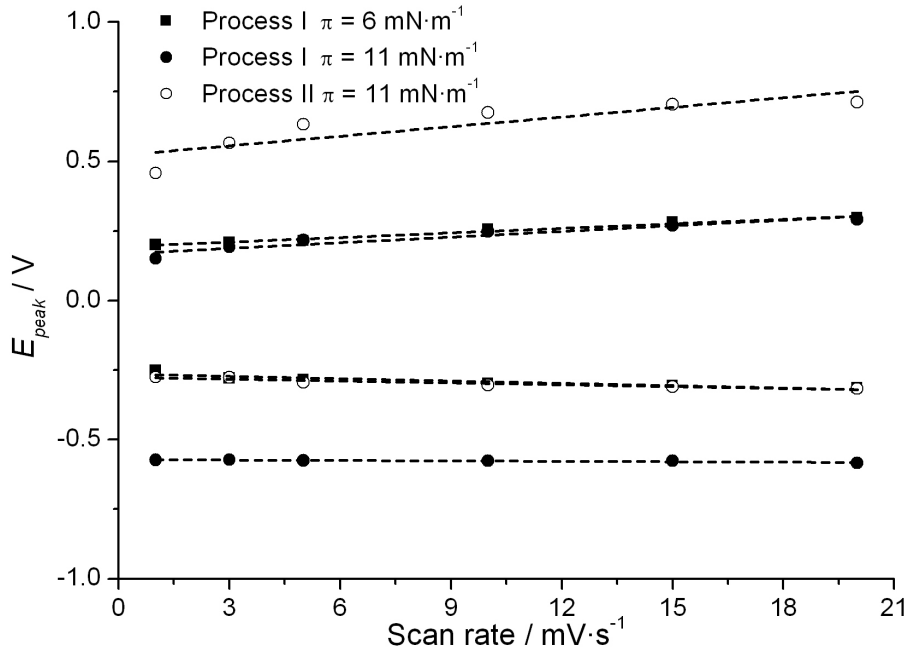

Figure 5.1.4. Reduction and oxidation peaks potential vs. the scan rate for the ITO-UQ/electrolyte electrode at π = 6 and 11 $mN \cdot m^{-1}$.

As it can be inferred from the Figure 5.1.4, an increase in the scan rate affects in a larger extent the oxidation peak position, which is moving faster to more anodic values than the

reduction peak to more cathodic values. So that, it indicates that the midpoint potential (midpoint potential between the oxidation and the reduction peak, both corresponding to the same redox process) for processes I and II has scan rate dependence. During the oxidation process, UQH_2 is the reactant so the possibilities of hydrogen bonds are larger, producing a stabilization of the UQH_2 molecule and making it more difficult to oxidise. Moreover, the stabilization of UQH·, which has been suggested [42], moves the second electron transfer peak potential to more anodic values, so that, the oxidation peak observed for each process is the convolution of two peaks that corresponds to each electron transfer which explains the larger width for the oxidation peak compared with the reduction one.

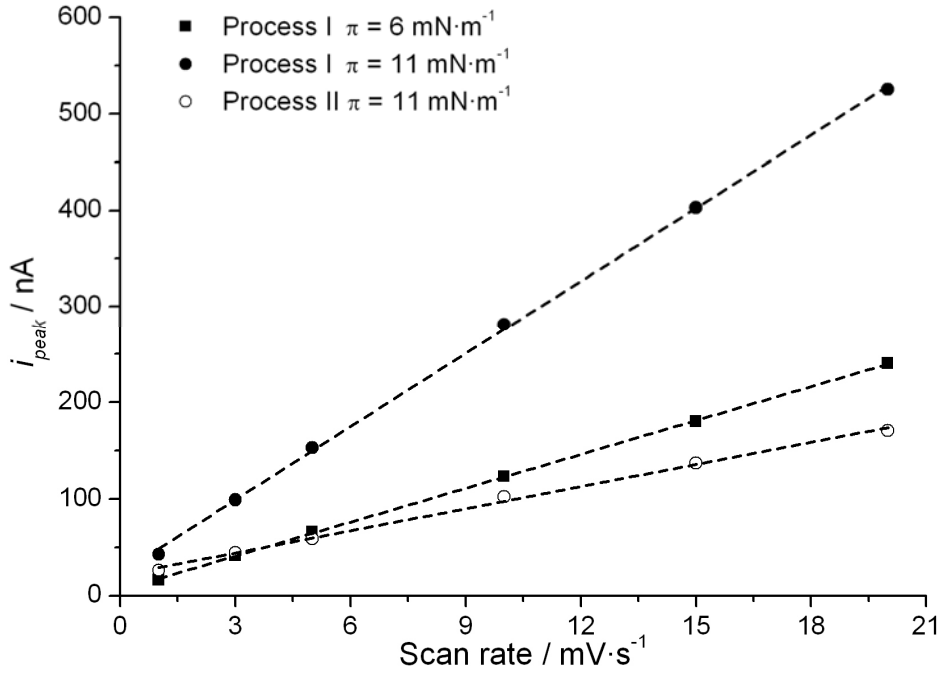

Figure 5.1.5. Oxidation peaks intensity vs. the scan rate for the ITO-UQ/electrolyte electrode at π = 6 and 11 $mN \cdot m^{-1}$.

Moreover, the dependence of the redox peaks current intensity vs. the scan rate has been studied for the ITO-UQ/electrolyte system and it has been obtained that either reduction or oxidation peak current intensity (i_{peak}) and scan rate are related by a linear dependence. Figure 5.1.5 shows this dependence for the oxidation peak current so indicating that UQ molecules are surface confined in both processes [16,29] and that the electron transfer process is not diffusion controlled, in line with the observations of Märtensson and Agmo [32] for scan rates < 1 V/s, Gordillo and Schiffrin [28] and Li et al. [43] for monolayers

containing UQ confined on the surface. This result also indicates that the redox UQ centres have enough presence of available protons close to them.

The charge involved at each surface pressure is obtained by integrating the area under the reduction or oxidation waves. The obtained experimental values of charge, presented as surface coverage, are shown in Table 5.1.2 and compared with the expected value to obtain the electroactive fraction of UQ. The expected surface coverage values are calculated assuming that UQ molecules are perfectly spread on the ITO surface and that they form no aggregates, being the resulting value corrected with the transfer ratio associated to it in the LB transfer process. We have chosen to show in Table 5.1.2 the oxidation surface charge of the redox processes which are similar but lower than the results obtained for the reduction processes which have the undesirable contribution of the hydrogen evolution.

Table 5.1.2. Expected and experimental total surface coverage, experimental surface coverage for process I and electroactive fraction involved in the whole redox process for ITO-UQ/electrolyte system using 0.150 M of KCl electrochemical cell and using potassium phosphate buffered solution at pH 7.4, at a scan rate of 10 $mV \cdot s^{-1}$.

π ($mN \cdot m^{-1}$)	Γ_{expec} (10^{-12} mol · cm^{-2})	$\Gamma_{O\ tot}$ (10^{-12} mol · cm^{-2})	$\Gamma_{O\ proc\ I}$ (10^{-12} mol · cm^{-2})	Electroactive fraction (%)
6	145.5	37.5	37.5	25.8
11	255.4	149.2	100	58.4

The results presented in Table 5.1.2 show that both the surface coverage and the electroactive fraction increase when increasing the surface pressure. The low electroactive fraction for both surface pressures indicates that part of the UQ molecules is electrochemically inactive. The low electroactive fraction can be attributed, on the one hand, to the formation of UQ head-to-head aggregates, as it has been proposed by previous authors on other systems using UQ and other prenylquinones [27,34-37]. In addition, the low electroactivity can be correlated with the electrical properties and surface structure of the substrate used as working electrode. Laval and Majda [41] observed 100% of electroactivity when the substrate employed was bare gold whereas after the deposition of an octadecanethiol monolayer (OM) on the gold substrate, the electroactivity of the pure UQ system was reduced below the 50%. In our case the non homogeneous electrode

surface and the semiconductive properties of ITO make it to behave different than metal surfaces.

Our results also contrast with the observations of Moncelli et al. [19] who observed a decrease in the surface charge when increasing the initial UQ content from 0.5 to 2 % on a monolayer of DOPC on HDME at pH 9.5. This different behaviour is explained by the differences in pH. Moncelli et al. [15,19] worked with pH 9.5 so the availability of protons in the proximity of the UQ heads is more limited than in our experiments at pH 7.4. The lack of protons affects the reduction rate determining step (1_b), so at high UQ concentrations or high scan rates, the step 1_b is not completed so the electroactive fraction is reduced. In our experiments the enough presence of available protons close to the UQ centres avoids the high local UQ concentration problem, so the electroactive fraction is enhanced when increasing the initial UQ content. This is observation is explained by the electron hopping effect (See Section 3.4.5). This process consists in a successive electron exchange between the oxidized and reduced form of the redox pair, in which the product (UQH·) of the first electroreduced UQ act as reductor for the UQ beside by the proximity of electronic levels.

The E_f (I) value shown in table 5.1.1 is comparable with the values given in the literature for other systems in which the UQ molecules are confined in monolayers on a substrate surface. Gordillo and Schiffrin [28] have studied the HDME-UQ/electrolyte system and they found at pH ≈ 9.5 the midpoint potential at ≈ -0.26 V which corrected by the pH differences, gives a $E_{f\mathrm{UQ/UQH2}}$ ≈ -0.13 V at pH 7.4. The hydrophobic character of HDME orients UQ with the tail in direct contact with the surface and the head pointing to the solution. In this line, Ma et al. [44,45] prepared SAMs of UQ on gold giving an extrapolated formal potential of $E_{f\mathrm{UQ/UQH2}}$ ≈ - 0.09 V and Petrangolini et al. [17] observed the formal potential for hydroquinone/benzoquinone in SAM on gold at $E_{f\mathrm{UQ/UQH2}}$ ≈ -0.05 V. Both studies with the UQ head environment and distance to the surface that can be assimilated to that of Gordillo and Schiffrin [28]. On the other hand, Laval and Majda [41] obtained a $E_{f\mathrm{UQ/UQH2}}$ ≈ -0.09 V for a LB film of UQ transferred at 10 $mN \cdot m^{-1}$ on pure gold in which the UQ is placed with the heads in direct touch with the substrate surface, which is a similar position to our experiments. The similar formal potential observed using several substrates and several UQ head-substrate surface distances indicates that in all the exposed

situations, the UQ head has a similar environment and experiences a similar redox mechanism regardless the distance to the electrode surface.

The slight differences observed on the formal potential between the literature and our results are related with the physicochemical properties of the substrate, the differences on the electrolyte solution and the differences in the distance UQ-substrate surface. Concretely, in the case of HDME the orientation of the headgroup and the more compact distribution of the molecules hinder the electron transfer so obtaining more cathodic formal potentials than our results on ITO. The position of UQ on ITO has not been studied although the work of Li et al. [43] using UQ on a hydrophilic substrate like silver indicate that UQ or UQH_2 head have face-on orientation, with the benzene ring lying flat on the substrate surface which favours the interactions substrate-UQ. In our case, the possibility of hydrogen bonds formation between UQ, UQH_2, water and ITO is added to the ITO-UQ hydrophilic interactions, so we conclude that UQ is reduced via process I and it has the head in contact with the ITO surface with the tails tilted and pointing to the solution.
On the other hand, although the process II is more irreversible and kinetically unfavourable [47] than process I, it has a more positive formal potential (close to that of benzoquinone/hydroquinone in aqueous solution E_f (I) ≈ 0.14 V vs. Ag/AgCl [48]) that can be correlated with a more aqueous environment for the UQ head group, which is translated in that they are placed in an environment with H^+ ion more available nearer to the aqueous electrolyte [9]. As this process only takes place when the UQ is transferred at surface pressure around the collapse pressure, we correlate this second redox process with the UQ patches lying above the first monolayer (Exposed in Figure 5.1.2 B).

So that, our results confirm that UQ is confined and does not diffuse to the working electrode surface to experience the redox processes, which indicates that the electron transfer takes place by two mechanisms. First, by direct transfer and electron hopping between the UQ placed in close contact with ITO (process I) and second, by electron hopping through the main UQ monolayer (process II). The electron hopping favours the rate determining step (1_b) so favouring the electroreduction in the timescale used. At low surface pressure the molecules are far enough to do not be affected by this phenomenon. Increasing the surface pressure the UQ headgroups are placed closer favouring the electron hopping redox process.

5.1.4 Global sight of the UQ system transferred on ITO using the LB technique

The results obtained indicate that UQ forms monolayers at the air|water interface, showing LE state during the entire isotherm, occurring the monolayer collapse at a relatively low surface pressure, ≈ 11 $mN \cdot m^{-1}$. The deposition of UQ on mica shows that after the collapse, UQ forms monolayers with some patches over it, which are correlated with UQ molecules expulsed from the monolayer and established in pools, placed parallel to the mica surface (Figure 5.1.6). The electrochemical response shows one redox process at low surface pressure and it appears a second redox process when increasing the surface pressure. The coincidence of the second redox process with the appearance of UQ patches indicates that both are related, and the first redox process corresponds to the molecules in direct contact with the ITO surface.

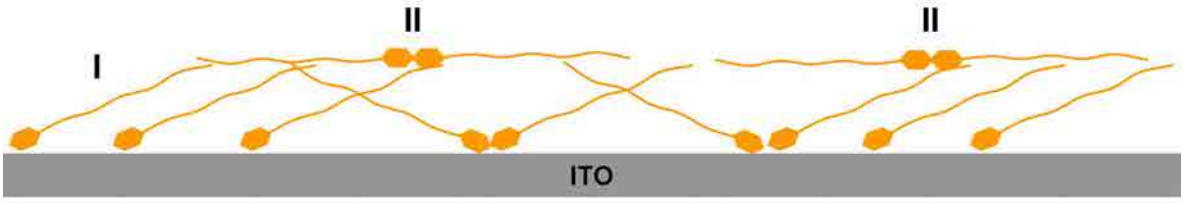

Figure 5.1.6. Scheme of the UQ molecules transferred on ITO at π = 11 $mN \cdot m^{-1}$. The labels I and II indicate the UQ positions that origin the redox processes I and II.

5.2 PQ system

5.2.1 π-A isotherms and physical states

The π-A isotherm of PQ and its corresponding C_s^{-1} curve (inset) calculated using the Expression 2.9 are presented in Figure 5.2.1. The isotherm shows that pure PQ presents the lift-off and limiting area at 76 Å^2·molec^{-1} and 72 Å^2·molec^{-1} respectively, and a very low collapse pressure ≈ 0.3 mN·m^{-1} in water subphase. The selection of this collapse pressure has been done according to the surface pressure at which the slope of the isotherm has been reduced and, in addition, at which the C_s^{-1} curve present a low decrease after the maximum. We correlate both observations with the collapse.

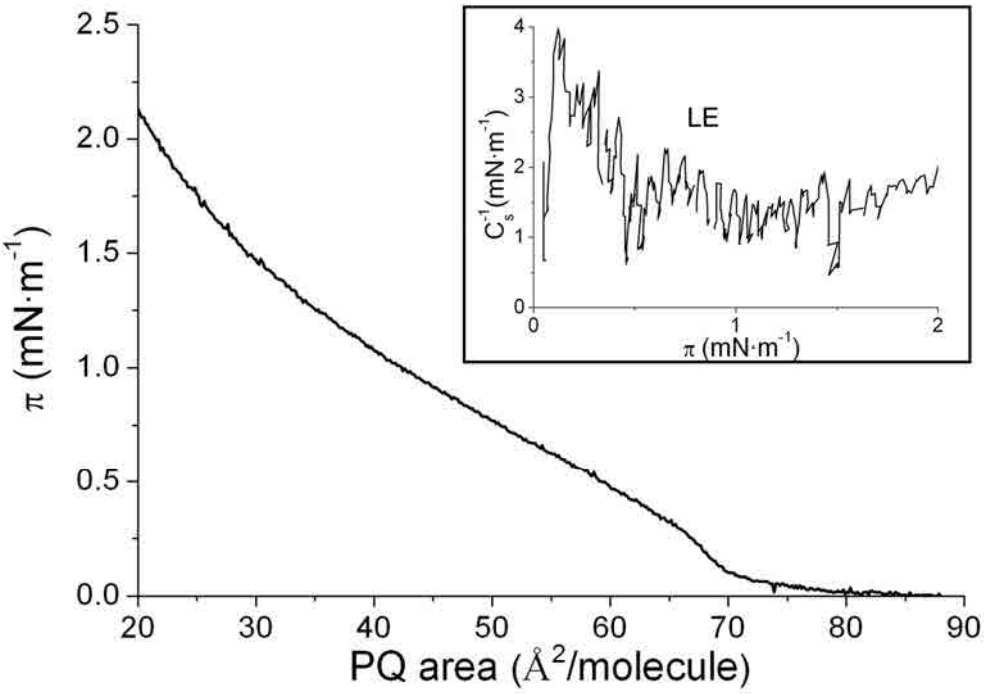

Figure 5.2.1 π-A isotherm of PQ at 21 ± 0.5 ºC on water subphase. Inset, inverse of the compressibility modulus vs. surface pressure.

The lift-off area obtained in our π-A isotherm is close to that observed by Kruk et al. [38] using phosphate buffered at pH 7 subphase. Other studies using phosphate buffered subphase presents 83 Å^2·molec^{-1} [49] and 92 Å^2·molec^{-1} [50]. The limiting area per molecule that we observe, 72 Å^2·molec^{-1}, is in line with the 68 Å^2·molec^{-1} seen by Es-Sounni and Leblanc [50], the 73 Å^2·molec^{-1} observed by Guay and Leblanc [49] and the 76

$Å^2 \cdot molec^{-1}$ observed by Kruk et al. [38]. On the other hand, the collapse pressure obtained in our experimenst is in line with the 1.2-1.4 $mN \cdot m^{-1}$ observed in the literature using as subphase a phosphate buffered solution at pH close to the biological one [49,50]. Further compression of the PQ monolayer provokes the collapse of the film forming multilayers. The differences between studies in the lift-off area and the limiting area of PQ may be related with the method used for PQ purification and/or the presence of impurities, as it was suggested by Es-Sounni and Leblanc [50], and the different solvent used for the PQ solution preparation. On the other hand, the inset of Figure 5.2.1 presents the C_s^{-1} curve corresponding to the PQ isotherm, although the extremely low collapse pressure indicates that the $C_{s\ \max}^{-1}$ values presented by Vitovic et al. [7] can not be applied to this system. Despite of this difficulty, the shape of the PQ isotherm and the behaviour observed in Section 5.1.1 for UQ suggest that the monolayer forms LE at 0.1 $mN \cdot m^{-1}$.

The low collapse pressure and the high limiting area are determined by the higher hydrophobicity of the PQ (See Figure 3.5B) tails compared with the low hydrophilicity of the heads and the large area of the tail.

It is also interesting to point that the use of the CPK model gives the approximated dimensions of the PQ molecule being the total height 32 Å, corresponding 23 Å to the hydrocarbon chain and 9 Å to the head. The width of the head is 6.6 Å and the depth is 4 Å. So that, the limiting area obtained in our experiments and in the literature for PQ is close to the ≈ 60 $Å^2 \cdot molec^{-1}$ calculated using a CPK atomic model for PQ polar head including the hydrophobic cross section. On the other hand, the literature [38] indicates that PQH_2 occupies a slightly larger surface area (83 $Å^2 \cdot molec^{-1}$) than the 76 $Å^2 \cdot molec^{-1}$ observed in the same study for PQ. However, the PQH_2 has higher stability presenting a collapse pressure of ≈13 $mN \cdot m^{-1}$ thanks to the slightly higher polarity of its head which favours the polar interactions with the subphase [1] and, especially, the ability of the quinol to stablish stronger hydrogen bonds with aqueous solvents [8].

5.2.2 AFM

The AFM topographic images of PQ at two surface pressures are presented to light which is the organization of these molecules once transferred to a hydrophilic substrate (mica) and to correlate this knowledge with the physical state proposed in the π-A isotherm section.

Figure 5.2.2 shows the AFM topographic images obtained for LB films of pure PQ transferred at π = 1 and 2 $mN \cdot m^{-1}$. We have chosen these surface pressures to avoid the extremely low transfer ratio at lower surface pressures than the collapse pressure.

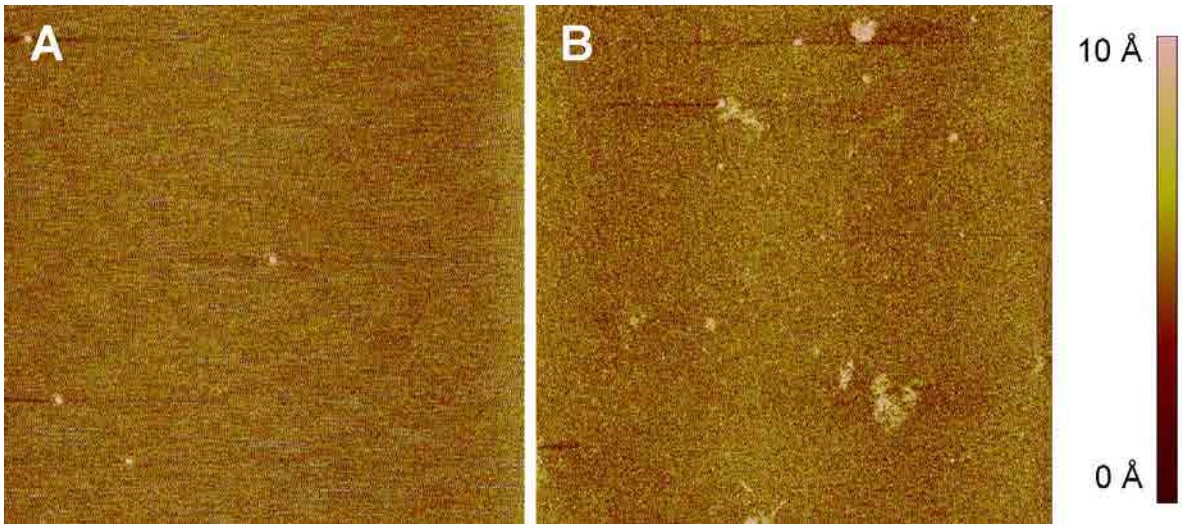

Figure 5.2.2. AFM images (5μm x 5μm) for LB films of PQ transferred on mica at 21 ºC at (A) π = 1 $mN \cdot m^{-1}$ (48 $Å^2 \cdot molec^{-1}$) and (B) at π = 2 $mN \cdot m^{-1}$ (29 $Å^2 \cdot molec^{-1}$).

Figure 5.2.2 shows that PQ is in a very fluid phase, most probably LE according to the previous explanation. It can also be observed the presence of small white circles with a height of ≈ 30 Å in Figure 5.2.2A that increase in number when the collapse has been taken place (Figure 5.2.2B). In addition, structures of diameter ≈ 200 nm and height ≈ 5 Å are seen at this high surface pressure. We correlate the presence of these structures to the formation of PQ aggregates [27,34-37] that are favoured when the PQ concentration is high [36] which is achieved thanks to the barrier compression. Similar structures have been observed for UQ (Figure 5.1.2), although in that figure, the distribution of them was more homogeneous.

The formation of such a fluid phase hindrances the formation of layer holes to measure the layer height so it is not possible to know whether it is a mono- or multilayer. Anyway, the low transfer ratios observed for pure PQ (≈ 10 %) and the results observed using other techniques indicate that the low stable multilayer formed at the air|water interface at higher surface pressure than the collapse is undone once it has been transferred to the mica, so occupying in monolayer form all the mica available space in a more fluid phase than at the air|water interface, which correlates with previous authors [51] failed attempts to depositing multilayers of PQ. So that, the AFM topographic images of pure PQ on mica contribute with little information of this system due to the extremely fluidness of the film deposition which is also the cause of the low transfer ratio.

5.2.3 Electrochemical behaviour

Figure 5.2.3 shows the cyclic voltammogram of a LB film of pure PQ transferred on ITO at a scan rate of 10 $mV \cdot s^{-1}$ in a 0.150 M KCl cell solution buffered at pH 7.4. The LB films have been transferred at three different surface pressures, all of them higher than the collapse pressure. Below that pressure, the transfer ratio is practically zero so the samples present no electrochemical response. The PQ behaviour exposed for the mica-PQ system is also worth for the ITO-PQ system, which implies that, regardless the PQ is forming multilayers at the air|water interface, the low compactness of them leads the PQ to form monolayers once transferred, as it has been explained in the previous section. So that, when transferring at higher surface pressure, the number of PQ molecules in the monolayer is increased. However, only one redox process is observed (process I) indicating that all the PQ molecules have a similar position on the ITO surface. Previously, the ITO/electrolyte system has been studied and it shows that ITO behaves as a polarizable electrode in the experimental conditions (see dashed line in Figure 5.2.3) as it has been explained in Section 5.1.3.

In the experimental conditions, the CVs start at several positive potentials at which the PQ has the quinone ring in its oxidised form [4]. The potential is first scanned towards cathodic potentials until a final potential, which is determined by the hydrogen evolution, and then, the scan is reversed till the initial potential. Despite the fact that wider potential window has been tested, the results show only one redox process that we will assign as process I. The redox peaks and formal potentials for process I at several surface pressures are summarized

in Table 5.2.1, all of them presenting the reduction peak at E_{pR} (I) = -0.30 ± 0.03 V and the oxidation peak at E_{pO} (I) = 0.24 ± 0.03 V which represents a formal potential of E_f (I) = -0.03 ± 0.03 V. It is also interesting to observe that the double layer capacity of the ITO/electrolyte experiments is fitted in the capacitive current of the ITO-PQ/electrolyte system at different surface pressures.

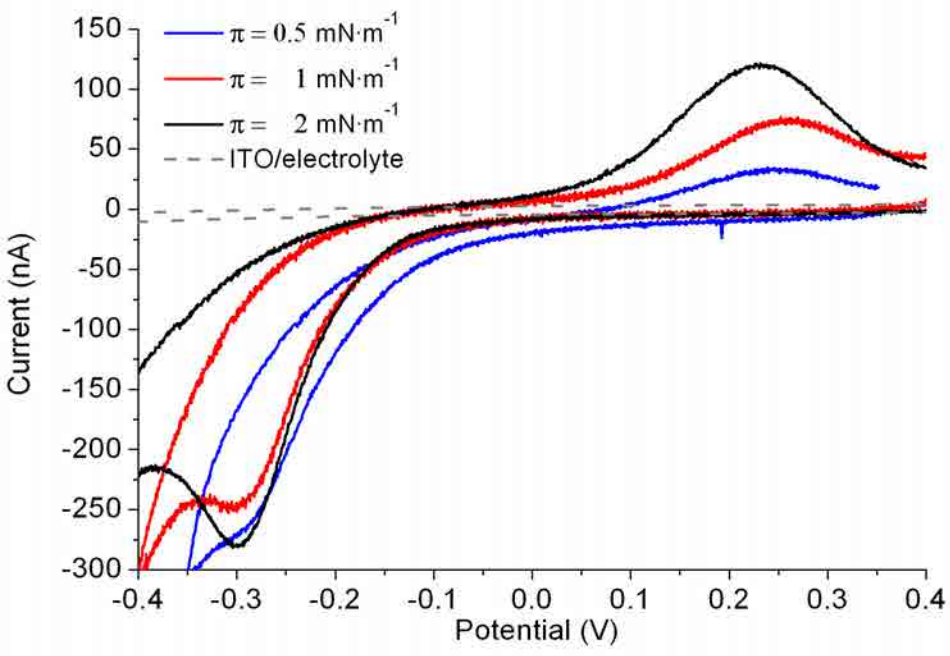

Figure 5.2.3. CVs of ITO-PQ LB films transferred at several surface pressures carried on a 0.150 M of KCl electrochemical cell using potassium phosphate buffered solution at pH 7.4 and at a scan rate of 10 mV·s^{-1}.

Table 5.2.1. Peak potentials and formal potentials of the redox processes I of ITO-PQ/electrolyte system.

π (mN·m^{-1})	E_{pR} (I) (V)	E_{pO} (I) (V)	E_f (I) (V)
0.5	-0.30 ± 0.02	0.25 ± 0.02	-0.03 ± 0.03
1	-0.31 ± 0.02	0.26 ± 0.02	-0.03 ± 0.03
2	-0.30 ± 0.02	0.23 ± 0.02	-0.04 ± 0.03

Discussion of the electrochemical response of the ITO-PQ/electrolyte system

The PQ/PQH$_2$ electrochemical response has only been previously studied by Marchal et al. [21,23] in a SPB of DMPC on gold. The results obtained were similar to those corresponding to the UQ/UQH$_2$ system using the same conditions. Moreover, the morphology and structure similarity between UQ and PQ and the similar redox behaviour observed (summarized in Table 5.1.1 and 5.2.1) from our own experiments leads us to treat and discuss PQ in the same line that it was expressed for UQ. So that, the global

electrochemical reaction of the PQ/PQH_2 redox couple proposed in our experimental conditions is the scenario 1.

(1) $PQ + 2e^- + 2H^+ \rightarrow PQH_2$

This scenario has three main sequential reactions:

Reduction

(1_{ra}) $PQ + e^- \rightarrow PQ^{\cdot -}$

(1_{rb}) $PQ^{\cdot -} + H^+ \rightarrow PQH^{\cdot}$ rds

(1_{rc}) $PQH^{\cdot} + H^+ + e^- \rightarrow PQH_2$

Oxidation

(1_{oc}) $PQH_2 - e^- \rightleftharpoons PQH_2^{\cdot +}$

(1_{ob}) $PQH_2^{\cdot +} + OH^- \rightarrow PQH^{\cdot} + H_2O$ rds

(1_{oa}) $PQH^{\cdot} + OH^- - e^- \rightleftharpoons PQ + H_2O$

As it can be seen, the global redox process is pH dependent. In this Ph. D thesis the influence of the pH has not been studied and then, only the global reaction will be considered to describe the electrochemical behaviour of the PQ/PQH_2 redox couple. It is also worth to comment that the first ionization constant of PQH_2 should be pKa ≈ 10 according to the values observed for similar quinones [52], then at the pH 7.4, the neutral form of PQH_2 is predominant.

The shape of the voltammograms presents two important deviations respect to the theoretical models proposed in the literature to describe the cyclic voltammetric response of a surface confined reaction [29-31]. First, the peak shape which is not symmetrical, presenting the reduction peaks a sharper shape than the oxidation ones, a similar behaviour than that seen by Märtensson and Agmo [32] and Hong and Park [22]. Second, the redox peak separation for process I is larger than the expected for such systems, indicating an irreversible behaviour for the redox process. Similar deviations have been also obtained studying the surface electrochemistry of the UQ/UQH_2 system at pH < 12 [21-24].

The redox peaks separation for process I is enhanced when increasing the scan rate, making the process more irreversible (see Figure 5.2.4) that represents a similar trend to that was observed by Marchal et al. [21] and by Laval and Majda [41]. This large separation for both processes arised from the slow charge transfer rates at ITO-monolayer|electrolyte interface [32].

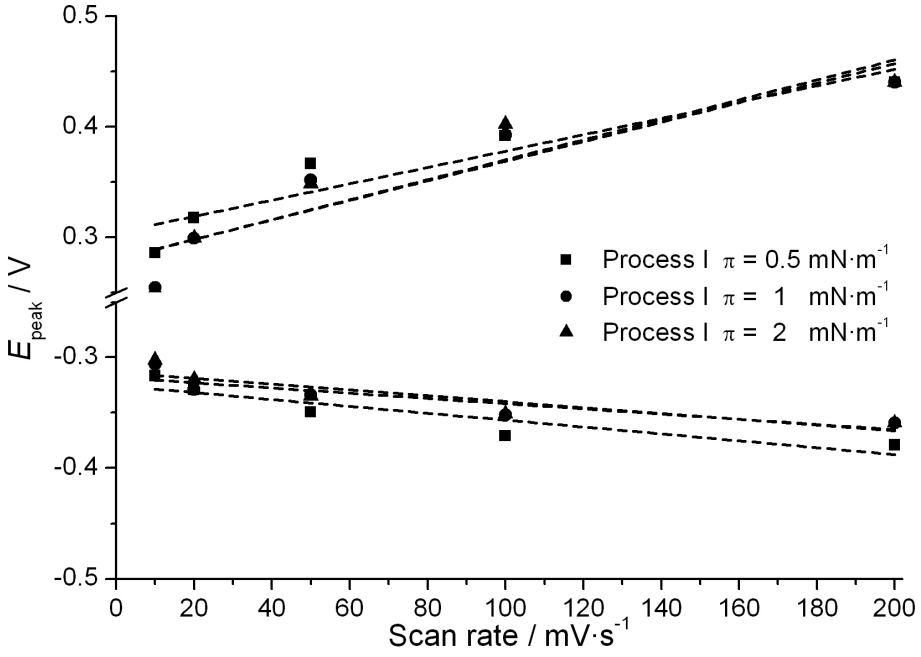

Figure 5.2.4. Peak potential vs. the scan rate for the ITO-PQ/electrolyte system at π = 0.5, 1 and 2 mN·m^{-1}.

As it can be inferred from the Figure 5.2.4, an increase in the scan rate affects in a larger extent the oxidation peak position, which is moving faster to more anodic values than the reduction peak to more cathodic values. So that, it indicates that the midpoint potential for process I has scan rate dependence.

As it has been discussed for the UQ/UQH_2 redox couple, the larger polarity of PQH_2 compared with PQ leads the former to place in a closer position to the ITO surface which favours the electron transfer. Moreover, the formation of hydrogen bonds between PQH_2-water [4, 25,26], the formation of PQH_2 aggregates [27,33-37] and the formation of PQ-PQH_2 charge-transfer complexes [33,38-40] overtake this effect obtaining a net oxidation hindrance. The reduction species present little stabilization due to PQH_2 is more hydrogen bond forming than PQ. Moreover the former is being produced during the reduction process whereas for the oxidation process, PQH_2 is the reactant so the possibilities of hydrogen bonds are larger, producing a stabilization of the PQH_2 molecule and making it more difficult to oxidise.

The stabilization of PQH·, which has been suggested [42], moves the second electron transfer peak potential to more anodic values, so that, the oxidation peak observed for each

process is the convolution of two peaks that corresponds to each electron transfer which explains the larger width for the oxidation peak compared with the reduction one.

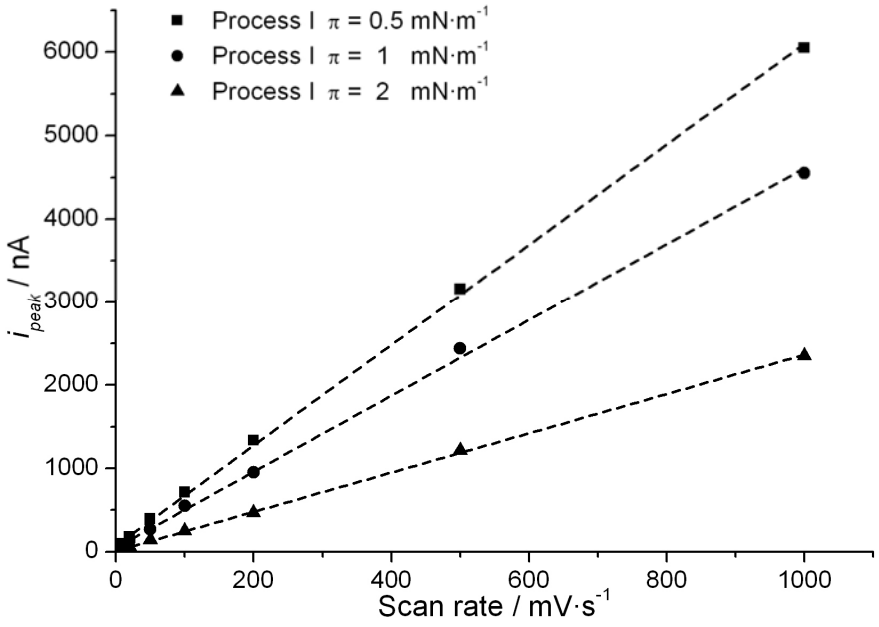

Figure 5.2.5. Peak intensity vs. the scan rate for the ITO-PQ/electrolyte electrode at π = 0.5, 1 and 2 mN·m^{-1}.

Moreover, the current intensity of the redox peaks has been studied for the ITO-PQ/electrolyte system and it has been shown that either reduction or oxidation peak current intensity (i_{peak}) and scan rate are related by a linear dependence. Figure 5.2.5 shows this dependence for the oxidation, so indicating that PQ molecules are surface confined in both processes [16,29] and that the electron transfer process is not diffusion controlled, in line with the observations of Märtensson and Agmo [32] for scan rates < 1 V/s, Gordillo and Schiffrin [28] and Li et al. [43] for monolayers containing UQ confined on the surface. In addition, the explained similarities between PQ and UQ permit to compare the UQ voltammetric results found in the literature presented in Section 5.1.3 with our experimental voltammetric results using PQ. The slight differences on the formal potential observed with our PQ results are related with the differences between both prenylquinones, the physicochemical properties of the substrate, the differences on the electrolyte solution and the differences in the distance prenylquinone head-substrate surface.

The charge involved at each surface pressure is obtained by integrating the area under the reduction or oxidation waves. The obtained experimental values of charge, presented as surface coverage, are shown in Table 5.2.2 and compared with the expected value to obtain the electroactive fraction of PQ. The expected surface coverage values are calculated assuming that PQ molecules are perfectly spread on the ITO surface and that they form no aggregates, being the resulting value corrected with the transfer ratio associated to it. We have chosen to show in Table 5.2.2 the oxidation surface charge of the redox process which is similar but lower than the results obtained for the reduction process which have the undesirable contribution of hydrogen evolution.

Table 5.2.2. Experimental, expected total surface coverage and electroactive fraction involved in the redox process for ITO-PQ/electrolyte system using 0.150 M of KCl electrochemical cell and using potassium phosphate buffered solution and at pH 7.4, at a scan rate of 10 $mV \cdot s^{-1}$.

π ($mN \cdot m^{-1}$)	Γ_{expec} (10^{-12} mol · cm^{-2})	$\Gamma_{O\,tot}$ (10^{-12} mol · cm^{-2})	Electroactive fraction (%)
0.5	23.1	5.2	22.6
1	39.5	18.0	45.5
2	48.8	27.0	55.3

The results presented in Table 5.2.2 show that both the surface coverage and the electroactive fraction increase when increasing the surface pressure. The low electroactive fraction for all the surface pressures indicates that part of the PQ molecules is electrochemically inactive. The low electroactive fraction can be attributed, on the one hand, to the formation of PQ head-to-head aggregates, as it has been proposed by previous authors on other systems using other prenylquinones [27,34-37]. In addition, the low electroactivity can be correlated with the electrical properties and surface structure of the substrate used as working electrode. Laval and Majda [41] observed 100% of UQ electroactivity when the substrate employed was bare gold whereas after the deposition of an OM on the gold substrate, the electroactivity of the pure UQ system was reduced below the 50%. In our case the non homogeneous electrode surface and the semiconductive properties of ITO makes it to behave different than metal surfaces. On the other hand, the electroactive fraction is enhanced when increasing the initial PQ content. In our case, the occurrence of an electron hopping effect can be proposed (See Section 3.4.5). So that, our results confirm that PQ is confined and does not diffuse to the working electrode surface to

experience the redox process, which indicates that the electron transfer takes place both by direct transfer and electron hopping between the PQ molecules placed in close contact with ITO.

5.2.4 Global sight of the PQ system transferred on ITO using the LB technique

The results obtained indicate that PQ, only at very low surface pressures, forms monolayers at the air|water interface showing LE state at the most compact state and, after the collapse, it forms multilayers. The AFM images of the deposition of PQ on mica show that, after the collapse, PQ forms fluid monolayers with some patches over it, which are correlated with PQ molecules expulsed from the monolayer and established in not well distributed aggregates pools. The electrochemical response shows only one redox process at several surface pressures, so that, the non-appearance of the second redox peak indicates that the proportion of PQ molecules located at a fixed position over the monolayer is not relevant once transferred on ITO, indicating furthermore, a lower order in the first monolayer of PQ molecules that does not let the formation of patches over it (Figure 5.2.6). The redox process observed includes all the PQ molecules on the ITO surface, which are mostly placed in direct contact with the ITO surface.

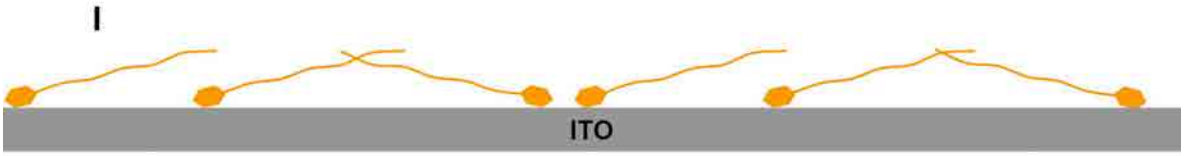

Figure 5.2.6. Scheme of the PQ molecules transferred on ITO at π = 2 mN·m^{-1}. The label I indicates the PQ position that origin the redox processes I. The low stability of the PQ monolayer and the low transfer ratio associated to it implies no order and no orientation of the film molecules.

5.3 DPPC

5.3.1 π-A isotherms and physical states

The π-A isotherm of DPPC and its corresponding C_s^{-1} curve (inset) calculated using the Expression 2.9 are presented in Figure 5.3.1. The isotherm shows that DPPC forms very stable monolayers that presents the lift-off and limiting area at 91 $Å^2 \cdot molec^{-1}$ and 52 $Å^2 \cdot molec^{-1}$ respectively, and it collapses at ≈ 54 $mN \cdot m^{-1}$.

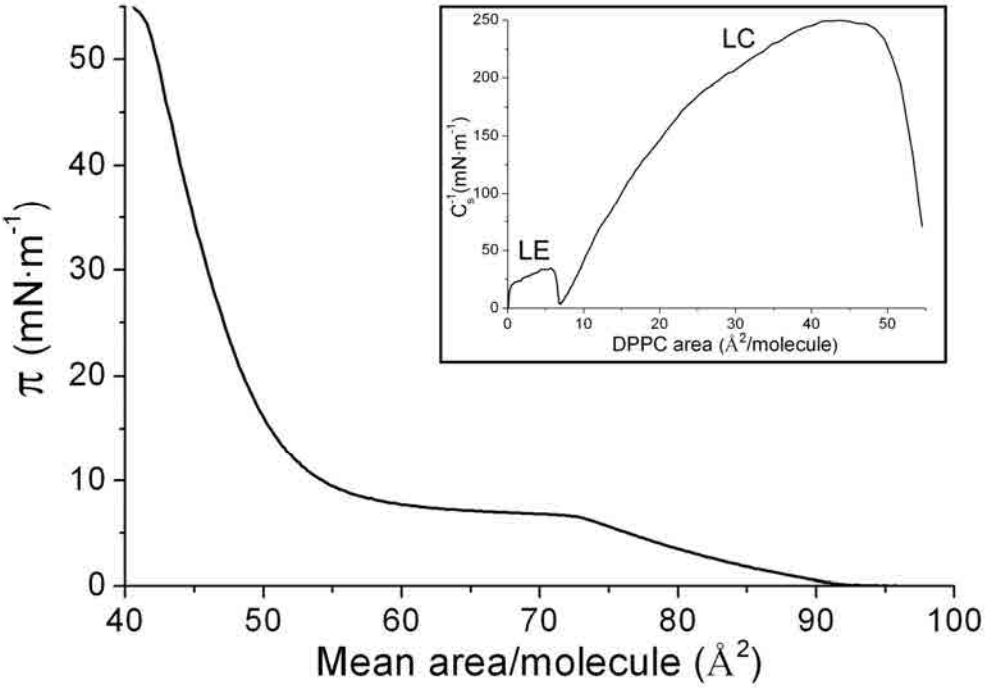

Figure 5.4.1 π-A isotherm of DPPC at 21 ± 0.5 ºC on water subphase. Inset, inverse of the compressibility modulus vs. surface pressure.

The DPPC lift-off and limiting area and collapse pressure are nearly the same than that observed in previous studies using similar conditions [53-55], showing also the plateau at similar surface pressure. Accordingly to the values presented by Vitovic et al. [7] our DPPC presents LE phase from low surface pressions till the plateau at π ≈ 6 $mN \cdot m^{-1}$ (inset of Figure 5.3.1) indicating phase change to LC state (More detailed information about the physical state is presented in Section 5.3.2). This physical state behaviour is in line with the observations of previous authors [53-55].

5.3.2 AFM

Figure 5.3.2 presents the AFM topographic images corresponding to DPPC transferred at several surface pressures on mica. The images A and B present two tonalities of brown (fair and dark) and both tonalities correspond to zones with different heights of the DPPC monolayer. The measurements of the relative heights of the higher zones referred to the dark zones are 12 ± 2 Å and 17 ± 2 Å for the image A and B respectively. This information indicates that the monolayer, once transferred to the mica surface, presents zones with different height, which is correlated with a different tilting of the DPPC molecules that indicate a different physical state. It is important to remark that each brown tonality indicates a different height but the physical state that is correlated with them depends on the surface pressure at which the monolayer has been transferred.

According to the values of $C_s^{-1}{}_{max}$ presented in the previous section, the complete vision of the situation indicates that DPPC on mica at π = 6 mN·m^{-1} (image A in Figure 5.3.2) forms a compact (fair brown zones) monolayer with a portion of fluid zones (dark zones). The compression of the film leads to the ordering of the fluid phase (image B in Figure 5.3.2) till the high ordered state covers the entire mica surface (images C and D in Figure 5.3.2). According to the $C_s^{-1}{}_{max}$ values presented in Section 5.3.1 at π = 6 mN·m^{-1}, the relative height of 17 ± 2 Å observed for the fair zones is LC referred to the LE state (dark brown). At $\pi \geq$ 25 mN·m^{-1} the monolayer is LC state with short depth (< 1 Å) grooves. The surface covered by the LC state at each surface pressure increases quickly when increasing the surface pressure from π = 6 mN·m^{-1} (67%) till the π = 25 mN·m^{-1} where the LC state monolayer covers the 100% of the available area. All these AFM topographic observations observations are in line with the AFM observations of Chu et al. [56]. A scheme of the DPPC molecules on a hydrophilic substrate is presented in Figure 5.3.3.

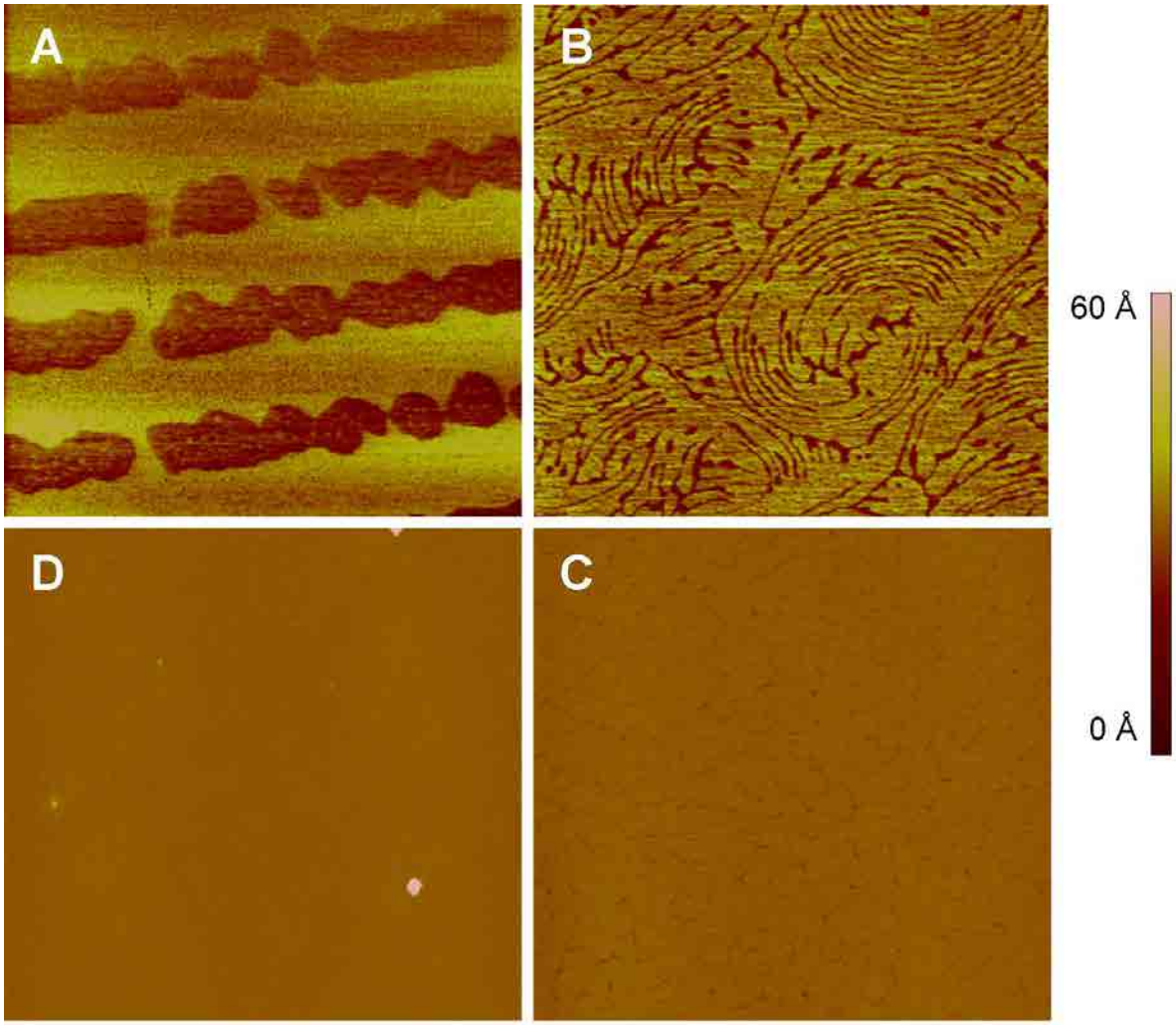

Figure 5.3.2. AFM images (5μm x 5μm) for LB films of DPPC transferred on mica at 21ºC at (A) π = 6 $mN \cdot m^{-1}$, (B) π = 15 $mN \cdot m^{-1}$, (C) π = 25 $mN \cdot m^{-1}$, (D) π = 40 $mN \cdot m^{-1}$.

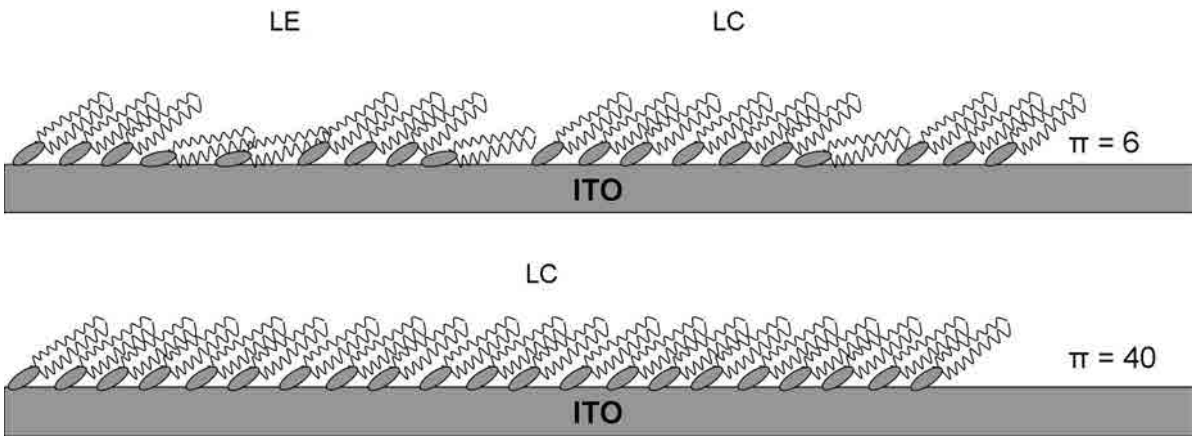

Figure 5.3.3. Scheme of the position of DPPC molecules at π = 6 and 40 $mN \cdot m^{-1}$.

The compact monolayer presents at π = 40 $mN \cdot m^{-1}$ some rounded shape structures. The origin of such structures is uncertain but we hypothesize that they are the result of a local surface pressure increase which induces a local collapse [57,58] of the film, forming flatten disks of ≈ 100 nm diameter and a height of 1 to 7 nm. These observations are consistent with small flatten bilayer vesicles, in line with previous observations for POPG [59] and DPPG [60].

The height of the LE phase observed in the literature for DPPC is 3-6 Å [53,54] in similar conditions than in our experiments. So that, we use this value to obtain the absolute height of the LC zones (22 ± 2 Å), in line with the ≈ 20 Å observed in the literature [53,54].

On the other hand, the use of the CPK model gives the approximated dimensions of the DPPC molecule being the total height 24 Å, corresponding 16 Å to the hydrocarbon chain and 8 Å to the head (Figure 3.3). The width of the head is 5.3 Å and the depth is 4 Å. Considering that the LC state is the most compact phase that DPPC can achieve, it is interesting to evaluate the angle between the monolayer normal and the lipid. Using basic trigonometry, the tilt angle obtained for LC is 24º which is in line with the generally expected values for LC (≈32º) [61].

5.3.3 Electrochemical behaviour

Figure 5.3.4 shows the cyclic voltammogram at a scan rate of 10 $mV \cdot s^{-1}$ of LB films of DPPC transferred on ITO in a 0.150 M KCl cell solution buffered at pH 7.4. The LB films have been transferred at two different surface pressures selected according to the criterion of being one surface pressure with part of the monolayer in the LE state and other surface pressure with absence of LE state. Previously, the ITO/electrolyte system has been studied and shows that ITO behaves as a polarizable electrode in the experimental conditions (see dashed line in Figure 5.3.4) as it has been explained in Section 5.1.3. In our experiments, three CVs are required to obtain the stationary state in the electrochemical response, presenting a good reproducibility from the third scan and at least 15 cycles. The voltammograms indicate that in the potential range between 0.80 and -0.40 V the ITO-DPPC electrode does not show faradaic response and that the effect of the applied electrical potential on the lipid monolayer is low. At more anodic potentials than -0.40 V a

continuous increase (not shown) of the intensity was obtained, indicating hydrogen evolution.

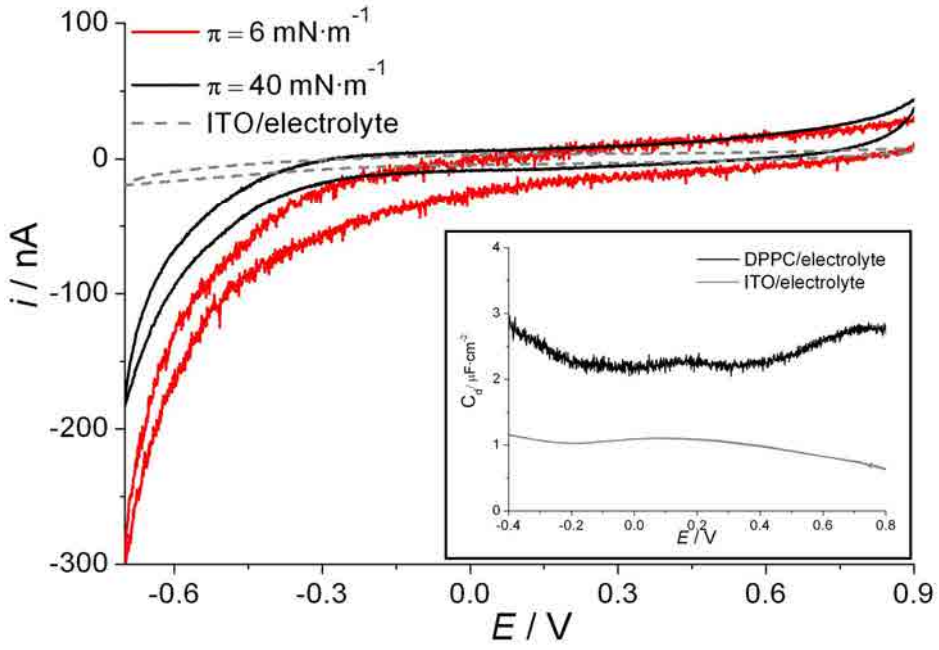

Figure 5.3.4. Cyclic voltammograms of the ITO/electrolyte and ITO-DPPC/electrolyte system. All CVs have been performed using 0.150 M of KCl electrochemical cell using potassium phosphate buffered solution at pH 7.4, at a scan rate of 10 $mV \cdot s^{-1}$. Inset: C_d of the ITO/electrolyte and ITO-DPPC/electrolyte system at π = 40 $mN \cdot m^{-1}$ obtained from the CVs presented in Figure 5.3.4.

The cyclic voltammogram of the ITO-DPPC/electrolyte system has been used to evaluate its C_d (Inset of Figure 5.3.4) from the values of voltammetric charging current [9] using the Expression 2.38. The ITO-DPPC electrode presents slightly higher C_d values than bare ITO, being constant (≈ 2.5 $\mu F \cdot cm^{-2}$) at the potential window used. C_d values ≈ 1.8 $\mu F \cdot cm^{-2}$ have been reported for high quality lipid monolayers [62] so indicating that our monolayer is not completely homogeneous and it presents few defects. The fact that the voltamogram presents a reproducible behaviour indicates that the lipid layer is permeable to water molecules and, after the third scan, the stable water content is achieved in the monolayer. Similar results showing the effect of an applied potential on LB monolayers of DPPC on ITO were obtained by Yang et al. [63] who explained the small changes when applying potentials on these monolayers and their reversible behaviour, as a consequence of the affinity between the lipid heads and the hydrophilic surface of ITO.

5.4 MGDG

5.4.1 π-A isotherms and physical states

The π-A isotherm of saturated MGDG (See Figure 3.4A and specifications in Section 4.1) and its corresponding C_s^{-1} curve (inset) calculated using the Expression 2.9 are presented in Figure 5.4.1. The isotherm shows that MGDG forms very stable monolayers that presents the lift-off and limiting area at 59 $Å^2 \cdot molec^{-1}$ and 49 $Å^2 \cdot molec^{-1}$ respectively, and it collapses at ≈ 53 $mN \cdot m^{-1}$.

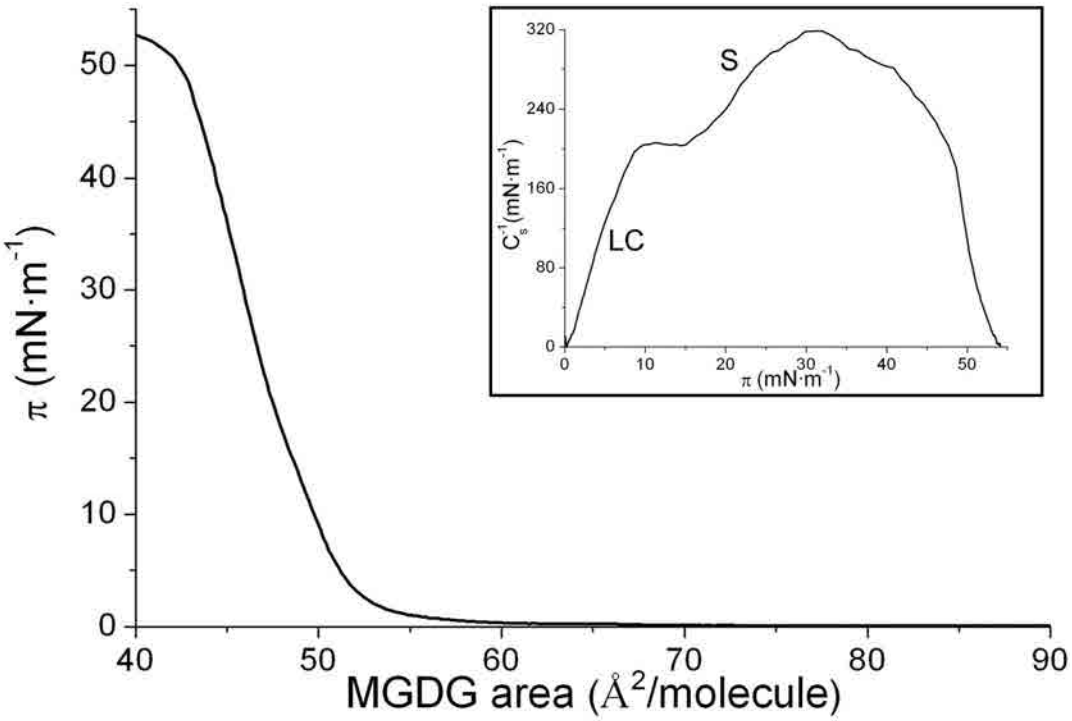

Figure 5.4.1 π-A isotherm of MGDG at 21 ± 0.5 ºC on water subphase. Inset, inverse of the compressibility modulus vs. surface pressure.

The MGDG lift-off area is in line with previous studies using similar conditions like the ≈ 60 $Å^2 \cdot molec^{-1}$ observed by Bishop et al. [64] but it is substantially different than the 50 $Å^2 \cdot molec^{-1}$ observed by Schneider et al. [65] and than the 80-100 $Å^2 \cdot molec^{-1}$ observed by Tomoaia-Cotişel et al. [66,67]. However, the limiting area observed in our results coincides with the observations of Bishop et al. [64] and Tomoaia-Cotişel et al. [66,67] but differs to the 39 $Å^2 \cdot molec^{-1}$ observed by Schneider et al. [65]. On the other hand, the collapse

pressure is in line with the observations of Tomoaia-Cotişel et al. [66,67] who found the same value in similar experimental conditions. This value contrasts with the observations of Schneider et al. [65] who observed this value at 62 $mN \cdot m^{-1}$. The differences observed may be attributed to the solvent used for the MGDG solution preparation.

The shape of the lipid π-A isotherm depends strongly on the unsaturation index of their acyl chains. So that, in order to understand the interactions present in our system, it is interesting to compare the results obtained using our saturated MGDG with the results for unsaturated MGDG found in the literature.

The lift-off area is found at 95-120 $Å^2 \cdot molec^{-1}$ for an unsaturation index below the unity, whereas the limiting area for the same experiments is found at 45 $Å^2 \cdot molec^{-1}$ [68], for an unsaturation index of ≈ 0.2 and at ≈ 75 $Å^2 \cdot molec^{-1}$ for an unsaturation index ≈ 0.8 [64,68,70]. MGDG in pure water or buffered solution using TRIS at pH 8 with an unsaturation index ≈ 2.7 presents the lift-off area at 140 $Å^2 \cdot molec^{-1}$ and a limiting area ≈ 91 $Å^2 \cdot molec^{-1}$ [71,72] whereas in the same conditions but pH 7 using phosphate [38], these areas are reduced to 120 and 82 $Å^2 \cdot molec^{-1}$ respectively. On the other hand, Bottier et al. [73] using NaCl electrolyte as subphase and MGDG with an unsaturation index ≈ 2 presents a limiting area of 82 $Å^2 \cdot molec^{-1}$. The results [71,72] obtained at an unsaturation index ≈ 2.7 indicate that the presence or absence of the buffer ions has no effect on the isotherm for unsaturated MGDG whereas the reduction of only one unit of pH reduces ≈ 10 % the lift-off and the limiting area. It is also important that, comparing the experiments using NaCl electrolyte [73] with the pure water subphase [71,72], the presence of hydrated ions of the electrolyte produce an expansion of the monolayer compared with the pure water subphase [66].

Looking at the collapse surface pressure, the value observed for saturated MGDG is higher than that for unsaturated MGDG found in the literature, being the later independent of unsaturation index and the experimental conditions. In pure water and unsaturation index below the unity, the collapse pressure is ≈ 42 $mN \cdot m^{-1}$ [68-70] being this value close to the ≈ 43 $mN \cdot m^{-1}$ obtained with an unsaturation index ≈ 2.7 in pure water [72], phosphate [38] or TRIS buffered solution at pH 7-8 [71,74]. In addition, Bottier et al. [73] observed the collapse at 46 $mN \cdot m^{-1}$ using NaCl electrolyte subphase with 2 unsaturations.

The lower collapse pressure and the larger lift-off and limiting area observed for unsaturated MGDG compared with our saturated MGDG results were expected. The headgroups are the same so they produce similar MGDG-MGDG interactions in both saturated and unsaturated, whereas the presence of these unsaturations in the lipid chains hindrances the tighter packing for both the heads and the tails [75]. Besides the presence of unsaturations, their position in the alkyl chain determine the area and volume occupied by the MGDG molecule and therefore, influencing the compactness of the monolayer [76]. The high collapse pressure and the low limiting area observed for saturated MGDG is a clear sign that two cooperative forces are involved. First, the hydrophilicity of the MGDG heads governs the packing, so reducing the distances between the MGDG chains thanks to the formation of hydrogen bonds. Second, these chains are completely saturated so the van der Waals forces between the hydrocarbon chains are favoured and therefore, enhancing the compactness and the stability of the monolayer.

Accordingly to the values presented by Vitovic et al. [7] our MGDG presents LC phase from low surface pressions till the solid state formation at $\pi \approx 10$ mN·m^{-1} (inset of Figure 5.4.1) where a plateau is observed until $\pi \approx 15$ mN·m^{-1} indicating phase change to S state (More detailed information about the physical state is presented in Section 5.4.2). The formation of the solid state is not observed in the experiments of Tomoaia-Cotişel et al. [66] who observed the $C_s^{-1}{}_{\max}$ for saturated MGDG in similar conditions to our experiments at 208 mN·m^{-1} being this value significantly different to the $C_s^{-1}{}_{\max} = 320$ mN·m^{-1} that we have obtained.

As it has been explained, the comparison of our saturated MGDG results with those of unsaturated MGDG found in the literature gives idea of the interactions present at each system and it is clear that the presence of unsaturations affects in a large extent the $C_s^{-1}{}_{\max}$ value. Unsaturated MGDG on water subphase presents a $C_s^{-1}{}_{\max}$ of ≈ 39 mN·m^{-1} [68] and ≈ 35 mN·m^{-1} [68,70] for an unsaturation index of 0.2 and 0.8 respectively. The use of TRIS buffered solution at pH 7.4 enhances the $C_s^{-1}{}_{\max}$ for a 0.4 unsaturation index to 54 mN·m^{-1} [77].

These comparisons confirm that an increase in the unsaturation of the acyl chains provokes a reduction of the monolayer $C_s^{-1}{}_{\max}$, especially the first unsaturation which produces a decrease of $C_s^{-1}{}_{\max}$ values from ≈ 320 to 39 mN·m^{-1}. It is interesting to point that there are also differences in the alkyl chain length between the MGDG used in the exposed experiments of several authors, but the small differences in hydrophobic interactions are largely overcome by the double bond hindrance in the monolayer stability. The low value of the inverse of the compressibility modulus for unsaturated MGDG confirms that, conversely to saturated MGDG, it presents LE phase from its appearance in the G-LE phase coexistence till the collapse [38,68,73,77].

Saturated MGDG forms solid state monolayer at the most compact state due to the favourable interactions of different MGDG molecules between the chains on the one hand, and between the heads on the other hand. The presence of unsaturations in the MGDG chains extends the LE phase due to the hindrances for a tight packing, even forbidding the formation of the condensed states. The different orientations that can be adopted by the sugar moiety of MGDG depend on the hydrogen bonds established [73,78].

5.4.2 AFM

Figure 5.4.2 presents the AFM topographic images corresponding to MGDG transferred at several surface pressures on mica. The images present two tonalities of brown (fair and dark), in addition, the image A also presents a medium brown tonality. All of these tonalities correspond to zones with different heights of the MGDG monolayer. The measurements of the relative heights of the higher zones referred to the dark zones are 15 ± 1 Å and 19 ± 1 Å for the medium and fair brown respectively in image A. This information indicates that the monolayer, once transferred to the mica surface, presents zones with different height, which is correlated with a different tilting of the MGDG molecules that indicate a different physical state. It is important to remark that each brown tonality indicates a different height but the physical state that is correlated with them depends on the surface pressure at which the monolayer has been transferred.

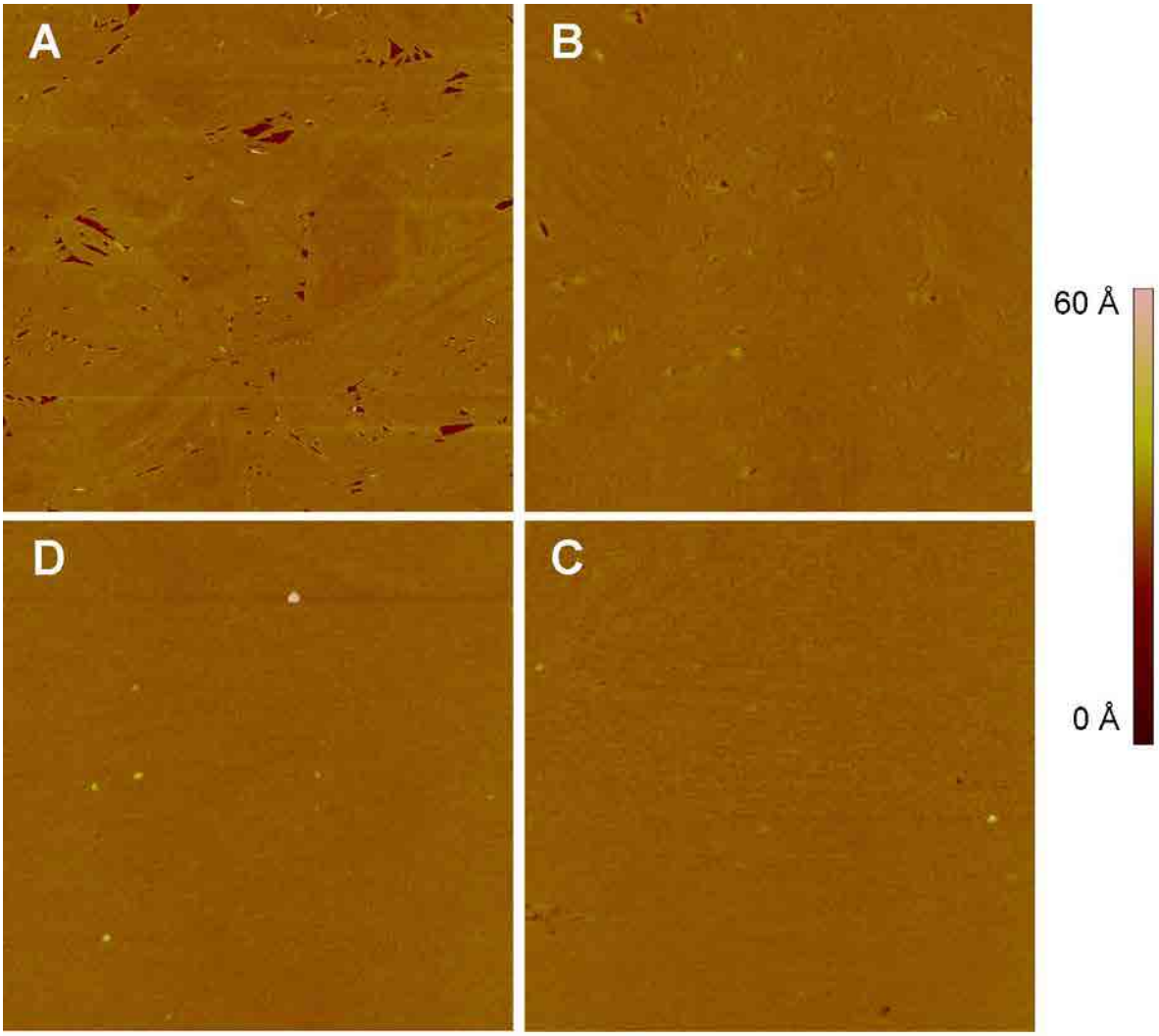

Figure 5.4.2. AFM images (5μm x 5μm) for LB films of MGDG transferred on mica at 21ºC at (A) π = 6 $mN \cdot m^{-1}$, (B) π = 15 $mN \cdot m^{-1}$, (C) π = 25 $mN \cdot m^{-1}$, (D) π = 40 $mN \cdot m^{-1}$.

According to the values of $C_s^{-1}{}_{max}$ presented in the previous section, the complete vision of the situation indicates that MGDG on mica at π = 6 $mN \cdot m^{-1}$ forms a LC (fair and medium brown zones) continuous monolayer with a low proportion of fluid zones (dark zones). Moreover, the tilting of the ordered phase to a more compact phase (fair brown) has begun occupying ≈ 60% of the mica surface. The compression of the film leads to the ordering of the fluid phase till the high ordered state covers the entire mica surface (images B, C and D in Figure 5.4.2). The $C_s^{-1}{}_{max}$ values presented in Section 5.4.1 does not indicate the presence of S state at π = 15 $mN \cdot m^{-1}$, so we correlate the two different heights (15 ± 1 Å and 19 ± 1 Å) observed for the compact state respectively with LC1, corresponding to

molecules in the beginning of the LC state (medium brown), and LC2, molecules at the more ordered state of the LC state (fair brown) both referred to the LE state (dark brown). At π = 25 mN·m^{-1} the highest zones present a relative height of ≈ 3 ± 1 Å respectively the dark zone, which in addition to the C_s^{-1} values observed for that surface pressure, indicate that the fair zones are in S state and the dark zones in LC2 state. The compression of the less ordered state transforms gradually the LC1 or LC2 zones on S; remaining small LC2 areas that achieve rounded shape when the surface pressure is increased (Figure 5.4.2 C). The surface covered by the more compact state at each surface pressure increases when increasing the surface pressure from its formation till the π = 40 mN·m^{-1} where the S state monolayer cover the 100% of the available area. A scheme of the MGDG molecules on a hydrophilic substrate is presented in Figure 5.4.3.

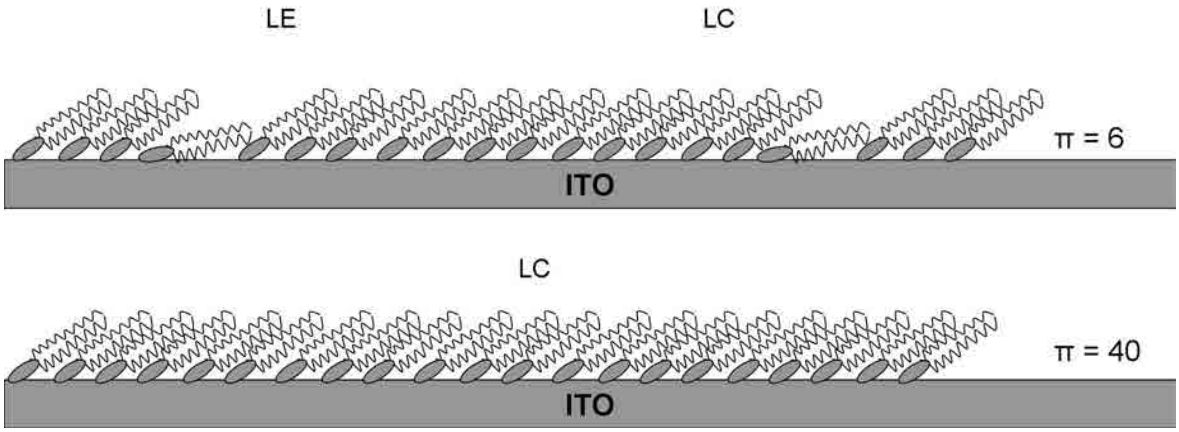

Figure 5.4.3. Scheme of the position of MGDG molecules at π = 6 and 40 mN·m^{-1}.

Although some undefined shape white zones (higher than the monolayer) are also seen at low surface pressure, the compact monolayer presents at $\pi \geq$ 25 mN·m^{-1} some rounded shape structures that increase in number when increasing the surface pressure. The origin of such structures is uncertain but we hypothesize that they are the result of a local surface pressure increase which induces a local collapse [57,58] of the film, forming flatten disks of 100 - 250 nm diameter and a height of 0.5 to 5 nm. These observations are consistent with small flatten bilayer vesicles, in line with previous observations for POPG [59] and DPPG [60].

Our observations for saturated MGDG differs to the studies of Bottier at al. [73] who observed homogeneous LE phase images with no visible phase separation for unsaturated

MGDG at several surface pressures. However, they observed irregular protrusions of ≈ 7 Å at π > 25 $mN \cdot m^{-1}$ which were attributed to a specific organization of the monogalactosyl head groups due to strong lateral interactions between themselves. In our saturated MGDG no segregation, no protrusions are observed even at 40 $mN \cdot m^{-1}$, so that, the different behaviour is correlated with the absence of the double bonds.

The height of the LE phase of galactolipid-prenylquinone systems is 6 ± 2 Å (for more information see Section 5.7.5 and 5.8.5) which is in accordance to the 3-6 Å observed in the literature for LE of DPPC [53,54]. Accepting that this value should be close to that of the MGDG, we calculate the absolute height of each physical state according to it and the relative heights previously measured. The results obtained indicate that LC1 state measures ≈ 21 ± 1 Å, LC2 state measures ≈ 25 ± 1 Å, and the S state ≈ 27 ± 1 Å. On the other hand, the use of the CPK model gives the approximated dimensions of the MGDG molecule (Figure 3.4A with R = stearolyl) being the total height 27 Å, corresponding 18 Å to the hydrocarbon chain and 9 Å to the head, in an extended and vertical orientation. The width of the head is 5.8 Å and the depth is 4 Å. The observation that S state presents a slightly higher height than the approximated using CPK model can be explained based on the accuracy of both the CPK model and the AFM instrument measurements. Nevertheless, using basic trigonometry the angle between the monolayer normal and the lipid chain can be obtained for the LC2 state, showing that this state of MGDG systems present a tilt angle ≈ 22º. This value is far from the observations of Bottier et al. [73] of 40º for unsaturated MGDG in the LC state and the 40.6º for the same physical state observed for DSPC [81] that is a lipid which has similar size and ordering behaviour to that corresponding for MGDG. In our case, the absence of unsaturations and the lipid head nature favour both interactions head-to-head and chain-to-chain, so enhancing the compactness of the monolayer so achieving a proximal position between MGDG molecules. On the other hand, the value expected for S phase of phospholipids (≈20º) [61] is similar to our observations for the LC2 state. The angle obtained can be used to calculate the surface occupied by the horizontal projection of the MGDG head using basic trigonometry and the dimensions of MGDG. The result is ≈ 55 $Å^2 \cdot molec^{-1}$ which is close to the 49 $Å^2 \cdot molec^{-1}$ limiting area value observed for the MGDG π-A isotherms in Section 5.5.1, which indicates that the monolayer transferred on mica has a similar display than that observed in the isotherms.

5.4.3 Electrochemical behaviour

Figure 5.4.4 shows the cyclic voltammogram at a scan rate of 10 $mV \cdot s^{-1}$ of LB films of MGDG transferred on ITO in a 0.150 M KCl cell solution buffered at pH 7.4. The LB films have been transferred at two different surface pressures selected according to the criterion of being one surface pressure predominated by the LC2 state and other surface pressure predominated by the S state. Previously, the ITO/electrolyte system has been studied and it shows that ITO behaves as a polarizable electrode in the experimental conditions (see dashed line in Figure 5.4.4) as it has been explained in Section 5.1.3. In our experiments, three CVs are required to obtain the stationary state in the electrochemical response, presenting a good reproducibility from the third scan and at least 15 cycles. The voltammograms indicate that in the potential range between 0.80 and -0.40 V the ITO-MGDG electrode does not show faradaic response and that the effect of the applied electrical potential on the lipid monolayer is low. At more anodic potentials than -0.40 V a continuous increase (not shown) of the intensity was obtained, indicating hydrogen evolution.

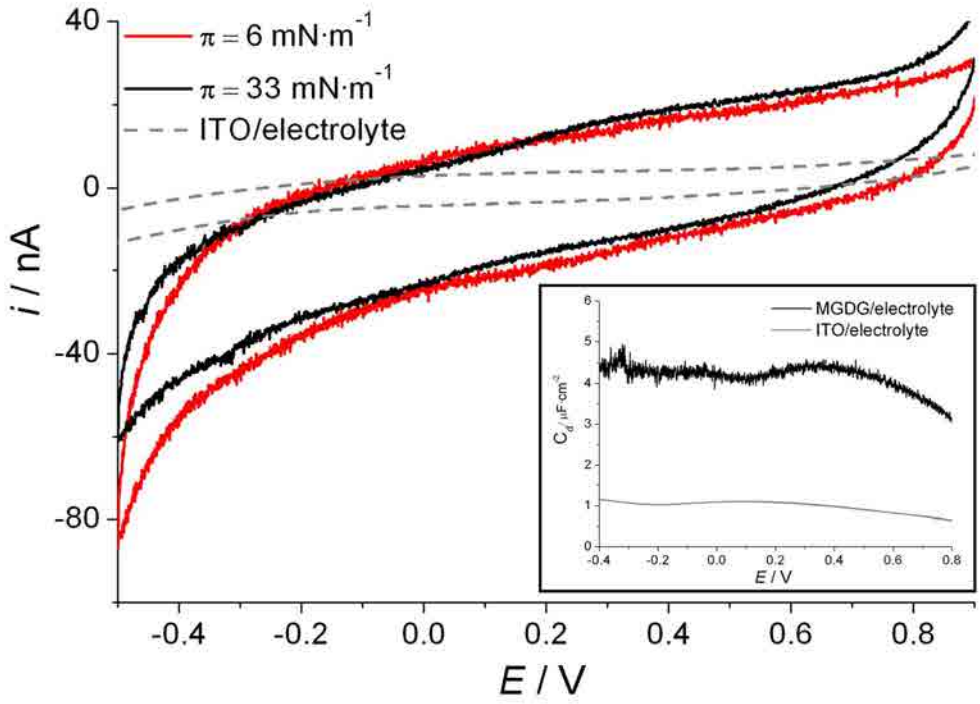

Figure 5.4.4. Cyclic voltammograms of the ITO/electrolyte and ITO-MGDG/electrolyte system. All CVs have been performed using 0.150 M of KCl electrochemical cell using potassium phosphate buffered solution at pH 7.4, at a scan rate of 10 $mV \cdot s^{-1}$. Inset: C_d of the ITO/electrolyte and ITO-MGDG/electrolyte at π = 33 $mN \cdot m^{-1}$ system obtained from the CVs presented in Figure 5.4.4.

The cyclic voltammogram of the ITO-MGDG/electrolyte system has been used to evaluate its C_d (Inset of Figure 5.4.4) from the values of voltammetric charging current [9] using the Expression 2.38. The ITO-MGDG electrode presents higher C_d value than bare ITO, presenting a constant $C_d \approx 4$ $\mu F \cdot cm^{-2}$ in the potential window used. C_d values ≈ 1.8 $\mu F \cdot cm^{-2}$ have been reported for high quality lipid monolayers [62] so indicating that our monolayer is not completely homogeneous and presents few defects. The fact that the voltamogram presents a reproducible behaviour indicates that the lipid layer is permeable to water molecules, and after the third scan, the stable water content is achieved in the monolayer. This effect, and its reversibility, of the applied potential on lipid LB monolayers on ITO are explained by the lipid heads-ITO affinity [63]. The case of pure MGDG is slightly different compared with the other lipids of this Ph.D. Thesis due to it presents a more stable C_d value when changing the applied potential, even in the case of low surface pressures. We correlate this behaviour to the higher compactness of the physical state of the MGDG.

5.5 DGDG

5.5.1 π-A isotherms and physical states

The π-A isotherm of saturated DGDG (See Figure 3.4B and specifications in Section 4.1) and its corresponding C_s^{-1} curve (inset) calculated using the Expression 2.9 are presented in Figure 5.5.1. The isotherm shows that DGDG forms very stable monolayers that presents the lift-off and limiting area at 59 Å^2·molec^{-1} and 51 Å^2·molec^{-1} respectively, and it collapses at ≈ 57 mN·m^{-1}.

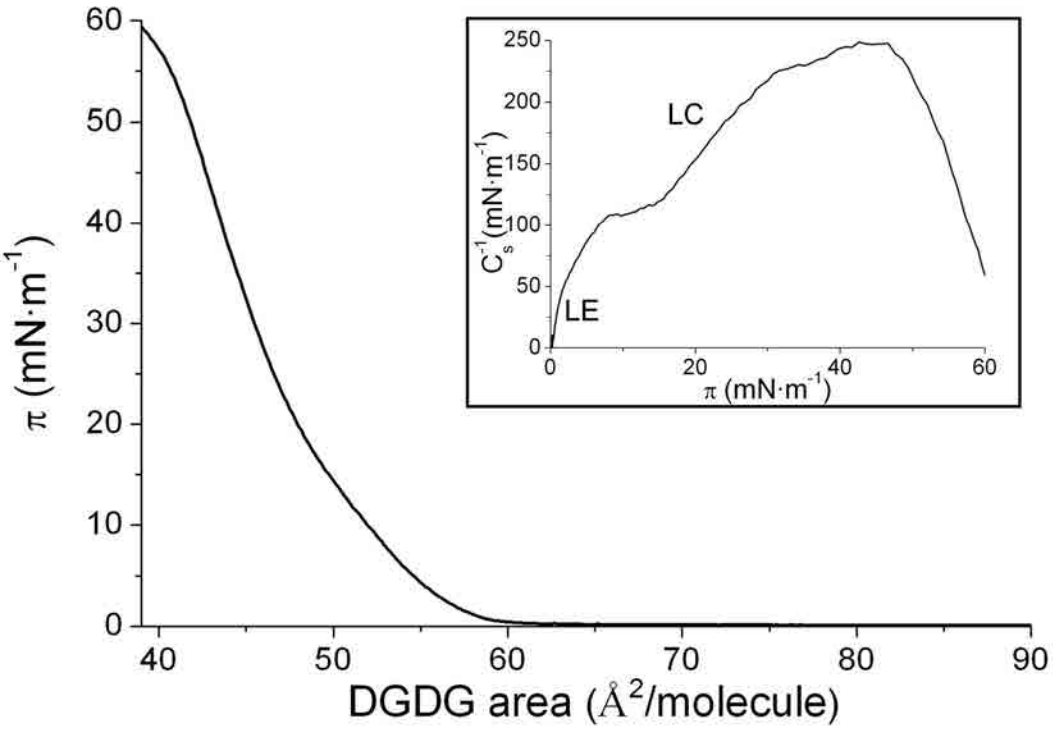

Figure 5.5.1 π-A isotherm of DGDG at 21 ± 0.5ºC on water subphase. Inset: Inverse of the compressibility modulus vs. surface pressure.

The DGDG lift-off area observed in our experiments differs substantially to that observed using similar conditions by Tomoaia-Cotişel et al. [66] at ≈ 85 Å^2·molec^{-1} and Bishop et al. [64] at ≈ 100 Å^2·molec^{-1}. Nevertheless, the limiting area observed at 51 Å^2·molec^{-1} coincides with that observed by Tomoaia-Cotişel et al. [66] although differs from the 70 Å^2·molec^{-1} observed by Bishop [64]. On the other hand, the collapse pressure observed in our isotherm is lower than that observed by Tomoaia-Cotişel et al. [66] who found it at 67

$mN \cdot m^{-1}$. The DGDG lipid used in the three studies is very similar, so the differences may be attributed to the method used for DGDG purification and/or the presence of impurities and the different solvent used for DGDG solution preparation.

The shape of the lipids π-A isotherms depends strongly on the unsaturation index of their acyl chains. So that, it is important to compare the results obtained using our saturated DGDG with the results found in the literature for unsaturated DGDG to understand the interactions present in our system. Looking at the lift-off area, DGDG with a 0.6 unsaturation index presents the mentioned area at 100 $Å^2 \cdot molec^{-1}$ [68], and increasing the unsaturation index to 1-1.3, this area is 105-125 [68,69]. In water at 37 ºC and 2.6 unsaturations per molecule, the lift-off area is observed at 165 $Å^2 \cdot molec^{-1}$ [56]. Moreover, DGDG with 1.7 unsaturations per molecule in water with NaCl electrolyte as subphase shows a lift-off area of 135 $Å^2 \cdot molec^{-1}$ [73] and DGDG with 1 unsaturation in TRIS buffered subphase at pH 7.4 marks this area at 120 $Å^2 \cdot molec^{-1}$ [77]. On the other hand, Gzyl-Malcher [68] found that the limiting area for DGDG with 0.6 unsaturation index is 52 $Å^2 \cdot molec^{-1}$. Increasing the unsaturation index to 1, the area is 80-90 [68-70] and 101 $Å^2 \cdot molec^{-1}$ with an unsaturation index of 1,3 [69]. In water at 37 ºC and 2.6 unsaturations per molecule, the limiting area is observed at 125 $Å^2 \cdot molec^{-1}$ [56]. Experiments in other subphases, like DGDG with 1.7 unsaturations per molecule in water with NaCl electrolyte presents the limiting area at 64 $Å^2 \cdot molec^{-1}$ [73] and DGDG with 1 unsaturation in TRIS buffered subphase at pH 7.4 shows this area at 95 $Å^2 \cdot molec^{-1}$[77]. These last results confirm that the presence of hydrated ions of the electrolyte also produce an expansion of the monolayer compared with the pure water subphase, whereas the presence of electrolytes does not affect the collapse pressure [66].

The high collapse pressure observed for saturated DGDG is well established but the specific value has disagreement. On the other hand, there is strong consensus in the collapse pressure for unsaturated DGDG regardless the conditions employed. In water subphase and similar temperature the collapse pressure was observed at 46-47 $mN \cdot m^{-1}$ with 0.6-1.3 unsaturations per DGDG molecule [68-70]. In water at 37 ºC and 2.6 unsaturations per molecule, the collapse was observed at 43 $mN \cdot m^{-1}$ [56]. Moreover, DGDG with 1-1.8 unsaturations in water with NaCl electrolyte subphase or in TRIS neutral pH subphase presents the collapse at 43-46 $mN \cdot m^{-1}$ [73,77,79].

The larger lift-off and limiting area and the lower collapse pressure observed for unsaturated DGDG compared with our saturated DGDG results were expected. The headgroups are the same so they produce a similar effect in the DGDG-DGDG interactions, mainly by higrogen bond, in both saturated and unsaturated molecules whereas the presence of these unsaturations in the hydrocarbon chains hindrances their tighter packing [75] and the intensity of van der Waals forces between them. Besides the presence of unsaturations, their position in the alkyl chain determine the area and volume occupied by the DGDG molecule and therefore, influencing the compactness of the monolayer [76].

Accordingly to the values presented by Vitovic et al. [7] our DGDG presents LE phase from low surface pressions till the compact state formation at $\pi \approx 8$ mN·m^{-1} (inset of Figure 5.5.1) where a plateau is observed until $\pi \approx 15$ mN·m^{-1} indicating phase change to the LC state (more detailed information about the physical state is presented in Section 5.5.2). These observations are in agreement with the experiments of Tomoaia-Cotişel et al. [66] who observed that the $C_s^{-1}{}_{\max}$ for saturated DGDG in similar conditions than our experiments was 240 mN·m^{-1} being this value close to our 249 mN·m^{-1} value. It has been observed that, even in the case of compact monolayers, the DGDG chains maintain free rotation in their vertical axe [67]. The compression of the saturated DGDG monolayer forces the reorientation of the heads favouring the formation of hydrogen bonds between DGDG molecules, which is reflected in an increase of the compressibility of the monolayer [67].

The presence of unsaturations in the alkyl chain of the DGDG molecule affects in a large extend the $C_s^{-1}{}_{\max}$. This is the case reported by Gzyl-Malcher et al. [68] who found that for DGDG with an unsaturation index of 0.6, the $C_s^{-1}{}_{\max}$ is ≈ 64 mN·m^{-1} and increasing the unsaturation index to 1, the $C_s^{-1}{}_{\max}$ is minored to 54 mN·m^{-1}. Experiments with similar conditions for DGDG with an unsaturation index of 1 present a $C_s^{-1}{}_{\max}$ of 63 mN·m^{-1} [70] and using TRIS buffered at pH 7.4 conditions with an unsaturation index of 1 DGDG presents a $C_s^{-1}{}_{\max}$ of 105 mN·m^{-1}. These comparisons confirm that an increase in the unsaturation of the alkyl chains provokes a reduction of the $C_s^{-1}{}_{\max}$, especially the first unsaturation which produces a decrease from ≈ 249 to 64 mN·m^{-1}. It is interesting to point

that there are also differences in the alkyl chain length between the DGDG used in the exposed experiments of several authors, but the small differences in hydrophobic interactions are largely overcome by the double bond hindrance in the monolayer stability. The low value of $C_s^{-1}{}_{max}$ for unsaturated DGDG confirms that, conversely to saturated DGDG, it presents LE phase from its appearance in the G-LE phase coexistence till the collapse [38,56,73,77]. The presence of unsaturations in the DGDG chains extends the LE phase due to the hindrances for a tight packing, even forbidding the formation of the LC state.

5.5.2 AFM

Figure 5.5.2 presents the AFM topographic images corresponding to DGDG transferred at several surface pressures on mica. The images present two tonalities of brown (fair and dark) and both correspond to zones with different heights of the DGDG monolayer. The measurements of the relative height of the higher fair zones referred to the dark zones in Figure 5.5.2A is 15 ± 1 Å. This information indicates that the monolayer, once transferred to the mica surface, presents zones with a different tilting of the DGDG molecules that indicate a different physical state. It is important to remark that each brown tonality indicates a different height but the physical state that is correlated with them depends on the surface pressure at which the monolayer has been transferred.

DGDG on mica at low surface pressures ($\pi \leq 3$ mN·m^{-1}) forms round edge domains of a compact state (Image A) whereas the rest of the molecules are in a more fluid state. The compression of the film leads to the ordering of the fluid phase till the ordered state covers the entire mica surface (Images B, C and D in Figure 5.5.2). At $\pi = 45$ mN·m^{-1} this compact monolayer surface presents some rounded shape structures which origin is uncertain but we hypothesize that they are the result of a local surface pressure increase which induces a local collapse [57,58] of the film, forming flatten disks of ≈100 - 200 nm diameter and a height of 3 to 20 nm. These observations are consistent with small flatten bilayer vesicles, in line with previous observations for POPG [59] and DPPG [60].

The relative height of the more ordered phase respectively to the less ordered phase has been measured in order to clarify which physical state predominates at each surface

pressure. The $C_s^{-1}{}_{\max}$ values presented in the previous section indicate that S state is never achieved by DGDG, so in Figure 5.5.2A, we correlate the relative height of 15 ± 1 Å to the LC1 state referred to the LE state (dark zones). The relative height of 3 ± 1 Å observed in Figure 5.5.2C is correlated with the LC2 (fair zones) referred to the LC1 (dark zones). Therefore, fair zones at π = 3 mN·m^{-1} corresponds to the LC1 state and at higher surface pressure, they represent the LC2 state. On the other hand, dark zones corresponds to the LE state at π = 3 mN·m^{-1} that changes to LC at higher surface pressures. The compression of the less ordered state transforms gradually the LC1 zones on LC2, remaining small LC1 areas that achieve rounded shape when the surface pressure is increased (Figure 5.5.2 C). The surface covered by the LC2 state increases when increasing the surface pressure from its formation till π = 45 mN·m^{-1} where the LC2 covers the 100% of the available area. In consequence, we explain the plateau formed at $C_s^{-1} \approx 105$ mN·m^{-1} in the inset of Figure 5.5.1 with the LE to LC phase change. A scheme of the DGDG molecules on a hydrophilic substrate is presented in Figure 5.5.3.

These topographic results for saturated DGDG differs to the observations of Bottier at al. [73] and Chu et al. [56] who observed homogeneous LE phase images with no visible phase separation for unsaturated DGDG at several surface pressures.

The height of the LE phase of galactolipid-prenylquinone systems is 6 ± 2 Å (for more information see Section 5.7.5 and 5.8.5) which is in accordance to the 3-6 Å observed in the literature for LE of DPPC [53,54]. Accepting that this value should be close to that of the DGDG, we calculate the absolute height of each physical state according to it and the relative heights previously measured. The results obtained are: LC1 state measures 21 ± 1 Å and the LC2 state measures 24 ± 1 Å. On the other hand, the use of the CPK model gives the approximated dimensions of the DGDG molecule (Figure 3.4B with R= stearolyl) being the total height 30 Å, corresponding 18 Å to the hydrocarbon chain and 12 Å to the head, in a extended and vertical orientation. The width of the head is 5.8 Å and depth is 4 Å. Considering that LC2 state is the most compact phase that DGDG can achieve, it is interesting to evaluate the angle between the monolayer normal and the lipid. Using basic trigonometry, the tilt angle obtained for LC2 is 37º and 46º for the LC1. These values are in line with the observations of Bottier et al. [73] of 40º for unsaturated MGDG in the LC

state and the 40.6º for the same physical state observed for DSPC [81] that is a lipid which has similar size and ordering behaviour, being both in line with the generally expected tilt angle for the LC state (≈32º) [61]. The angle obtained can be used to calculate the surface occupied by the horizontal projection of the DGDG head using basic trigonometry and the dimensions of DGDG. The result is ≈ 57 $Å^2 \cdot molec^{-1}$, which is close to the 51 $Å^2 \cdot molec^{-1}$ limiting value observed for the DGDG isotherms in Section 5.5.1, which indicates that the monolayer transferred on mica has a similar display than that observed in the π-A isotherms.

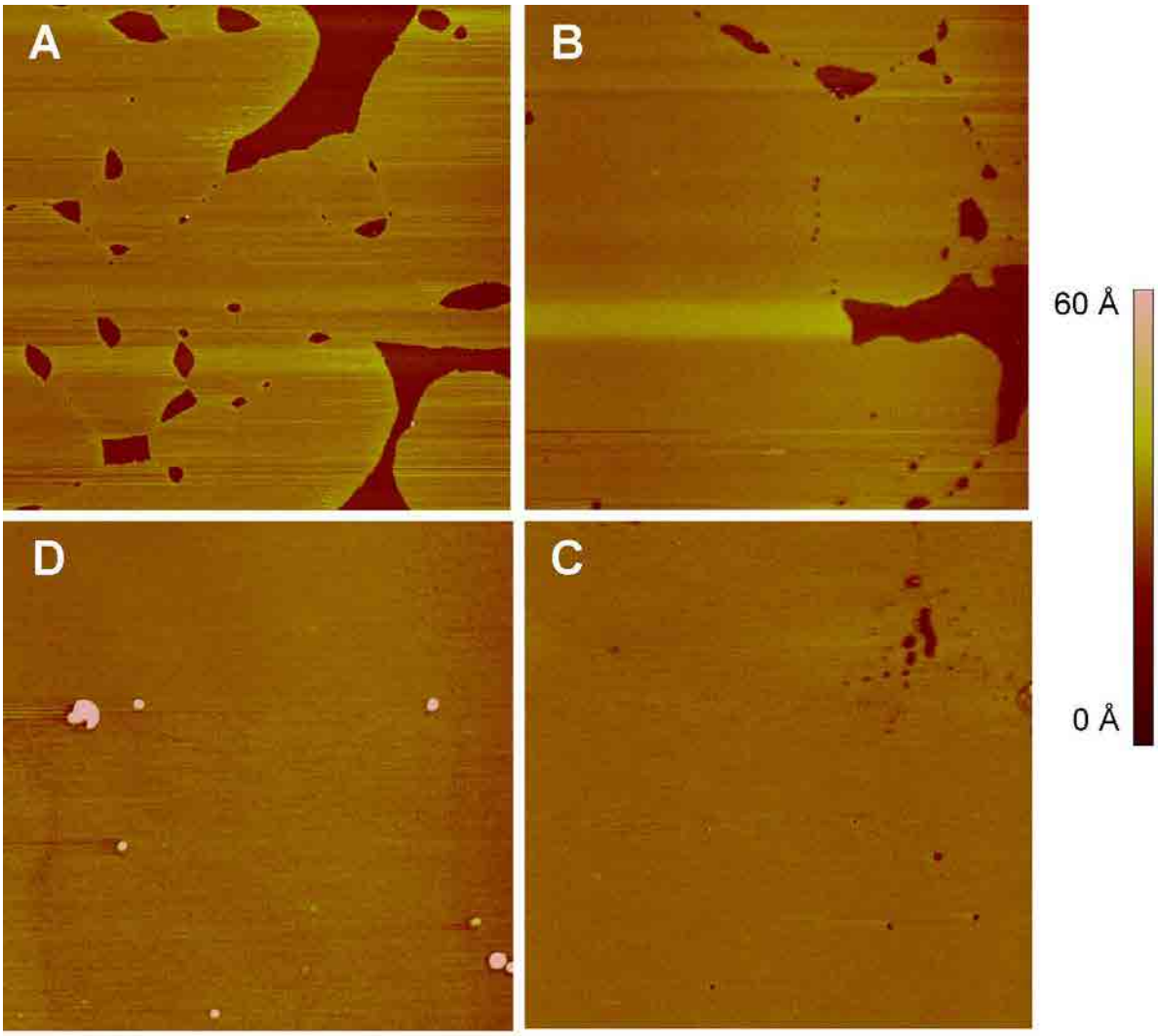

Figure 5.5.2. AFM images (5μm x 5μm) for LB films of DGDG transferred on mica at 21ºC at (A) π = 3 $mN \cdot m^{-1}$, (B) π = 15 $mN \cdot m^{-1}$, (C) π = 33 $mN \cdot m^{-1}$, (D) π = 45 $mN \cdot m^{-1}$.

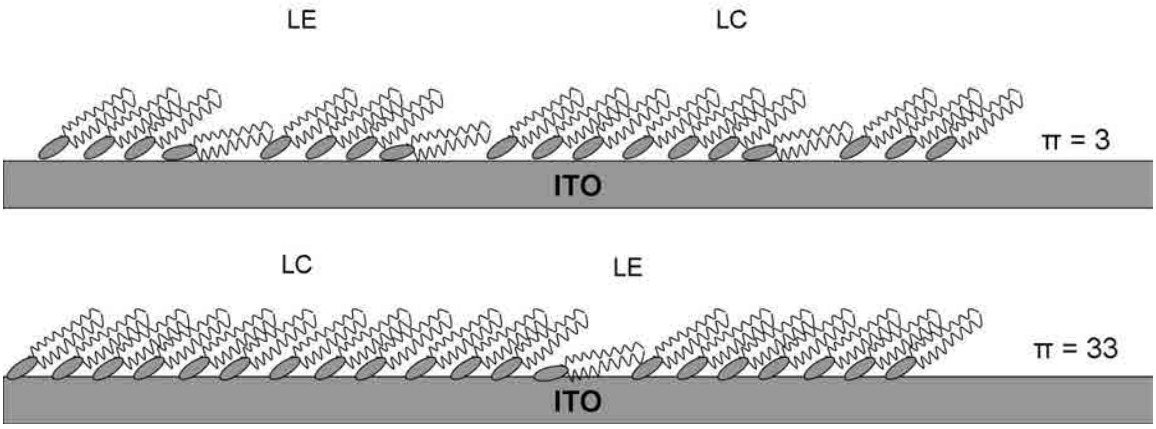

Figure 5.5.3. Scheme of the position of DGDG molecules at π = 3 and 33 $mN \cdot m^{-1}$.

5.5.3 Electrochemical behaviour

Figure 5.5.4 shows the cyclic voltammogram at a scan rate of 10 $mV \cdot s^{-1}$of LB films of DGDG transferred on ITO in a 0.150 M KCl cell solution buffered at pH 7.4. The LB films have been transferred at two different surface pressures selected according to the criterion of being one surface pressure predominated by the LC1 state and other surface pressure predominated by the LC2 state. Previously, the ITO/electrolyte system has been studied and it shows that ITO behaves as a polarizable electrode in the experimental conditions (see dashed line in Figure 5.5.4) as it has been explained in Section 5.1.3. In our experiments, three CVs are required to obtain the stationary state in the electrochemical response, presenting a good reproducibility from the third scan and at least 15 cycles. The voltammograms indicate that in the potential range between 0.80 and -0.40 V the ITO-DGDG electrode does not show faradaic response and that the effect of the applied electrical potential on the lipid monolayer is low. At more anodic potentials than -0.40 V a continuous increase (not shown) of the intensity was obtained, indicating hydrogen evolution.

The cyclic voltammogram of the ITO-DGDG/electrolyte system has been used to evaluate its C_d (Inset of Figure 5.5.4) from the values of voltammetric charging current [9] using the Expression 2.38. The ITO-DGDG electrode presents higher C_d values than bare ITO, increasing from 2 to 5.5 $\mu F \cdot cm^{-2}$ when scanning from 1.00 to -0.40 V. C_d values $\approx$ 1.8 $\mu F \cdot cm^{-2}$ have been reported for high quality lipid monolayers [62] so indicating that our monolayer is not completely homogeneous and presents few defects. The fact that the

voltamogram presents a reproducible behaviour indicates that the lipid layer is permeable to water molecules, and after the third scan, the stable water content is achieved in the monolayer. This effect, and its reversibility, of the applied potential on lipid LB monolayers on ITO are explained by the lipid heads-ITO affinity [63].

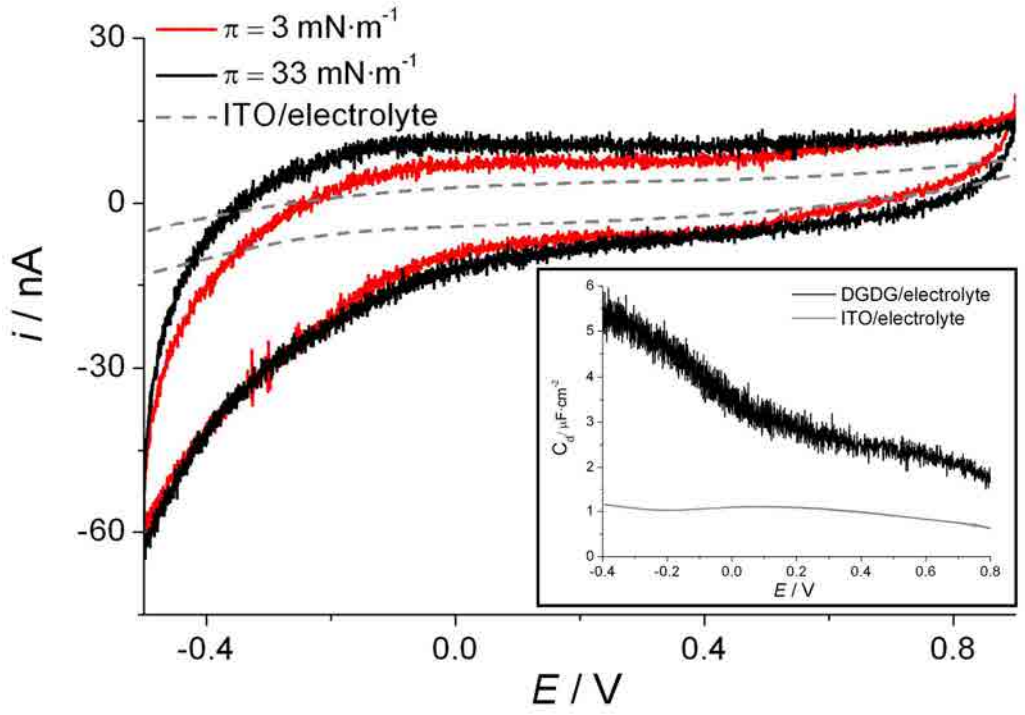

Figure 5.5.4. Cyclic voltammograms of the ITO/electrolyte and ITO-DGDG/electrolyte system. All CVs have been performed using 0.150 M of KCl electrochemical cell using potassium phosphate buffered solution at pH 7.4, at a scan rate of 10 $mV \cdot s^{-1}$. Inset: C_d of the ITO/electrolyte and ITO-DGDG/electrolyte at π = 33 $mN \cdot m^{-1}$ system obtained from the CVs presented in Figure 5.5.4.

5.6 MGDG:DGDG 2:1 (MD)

5.6.1 π-A isotherms and physical states

The π-A isotherm of a mixture of saturated MGDG:DGDG 2:1 (MD) and its corresponding C_s^{-1} curve (inset) calculated using the Expression 2.9 are presented in Figure 5.6.1. The isotherm shows that MD forms very stable monolayers that presents the lift-off and limiting area at 57 $Å^2$·molec^{-1} and 51 $Å^2$·molec^{-1} respectively, and it collapses at ≈ 49 mN·m^{-1}. The similarities in the lift-off and limiting area between the MGDG (Section 5.4.1) and DGDG (Section 5.5.1) in this Ph.D. Thesis and in the literature [64,66,67] are also maintained in the MD mixture although the collapse pressure is lower than that of both components. This phenomenon will be explained in Section 5.6.2.

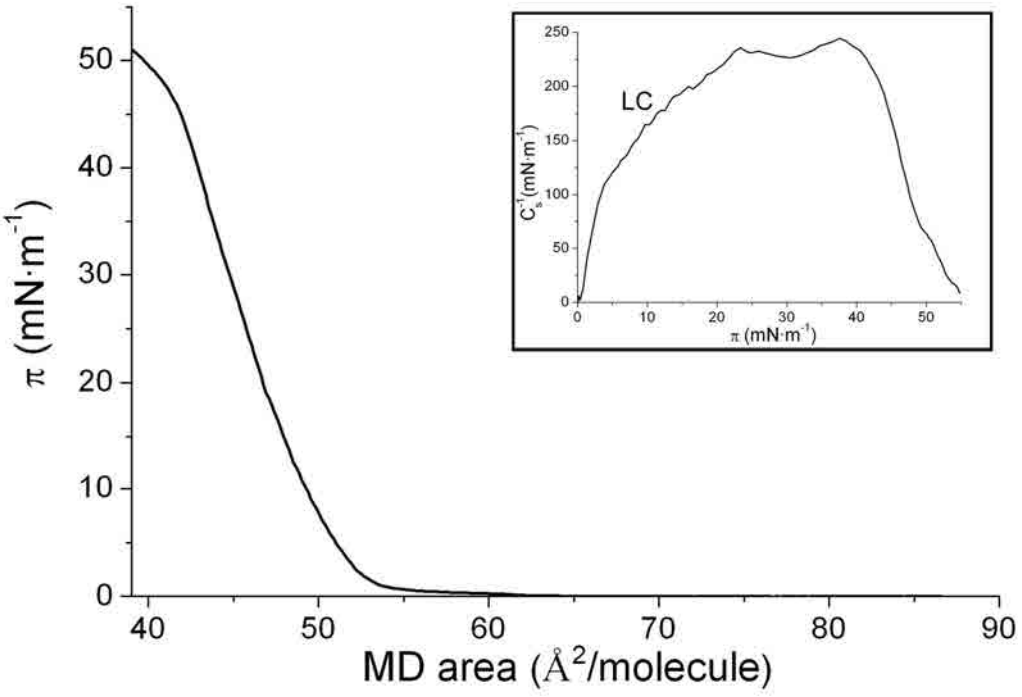

Figure 5.6.1 π-A isotherm of MD at 21 ± 0.5ºC on water subphase. Inset, inverse of the compressibility modulus vs. surface pressure.

The inset of Figure 5.6.1, in accordance with the $C_{s\ max}^{-1}$ values presented by Vitovic et al. [7], shows that MD presents LC phase during the entire isotherm (More detailed information about the physical state is presented in Section 5.6.2). The MD mixture

presents a $C_s^{-1}{}_{max}$ value of ≈ 250 mN·m^{-1} closer to that of DGDG rather than the MGDG (see Sections 5.4.1 and 5.5.1), being this behaviour explained by that the most fluid component leads the mixture compactness. It has been explained in previous sections that the reorientation of the galactosyl headgroups molecules favours the formation of hydrogen bonds between the headgroups and water molecules [73,78]. So that, the presence of different kind of galactosyl headgroups will restrict the optimal orientation of the MGDG headgroups.

The representation of the mean area per molecule vs. the molar fraction at selected pressures gives idea about the ideality of a mixture at these surface pressures (See Section 2.1.1.5). The Figure 5.6.2 plots the area per molecule for MGDG:DGDG (2:1) (MD) mixture at several surface pressures. This figure shows that MGDG and DGDG form non-ideal mixtures with negative deviation at the entire range of surface pressures, which can indicate attractive interactions between MGDG and DGDG molecules.

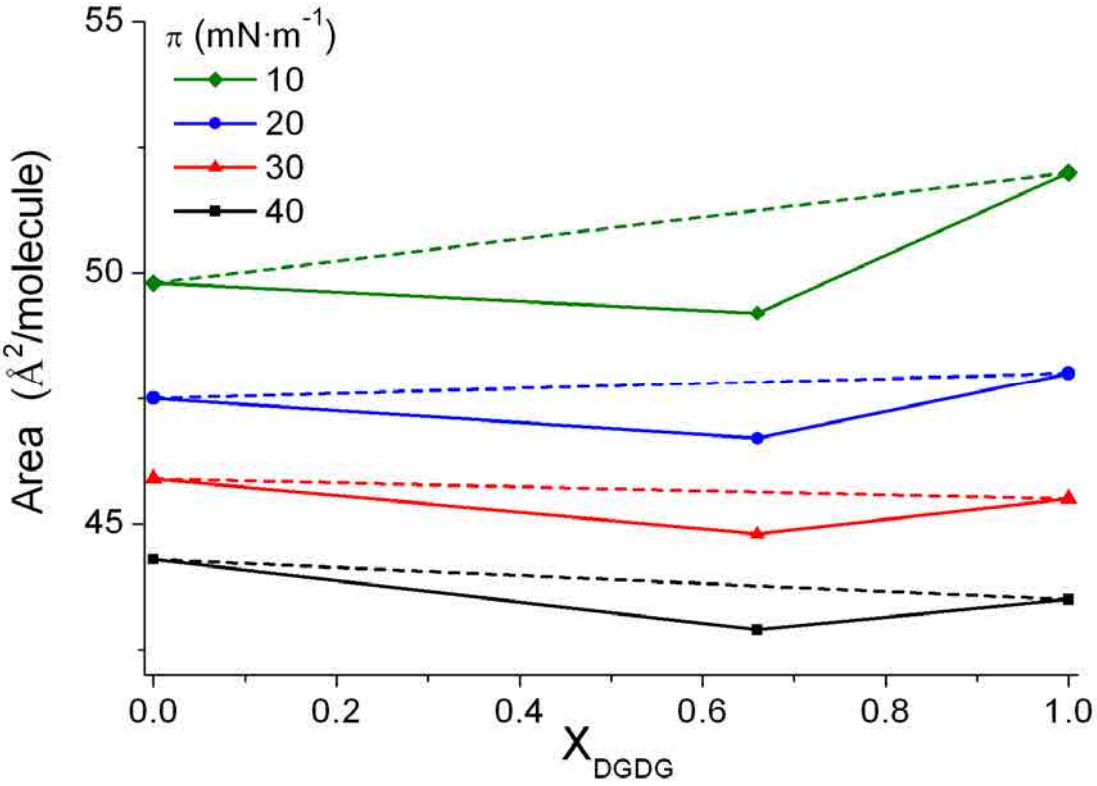

Figure 5.6.2. Plot of the mean area per molecule vs. the molar fraction for MGDG, DGDG and MGDG:DGDG (2:1) (MD) mixtures. Discontinuous straight line represents the ideal behaviour for each surface pressure.

The shape of the lipids π-A isotherms depends strongly on the saturation index of their acyl chains. So that, in order to understand the strength of the interactions present in our system, it is interesting to compare the results obtained using our 2:1 mixture of MGDG and DGDG both saturated with the results for similar mixtures with unsaturated galactolipids found in the literature.

MD in water subphase with an unsaturation index of ≈ 0.2 shows the lift-off and limiting area at 55 $Å^2 \cdot molec^{-1}$ and 50 $Å^2 \cdot molec^{-1}$ respectively [68] whereas for an unsaturation index of ≈ 0.8, these areas are placed at 100 $Å^2 \cdot molec^{-1}$ and 75 $Å^2 \cdot molec^{-1}$ respectively [68,70]. The unsaturated MD mixture in NaCl electrolyte subphase and unsaturation index of ≈ 2 [73] present the lift-off and the limiting area at 150 $Å^2 \cdot molec^{-1}$ and 70 $Å^2 \cdot molec^{-1}$ respectively. This last result indicates that comparing the experiments using NaCl electrolyte with the pure water subphase, the presence of hydrated ions of the electrolyte produce an expansion of the monolayer compared with the pure water subphase [66]. On the other hand, the collapse surface pressure for the unsaturated MD mixture in water is ≈ 43 $mN \cdot m^{-1}$ for an unsaturation index lower than the unity [68,70]. On the other hand, in NaCl electrolyte subphase and unsaturation index of ≈ 2, the collapse pressure observed is 47 $mN \cdot m^{-1}$[73].

The larger lift-off and limiting area and the lower collapse pressure observed for unsaturated MD compared with our saturated MD results indicate, as it has been observed for pure components, that the presence of these unsaturations in the lipid chains hindrance the tighter packing for both the heads and the tails [75] of the lipid molecules. Bottier et al. [73] observed that in an unsaturated MGDG:DGDG mixture, the MGDG headgroup forces the DGDG head to a different orientation than in pure DGDG monolayers, and that the presence of both galactolipids induced a higher hydration than in pure components. In our case, the absence of unsaturations permits the chains of both lipids to compete with the heads for leading the packing.

The $C_{s^{-1}\,\max}$ for unsaturated MD on water subphase has been observed at ≈ 47 $mN \cdot m^{-1}$ [68] and ≈ 40 $mN \cdot m^{-1}$ [68,70] for an unsaturation index of 0.2 and 0.8 respectively. These comparisons confirm that an increase in the unsaturation of the acyl chains provokes a

reduction of the compressibility of the monolayer, especially the first unsaturation which produces a decrease from ≈ 240 to 40 $mN \cdot m^{-1}$. It is interesting to point that there are also differences in the alkyl chain length between the MGDG and DGDG used in the exposed mixture experiments of several authors, but the small differences in hydrophobic interactions are largely overcome by the double bond hindrance in the monolayer stability. The low $C_s^{-1}{}_{max}$ value for unsaturated MD mixture confirms that, conversely to saturated MD, it presents LE phase from its appearance in the G-LE phase coexistence till the collapse [68,70,73].

The literature shows that unsaturated MD mixtures form non-ideal monolayers at the air|water interface and exhibit strong tendency towards phase separation although remain miscible, especially at MGDG:DGDG molar ratio similar to our experiments at which the non-attractive interactions between MGDG and DGDG are the weakest [68,70]. In our MD mixture, the attractive interactions suggested from Figure 5.6.2, the absence of an inflexion in the MD isotherm corresponding to one component collapse or expulsion and the high similarities between saturated MGDG and DGDG pure components suggests the favourable mixing behaviour [70] previously the collapse. On the other hand, the lower collapse pressure for MD than MGDG may indicate phase segregation at high surface pressures which correlates with the phase separation observed for the unsaturated mixture [68,70].

5.6.2 AFM

Figure 5.6.3 presents the AFM topographic images corresponding to MD transferred at several surface pressures on mica. The images present two tonalities of brown (fair and dark). In addition, the image A also presents a medium brown tonality. All of these tonalities correspond to zones with different heights of the MD monolayer. The measurements of the relative heights of the higher zones referred to the dark zones are 15 ± 1 Å and 19 ± 1 Å for the medium and fair brown respectively in image A. This information indicates that the monolayer, once transferred to the mica surface, presents zones with different height which is correlated with a different tilting of the MD molecules that indicate a different physical state. It is important to remark that each brown tonality indicates a different height but the physical state that is correlated with them depends on the surface pressure at which has been transferred the monolayer.

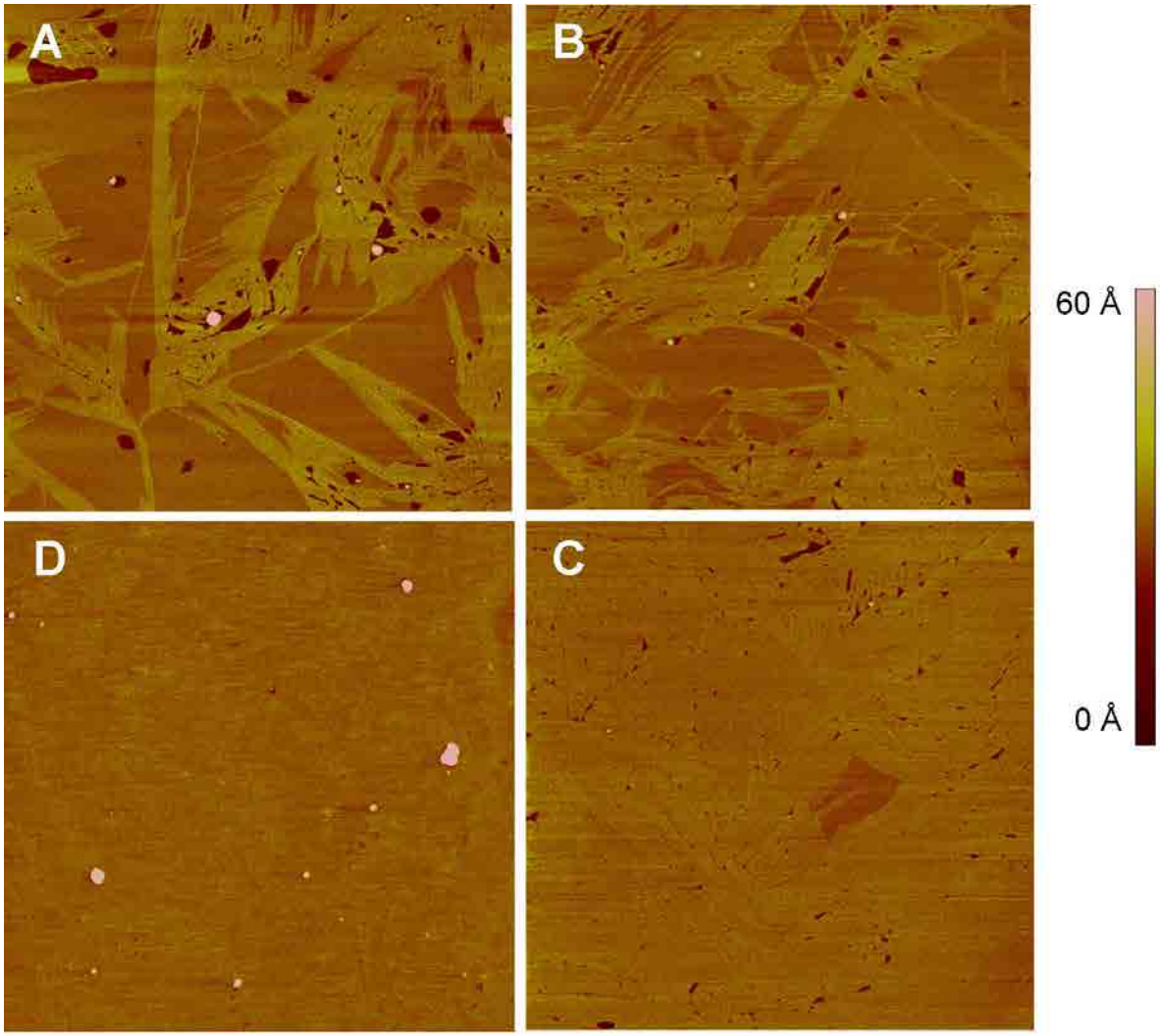

Figure 5.6.3. AFM images (5μm x 5μm) for LB films of MD transferred on mica at 21ºC at (A) π = 1 mN·m^{-1}, (B) π = 6 mN·m^{-1}, (C) π = 15 mN·m^{-1}, (D) π = 33 mN·m^{-1}.

According to the values of $C_s^{-1}{}_{max}$ presented in the previous section, the complete vision of the situation indicates that MD on mica at π = 1 mN·m^{-1} forms a LC (fair and medium brown zones) continuous monolayer with a low proportion of fluid zones (dark zones). Moreover, the tilting of the ordered phase to a more compact phase (fair brown) has begun, occupying ≈ 45 % of the mica surface. The compression of the film leads to the ordering of the fluid phase till the high ordered state covers the entire mica surface (images B, C and D in Figure 5.6.2). The $C_s^{-1}{}_{max}$ values presented in Section 5.4.1 indicates that MD is incapable of forming S state, so we correlate the two different heights (15 ± 1 Å and 19 ± 1 Å) observed for the compact state respectively with LC1, corresponding to molecules in the beginning of the LC state (medium brown), and LC2, molecules at the more ordered state

of the LC state (fair brown) both referred to the LE state (dark brown). At π = 25 mN·m^{-1} the highest zones presents a relative height of 4 ± 1 Å respectively the dark zone which in addition to the C_s^{-1} values observed for that surface pressure, indicate that the fair zones are in LC2 state and the dark zones in LC1 state. The compression of the less ordered state transforms gradually the LC1 on LC2; remaining small LC1 areas that achieve rounded shape when the surface pressure is increased (Figure 5.6.2 C). The surface covered by the more compact state at each surface pressure increases when increasing the surface pressure from its formation till the π = 40 mN·m^{-1} where the LC2 state monolayer cover the 100% of the available area. A scheme of the MD molecules on a hydrophilic substrate is presented in Figure 5.6.4.

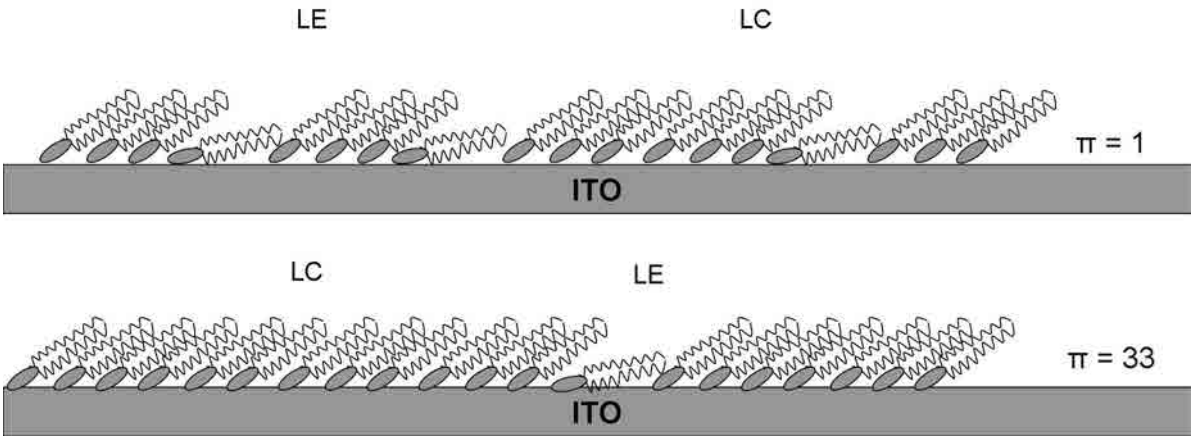

Figure 5.6.4. Scheme of the position of MD molecules at π = 1 and 33 mN·m^{-1}.

At all surface pressures, the monolayer presents some rounded shapes that are placed in the more fluid zones and when these zones disappear, they are localized on top of the monolayer. The origin of such structures is uncertain but we hypothesize that they are the result of a local surface pressure increase which induces a local collapse [57,58] of the film, forming flatten disks of ≈ 50-150 nm diameter and a height of 3 to 12 nm. These observations are consistent with small flatten bilayer vesicles, in line with previous observations for POPG [59] and DPPG [60]. Moreover, the presence of the two different galactolipids facilitates the formation of local tension zones, which explains the existence of these flatten disks even at very low surface pressure. On the other hand, the lower collapse pressure observed for MD compared with the pure MGDG and DGDG can be explained by the formation of the presented white round shape structures which, once formed, hindrance the perfect packing of the rest of the molecules that remain at the

air|water interface, so facilitanting the collapse. The slightly lower limiting area observed for MD is also related with the formation of these structures which provoke the lost of molecules at the air|water interface so inducing a higher compression. This white round shape structures affects the area per molecule values of Figure 5.6.2, although it seems to not modify the conclusions of this figure.

The surface covered by the LC2 state increases when scaling the surface pressure from its formation till the π = 33 $mN \cdot m^{-1}$, where the LC2 covers nearly the 100% of the available area. Our observations for saturated MD differs to the studies of Bottier at al. [73] who observed homogeneous LE phase images with no visible phase separation for an unsaturated MD (1:1) mixture at several surface pressures. On the other hand, they also observed rounded protrusions of $\approx$ 4 Å with a diameter of $\approx$100 nm at π > 25 $mN \cdot m^{-1}$, which were attributed to a specific organization of the monogalactosyl headgroups due to the strong lateral interactions between both galactolipids. In our saturated MD mixture no segregation is observed even at 33 $mN \cdot m^{-1}$. The flatten disks sometimes observed in our AFM images seem to have no relation with the lower protrusions observed by Bottier et al. that covers an important area of the monolayer. The different behaviour is correlated with the absence of the double bonds.

The height of the LE phase of galactolipid-prenylquinone systems is 6 ± 2 Å (for more information see Section 5.7.5 and 5.8.5) which in accordance to the 3-6 Å observed in the literature for LE of DPPC [53,54]. Assuming that this value should be close to that of the MD, we calculate the absolute height of each physical state according to it and the relative heights previously measured. The results obtained are that LC1 state measures 21 ± 1 Å and the LC2 state measures 25 ± 1 Å.

5.6.3 Electrochemical behaviour

Figure 5.6.5 shows the cyclic voltammogram at a scan rate of 10 $mV \cdot s^{-1}$of LB films of MD transferred on ITO in a 0.150 M KCl cell solution buffered at pH 7.4. The LB films have been transferred at two different surface pressures selected according to the criterion of being one surface pressure predominated by the LC1 state and other surface pressure predominated by the LC2 state. Previously, the ITO/electrolyte system has been studied and shows that ITO behaves as a polarizable electrode in the experimental conditions (see dashed line in Figure 5.6.5) as it has been explained in Section 5.1.3. In our experiments, three CVs are required to obtain the stationary state in the electrochemical response, presenting a good reproducibility from the third scan and at least 15 cycles. The voltammograms indicate that in the potential range between 0.80 and -0.40 V the ITO-MD electrode does not show faradaic response and that the effect of the applied electrical potential on the lipid monolayer is low. At more anodic potentials than -0.40 V a continuous increase (not shown) of the intensity was obtained, indicating hydrogen evolution.

The cyclic voltammogram of the ITO-MD/electrolyte system has been used to evaluate its C_d (Inset of Figure 5.6.5) from the values of voltammetric charging current [9] using the Expression 2.38. The ITO-MD electrode presents higher C_d values than bare ITO, increasing from 2 to 4.5 $\mu F \cdot cm^{-2}$ when scanning from 0.90 to -0.30 V. C_d values $\approx$ 1.8 $\mu F \cdot cm^{-2}$ have been reported for high quality lipid monolayers [62] so indicating that our monolayer is not completely homogeneous and it presents few defects. The fact that the voltamogram presents a reproducible behaviour indicates that the lipid layer is permeable to water molecules, and after the third scan, the stable water content is achieved in the monolayer. This effect, and its reversibility, of the applied potential on lipid LB monolayers on ITO are explained by the lipid heads-ITO affinity [63].

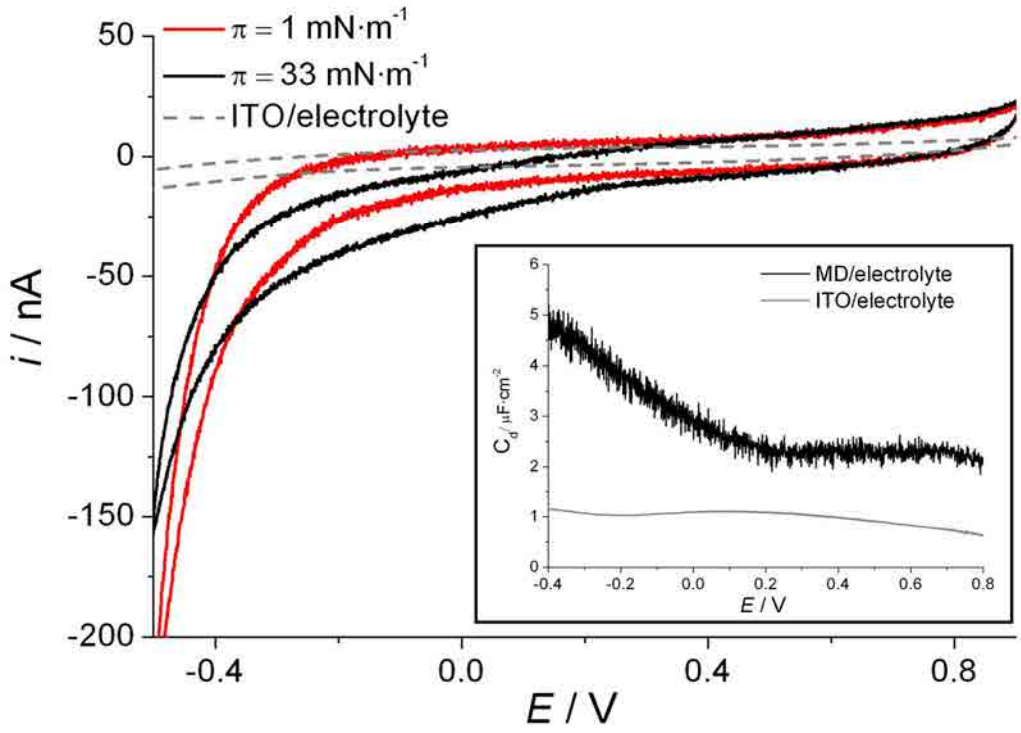

Figure 5.6.5. Cyclic voltammograms of the ITO/electrolyte and ITO-MD/electrolyte system. All CVs have been performed using 0.150 M of KCl electrochemical cell using potassium phosphate buffered solution at pH 7.4, at a scan rate of 10 $mV \cdot s^{-1}$. Inset: C_d of the ITO/electrolyte and ITO-MD/electrolyte at π = 33 $mN \cdot m^{-1}$ system obtained from the CVs presented in Figure 5.6.5.

5.7 DPPC:UQ

5.7.1 π-A isotherms and physical states

The π-A isotherms of the DPPC:UQ system at biological relevant ratios are presented in Figure 5.7.1 referred to the weighted (mean) area per molecule according to the DPPC:UQ ratio. The C_s^{-1} curves (Figure 5.7.2) corresponding to the described π-A isotherms (Figure 5.7.1) are calculated according to the Expression 2.9. The most significant values of Figure 5.7.1 and 5.7.2 are summarized in Table 5.7.1. The description and discussion of the π-A isotherms and the C_s^{-1} results for the DPPC and UQ pure components were explained in Section 5.3.1 and 5.1.1 respectively. So that, we present in this section only the results of the mixtures and their corresponding discussion.

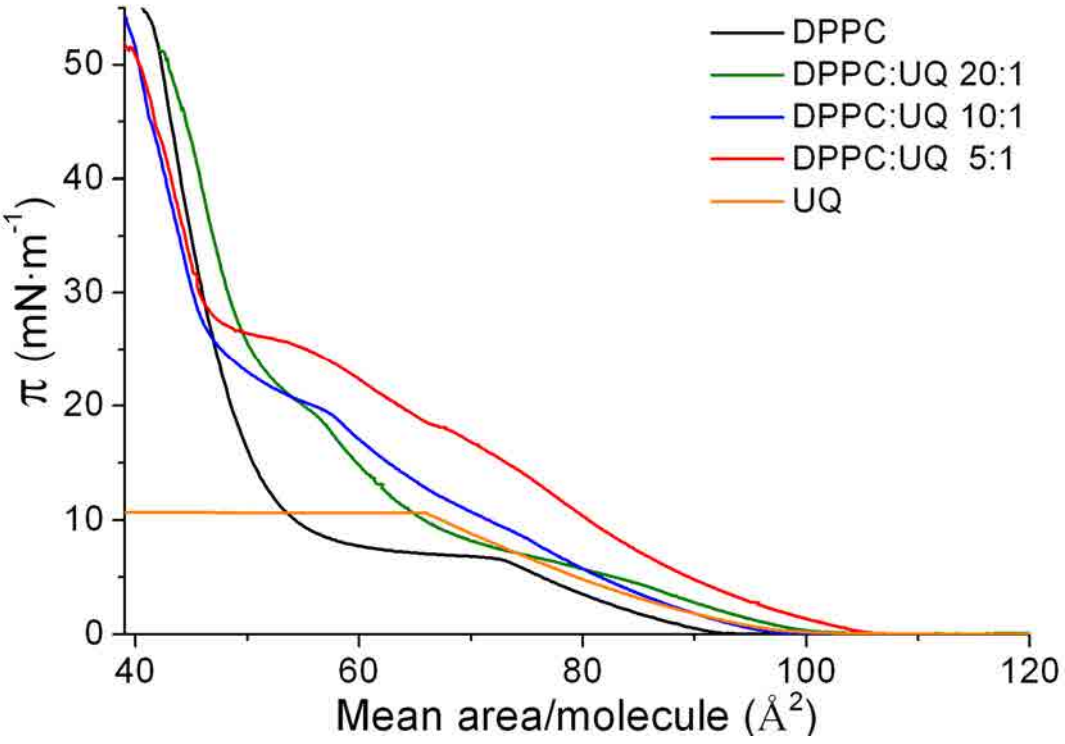

Figure 5.7.1 π-A isotherms for DPPC, UQ and DPPC:UQ mixtures at 21 ± 0.5 ºC on water subphase.

Figure 5.7.1 shows that the π-A isotherms of the DPPC:UQ mixtures present different behaviour according to the UQ presence in the mixture, showing an important influence of the incorporated UQ in comparison with the isotherm of pure DPPC. On the other hand, Figure 5.7.2 shows that each C_s^{-1} curve presents three local minimum points, which represents three changes from concave to convex or vice-versa in the π-A isotherms and

they are called kink points. In reference to the second kink point, present at ≈ 26 $mN \cdot m^{-1}$ for the 5:1 ratio and at ≈ 21 $mN \cdot m^{-1}$ for the 10:1 and 20:1 ratios, the isotherms shown in Figure 5.7.1 can be divided in two zones, establishing the border value at this kink point. At surface pressure below the second kink point, the presence of high content of UQ (see DPPC:UQ 5:1 system) hindrances in a quite larger extent the packing of the monolayer than the low ratios (See DPPC:UQ 20:1 and 10:1 systems). Above the surface pressure of this kink point, the most UQ molecules have been expulsed, as it will be explained. In addition, all the π-A isotherms of the mixtures have a similar slope, showing also a similar area per molecule till the collapse. On the other hand, the different slope of the π-A isotherms of the mixtures compared with that of pure DPPC indicates that part of the UQ is still remaining in the DPPC matrix, although it seems to be with low content.

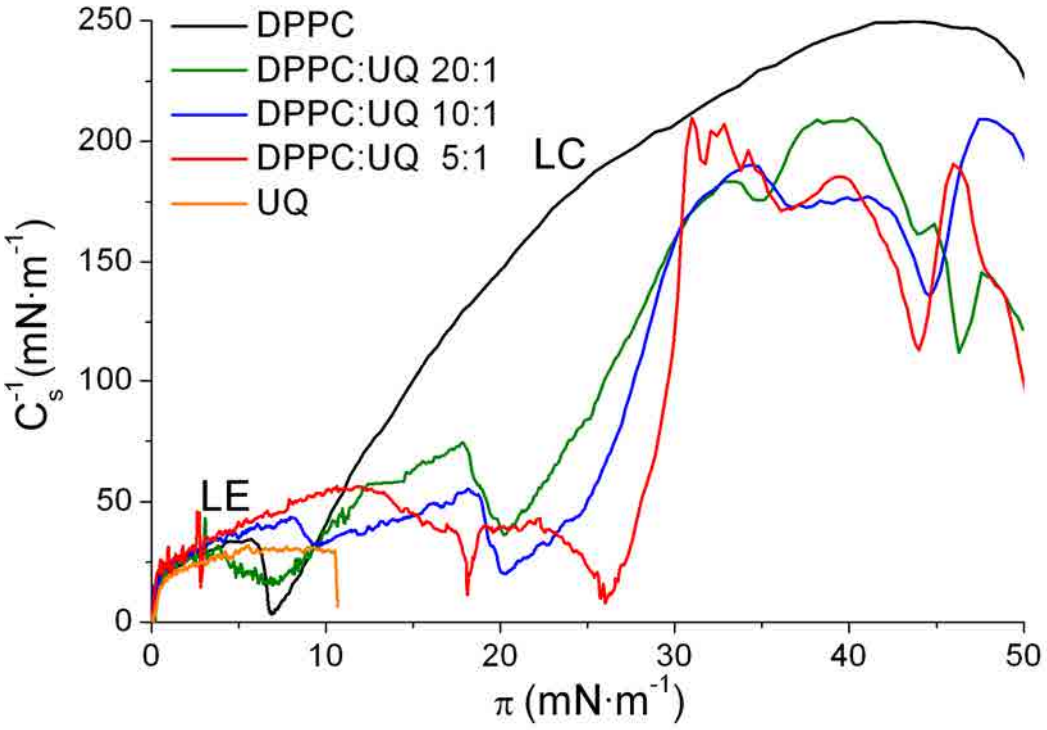

Figure 5.7.2. Inverse of the compressibility modulus vs. surface pressure for DPPC, UQ and DPPC:UQ mixtures on water subphase.

The lift-off area increases as the UQ content in the DPPC:UQ mixture is enlarged (Table 5.7.1), and it is correlated with the distorting effect of UQ in the DPPC matrix [80]. This phenomena was also observed by Bilewicz et al. [1] using UQ and $C_{18}SH/C_{18}OH$ and also by Kruk et al. [38] using PQ and unsaturated MGDG mixtures. The presence of UQ in the

initial zone hindrances the packing of the DPPC headgroups, and therefore, the hydrophobic interactions between the DPPC chains are also reduced, as it was seen in the case of UQ inserted in phospholipids [25]. When UQ is present at low concentrations, it is better retained in the matrix due to it affects in a lower extent the formation and shape of the ordered phases. After the main rejection of the UQ (second kink point), the compactness of the mixture monolayer is rapidly enhanced.

Table 5.7.1. Collapse pressure, lift-off area and phase change of the second kink point position for the DPPC, UQ and their biological mixtures obtained from Figure 5.7.1. The presentation only of the second kink point is due to it is correlated with the phase change.

	Collapse pressure ($mN \cdot m^{-1}$)	Lift-off area ($Å^2 \cdot molec^{-1}$)	2nd Kink point pressure ($mN \cdot m^{-1}$)	2nd Kink point area ($Å^2 \cdot molec^{-1}$)
DPPC	55	91	-	-
DPPC:UQ 20:1	52	98	21	55
DPPC:UQ 10:1	55	97	21	56
DPPC:UQ 5:1	52	105	26	52
UQ	11	102	-	-

The C_s^{-1} curves of DPPC:UQ mixtures present similar shape with differences according to the UQ content around the kink points. Accordingly to the values presented by Vitovic et al. [7] and the characteristics of the system, it is suggested that the first kink point, at ≈ 18 $mN \cdot m^{-1}$ for the 5:1 ratio and at ≈ 8 $mN \cdot m^{-1}$ for the 10:1 and 20:1 ratios, indicates an increase of the DPPC molecules ordering which implies the beginning of a progressive expulsion of the UQ molecules from the matrix. The second kink point indicates the phase change from LE to LC of the DPPC molecules, which implies the expulsion from the matrix of the most part of the remaining UQ molecules. So that, the compactness of the mixture monolayer is rapidly enhanced. The third kink point (placed at ≈ 44 $mN \cdot m^{-1}$) seems to represent a reorientation of the DPPC molecules, which implies the last stage of UQ molecules expulsion from the matrix. Quinn and Esfahani [4] proposed for the DMPC:UQ mixtures the surface pressure of 35 $mN \cdot m^{-1}$ to be the initial surface pressure at which UQ is completely separated from DMPC and overlies the DMPC monolayer. Probably, this pressure depends on the physico-chemical properties of the lipid and the prenylquinone.

Phase rule

The collapse pressure of a mixed monolayer of different components is related to the miscibility of its components, being dependent on the film composition in a miscible system [50,68]. In our DPPC and DPPC:UQ mixtures isotherms, the collapse pressure is ≈ 53 $mN \cdot m^{-1}$. Therefore, the similar collapse pressure can be used to elucidate the expulsion of one of the components in a mixed film. In a two component monolayer, if components are completely immiscible, a lower collapse pressure of one of the components will be observed as predicted by the phase rule. Maintaining temperature and external pressure constant, the number of degrees of freedom F of the monolayer system is given by the Expression 2.14 [82,83] that is reproduced below:

$$F = C_B + C_S - P_B - P_S + 1$$

In our DPPC:UQ experiments, at the air|water interface, $C_B = 2$ (air and water), $C_S = 2$ (DPPC and UQ), and $P_B = 2$ (gas and liquid), thus $F = 3 - P_S$. According to that, homogenous mixed films achieve the collapse equilibrium with $P_S = 2$ (condensed and collapsed state) so the system will have one degree of freedom. According to our results, the collapse pressure is practically fixed, discarding the experimental deviations, for pure DPPC and DPPC:UQ mixtures. This indicates zero degrees of freedom and therefore, following the previous reasoning, $P_S = 3$. So that, at the collapse equilibrium of the mixtures isotherms coexist: DPPC (LC), DPPC (collapse) and expelled UQ. The same statements can also be applied to the second kink point zone, where the π is practically fixed indicating zero degrees of freedom. Thus $P_S = 3$ which indicates that three phases coexist: DPPC:UQ (LE), DPPC:UQ (LC) and expelled UQ, confirming the phase change. This observation coincides with the AFM conclusions (Section 5.7.3).

5.7.2 Thermodynamic study

The representation of the mean area per molecule vs. the molar fraction at selected surface pressures gives idea about the ideality of a mixture at these surface pressures. The reader is addressed to Section 2.1.1.5 where the mathematical treatment (Expressions 2.10 - 2.13) for the figures of this part is explained. Figure 5.7.3 plots the area per molecule and Figure 5.7.4 plots G^E both vs. the UQ molar fraction for DPPC:UQ mixtures at several surface pressures before the main UQ expulsion at the second kink point. At surface pressures

above this event, the thermodynamic study has not been performed due to the UQ content in the DPPC:UQ matrix is unknown and significantly lower than the initial presence.

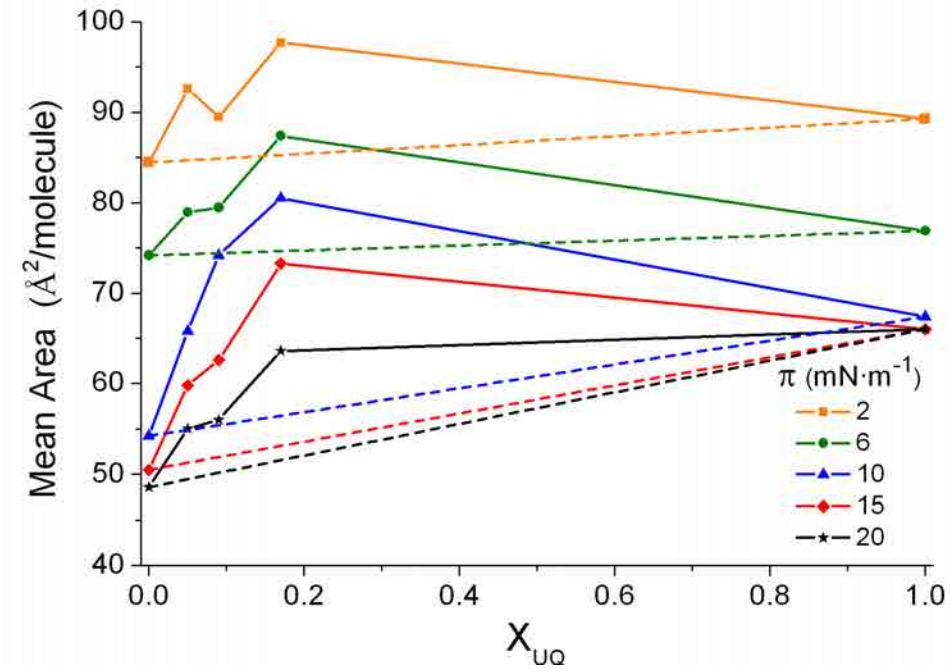

Figure 5.7.3. Plot of the mean area per molecule vs. the molar fraction for DPPC, UQ and DPPC:UQ mixtures at several surface pressures before the main UQ expulsion. Discontinuous straight line represents the ideal behaviour for each surface pressure.

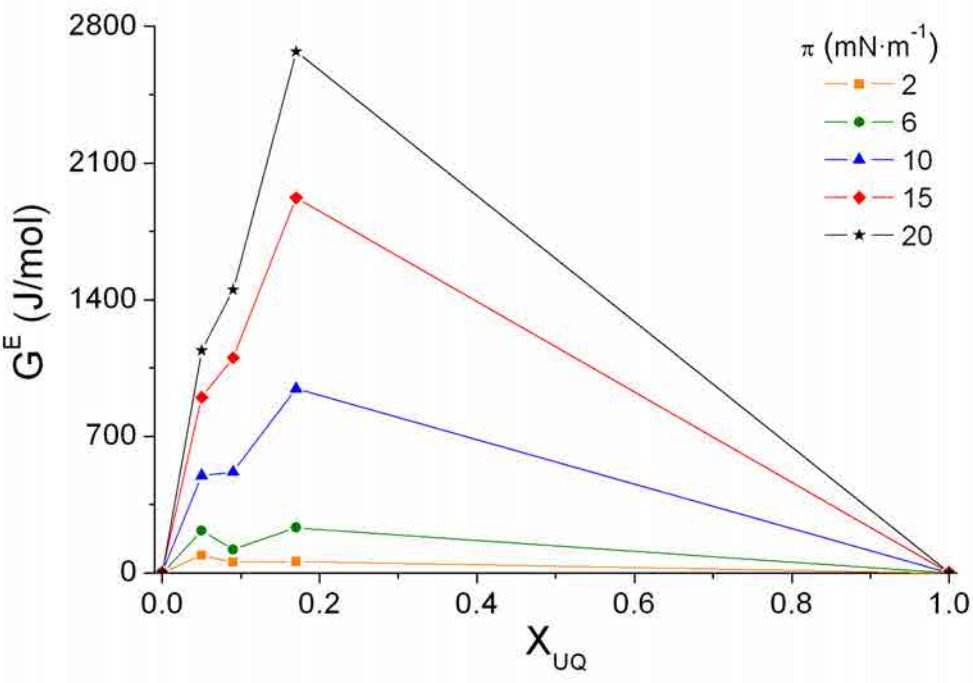

Figure 5.7.4. Plot of the excess energy vs. the molar fraction for DPPC, UQ and DPPC:UQ mixtures at several surface pressures before the main UQ expulsion.

Both figures (Figure 5.7.3 and 5.7.4) show that DPPC and UQ form non-ideal mixtures with positive deviation at $\pi \leq 20$ mN·m^{-1}, which indicates that, at these surface pressures, the interactions between the two components are weaker than the interactions between pure components [6] suggesting the possible formation of enriched domains or aggregates of molecules [68,83] at high UQ content.

The Figure 5.7.5 represents the ΔG_{mix} vs. UQ molar content at several surface pressures before the main UQ expulsion. The negative values observed for ΔG_{mix} at $\pi \leq 10$ mN·m^{-1} indicate that the mixed monolayers of DPPC:UQ are more stable than pure components [6]. At higher surface pressures, the mixed monolayer is not stable which favours the UQ expulsion.

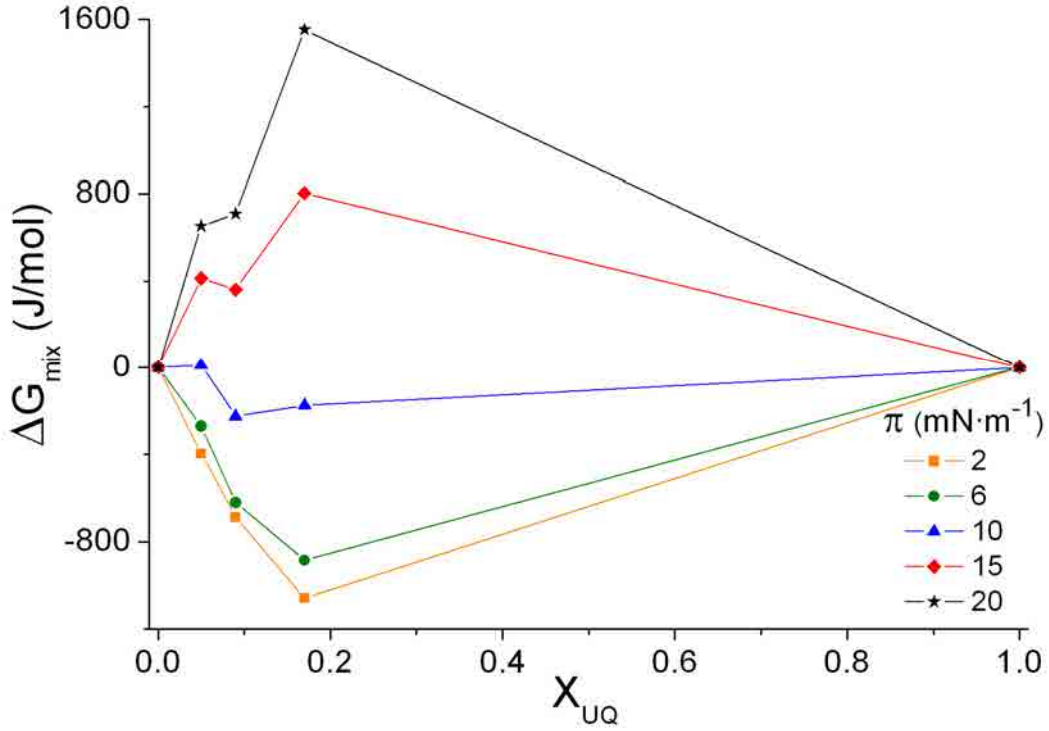

Figure 5.7.5. Plot of the mixing energy vs. the molar fraction for DPPC, UQ and DPPC:UQ mixtures at several surface pressures before the main UQ expulsion.

The formation of non-ideal mixtures between UQ and DPPC at low surface pressure, as it was previously observed [6], is explained by the difference in the chain length between UQ and DPPC, which permits a free rotation of the UQ part that protrudes over the DPPC producing also a motion of the DPPC molecules, which induces an increase of the molecular area [6,38]. The difference between the ideal line (dashed) and the experimental

data of Figure 5.7.4 is the excess area per molecule, which decreases when increasing the surface pressure and this may be interpreted as an indication that the DPPC:UQ system tends towards a total segregation [6].

5.7.3 AFM

In this part we present the topographic images of different DPPC:UQ mixtures at several surface pressures to light which is the organization of these molecules once transferred to a hydrophilic substrate (mica) and ultimately, correlate this knowledge with the predicted results in previous sections. The description and discussion of the AFM topographic images and their mathematical treatment for the pure components DPPC and UQ are explained in Section 5.3.2 and 5.1.2 respectively. So that, we present in this section only the results of the mixtures and their corresponding discussion.

Figure 5.7.6 shows the AFM topographic images corresponding to pure DPPC and pure UQ and the selected DPPC:UQ mixtures transferred on mica at π = 6 $mN \cdot m^{-1}$. This surface pressure permits us to ensure that most of the initial UQ is present in all the mixtures showing the larger differences for these systems. The images A, B and C show two different tonalities of brown (fair and dark) and both correspond to the DPPC or DPPC:UQ monolayer, being each tonality correlated with a different physical state of the system monolayer respectively. Moreover, the images A, B and C show that the presence of UQ has a strong influence on the DPPC matrix.

In order to explain the behaviour of the DPPC:UQ mixtures at several surface pressures, we have selected the 5:1 ratio (Figure 5.7.7) due to it is the most different from the pure DPPC (Figure 5.3.2) of the ratios we have studied and represents the best option to compare them. As it has been shown for pure DPPC, DPPC:UQ 5:1 presents two different tonalities of brown (fair and dark) and each one corresponds to zones with a different order of the molecules. Moreover, it is interesting to point that at π = 6 $mN \cdot m^{-1}$ and only for the 5:1 ratio, the image presents small black zones (holes) which corresponds to the mica surface (See inset in Figure 5.7.7A). The compression leads to a more compact fashion of the more ordered zones till π = 33 $mN \cdot m^{-1}$ where the monolayer presents uniform phase with rounded shaped protrusions of diameter 75 to 150 nm and 8 ± 2 Å height over it. On the other hand,

AFM topographic images have been performed with the systems DPPC:UQ 10:1 and 20:1 (not shown) obtaining a behaviour comprised between the pure DPPC (Figure 5.3.2) and the DPPC:UQ 5:1 (Figure 5.7.7), so only the image corresponding to π = 6 $mN \cdot m^{-1}$ for DPPC:UQ 10:1 is presented (Figure 5.7.6).

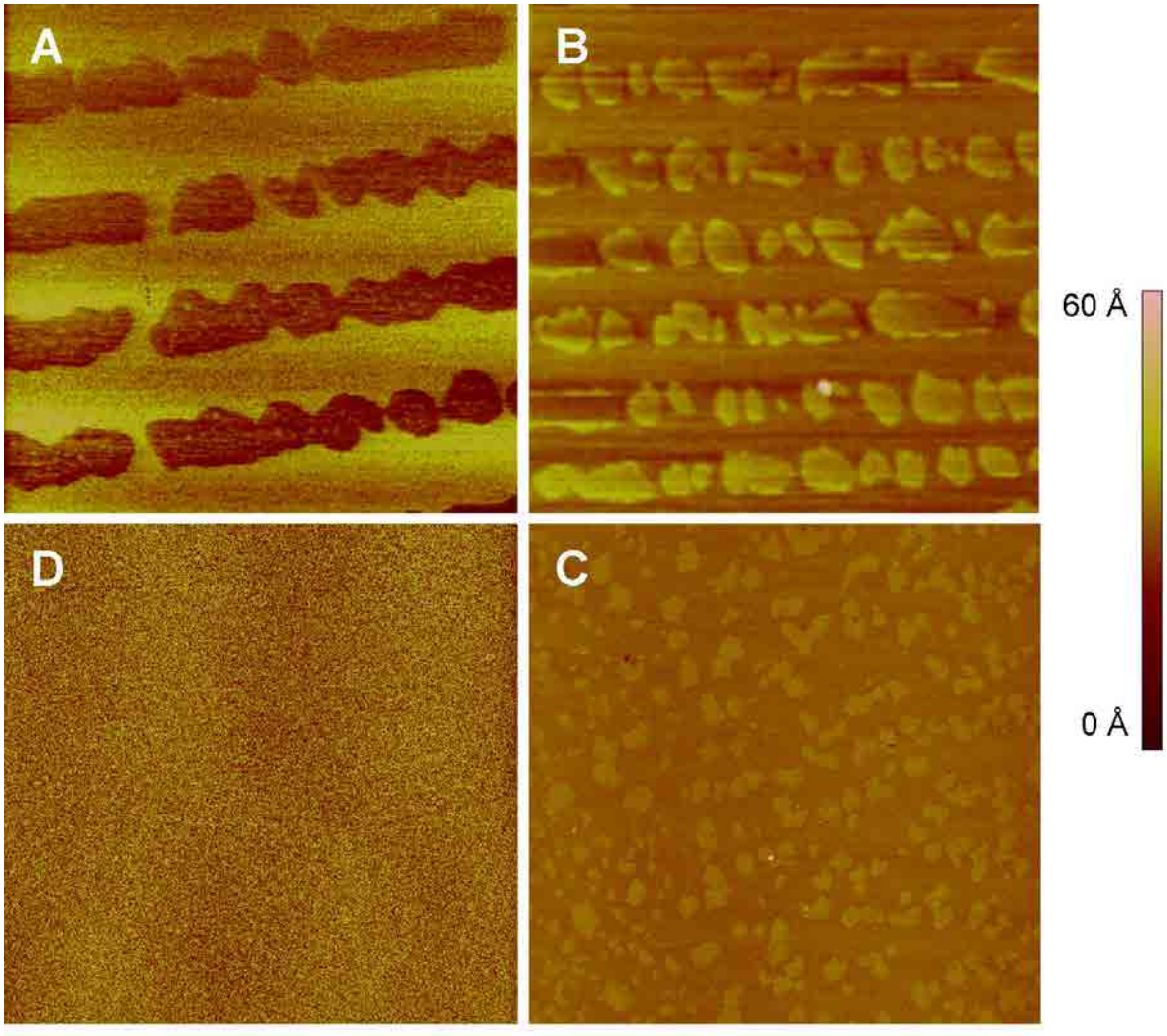

Figure 5.7.6. AFM images (5µm x 5µm) for LB films transferred on mica at 21ºC at π = 6 $mN \cdot m^{-1}$ for (A) pure DPPC, DPPC:UQ systems (B) 10:1, (C) 5:1 and (D) pure UQ.

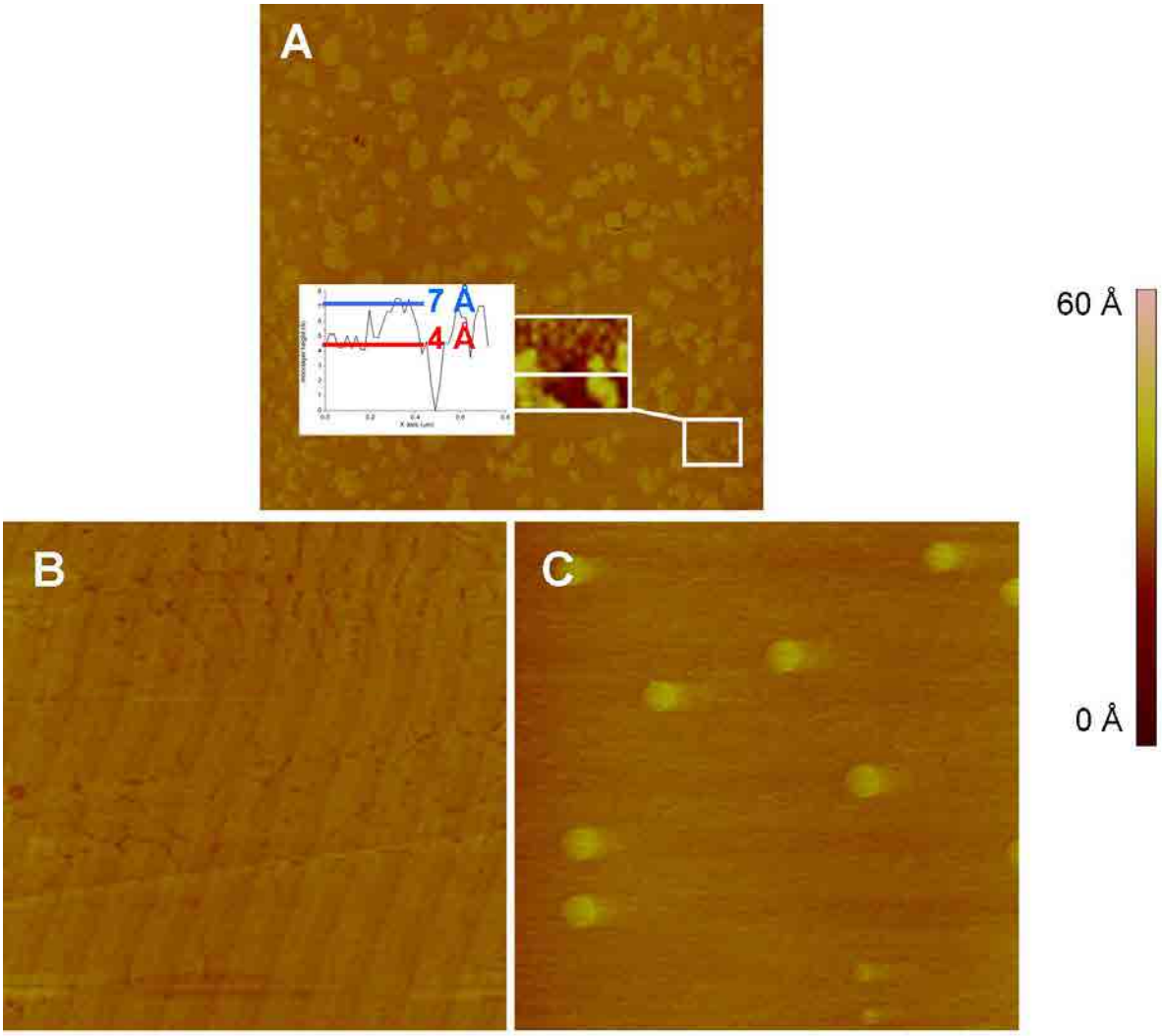

5.7.7. AFM images (5μm x 5μm) for LB films of DPPC:UQ 5:1 system transferred on mica at 21ºC at (A) π = 6 mN·m^{-1}, (B) π = 25 mN·m^{-1} and (C) π = 33 mN·m^{-1}.

AFM discussion

As it has been explained for pure DPPC (Section 5.3.2) each tonality indicates a different tilt order of the molecules that depends on the surface pressure and the interactions established between molecules and between the molecules with the substrate. The appearance simultaneously of zones with a high order (fair zones) with zones of low order (dark zones) in pure DPPC indicates that the meaning of the tonalities is also the same for the mixtures.

In order to light each physical state, we have measured the relative height between fair and dark zones, and assuming the height of 4 ± 1 Å for the dark brown zones referred to the mica surface (Inset of Figure 5.7.7A) , the absolute height is presented in Table 5.7.2. The

selection of this height value for the dark zones is done based on that this is the height measured between the dark brown zones and the black zones seen at low surface pressure for the DPPC:UQ 5:1 system (Inset of Figure 5.7.7A) and, moreover, this height is in accordance with the 3-6 Å observed in the literature for LE state of DPPC monolayers [53,54].

Table 5.7.2. Height of each physical state for the LB monolayers of DPPC and DPPC:UQ mixtures on mica. *Estimated value (more information in the text).

	LE	LC
DPPC	4 ± 1 *	22 ± 2
DPPC:UQ 20:1	4 ± 1 *	16 ± 2
DPPC:UQ 10:1	4 ± 1 *	17 ± 2
DPPC:UQ 5:1	4 ± 1	-

The absolute heights obtained at each surface pressure and considering the C_s^{-1} results permit the obtaining of the physical state corresponding to each tonality for all the systems (Table 5.7.3).

Table 5.7.3. Physical states of each zone (dark and fair brown) corresponding to the DPPC and DPPC:UQ systems at several surface pressures.

	DPPC		DPPC:UQ 20:1		DPPC:UQ 10:1		DPPC:UQ 5:1	
π (mN·m^{-1})	Dark	Fair	Dark	Fair	Dark	Fair	Dark	Fair
6	LE	LC	LE	LC	LE	LC	LE	LC
15	LE	LC	LE	LC	LE	LC	LE	LC
25	-	LC	LE	LC	LE	LC	LE	LC

The height observed for the DPPC:UQ mixtures LC phase is in line with that of pure DPPC. In Table 5.7.2, the height value for the DPPC:UQ 5:1 system is not reported because the quality of the images do not permit to obtain this value with enough precision. At $\pi \geq 25$ mN·m^{-1} the AFM images give little information about the physical state, although when also considering the C_s^{-1} values of these mixtures (Figure 5.7.2), it is suggested that all mixtures present LC state (Figure 5.7.7B). On the other hand, it is also interesting to point that DPPC and DPPC:UQ mixtures present grooves of depth < 4 Å at the LC phase which suggest that the continuous phase has been formed by fusion of rigid domains.

The DPPC and DPPC:UQ mixtures monolayers cover the entire mica surface at all surface pressures, except for the explained case of DPPC:UQ 5:1 at π = 6 mN·m^{-1}. The non-observation of uncovered mica zones permits to obtain the proportion of each physical state at each surface pressure. The Figure 5.7.8 presents the percentage of the monolayer in fair brown, so that, according to the Table 5.7.3, the proportion of each physical state can be elucidated. For the particular case of DPPC:UQ 5:1 at π = 6 mN·m^{-1}, the result shown is also the fair brown zones but the complementary value indicates the area occupied for both the LE zones and the uncovered regions.

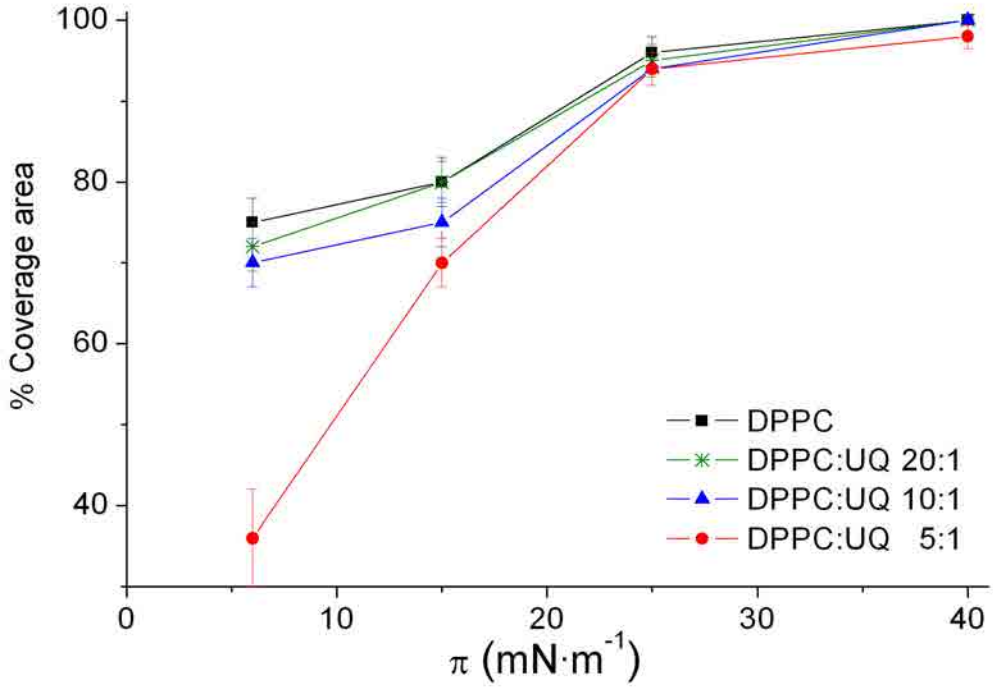

Figure 5.7.8. Monolayer coverage of the fair brown zones on the mica surface for the pure DPPC and the DPPC:UQ mixtures, calculated from AFM images.

The results obtained in Figure 5.7.8 shows that DPPC and DPPC:UQ mixtures present similar tendency of covered area by the compact phase although the height of the pure DPPC is higher (see Table 5.7.2), so that, this behaviour suggests that, once transferred, the interactions mica-DPPC or mica-DPPC:UQ are similar when the UQ content is low and the UQ presence mainly affects the DPPC molecules tilting. On the other hand, the DPPC:UQ systems show at the most surface pressures, the expected trend of more surface covered by the compact state when decreasing the UQ content. The reason for this behaviour is that the presence of UQ hindrances the ordering of the DPPC molecules. The tendency is clear and the surface pressures at which this trend is not followed is due to slight experimental

deviations. Increasing the surface pressure all the DPPC:UQ systems increase the presence of LC achieving at π = 25 $mN \cdot m^{-1}$ a nearly flat increase which is correlated with that the major content of UQ has been rejected from the lipid matrix.

The simultaneous presence of two different physical states at each surface pressure for both the DPPC and DPPC:UQ systems indicates that both systems starts the LE to LC physical state change at very low surface pressure. The pure DPPC system achieves at lower surface pressure than the DPPC:UQ system the entire mica surface covered by the LC state (Figure 5.7.8), which is explained by the presence of UQ in the DPPC:UQ mixtures hindrances the packing of the DPPC molecules. The size of the LC domains are reduced when increasing the UQ content in the DPPC:UQ mixture (Figure 5.7.6), which indicates that part of the UQ is in the LC domains. Roche et al. [6] using fluorescence microscopy for the DPPC:UQ system observed that a UQ presence > 5 mol% reduces the surface occupied by the LC phase, it decreases the LC domain size and it produces a change in the domain shape compared with pure DPPC. We observe in our DPPC:UQ system AFM topographic images the same behaviour to Roche et al. [6].

5.7.4 Electrochemical behaviour

In this section, the electrochemical behaviour of the ITO-DPPC:UQ/electrolyte systems and its mathematical treatment are presented. On the other hand, the results and their corresponding discussion of the pure components DPPC and UQ are exposed in Section 5.3.4 and 5.1.3 respectively, so that, they will be only presented in this section in case it is necessary to compare with the mixtures results. In our experiments, three CVs are required to obtain the stationary state in the electrochemical response, presenting a good reproducibility from the third scan and at least 15 cycles.

Figure 5.7.9 and 5.7.10 present the cyclic voltammograms at 10 $mV \cdot s^{-1}$ of the ITO-DPPC:UQ/electrolyte 5:1 and 10:1 systems respectively, transferred on ITO at several surface pressures which, in part, are the same that were selected for topographic AFM imaging on mica. It must be considered that the topographic images observed for the DPPC:UQ system on mica are not directly correlated with the film deposited on ITO due to

the differences between substrates in surface roughness and physico-chemical properties, although it can be extrapolated.

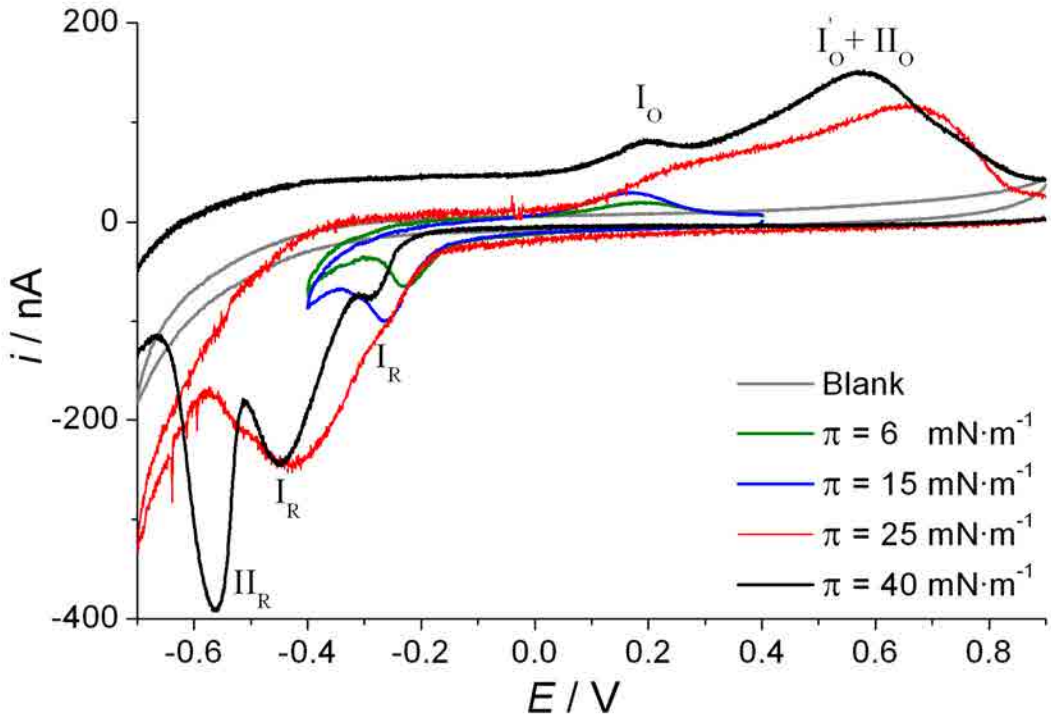

Figure 5.7.9. Cyclic voltammogram of ITO-DPPC:UQ 5:1 LB films transferred at several surface pressures. Blank line represents CV of the ITO-DPPC electrode. All CVs have been performed using 0.150 M of KCl electrochemical cell using potassium phosphate buffered solution at pH 7.4 and at a scan rate of 10 $mV \cdot s^{-1}$.

The ITO-DPPC:UQ 5:1/electrolyte system at $\pi \leq 15$ $mN \cdot m^{-1}$ (Figure 5.7.9), presents only a main irreversible process that we label as process I according to the similarity between the reduction and oxidation peak potentials and the formal potential of ITO-UQ/electrolyte (Section 5.1.3) and the ITO-DPPC:UQ/electrolyte systems (Table 5.7.4). The ITO-DPPC:UQ/electrolyte systems at $\pi = 25$ $mN \cdot m^{-1}$ shows a wide reduction peak, that draws three waves, and two wide oxidation peaks are obtained; whereas at $\pi = 40$ $mN \cdot m^{-1}$ three reduction peaks are clearly differentiated in the cathodic scan and two oxidation peaks in the anodic scan. In Figure 5.7.9, the peaks have been labelled as I_R, I_R' and II_R, for the cathodic scan, and I_O and I_O' + II_O for the anodic scan and their potentials are summarized in Table 5.7.4. The redox process II assignment has also been done according to the CVs presented in Figure 5.7.11, considering the similarity in the reduction peak position (II_R) between the CVs of the ITO-DPPC:UQ 5:1/electrolyte and the ITO-UQ/electrolyte (Section 5.1.3) systems, but in the case of the DPPC:UQ mixture a new reduction peak labelled as

I_R' appears. The second oxidation peak that appear at π = 25 mN·m^{-1} and π = 40 mN·m^{-1} has been labelled as I_O'+II_O. The peak I_O'+II_O is wide and asymmetric and it is shifted to more cathodic potentials with respect to the position of peak II_o for ITO-UQ/electrolyte system indicating that two processes are convoluted.

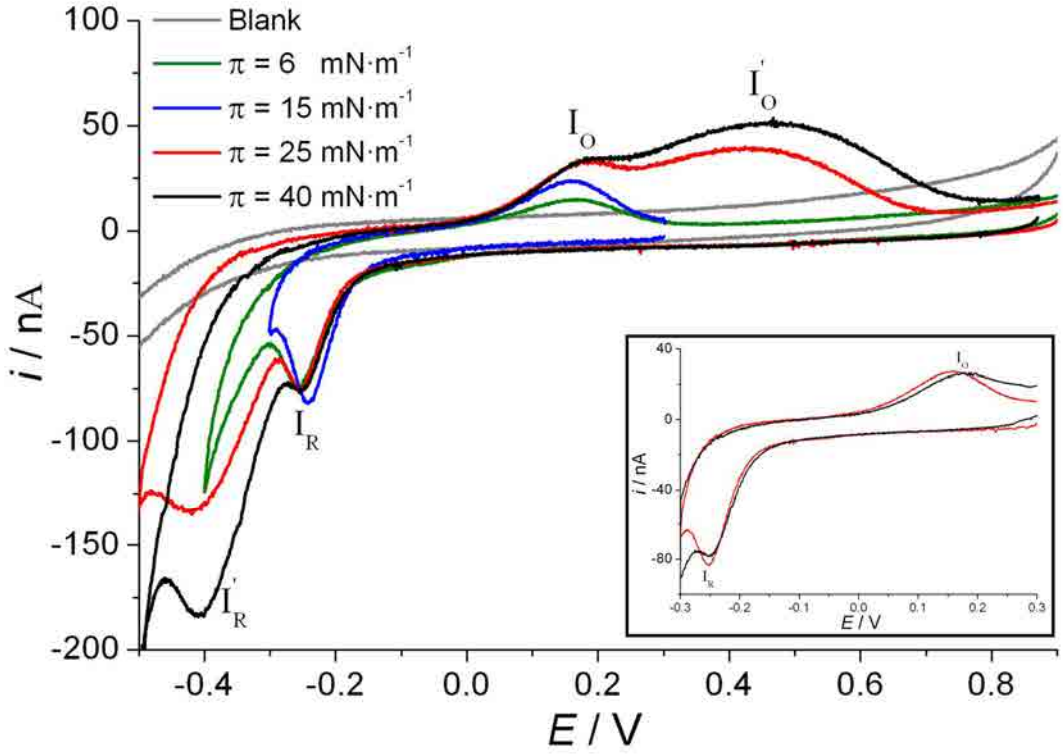

Figure 5.7.10. Cyclic voltammogram of ITO-DPPC:UQ 10:1 LB films transferred at several surface pressures. Blank line represents the CV of the ITO-DPPC electrode. Inset corresponds to the ITO-DPPC:UQ/electrolyte system at 10:1 ratio in short potential window transferred at π = 25 and 40 mN·m^{-1}. All CVs have been performed using 0.150 M of KCl electrochemical cell using potassium phosphate buffered solution at pH 7.4 and at a scan rate of 10 mV·s^{-1}.

The redox peak potentials of the ITO-DPPC:UQ 10:1/electrolyte system (Figure 5.7.10) are presented in Table 5.7.5. This mixture shows the oxidation peak I_O' position without the influence of the process II due to the later is not present in the CVs of this system. Therefore, the formal potential of process I' can also be calculated (Table 5.7.5). On the other hand, it is interesting to observe that the double layer capacity of the ITO-DPPC/electrolyte experiments is fitted in the capacitive current of all the ITO-DPPC:UQ/electrolyte systems (See Blank line in Figures 5.7.9 and 5.7.10).

Table 5.7.4. Redox peaks potentials and the formal potential that process I represents for the ITO-DPPC:UQ 5:1/electrolyte system and the redox peak potentials for process I' and II for the same system.

π ($mN \cdot m^{-1}$)	E_{pR} (I) (V)	E_{pO} (I) (V)	E_f (I) (V)	E_{pR} (I') (V)	E_{pO} (I') (V)	E_{pR} (II) (V)	E_{pO} (I'+II)(V)
6	-0.22 ± 0.02	0.18 ± 0.02	-0.02 ± 0.02	-	-	-	-
15	-0.24 ± 0.02	0.17 ± 0.02	-0.04 ± 0.02	-	-	-	-
25	-0.28 ± 0.02	0.22 ± 0.02	-0.05 ± 0.02	-0.42 ± 0.02	-	-0.52 ± 0.02	0.63 ± 0.02
40	-0.28 ± 0.02	0.20 ± 0.02	-0.04 ± 0.02	-0.44 ± 0.02	-	-0.56 ± 0.01	0.58 ± 0.02

Table 5.7.5. Redox peaks potentials and the formal potential that they represent for the ITO-DPPC:UQ 10:1/electrolyte system.

π ($mN \cdot m^{-1}$)	E_{pR} (I) (V)	E_{pO} (I) (V)	E_f (I) (V)	E_{pR} (I') (V)	E_{pO} (I') (V)	E_f (I') (V)
6	-0.23 ± 0.01	0.16 ± 0.02	-0.04 ± 0.02	-	-	
15	-0.23 ± 0.01	0.16 ± 0.02	-0.04 ± 0.02	-	-	
25	-0.23 ± 0.01	0.18 ± 0.02	-0.03 ± 0.02	-0.43 ± 0.02	0.41 ± 0.02	-0.01 ± 0.01
40	-0.23 ± 0.01	0.18 ± 0.02	-0.03 ± 0.02	-0.43 ± 0.02	0.43 ± 0.02	0.00 ± 0.01

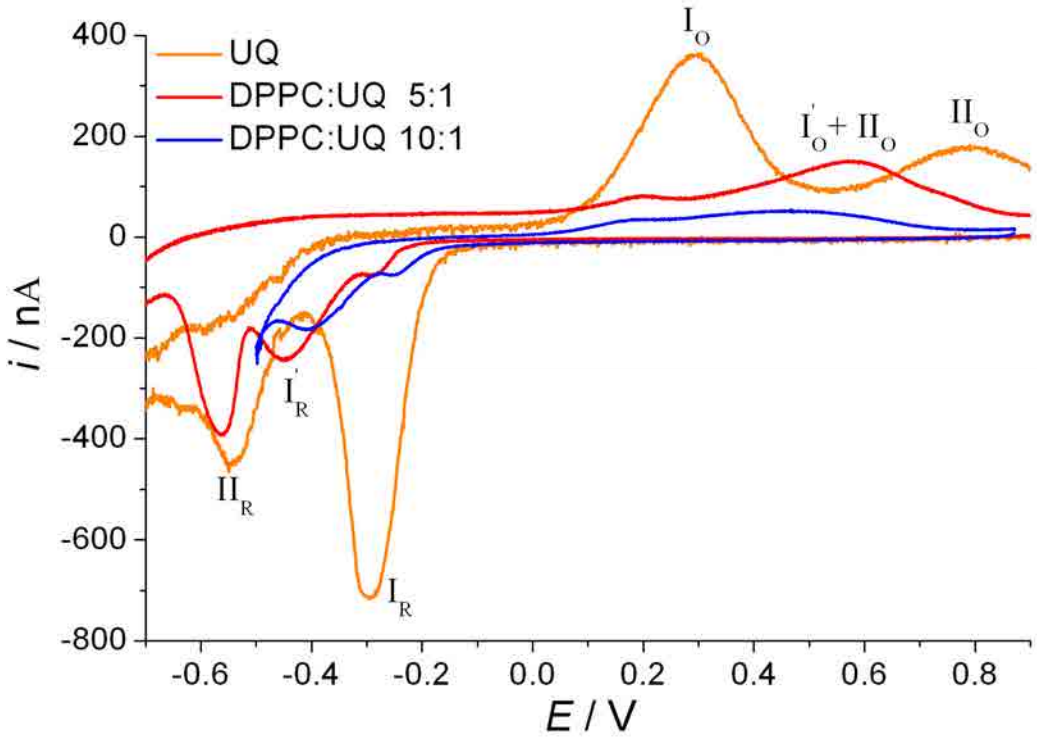

Figure 5.7.11. Cyclic voltammograms of ITO-DPPC:UQ 5:1 and 10:1 LB films transferred at π = 40 $mN \cdot m^{-1}$ and pure UQ transferred at π = 11 $mN \cdot m^{-1}$. All CVs have been performed at 10 $mV \cdot s^{-1}$, using 0.150 M of KCl electrochemical cell using potassium phosphate buffered solution at pH 7.4.

Discussion of the electrochemical response of the DPPC:UQ-ITO/electrolyte system

We understand that the global reaction and the mechanism proposed for pure UQ in confined situation (Section 5.1.3) is the same for the UQ of the ITO-DPPC:UQ/electrolyte system. The shape of the voltammograms for the ITO-DPPC:UQ/electrolyte systems presents two important deviations respect to the theoretical models proposed in the literature to describe the cyclic voltammetric response of a surface confined reaction [29-31]. First, the peak shape which is not symmetrical, presenting the reduction peaks a sharper shape than the oxidation ones, a similar situation that was observed by Märtensson and Agmo [32] and Hong and Park [22] studying UQ and hydroquinone respectively. Second, the redox peaks separation for process I, I' or II is larger than the expected for such systems.

The different shape of reduction and oxidation peaks can be explained by the different hydrophilic character of the redox couple UQ/UQH_2 as it was pointed for the UQ-ITO system (Section 5.1.3). The larger polarity of UQH_2 compared with UQ leads the former to establish better attractive interactions by dipole-dipole or hydrogen bond between UQH_2 and DPPC headgroups and, in addition, the UQH_2-ITO, UQH_2-UQH_2 and UQH_2-water interactions are also enhanced [4,25-27,32-38,84,85,93]. During the oxidation scan UQH_2 is the reactant so the possibilities of hydrogen bonds are larger, increasing the stabilization of the UQH_2 molecule and making it more difficult to oxidise. These arguments are also valid for explaining the larger width of the oxidation peak compared with that of the reduction process.

The Figure 5.7.12 presents the redox peak potentials of processes I and I' vs. the scan rate for the ITO-DPPC:UQ/electrolyte 10:1 system. The redox peaks separation for process I' is larger than for process I indicating that process I' is even more irreversible than process I. Moreover, the redox peaks separation for all the processes I and I' is enhanced when increasing the scan rate and similar behaviour is observed for the ITO-DPPC:UQ 5:1/electrolyte system (not shown). This separation makes both processes (I and I') more irreversible and it represents a similar trend to that it was observed by Marchal et al. [21] and by Laval and Majda [41]. This large separation for both processes aroused from the slow charge transfer rates at the ITO-monolayer|electrolyte interface [32]. The

irreversibility of process II can be studied comparing the peak potential of II_R and that of the oxidation peak I_o'+ II_o, obtaining that process II is more irreversible than process I or I'.

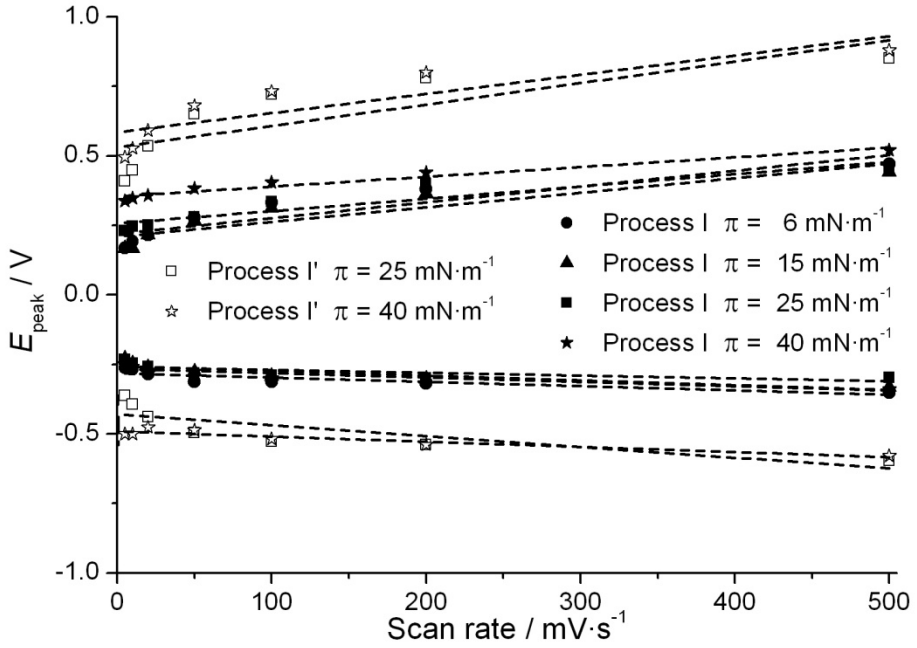

Figure 5.7.12. Peak potential vs. the scan rate for the ITO-DPPC:UQ 10:1/electrolyte system transferred at several surface pressures.

As it can be inferred from the Figure 5.7.12, the increase in the scan rate affects in a larger extent the oxidation peak potential than the reduction one, which produces that the midpoint potential (midpoint potential between the oxidation and the reduction peak both corresponding to the same redox process) for process I and I' has scan rate dependence. On the other hand, it is interesting to observe that all the linear adjustments of the process I and I' reduction peaks for the ITO-DPPC:UQ/electrolyte 10:1 system (Figure 5.7.12) have a similar slope and similar trend is shown for the oxidation peaks of the same process. However, the y-intercept of the linear adjustment of the reduction peaks is displaced to more cathodic values when increasing the surface pressure and similar occurs with the y-intercept of the linear adjustment of the oxidation peaks that are displaced to more anodic values. These trends are similar to those observed for the process I and I' of the ITO-DPPC:UQ/electrolyte 5:1 system and both are explained by the hindrance increase of the electrochemical process when increasing the scan rate. The process II, that it is only observed in the ITO-DPPC:UQ/electrolyte 5:1 system, also presents a reduction peak potential that it is displaced to more cathodic potential when increasing the scan rate (not shown).

Moreover, the current intensity of the redox peaks (i_{peak}) has been studied for the ITO-DPPC:UQ/electrolyte 10-1 system at several scan rates and it has been shown that the reduction (not shown) and the oxidation current intensity are related by a linear dependence with the scan rate (Figure 5.7.13) so indicating that UQ molecules are surface confined in all the processes [16,29] and that the electron transfer process is not diffusion controlled. These observations are also valid for ITO-DPPC:UQ/electrolyte 10:1 (not shown). Our results are in line with the observations of Märtensson and Agmo [32] for scan rates < 1 $V \cdot s^{-1}$, Gordillo and Schiffrin [28] and Li et al. [43] for monolayers containing UQ confined on the electrode surface.

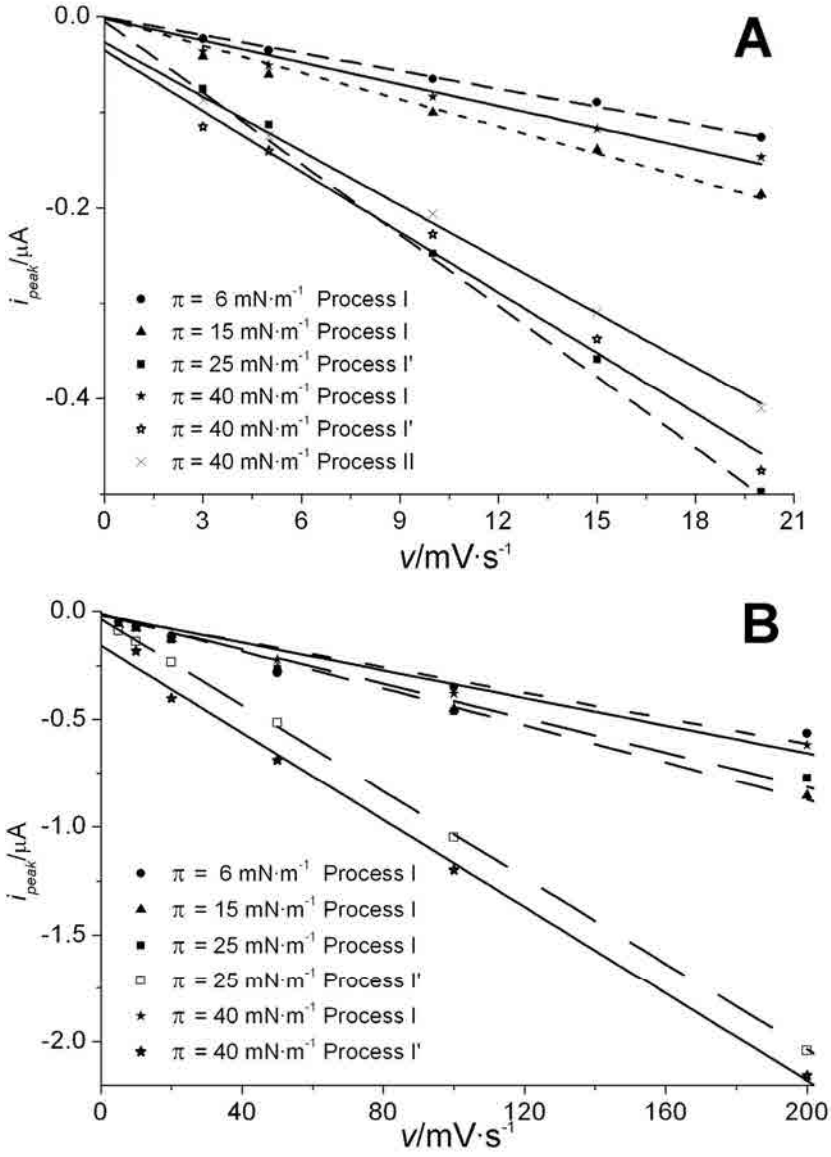

Figure 5.7.13. Oxidation peak intensity vs. the scan rate for the A) ITO-DPPC:UQ 5:1/electrolyte system and B) ITO-DPPC:UQ 10:1/electrolyte both transferred at several surface pressures.

The charge involved in the LB monolayer transferred at each surface pressure is obtained by integrating the area under the reduction or oxidation waves. The surface coverage (Γ) is obtained from the experimental values of charge and considering the global reaction for UQ in confined situation (Section 5.1.3). The Γ for the ITO-DPPC:UQ/electrolyte system are shown in Table 5.7.6 and compared with the expected value to obtain the electroactive fraction of UQ. The expected surface coverage (Γ_{expec}) values are calculated assuming that UQ and DPPC molecules are perfectly spread, accordingly to the corresponding ratio, on the ITO surface, being the resulting value corrected with the transfer ratio associated to it in the LB transfer process. We have chosen to show in Table 5.7.6 the oxidation surface coverage (Γ_O) of the redox processes, which are similar but lower than the results obtained for the reduction scan that have the undesirable contribution of hydrogen evolution.

Table 5.7.6. Expected (Γ_{expec}) and experimental total ($\Gamma_{O\,tot}$) surface coverage, experimental surface coverage for process I, Γ_O (I), and electroactive fraction involved in the whole redox process for ITO-DPPC:UQ/ electrolyte system using 0.150 M of KCl electrochemical cell, using potassium phosphate buffered solution at pH 7.4 and at a scan rate of 10 $mV \cdot s^{-1}$.

π ($mN \cdot m^{-1}$)	Γ_{expec} (10^{-12} mol · cm^{-2})	$\Gamma_{O\,tot}$ (10^{-12} mol · cm^{-2})	Γ_O (I) (10^{-12} mol · cm^{-2})	Electroactive fraction (%)
ITO-DPPC:UQ/electrolyte 5:1				
6	21.3	3.5	3.5	16.5
15	37.9	7.7	7.7	20.3
25	49.4	33.9	11.3	68.6
40	62.9	55.8	8.7	88.7
ITO-DPPC:UQ/electrolyte 10:1				
6	12.9	2.0	2	15.8
15	24.1	4.2	4.2	17.3
25	31.8	17.1	6.4	53.8
40	35.5	24.0	7.1	67.6

The Table 5.7.6 shows that an increase in the initial UQ content in ITO-DPPC:UQ/electrolyte systems leads to an increase of the electroactive fraction. Our results contrast with the observations of Moncelli et al. [19] who observed a decrease in the surface coverage when increasing the initial UQ content from 0.5 to 2 % on a monolayer of DOPC on HDME at pH 9.5. This different behaviour is explained by the differences in pH. Moncelli et al. [15,19] worked with pH 9.5 so the availability of protons in the proximity of

the UQ heads is more limited than in our experiments at pH 7.4. The lack of protons affects the reduction rate determining step (1_b) (see Section 5.1.3) so at high UQ concentrations or high scan rates, the step 1_b is not completed so the electroactive fraction is reduced. In our experiments the enough presence of available protons close to the UQ heads avoids the high local UQ concentration problem. The fact that the electroactive fraction is enhanced when increasing the initial UQ content is explained by the electron hopping effect (See Section 3.4.5). Moreover, the non homogeneous electrode surface and the semiconductive properties of ITO induce it to behave different to metal surfaces like gold or mercury contributing with the different environments that UQ head experiences in the chain region [41] to reduce the electroactive fraction [9].

On the other hand, Γ_O (I) values (Table 5.7.6) are represented in Figure 5.7.14 vs. the surface pressure. At low surface pressures, when only process I is present in the voltammograms, the Γ_O (I) values are equal to the total surface coverage (Γ_{Otot}), but increasing the surface pressure, when peaks I' and II appear, Γ_O (I) attains a maximum value, whereas Γ_{Otot} continues increasing. This process I has a surface coverage limiting value $\approx 11 \cdot 10^{-12}$ mol·cm^{-2} for the ITO/DPPC:UQ 5:1 system. The exceeding surface coverage of UQ correspond to processes I' and II that increase as the monolayer order is enhanced, in according to Hong and Park [22], and it seems to have no limit at the experimented surface pressures.

Finally we compare the formal potential values obtained in our system (Table 5.7.4 and 5.7.5) with that reported in the literature for UQ confined on an electrode surface. Previous authors [16,19,28] have studied the UQ redox processes on HDME. All of them found a formal potential value of $E_f \approx$ -0.13 V vs. Ag/AgCl at pH 7.4. On the other hand, Marchal et al. [21,23], Jeuken et al. [86] and Laval and Majda [41] performed experiments in a biomimetic membrane on gold. The formal potential obtained was, respectively, $E_f \approx$ -0.14 V vs. Ag/AgCl, $E_f \approx$ -0.15 V vs Ag/AgCl and $E_f \approx$ -0.09 V vs. Ag/AgCl. All the formal potential observed by previous authors for the UQ redox processes are less thermodynamically favourable than that observed in this work for process I which is correlated with the higher availability of protons in our system. The process I or I' observed in our experiments requires, respectively, direct contact or short distance between ITO and the UQ head, which can be correlated with the exposed situations [21,23,41,86] at which the UQ is

forced to diffuse to contact the substrate surface to take place the redox process. On the other hand, our process II is more irreversible and kinetically unfavourable [29] than process I or I', but it has more positive formal potential (close to that of benzoquinone/hydroquinone in aqueous solution $E_f \approx 0.14$ V vs. Ag/AgCl [48]) that can be correlated with a more aqueous environment for the UQ headgroup, which is correlated to that they are placed in an environment with higher H^+ ion availability nearer to the aqueous electrolyte. Therefore, we correlate process II with the redox behaviour of the UQ molecules that have been expelled from the DPPC matrix and they are placed on top of the monolayer. On the other hand, as process I' presents a formal potential placed between that of processes I and II, we correlate the process I' with the UQ molecules that are placed in an intermediate position between process I and II, but still confined in the DPPC matrix [9]. The major irreversibility of process II compared with process I and I' is correlated with the larger distance that the electron transfer is forced to proceed from the ITO surface to the UQ head which induces a slowing of the overall electron-transfer rate which is often observed in SAMs of electro-active molecules [22,45] and in SPB [87].

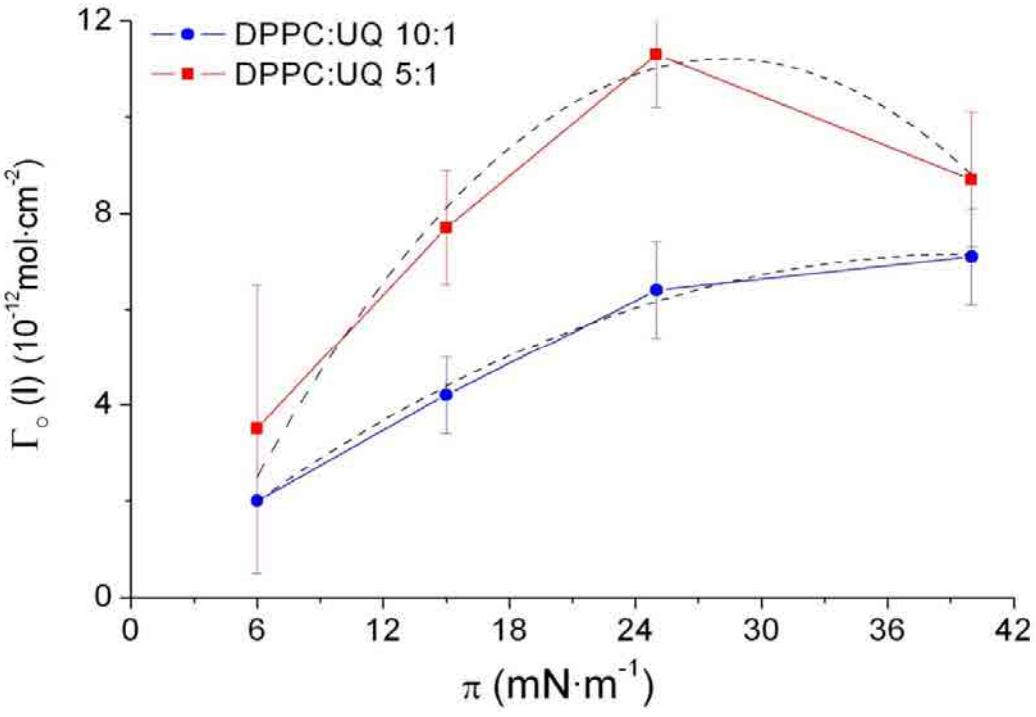

Figure 5.7.14. Surface coverage of the UQH_2 fraction oxidized via process I, Γ_O (I), vs. surface pressure, π, for ITO-DPPC:UQ/electrolyte 5:1 and 10:1 mixtures.

5.7.5 Global sight of the DPPC:UQ system transferred on ITO using the LB technique

In this section we explain the global behaviour of the DPPC:UQ system and the position of the UQ molecules in the monolayer summarizing the results obtained from the used techniques.

The different shape of the C_s^{-1} curves and the lower C_s^{-1} values observed for the DPPC:UQ mixtures compared to the pure DPPC indicate the presence of UQ molecules in the matrix of the DPPC:UQ mixtures ("diving" position, see Section 3.4.2), and it leads to less compact physical states. The shape of the π-A isotherms, the shape of the C_s^{-1} curves and the shape of the second kink point in the C_s^{-1} curves suggest that the system experiences a gradual UQ expulsion from the first kink point to the second where a sudden UQ expulsion takes place. Then, it is followed by a gradual expelling of the remaining UQ molecules until the third kink point. The expulsion of the UQ from the lipid heads region leads mainly to the "swimming" position, being this position and the formation of aggregates favoured at large initial content of UQ and at ordered states, as it was previously observed [3,25,27,36]. So that, the expulsion of UQ is the way chosen by the DPPC:UQ mixture to minimize its energy at the interface [49] and to minimize the low favourable interactions between UQ and the DPPC chains. The proportion of UQ at each position (diving [4,15, 36,88-95], or swimming [4,84,85,88,91-94,96-103,107] is defined by the DPPC physical state and the initial UQ content.

A complete vision of the UQ positions in the DPPC:UQ monolayer can be obtained considering the thermodynamic description of the physical states, the AFM results of the DPPC:UQ 5:1 system on mica (Figure 5.7.7) and the CVs of Figures 5.7.9-5.7.11. Therefore, these UQ positions will be extrapolated to all the ITO-DPPC:UQ systems. The DPPC and the DPPC:UQ mixtures with low UQ content, both at low surface pressure, present similar covered area by the LC state (Figure 5.7.8) whereas the DPPC:UQ 5:1 ratio presents a markedly lower covered area by this LC state. In addition, the height measured for the LC state of pure DPPC is higher than that of the DPPC:UQ mixtures. These observations indicate that UQ is present in both physical states (LE and LC) in the

DPPC:UQ mixtures. At π = 6 mN·m^{-1}, the CVs of Figures 5.7.9 and 5.7.10 show that only the redox process I is obtained and it presents a similar formal potential (E_f (I) = -0.04 ± 0.02 V) to that of process I for the ITO-UQ/electrolyte system (inset of Figure 5.7.11), which indicates that the local environment around each UQ is uniform in both situations [22]. So that, at low surface pressures, regardless the DPPC:UQ domains are in LE or LC state, we correlate the "diving" position with the UQ placed in the DPPC matrix and located in direct contact with the electrode surface (Figure 5.7.7A). The monolayer of DPPC:UQ 5:1 at π = 6 mN·m^{-1} is especially interesting due to the low surface pressure, the large zones in LE and the high UQ content compared with the other ratios used lead the LE to be non-uniform leaving some pinholes that arrive to the mica surface (Figure 5.7.7A inset).

The compression of the explained monolayer induces two actions: First the compactness of the LC state, so favouring the rejection of part of the UQ in "diving" position. On the one hand, it can be vertically rejected to the diving position without contact to the substrate and, on the other hand, horizontally to the remaining LE zones. Second, the phase change from LE to LC of the remaining LE zones (Figure 5.7.7B). The CVs of Figures 5.7.9 and 5.7.10 show that at π = 25 mN·m^{-1} the DPPC:UQ system present mainly the redox process I' with a more positive formal potential (E_f (I') = 0.00 ± 0.01 V) than that of process I, indicating that the environment has more available H^+ for UQ molecules. Therefore, we correlate process I$^{'}$ with the UQ molecules located still in diving position but without contact to the ITO surface. Further compression results in a more compact LC state with absence of LE state and the formation of rounded shaped protrusions (Figure 5.7.7C), which we relate with the presence of UQ molecules in "swimming" position forming pools on top of the monolayer. We correlate this "swimming" position with the process II observed in the CVs of Figure 5.7.9, only for the ITO-DPPC:UQ/electrolyte 5:1 system. The process II for ITO-DPPC:UQ/electrolyte 10:1 is not observed, even at high scan rate. This observation indicates that at low initial UQ content, the "swimming" position is not favoured due to the fast ordering of the LE to LC state favours the diving position without ITO-UQ contact. According to the literature and considering the monolayer|air interface, the "swimming" position is more stable than the "diving" position due to the later disrupts the cooperative motions between the DPPC chains [102]. Moreover, above the DPPC chains, the medium is air whose hydrophobicity [104] added to the hydrophobicity of the end part of the DPPC

chains stabilize the UQ [6] avoiding the distortion of being inserted between the DPPC chains. However, the "diving" position can be stabilized thanks to part of the UQ molecules can self-aggregate, in accordance with Roche et al. [6], forming head to head aggregates to withstand the hydrophobic environment of the lipid chain region. It is important to consider that our experiments always presents a higher UQ content than the minimum observed in the literature for aggregation (0.5-2 mol%) [1,15,36].

The presence of enriched domains is predictable based on the Van Dijck et al. [105] observations for saturated phospholipids with the same headgroup and others studies presented in the literature [27,35,36,41,93,95,98,106,107]. However, the results obtained for the DPPC:UQ system indicates that the formation of enriched domains are unfavoured in our experimental conditions. Moreover, the formation of grooves in the AFM images may indicate that the composition of the present phases is similar. On the other hand, the non-presence of LE zones at high surface pressures and the saturation of the Γ_O (I) when the surface pressure increases (Figure 5.7.14) indicate that the diving position with ITO-UQ contact in the LC state is saturated. Therefore, it can be concluded for the system DPPC:UQ that the increased compression favours the vertical rejection of "diving" quinones in contact with the substrate, first to the "diving" position without contact and finally to the "swimming" position.

Our results confirm that UQ is confined and the electron transfer takes place mainly by two mechanisms, first, by direct transfer and electron hopping between the UQ placed in "diving" position with ITO (process I and I'), and second, by electron hopping through the lipid matrix (process II). The electron hopping favours the rate determining step (1_b) so favouring the electroreduction in the timescale used. At low surface pressure the molecules are far enough each other to do not be affected by the electron hopping mechanism. Increasing the surface pressure the UQ headgroups are placed closer favouring the electron hopping redox process.

In order to clarify the position and organization of the DPPC and UQ molecules at each physical state the Figure 5.7.15 represents the position of DPPC and UQ molecules of the DPPC:UQ 5:1 system at the surface pressures studied. This Figure 5.7.15 explains the

different meaning of the fair and dark colours observed in the AFM images summarized in Table 5.7.3 and the UQ positions that origin the redox processes I, I' and II.

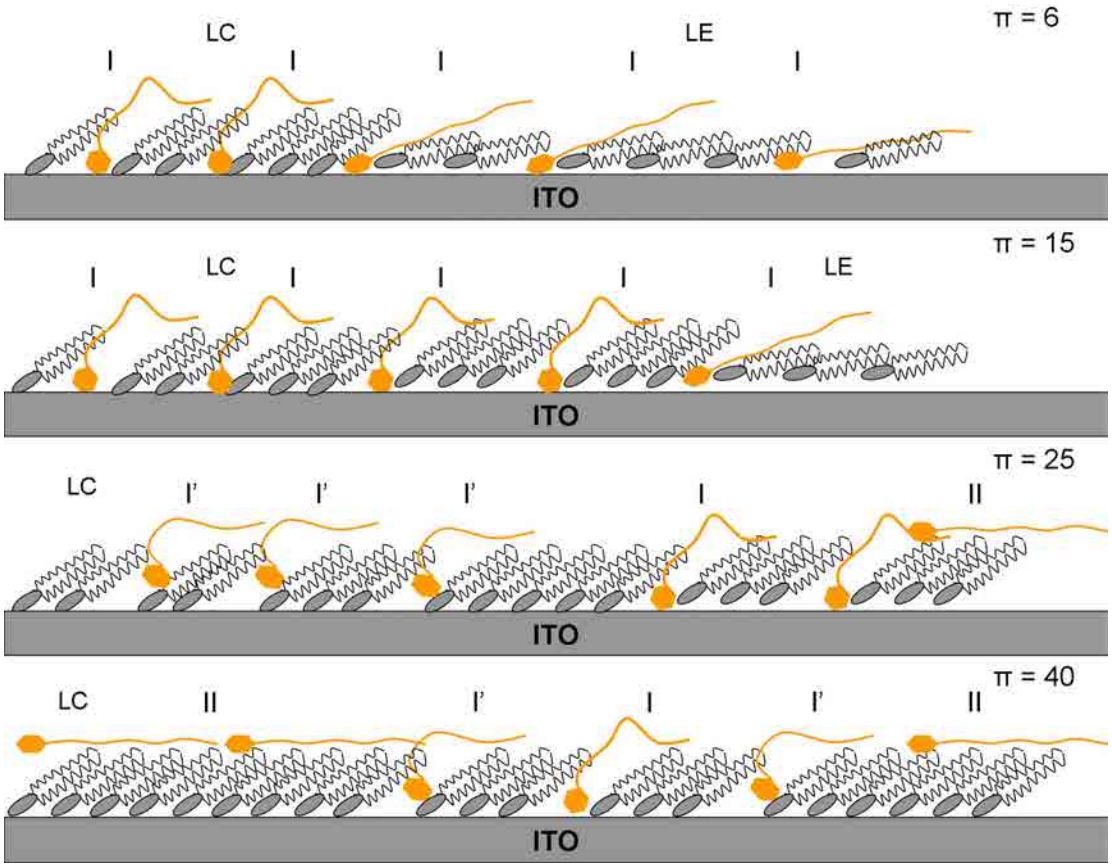

Figure 5.7.15. Scheme of the position of DPPC and UQ molecules of the DPPC:UQ 5:1 system at several surface pressures. The labels I, I' and II indicate the UQ positions that origin the redox processes I, I' and II.

5.7.6 ITO-DPPC:UQ biomimetic system studied using the SPB technique

In this section, we will present the ITO-DPPC:UQ system prepared using the SPB technique. The differences between the LB and SPB techniques in preparation method and how it affects to the resulting pure lipid layer has been explained in Section 2.1. It is important to study the differences between both preparation methods when, in addition to the lipid, a redox molecule (UQ) is present. So that, we characterize the topography and mechanical properties of DPPC and DPPC:UQ SPB samples using AFM and Force curves, so as to correlate the different behavior of SPBs on ITO referred to bare ITO. The SPBs are also characterized using cyclic voltammetry in order to obtain the electrochemical response of the inserted UQ.

5.7.6.1 Topography and mechanical properties

Topography

Figure 5.7.16 corresponds to an AFM image of bare ITO. This image shows large flat areas with rounded structures corresponding to nanometric inhomogeneities for the ITO film. The mean roughness of this ITO is 12 ± 6 Å, being this value slightly lower than the values of 14-20 Å observed by previous authors [63,108]. This low surface roughness permits the formation and observation of larger SPB islands.

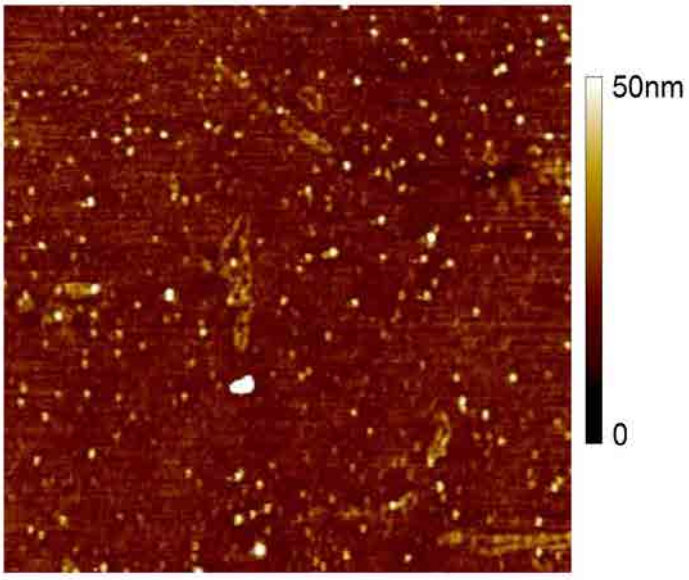

Figure 5.7.16. Topographic AFM image (5 μm x 5μm) of bare ITO.

Figure 5.7.17 depicts the AFM images of SPBs of DPPC and DPPC:UQ 5:1 mixture respectively. AFM images of DPPC:UQ 10:1 and 20:1 mixtures show similar appearance

than those of DPPC:UQ 5:1. These images confirm that the SPB is formed on ITO. The images presented in Figure 5.7.17 show two main zones corresponding to two different materials, confirmed both topographically and by the respective contrast phase images (not shown). Dark zones correspond to naked ITO surface, which is taken as zero level for further studies, and fair zones correspond to SPB islands.

SPBs shown in this work represent a surface coating from 50% to 70%, being lower than the 89% achieved on mica [109], which is an atomically flat substrate with subnanometric roughness. Patches of multilayers corresponding to the spreading of non unilamellar vesicles are rarely seen.

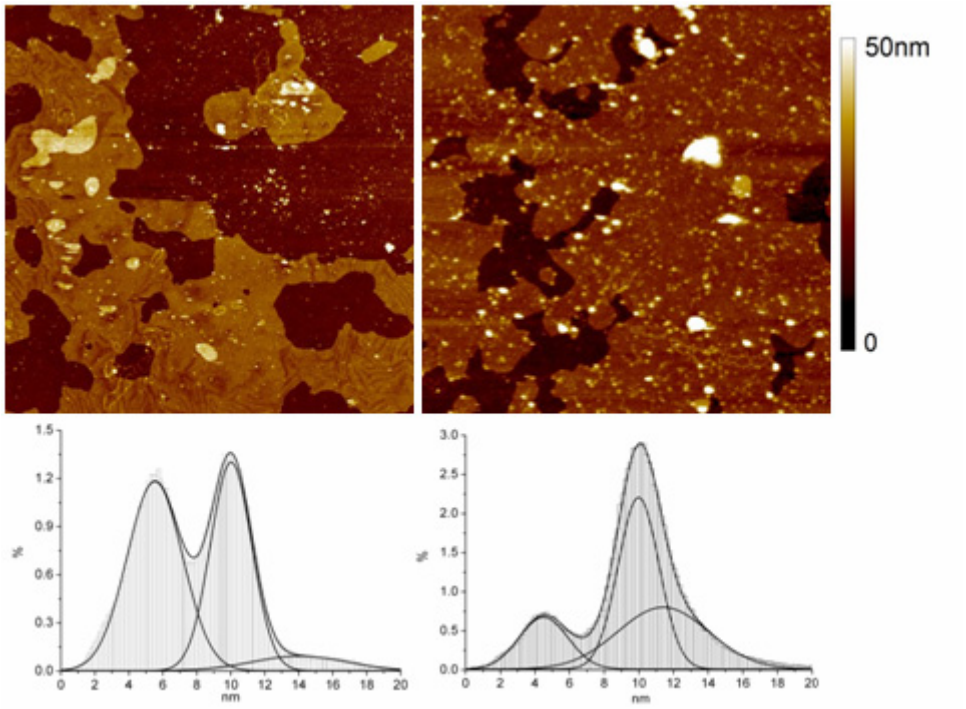

Figure 5.7.17. Topographic AFM images (5 μm x 5μm) of SPB of DPPC (left) and DPPC:UQ 5:1 (right), and height distributions. The SPB height respect to ITO surface was calculated from the distance between distribution peaks. Images were acquired in liquid tapping mode.

The topographic images permit to quantify the average height of the SPBs, by comparing height histograms of the pixels corresponding to the top of the SPBs and ITO regions. Then, the height difference between the two peaks of the histogram was calculated and presented as reported SPBs height values. This height is measured to be 46 ± 3 Å for all the studied compositions except for DPPC:UQ 5:1, which present a height of 57 ± 3 Å, indicating an expansion of the bilayer. A more accurate analysis of the heights distribution (see Figure 5.7.17) shows a deconvolution in two peaks for the DPPC:UQ 5:1, centered at

55 ± 3 Å and 69 ± 3 Å, the later with lower frequencies. It can be inferred that the pure DPPC bilayer spread on ITO has a similar thickness as the pure DPPC SPBs spread on mica, 47 ± 2 Å [110] or 48 ± 3 Å [111], but slightly lower than the values of 57 ± 3 Å [112], of 55 Å [113] and of 55 ± 1 Å [114] obtained by other authors, whereas molecular dynamic simulations [115] provide a value of 42 Å for the DPPC bilayer, in more accordance with our value. The higher reported values can be attributed to the presence of a thin layer of water between the ITO surface and the bilayer [112,116-118]. The second peak in the DPPC height distribution of Figure 5.7.17, which presents low frequencies, corresponds to a double SPB, in concordance with the patches observed in the topographic image. Nussio et al. [110] also studied the pure DPPC SPB's height on several hydrophilic substrates with different roughness. The results obtained by Nussio et al. are in agreement with our experimental observations, indicating that the substrate roughness has no significant influence in the bilayer height. Another observation is that the insertion of UQ in the DPPC SPB has no influence on the average height for low UQ concentrations, indicating that these molecules mainly embed and distribute uniformly between the DPPC matrix in "diving" and swimming" position. At higher UQ concentrations (5:1), these molecules cannot be correctly distributed so they may form pools or aggregates of UQ [36] in "swimming" position that locally expand the bilayer thickness. This fact is commented in the next section in correspondence with the Force curves results.

Force curves

Force spectroscopy characterization of samples was performed using force-extension curves, which provide information on the interaction forces between neighboring molecules and on the mechanical properties of the SPB. Force extension curves were performed on the central regions of SPBs to avoid rim effects.

The threshold force (*Fy*) is the force at which the SPB locally collapses due to the vertical force exerted by the AFM tip. In fact, it can be regarded as a fingerprint of a given sample, as it was demonstrated in a previous work [110]. Conceptually, *Fy* marks the transition between the elastic regime and the plastic deformation or fragile rupture. Because of that, *Fy* gives an accurate idea of the intermolecular interaction forces that arise inside the SPB and also of the possible electrostatic interactions that bind SPBs to substrates. In our case, experimental *Fy* values are used to assess molecular rearrangements when preparing DPPC SPBs with different UQ ratios at a selected temperature and buffer conditions.

Figure 5.7.18A shows the basic scheme of an AFM working on the Force Spectroscopy mode. In each force curve, the cantilever deflection, which is proportional to the vertical force exerted on the sample, is 0 before the tip-sample contact (Point 1, Figure 5.7.18B). Increasing the tip compression on the SPB, the vertical force increases until the layer breaks due to the pressure exerted on it. This breakthrough appears as a sudden jump in the force curve (Point 2). As vertical force keeps on increasing, the tip is in contact with the sample substrate. A more handy representation of the force curve (vertical piezo displacement vs. Vertical force) is the Penetration curve (FvP), that is, sample penetration depth vs. vertical force.

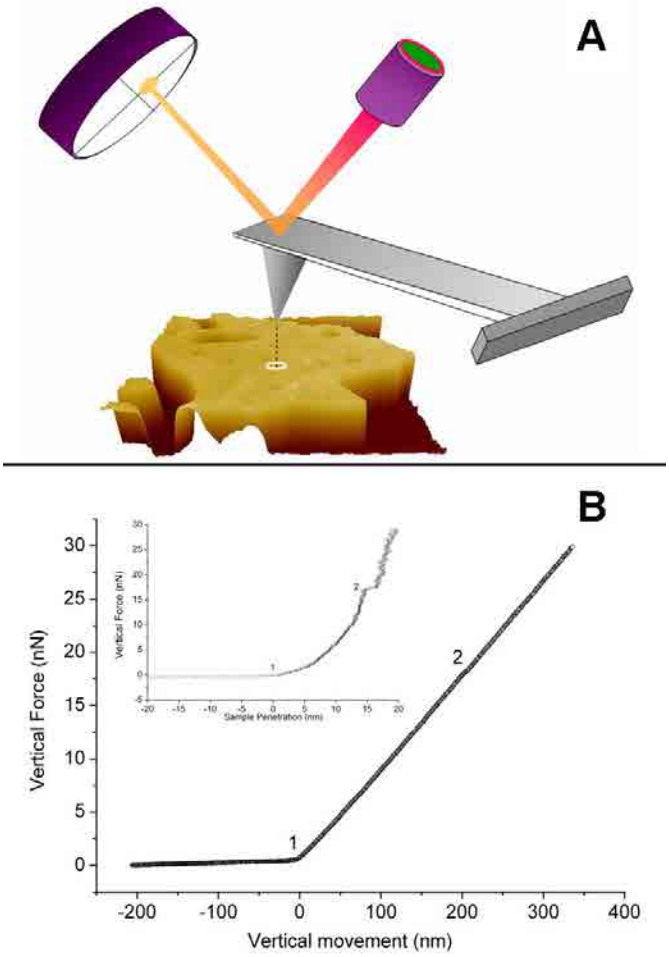

Figure 5.7.18. A) AFM tip-sample scheme when executing a force curve. B) Characteristic force curve for a DPPC:UQ 5:1 mixture. B Inset) FvP of a characteristic force curve for a DPPC:UQ 5:1 mixture.

Inset of Figure 5.7.18B shows this kind of representation, where two characteristic regions can be easily recognized; from point 1 to 2 the curve shows the elastic compression of the sample. At higher forces (after the breakthrough event), the plastic compression of the substrate is represented. Interestingly, the elastic region of the FvP comprises two different interactions. First of all, electrostatic forces between tip and sample, which arise when the electrical double layer induced by the zwitterionic headgroups of DPPC meet the slightly negative charge of the AFM tip. This force was measured to be extremely small for similar AFM probes in these conditions of ionic strength and pH so its effects will be neglected in the analysis of the data. And secondly, the mechanical deformation of the sample, which will be considered to account for the totality of the measured interaction.

Figure 5.7.19 shows histograms corresponding to *Fy* values obtained from individual FvP curves for different composition of SPBs. The obtained results are 32.8 ± 7.1 nN for pure DPPC, 24.0 ± 6.6 nN for DPPC:UQ 20:1 and 20.8 ± 5.7 nN for DPPC:UQ 10:1. DPPC:UQ 5:1 presents a bimodal distribution being the first mode centered at 15.2 ± 6.0 nN and the second at 38.7 ± 5.7 nN. It can be clearly seen that *Fy* value decreases when the UQ content in the SPB increases. This fact can be explained by the increase of the area per molecule caused by the insertion of UQ in the DPPC matrix, which causes a weakening of lateral alkyl-alkyl interactions producing a decrease in the compactness of the layer. On previous works, *Fy* values measured on a DPPC SPB on mica and on similar buffer conditions presented a mean value of 28.6 nN [110], 25 nN [119] or 21.4 nN [120], being lower than the value of 32.8 nN determined by us on ITO. ITO and mica are hydrophilic substrates with similar isoelectric point, so these small differences can be explained by the different chemical composition of the surface and by the different cations present in the buffer as seen by Redondo-Morata et al. [120] who observed a 7 nN increase of the *Fy* value for DPPC SPBs on mica when Na^+ was exchanged by K^+ in the buffer.

The existence of a bimodal distribution for the DPPC:UQ 5:1 system is explained by the formation of UQ pools or aggregates in “swimming” position when the UQ concentration is high. These pools provoke bilayer local expansions, as it has been explained in the previous section, where two heights are observed in the AFM images. The indentation in these expanded zones, with higher height, is more difficult than in the standard zones, so a higher

Fy is required. Thus, the presence of standard (15.2 ± 6.0 nN) and expanded zones (38.7 ± 5.7 nN) lead to each mode of the histogram.

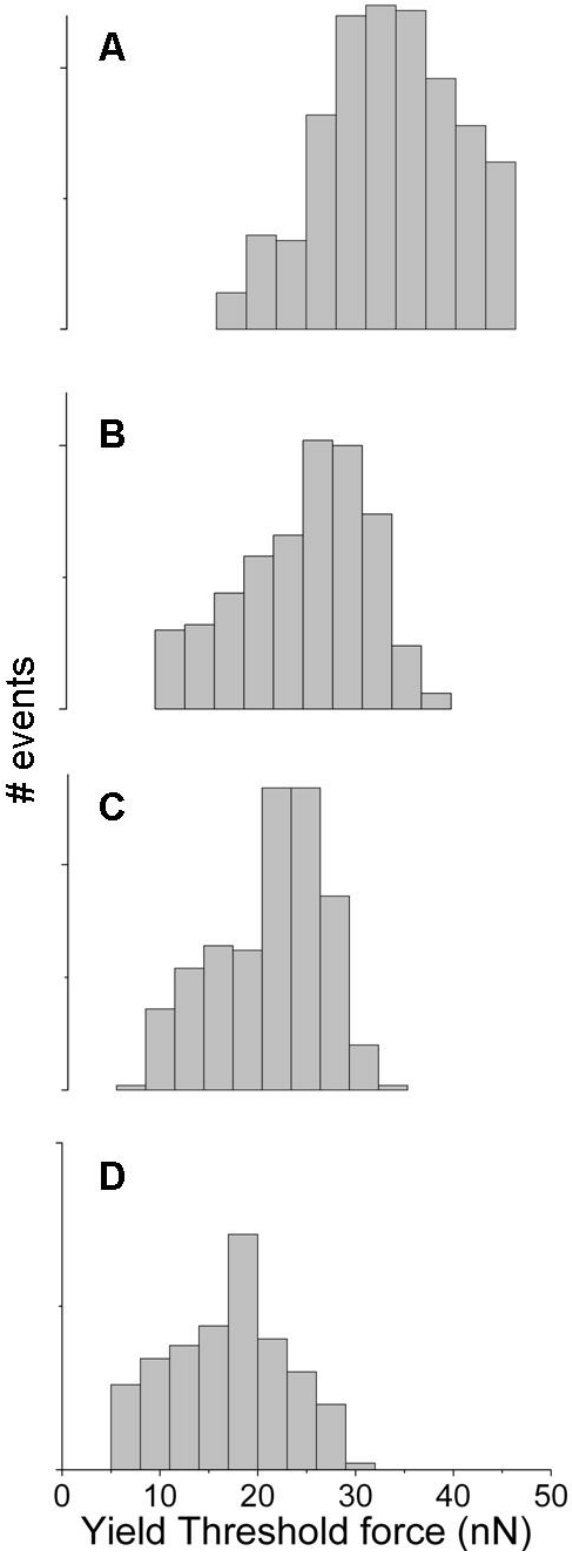

Figure 5.7.19. Yield threshold histograms obtained from force-curves on SPBs of DPPC (A), DPPC:UQ 20:1 (B), DPPC:UQ 10:1 (C), DPPC:UQ 5:1 (D).

5.7.6.2 Electrochemical characterization

The electrochemical behavior of bare ITO electrode, ITO-DPPC SPB and ITO-DPPC:UQ SPB has been studied by cyclic voltammetry in the electrolyte solution at pH 7.4. Bare ITO electrode (See Section 5.1.3) presents no redox response in the potential window placed between 1 to -0.7 V and presents an interfacial capacitance (C_d) around 1 $\mu F \cdot cm^{-2}$. The ITO-DPPC bilayer presents C_d values between 2 and 4 $\mu F \cdot cm^{-2}$ for the potential window compressed between 1 to -0.2 V indicating that the ITO-DPPC bilayer system is more accessible to the electrolyte ions than the bare ITO electrode surface, and that the lipid bilayer presents few defects [37,121,122]. At more cathodic potentials than -0.2 V a continuous increasing of the current values is obtained for the ITO-DPPC bilayer indicating that the hydrogen evolution becomes important. The capacitance values are in accordance with that obtained for an ITO/DPPC monolayer extracted by the Langmuir-Blodgett technique (See Section 5.3.3) although in this case hydrogen evolution starts at -0.4 V at a surface pressure of 40 $mN \cdot m^{-1}$. The fact that the hydrogen evolution starts at more cathodic potentials in the case of the vesicle fusion SPB system can be attributed to a lower order and lower uniformity in the bilayer obtained by this technique [123]. Studies of the effect of electrical potential on supported lipid bilayers [10,63,121-123] show that imposing a progressively more negative potential at the electrode surface, the bilayer becomes less ordered, apparently swells and finally is detached from the electrode surface. In this reversible process, the bilayer remains near the surface only separated by a layer of electrolyte.

Figure 5.7.20 shows the cyclic voltammetric response of the ITO-DPPC:UQ system using the buffered electrolyte solution, scanning towards negative potentials. The DPPC:UQ 5:1 system presents two peaks for oxidation that we label oxidation peaks as I_O and II_O and one main peak for reduction. The DPPC:UQ 10:1 system presents a similar behavior but having a peak intensity quite shorter than 5:1. On the other hand, DPPC:UQ 20:1 presents a wave without appreciable intensity peaks, having a cyclic voltammetric response close to the pure DPPC. In this last case, the electrochemical response is similar to that obtained for adsorbed vesicles of liposomes containing UQ [124]. Figure 5.7.20 inset presents the cyclic voltammetric response of the DPPC:UQ 10:1 system on ITO in a shorter potential window than Figure 5.7.20. Comparing both figures it can be seen an increase in the current intensity of peak II_O when scanning to more cathodic potentials. This observation confirms

that the reduction peak is a convolution of two processes, I and II, so we label it as $I_R + II_R$. The inset also confirms that process I is more reversible than process II.

The formal potential of process I and II referred to the Ag/AgCl can be calculated by taking the average of the reduction peak potential $I_R + II_R$ and the oxidation potentials of peaks I_O and II_O, being E_f(I) = -0.02 ± 0.03 V for the process I and E_f(II) = +0.08 ± 0.02 V for the process II. These values are very close to those observed for ITO-DPPC:UQ monolayers in Section 5.7.4. Further information of the ITO-DPPC:UQ electrochemical system can be obtained using cyclic voltammetry at different scan rates. Discarding the DPPC:UQ 20:1 system because no redox response was obtained, both 5:1 and 10:1 systems presents a good linear dependence between the scan rate and the peak current intensity (Figure 5.7.21). The linear dependence indicates that UQ molecules are surface confined [29] and the electrochemical processes are not diffusion controlled.

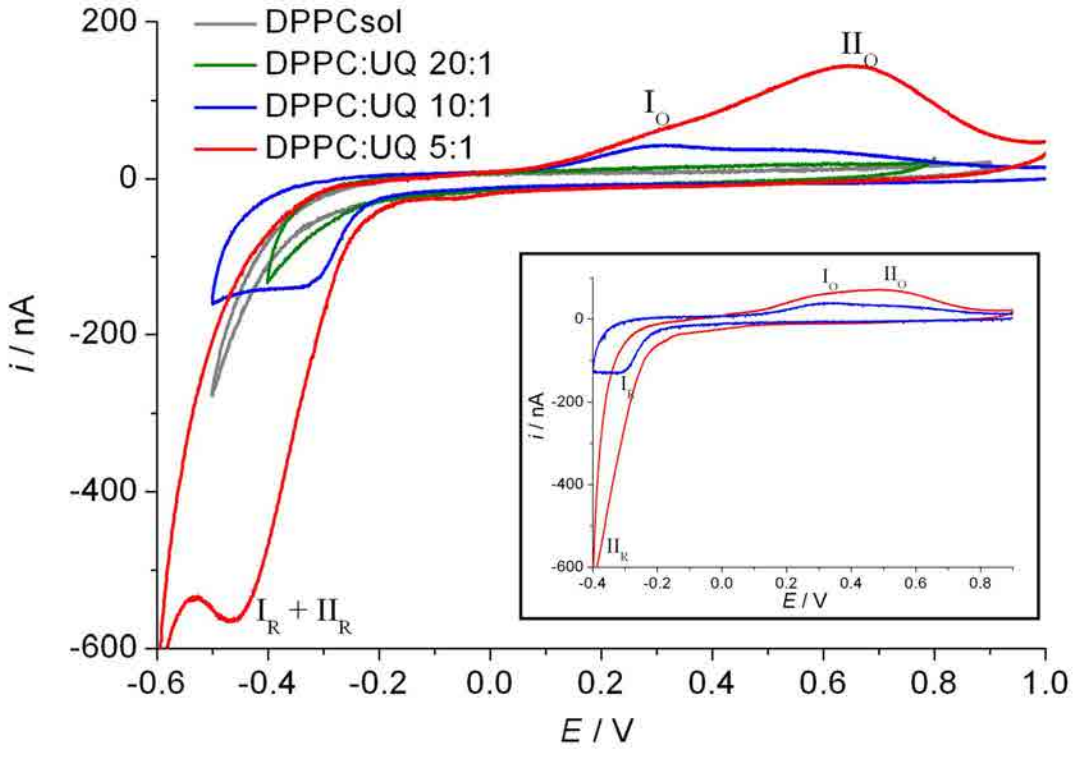

Figure 5.7.20. CVs of SPBs of DPPC and DPPC:UQ mixtures using the buffered solution at 23 ± 1ºC. Inset: CVs for the same systems but in a shorter potential window.

The global reaction and the mechanism proposed for pure UQ in confined situation (Section 5.1.3) is the same for the UQ of the DPPC:UQ system. Moreover, the main difference

between process I and II is the position of UQ in the bilayer [9] not the mechanism. On the other hand, the E_f values obtained in this section for the ITO-DPPC:UQ bilayer system and those obtained for ITO-DPPC:UQ monolayer system (Section 5.7.4) are closer to the benzoquinone/hydroquinone system in aqueous solution than in an aprotic solvent, fact that indicates that UQ molecules have H^+ ions available. This observation is also corroborated by Figure 5.7.21 where not diffusion dependence is obtained for the electrochemical process.

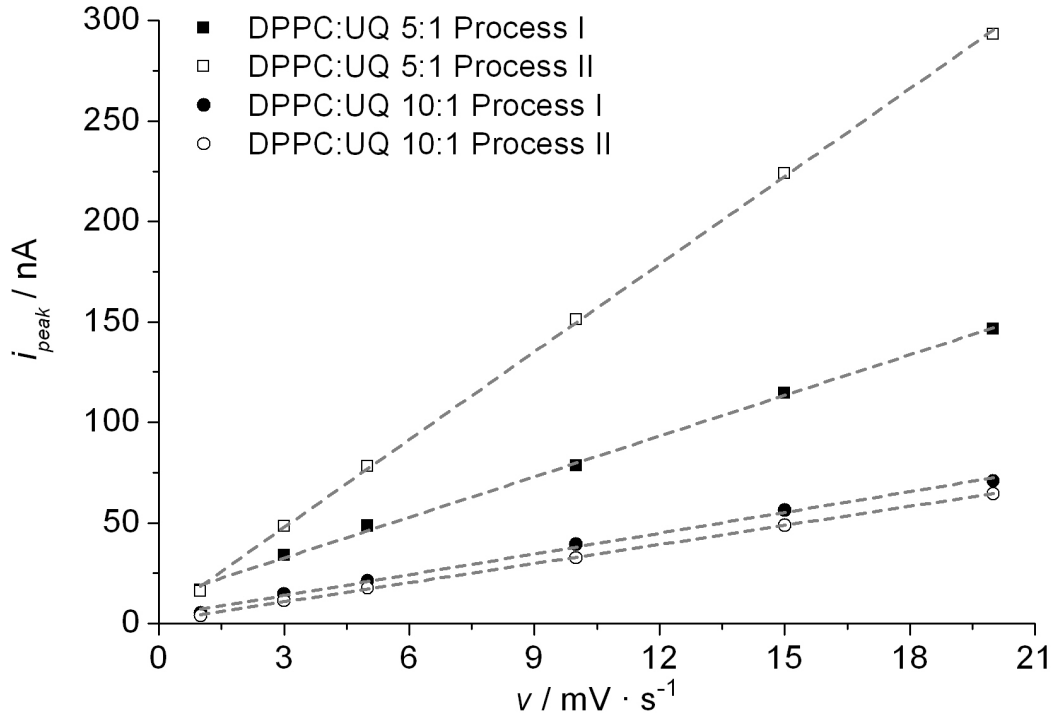

Figure 5.7.21. Oxidation peak intensity dependence vs. scan rate for SPB's of DPPC:UQ 5:1 and 10:1.

From these results and the studies of the electrical properties of SPB [123,125], the ITO-DPPC:UQ system can be described as a two component fluid supported membrane where the DPPC molecules act as electroinactive solvent and forms a stable bilayer. The transport of ions through this bilayer was attributed to the ion diffusion in the hydrocarbon region after entrapment, so following the Nagle and Scott´s ion permeability theory. The diffusive movement is not the permeation-limiting process, but the ion entrapment is. This entrapment is produced by lateral density fluctuations that open short-lived cavities in the headgroup region of the bilayers into which ions can enter [126].

Process I corresponds to the UQ/UQH_2 redox process for UQ molecules in "diving position", being mainly inserted in the bottom leaflet of the lipid bilayer. Process II

correlates with the redox response for the UQ molecules in “swimming” position well in the midplain of the SPB or in the upper leaflet of the lipid bilayer. On the other hand, as it can be seen in Figure 5.7.20, when increasing the UQ content, the process II become more important, being the “swimming” position favoured at high UQ content [36]. These UQ clusters produce local expansions in the lipid bilayer as it has been explained in previous sections. Scanning towards negative potentials, the proton permeability of the SPB starts at more positive potentials than in the LB monolayers (Section 5.7.4). In the reduction process, this higher permeability produces the competition between the hydrogen evolution process and the UQ reduction at less negative potentials. The consequence of this earlier competition is the impossibility to deconvolute the reduction process in its three components: Hydrogen evolution, I_R and II_R.

The charge involved in the oxidation peak of DPPC:UQ 5:1 system is 4.5 μC being more than two times larger than the involved in DPPC:UQ 10:1 (1.8 μC). This result is in concordance with that obtained for a DPPC:UQ monolayer (See Section 5.7.4) and it implies that the electroactive fraction increases with the UQ content in the bilayer. This behavior could be attributed to an electron hopping mechanism between UQ molecules in the electron transfer process that is favoured at high densities of UQ in the bilayer [127]. From the oxidation charge, the surface coverage of UQ in the bilayer can be calculated, obtaining the values of $70 \cdot 10^{-12}$ mol·cm^{-2} and $27 \cdot 10^{-12}$ mol·cm^{-2} for DPPC:UQ 5:1 and DPPC:UQ 10:1, respectively. The surface coverage for the DPPC:UQ 5:1 system, $70 \cdot 10^{-12}$ mol·cm^{-2}, is higher than the expected value, $21 \cdot 10^{-12}$ mol·cm^{-2}, calculated according to the mean area per molecule occupied by UQ, obtained at Section 5.1.1, at the equivalent surface pressure of 33 mN·m^{-1} for biological membranes [128]. This can be explained by a higher insertion of UQ than it was expected and the formation of UQ pools at the highest UQ concentration that enhances the electron hopping effect. On the other hand, this value is comparable with the value of $55.8 \cdot 10^{-12}$ mol·cm^{-2} obtained at high surface pressure for a DPPC:UQ 5:1 monolayer (Section 5.7.4). Lowering the UQ concentration, the surface coverage obtained for DPPC:UQ 10:1 system, $27 \cdot 10^{-12}$ mol·cm^{-2}, is closer to the expected value of $21 \cdot 10^{-12}$ mol·cm^{-2}.

5.7.6.3 Global sight of the DPPC:UQ system deposited by SPB.

DPPC:UQ SPBs were deposited (Figure 5.7.22) on ITO, a transparent and conducting material. The AFM images show no topographically significant visual differences according to the DPPC:UQ ratio, although the SPB height increases for the DPPC:UQ 5:1 system, fact that can be explained by the formation of UQ pools or aggregates in the bilayer. On the other hand, force curves performed on top of the SPBs reveal a decrease of breakthrough force values when increasing the UQ content in the mixture, being this behavior due to the weakening of the phospholipid intermolecular forces when UQ is added. DPPC:UQ 5:1 shows a bimodal distribution explained by the two structures detected topographically. Firstly, zones of DPPC:UQ leaflets with UQ molecules uniformly distributed, and the second, DPPC:UQ leaflets with UQ pools or aggregations in "swimming" position.

The cyclic voltammetry shows two differentiated processes; the first one corresponds to the redox behaviour of the UQ molecules in "diving" position and process II corresponds to the UQ molecules in "swimming" position. Process II becomes more important when increasing the UQ content, which is in accordance with the UQ saturation in the DPPC matrix and its expulsion to the "swimming" position.

The results obtained show that the employed technique is suitable for SPB formation on non-atomically flat hydrophilic substrates, as ITO, fact that opens prospect for artificial photosynthesis studies.

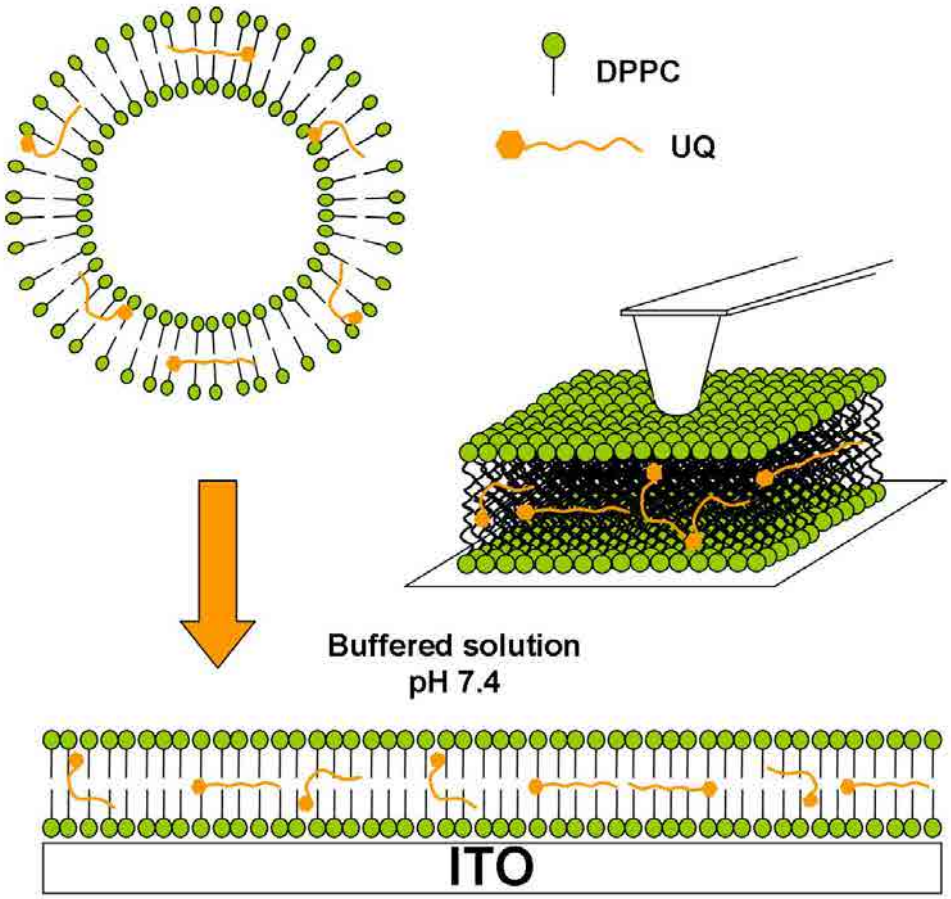

5.7.22. Scheme of the deposition of liposomes of DPPC:UQ on ITO showing the UQ molecules positions.

5.8 MGDG:UQ

5.8.1 π-A isotherms and physical states

The π-A isotherms of the MGDG:UQ system at biological relevant ratios are presented in Figure 5.8.1 referred to the weighted (mean) area per molecule according to the MGDG:UQ ratio. The C_s^{-1} curves (Figure 5.8.2) corresponding to the described π-A isotherms (Figure 5.8.1) are calculated according to the Expression 2.9. The most significant values of Figure 5.8.1 and 5.8.2 are summarized in Table 5.8.1. The description and discussion of the π-A isotherms and the C_s^{-1} results for the MGDG and UQ pure components were explained in Section 5.4.1 and 5.1.1 respectively. So that, we present in this section only the results of the mixtures and their corresponding discussion.

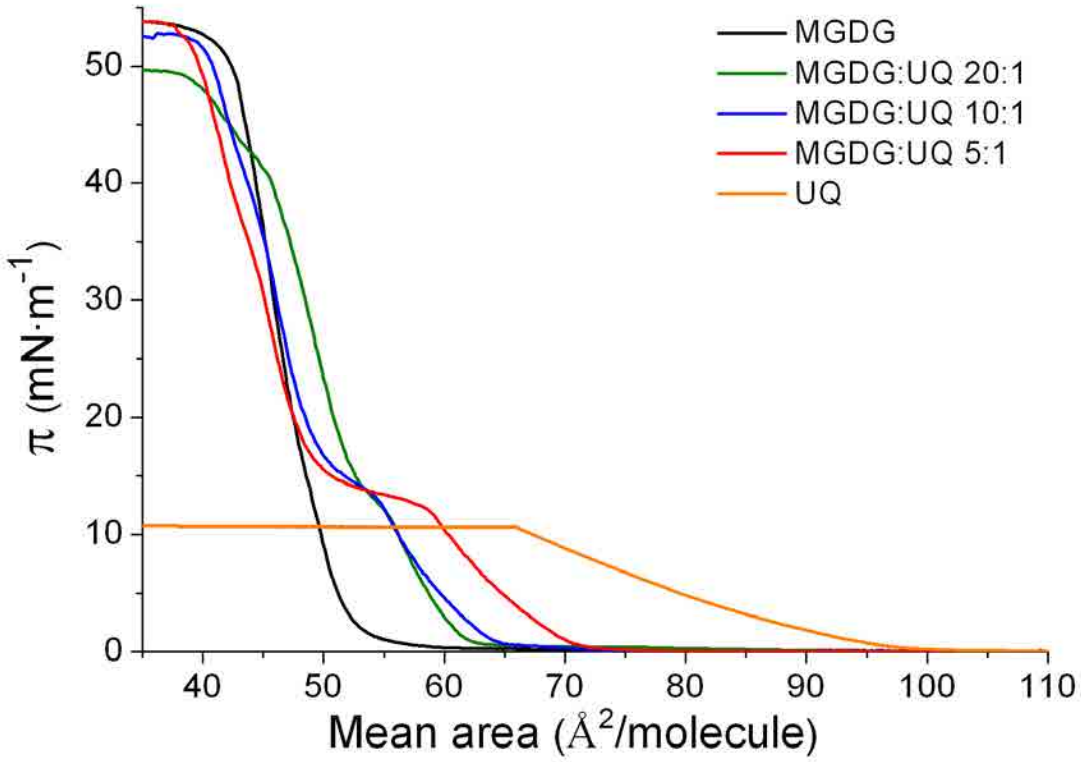

Figure 5.8.1 π-A isotherms for MGDG, UQ and MGDG:UQ mixtures at 21 ± 0.5 ºC on water subphase.

Figure 5.8.1 shows that the π-A isotherms of the MGDG:UQ mixtures present different behaviour according to the UQ presence in the mixture, showing an important influence of the incorporated UQ in comparison with the isotherm of pure MGDG. On the other hand, Figure 5.8.2 shows that each C_s^{-1} curve presents two kink points. In accordance to the first

kink point at ≈ 14 $mN \cdot m^{-1}$, corresponding to the first main UQ expulsion, the isotherms shown in Figure 5.8.1 can be divided in two zones establishing the border value at this kink point.

It can be observed in Figure 5.8.1 that below the surface pressure of the first kink point, the presence of high content of UQ (see MGDG:UQ 5:1 system) hindrances in a quite larger extent the packing of the monolayer than the low ratios (See MGDG:UQ 20:1 and 10:1 systems). The isotherms have a similar slope after the first main UQ expulsion, showing also a similar area per molecule till the next kink point at ≈ 40 $mN \cdot m^{-1}$ where the MGDG:UQ 20:1 presents a lower slope and collapse pressure than the other mixtures. On the other hand, the different slope of the mixtures isotherms compared with that of pure MGDG indicates that part of the UQ is still remaining in the MGDG matrix, although it seems to be with low content.

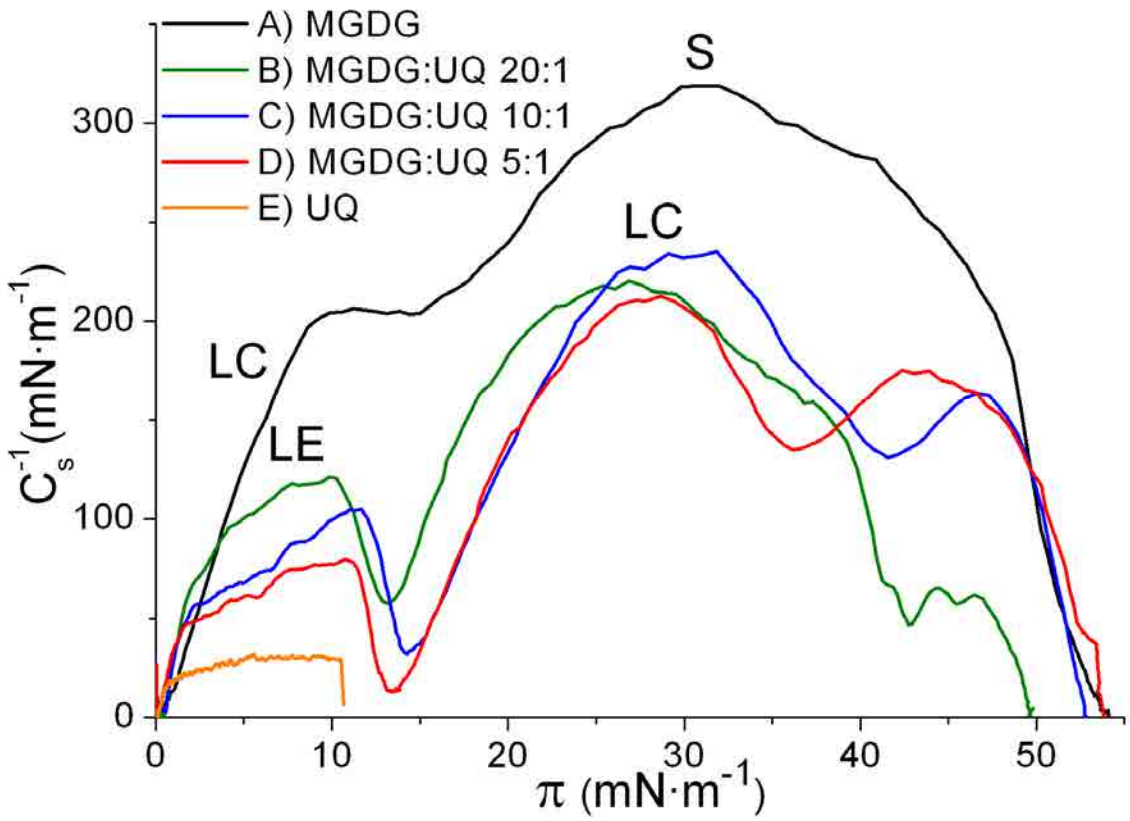

Figure 5.8.2. Inverse of the compressibility modulus vs. surface pressure for MGDG, UQ and MGDG:UQ mixtures on water subphase.

Table 5.8.1. Collapse pressure, lift-off area and phase change kink point position for the MGDG, UQ and their biological mixtures obtained from Figure 5.8.1 and 5.8.2. The presentation only of the first kink point is due to it is correlated with the phase change.

	Collapse pressure ($mN \cdot m^{-1}$)	Lift-off area ($Å^2 \cdot molec^{-1}$)	1st Kink point pressure ($mN \cdot m^{-1}$)	1st Kink point area ($Å^2 \cdot molec^{-1}$)
MGDG	53	59	-	-
MGDG:UQ 20:1	49	64	13.1	53.2
MGDG:UQ 10:1	52	65	14.3	53.1
MGDG:UQ 5:1	53	72	13.4	55.1
UQ	11	102	-	-

Both the lift-off area and the area at which appears the first kink point increase as the UQ content in the MGDG:UQ mixture is enlarged (Table 5.8.1), and it is correlated with the distorting effect of UQ in the MGDG matrix [80]. This phenomena was also observed by Bilewicz et al. [1] using UQ and $C_{18}SH/C_{18}OH$ and also by Kruk et al [38] using PQ and unsaturated MGDG. The presence of UQ in the initial zone hindrances the packing of the MGDG headgroups, and therefore, the hydrophobic interactions between the MGDG chains are also reduced, as it was seen in the case of UQ inserted in phospholipids Section 5.7.1. After the main rejection of the UQ molecules (first kink point), the compactness of the mixture monolayer is rapidly enhanced. The explanation for this phenomenon is that UQ is better retained in the lipid matrix when present at low concentrations due to it affects in a lower extent the formation and shape of the ordered phases.

All the MGDG:UQ mixtures C_s^{-1} curves present similar shape with slight differences according to the UQ content around the kink points. Accordingly to the values presented by Vitovic et al. [7] and the characteristics of this system, the first kink point indicates the phase change from LE to LC which implies the main UQ expulsion from the lipid matrix. The extent of this rejection (difference between the local maximum and local minimum at the LE-LC phase change) is accorded to the initial UQ content. The surface pressure at which this first kink point takes place is similar in all the mixtures discarding the experimental deviations. However, the second kink point (at ≈ 40 $mN \cdot m^{-1}$) may be related with an orientation change which implies also a second UQ expulsion. The surface pressure of this second kink point is close to the surface pressure of 35 $mN \cdot m^{-1}$ proposed by Quinn and Esfahani [4] for the DMPC:UQ mixtures at which UQ is completely separated from

DMPC. Probably, this surface pressure depends on the physico-chemical properties of the lipid and the prenylquinone.

Phase rule

The collapse pressure of a mixed monolayer of different components is related to the miscibility of its components, being dependent on the film composition in a miscible system [50,68]. In our MGDG and MGDG:UQ mixtures isotherms, the collapse pressure is ≈ 51 mN·m^{-1}. Therefore, the similar collapse pressure can be used to elucidate the expulsion of one of the components in a mixed film. In a two component monolayer, if components are completely immiscible, a lower collapse pressure of one of the components will be observed as it is predicted by the phase rule. Maintaining temperature and external pressure constant, the number of degrees of freedom F of the monolayer system is given by the Expression 2.14 [82,83] that is reproduced below:

$$F = C_B + C_S - P_B - P_S + 1$$

In our MGDG:UQ experiments, at the air|water interface, $C_B = 2$ (air and water), $C_S = 2$ (MGDG and UQ), and $P_B = 2$ (gas and liquid), thus $F = 3-P_S$. According to that, homogenous mixed films achieve the collapse equilibrium with $P_S = 2$ (condensed and collapsed state) so the system will have one degree of freedom. According to our results, the collapse pressure is practically fixed, discarding the experimental deviations, for pure MGDG and MGDG:UQ mixtures. This indicates zero degrees of freedom and therefore, following the previous reasoning, $P_S = 3$. So that, at the collapse equilibrium of the mixtures isotherms coexist MGDG (LC), MGDG (collapse) and expelled UQ. The same statements can also be applied to the phase change zone at $\pi \approx 14$ mN·m^{-1}, where the π is practically fixed indicating zero degrees of freedom. Thus $P_S = 3$ which indicate that three phases coexist: MGDG:UQ (LE), MGDG:UQ (LC) and expelled UQ, confirming the beginning of the UQ expulsion at this surface pressure. This observation coincides with the AFM conclusions (Section 5.8.4).

5.8.2 BAM

BAM images give information about the film structure at the air|water interface at microscopic scale. These images permit to distinguish the phases deduced from the π-A isotherms (See Section 5.8.1). Figure 5.8.3A presents the gas phase (foam structure) that appears for $\pi < 0.6$ mN·m^{-1}. The Figure 5.8.3B corresponds to the LE phase and the Figure 5.8.3C shows the LE to LC phase change being both phases present at $\pi \approx 14$ mN·m^{-1}. Above this surface pressure, the monolayer is practically homogeneous, and corresponds to the LC state (Figure 5.8.3D).

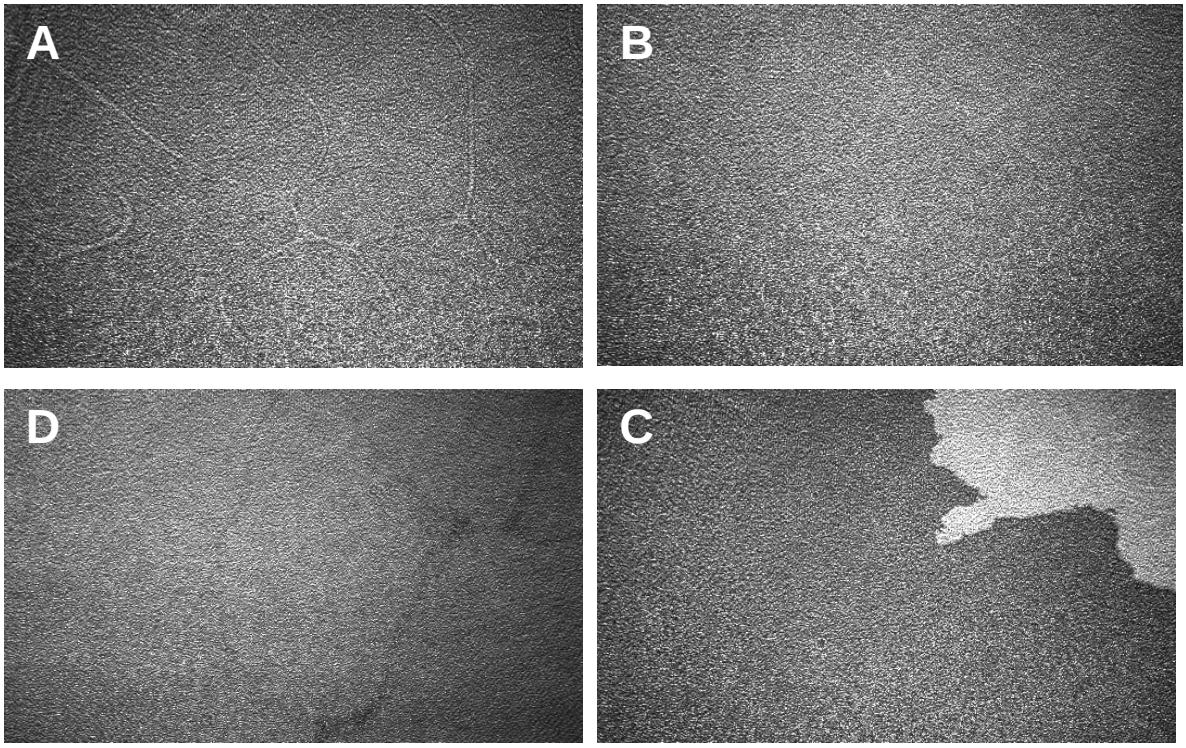

Figure 5.8.3. BAM images of a MGDG:UQ 10:1 mixture monolayer at 21 ºC and at selected phase states. A) $\pi = 0.25$ mN·m^{-1}, B) $\pi = 4.7$ mN·m^{-1}, C) $\pi = 13.9$ mN·m^{-1}, D) $\pi = 40.0$ mN·m^{-1}.

5.8.3 Thermodynamic study

The representation of the mean area per molecule vs. the molar fraction at selected surface pressures gives idea about the ideality of a mixture at these surface pressures. The reader is addressed to Section 2.1.1.5 where the mathematical treatment (Expressions 2.10 - 2.13) for the figures of this part is explained. The Figure 5.8.4 plots the area per molecule and the Figure 5.8.5 plots G^E both vs. the UQ molar fraction, represented for MGDG:UQ mixtures at several surface pressures before the main UQ expulsion (≈ 14 $mN \cdot m^{-1}$). At surface pressures above this event, the thermodynamic study has not been performed due to the UQ content in the MGDG:UQ matrix is unknown and significantly lower than the initial presence.

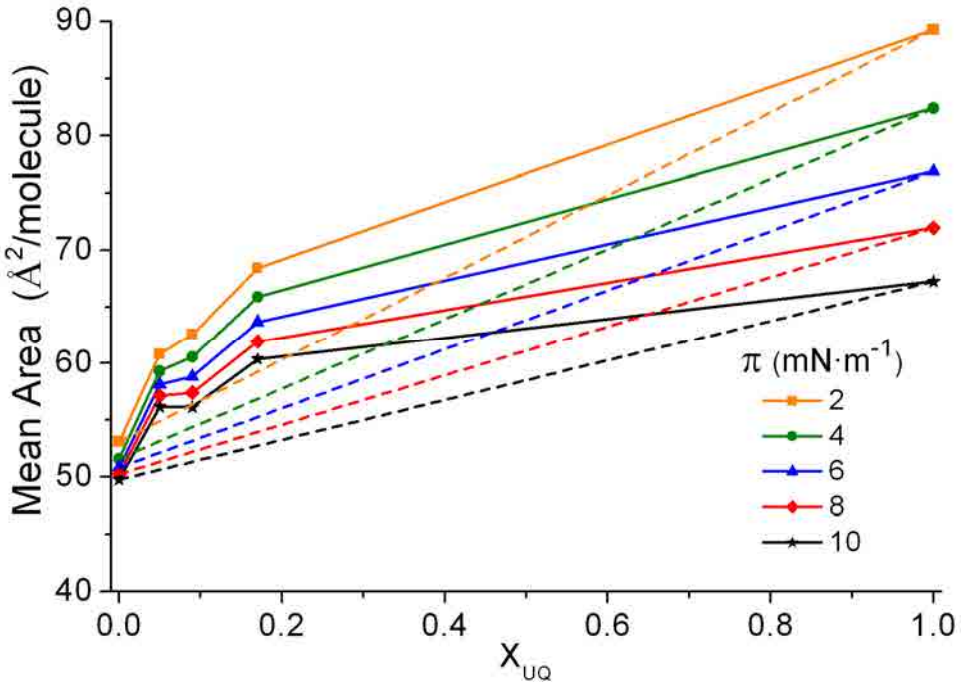

Figure 5.8.4. Plot of the mean area per molecule vs. the molar fraction for MGDG, UQ and MGDG:UQ mixtures at several surface pressures before the main UQ expulsion. Discontinuous straight line represents the ideal behaviour for each surface pressure.

Both figures (Figure 5.8.4 and 5.8.5) show that MGDG and UQ form non-ideal mixtures with positive deviation at $\pi \leq 10$ $mN \cdot m^{-1}$ which indicates that, at these surface pressures, the interactions between the two components are weaker than the interactions between pure components [6] suggesting the possible formation of enriched domains or aggregates of molecules [68,83] at high UQ content.

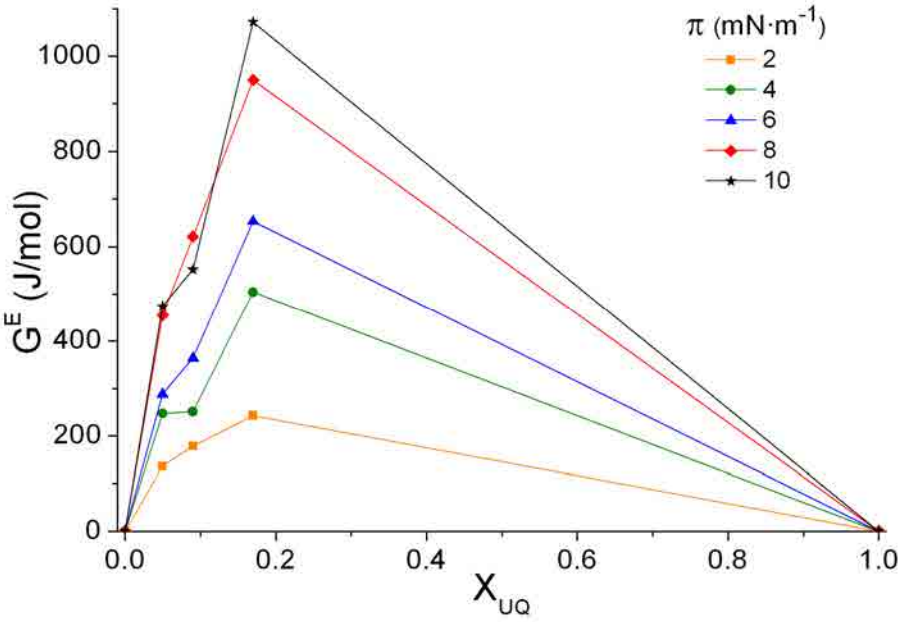

Figure 5.8.5. Plot of the excess energy vs. the molar fraction for MGDG, UQ and MGDG:UQ mixtures at several surface pressures before the main UQ expulsion.

The Figure 5.8.6 represents the ΔG_{mix} vs. UQ molar content at several surface pressures before the main UQ expulsion. The negative values observed for ΔG_{mix} at $\pi \leq 10$ mN·m^{-1} indicate that the mixed monolayers of MGDG:PQ are more stable than pure components [6], although the low ΔG_{mix} values corroborate the low stability of the mixture.

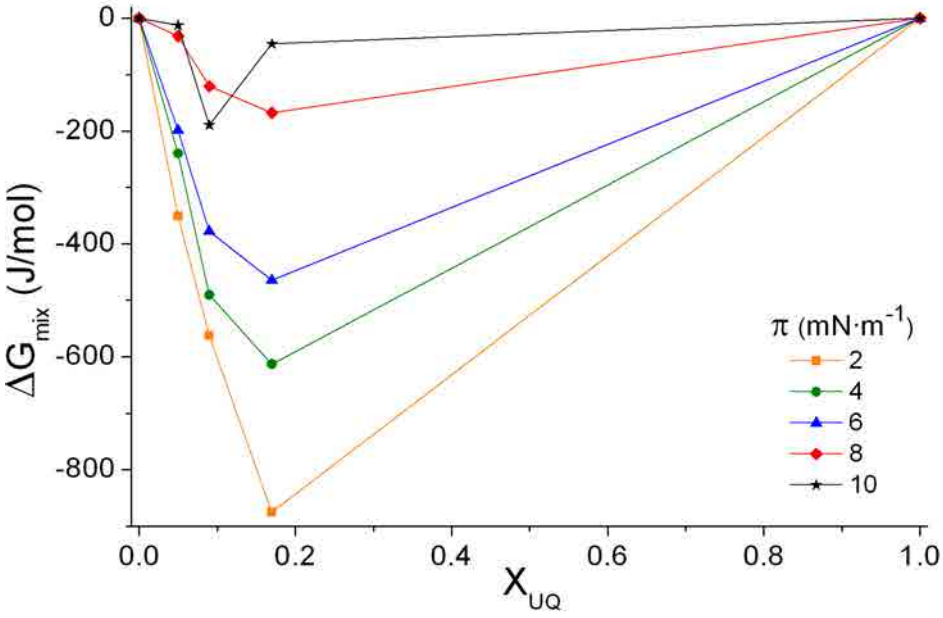

Figure 5.8.6. Plot of the mixing energy vs. the molar fraction for MGDG, UQ and MGDG:UQ mixtures at several surface pressures before the main UQ expulsion.

The formation of non-ideal mixtures between UQ and MGDG at low surface pressure, as it was observed in the DPPC:UQ system (Section 5.7.2), is explained by the difference in the chain length between UQ and MGDG which permits a free rotation of the UQ part that protrudes over the MGDG producing also a motion of the MGDG molecules which induces an increase of the molecular area [6,38].

5.8.4 AFM

In this part we present the topographic images of different MGDG:UQ mixtures at several surface pressures to light which is the organization of these molecules once transferred to a hydrophilic substrate (mica) and ultimately, correlate this knowledge with the predicted results in previous sections. The description and discussion of the AFM topographic images and their mathematical treatment for the pure components MGDG and UQ are explained in Section 5.4.2 and 5.1.2 respectively. So that, we present in this section only the results of the mixtures and their corresponding discussion.

Figure 5.8.7 shows the AFM topographic images corresponding to pure MGDG and the selected MGDG:UQ mixtures transferred on mica at π = 6 $mN \cdot m^{-1}$. This surface pressure permits us to ensure that most of the initial UQ is present in all the mixtures showing the larger differences for these systems. The images A-D show two different tonalities of brown (fair and dark) and both correspond to the MGDG or MGDG:UQ monolayer, being each tonality correlated with a different physical state of the system monolayer. Moreover, the images A-D show that the presence of UQ has a strong influence on the MGDG matrix.

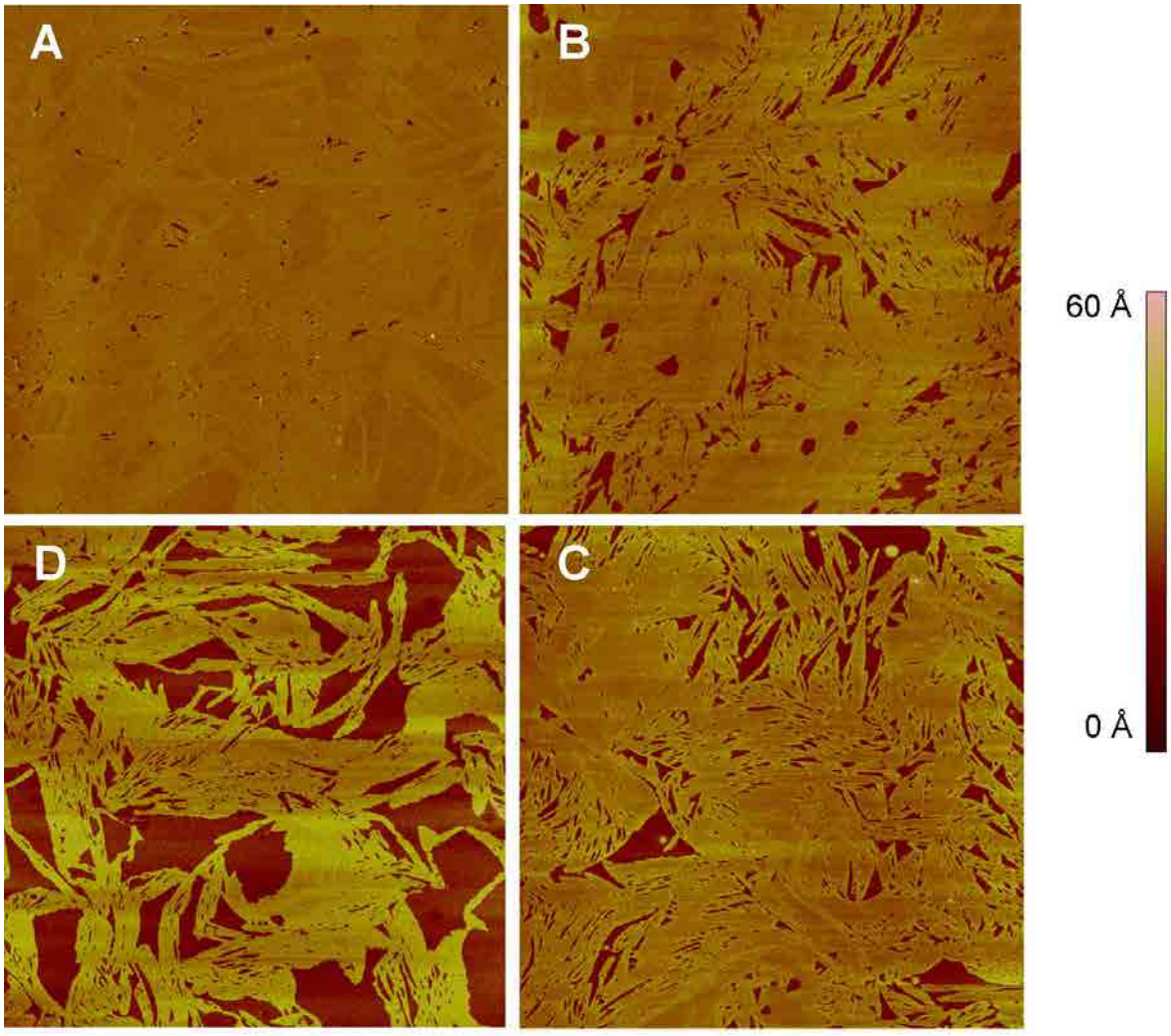

Figure 5.8.7. AFM images (10μm x 10μm) for LB films transferred on mica at 21ºC at π = 6 mN·m^{-1} for (A) pure MGDG and MGDG:UQ systems (B) 20:1, (C) 10:1, (D) 5:1.

In order to explain the behaviour of the MGDG:UQ mixtures at several surface pressures, we have selected the 5:1 ratio (Figure 5.8.8) due to it is the most different from the pure MGDG (Figure 5.4.2) of the ratios we have studied and represents the best option to compare them. As it has been shown for pure MGDG, MGDG:UQ 5:1 presents two different tonalities of brown (fair and dark) and each one corresponds to zones with a different order of the molecules. Moreover, it is interesting to point that at π = 6 mN·m^{-1} and only for the 5:1 ratio, the image presents black zones which corresponds to the mica surface (See inset in Figure 5.8.8A). The compression leads to a more compact fashion of the more ordered zones till π = 40 mN·m^{-1} where the monolayer presents uniform phase with filament protrusions of ≈ 2.5 Å height over it. In addition, at this high surface pressure the monolayer still presents rounded small zones with the molecules in a less ordered state.

On the other hand, AFM topographic images have been performed with the systems MGDG:UQ 10:1 and 20:1 (not shown) obtaining a behaviour comprised between the pure MGDG (Figure 5.4.2) and the MGDG:UQ 5:1 (Figure 5.8.8), so only the images corresponding to π = 6 mN·m^{-1} for MGDG:UQ 10:1 and 20:1 are presented (Figure 5.8.7).

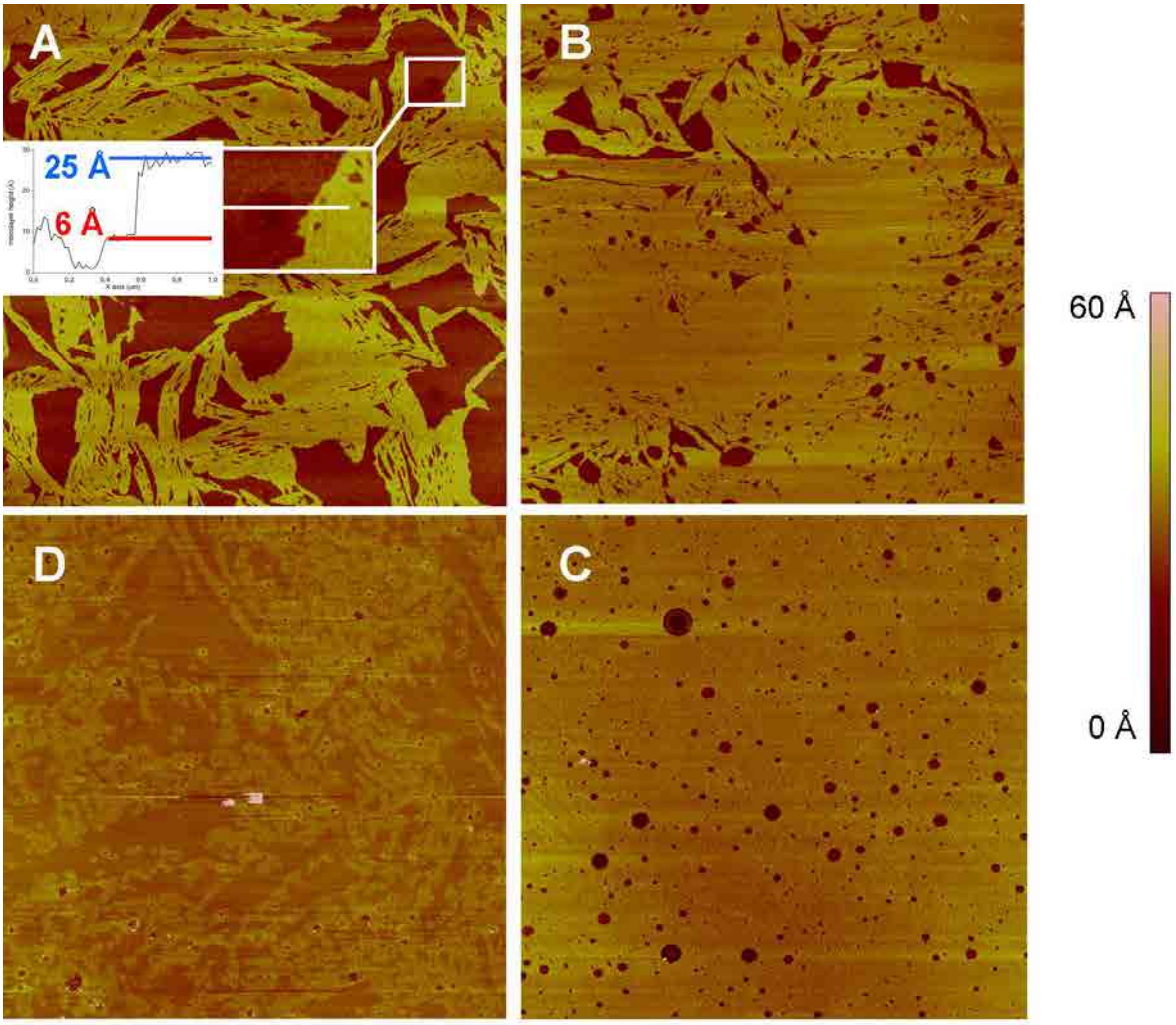

5.8.8. AFM images (10µm x 10µm) for LB films of MGDG:UQ 5:1 system transferred on mica at 21ºC at (A) π = 6 mN·m^{-1}, (B) π = 15 mN·m^{-1}, (C) π = 25 mN·m^{-1}, (D) π = 40 mN·m^{-1}.

AFM discussion

As it has been explained for pure MGDG (Section 5.4.2) each tonality indicates a different tilt order of the molecules that depends on the surface pressure and the interactions established between molecules and between the molecules with the substrate. The appearance simultaneously of zones with a high order (fair zones) with zones of low order (dark zones) in pure MGDG indicates that the meaning of the tonalities is also the same for

the mixtures. On the other hand, it seems clear that the physical states deduced using the C_s^{-1} curves for pure MGDG are more ordered than the corresponding to MGDG:UQ at the same surface pressure, so that, the different tonalities are correlated with different ordering state but the order that represents each tonality depends on the presence of UQ.

In order to light each physical state, we have measured the relative height between fair and dark zones, and assuming the height of 6 ± 2 Å for the dark brown zones referred to the mica surface, the absolute height is presented in Table 5.8.2. The selection of this height value for dark zones is done based on that this is the height measured between the dark brown zones and the black zones seen at low surface pressure for the MGDG:UQ 5:1 system (Inset of Figure 5.8.8A) and, moreover, this height is in accordance with the 3-6 Å observed in the literature for LE of DPPC monolayers [53,54]. The absolute heights obtained at each surface pressure and considering the C_s^{-1} results permit the obtaining of the physical state corresponding to each tonality for all the systems (Table 5.8.3) where LC1 and LC2 have the meaning explained for pure MGDG (see Section 5.4.2).

Table 5.8.2. Height of each physical state for the LB monolayers of MGDG and MGDG:UQ mixtures on mica. *Estimated value (more information in the text).

	LE	LC1	LC2	S
MGDG	6 ± 2 *	21 ± 2	25 ± 2	27 ± 2
MGDG:UQ 20:1	6 ± 2 *		24 ± 2	
MGDG:UQ 10:1	6 ± 2 *		24 ± 2	
MGDG:UQ 5:1	6 ± 2		24 ± 2	

Table 5.8.3. Physical states of each zone (dark and fair brown) corresponding to the MGDG and MGDG:UQ systems at several surface pressures.

	MGDG		MGDG:UQ 20:1		MGDG:UQ 10:1		MGDG:UQ 5:1	
π (mN·m^{-1})	Dark	Fair	Dark	Fair	Dark	Fair	Dark	Fair
6	LE	LC2	LE	LC2	LE	LC2	LE	LC2
15	LC1	LC2	LE	LC2	LE	LC2	LE	LC2
25	LC2	S	LE	LC2	LE	LC2	LE	LC2
40		S		LC2		LC2		LC2

The MGDG and MGDG:UQ mixtures monolayers cover the entire mica surface at all the studied surface pressures, except for the explained case of MGDG:UQ 5:1 at π = 6 mN·m^{-1}. The no observation of uncovered mica zones permits obtaining the proportion of each physical state. The Figure 5.8.9 presents the percentage of the monolayer in fair brown, so that, according to the Table 5.8.3, the proportion of each physical state can be elucidated. For the particular case of MGDG:UQ 5:1 at π = 6 mN·m^{-1}, the result shown is also the fair brown zones but the complementary value indicates the area occupied for both the LE zones and the uncovered regions.

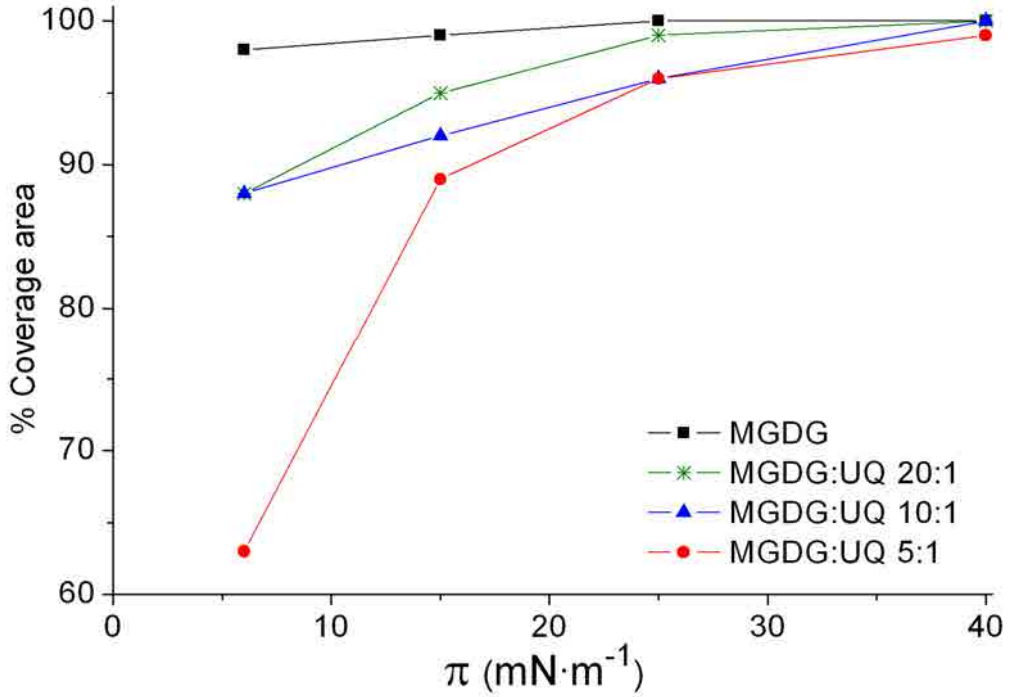

Figure 5.8.9. Monolayer coverage of the fair brown zones on the mica surface for the pure MGDG and the MGDG:UQ mixtures, calculated from AFM images.

The results obtained in Figure 5.8.9 for the MGDG:UQ systems show, at the most surface pressures, the expected trend of more surface covered by the compact state when decreasing the UQ content. The reason for this behaviour is that the reduced presence of UQ enhances the ordering of the MGDG molecules. The surface pressures at which this trend is not accomplished is due to slight experimental deviations. Increasing the surface pressure, all the MGDG:UQ systems increases the ratio of LC achieving a nearly flat increase at π = 25 mN·m^{-1} which is correlated with that the major content of UQ has been rejected from the lipid matrix. On the other hand, pure MGDG presents a nearly flat

increase of the area covered by the more compact phase from low surface pressure. The explanation is the quick transformation of the LE or LC1 state in LC2 which leads that the entire monolayer is in a high ordered state at 15 $mN \cdot m^{-1}$.

The simultaneous presence of two different physical states at each surface pressure for both the MGDG and MGDG:UQ systems indicates that both systems starts the LE to LC physical state change at very low surface pressure. The pure MGDG system achieves at lower surface pressure than the MGDG:UQ system the entire mica surface covered by the LC state (Figure 5.8.8) which is explained by the presence of UQ in the MGDG:UQ mixtures hindrances the packing of the MGDG molecules, so the area occupied by the LC domains are reduced when increasing the UQ content in the MGDG:UQ mixture (Figure 5.8.6). Roche et al. [6**]** using fluorescence microscopy for the DPPC:UQ system observed that a UQ presence > 5 mol% reduces the surface occupied by the LC phase, decreases the LC domain size and produces a change in the domain shape compared with pure DPPC, in line with our DPPC:UQ results observations. We observe a similar behaviour in our results for the MGDG:UQ system compared with that observed for the DPPC:UQ, although we can not appreciate changes in the domains shape in the topographic images.

5.8.5 Electrochemical behaviour

In this section, the electrochemical behaviour of the ITO-MGDG:UQ/electrolyte systems and its mathematical treatment are presented. On the other hand, the results and their corresponding discussion of the pure components MGDG and UQ are exposed in sections 5.4.3 and 5.1.3 respectively, so that, they will be only presented in this section in case it is necessary to compare with the mixtures results. In our experiments, three CVs are required to obtain the stationary state in the electrochemical response, presenting a good reproducibility from the third scan and at least 15 cycles.

Figure 5.8.10 and 5.8.11 present the cyclic voltammograms at 10 $mV \cdot s^{-1}$ of the ITO-MGDG:UQ/electrolyte 5:1 and 10:1 systems respectively, transferred on ITO at several surface pressures which, in part, are the same that were selected for topographic AFM imaging on mica. It must be considered that the topographic images observed for the MGDG:UQ system on mica are not directly correlated with the film deposited on ITO due

to the differences between substrates in surface roughness and the physico-chemical properties, although it can be extrapolated.

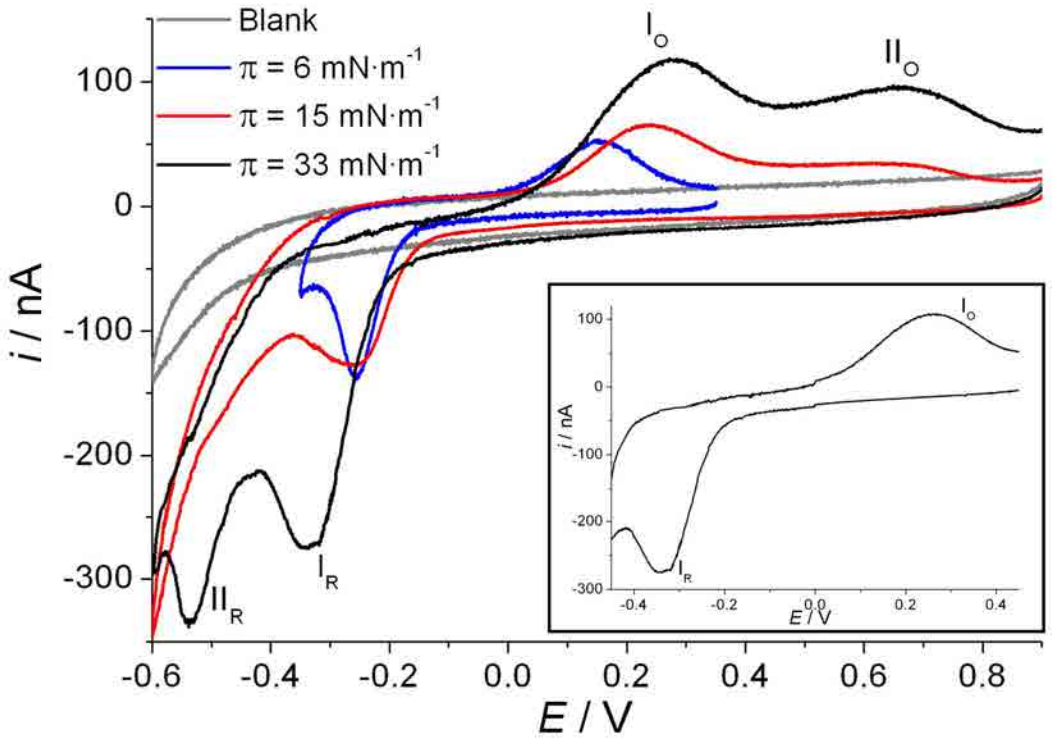

Figure 5.8.10. Cyclic voltammogram of ITO-MGDG:UQ/electrolyte 5:1 LB films transferred at several surface pressures. Blank line represents CV of the ITO-MGDG electrode. Inset corresponds to the MGDG:UQ system at 5:1 ratio in short potential window transferred at π = 33 mN·m^{-1}. All CVs have been performed using 0.150 M of KCl electrochemical cell using potassium phosphate buffered solution at pH 7.4 and at a scan rate of 10 mV·s^{-1}.

The ITO-MGDG:UQ/electrolyte 5:1 at π = 33 mN·m^{-1} shows two reduction and two oxidation peaks whereas at π = 6 mN·m^{-1} only a reduction and an oxidation peak are present. At π = 15 mN·m^{-1} one wide wave is observed for reduction and two peaks are observed for the oxidation process. On the other hand, the ITO-MGDG:UQ/electrolyte 10:1 presents only one reduction and one oxidation peak at all the surface pressures studied. The redox processes have been labelled according to those observed fo the ITO-UQ and ITO-DPPC:UQ systems (Section 5.1.3 and 5.7.4, respectively). The main differences between the DPPC:UQ and the MGDG:UQ systems are on the one hand, the non-appearance of the reduction peak of process I' in the later system, although the broadness of the process I peak and the results obtained for the MGDG:PQ system (See Section 5.9.5) may indicate

that more than one process are involved. On the other hand, the process I_O becomes more important than II_O in the MGDG:UQ system when increasing the surface pressure.

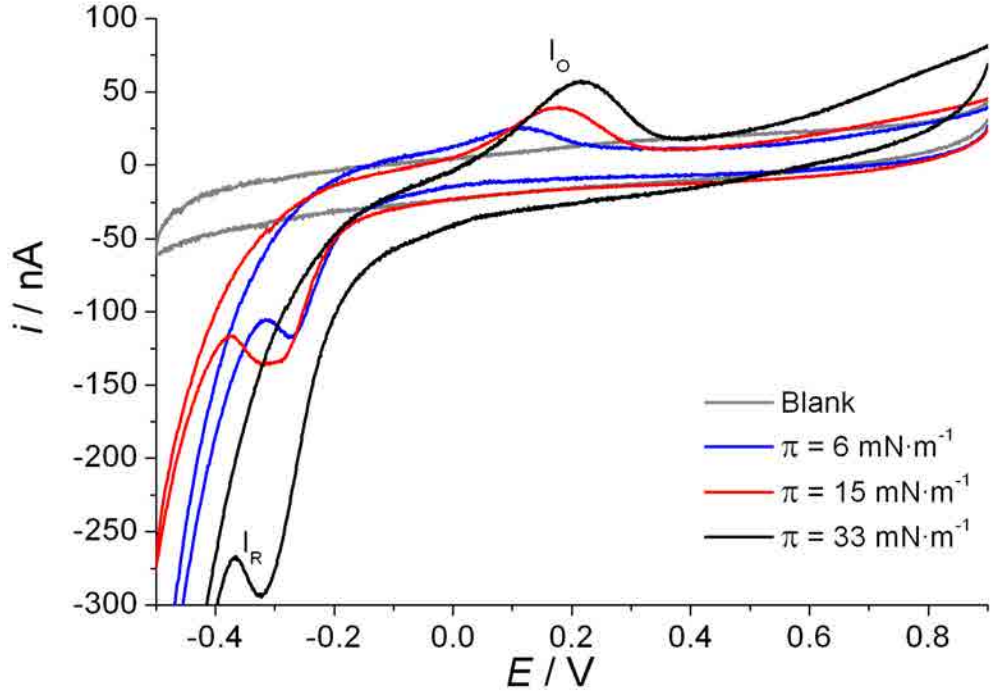

Figure 5.8.11. Cyclic voltammogram of ITO-MGDG:UQ 10:1 LB films transferred at several surface pressures. Blank line represents the CV of the ITO-MGDG electrode. All CVs have been performed using 0.150 M of KCl electrochemical cell using potassium phosphate buffered solution at pH 7.4 and at a scan rate of 10 $mV \cdot s^{-1}$.

In order to gain more information about the system, voltammograms at different scan rates have been performed and Figure 5.8.12 shows the CVs of the MGDG:UQ/electrolyte 5:1 and 10:1 systems on ITO for π = 33 $mN \cdot m^{-1}$, being both experiments scanned at 200 $mV \cdot s^{-1}$. In addition, the inset of Figure 5.8.12 represents the CVs at 10 $mV \cdot s^{-1}$ of the same systems and also, the corresponding to the ITO-UQ/electrolyte system at π = 11 $mN \cdot m^{-1}$. Despite of the increase in the scan rate for the ITO-MGDG:UQ/electrolyte systems, the deconvolution of both processes that seems involved in the cathodic and anodic scan of process I is not possible. In addition, the Figure 5.8.12 confirms that the ITO-MGDG:UQ/electrolyte 10:1 system at π = 33 $mN \cdot m^{-1}$ only shows process I although a wider potential window has been tested (not shown). In this figure, the scan rate is increased in such way that the hydrogen evolution present in all the voltammograms at all compositions starts at more negative potentials than at 10 $mV \cdot s^{-1}$, indicating that this evolution is a quite slower process than process II. The peak and formal potentials of

processes I and II for the ITO-MGDG:UQ/electrolyte 5:1 and 10:1 systems are summarized in Table 5.8.4. On the other hand, it is also interesting to observe that the double layer capacity of the ITO-MGDG/electrolyte experiments is fitted in the capacitive current of the ITO-MGDG:UQ/electrolyte systems (See Blank line in Figures 5.8.10 and 5.8.11).

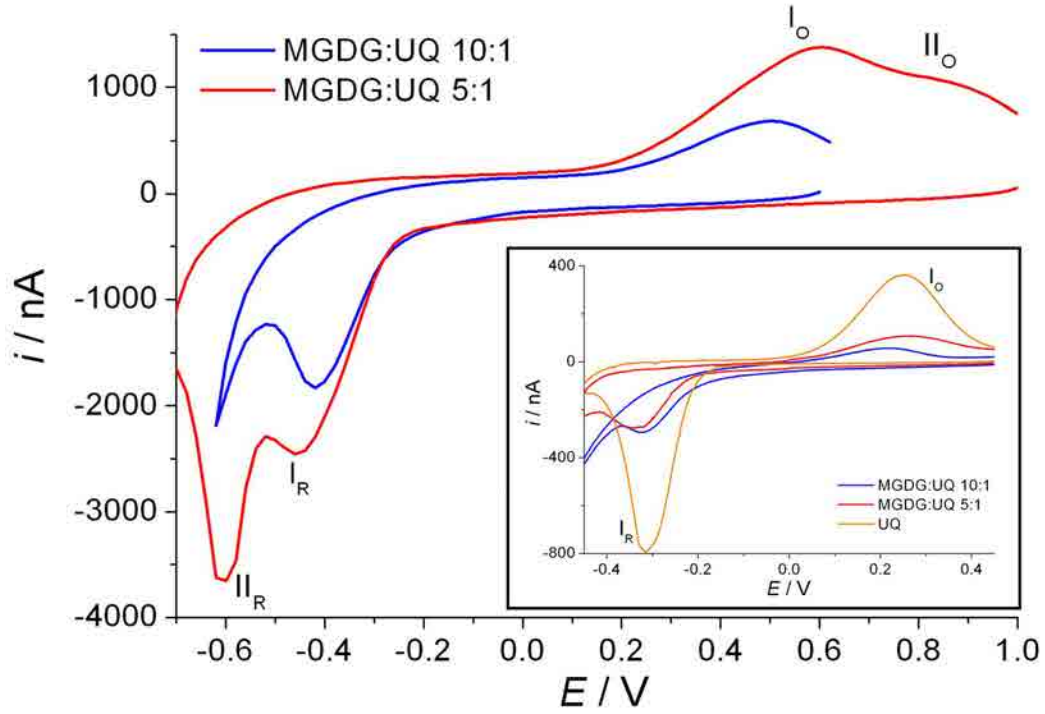

Figure 5.8.12. Cyclic voltammograms of ITO-MGDG:UQ 5:1 and 10:1 LB films transferred at π = 33 mN·m^{-1} and at 200 mV·s^{-1}. Inset presents the cyclic voltammograms of the same systems and the ITO-UQ system transferred at π = 11 mN·m^{-1} in a shorter potential window and at 10 mV·s^{-1}. All CVs have been performed using 0.150 M of KCl electrochemical cell using potassium phosphate buffered solution at pH 7.4.

Table 5.8.4. Redox peaks potentials and the formal potential that they represent for the ITO-MGDG:UQ /electrolyte 5:1 and 10:1 systems.

π (mN·m^{-1})	E_{pR} (I) (V)	E_{pO} (I) (V)	E_f (I) (V)	E_{pR} (II) (V)	E_{pO} (II) (V)	E_f (II) (V)
ITO-MGDG:UQ/electrolyte 5:1						
6	-0.25 ± 0.02	0.16 ± 0.02	-0.04 ± 0.02	-	-	-
15	-0.27 ± 0.02	0.24 ± 0.02	-0.02 ± 0.02	-	0.62± 0.03	-
33	-0.34 ± 0.02	0.28 ± 0.02	-0.03 ± 0.02	-0.54 ± 0.01	0.65 ± 0.02	0.06 ± 0.03
ITO-MGDG:UQ/electrolyte 10:1						
6	-0.28 ± 0.02	0.12 ± 0.02	-0.08 ± 0.02	-	-	-
15	-0.31 ± 0.02	0.18 ± 0.03	-0.07 ± 0.03	-	-	-
33	-0.33 ± 0.02	0.22 ± 0.02	-0.06 ± 0.02	-	-	-

Discussion of the electrochemical response of the MGDG:UQ-ITO/electrolyte system

We understand that the global reaction and the mechanism proposed for pure UQ in confined situation (Section 5.1.3) is the same for the UQ of the ITO-MGDG:UQ/electrolyte system. The shape of the voltammograms for the ITO-MGDG:UQ/electrolyte systems presents two important deviations respect to the theoretical models proposed in the literature to describe the cyclic voltammetric response of a surface confined reaction [29-31]. First, the peak shape, which is not symmetrical, presenting the reduction peak a sharper shape than the oxidation one, a similar situation that it was observed by Märtensson and Agmo [32] and Hong and Park [22] studying UQ and hydroquinone respectively. Second, the redox peaks separation for process I or process II is larger than the expected for such systems.

The different shape of reduction and oxidation peaks can be explained by the different hydrophilic character of the redox couple UQ/UQH_2 as it was pointed for the UQ-ITO system (Section 5.1.3). The larger polarity of UQH_2 compared with UQ leads the former to establish better attractive interactions by dipole-dipole or hydrogen bond between UQH_2 and MGDG headgroups and, in addition, the UQH_2-ITO, UQH_2-UQH_2 and UQH_2-water interactions are also enhanced [4,25-27,32-38,84,85,93]. During the oxidation scan UQH_2 is the reactant so the possibilities of hydrogen bonds are larger, increasing the stabilization of the UQH_2 molecule and making it more difficult to oxidise. These arguments are also valid for explaining the larger width of the oxidation peak compared with that of the reduction process.

The Figure 5.8.13 presents the redox peak potentials of processes I and II vs. the scan rate for the ITO-MGDG:UQ/electrolyte 5:1 system. The redox peaks separation for process II is larger than for process I indicating that process II is even more irreversible than process I. Moreover, the redox peaks separation for both processes is enhanced when increasing the scan rate and similar behaviour is observed for process I of the ITO-MGDG:UQ 10:1/electrolyte system (not shown). This separation makes both processes (I and II) more irreversible and it represents a similar trend to that it was observed by Marchal et al. [21] and by Laval and Majda [41]. This large separation for both processes aroused from the slow charge transfer rates at the ITO-monolayer|electrolyte interface [32]. In addition, it can be also inferred from Figure 5.8.13 that the increase in the scan rate affects in a larger

extent the oxidation peak potential than the reduction one, which produces that the midpoint potential for process I and II has scan rate dependence. On the other hand, it is interesting to observe that all the linear adjustments of the processes I and II reduction peaks for the ITO-MGDG:UQ/electrolyte 5:1 system (Figure 5.8.13) have a similar slope and similar trend is shown for the oxidation peaks of the same processes. However, the y-intercept of the linear adjustment of the reduction peaks is displaced to more cathodic values when increasing the surface pressure and similar occurs with the y-intercept of the linear adjustment of the oxidation peaks that are displaced to more anodic values. This displacement can be explained by the existence of a different environment around the UQ head that is less favourable at low surface pressures or at low UQ content, according to the values of E_f (I) shown in Table 5.8.4. Moreover, the figure has been separated in low and high scan rates because at low scan rates (< 20 $mV \cdot s^{-1}$) the linear adjustments of the reduction and oxidation peak potentials of processes I and II present a higher slope (Figure 5.8.13A) than at high scan rates (Figure 5.8.13B). The trends observed for process I of the MGDG:UQ/electrolyte 5:1 system are similar to that observed for the process I of the ITO-MGDG:UQ/electrolyte 10:1 system and both are explained by the hindrance increase of the electrochemical process when increasing the scan rate.

Moreover, the current intensity of the redox peaks (i_{peak}) has been studied for the ITO-MGDG:UQ/electrolyte 5-1 system at several scan rates and it has been shown that the reduction (not shown) and the oxidation current intensity are related by a linear dependence with the scan rate (Figure 5.8.14) so indicating that UQ molecules are surface confined in all the processes [16,29] and that the electron transfer process is not diffusion controlled. These observations are also valid for ITO-MGDG:UQ/electrolyte 10:1 (not shown). Our results are in line with the observations of Märtensson and Agmo [32] for scan rates < 1 $V \cdot s^{-1}$, Gordillo and Schiffrin [28] and Li et al. [43] for monolayers containing UQ confined on the electrode surface.

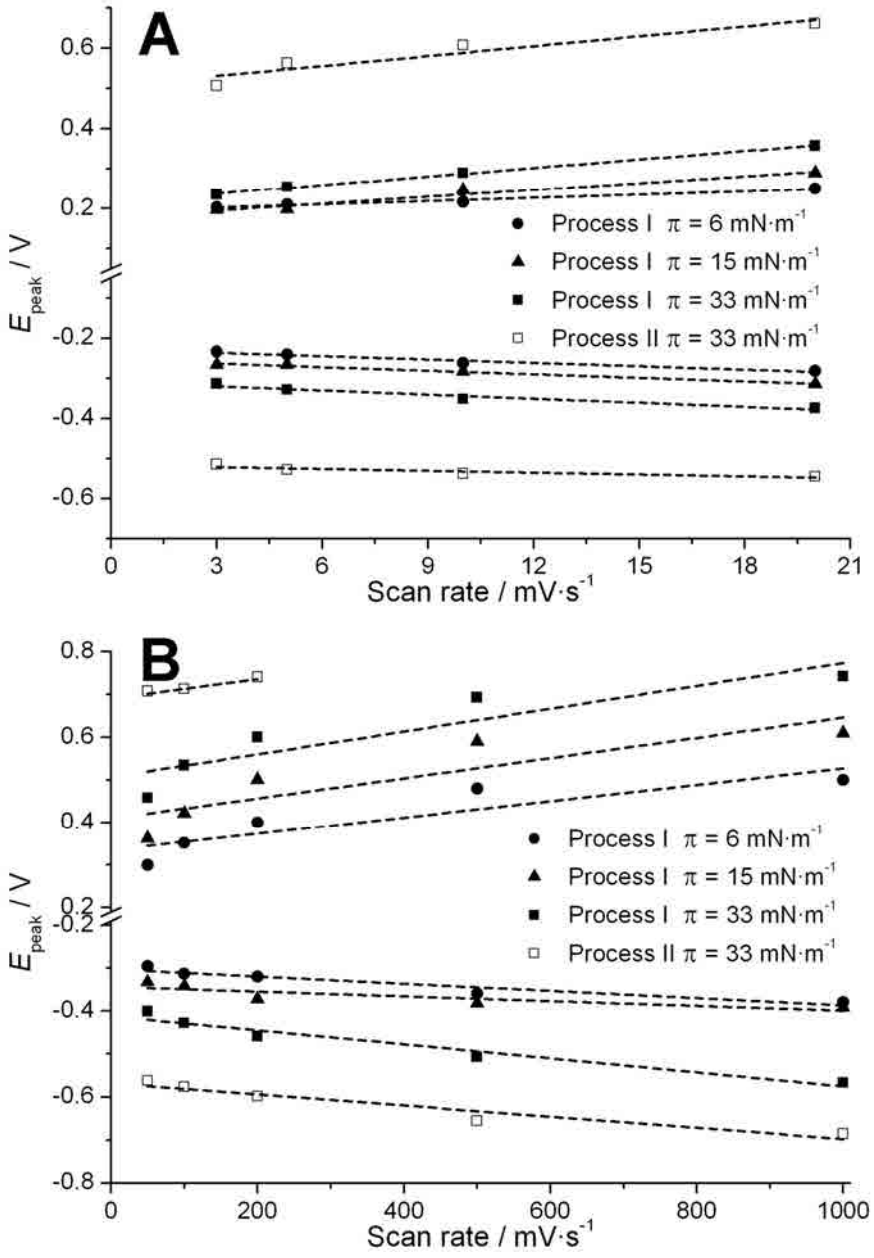

Figure 5.8.13. Peak potential vs. the scan rate for the ITO-MGDG:UQ 5:1/electrolyte system transferred at several surface pressures. A) low scan rates and B) high scan rates.

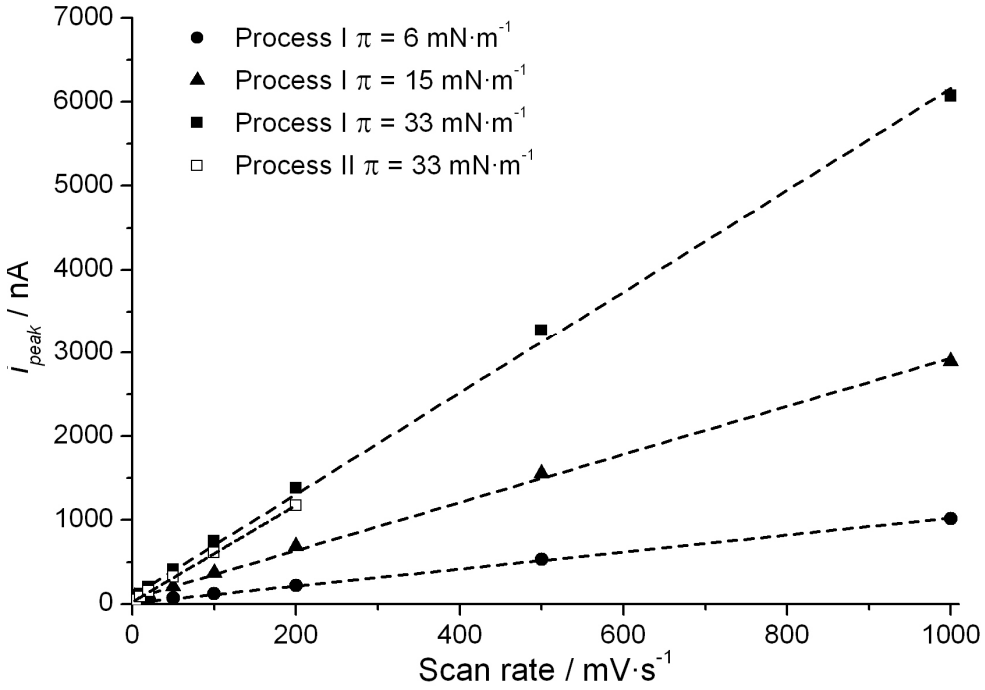

Figure 5.8.14. Oxidation peak intensity vs. the scan rate for the ITO-MGDG:UQ 5:1/electrolyte system at π = 6, 15 and 33 mN·m^{-1}.

The charge involved in the LB monolayer transferred at each surface pressure is obtained by integrating the area under the reduction or oxidation waves. The surface coverage (Γ) is obtained from the experimental values of charge and considering the global reaction for UQ in confined situation (Section 5.1.3). The Γ for the ITO-MGDG:UQ/electrolyte system are shown in Table 5.8.5 and compared with the expected value to obtain the electroactive fraction of UQ. The expected surface coverage (Γ_{expec}) values are calculated assuming that UQ and MGDG molecules are perfectly spread, accordingly to the corresponding ratio, on the ITO surface, being the resulting value corrected with the transfer ratio associated to it in the LB transfer process. We have chosen to show in Table 5.8.5 the oxidation surface coverage (Γ_O) of the redox processes which are similar but lower than the results obtained for the reduction scan which have the undesirable contribution of hydrogen evolution.

Table 5.8.5. Expected (Γ_{expec}), experimental total oxidation ($\Gamma_{O\,tot}$) surface coverage, experimental surface coverage for process I, Γ_O (I), and electroactive fraction involved in the whole redox process for the ITO-MGDG:UQ/electrolyte system using 0.150 M of KCl electrochemical cell, with potassium phosphate buffered solution at pH 7.4 and at a scan rate of 10 $mV \cdot s^{-1}$.

π ($mN \cdot m^{-1}$)	Γ_{expec} (10^{-12} mol · cm^{-2})	$\Gamma_{O\,tot}$ (10^{-12} mol · cm^{-2})	Γ_O *(I)* (10^{-12} mol · cm^{-2})	Electroactive fraction (%)
ITO-MGDG:UQ/electrolyte 5:1				
6	19.0	10.4	10.4	54.9
15	41.5	21.4	15.8	51.6
33	50.3	47.7	32.8	94.7
ITO-MGDG:UQ/electrolyte 10:1				
6	14.2	4.4	4.4	31.0
15	24.7	9.9	9.9	40.1
33	28.2	11.8	11.8	41.8

The Table 5.8.5 shows that an increase in the initial UQ content in ITO-MGDG:UQ/electrolyte systems leads to an increase of the electroactive fraction. Our results contrast with the observations of Moncelli et al. [19] who observed a decrease in the surface coverage when increasing the initial UQ content from 0.5 to 2 % on a monolayer of DOPC on HDME at pH 9.5. This different behaviour is explained by the differences in pH. Moncelli et al. [15,19] worked with pH 9.5 so the availability of protons in the proximity of the UQ heads is more limited than in our experiments at pH 7.4. The lack of protons affects the reduction rate determining step (1_b) (see Section 5.1.3) so at high UQ concentrations or high scan rates, the step 1_b is not completed so the electroactive fraction is reduced. In our experiments the enough presence of available protons close to the UQ heads avoids the high local UQ concentration problem. The fact that the electroactive fraction is enhanced when increasing the initial UQ content is explained by the electron hopping effect (See Section 3.4.5). Moreover, the non homogeneous electrode surface and the semiconductive properties of ITO induce it to behave different to metal surfaces like gold or mercury contributing with the different environments that UQ head experiences in the chain region [41] to reduce the electroactive fraction [9]. On the other hand, Γ_O (I) values (Table 5.8.5) are represented in Figure 5.8.15 vs. the surface pressure, and it shows that Γ_O (I) for the ITO/MGDG:UQ 10:1 system attains a maximum value $\approx 10 \cdot 10^{-12}$ $mol \cdot cm^{-2}$, whereas Γ_O (I) of the ITO/MGDG:UQ 5:1 system continues increasing.

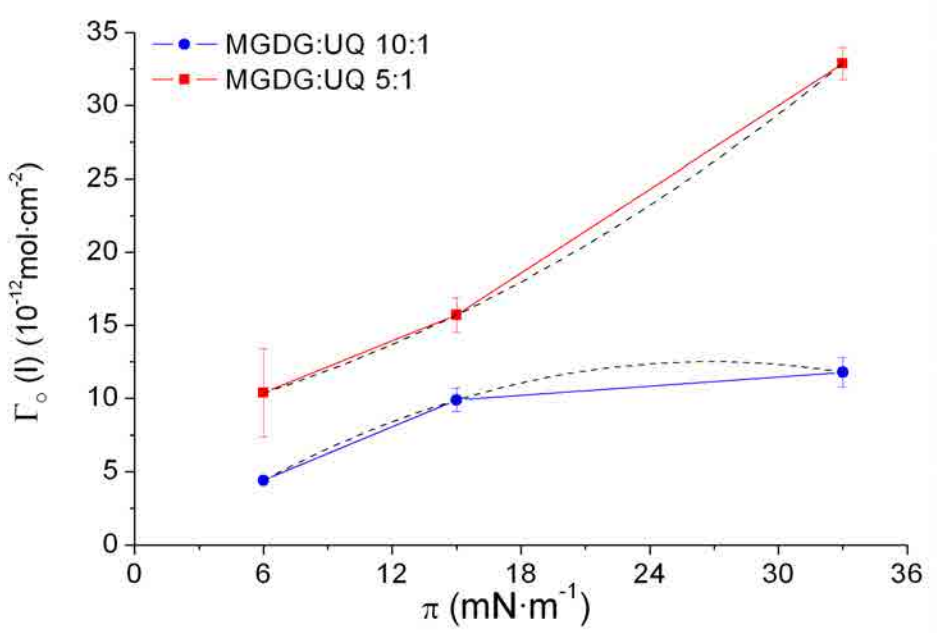

Figure 5.8.15. Surface coverage of the UQH_2 fraction oxidized via process I, Γ_O (I), vs surface pressure, π, for ITO-MGDG:UQ/electrolyte 5:1 and 10:1 mixtures.

Finally, we compare the formal potential values obtained in our system (Table 5.8.4) with that reported in the literature for UQ confined on an electrode surface. Previous authors [16,19,28] have studied the UQ redox processes on HDME. All of them found at pH ≈ 9.5 the midpoint potential of E_f ≈ -0.26 V, which corrected by the pH differences it is obtained a formal potential value of E_f (I) ≈ -0.13 V vs. Ag/AgCl at pH 7.4. On the other hand, Marchal et al. [21,23] performed experiments in a biomimetic membrane approach in which the PQ or UQ was encapsulated between a bottom layer of Octadecyltrichlorosilane (OTS) and a top layer of DMPC so as to have the redox processes laterally on a gold wall. The formal potential E_f ≈ -0.14 V vs. Ag/AgCl observed is close to the E_f ≈ -0.15 V vs Ag/AgCl observed by Jeuken et al. [86] and to that formal potential obtained by the Laval and Majda [41] of E_f ≈ -0.09 V vs. Ag/AgCl on gold for a LB film of UQ transferred at 10 $mN \cdot m^{-1}$. In all the exposed situations [21,23,41,86], the UQ/UQH_2 redox process is diffusion controlled. In this line, Ma et al. [44,45] prepared SAMs of UQ on gold using similar conditions giving an extrapolated formal potential of E_f ≈ - 0.09 V vs. Ag/AgCl in a situation that can be assimilated to that explained for the HDME electrode. On the other hand, the same authors [44] studied in similar conditions the cyclic voltammetry of UQ in phospholipid bilayers on gold giving an extrapolated formal potential of E_f ≈ -0.05 V vs. Ag/AgCl which coincides with the formal potential for hydroquinone/benzoquinone

observed in SAM on gold by Petrangolini et al. [17]. All the formal potential observed by previous authors for the UQ redox processes are less thermodynamically favourable than that observed in this work for process I, which is correlated with the higher availability of protons in our system. The process I observed in our experiments requires, direct contact or short distance between ITO and the UQ head, which can be correlated with the exposed situations [21,23,41,86]. On the other hand, our process II is more irreversible and kinetically unfavourable [29] than process I, but it has more positive formal potential (close to that of benzoquinone/hydroquinone in aqueous solution E_f (II) ≈ 0.14 V vs. Ag/AgCl [48]) that can be correlated with a more aqueous environment for the UQ headgroup which is correlated to that they are placed in an environment with higher H^+ ion availability nearer to the aqueous electrolyte. Therefore, we correlate process II with the redox behaviour of the UQ molecules that have been expelled from the MGDG matrix and they are placed on top of the monolayer. The major irreversibility of process II compared with process I is correlated with the larger distance that the electron transfer is forced to proceed from the ITO surface to the UQ head, which induces a slowing of the overall electron-transfer rate that is often observed in SAM of electro-active molecules [22,45] and in SPB [87].

5.8.6 Global sight of the MGDG:UQ system transferred on ITO using the LB technique

In this section we explain the global behaviour of the MGDG:UQ system and the position of the UQ molecules in the monolayer studying the results obtained from the used techniques.

The different shape of the C_s^{-1} curves and the lower C_s^{-1} values observed for the MGDG:UQ mixtures compared to the pure MGDG indicate the presence of of UQ molecules in the matrix of the MGDG:UQ mixtures (“diving” position, see Section 3.4.2), and it leads to less compact physical states. The shape of the π-A isotherms, the shape of the C_s^{-1} curves and the shape of the first kink point in the C_s^{-1} curves suggest that the system experiences a sudden UQ expulsion followed by a gradual expelling. The expulsion of the UQ from the lipid heads region leads to the diving position without ITO-UQ contact and the “swimming” position, being this last position and the formation of aggregates favoured at large initial content of UQ and at ordered states, as it was previously observed

[3,25,27,36]. So that, the expulsion of UQ is the way chosen by the MGDG:UQ mixture to minimize its energy at the interface [49] and to minimize the low favourable interactions between UQ and the MGDG chains. The proportion of UQ at each position (diving [4,15, 36,88-95] or swimming [4,84,85,88,91-94,96-103,107]) is defined by the MGDG physical state and the initial UQ content.

A complete vision of the UQ positions in the MGDG:UQ monolayer can be obtained considering the thermodynamic description of the physical states, the AFM results of the MGDG:UQ 5:1 system on mica (Figure 5.8.8) and the CVs of Figures 5.8.10-5.8.12. Therefore, these UQ positions will be extrapolated to all the ITO-MGDG:UQ systems. The MGDG and the MGDG:UQ mixtures with low UQ content, both at low surface pressure, present similar covered area by the LC state (Figure 5.8.9) whereas the MGDG:UQ 5:1 ratio presents a markedly lower covered area by this LC state. In addition, the height measured for the LC state of pure MGDG is higher than that of the MGDG:UQ mixtures. These observations indicate that UQ is present in both physical states (LE and LC) in the MGDG:UQ mixtures. At π = 6 $mN \cdot m^{-1}$, the CVs of Figures 5.8.10 show the formal potential at E_f (I) = -0.03 ± 0.02 V for the ITO-MGDG:UQ/electrolyte 5:1 system and the 5.8.11 show the same process at E_f (I) = -0.07 ± 0.02 V for the ITO-MGDG:UQ/electrolyte 10:1 system. Both are close to the formal potential of the redox process I obtained for the ITO-UQ/electrolyte system (inset of Figure 5.8.12) which indicates that the local environment around each UQ is similar in these situations [22]. However, the more cathodic formal potential obtained for the ITO-MGDG:UQ/electrolyte 10:1 system may be related with the higher proportion of compact LC state compared with the pure UQ or the ITO-MGDG:UQ/electrolyte 5:1 system which induces slight changes in the UQ environment that hindrance the electron transfer. Despite of these small differences, at low surface pressures, regardless the MGDG:UQ domains are in LE or LC state (Figure 5.8.8A), we correlate process I with the “diving” position at which the UQ is placed in the MGDG matrix and located in direct contact with the electrode surface. The monolayer of MGDG:UQ 5:1 at π = 6 $mN \cdot m^{-1}$ is especially interesting due to the low surface pressure, the large zones in LE and the high UQ content compared with the other ratios used lead the LE to be non-uniform leaving some pinholes that arrive to the mica surface (Figure 5.8.8A inset).

The compression of the explained monolayer induces two actions: First the compactness of the LC2 state, so favouring the rejection of part of the UQ in “diving” position. On the one hand, it can be vertically rejected to the diving position without contact to the substrate and, on the other hand, horizontally to the remaining LE zones so enriching them in UQ. Second, the phase change from LE to LC2 of the remaining LE zones (Figure 5.8.8B and C). Further compression results in a more compact LC2 state with very low proportion of covered areas by the LE state and the formation of filament shaped protrusions (Figure 5.8.8D), which we relate with the presence of UQ molecules in “swimming” position forming pools on top of the monolayer. We correlate this “swimming” position with the process II observed in the CVs of Figure 5.8.10, only for the ITO-MGDG:UQ/electrolyte 5:1 system. The process II for ITO-MGDG:UQ/electrolyte 10:1 is not observed, even at high scan rate.

The presence of enriched domains is predictable based on the Van Dijck et al. [105] observations for saturated phospholipids with the same headgroup and others studies presented in the literature [27,35,36,41,93,95,98,106,107]. In addition, Figure 5.8.8C and D present small LE zones in circular shape which is the shape adopted by the monolayers to minimize the surface tension of the nascent boundary when lipid reorientate in the layer boundaries [118]. They may indicate that the composition in and out the rounded shape is different. On the other hand, the non-saturation of the Γ_O (I) (Figure 5.8.15) when increasing the surface pressure at which the LB film has been transferred suggests that, when changing from LE to LC, the lateral rejection is favoured placing most of the UQ molecules in the “diving” position in the LE zones. The fast LE to LC physical state change entraps the UQ molecules in the MGDG matrix, favouring the diving position over the swimming position. The later position is only achieved at high initial UQ content due to the exceeding UQ molecules are horizontal rejected and they are placed above the UQ molecules in “diving” position. Moreover, the “diving” position present wide redox peaks that, based on the observations for the ITO-MGDG:PQ/electrolyte system (Section 5.9.5), comprises two redox processes I_α and I_β corresponding, respectively, to the UQ molecules in direct contact and the UQ molecules close to the ITO surface. The difficult deconvolution of these peaks in the ITO-MGDG:UQ/electrolyte system, even at high scan rate, indicates that both peaks present similar formal potential, and similar electron transfer rate constants. However, their presence can explain the slight dependency of the formal

potential with the surface pressure observed in Figure 5.8.13. On the other hand, the two different redox processes for a substrate-UQ/electrolyte system at the same voltammogram have only been previously observed by Moncelli et al. [19]. They argued that each reduction peak they observed correlate to the intercalated UQ in the phospholipid matrix and to a UQ rich phase respectively.

According to the literature and considering the monolayer|air interface, the “swimming” position is more stable than the “diving” position due to the later disrupts the cooperative motions between the MGDG chains [102]. Moreover, above the MGDG chains, the medium is air whose hydrophobicity [104] added to the hydrophobicity of the end part of the MGDG chains stabilize the UQ [6] avoiding the distortion of being inserted between the MGDG chains. However, the “diving” position can be stabilized thanks to fast physical state change and/or part of the UQ molecules self-aggregate, forming head to head aggregates to withstand the hydrophobic environment of the lipid chain region in accordance with Roche et al. [6]. It is important to consider that our experiments always presents a higher UQ content than the minimum observed in the literature for aggregation (0.5-2 mol%) [1,15,36].

Our results confirm that UQ is confined at the electrode surface and the electron transfer takes place mainly by two mechanisms, first, by direct transfer and electron hopping between the UQ placed in “diving” position (process I), and second, by electron hopping through the lipid matrix (process II). The electron hopping favours the rate determining step (1_b) (Section 5.2.3) so favouring the electroreduction in the timescale used. At low surface pressure or at low UQ initial content, the molecules are far enough each other to do not be affected by the electron hopping mechanism. Increasing the surface pressure the UQ headgroups are placed closer facilitanting the electron hopping redox process.

In order to clarify the position and organization of the MGDG and UQ molecules at each physical state, the Figure 5.8.16 represents the position of MGDG and UQ molecules of the MGDG:UQ 5:1 system at the surface pressures studied. This Figure 5.8.16 explains the different meaning of the fair and dark colours observed in the AFM images summarized in Table 5.8.3 and the UQ positions that origin the redox processes I_α, I_β and II.

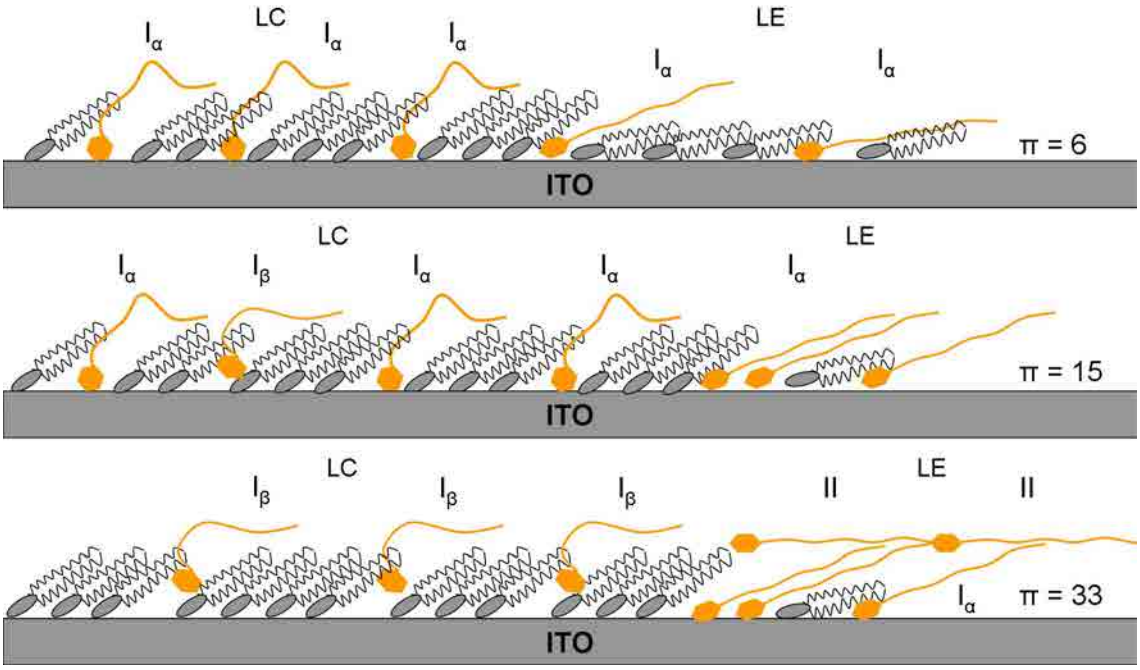

Figure 5.8.16. Scheme of the position of MGDG and UQ molecules of the MGDG:UQ 5:1 system at several surface pressures. The labels I_α, I_β and II indicate the UQ positions that origin the redox processes I_α, I_β and II.

5.9 MGDG:PQ

5.9.1 π-A isotherms and physical states

The π-A isotherms of the MGDG:PQ system at biological relevant ratios are presented in Figure 5.9.1 referred to the MGDG area per molecule. The C_s^{-1} curves (Figure 5.9.2) corresponding to the described π-A isotherms (Figure 5.9.1) are calculated according to the Expression 2.9. The most significant values of Figures 5.9.1 and 5.9.2 are summarized in Table 5.9.1. The usual representation of isotherms corresponding to binary mixtures is the π vs. mean area per molecule, being each isotherm referred to the weighted (mean) area per molecule according to the MGDG:PQ ratio. In the present case, we have discarded this kind of representation due to PQ is mostly expelled from the lipid matrix at low surface pressures (as it will be commented in this section). This kind of representation of the MGDG:PQ system above the main expulsion has non-sense and distorts the global sight. The description and discussion of the π-A isotherms and the C_s^{-1} results for the MGDG and PQ pure components were explained in Section 5.4.1 and 5.2.1 respectively. So that, we present in this section only the results of the mixtures and their corresponding discussion.

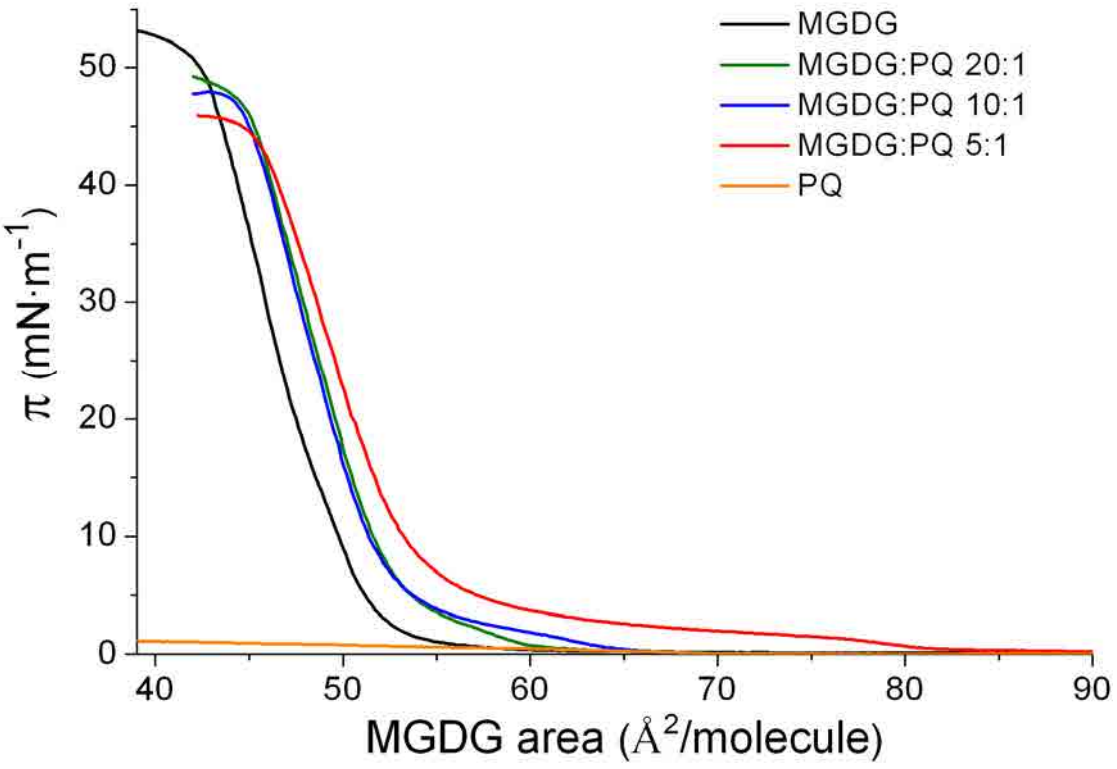

Figure 5.9.1 π-A isotherms for MGDG, PQ and MGDG:PQ mixtures at 21 ± 0.5 ºC on water subphase.

MGDG:PQ mixtures present different behaviour according to the PQ presence in the mixture. The isotherm can be divided in two zones being the kink point at ≈ 2 $mN \cdot m^{-1}$, the border value. Below that surface pressure, the presence of high content of PQ (see MGDG:PQ 5:1 system) hindrances in a quite larger extent the packing of the MGDG monolayer than the low ratios (See MGDG:PQ 20:1 and 10:1 systems). Above 2 $mN \cdot m^{-1}$, the isotherms of MGDG:PQ systems tend to meet each other at high surface pressure. On the other hand, the mixtures only meet the pure MGDG isotherm at the collapse, indicating the presence of PQ in the MGDG matrix even at high surface pressures.

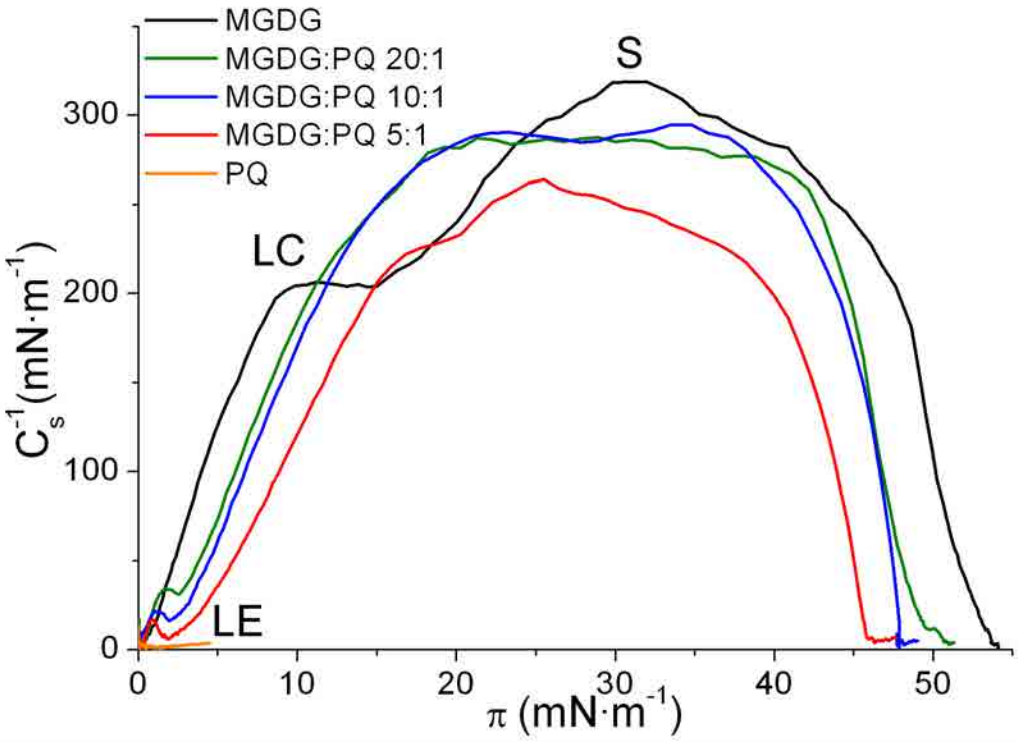

Figure 5.9.2. Inverse of the compressibility modulus vs. surface pressure for MGDG, PQ and MGDG:PQ mixtures on water subphase.

Table 5.9.1. Collapse pressure, lift-off area and kink point position for the MGDG, PQ and their biological mixtures obtained from Figure 5.9.1 and 5.9.2.

	Collapse pressure ($mN \cdot m^{-1}$)	Lift-off area ($Å^2 \cdot molec^{-1}$)	Kink point pressure ($mN \cdot m^{-1}$)	Kink point area ($Å^2 \cdot molec^{-1}$)
MGDG	53	59	-	-
MGDG:PQ 20:1	48	70	2.5	56.6
MGDG:PQ 10:1	48	72	1.9	59.8
MGDG:PQ 5:1	46	90	1.8	71.9
PQ	0.3	76	-	-

Both the lift-off area and the area at which appears the kink point increase as the PQ content in the MGDG:PQ mixture is enlarged (Table 5.9.1), and it is correlated with the distorting effect of PQ in the MGDG matrix [80]. This phenomena was also observed by Kruk et al [38] using PQ and unsaturated MGDG and also by Bilewicz et al. [1] using UQ and $C_{18}SH/C_{18}OH$. The presence of PQ in the initial zone hindrances the packing of the MGDG headgroups, and therefore, the hydrophobic interactions between the MGDG chains are also reduced, as it was seen in the case of UQ inserted in phospholipids [25]. The explanation for this phenomenon is that PQ is better retained in the lipid monolayer when present at low concentrations due to it affects in a lower extent the formation and shape of the ordered phases. After the main rejection of PQ (kink point), the monolayer compactness is rapidly enhanced.

The behaviour of the saturated MGDG:PQ π-A isotherms is similar to that observed using unsaturated MGDG [38] in which the MGDG:PQ mixtures π-A isotherms maintain the separation, with the pure lipid. However, when working with the saturated lipid, this separation is lower. On the other hand, we do not observe shifts in the collapse pressure and it may be caused by the shorter range of PQ ratios used in comparison to Kruk et al. [38] experiments. However, we do observe differences in the lift-off area. This observation indicates that unsaturated MGDG maintains a larger extent of PQ content in its matrix than the saturated MGDG, which can be correlated with the more fluid phase of the unsaturated MGDG, as it has been explained in Section 5.4.1.

All the C_s^{-1} curves for the MGDG:PQ mixtures present a similar behaviour, showing at $\pi \approx$ 2 $mN \cdot m^{-1}$ a kink point, which accordingly to the values presented by Vitovic et al. [7] and the characteristics of this system indicates the phase change from LE to LC and it implies the main PQ expulsion from the lipid matrix. The extent of this rejection and the specific surface pressure at which takes place depends on the initial PQ content. At $\pi > 2$ $mN \cdot m^{-1}$ the C_s^{-1} values presented by the MGDG:PQ 20:1 and 10:1 systems, that are the mixtures with the lowest PQ presence, are similar to that shown by pure MGDG and presents a $C_{s\ \max}^{-1}$ little higher than the border value proposed by Vitovic et al. [7] for the S state. However, the proximity between both values suggests the possibility that the monolayer is still in the LC state being this possibility discussed in Section 5.9.4. On the other hand, the

behaviour shown by the C_s^{-1} curve of MGDG:PQ 5:1 mixture resembles the C_s^{-1} curves of the 20:1 and 10:1 mixtures but with marked lower C_s^{-1} values.

Phase rule

The collapse pressure of a mixed monolayer of different components is related to the miscibility of its components, being dependent on the film composition in a miscible system [50,68]. In our MGDG and MGDG:PQ mixtures isotherms, the collapse pressure is ≈ 50 $mN \cdot m^{-1}$. Therefore, the similar collapse pressure can be used to elucidate the expulsion of one of the components in a mixed film. In a two component monolayer, if components are completely immiscible, a lower collapse pressure of one of the components will be observed as it is predicted by the phase rule. Maintaining temperature and external pressure constant, the number of degrees of freedom F of the monolayer system is given by the Expression 2.14 [82,83] that is reproduced below:

$$F = C_B + C_S - P_B - P_S + 1$$

In our MGDG:PQ experiments, at the air|water interface, $C_B = 2$ (air and water), $C_S = 2$ (MGDG and PQ), and $P_B = 2$ (gas and liquid), thus $F = 3 - P_S$. According to that, homogenous mixed films achieve the collapse equilibrium with $P_S = 2$ (condensed and collapsed state), so the system will have one degree of freedom. According to our results, the collapse pressure is practically fixed, discarding the experimental deviations, for pure MGDG and MGDG:PQ mixtures. This indicates zero degrees of freedom and therefore, following the previous reasoning, $P_S = 3$. So that, at the collapse equilibrium of the mixtures isotherms coexist MGDG (LC), MGDG (collapse) and expelled PQ. The same statements can be also applied to the phase change zone at $\pi \approx 2$ $mN \cdot m^{-1}$, where the π is practically fixed indicating zero degrees of freedom. Thus $P_S = 3$ which indicate that three phases coexist: MGDG:PQ (LE), MGDG:PQ (LC) and expelled PQ, confirming the beginning of the PQ expulsion at this surface pressure. This observation coincides with the AFM conclusions (Section 5.9.4).

5.9.2 BAM

BAM images give information about the film structure at the air|water interface at microscopic scale. In this case, we have selected for the MGDG:PQ 20:1 mixture, Figure 5.9.3A in which the LE phase formation is observed, Figure 5.9.3B and Figure 5.9.3C which represents the LC state at different surface pressures.

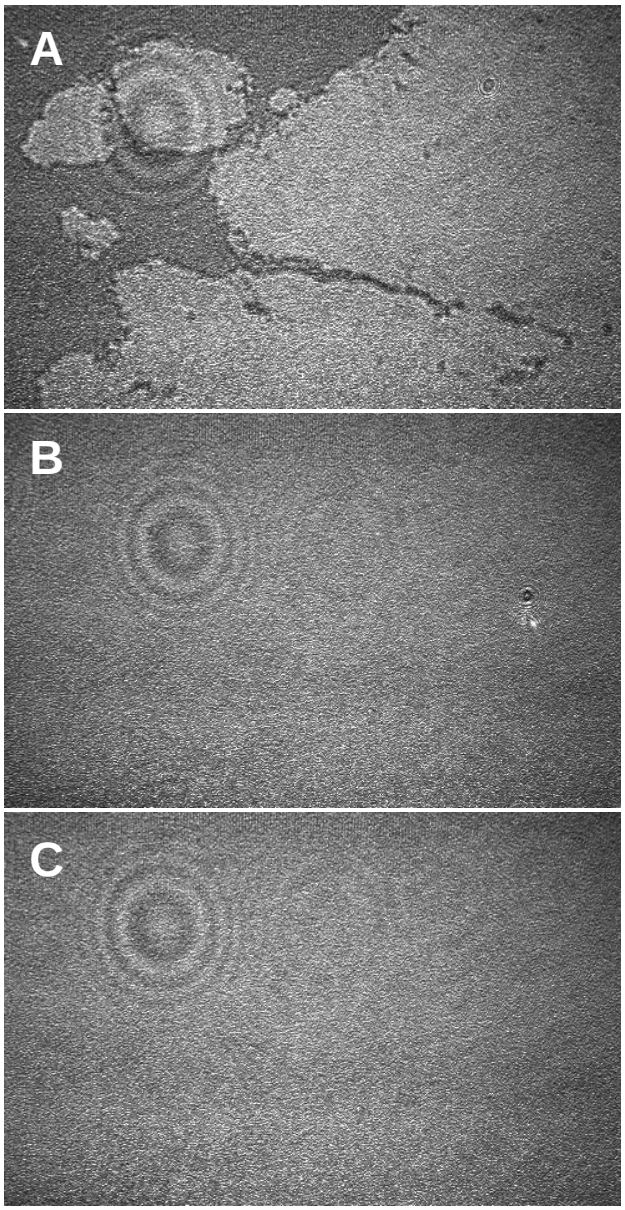

Figure 5.9.3. BAM images of the MGDG:PQ 20:1 mixture. A) at 0.2 $mN \cdot m^{-1}$, B) at 15 $mN \cdot m^{-1}$ and C) at 33 $mN \cdot m^{-1}$ on water subphase.

5.9.3 Thermodynamic study

The representation of the mean area per molecule vs. the molar fraction at selected pressures gives idea about the ideality of a mixture at these surface pressures. The reader is addressed to Section 2.1.1.5 where the mathematical treatment (Expressions 2.10 - 2.13) for the figures of this part is explained. The Figure 5.9.4 plots the area per molecule and the Figure 5.9.5 plots G^E both vs. the PQ molar fraction, represented for MGDG:PQ mixtures at several surface pressures before the main PQ expulsion (≈ 2 $mN \cdot m^{-1}$). At surface pressures above this event, the thermodynamic study has not been performed due to the PQ content in the MGDG:PQ matrix is unknown and significantly lower than the initial presence.

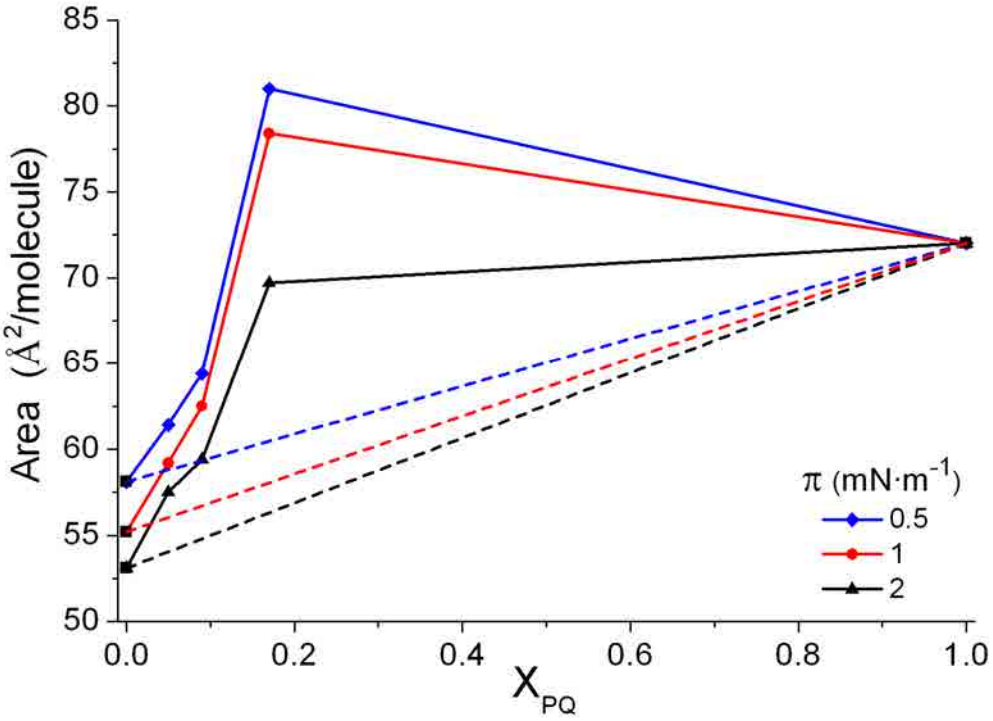

Figure 5.9.4. Plot of the mean area per molecule vs. the molar fraction for MGDG, PQ and MGDG:PQ mixtures at several surface pressures before the main PQ expulsion. Discontinuous straight line represents the ideal behaviour for each surface pressure.

Both figures (5.9.4 and 5.9.5) show that MGDG and PQ form non-ideal mixtures with positive deviation at $\pi \leq 2$ $mN \cdot m^{-1}$, which indicates that, at these surface pressures, the interactions between the two components are weaker than the interactions between pure components [6], suggesting the possible formation of enriched domains or aggregates of molecules [68,83] at high PQ content.

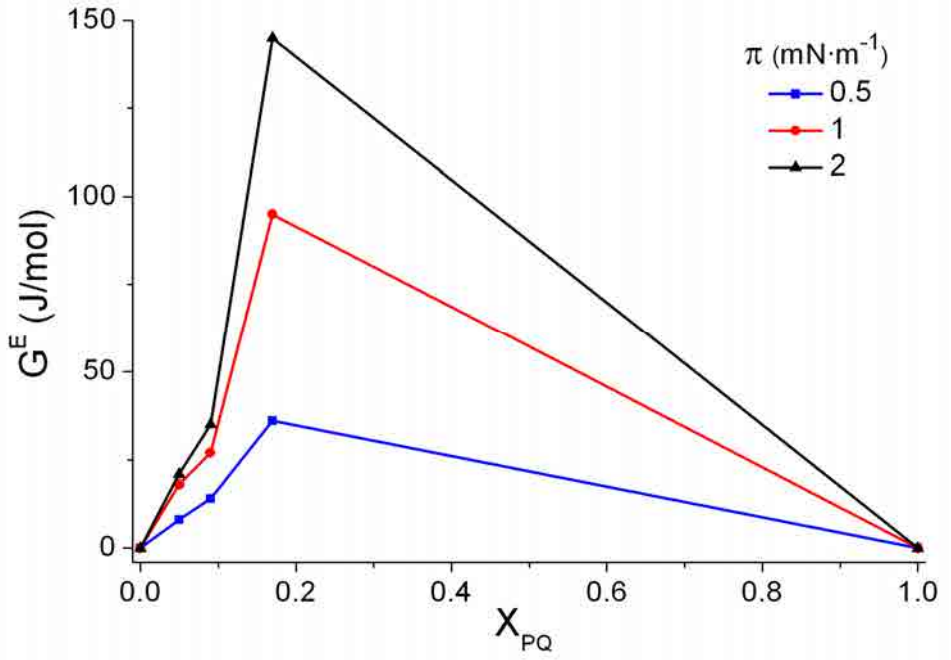

Figure 5.9.5. Plot of the excess energy vs. the molar fraction for MGDG, PQ and MGDG:PQ mixtures at several surface pressures before the main PQ expulsion.

The Figure 5.9.6 represents the ΔG_{mix} vs. PQ molar content at several surface pressures before the main PQ expulsion. The negative values observed for ΔG_{mix} at $\pi \leq 2$ mN·m^{-1} indicate that the mixed monolayers of MGDG:PQ are more stable than pure components [6], although the low ΔG_{mix} values corroborate the low stability of the mixture.

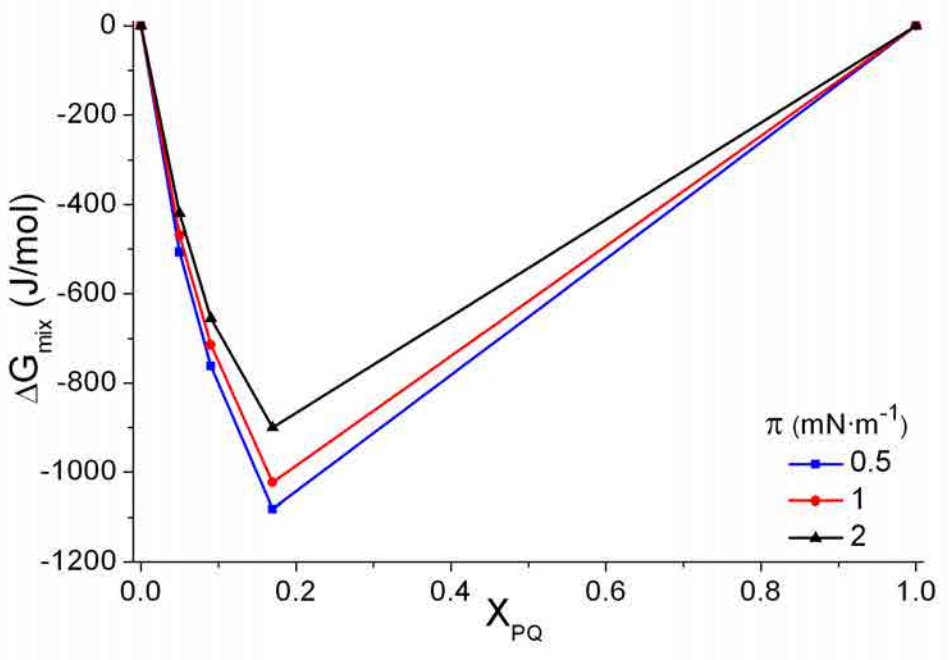

Figure 5.9.6. Plot of the mixing energy vs. the molar fraction for MGDG, PQ and MGDG:PQ mixtures at several surface pressures before the main PQ expulsion.

The formation of non-ideal mixtures between PQ and MGDG at low surface pressure, as it was observed in the MGDG:UQ system (Section 5.8.2), is explained by the difference in the chain length between PQ and MGDG which permits a free rotation of the PQ part that protrudes over the MGDG producing also a motion of the MGDG molecules which induces an increase of the molecular area [6,38].

5.9.4 AFM

In this part we present the topographic images of the selected MGDG:PQ mixtures at several surface pressures to light which is the organization of these molecules once transferred to an hydrophilic substrate (mica) and ultimately, correlate this knowledge with the predicted results in previous sections. The description and discussion of the AFM topographic images for the pure components MGDG and PQ are explained in section 5.4.2 and 5.2.2 respectively. So that, we present in this section only the results of the mixtures and their corresponding discussion.

Figure 5.9.7 shows the AFM topographic images corresponding to pure MGDG and the selected MGDG:PQ mixtures transferred on mica at π = 15 $mN \cdot m^{-1}$. The selection of π = 15 $mN \cdot m^{-1}$ has been done to confirm that PQ is still present in the monolayer of the MGDG:PQ mixture, showing large differences according to the PQ content. The images A-D show two different tonalities of brown (fair and dark) and both correspond to the MGDG or MGDG:PQ monolayer, being each tonality correlated with a different physical state of the system monolayer. Moreover, the images A-D show that the size of the dark zones is accorded to the PQ content.

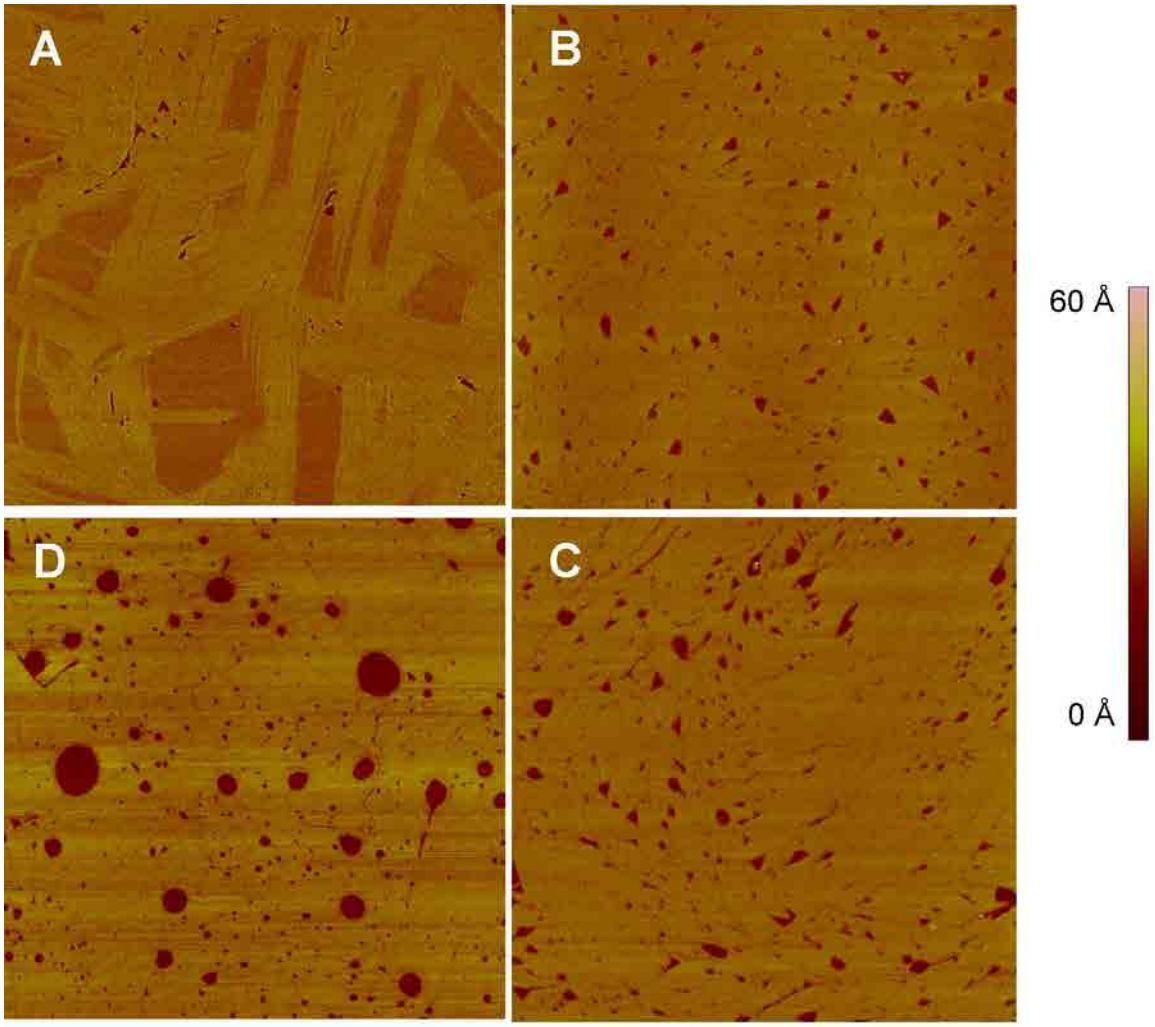

Figure 5.9.7. AFM images (5μm x 5μm) for LB films transferred on mica at 21ºC at π = 15 mN·m^{-1} for (A) pure MGDG and MGDG:PQ systems (B) 20:1, (C) 10:1, (D) 5:1.

In order to explain the behaviour of the MGDG:PQ mixtures at several surface pressures, we have selected the 5:1 ratio (Figure 5.9.8) due to it is the most different from the pure MGDG (Figure 5.4.2) of the ratios we have studied and it represents the best option to compare them. As it has been explained for pure MGDG, MGDG:PQ 5:1 presents two different tonalities of brown (fair and dark) and each one corresponds to zones with a different order of the molecules. Moreover, it is interesting to point that at π = 1 mN·m^{-1} and only for the 5:1 ratio, the image presents black zones which corresponds to the mica surface (See inset in Figure 5.9.8A). The compression leads to a more compact fashion of the more ordered zones till π = 33 mN·m^{-1} where practically all the monolayer is compact remaining only small rounded zones with the molecules in a less ordered state. On the other hand, AFM topographic images have been performed with the systems MGDG:PQ 10:1

and 20:1 (not shown) obtaining a behaviour comprised between the pure MGDG (Figure 5.4.2) and the MGDG:PQ 5:1 (Figure 5.9.8), so only the images corresponding to π = 15 $mN \cdot m^{-1}$ for MGDG:UQ 10:1 and 20:1 are presented (Figure 5.9.7).

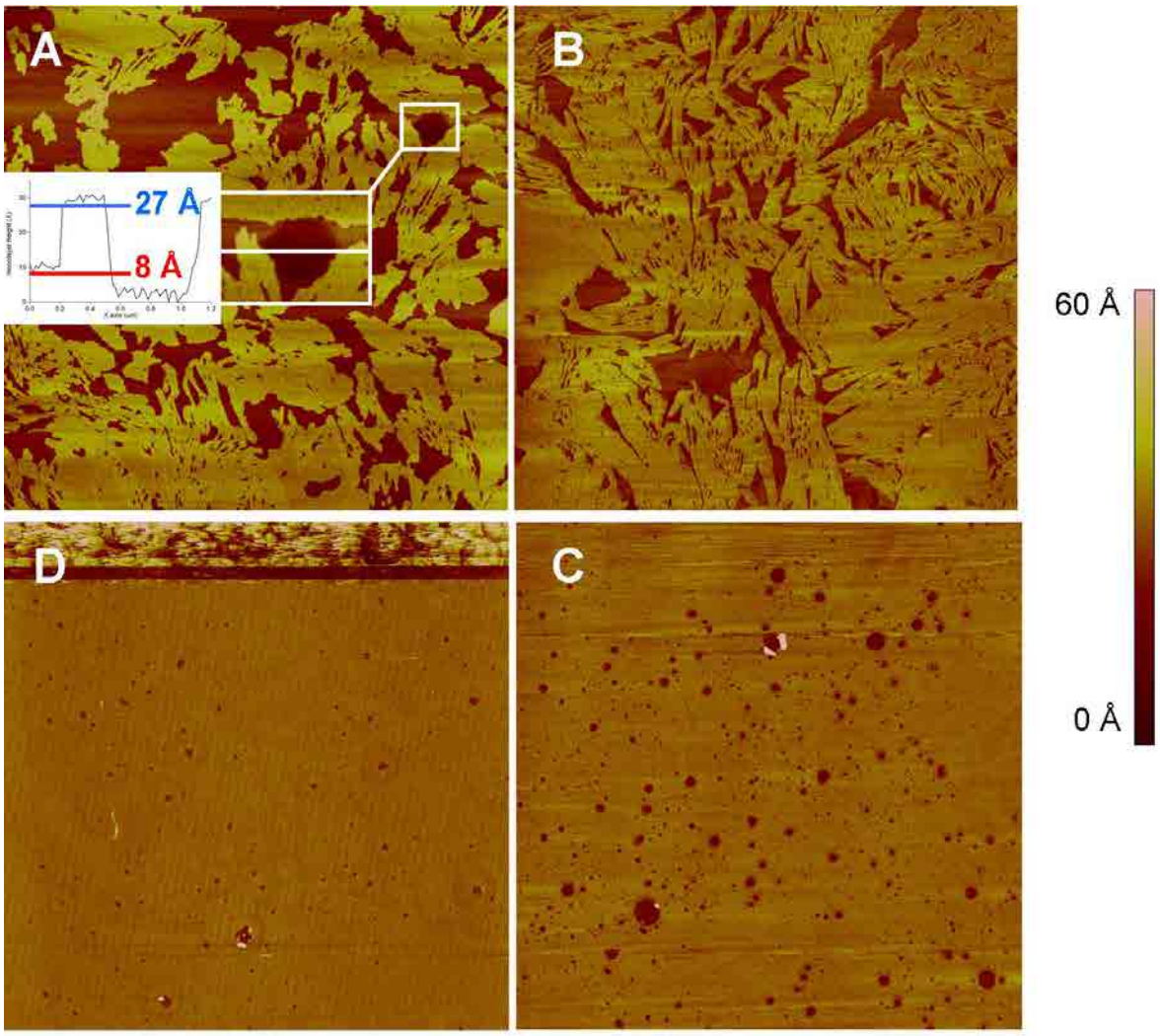

5.9.8. AFM images (10µm x 10µm) for LB films of MGDG:PQ 5:1 system transferred on mica at 21ºC at (A) π = 1 $mN \cdot m^{-1}$, (B) π = 3 $mN \cdot m^{-1}$, (C) π = 15 $mN \cdot m^{-1}$, (D) π = 33 $mN \cdot m^{-1}$.

AFM discussion

As it has been explained for pure MGDG (Section 5.4.2), each brown tonality indicates a different tilt order of the molecules that depends on the surface pressure and the interactions established between molecules and between the molecules with the substrate. The appearance simultaneously of zones with a high order (fair brown zones) with zones of low order (dark brown zones) in pure MGDG indicates that the meaning of the tonalities is also

the same for the mixtures. On the other hand, it seems clear that the physical states deduced using the C_s^{-1} curves for pure MGDG are more ordered than the corresponding to MGDG:PQ at the same surface pressure, so that, the different tonalities are correlated with different ordering state but the order that represents each tonality depends on the PQ presence. In order to light each physical state, we have measured the relative height between fair and dark zones, and assuming the height of 6 ± 2 Å for the dark brown zones referred to the mica surface, the absolute height is presented in Table 5.9.2. The selection of this height value for the dark zones is done based on that this is the height measured between the dark brown zones and the black zones seen at low surface pressure for the MGDG:PQ 5:1 system (Inset of Figure 5.9.8A) and, moreover, this height is in accordance with the 3-6 Å observed in the literature for the LE state of DPPC monolayers [53,54]. The absolute heights obtained at each surface pressure and considering the C_s^{-1} results permit the obtaining of the physical state corresponding to each tonality for all the systems (Table 5.9.3) where LC1 and LC2 have the meaning explained for pure MGDG (see Section 5.4.2).

Table 5.9.2. Height of each physical state for the LB monolayers of MGDG and MGDG:PQ mixtures on mica. *Estimated value (more information in the text).

	LE	LC1	LC2	S
MGDG	6 ± 2 *	21 ± 2	25 ± 2	27 ± 2
MGDG:PQ 20:1	6 ± 2 *	20 ± 2	24 ± 2	
MGDG:PQ 10:1	6 ± 2 *	22 ± 2	26 ± 2	
MGDG:PQ 5:1	6 ± 2	24 ± 2	26 ± 2	

Table 5.9.3. Physical states of each zone (dark and fair brown) corresponding to the MGDG and MGDG:PQ systems at several surface pressures.

	MGDG			MGDG:PQ 20:1		MGDG:PQ 10:1		MGDG:PQ 5:1	
π ($mN \cdot m^{-1}$)	Dark	Fair	π ($mN \cdot m^{-1}$)	Dark	Fair	Dark	Fair	Dark	Fair
6	LE	LC2	1	LE	LC2	LE	LC1	LE	LC1
15	LC1	LC2	3	LE	LC2	LE	LC2	LE	LC2
25	LC2	S	15	LE	LC2	LE	LC2	LE	LC2
40		S	33	LC1	LC2	LE	LC2	LE	LC2

The MGDG and MGDG:PQ mixtures monolayers cover the entire mica surface at all the studied surface pressures, except for the explained case of MGDG:PQ 5:1 at π = 1 mN·m^{-1}. The non-observation of uncovered mica zones permits obtaining the proportion of each physical state. The Figure 5.9.9 presents the percentage of the monolayer in fair brown, so that, according to the Table 5.9.3, the proportion of each physical state can be elucidated. For the particular case of MGDG:PQ 5:1 at π = 1 mN·m^{-1}, the result shown is also the fair brown zones but the complementary value indicates the area occupied for both the LE zones and the uncovered regions.

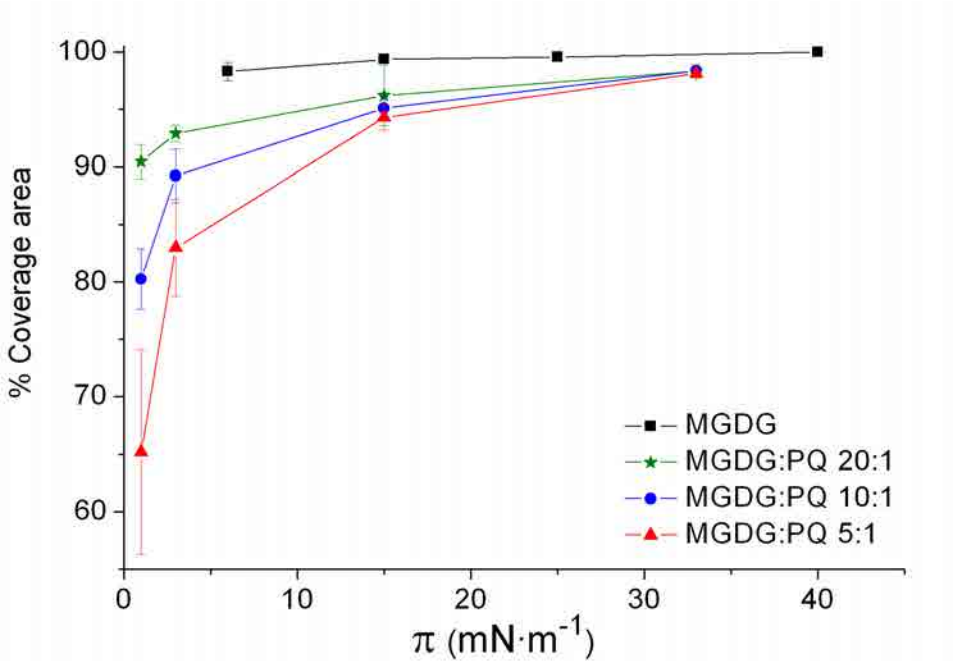

Figure 5.9.9. Monolayer coverage of the fair brown zones on the mica surface for the pure MGDG and the MGDG:PQ mixtures, calculated from AFM images.

The results obtained in Figure 5.9.9 for the MGDG:PQ systems show the expected trend of more surface covered by the compact state when decreasing the PQ content. The reason for this behaviour is that the reduced presence of PQ enhances the ordering of the MGDG molecules. Increasing the surface pressure all the MGDG:PQ systems increases the ratio of LC zones achieving at π = 15 mN·m^{-1} a nearly flat increase which is correlated with that the major content of PQ has been rejected from the lipid matrix. On the other hand, pure MGDG presents a nearly flat increase of the area covered by the more compact phase when increasing the surface pressure. The explanation is the quick transformation of the LE or LC1 state in LC2 which leads that the entire monolayer is in a high ordered state at 15 mN·m^{-1}.

The simultaneous presence of two different physical states at each surface pressure for both the MGDG and MGDG:PQ systems indicates that both systems presents a physical state change that implies the coexistence, from low surface pressure, of zones with low and high order of molecules (See Table 5.9.3). The pure MGDG system achieves the S state (Table 5.9.3) whereas the MGDG:PQ mixtures present LC2 at the most compact state, which is explained by the presence of PQ in the MGDG:PQ mixtures hindrances the packing of the MGDG molecules. At the same surface pressure, the MGDG presents similar or higher ordered state for the fair zones than the MGDG:PQ mixtures (See Table 5.9.3) which indicates that part of the PQ is in the LC domains. A similar behaviour is observed for the dark zones, which also indicates the presence of PQ in the LE state. These observations indicates that PQ is present in both physical states of the MGDG:PQ mixtures and the higher affinity of the PQ for the LE state points the formation of MGDG:PQ domains (LC2 zones) with low PQ content and MGDG:PQ domains with high PQ content (LE zones forming PQ enriched domains). On the other hand, the height observed for the fair zones of the MGDG:PQ 20:1 and 10:1, in addition to the to proximity to the C_s^{-1} values for LC-S change (Section 5.9.1), indicate that these mixtures are still in the LC state.

5.9.5 Electrochemical behaviour

In this section, the electrochemical behaviour of the ITO-MGDG:PQ/electrolyte system and its mathematical treatment are presented. On the other hand, the results and their corresponding discussion of the pure components MGDG and PQ are exposed in sections 5.4.3 and 5.2.3 respectively, so that, they will be only presented in this section in case it is necessary to compare with the mixtures results. In our experiments, three CVs are required to obtain the stationary state in the electrochemical response, presenting a good reproducibility from the third scan and at least 15 cycles.

Figure 5.9.10 and 5.9.11 present the cyclic voltammograms at 10 $mV \cdot s^{-1}$ of the ITO-MGDG:PQ/electrolyte 5:1 and 10:1 systems respectively, transferred on ITO at several surface pressures which, in part, are the same that were selected for topographic AFM imaging on mica.

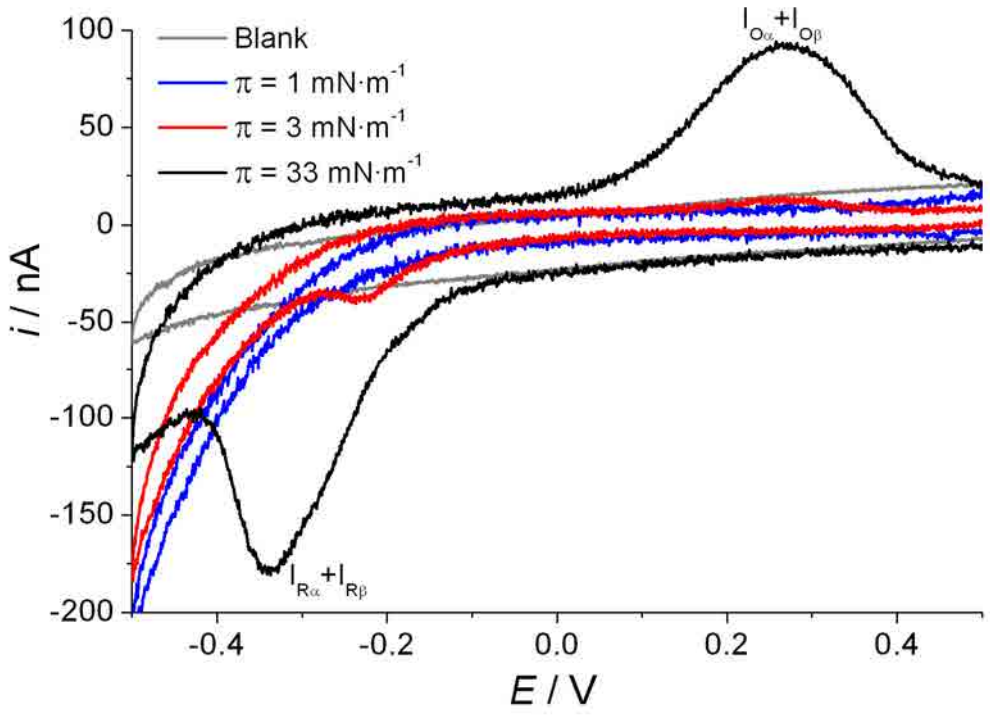

Figure 5.9.10. CV of ITO-MGDG:PQ 5:1 LB films transferred at several surface pressures. Blank line represents CV of the ITO-MGDG/electrolyte electrode. All CVs have been performed using 0.150 M of KCl electrochemical cell and a potassium phosphate buffered solution at pH 7.4 and at a scan rate of 10 $mV \cdot s^{-1}$.

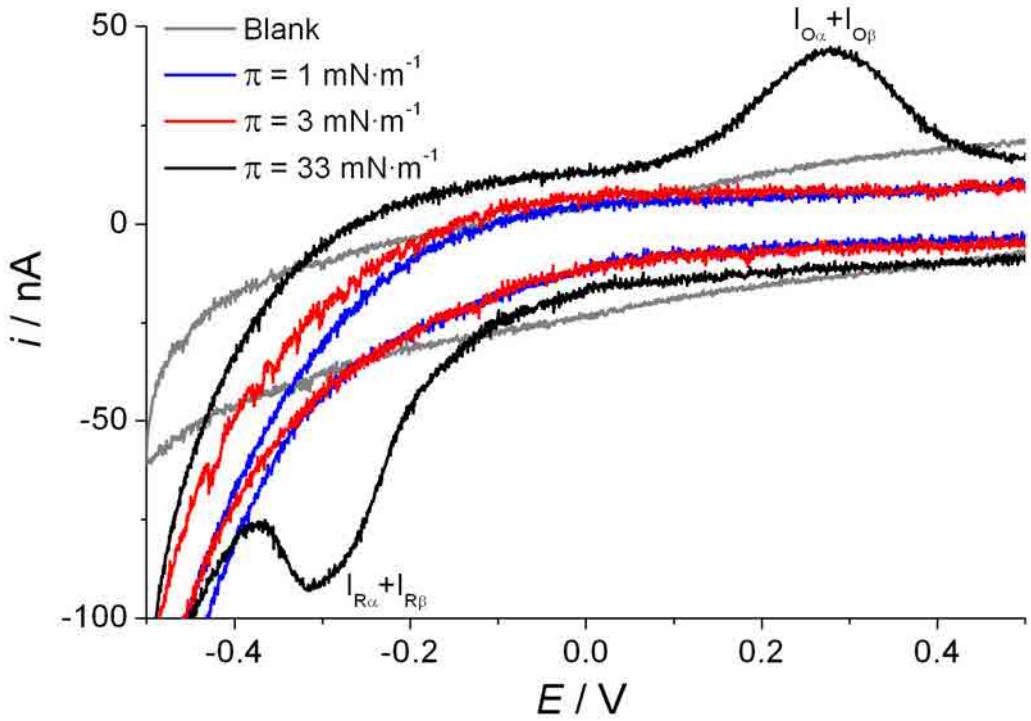

Figure 5.9.11. CV of ITO-MGDG:PQ 10:1 LB films transferred at several surface pressures. Blank line represents the CV of ITO-MGDG electrode. All CVs have been performed using 0.150 M of KCl electrochemical cell and a potassium phosphate buffered solution at pH 7.4, at a scan rate of 10 $mV \cdot s^{-1}$.

Both ITO-MGDG:PQ/electrolyte 5:1 and 10:1 systems present only one reduction and one oxidation wave. For the ITO-MGDG:PQ/electrolyte 5:1 system the reduction and oxidation waves are visible at surface pressures 3 and 33 $mN \cdot m^{-1}$, whereas for the system ITO-MGDG:PQ/electrolyte 10:1, they are observed only at π = 33 $mN \cdot m^{-1}$. The shape and width of the peaks obtained at π = 33 $mN \cdot m^{-1}$ suggest that each wave convolute more than one redox process. On the other hand, the main difference between the MGDG:UQ and the MGDG:PQ systems are the non-appearance of process II in the later, even at high surface pressure.

In order to gain more information about the system, voltammograms at different scan rates have been performed and Figure 5.9.12 shows the cyclic voltammograms of the ITO-MGDG:PQ/electrolyte 5:1 and 10:1 systems on ITO for π = 33 $mN \cdot m^{-1}$ and ITO-PQ/electrolyte system at π = 2 $mN \cdot m^{-1}$, being all experiments scanned at 200 $mV \cdot s^{-1}$. The increase of the scan rate allows a better sight of the presence of two reduction peaks in the cathodic scan for the ITO-MGDG:PQ/electrolyte mixtures which, comparing with the response of the ITO-PQ/electrolyte system, are labelled as $I_{R\alpha}$ and $I_{R\beta}$ in all Figures 5.9.10-5.9.12. In the anodic scan the peak becomes wider indicating also the presence of two peaks. The deconvolution of the peaks is presented only for Figure 5.9.12 where the peak separation is mathematically reliable. On the other hand, the inset of Figure 5.9.12 shows process I at 10 $mV \cdot s^{-1}$ for ITO-PQ/electrolyte system transferred at π = 2 $mN \cdot m^{-1}$ (on the collapse), and ITO-MGDG:PQ/electrolyte 5:1 and 10:1 systems at π = 33 $mN \cdot m^{-1}$ which permit to compare these systems at low scan rate. The figure shows that the position of $I_{R\alpha}$ and $I_{O\alpha}$ are similar regardless being the ITO-PQ or the ITO-MGDG:PQ systems. The Table 5.9.4 presents the peak and formal potentials for the redox process $I_\alpha + I_\beta$ of ITO-MGDG:PQ/electrolyte 5:1 and 10:1 system. The Figure 5.9.12 also confirms that the ITO-MGDG:PQ/electrolyte system does not show the process II observed for the ITO-MGDG:UQ/electrolyte 5:1 system even working at high scan rate. In this figure, the scan rate is increased in such way that the hydrogen evolution present in all the voltammograms at all compositions starts at more negative potentials than at 10 $mV \cdot s^{-1}$, indicating that this evolution is a quite slower process than process I_α and I_β. On the other hand, it is also interesting to observe that the double layer capacity of the ITO-MGDG/electrolyte experiments is fitted in the capacitive current of the ITO-MGDG:PQ/electrolyte systems (See Blank line in Figures 5.9.10 and 5.9.11).

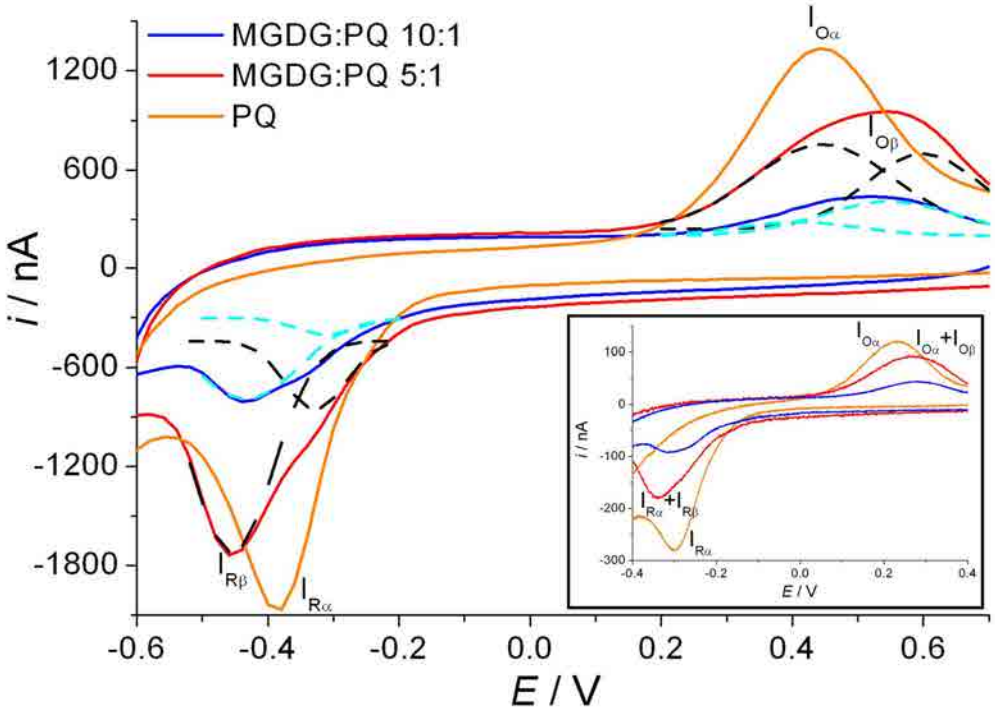

Figure 5.9.12. Cyclic voltammograms of ITO-MGDG:PQ/electrolyte 5:1 and 10:1 LB films transferred at π = 33 mN·m^{-1} and ITO-PQ/electrolyte system at π = 2 mN·m^{-1} all of them scanned at 200 mV·s^{-1}. Dashed black and light blue lines correspond to the deconvolution of I_α and I_β in the CVs of the ITO-MGDG:PQ/electrolyte 5:1 and 10:1 respectively. Inset presents the cyclic voltammograms of the same systems in a shorter potential window and at 10 mV·s^{-1}. All CVs have been performed using 0.150 M of KCl electrochemical cell and a potassium phosphate buffered solution at pH 7.4.

Table 5.9.4. Peak potentials and formal potentials for the redox process $I_\alpha + I_\beta$ of ITO-MGDG:PQ/electrolyte 5:1 and 10:1 system.

π (mN·m^{-1})	E_{pR} (I_α+ I_β) (V)	E_{pO} (I_α+ I_β) (V)	E_f (I_α+ I_β) (V)
ITO-MGDG:PQ/electrolyte 5:1			
3	-0.23 ± 0.02	0.25 ± 0.02	0.01 ± 0.02
33	-0.34 ± 0.02	0.26 ± 0.02	-0.04 ± 0.02
ITO-MGDG:PQ/electrolyte 10:1			
33	-0.31 ± 0.02	0.29 ± 0.02	-0.01 ± 0.02

Discussion of the electrochemical response of the ITO-MGDG:PQ/electrolyte system

We understand that the global reaction and the mechanism proposed for pure PQ in confined situation (Section 5.2.3) is the same for the PQ of the ITO-MGDG:PQ/electrolyte system. The shape of the voltammograms for the ITO-MGDG:PQ/electrolyte systems presents two important deviations respect to the theoretical models proposed in the literature to describe the cyclic voltammetric response of a surface confined reaction [29-31]. First, the peak shape which is not symmetrical, presenting the reduction peak a sharper shape than the oxidation one, a similar situation that it was observed by Märtensson and Agmo [32] and Hong and Park [22] studying other quinones. Second, the redox peaks separation is larger than the expected for such systems.

The different shape of reduction and oxidation peaks can be explained by the different hydrophilic character of the redox couple PQ/PQH_2 as it was pointed for the ITO-PQ system (Section 5.2.3). The larger polarity of PQH_2 compared with PQ leads the former to establish better attractive interactions by dipole-dipole or hydrogen bond between PQH_2 and MGDG headgroups and, in addition, the PQH_2-ITO, PQH_2-PQH_2 and PQH_2-water interactions are also enhanced [4,25-27,32-38,84,85,93] . During the oxidation scan PQH_2 is the reactant so the possibilities of hydrogen bonds are larger, increasing the stabilization of the PQH_2 molecule and making it more difficult to oxidise. These arguments are also valid for explaining the larger width of the oxidation peak compared with that of the reduction process.

The Figure 5.9.13A presents the redox waves potentials vs. the scan rate at low scan rates (< 20 mV·s^{-1}) only for the MGDG:PQ 5:1 at $\pi = 3$ mN·m^{-1} due to the absence of peaks or the impossibility of a reliable redox peaks deconvolution. On the other hand, the Figure 5.9.13B presents the redox peaks potentials once deconvoluted. At $\pi = 3$ mN·m^{-1}, despite of the increase of the scan rate, only one process labelled as I_α is obtained. At $\pi = 33$ mN·m^{-1}, Figure 5.9.13B shows that the redox peaks separation for process I_β is larger than for process I_α indicating that process I_β is even more irreversible than process I_α. Moreover, the redox peaks separation for the ITO-MGDG:PQ/electrolyte 5:1 system, for both processes I_α and I_β is enhanced when increasing the scan rate and similar behaviour is observed for the ITO-MGDG:PQ/electrolyte 10:1 system (not shown). This separation makes both processes (I_α and I_β) more irreversible, that represents a similar trend to that it was observed by

Marchal et al. [21] and by Laval and Majda [41]. This large separation for both processes aroused from the slow charge transfer rates at ITO-monolayer|electrolyte interface [32].

In addition, it can be also inferred from Figure 5.9.13 that the increase in the scan rate affects in a larger extent the oxidation peak potential than the reduction one, which produces that the midpoint potential for processes I_α and I_β has scan rate dependence. On the other hand, it is interesting to observe that all the linear adjustments of the processes I_α and I_β reduction peaks for the ITO-MGDG:PQ/electrolyte 5:1 system (Figure 5.9.13 B) have a similar slope and similar trend is shown for the oxidation peaks of the same processes. However, the y-intercept of the linear adjustment of the reduction peaks is displaced to more cathodic values when increasing the surface pressure and similar occurs with the y-intercept of the linear adjustment of the oxidation peaks that are displaced to more anodic values. This displacement can be explained by the existence of a different environment around the PQ head. The values of E_f (I) shown in Table 5.9.4, have been experimentally calculated at low scan rates for the convoluted I_α+I_β waves. The process I_α is favourable at low surface pressures or at low PQ content, and process I_β is favoured when increasing the PQ concentration, regardless by increasing the surface pressure or the initial PQ content. Moreover, the figure has been separated in low and high scan rates because at low scan rates (< 20 $mV \cdot s^{-1}$) the linear adjustments of the reduction and oxidation peak potentials of process I_α presents a higher slope (Figure 5.9.13A) than at high scan rates (Figure 5.8.13B), which is explained by the hindrance increase of the electrochemical process when increasing the scan rate. The trend observed for process I_α of the MGDG:PQ/electrolyte 5:1 system can not be compared with the 10:1 system or the I_β process due to the absence of redox peaks.

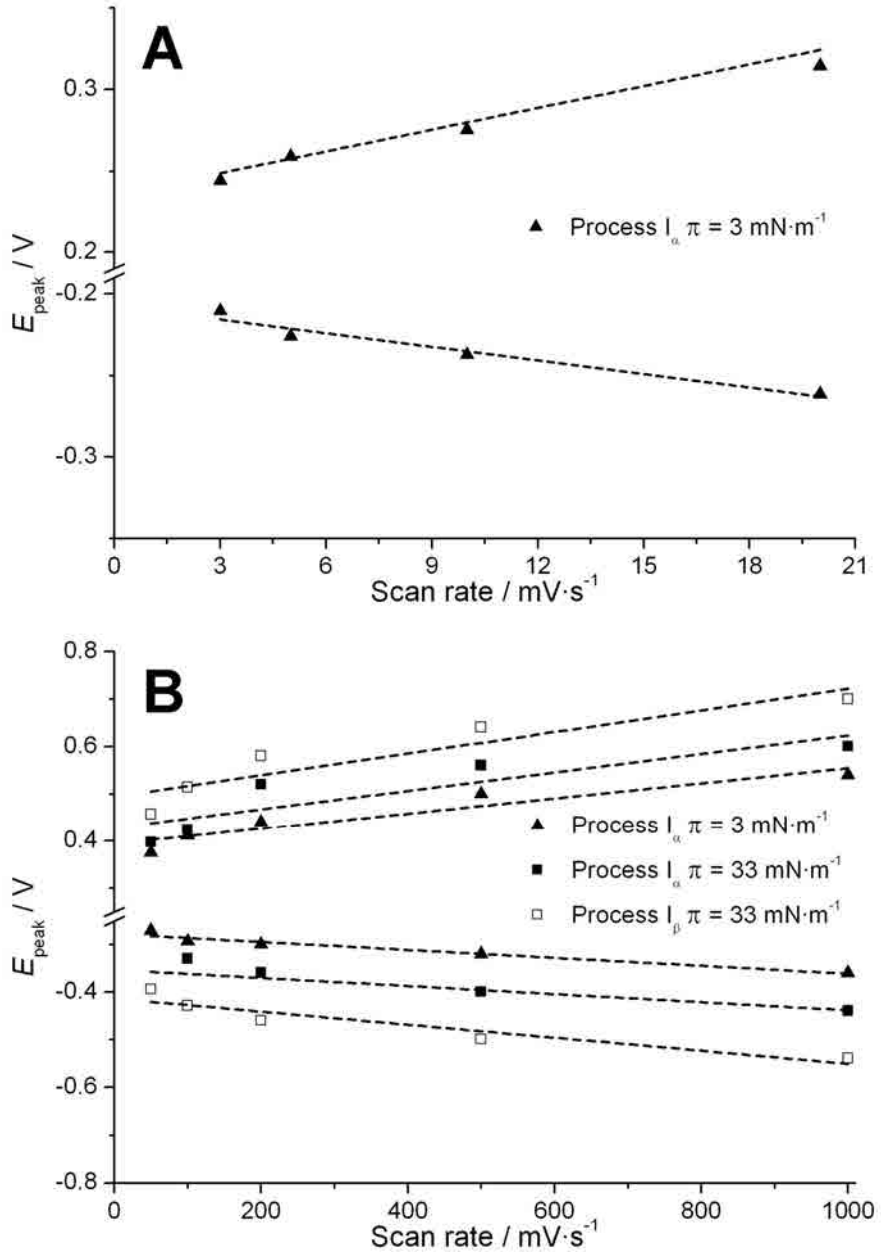

Figure 5.9.13. Peak potential vs. the scan rate for the ITO-MGDG:PQ 5:1/electrolyte system at π = 3 and 33 mN·m^{-1} at A) low scan rates and B) high scan rates.

Moreover, the current intensity of the redox peaks (i_{peak}) has been studied for the ITO-MGDG:PQ /electrolyte 5:1 system at several scan rates and it has been shown that the reduction (not shown) and the oxidation current intensity are related by a linear dependence with the scan rate (Figure 5.8.14), so indicating that UQ molecules are surface confined in all the processes [16,29] and that the electron transfer process is not diffusion controlled. These observations are also valid for ITO-MGDG:PQ/electrolyte 10:1 (not shown). Our

results are in line with the observations of Märtensson and Agmo [32] for scan rates < 1 $V \cdot s^{-1}$, Gordillo and Schiffrin [28] and Li et al. [43] for monolayers containing UQ confined on the electrode surface.

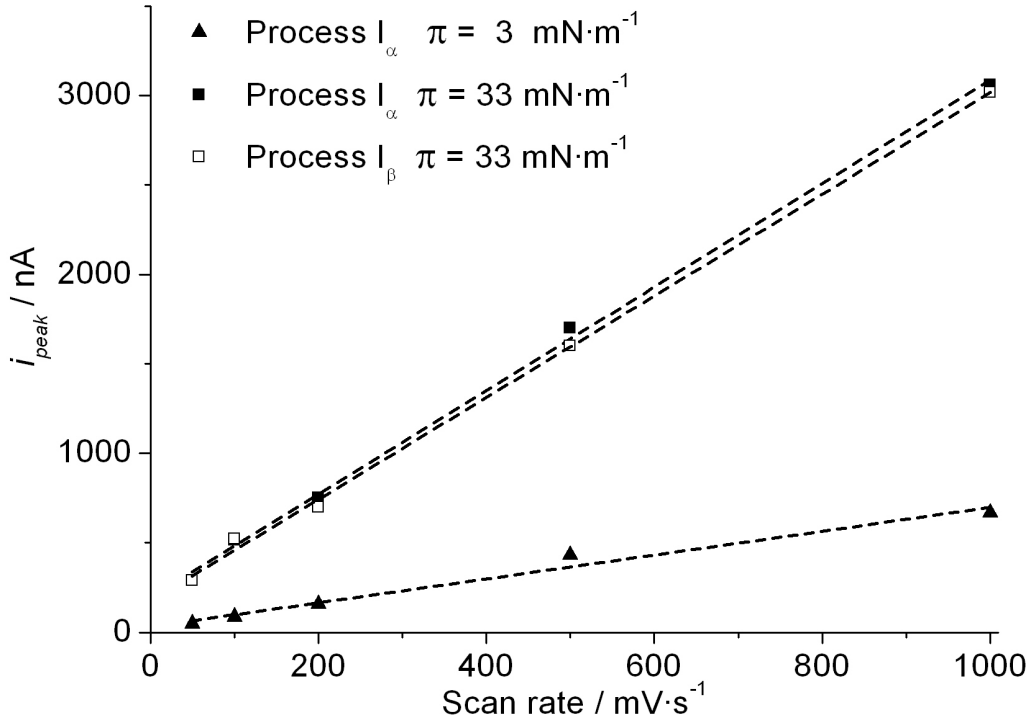

Figure 5.9.14. Oxidation peak intensity vs. the scan rate for the ITO-MGDG:PQ 5:1/electrolyte system at several surface pressures.

The charge involved in the LB monolayer transferred at each surface pressure is obtained by integrating the area under the reduction or oxidation waves. The surface coverage (Γ) is obtained from the experimental values of charge and considering the global reaction for PQ in confined situation (Section 5.2.3). The Γ for the ITO-MGDG:PQ/electrolyte system is shown in Table 5.9.5 and compared with the expected value to obtain the electroactive fraction of PQ. The expected surface coverage (Γ_{expec}) values are calculated assuming that PQ and MGDG molecules are perfectly spread on the ITO surface, accordingly to the corresponding ratio, being the resulting value corrected with the transfer ratio associated to it in the LB transfer process. We have chosen to show in Table 5.9.5 the oxidation surface coverage (Γ_O) of the redox processes which are similar but lower than the results obtained for the reduction scan which have the undesirable contribution of hydrogen evolution.

Table 5.9.5. Expected (Γ_{expec}) and experimental total oxidation ($\Gamma_{O\,tot}$) surface coverage and electroactive fraction involved in the whole redox process for ITO-MGDG:PQ/electrolyte system using 0.150 M of KCl electrochemical cell, with potassium phosphate buffered solution at pH 7.4 and at a scan rate of 10 $mV \cdot s^{-1}$.

π ($mN \cdot m^{-1}$)	Γ_{expec} (10^{-12} mol · cm^{-2})	$\Gamma_{O\,tot}$ (10^{-12} mol · cm^{-2})	Electroactive fraction (%)
ITO-MGDG:PQ/electrolyte 5:1			
3	22.1	1.3	5.9
33	46.1	23	49.9
ITO-MGDG:PQ/electrolyte 10:1			
33	25.8	7.5	29.2

The Table 5.9.5 shows that an increase in the initial PQ content in the ITO-MGDG:PQ/electrolyte systems leads to an increase of the electroactive fraction. Our results contrast with the observations of Moncelli et al. [19] who observed a decrease in the Γ_{Otot} when increasing the initial UQ content from 0.5 to 2 % on a monolayer of DOPC on HDME at pH 9.5. This different behaviour is explained by the differences in pH. Moncelli et al. [15,19] worked with pH 9.5 so the availability of protons in the proximity of the UQ heads is more limited than in our experiments at pH 7.4. The lack of protons affects the reduction rate determining step (1_b) (See Section 5.2.3) so at high PQ concentrations or high scan rates, the step 1_b is not completed so the electroactive fraction is reduced. In our experiments the enough presence of available protons close to the PQ heads avoids the high local PQ concentration problem. The fact that the electroactive fraction is enhanced when increasing the initial PQ content is explained by the electron hopping effect (See Section 3.4.5). Moreover, the non homogeneous electrode surface and the semiconductive properties of ITO induce it to behave different than metal surfaces like gold or mercury contributing with the different environments that PQ head experiences in the chain region [41] to reduce the electroactive fraction [9].

The explanations given in Section 5.9.5 when comparing our ITO-MGDG:UQ/electrolyte system with the literature, are also valid for the ITO-MGDG:PQ/electrolyte due to the similarities between PQ and UQ induces a similar formal potential for process $I_\alpha + I_\beta$ in the experimental conditions, as it has been shown in Sections 5.8.5 and 5.9.5. The slight differences observed between the literature for UQ and our results for PQ are related with the differences between both prenylquinones, the physicochemical properties of the substrate, the differences on the electrolyte solution and the differences in the distance

prenylquinone head-substrate surface. All the formal potential observed by previous authors for the quinone redox process are less thermodynamically favourable than that observed in this work which is correlated with the higher availability of protons in our system. The processes I_α and I_β observed in our experiments requires, respectively, direct contact or short distance between ITO and the PQ head, which can be correlated with the exposed situations [21,23,41,86].

5.9.6 Global sight of the MGDG:PQ system transferred on ITO using the LB technique

In this section we explain the global behaviour of the MGDG:PQ system and the position of the PQ molecules in the monolayer studying the results obtained from the used techniques.

The separation maintained between pure MGDG and the MGDG:PQ mixtures both in π-A isotherms and C_s^{-1} curves after the main PQ expulsion indicate that PQ is, even at high surface pressures, present in the matrix of MGDG:PQ ("diving" position, see Section 3.4.2), and it leads to less compact physical states. The shape of the π-A isotherms, the shape of the C_s^{-1} curves and the shape of the kink point in the C_s^{-1} curves, in addition to the separation observed, suggest that the system experiences a sudden PQ expulsion followed by a gradual expelling.

A complete vision of the PQ positions in the MGDG:PQ monolayer can be obtained considering the thermodynamic description of the physical states, the AFM results of the MGDG:PQ 5:1 system on mica (Figure 5.9.8) and the CVs of Figures 5.9.10-5.9.12. Therefore, these PQ positions will be extrapolated to all the ITO-MGDG:PQ systems. The MGDG:PQ mixtures at low surface pressure, present less covered area by the LC state when increasing the PQ initial content (Figure 5.9.9). In addition, the height measured for the most compact state of pure MGDG is higher than that of the MGDG:PQ mixtures. These observations indicate that PQ is present in both physical states (LE and LC) of the MGDG:PQ mixtures. The monolayer of MGDG:PQ 5:1 at π = 1 $mN \cdot m^{-1}$ is especially interesting due to the low surface pressure, the large zones occupied by LE and the high PQ

content compared with the other ratios used, lead the LE to be non-uniform leaving some pinholes that arrive to the mica surface (Figure 5.9.8A inset).

At π = 1 mN·m^{-1}, the CVs of Figures 5.9.10 and 5.9.11 do not show voltammetric response. At π = 3 mN·m^{-1} only the redox process I_α is obtained for the ITO-MGDG:PQ/electrolyte 5:1 system and at π = 33 mN·m^{-1} a convolution of processes I_α and I_β is obtained either for the ITO-MGDG:PQ/electrolyte 5:1 or 10:1 system. At low surface pressures, regardless the MGDG:PQ domains are in LE or LC state (Figure 5.9.8B), we correlate the process I_α with "diving" position [4,15, 36,88-95] with the PQ placed in the MGDG matrix and located in direct contact with the electrode surface.

The compression of the explained monolayer induces two actions: First, the compactness of the LC2 state, so favouring the rejection of part of the PQ in "diving" position. On the one hand, it can be vertically rejected to the diving position without ITO-PQ contact and, on the other hand, horizontally to the remaining LE zones so enriching them in PQ. Second, the phase change from LE to LC2 of the remaining LE zones (Figure 5.9.8 C). The presence of enriched domains is predictable based on the Van Dijck et al. [105] observations for saturated phospholipids with the same headgroup and others studies presented in the literature [27,35,36,41,93,95,98,106,107], which we relate with the presence of small LE zones in Figure 5.9.8C and D in circular shape which is the shape adopted by the monolayers to minimize the surface tension of the nascent boundary when lipid reorientate in the layer boundaries [118], and they may indicate that the composition in and out the rounded shape are different. These observations suggest that, when changing from LE to LC, the lateral rejection is favoured placing most of the PQ molecules in the "diving" position in the LE zones. In addition, the fast change LE to LC physical state entraps the PQ molecules in "diving" position in the MGDG matrix, favouring the diving position without ITO-PQ contact but close to the ITO surface and forbidding the swimming position. Therefore, the "diving" position comprises two redox processes I_α and I_β corresponding respectively to the PQ molecules in direct contact and the PQ molecules close to the ITO surface. The difficult deconvolution of these peaks in the ITO-MGDG:PQ/electrolyte system, even at high scan rate, indicates that both peaks are close each other, suggesting slight changes in the environment that the PQ molecules experience at each position, being the process I_α favoured at low surface pressure. Further compression

results in a more compact LC2 state with lower proportion covered areas by the LE state (Figure 5.9.8D). However, the redox peaks corresponding to the “swimming” position are not observed for the ITO-MGDG:PQ/electrolyte system, even at high scan rate. Therefore, the PQ molecules forming pools in the LE zones are predominant, which we relate with the difficulty on performing topographic images on tapping mode at high surface pressures.

Our results confirm that PQ is confined on the electrode surface and the electron transfer takes place mainly by two mechanisms: First, by direct transfer and electron hopping between the PQ placed in “diving” position with ITO-PQ contact (process I_α), and second, by electron hopping through the lipid matrix (process I_β) to the PQ molecules in “diving” position without ITO-PQ contact. The electron hopping favours the rate determining step (1_b) (Section 5.2.3) so favouring the electroreduction in the timescale used. At low surface pressure the molecules are far enough each other to do not be affected by the electron hopping mechanism. Increasing the surface pressure the PQ headgroups are placed closer favouring the electron hopping redox process.

In order to clarify the position and organization of the MGDG and PQ molecules at each physical state the Figure 5.9.15 represents the position of MGDG and PQ molecules of the MGDG:PQ 5:1 system at the studied surface pressures. This Figure 5.9.15 explains the different meaning of the fair and dark colours observed in the AFM images summarized in Table 5.8.3 and the PQ positions that origin the redox processes I_α and I_β.

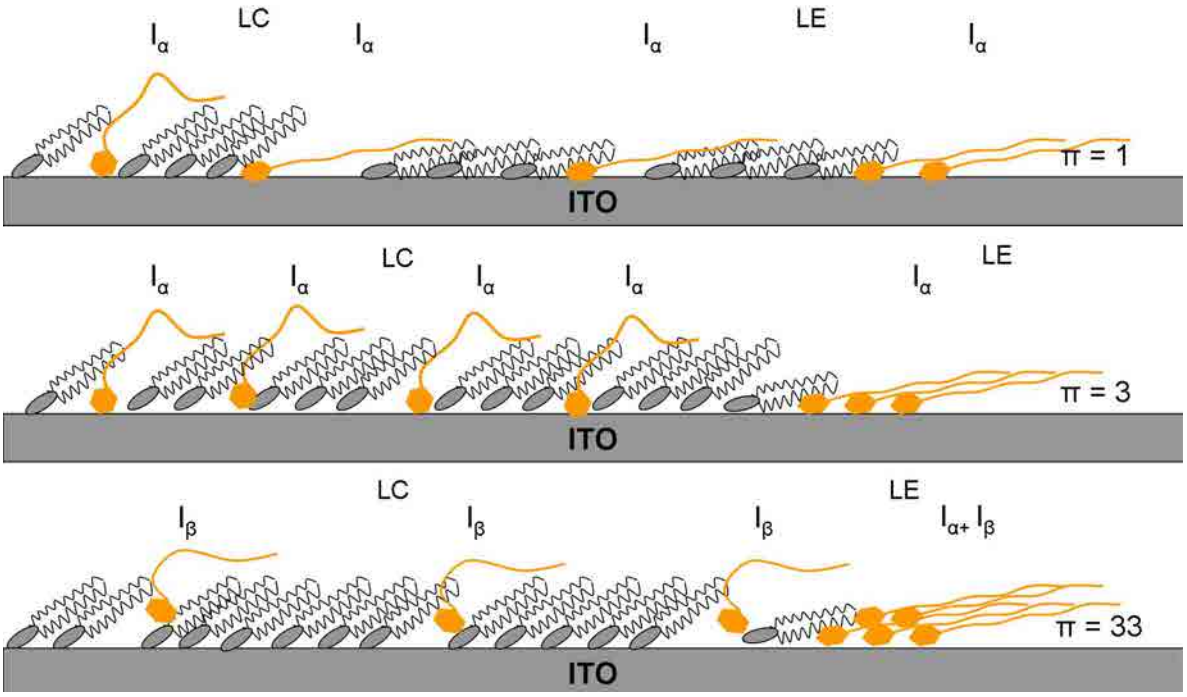

Figure 5.9.15. Scheme of the position of MGDG and PQ molecules of the MGDG:PQ 5:1 system at several surface pressures. The labels I_α and I_β indicate the PQ positions that origin the redox processes I_α and I_β.

5.10 DGDG:PQ

5.10.1 π-A isotherms and physical states

The π-A isotherms of the DGDG:PQ system at biological relevant ratios are presented in Figure 5.10.1 referred to the DGDG area per molecule. The C_s^{-1} curves (Figure 5.10.2) corresponding to the described π-A isotherms (Figure 5.10.1) are calculated according to the Expression 2.9. The most significant values of Figures 5.10.1 and 5.10.2 are summarized in Table 5.10.1. The usual representation of isotherms corresponding to binary mixtures is the π vs. mean area per molecule, being each isotherm referred to the weighted (mean) area per molecule according to the DGDG:PQ ratio. In the present case, we have discarded this kind of representation due to PQ is mostly expelled from the lipid matrix at low surface pressures (as it will be commented in this section). This kind of representation of the DGDG:PQ system above the main expulsion has non-sense and distorts the global sight. The description and discussion of the π-A isotherms and the C_s^{-1} results for the DGDG and PQ pure components were explained in Section 5.5.1 and 5.2.1 respectively. So that, we present in this section only the results of the mixtures and their corresponding discussion.

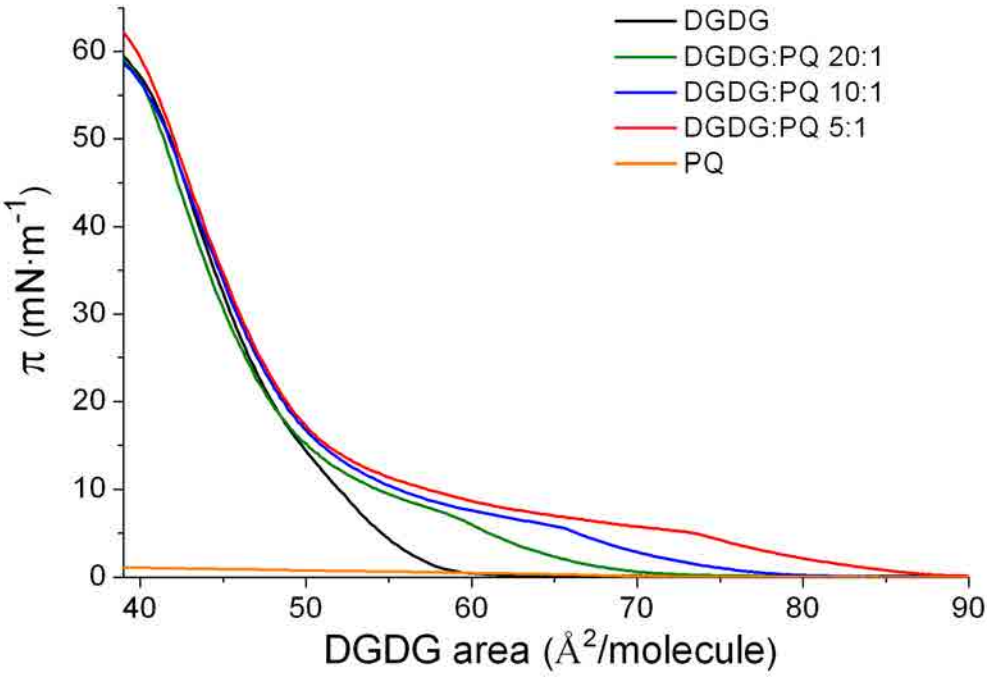

Figure 5.10.1 π-A isotherms for DGDG, PQ and DGDG:PQ mixtures at 21 ± 0.5 ºC on water subphase.

DGDG:PQ mixtures present different initial zone ($\pi \leq 15$ mN·m^{-1}) behaviour according to the PQ presence in the mixture. At $\pi > 15$ mN·m^{-1}, all π-A isotherms of the mixtures resemble the pure DGDG indicating that the PQ has been mostly expelled from the DGDG matrix after the kink point. So that, the remaining PQ molecules have been accommodated producing little effect on the headgroups packing.

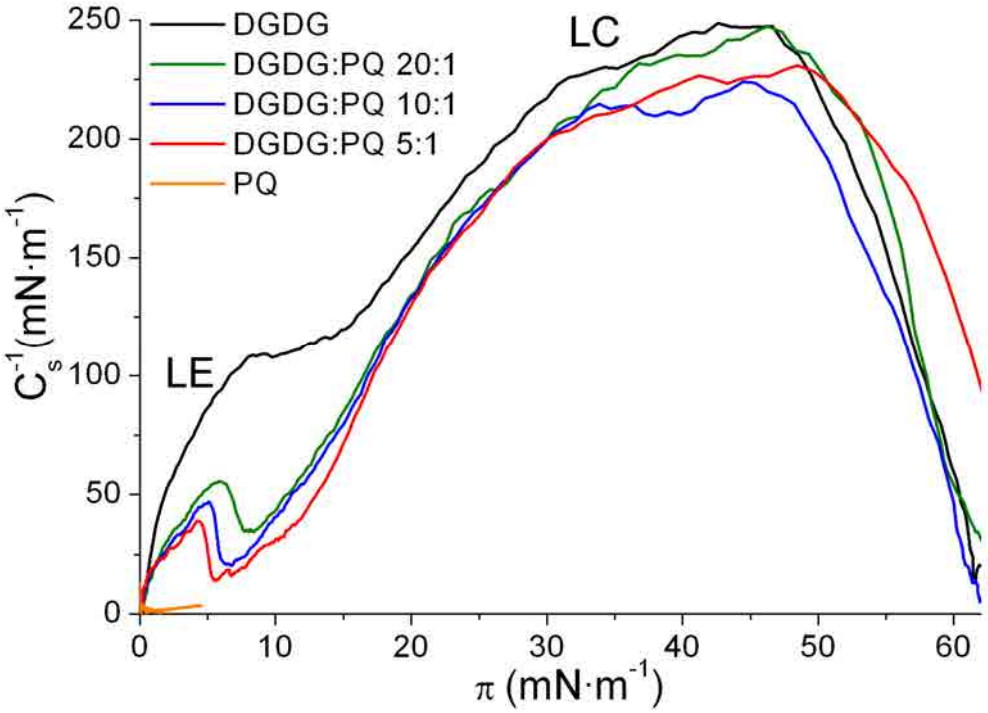

Figure 5.10.2. Inverse of the compressibility modulus vs. surface pressure for DGDG, PQ and DGDG:PQ mixtures on water subphase.

Table 5.10.1. Collapse pressure, lift-off area and kink point position for the DGDG, PQ and their biological mixtures obtained from Figure 5.10.1 and 5.10.2.

	Collapse pressure (mN·m^{-1})	Lift-off area (Å^2·molec^{-1})	Kink point pressure (mN·m^{-1})	Kink point area (Å^2·molec^{-1})
DGDG	57	59	-	-
DGDG:PQ 20:1	58	72	5.7	60.3
DGDG:PQ 10:1	58	77	5.1	66.3
DGDG:PQ 5:1	60	86	4.3	74.9
PQ	0.3	76	-	-

Both the lift-off area and the area at which appears the kink point increase as the PQ content in the DGDG:PQ mixture is enlarged (Table 5.10.1) and it is correlated with the distorting effect of PQ in the DGDG matrix [80]. This phenomena was also observed by

Kruk et al. [38] using PQ and unsaturated MGDG and also by Bilewicz et al. [1] using UQ and $C_{18}SH/C_{18}OH$. The presence of PQ in the initial zone hindrances the packing of the DGDG headgroups, and therefore, the hydrophobic interactions between the DGDG chains are also reduced, as it has been explained for the case of UQ inserted in MGDG (Section 5.9.1). The explanation for this phenomenon is that PQ is better retained in the lipid monolayer when present at low concentrations due to it affects in a lower extent the formation and shape of the ordered phases. After the main rejection of the PQ (kink point), the monolayer compactness is rapidly enhanced.

All the C_s^{-1} curves for the DGDG:PQ mixtures present a similar behaviour showing at $\pi \approx 5$ mN·m^{-1} a kink point, which accordingly to the values presented by Vitovic et al. [7] and the characteristics of this system indicates the phase change from LE to LC and it implies the main PQ expulsion from the lipid matrix. The extent of this rejection and the surface pressure at which takes place depends on the initial PQ content. At $\pi > 15$ mN·m^{-1} the mixtures and the pure DGDG present a similar C_s^{-1} curves shape (Figure 5.10.2) which is correlated with a similar PQ content remaining between the lipid chains. However, the mixtures present slightly lower C_s^{-1} values than the pure DGDG, which indicates that the presence of the remaining PQ slightly hindrances the perfect packing of the mixtures.

Phase rule

The collapse pressure of a mixed monolayer of different components is related to the miscibility of its components, being dependent on the film composition in a miscible system [50,68]. In our DGDG and DGDG:PQ mixtures isotherms, the collapse pressure is ≈ 58 mN·m^{-1}. Therefore, the similar collapse pressure can be used to elucidate the expulsion of one of the components in a mixed film. In a two component monolayer, if components are completely immiscible, a lower collapse pressure of one of the components will be observed as predicted by the phase rule. Maintaining temperature and external pressure constant, the number of degrees of freedom F of the monolayer system is given by the Expression 2.14 [82,83] that is reproduced below:

$$F = C_B + C_S - P_B - P_S + 1$$

In our DGDG:PQ experiments, at the air|water interface, $C_B = 2$ (air and water), $C_S = 2$ (DGDG and PQ), and $P_B = 2$ (gas and liquid), thus $F = 3 - P_S$. According to that, homogenous mixed films achieve the collapse equilibrium with $P_S = 2$ (condensed and collapsed state), so the system will have one degree of freedom. According to our results, the collapse pressure is practically fixed, discarding the experimental deviations, for pure DGDG and DGDG:PQ mixtures. This indicates zero degrees of freedom and therefore, following the previous reasoning, $P_S = 3$. So that, at the collapse equilibrium of the mixtures isotherms coexist DGDG (LC), DGDG (collapse) and expelled PQ. The same statements can also be applied to the phase change zone at $\pi \approx 5$ mN·m^{-1}, where the π is practically fixed indicating zero degrees of freedom. Thus $P_S = 3$ which indicate that three phases coexist: DGDG:PQ (LE), DGDG:PQ (LC) and expelled PQ, confirming the beginning of the PQ expulsion at this surface pressure. This observation coincides with the AFM conclusions (Section 5.10.4).

5.10.2 BAM

BAM images give information about the film structure at the air|water interface at microscopic scale. In this case, we have selected Figure 5.10.3A in which the gas phase is observed. In addition, we have chosen Figure 5.10.3B and Figure 5.10.3C that presents the LC state at different surface pressures.

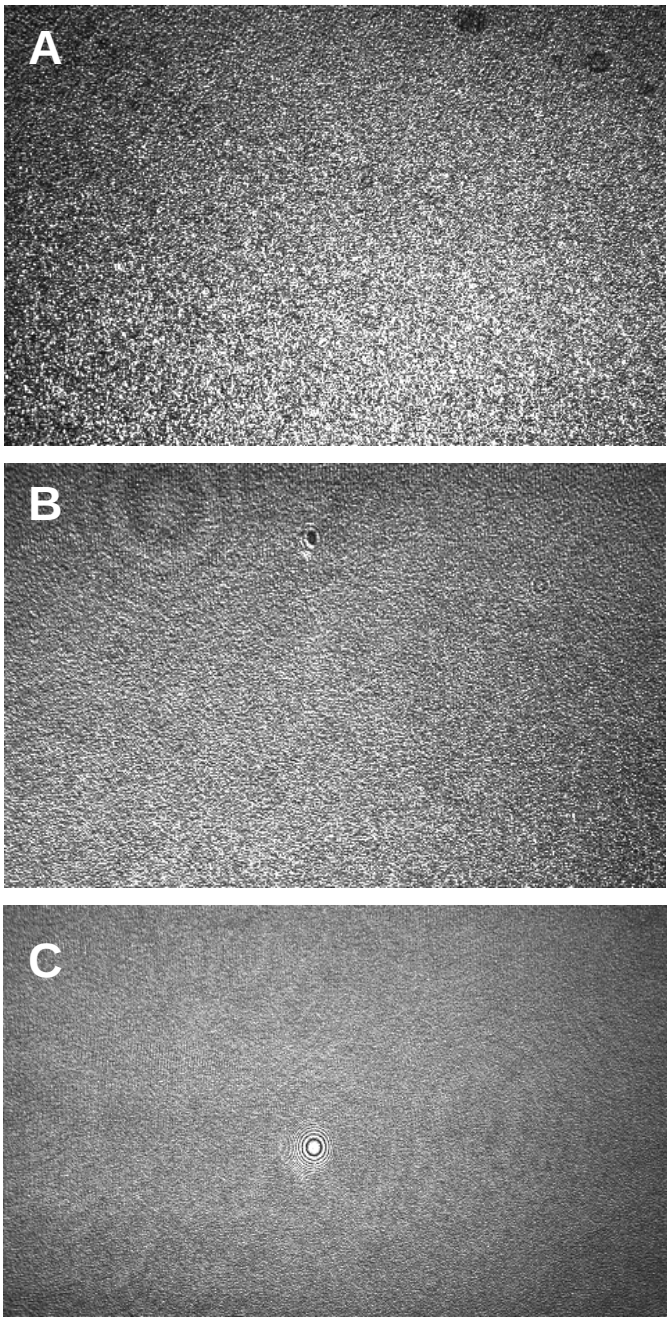

Figure 5.10.3. BAM images of the DGDG:PQ 5:1 mixture. A) at 0.2 $mN \cdot m^{-1}$, B) at 15 $mN \cdot m^{-1}$, C) at 33 $mN \cdot m^{-1}$ on water subphase.

5.10.3 Thermodynamic study

The representation of the mean area per molecule vs. the molar fraction at selected pressures gives idea about the ideality of a mixture at these surface pressures. The reader is addressed to Section 2.1.1.5 where the mathematical treatment (Expressions 2.10 - 2.13) for the figures of this part is explained. The Figure 5.10.4 plots the area per molecule and the Figure 5.10.5 plots G^E both vs. the PQ molar fraction, represented for DGDG:PQ mixtures at several surface pressures before the main PQ expulsion (≈ 5 $mN \cdot m^{-1}$). At surface pressures above this event, the thermodynamic study has not been performed due to the PQ content in the DGDG:PQ matrix is unknown and significantly lower than the initial presence.

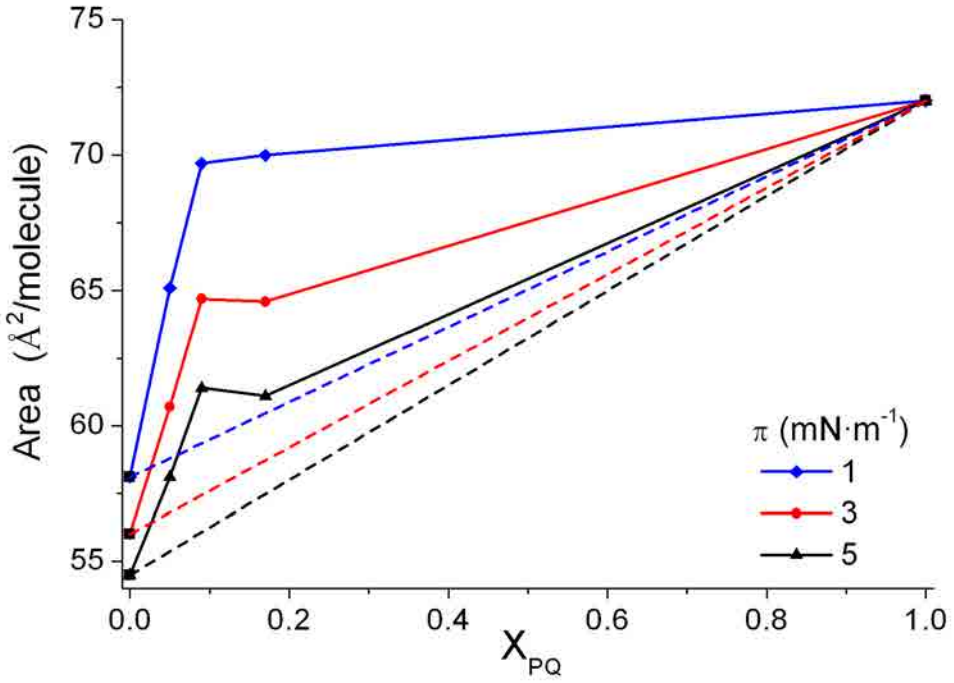

Figure 5.10.4. Plot of the mean area per molecule vs. the molar fraction for DGDG, PQ and DGDG:PQ mixtures at several surface pressures before the main PQ expulsion. Discontinuous straight line represents the ideal behaviour for each surface pressure.

Both figures (5.10.4 and 5.10.5) show that DGDG and PQ form non-ideal mixtures with positive deviation at $\pi \leq 5$ $mN \cdot m^{-1}$ which indicates that, at these surface pressures, the interactions between the two components are weaker than the interactions between pure components [6] suggesting the possible formation of enriched domains or aggregates of molecules [68,83] at high PQ content.

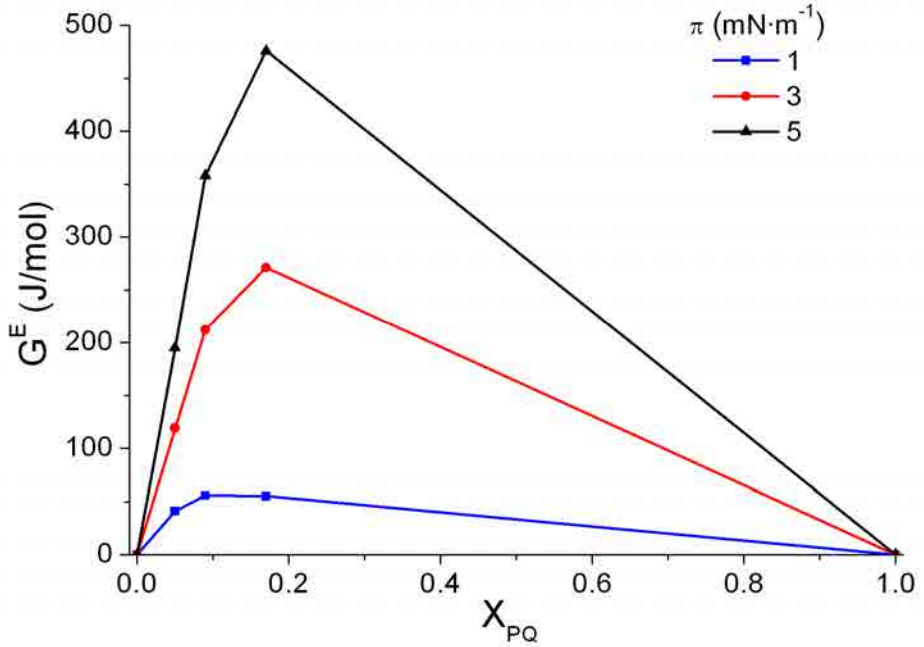

Figure 5.10.5. Plot of the excess energy vs. the molar fraction for DGDG, PQ and DGDG:PQ mixtures at several surface pressures before the main PQ expulsion.

The Figure 5.10.6 represents the ΔG_{mix} vs. PQ molar content at several surface pressures before the main PQ expulsion. The negative values observed for ΔG_{mix} at $\pi \leq 5$ mN·m^{-1} indicate that the mixed monolayers of DGDG:PQ are more stable than pure components [6], although the low ΔG_{mix} values corroborate the low stability of the mixture.

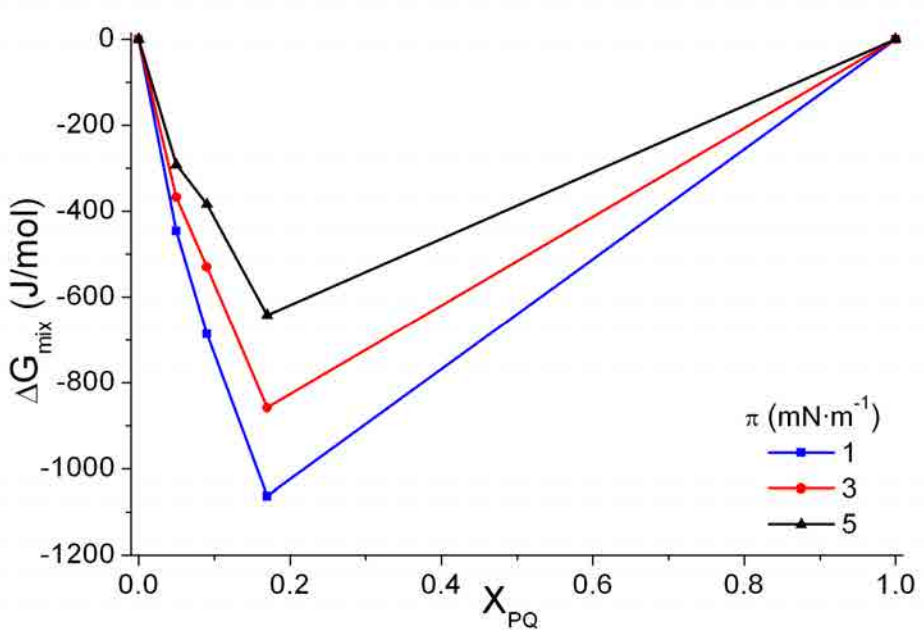

Figure 5.10.6. Plot of the mixing energy vs. the molar fraction for DGDG, PQ and DGDG:PQ mixtures at several surface pressures before the main PQ expulsion.

The formation of non-ideal mixtures between PQ and DGDG at low surface pressure, as it was observed in the MGDG:PQ system (Section 5.9.2), is explained by the difference in the chain length between PQ and DGDG, which permits a free rotation of the PQ part that protrudes over the DGDG, producing also a motion of the DGDG molecules that induces an increase of the molecular area [6,38].

5.10.4 AFM

In this part we present the topographic images of different DGDG:PQ mixtures at several surface pressures to light which is the organization of these molecules once transferred to a hydrophilic substrate (mica) and ultimately, correlate this knowledge with the predicted results in previous sections. The description and discussion of the AFM topographic images and their mathematical treatment for the pure components DGDG and PQ are explained in Section 5.5.2 and 5.2.2 respectively. So that, we present in this section only the results of the mixtures and their corresponding discussion.

Figure 5.10.7 shows the AFM topographic images corresponding to pure DGDG and the selected DGDG:PQ mixtures transferred on mica at π = 3 $mN \cdot m^{-1}$. The surface pressure used permits us to ensure that PQ is present in all the mixtures showing the larger differences for these systems. The images A-D show two different tonalities of brown (fair and dark) and both correspond to the DGDG or DGDG:PQ monolayer, being each tonality correlated with a different physical state of the system monolayer. On the other hand, the images A-D show that the PQ content has non-influence on the ordered domains size whereas it affects to the area occupied by these domains, being increased when lowering the initial PQ content, as it was expected.

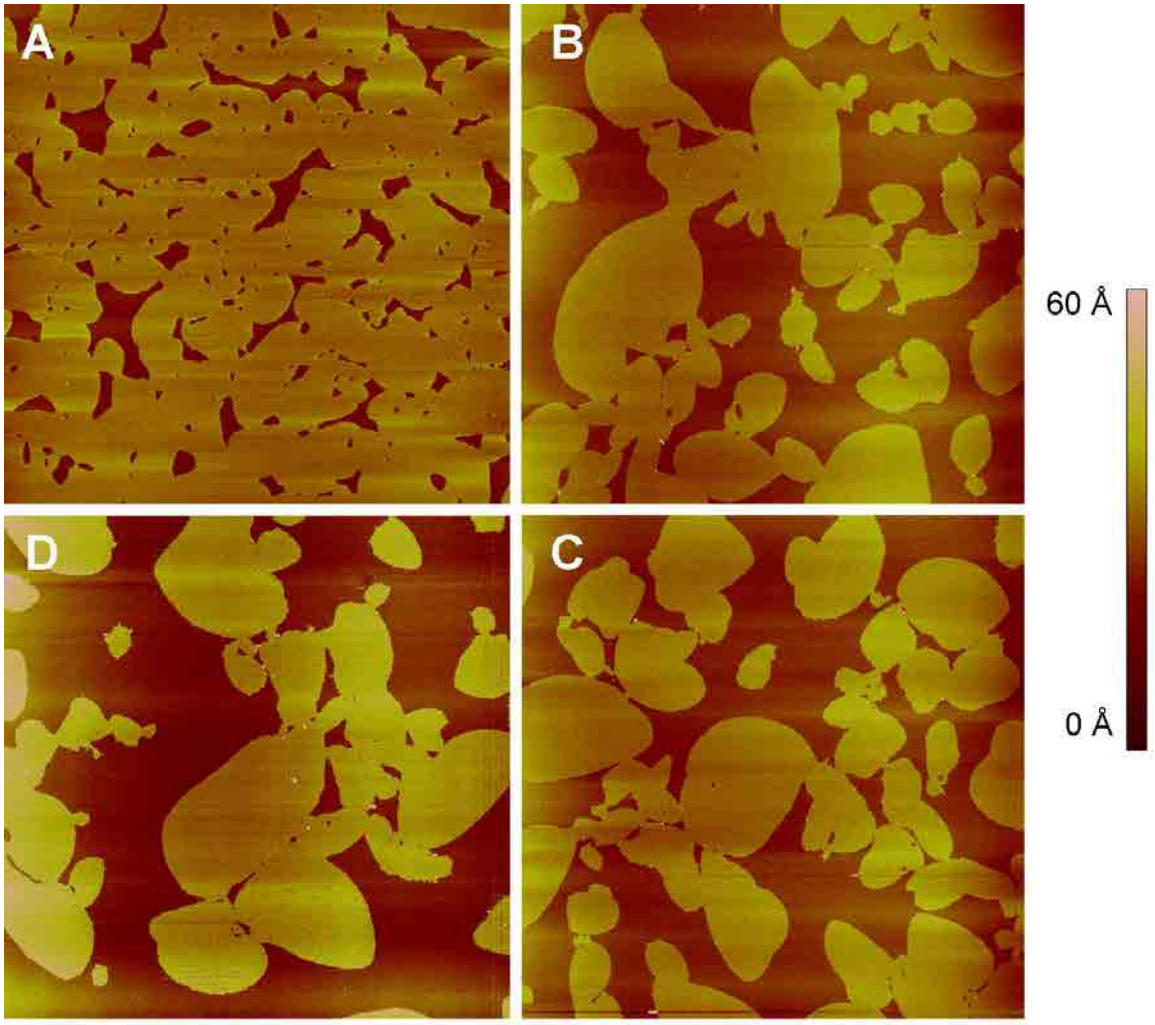

Figure 5.10.7. AFM images (20µm x 20µm) for LB films transferred on mica at 21ºC at π = 3 mN·m^{-1} for (A) pure DGDG and DGDG:PQ systems (B) 20:1, (C) 10:1, (D) 5:1.

In order to explain the behaviour of the DGDG:PQ mixtures at several surface pressures, we have selected the 5:1 ratio (Figure 5.10.8) due to it is the most different from the pure DGDG (Figure 5.5.2) of the ratios we have studied and it represents the best option to compare them. As it has been explained for pure DGDG, DGDG:PQ 5:1 presents two different tonalities of brown (fair and dark) and each one corresponds to zones with a different order of the molecules. The compression leads to a more compact fashion of the more ordered domains as it can be seen in Figure 5.10.8C at π = 33 mN·m^{-1} and in Figure 5.10.8D at π = 45 mN·m^{-1}, where practically the entire monolayer is compact, remaining only small rounded zones with the molecules in a less ordered state. On the other hand, AFM topographic images have been performed with the systems DGDG:PQ 10:1 and 20:1 (not shown) obtaining a behaviour comprised between the pure DGDG (Figure 5.5.2) and

the DGDG:PQ 5:1 (Figure 5.10.8), so only the images corresponding to π = 3 mN·m^{-1} for DGDG:PQ 10:1 and 20:1 are presented (Figure 5.10.7).

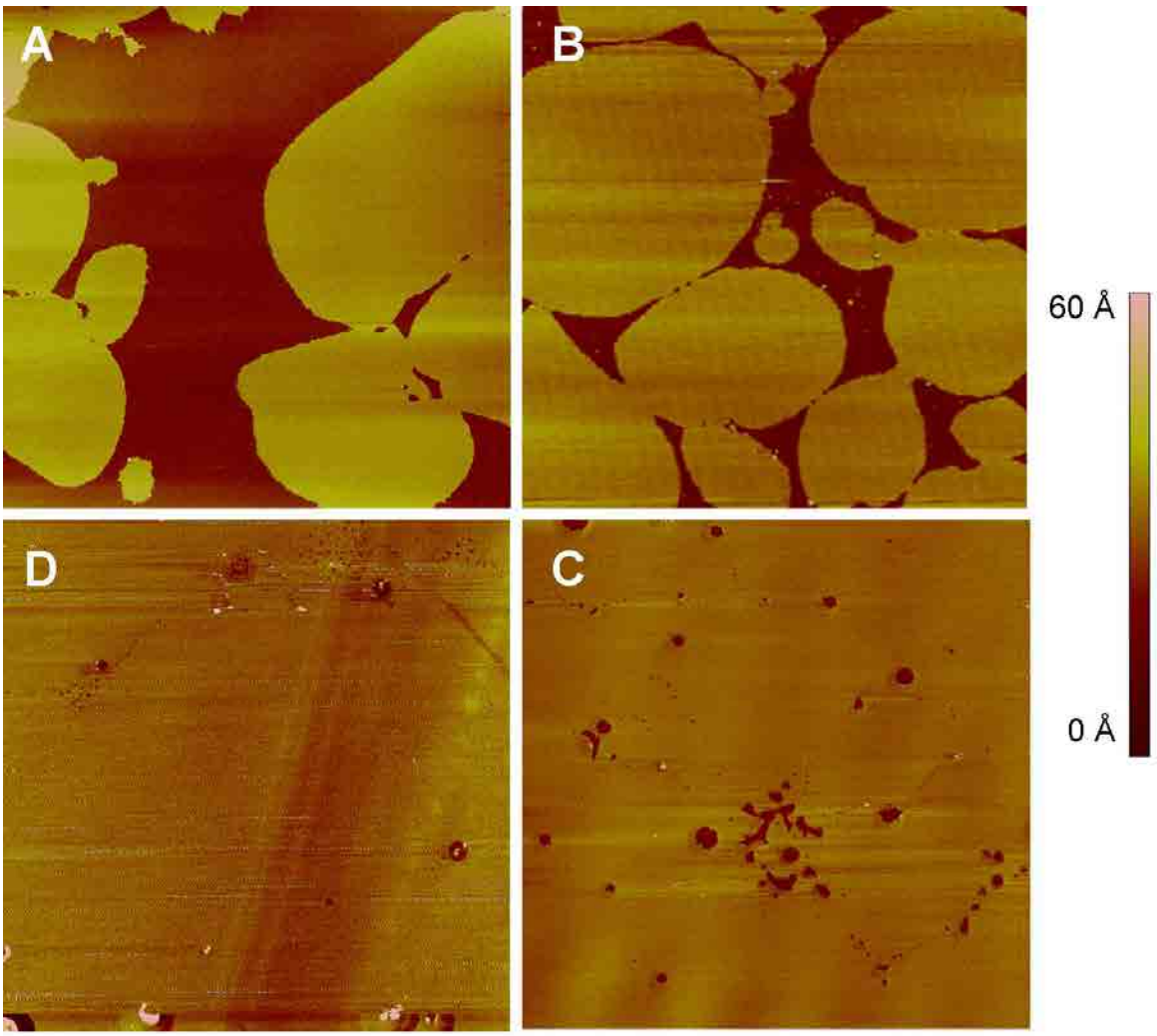

5.10.8. AFM images (10μm x 10μm) for LB films of DGDG:PQ 5:1 system transferred on mica at 21ºC at (A) π = 3 mN·m^{-1}, (B) π = 15 mN·m^{-1}, (C) π = 33 mN·m^{-1}, (D) π = 45 mN·m^{-1}.

AFM discussion

As it has been explained for pure DGDG (Section 5.5.2) each tonality indicates a different tilt order of the molecules that depends on the surface pressure and the interactions established between molecules and between the molecules with the substrate. The appearance simultaneously of zones with a high order (fair zones) with zones of low order (dark zones) in pure DGDG indicates that the meaning of the tonalities is also the same for the mixtures. On the other hand, it seems clear that the physical states deduced using the

C_s^{-1} curves for pure DGDG are more ordered than the corresponding to DGDG:PQ at the same surface pressure, so that, the different tonalities are correlated with different ordering state, but the order that represents each tonality depends on the presence of PQ.

In order to light each physical state, we have measured the relative height between fair and dark zones, and assuming the height of 6 ± 2 Å for the dark brown zones referred to the mica surface, the absolute height is presented in Table 5.10.2. The selection of this height value for the dark zones is done based on that this is the height measured between the dark brown zones and the black zones seen at low surface pressure for the MGDG:PQ 5:1 system (Inset of Figure 5.9.8A) and, moreover, this height is in accordance with the 3-6 Å observed in the literature for LE of DPPC monolayers [53,54]. The absolute heights obtained at each surface pressure and considering the C_s^{-1} results permit the obtaining of the physical state corresponding to each tonality for all the systems (Table 5.10.3) where LC1 and LC2 have the meaning explained for pure DGDG (see Section 5.5.2).

Table 5.10.2. Height of each physical state for the LB monolayers of DGDG and DGDG:PQ mixtures on mica. *Estimated value (more information in the text).

	LE	LC1	LC2
DGDG	6 ± 2 *	21 ± 2	24 ± 2
DGDG:PQ 20:1	6 ± 2 *	22 ± 2	24 ± 2
DGDG:PQ 10:1	6 ± 2 *	19 ± 2	25 ± 2
DGDG:PQ 5:1	6 ± 2 *	21 ± 2	23 ± 2

Table 5.10.3. Physical states of each zone (dark and fair brown) corresponding to the DGDG and DGDG:PQ systems at several surface pressures.

	DGDG		DGDG:PQ 20:1		DGDG:PQ 10:1		DGDG:PQ 5:1	
π (mN·m^{-1})	Dark	Fair	Dark	Fair	Dark	Fair	Dark	Fair
3	LE	LC1	LE	LC1	LE	LC1	LE	LC1
15	LC1	LC2	LE	LC2	LE	LC2	LE	LC1
33	LC1	LC2	LE	LC2	LE	LC2	LE	LC2

The DGDG and DGDG:PQ mixtures monolayers cover the entire mica surface at all the studied surface pressures. The non-observation of uncovered mica zones permits obtaining

the proportion of each physical state. The Figure 5.10.9 presents the percentage of the monolayer in fair brown, so that, according to the Table 5.10.3, the proportion of each physical state can be elucidated.

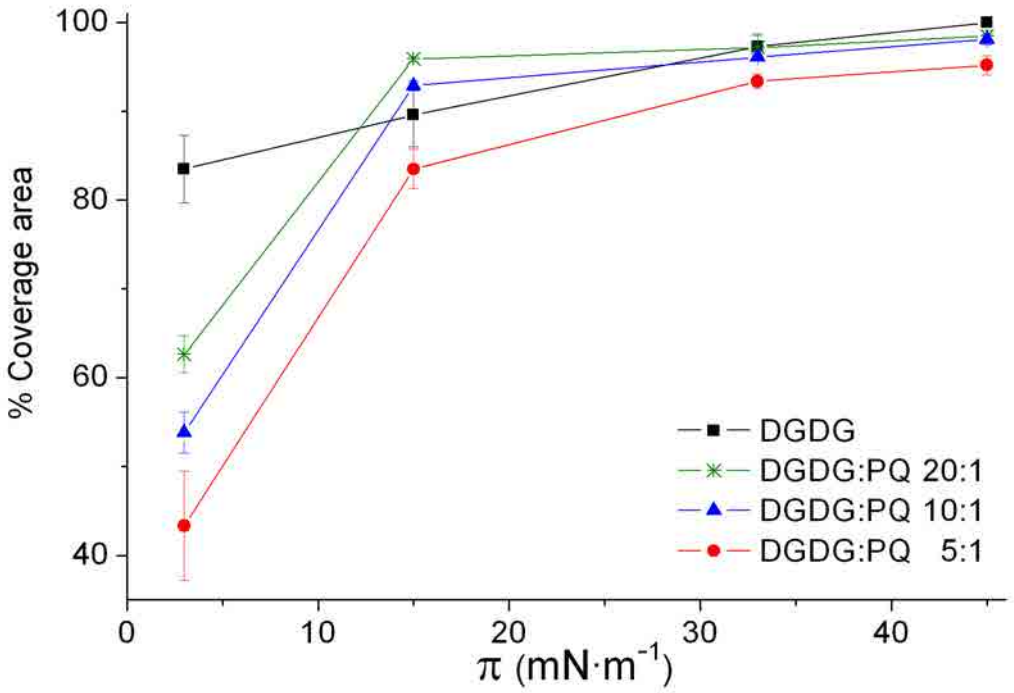

Figure 5.10.9. Monolayer coverage of the fair brown zones on the mica surface for the pure DGDG and the DGDG:PQ mixtures, calculated from AFM images.

The results obtained in Figure 5.10.9 for the DGDG:PQ systems show the expected trend of more surface covered by the compact state when decreasing the PQ content. The reason for this behaviour is that the reduced presence of PQ enhances the ordering of the DGDG molecules. Increasing the surface pressure, all the DGDG:PQ systems increases the ratio of LC zones achieving at π = 15 mN·m^{-1} a nearly flat increase which is correlated with that the major content of PQ has been rejected from the lipid matrix. On the other hand, pure DGDG presents a nearly flat increase of the area covered by the more compact phase when increasing the surface pressure. The explanation is the quick transformation of the LE or LC1 state in LC2 which leads that the entire monolayer is in a LC state at 15 mN·m^{-1}.

The simultaneous presence of two different physical states at each surface pressure for both the DGDG and DGDG:PQ systems indicates that both systems presents a physical state change that implies the coexistence, from low surface pressures, of zones with low and high order of molecules (See Table 5.10.3). The pure DGDG system achieves the complete LC state (Table 5.10.3) at lower surface pressure than the DGDG:PQ mixtures, which is explained by the presence of PQ in the DGDG:PQ mixtures hindrances the packing of the DGDG molecules. At the same surface pressure, the DGDG presents similar or higher ordered state for the fair zones than the DGDG:PQ mixtures (See Table 5.10.3), which indicates that part of the PQ is in the LC domains. A similar behaviour is observed for the dark zones, which also indicates the presence of PQ in the LE state. These observations indicates that PQ is present in both physical states of the DGDG:PQ mixtures and the higher affinity of the PQ for the LE state points the formation of DGDG:PQ domains (LC zones) with low PQ content and DGDG:PQ domains with high PQ content (LE zones), so establishing the LE zones as PQ rich zones. On the other hand, the LC areas correspond to DGDG zones where the low presence of PQ slightly hinders the compactness of this physical state (Figure 5.10.7).

5.10.5 Electrochemical behaviour

In this section, the electrochemical behaviour of the ITO-DGDG:PQ/electrolyte systems and its mathematical treatment are presented. On the other hand, the results and their corresponding discussion of the pure components DGDG and PQ are exposed in Sections 5.5.3 and 5.2.3 respectively, so that, they will be only presented in this section in case it is necessary to compare with the mixtures results. In our experiments, three CVs are required to obtain the stationary state in the electrochemical response, presenting a good reproducibility from the third scan and at least 15 cycles.

Figure 5.10.10 and 5.10.11 present the cyclic voltammograms at 10 $mV \cdot s^{-1}$ of the ITO-DGDG:PQ/electrolyte 5:1 and 10:1 systems respectively, transferred on ITO at several surface pressures which, in part, are the same that were selected for topographic AFM imaging on mica.

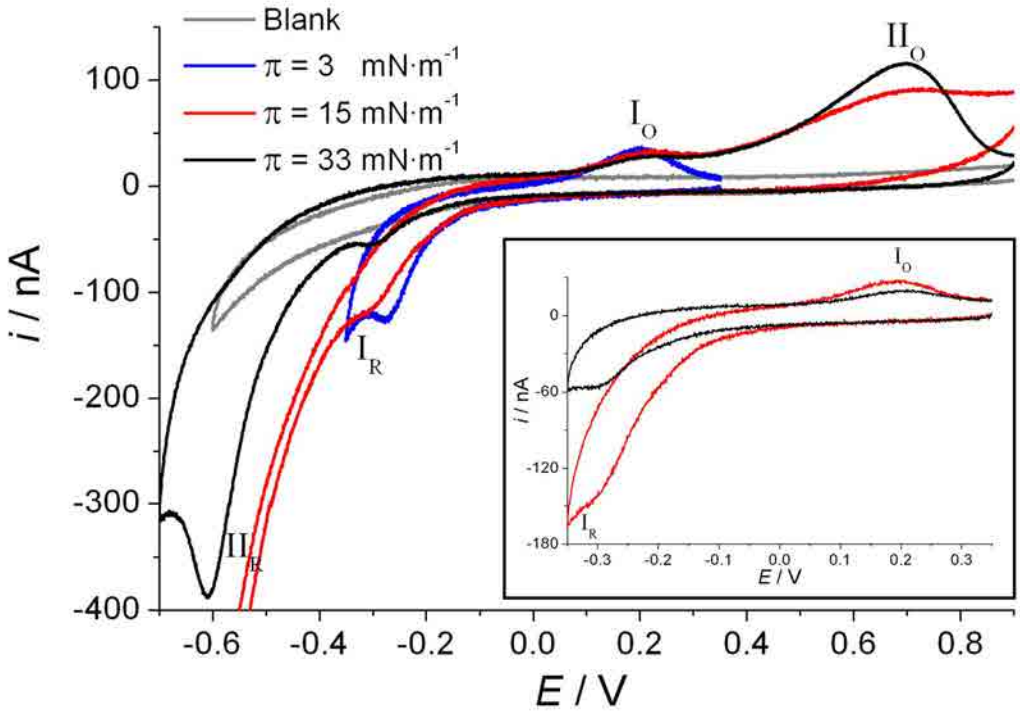

Figure 5.10.10. CV of ITO-DGDG:PQ 5:1 LB films transferred at several surface pressures. Blank line represents CV of the ITO-DGDG electrode. Inset: ITO-DGDG:PQ/electrolyte system at 5:1 ratio in short potential window transferred at π = 15 and 33 mN·m^{-1}. All CVs have been performed using 0.150 M of KCl electrochemical cell and a potassium phosphate buffered solution, at pH 7.4 and at a scan rate of 10 mV·s^{-1}.

The ITO-DGDG:PQ/electrolyte 5:1 system at π = 33 mN·m^{-1} shows two reduction and two oxidation peaks, whereas at π = 15 mN·m^{-1} one reduction and two oxidation peaks are observed, and at π = 3 mN·m^{-1} only one reduction and one oxidation peak are present. On the other hand, the ITO-DGDG:PQ/electrolyte 10:1 system (Figure 5.10.11) presents only one reduction and one oxidation peak (process I) at all the surface pressures studied. The non-observation of redox peaks at π = 3 mN·m^{-1} for the ITO-DGDG:PQ/electrolyte 10:1 system is based on that the low electrochemical response is overlapped by the ITO-DGDG/electrolyte signal. The shape and width of the process I peaks suggest that each wave convolute more than one redox process. The redox processes have been labelled according to those observed for the ITO-UQ and ITO-MGDG:UQ systems (Section 5.1.3 and 5.8.5, respectively). The main difference between the MGDG:UQ and the DGDG:PQ systems is that the process II_O becomes more important than I_O when increasing the surface pressure in the DGDG:PQ system.

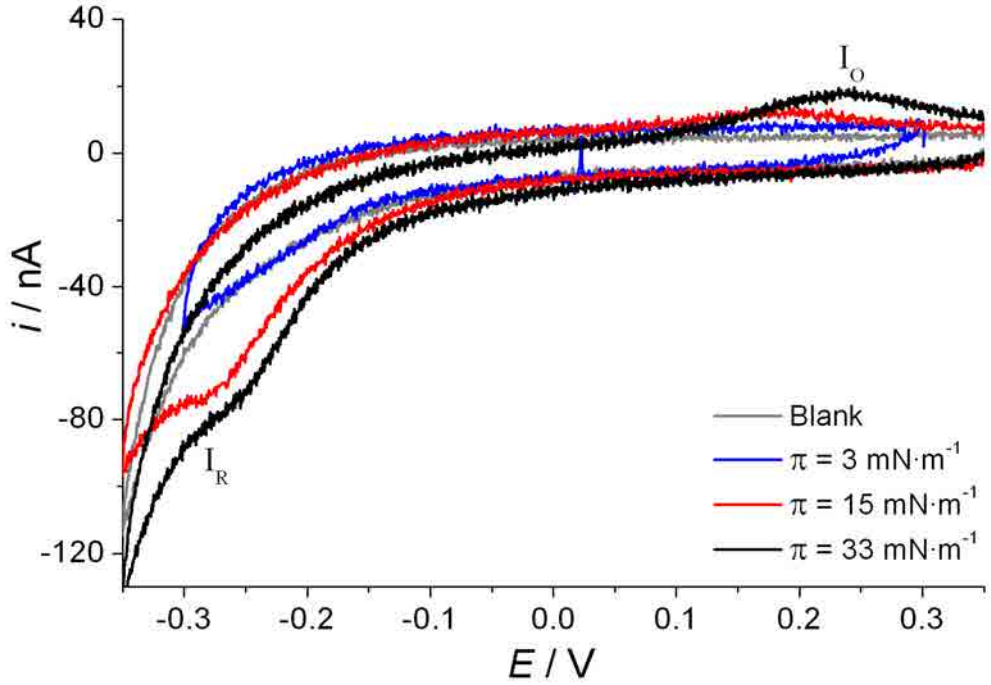

Figure 5.10.11. CVs of ITO-DGDG:PQ 10:1 LB films transferred at several surface pressures. Blank line represents the CV of the ITO-DGDG/electrolyte electrode. All CVs have been performed using 0.150 M of KCl electrochemical cell using potassium phosphate buffered solution at pH 7.4, at a scan rate of 10 $mV \cdot s^{-1}$.

In order to gain more information about the system, voltammograms at different scan rates have been performed and Figure 5.10.12 shows the CVs of the ITO-DGDG:PQ/electrolyte 5:1 and 10:1 systems for π = 33 $mN \cdot m^{-1}$ and ITO-PQ/electrolyte system at π = 2 $mN \cdot m^{-1}$, being all experiments scanned at 200 $mV \cdot s^{-1}$. In addition, the inset of Figure 5.10.12 represents the CVs at 10 $mV \cdot s^{-1}$ of the same systems. In Figure 5.10.12, the scan rate is increased in such way that the hydrogen evolution present in all the voltammograms at all compositions starts at more negative potentials than at 10 $mV \cdot s^{-1}$, indicating that this evolution is a quite slower process than process II. In consequence, the reduction of process I and II is unmasked as it occurred in the MGDG:UQ system (Section 5.7.4). On the other hand, the Figure 5.10.12 confirms that the ITO-DGDG:PQ/electrolyte 10:1 system at π = 33 $mN \cdot m^{-1}$ also shows process II. The peak and formal potentials of processes I and II for the ITO-DGDG:PQ/electrolyte 5:1 and 10:1 systems are summarized in Table 5.10.4. On the other hand, it is also interesting to observe that the double layer capacity of the ITO-DGDG/electrolyte experiments is fitted in the capacitive current of the ITO-DGDG:PQ/electrolyte systems (See Blank line in Figures 5.10.10 and 5.10.11).

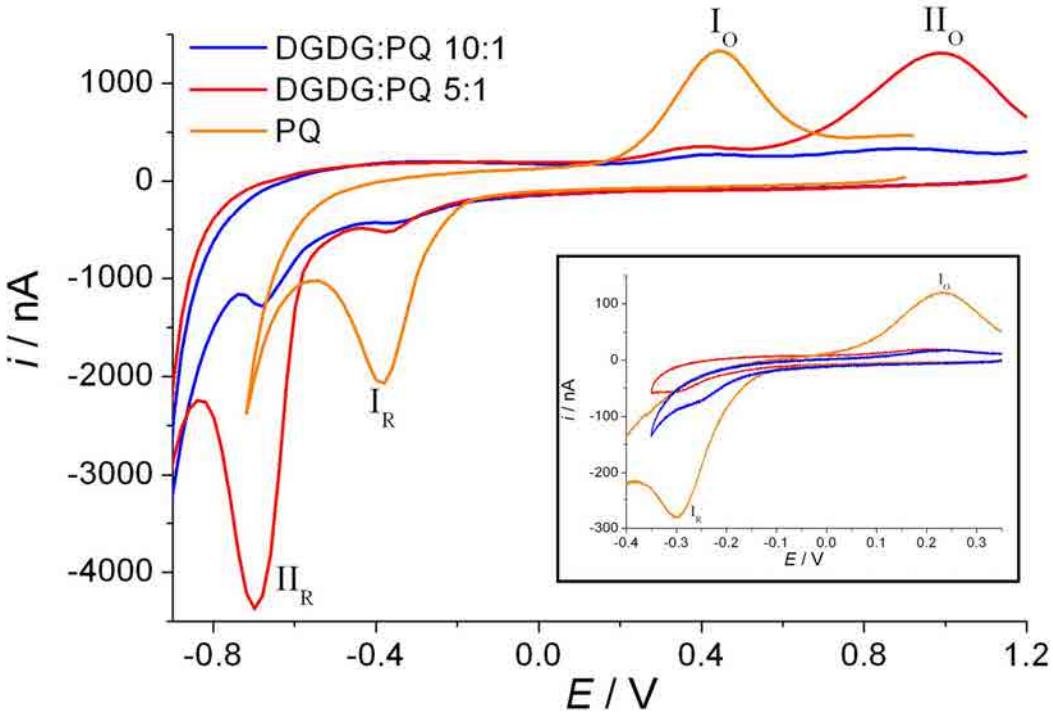

Figure 5.10.12. Cyclic voltammograms of ITO-DGDG:PQ/electrolyte 5:1 and 10:1 LB films transferred at π = 33 mN·m^{-1} and ITO-PQ/electrolyte system transferred at π = 2 mN·m^{-1}, all scanned at 200 mV·s^{-1}. Inset: CVs of the same systems in a shorter potential window and at 10 mV·s^{-1}. All CVs have been performed using 0.150 M of KCl electrochemical cell using potassium phosphate buffered solution at pH 7.4.

Table 5.10.4. Redox peaks potentials and the formal potential that they represent for the ITO-DGDG:PQ /electrolyte 5:1 and 10:1 systems.

π (mN·m^{-1})	E_{pR} (I) (V)	E_{pO} (I) (V)	E_f (I) (V)	E_{pR} (II) (V)	E_{pO} (II) (V)	E_f (II) (V)
ITO-DGDG:PQ/electrolyte 5:1						
3	-0.28 ± 0.02	0.19 ± 0.02	-0.05 ± 0.03	-	-	-
15	-0.31 ± 0.02	0.19 ± 0.02	-0.06 ± 0.03	-	-	-
33	-0.32 ± 0.02	0.20 ± 0.02	-0.06 ± 0.03	-0.61 ± 0.02	0.70± 0.02	0.05 ± 0.03
ITO-DGDG:PQ/electrolyte 10:1						
15	-0.29 ± 0.02	0.18 ± 0.02	-0.05 ± 0.03	-	-	-
33	-0.29 ± 0.02	0.23 ± 0.03	-0.03 ± 0.02	-	-	-

Discussion of the electrochemical response of the ITO-DGDG:PQ /electrolyte system

We understand that the global reaction and the mechanism proposed for pure PQ in confined situation (Section 5.2.3) is the same for the PQ of the ITO-DGDG:PQ/electrolyte system. The shape of the voltammograms for the ITO-DGDG:PQ/electrolyte systems presents two important deviations respect to the theoretical models proposed in the literature to describe the cyclic voltammetric response of a surface confined reaction [29-31]. First, the peak shape, which is not symmetrical, presenting the reduction peak a sharper shape than the oxidation one, a similar situation that it was observed by Märtensson and Agmo [32] and Hong and Park [22] studying UQ and hydroquinone respectively. Second, the redox peaks separation for process I or process II is larger than the expected for such systems.

The different shape of reduction and oxidation peaks can be explained by the different hydrophilic character of the redox couple PQ/PQH_2, as it was pointed for the ITO-PQ system (Section 5.2.3). The larger polarity of PQH_2 compared with PQ leads the former to establish better attractive interactions by dipole-dipole or hydrogen bond between PQH_2 and DGDG headgroups and, in addition, the PQH_2-ITO, PQH_2-PQH_2 and PQH_2-water interactions are also enhanced [4,25-27,32-38,84,85,93] . During the oxidation scan PQH_2 is the reactant so the possibilities of hydrogen bonds are larger, increasing the stabilization of the PQH_2 molecule and making it more difficult to oxidise. These arguments are also valid for explaining the larger width of the oxidation peak compared with that of the reduction process.

The Figure 5.10.13 presents the redox peak potentials of processes I and II vs. the scan rate for the ITO-DGDG:PQ/electrolyte 5:1 system. The redox peaks separation for process II is larger than for process I indicating that process II is even more irreversible than process I. Moreover, the redox peaks separation for both processes is enhanced when increasing the scan rate and similar behaviour is observed for process I of the ITO-DGDG:PQ 10:1/electrolyte system (not shown). This separation makes both processes (I and II) more irreversible and it represents a similar trend to that it was observed by Marchal et al. [21] and by Laval and Majda [41]. This large separation for both processes aroused from the slow charge transfer rates at the ITO-monolayer|electrolyte interface [32]. In addition, it can be also inferred from Figure 5.10.13 that the increase in the scan rate affects in a larger

extent the oxidation peak potential than the reduction one, which produces that the midpoint potential for process I and II has scan rate dependence. On the other hand, it is interesting to observe that all the linear adjustments of the processes I and II reduction peaks for the ITO-DGDG:PQ/electrolyte 5:1 system (Figure 5.10.13) have a similar slope and similar trend is shown for the oxidation peaks of the same processes. However, the y-intercept of the linear adjustment of the reduction peaks is displaced to more cathodic values when increasing the surface pressure and similar occurs with the y-intercept of the linear adjustment of the oxidation peaks that are displaced to more anodic values. This displacement can be explained by the existence of a different environment around the PQ head that is less favourable at low surface pressures or at low PQ content, according to the values of E_f (I) shown in Table 5.10.4. Moreover, the figure has been separated in low and high scan rates because at low scan rates (< 20 $mV \cdot s^{-1}$) the linear adjustments of the reduction and oxidation peak potentials of processes I and II present a higher slope (Figure 5.8.13A) than at high scan rates (Figure 5.8.13B). The trends observed for process I of the ITO-DGDG:PQ/electrolyte 5:1 system are similar to that observed for the process I of the ITO-ITO-DGDG:PQ/electrolyte 10:1 system and both are explained by the hindrance increase of the electrochemical process when increasing the scan rate.

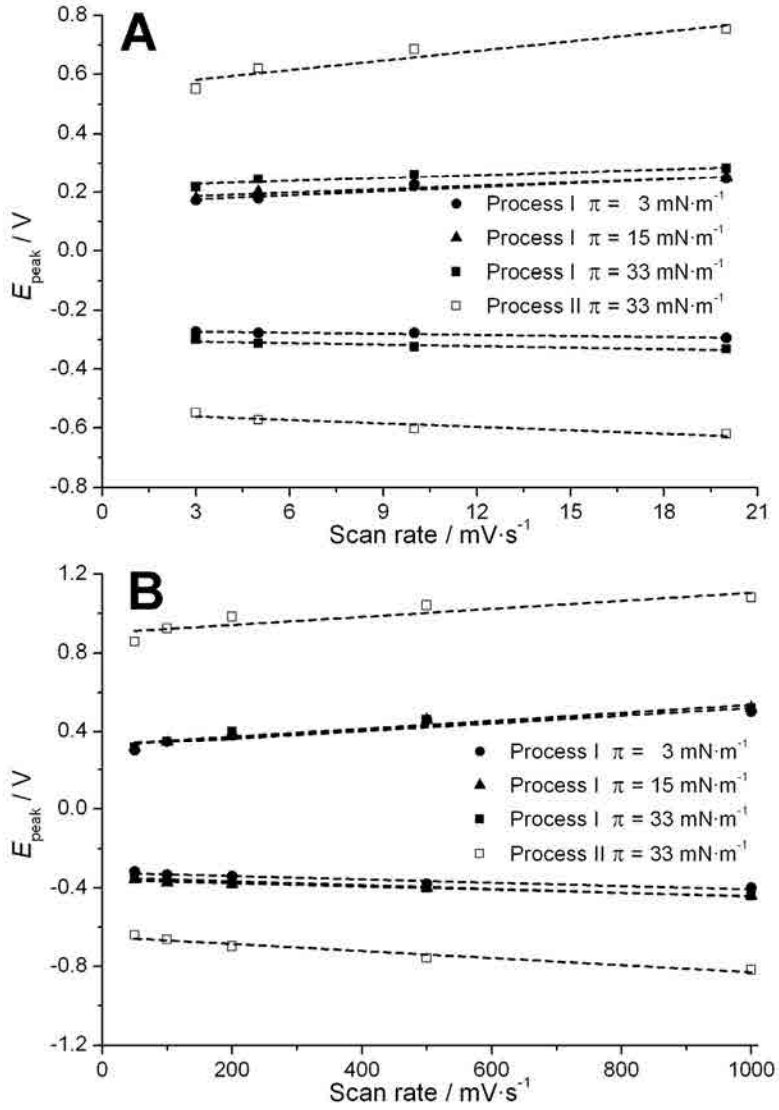

Figure 5.10.13. Peak potential vs. the scan rate for the ITO-DGDG:PQ 5:1/electrolyte system at π = 3, 15 and 33 mN·m^{-1} at A) low scan rates and B) high scan rates.

Moreover, the current intensity of the redox peaks (i_{peak}) has been studied for the ITO-DGDG:PQ/electrolyte 5:1 system at several scan rates, and it has been shown that the reduction (not shown) and the oxidation current intensity are related by a linear dependence with the scan rate (Figure 5.10.14), so indicating that PQ molecules are surface confined in both processes [16,29] and that the electron transfer process is not diffusion controlled. These observations are also valid for ITO-DGDG:PQ/electrolyte 10:1 (not shown). Our results are in line with the observations of Märtensson and Agmo [32] for scan rates < 1 V·s^{-1}, Gordillo and Schiffrin [28] and Li et al. [43] for monolayers containing UQ confined on the electrode surface.

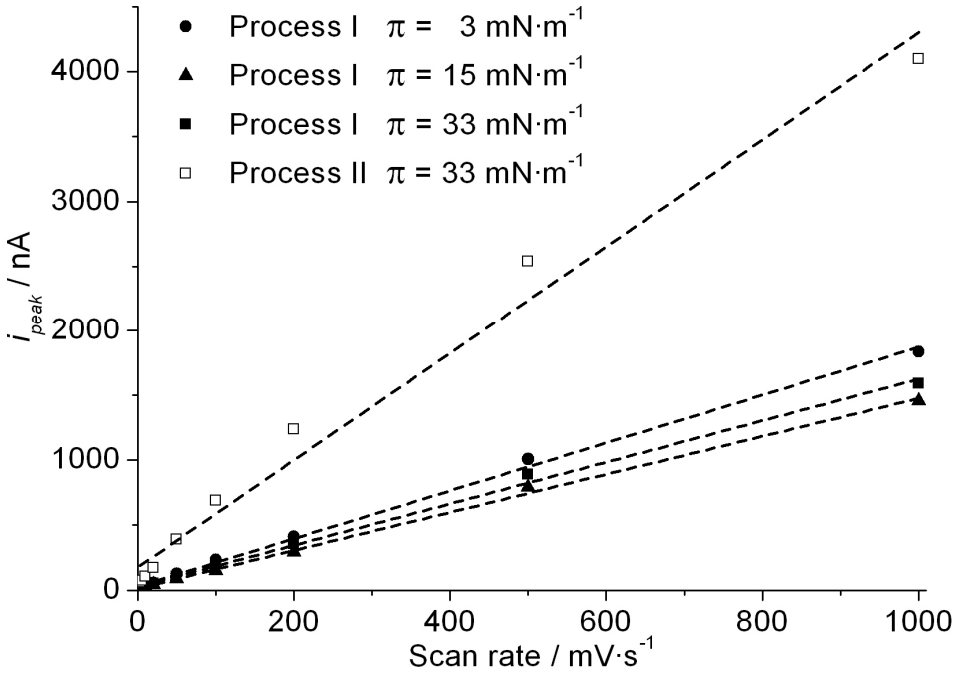

Figure 5.10.14. Oxidation peak intensity vs. the scan rate for the ITO-DGDG:PQ 5:1/electrolyte system at several surface pressures.

The charge involved in the LB monolayer transferred at each surface pressure is obtained by integrating the area under the reduction or oxidation waves. The surface coverage (Γ) is obtained from the experimental values of charge and considering the global reaction for PQ in confined situation (Section 5.2.3). The Γ for the ITO-DGDG:PQ/electrolyte system is shown in Table 5.10.5 and compared with the expected value to obtain the electroactive fraction of PQ. The expected surface coverage (Γ_{expec}) values are calculated assuming that PQ and DGDG molecules are perfectly spread, accordingly to the corresponding ratio, on the ITO surface, being the resulting value corrected with the transfer ratio associated to it in the LB transfer process. We have chosen to show in Table 5.10.5 the oxidation surface coverage (Γ_O) of the redox processes, which are similar but lower than the results obtained for the reduction scan that have the undesirable contribution of hydrogen evolution.

Table 5.10.5. Expected (Γ_{expec}) and experimental total oxidation ($\Gamma_{O\,tot}$) surface coverage, experimental surface coverage for process I, Γ_O (I), and electroactive fraction involved in the whole redox process for ITO-DGDG:PQ/electrolyte system using 0.150 M of KCl electrochemical cell, with potassium phosphate buffered solution at pH 7.4 and at a scan rate of 10 $mV \cdot s^{-1}$.

π ($mN \cdot m^{-1}$)	Γ_{expec} (10^{-12} mol · cm^{-2})	$\Gamma_{O\,tot}$ (10^{-12} mol · cm^{-2})	Γ_O (I) (10^{-12} mol · cm^{-2})	Electroactive fraction (%)
ITO-DGDG:PQ/electrolyte 5:1				
3	21.3	6.6	6.6	31.0
15	42.6	17.7	6.1	41.5
33	57.1	43.8	4.8	76.6
ITO-DGDG:PQ/electrolyte 10:1				
15	34.8	2.1	2.1	6.0
33	36.1	7.9	3.5	21.9

The Table 5.10.5 shows that an increasing in the initial PQ content in ITO-DGDG:PQ/electrolyte systems, the electroactive fraction is increased. Our results for PQ contrast with the observations of Moncelli et al. [19] who observed a decrease in the Γ_{tot} when increasing the initial UQ content from 0.5 to 2 % on a monolayer of DOPC on HDME at pH 9.5. This different behaviour is explained by the differences in pH. Moncelli et al. [15,19] worked with pH 9.5 so the availability of protons in the proximity of the UQ heads is more limited than in our experiments at pH 7.4. The lack of protons affects the reduction rate determining step (1_b) (see Section 5.2.3), so at high PQ concentrations or high scan rates, the step 1_b is not completed so the electroactive fraction is reduced. In our experiments the enough presence of available protons close to the PQ heads avoids the high local PQ concentration problem. The fact that the electroactive fraction is enhanced when increasing the initial PQ content is explained by the electron hopping effect (See Section 3.4.5). Moreover, the non-homogeneous electrode surface and the semiconductive properties of ITO induce it to behave different to metal surfaces like gold or mercury contributing with the different environments that UQ head experiences in the chain region [41] to reduce the electroactive fraction [9].

Γ_O (I) values (Table 5.10.5) are represented in Figure 5.10.15 vs. the surface pressure. At low surface pressures, when only process I is present in the voltammograms, the Γ_O (I) values are equal to the total surface coverage (Γ_{Otot}), but increasing the surface pressure, when process II_O appears, Γ_O (I) for the ITO-DGDG:PQ system attains a maximum value ≈

$3.5 \cdot 10^{-12}$ mol·cm^{-2}. It is important to consider that the large hydrogen evolution present where should appear the reduction peak of process II affects the shape of the corresponding oxidation peak so the surface coverage Γ_{Otot} has a larger error value.

The explanations given in Section 5.9.5 when comparing our ITO-MGDG:UQ/electrolyte system with the literature, are also valid for the ITO-DGDG:PQ/electrolyte due to the similarities on the one hand between MGDG and DGDG, and on the other hand, between PQ and UQ, which induce a similar formal potential for processes I and II in our experimental conditions, as it has been shown in Sections 5.8.5 and 5.10.5. The slight differences observed between the literature for UQ and our results for PQ are related with the differences between both prenylquinones, the physicochemical properties of the substrate, the differences on the electrolyte solution and the differences in the distance prenylquinone head-substrate surface. All the formal potential observed by previous authors for the quinone redox process are less thermodynamically favourable than that observed in this work which is correlated with the higher availability of protons in our system. The process I observed in our experiments requires direct contact or short distance between ITO and the PQ head, which can be correlated with the exposed situations [21,23,41,86].

PQs are present in two main positions in natural cell membranes being PQ_A bounded to the PSII and PQ_B that can free move. The electron flow from PQ_A to PQ_B is possible thanks to the higher redox potential for the latter due to the hydrogen bonds between the keto-oxygens and surrounding protein residues [130]. This natural behaviour can be compared with our system in which the different positions “diving” and “swimming” has also different redox potential. The redox potential for the “swimming” PQ is ≈ 110 mV higher than that of the “diving” PQ, which, by chance, is in line with the ≈ 80 mV that the redox potential of PQ_A is higher than PQ_B [130]. The higher redox potential permit the electron flow from the diving position to the swimming position, so favouring the electron hopping explained.

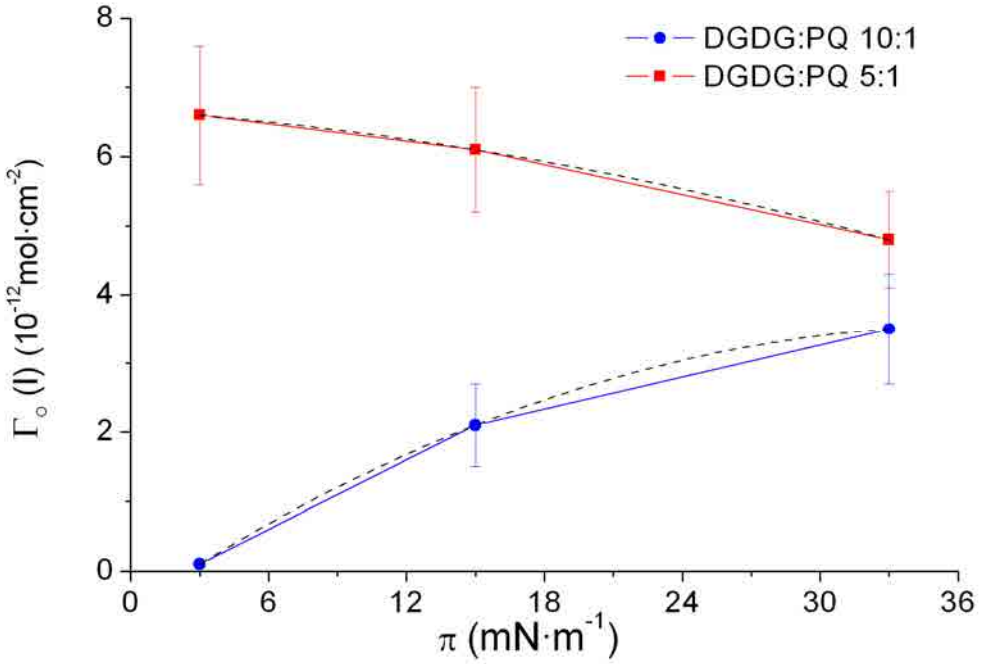

Figure 5.10.15. Surface coverage of the PQH_2 fraction oxidized via process I, Γ_O (I), vs surface pressure, π, for ITO-DGDG:PQ/electrolyte 5:1 and 10:1 mixtures.

5.10.6 Global sight of the DGDG:PQ system transferred on ITO using the LB technique

In this section we explain the global behaviour of the DGDG:PQ system and the position of the PQ molecules in the monolayer studying the results obtained from the used techniques.

The slightly lower C_s^{-1} values observed for the DGDG:PQ mixtures compared to the pure DGDG after the kink point indicate that the presence of remaining PQ molecules ("diving" position, see Section 3.4.2) have little effect on the monolayers of the DGDG:PQ mixtures. The shape of the π-A isotherms, the shape of the C_s^{-1} curves and the shape of the kink point in the C_s^{-1} curves suggest that the system experiences a sudden PQ expulsion of most of the PQ content. The expulsion of the PQ from the lipid heads region leads to the "diving" position without ITO-PQ contact and the "swimming" position, being this last position and the formation of aggregates favoured at large initial content of PQ and at ordered states, as it was previously observed [3,25,27,36]. So that, the expulsion of PQ is the way chosen by the DGDG:PQ mixture to minimize its energy at the interface [49] and to minimize the low

favourable interactions between PQ and the DGDG chains. The proportion of PQ at each position (diving [4,15, 36,88-95] or swimming [4,84,85,88,91-94,96-103,107]) is defined by the DGDG physical state and the initial PQ content.

A complete vision of the PQ positions in the DGDG:PQ monolayer can be obtained considering the thermodynamic description of the physical states, the AFM results of the DGDG:PQ 5:1 system on mica (Figure 5.10.8) and the CVs of Figures 5.10.10-5.10.12. Therefore, these PQ positions will be extrapolated to all the ITO-DGDG:PQ systems. The DGDG:PQ mixtures at low surface pressure, present lower covered area by the LC state when increasing the PQ initial content (Figure 5.10.9). This observation indicates that PQ is present in both physical states (LE and LC) of the DGDG:PQ mixtures. At π = 3 mN·m^{-1}, the CVs of Figures 5.10.10 and 5.10.11 show that only the redox process I is obtained and it presents a similar formal potential (E_f (I) = -0.05 ± 0.02 V) to that of process I for the ITO-PQ/electrolyte system (inset of Figure 5.10.12), which indicates that the local environment around each PQ is uniform in both situations [22]. So that, at low surface pressures, regardless the DGDG:PQ domains are in LE or LC state (Figure 5.10.8A), we correlate process I to the "diving" position with the PQ placed in the DGDG matrix and located in direct contact with the electrode surface. The compression of the explained monolayer induces two actions: First the compactness of the LC state, so favouring the rejection of part of the PQ in "diving" position. On the one hand, it can be vertically rejected to the diving position without ITO-PQ contact and, on the other hand, horizontally to the remaining LE zones so enriching them in PQ. Second, the phase change from LE to LC of the remaining LE zones (Figure 5.10.8 C). Further compression results in smaller but more enriched LE zones and a more compact LC state as seen in Figure 5.10.8C and D. In this case, the low quality of the topographic images for ITO-DGDG:PQ/electrolyte mixtures at π = 33 mN·m^{-1} complicate the observation of the PQ physical state but the no observation of localized higher zones suggest that the PQ are present as single molecules or small pools of molecules in LE state, which we relate with the difficulty on performing topographic images on tapping mode at high surface pressures. These observations are different to that explained for the MGDG:UQ (see Section 5.8.5) where filament protrusions were seen.

Moreover, the “diving” position present wide redox peaks that, based on the observations for the ITO-MGDG:PQ/electrolyte system (Section 5.9.5), comprises two redox processes I_α and I_β corresponding respectively to the PQ molecules in direct contact and the PQ molecules close to the ITO surface. The difficult deconvolution of these peaks in the ITO-DGDG:PQ/electrolyte system, even at high scan rate, indicates that both peaks are close each other, suggesting slight changes in the environment that the PQ molecules experience at each position, being the process I_α favoured at low surface pressure. Both peaks of PQ molecules in “diving” position are not distinguished in the voltammograms because present similar formal potential, but can explain the slight dependency of formal potential with the surface pressure observed in Figure 5.10.13.

The presence of enriched domains is predictable based on the Van Dijck et al. [105] observations for saturated phospholipids with the same headgroup and others studies presented in the literature [27,35,36,41,93,95,98,106,107]. In addition, Figure 5.10.8 C and D present small LE zones in circular shape, which is the shape adopted by the monolayers to minimize the surface tension of the nascent boundary when lipid reorientate in the layer boundaries [118], and they may indicate that the composition in and out the rounded shape are different. On the other hand, the saturation of the Γ_O (I) (Figure 5.10.15) when increasing the surface pressure at which the LB film has been transferred suggests that, when changing from LE to LC, the vertical rejection is also favoured, placing part of the PQ molecules in the “swimming” position in the LC zones. The gradual LE to LC physical state change permits that part of the PQ molecules get the most stable position that is the “swimming position”. According to the literature and considering the monolayer|air interface, the “swimming” position is more stable than the “diving” position due to the later disrupts the cooperative motions between the DGDG chains [102]. Moreover, above the DGDG chains, the medium is air whose hydrophobicity [104] added to the hydrophobicity of the end part of the DGDG chains stabilize the PQ [6] avoiding the distortion of being inserted between the DGDG chains. However, the “diving” position can be favoured thanks to fast physical state change and/or part of the PQ molecules self-aggregate, in accordance with Roche et al. [6], forming head to head aggregates to withstand the hydrophobic environment of the lipid chain region. It is important to consider that our experiments always presents a higher PQ content than the minimum observed in the literature for UQ aggregation (0.5-2 mol%) [1,15,36].

Our results confirm that PQ is confined on the electrode surface and the electron transfer takes place mainly by two mechanisms: First, by direct transfer and electron hopping between the PQ placed in "diving" position (process I), and second, by electron hopping through the lipid matrix (process II). The electron hopping favours the rate determining step (1_b) (Section 5.2.3) so favouring the electroreduction in the timescale used. At low surface pressure the molecules are far enough each other to do not be affected by the electron hopping mechanism. Increasing the surface pressure the PQ headgroups are placed closer favouring the electron hopping redox process.

In order to clarify the position and organization of the DGDG and PQ molecules at each physical state, the Figure 5.10.16 represents the position of DGDG and PQ molecules of the DGDG:PQ 5:1 system at the surface pressures studied. This Figure 5.10.16 explains the different meaning of the fair and dark colours observed in the AFM images summarized in Table 5.10.3 and the PQ positions that origin the redox processes I (positions I_α and I_β) and II.

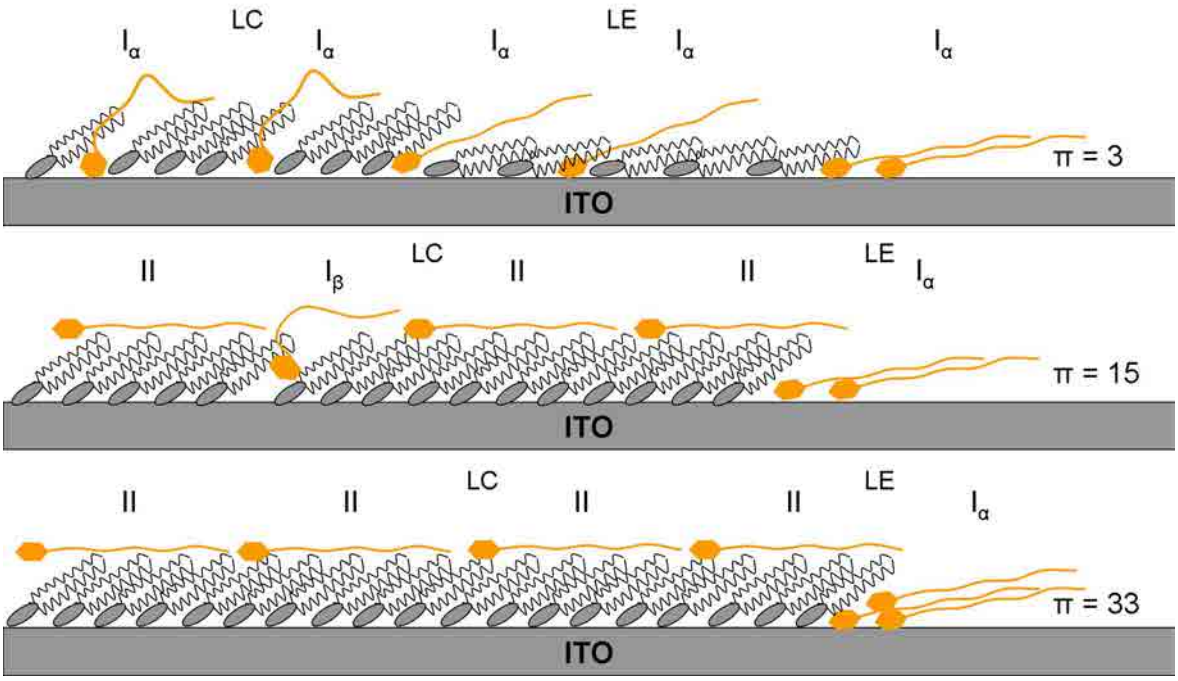

Figure 5.10.16. Scheme of the position of DGDG and PQ molecules of the DGDG:PQ 5:1 system at several surface pressures. The labels I_α, I_β and II indicate the PQ positions that origin the redox processes I_α, I_β and II.

5.11 MD:PQ

5.11.1 π-A isotherms and physical states

The π-A isotherms of the MGDG:DGDG:PQ (MD:PQ) system at biological relevant ratios are presented in Figure 5.11.1 referred to the MD area per molecule. The C_s^{-1} curves (Figure 5.11.2) corresponding to the described π-A isotherms (Figure 5.11.1) are calculated according to the Expression 2.9. The most significant values of Figures 5.11.1 and 5.11.2 are summarized in Table 5.11.1. The usual representation of isotherms corresponding to binary mixtures is the π vs. mean area per molecule, being each isotherm referred to the weighted (mean) area per molecule according to the MD:PQ ratio. In the present case, we have discarded this kind of representation due to PQ is mostly expelled from the lipid matrix at low surface pressures (as it will be commented in this section). This kind of representation of the MD:PQ system above the main expulsion has non-sense and distorts the global sight. The description and discussion of the π-A isotherms and the C_s^{-1} results for the MD and PQ pure components were explained in Section 5.6.1 and 5.2.1 respectively. So that, we present in this section only the results of the mixtures and their corresponding discussion.

MD:PQ mixtures (Figure 5.11.1 and 5.11.2) present different behaviour according to the PQ presence in the mixture. The isotherm can be divided in two zones being the kink point at $\pi \approx 3$ mN·m^{-1}, the border value. Below that surface pressure the higher the initial PQ content, the higher hindrance in the packing of the MD molecules. Unexpectedly, above 3 mN·m^{-1}, the isotherms of MD:PQ systems with low PQ content (See MD:PQ 20:1 and 10:1 systems) present higher deviation referred to the π-A isotherm and C_s^{-1} curve of the pure MD, presenting also higher collapse pressure and $C_{s\ \max}^{-1}$ value than the MD:PQ 5:1 system. On the other hand, all the mixtures never meet the pure MD π-A isotherm, indicating the presence of PQ in the MD matrix even at high surface pressures.

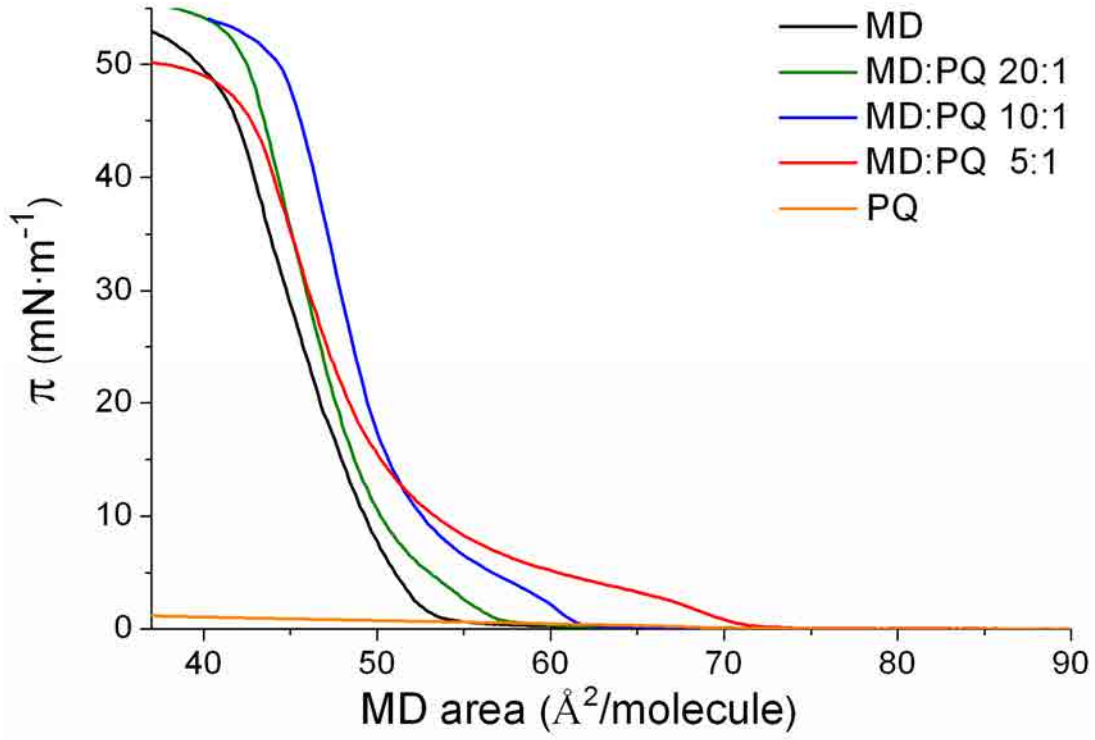

Figure 5.11.1 π-A isotherms for MD, PQ and MD:PQ mixtures at 21 ± 0.5 ºC on water subphase.

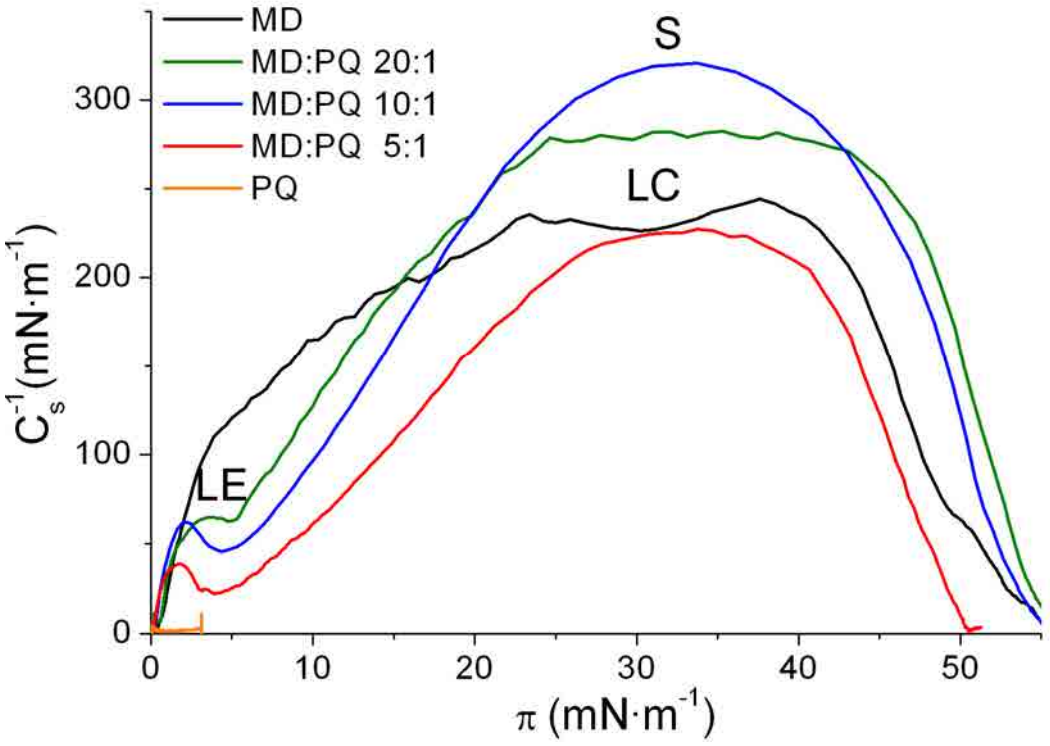

Figure 5.11.2. Inverse of the compressibility modulus vs. surface pressure for MD, PQ and MD:PQ mixtures on water subphase.

Table 5.11.1. Collapse pressure, lift-off area and kink point position for the MD, PQ and their biological mixtures obtained from Figure 5.11.1.

	Collapse pressure ($mN \cdot m^{-1}$)	Lift-off area ($Å^2 \cdot molec^{-1}$)	Kink point pressure ($mN \cdot m^{-1}$)	Kink point area ($Å^2 \cdot molec^{-1}$)
MD	48	57	-	-
MD:PQ 20:1	53	58	3.5	54
MD:PQ 10:1	52	62	2.0	60
MD:PQ 5:1	49	72	1.7	68
PQ	0.3	76	-	-

Both the lift-off area and the area at which appears the kink point increase as the PQ content in the MD:PQ mixture is enlarged (Table 5.11.1) and it is correlated with the distorting effect of PQ in the MD matrix [80]. This phenomena was also observed for the MGDG:quinone or DGDG:PQ systems (Section 5.8.1, 5.9.1 and 5.10.1). The presence of PQ in the initial zone hindrances the packing of the galactolipids headgroups, and therefore, the hydrophobic interactions between the galactolipids chains are also reduced. The explanation for this phenomenon is that PQ is better retained in the lipid monolayer when present at low concentrations due to it affects in a lower extent the formation and shape of the ordered phases. After the main rejection of the PQ (kink point), the monolayer compactness is rapidly enhanced.

The C_s^{-1} curves of all the MD:PQ mixtures present similar shape with differences at the $C_{s\ \max}^{-1}$ values and around the kink point (at $\pi \approx 3$ $mN \cdot m^{-1}$). Accordingly to the values presented by Vitovic et al. [7] and the characteristics of this system, this kink point indicates the phase change from LE to LC, which implies the main PQ expulsion from the lipid matrix. The extent of this rejection and the surface pressure at which takes place depends on the initial PQ content. The MD:PQ 5:1 system presents a lower $C_{s\ \max}^{-1}$ value than the MD, as it was expected. However, it is surprising the higher $C_{s\ \max}^{-1}$ value than MD presented by the MD:PQ 20:1 and, especially, the 10:1 system. This behaviour indicates a high stability of the MD:PQ system at low PQ content.

Phase rule

The collapse pressure of a mixed monolayer of different components is related to the miscibility of its components, being dependent on the film composition in a miscible system [50,68]. In our MD and MD:PQ mixtures isotherms, we can distinguish two different behaviours, as it has been explained, presenting the collapse pressure at ≈ 48 $mN \cdot m^{-1}$ and ≈ 52 $mN \cdot m^{-1}$ respectively. Therefore, the similar collapse pressure for each behaviour can be used to elucidate the expulsion of one of the components in a mixed film. In a two component monolayer, if components are completely immiscible, a lower collapse pressure of one of the components will be observed as predicted by the phase rule. Maintaining temperature and external pressure constant, the number of degrees of freedom F of the monolayer system is given by the Expression 2.14 [82,83] that is reproduced below:

$$F = C_B + C_S - P_B - P_S + 1$$

In our MD:PQ experiments, at the air|water interface, $C_B = 2$ (air and water), $C_S = 2$ (MD and PQ), and $P_B = 2$ (gas and liquid), thus $F = 3 - P_S$. According to that, homogenous mixed films achieve the collapse equilibrium with $P_S = 2$ (condensed and collapsed state) so the system will have one degree of freedom. According to our results, the collapse pressure is practically fixed, discarding the experimental deviations, for pure MD and MD:PQ 5:1 mixture. This indicates zero degrees of freedom and therefore, following the previous reasoning, $P_S = 3$. So that, at the collapse equilibrium of the mixtures isotherms coexist MD (LC), MD (collapse) and expelled PQ. On the other hand, the collapse pressure is practically fixed for the MD:PQ 20:1 and MD:PQ 10:1 mixtures, which also indicates zero degrees of freedom and therefore, following the previous reasoning, $P_S = 3$, although, the phases that coexist at the collapse are different, being MD:PQ (LC), MD:PQ (collapse) and expelled PQ. The same statements can also be applied to the phase change zone at $\pi \approx 3$ $mN \cdot m^{-1}$, where the π is practically fixed indicating zero degrees of freedom. In this case, all the mixtures present the coexistence of the same three phases, which are MD:PQ (LE), MD:PQ (LC) and expelled PQ, confirming the beginning of the PQ expulsion at this surface pressure. This observation coincides with the AFM conclusions (Section 5.11.3).

5.11.2 Thermodynamic study

The representation of the mean area per molecule vs. the molar fraction at selected pressures gives idea about the ideality of a mixture at these surface pressures. The reader is addressed to Section 2.1.1.5 where the mathematical treatment (Expressions 2.10 - 2.13) for the figures of this part is explained. The Figure 5.11.3 plots the area per molecule and the Figure 5.11.4 plots G^E both vs. the PQ molar fraction, represented for MD:PQ mixtures at several surface pressures before the main PQ expulsion (≈ 3 $mN \cdot m^{-1}$). At surface pressures above this event, the thermodynamic study has not been performed due to the PQ content in the MD:PQ matrix is unknown and significantly lower than the initial presence.

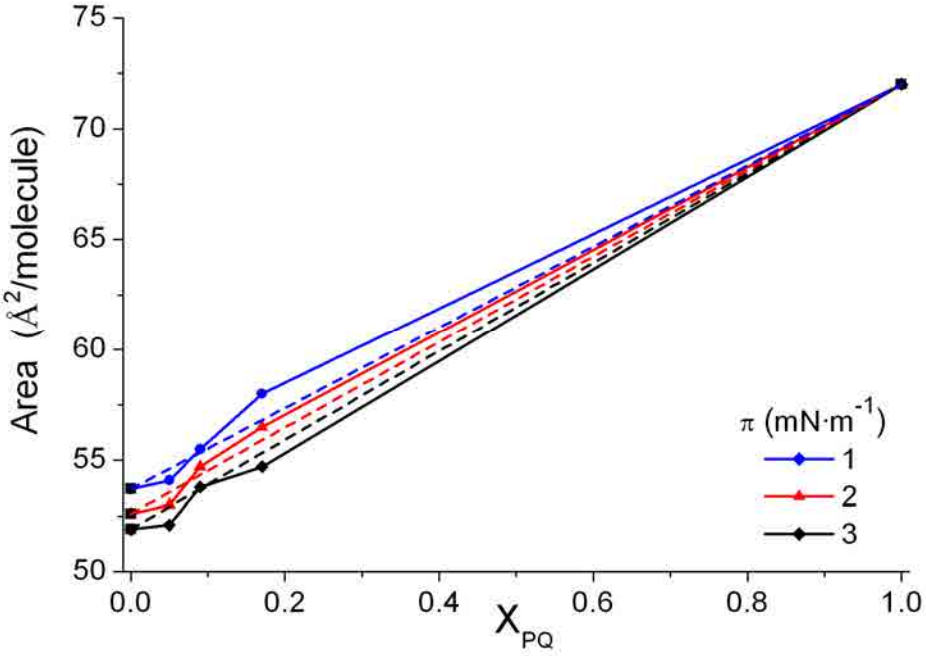

Figure 5.11.3. Plot of the mean area per molecule vs. the molar fraction for MD, PQ and MD:PQ mixtures at several surface pressures before the main PQ expulsion. Discontinuous straight line represents the ideal behaviour for each surface pressure.

Figure 5.11.3 shows that MD and PQ resemble the dashed line, discarding the experimental deviations, which indicates that the two components are inmiscible or they form ideal mixtures. On the other hand, the Figure 5.11.4 show that MD and PQ form non-ideal mixtures with slight positive deviation at $\pi \leq 3$ $mN \cdot m^{-1}$ which indicates that, at these surface pressures, the interactions between the two components are slightly weaker than the interactions between pure components [6].

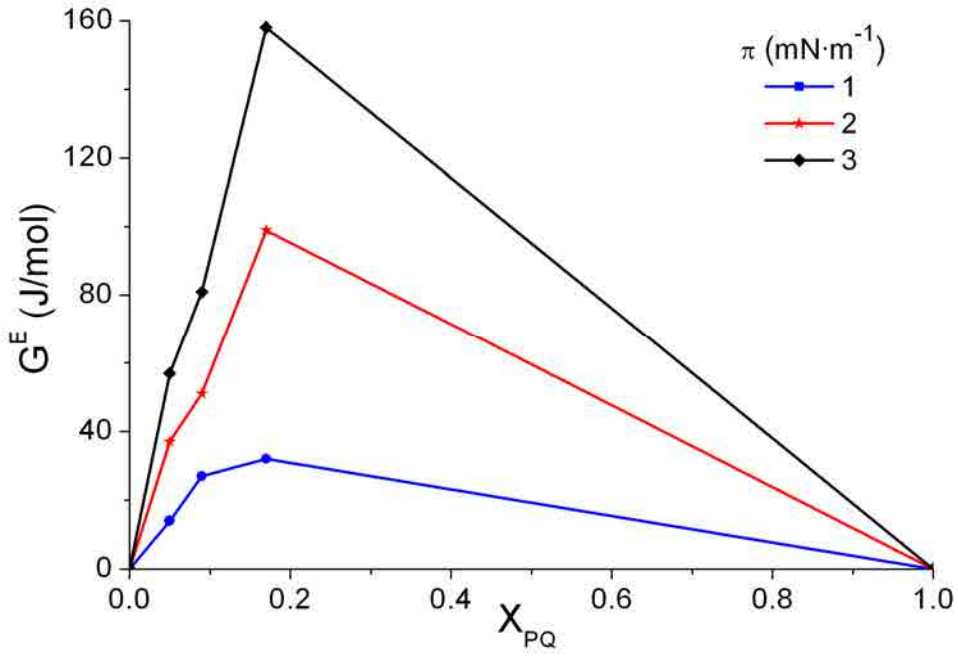

Figure 5.11.4. Plot of the excess energy vs. the molar fraction for MD, PQ and MD:PQ mixtures at several surface pressures before the main PQ expulsion.

The Figure 5.11.5 represents the ΔG_{mix} vs. PQ molar content at several surface pressures before the main PQ expulsion. The negative values observed for ΔG_{mix} at $\pi \leq 3$ mN·m^{-1} indicate that the mixed monolayers of MD:PQ are more stable than pure components [6].

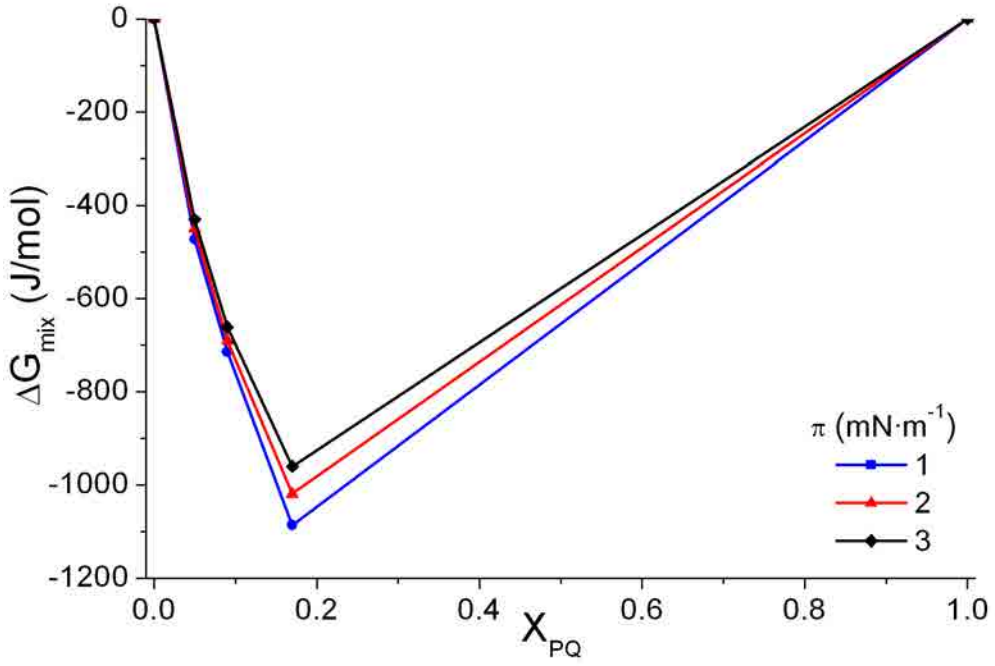

Figure 5.11.5. Plot of the mixing energy vs. the molar fraction for MD, PQ and MD:PQ mixtures at several surface pressures before the main PQ expulsion.

5.11.3 AFM

In this part we present the topographic images of different MD:PQ mixtures at several surface pressures to light which is the organization of these molecules once transferred to an hydrophilic substrate (mica) and ultimately, correlate this knowledge with the predicted results in previous sections. The description and discussion of the AFM topographic images and their mathematical treatment for the pure components MD and PQ are explained in Section 5.6.2 and 5.2.2 respectively. So that, we present in this section only the results of the mixtures and their corresponding discussion.

Figure 5.11.6 shows the AFM topographic images corresponding to pure MD and the selected MD:PQ mixtures transferred on mica at π = 6 $mN \cdot m^{-1}$. The surface pressure used permits us to ensure that PQ is present in all the mixtures showing the larger differences for these systems. The images A-D show two different tonalities of brown (fair and dark) and both correspond to the MD or MD:PQ monolayer, being each tonality correlated with a different physical state of the system monolayer. On the other hand, it is also important to observe that the topographic images corresponding to the MD:PQ 20:1 and 10:1 are alike, whereas the pure MD and MD:PQ 5:1 systems are quite similar, confirming the two different behaviours observed in the π-A isotherms. Moreover, the images present at all the MD:PQ ratios some rounded shape structures with a diameter of $\approx$ 80-150 nm and a variable height of 4 - 8 nm, corresponding the higher height to the higher PQ content.

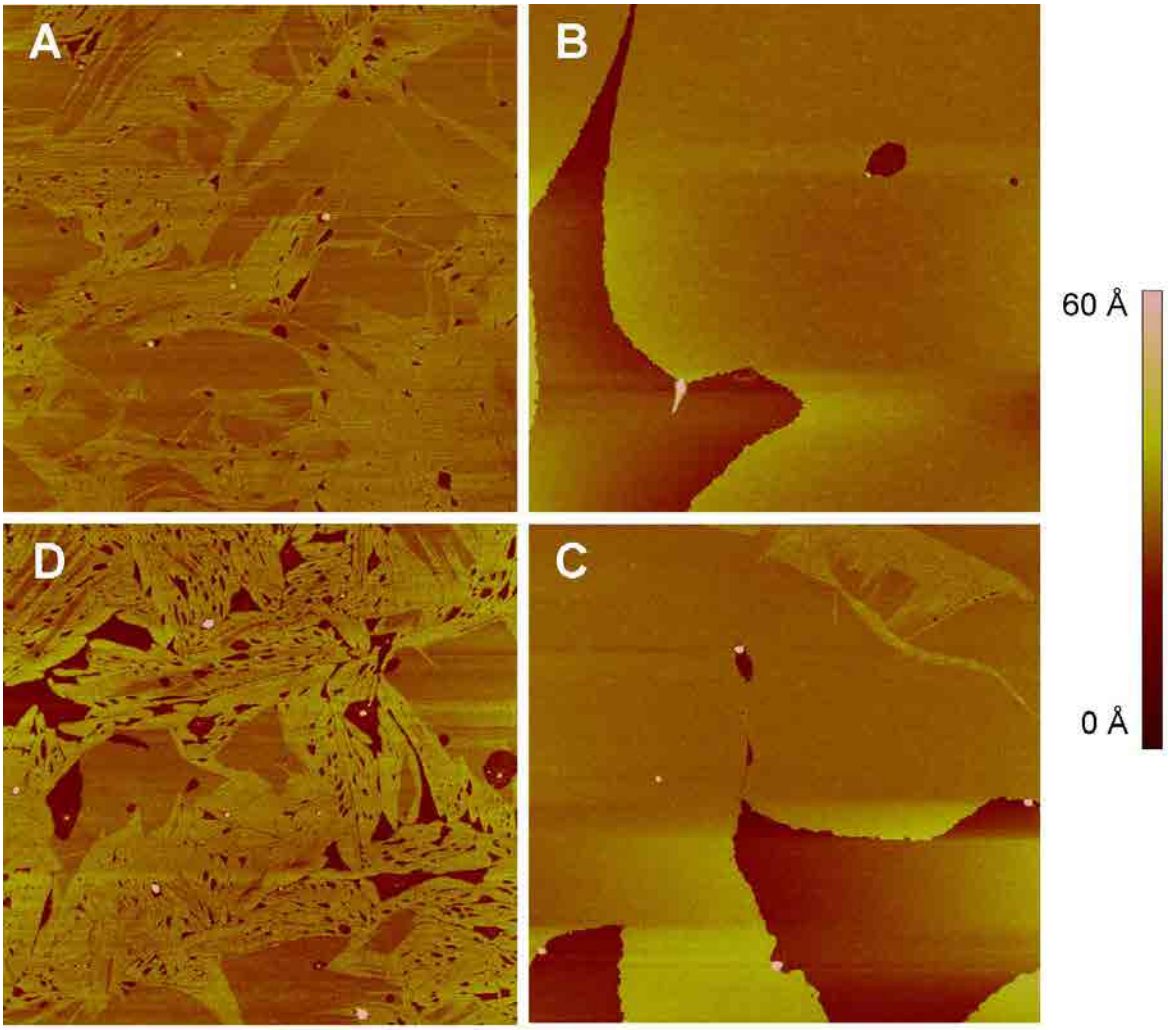

Figure 5.11.6. AFM images (5μm x 5μm) for LB films transferred on mica at 21ºC at π = 6 mN·m^{-1} for (A) pure MD and MD:PQ systems (B) 20:1, (C) 10:1, (D) 5:1.

In order to explain the behaviour of the MD:PQ mixtures at several surface pressures, we have selected the 5:1 ratio (Figure 5.11.7) and the 10:1 ratio (Figure 5.11.8) due to the large differences observed between them. As it has been explained for pure MD, the MD:PQ systems presents three different tonalities of brown (fair, medium and dark) and each one corresponds to zones with a different order of the molecules. On the other hand, it is interesting to point that at π = 1 mN·m^{-1} and only for the 5:1 ratio (Figure 5.11.7A), the image presents dark brown zones which corresponds to a very fluid LE phase. The compression of the MD:PQ 5:1 or 10:1 systems leads to a more compact fashion of the more ordered zones till π = 33 mN·m^{-1} where practically all the monolayer is compact remaining only small rounded zones with the molecules in a less ordered state. The topographic differences between MD:PQ 5:1 and 10:1, are especially important at $\pi \leq$ 15

$mN \cdot m^{-1}$ where different morphologies of the higher domains are observed (See Figure 5.11.7 and 5.11.8). The MD:PQ 20:1 system (not shown) is very similar to the 10:1. It is also interesting to point that the white rounded structures observed at low surface pressure increases in number when increasing the surface pressure, presenting a diameter of 80-160 nm with a height of 4-10 nm for the MD:PQ 5:1 system, and a diameter of 80-200 nm with a height of 4-14 nm for the MD:PQ 10:1 system.

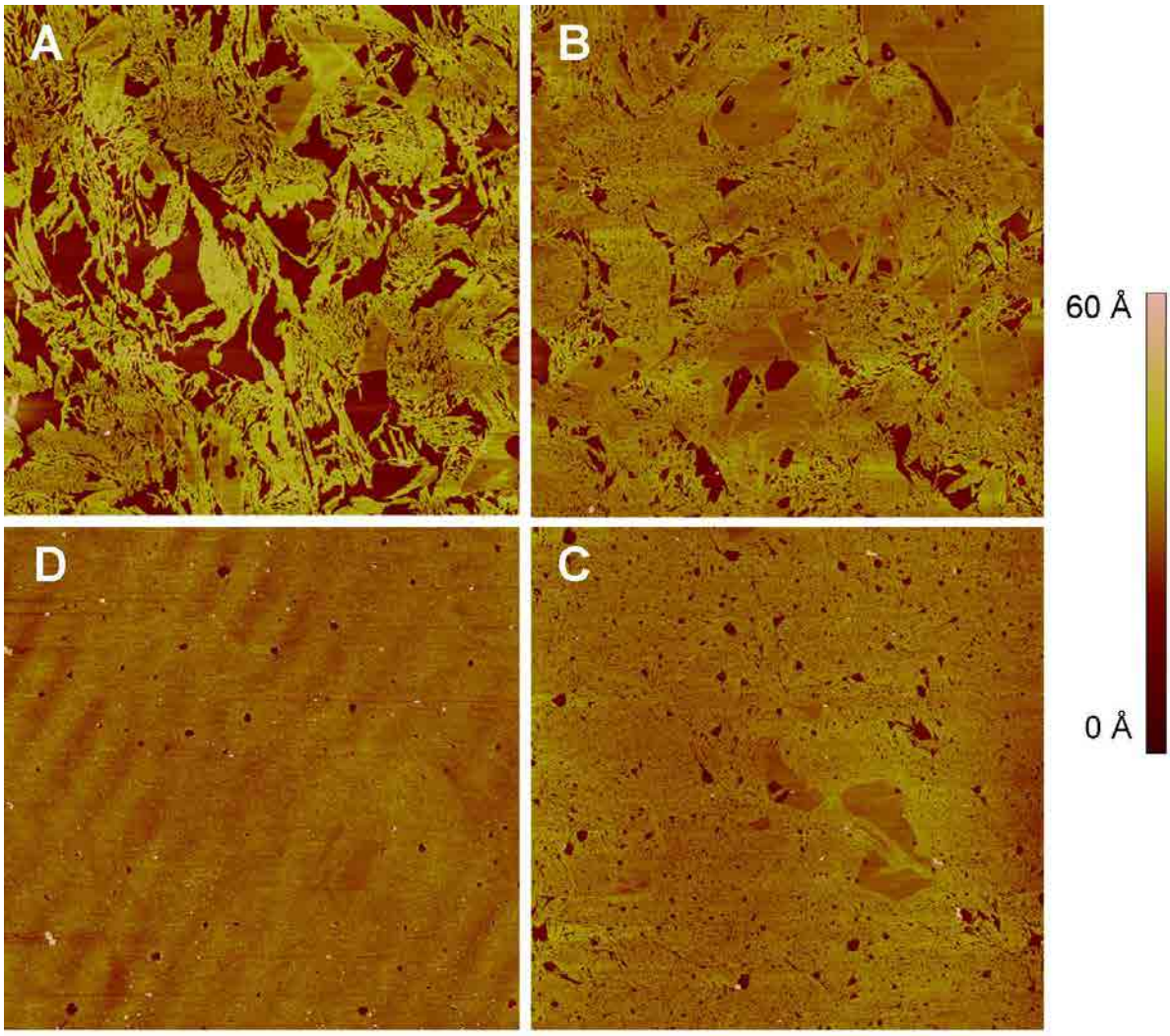

5.11.7. AFM images (20μm x 20μm) for LB films of MD:PQ 5:1 system transferred on mica at 21ºC at (A) π = 1 $mN \cdot m^{-1}$, (B) π = 6 $mN \cdot m^{-1}$, (C) π = 15 $mN \cdot m^{-1}$, (D) π = 33 $mN \cdot m^{-1}$.

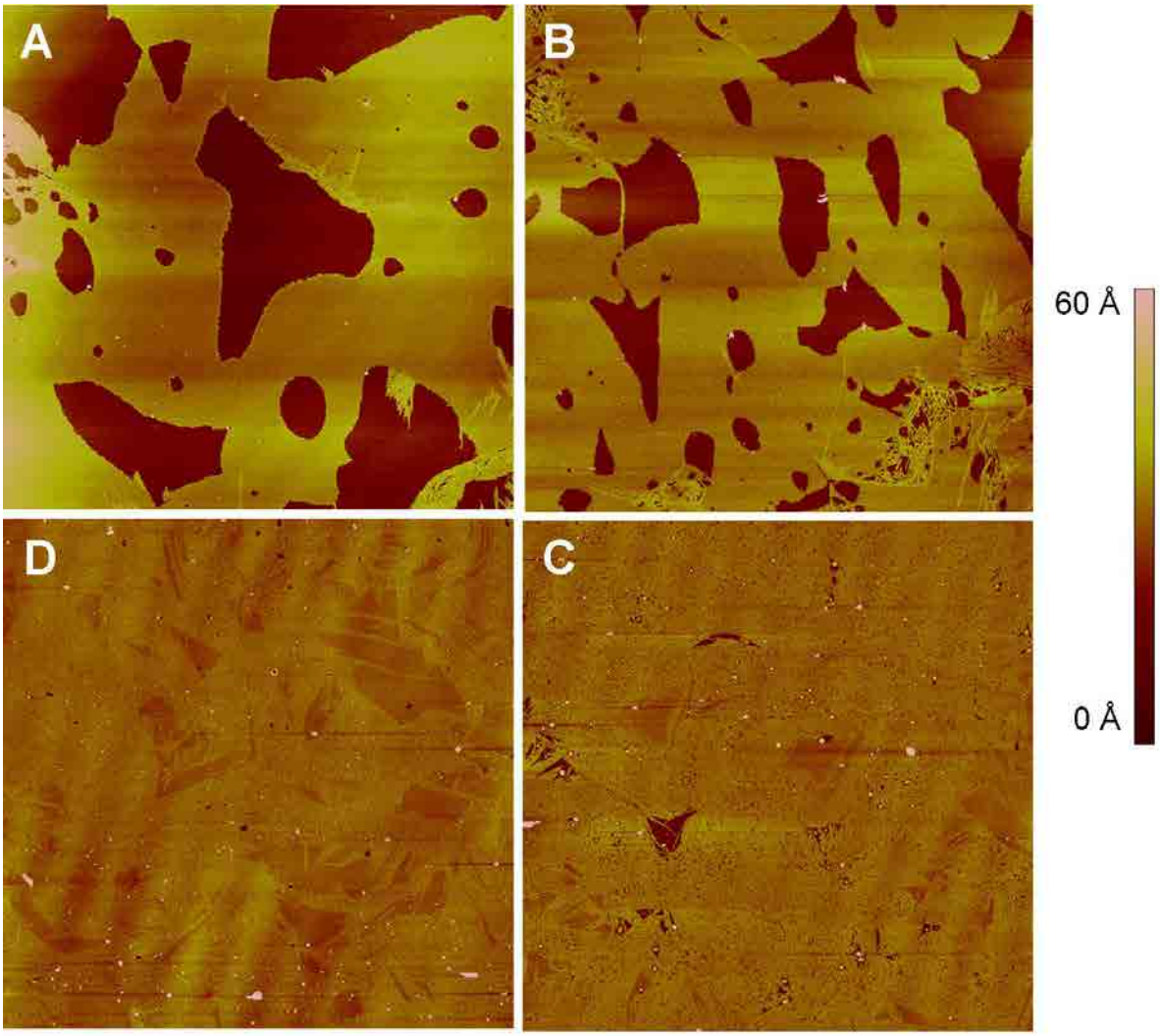

5.11.8. AFM images (20μm x 20μm) for LB films of MD:PQ 10:1 system transferred on mica at 21ºC at (A) π = 1 mN·m^{-1}, (B) π = 6 mN·m^{-1}, (C) π = 15 mN·m^{-1}, (D) π = 33 mN·m^{-1}.

AFM discussion

As it has been explained for pure MD (Section 5.6.2), each brown tonality indicates a different tilt order of the molecules that depends on the surface pressure and the interactions established between molecules and between the molecules with the substrate. The appearance simultaneously of zones with a high order (fair brown zones) with zones of low order (dark brown zones) in pure MD indicates that the meaning of the tonalities is also the same for the mixtures. However, the different physical states deduced using the C_s^{-1} curves for MD and the several MD:PQ systems suggest, that the different tonalities are correlated with different ordering state, but the order that represents each tonality depends on the PQ presence.

In order to light each physical state, we have measured the relative height between fair and medium brown zones referred to the dark zones. Assuming the height of 6 ± 2 Å for the dark brown zones referred to the mica surface, the absolute height is presented in Table 5.11.2. The selection of this height value for the dark zones is done based on that this is the height measured between the dark brown zones and the black zones seen at low surface pressure for the MGDG:PQ 5:1 system (Inset of Figure 5.9.8A) and moreover, this height is in accordance with the 3-6 Å observed in the literature for the LE state of DPPC monolayers [53,54]. It is relevant to observe that the high LC state height of the topographic images of the MD:PQ 10:1 and 5:1 systems suggest the presence of a more fluid LE state at π = 1 mN·m^{-1} compared with higher surface pressures. The absolute heights obtained at each surface pressure and considering the C_s^{-1} results permit the obtaining of the physical state corresponding to each tonality for all the systems (Table 5.11.2), where LC1 and LC2 have the meaning explained for pure MD (see Section 5.6.2). On the other hand, it is important to explain that despite the $C_s^{-1}{}_{\max}$ value for the MD:PQ 20:1 system indicates the S physical state, the AFM results indicate the LC2 phase as the most compact state. This behaviour can be explained due to the $C_s^{-1}{}_{\max}$ value is only slightly higher than the expected value for the S state.

Table 5.11.2. Height of each physical state for the LB monolayers of MD and MD:PQ mixtures on mica. *Estimated value (more information in the text).

	LE	LC1	LC2	S
MD	6 ± 2 *	21 ± 1	25 ± 1	
MD:PQ 20:1	6 ± 2 *	20 ± 1	23 ± 1	
MD:PQ 10:1	6 ± 2 *	22 ± 1	24 ± 1	27 ± 1
MD:PQ 5:1	6 ± 2 *	22 ± 1	24 ± 1	

The MD and MD:PQ mixtures monolayers cover the entire mica surface at all the studied surface pressures. The non-observation of uncovered mica zones permits obtaining the proportion of each physical state. The Figure 5.11.9 presents the percentage of the monolayer in the most compact state, so that, according to the Table 5.11.3, the proportion of each physical state can be elucidated.

Table 5.11.3. Physical states of each zone (dark and fair brown) corresponding to the MD and MD:PQ systems at several surface pressures.

	MD		MD:PQ 20:1		MD:PQ 10:1		MD:PQ 5:1	
π ($mN \cdot m^{-1}$)	Dark	Fair	Dark	Fair	Dark	Fair	Dark	Fair
1	LE	LC1	LE	LC1	LE	LC1	LE	LC1
6	LE	LC1	LE	LC1	LE	LC1	LE	LC1
15	LE	LC2	LE	LC2	LE	LC2	LE	LC1
33	LC1	LC2	LE	LC2	LE	S	LE	LC2

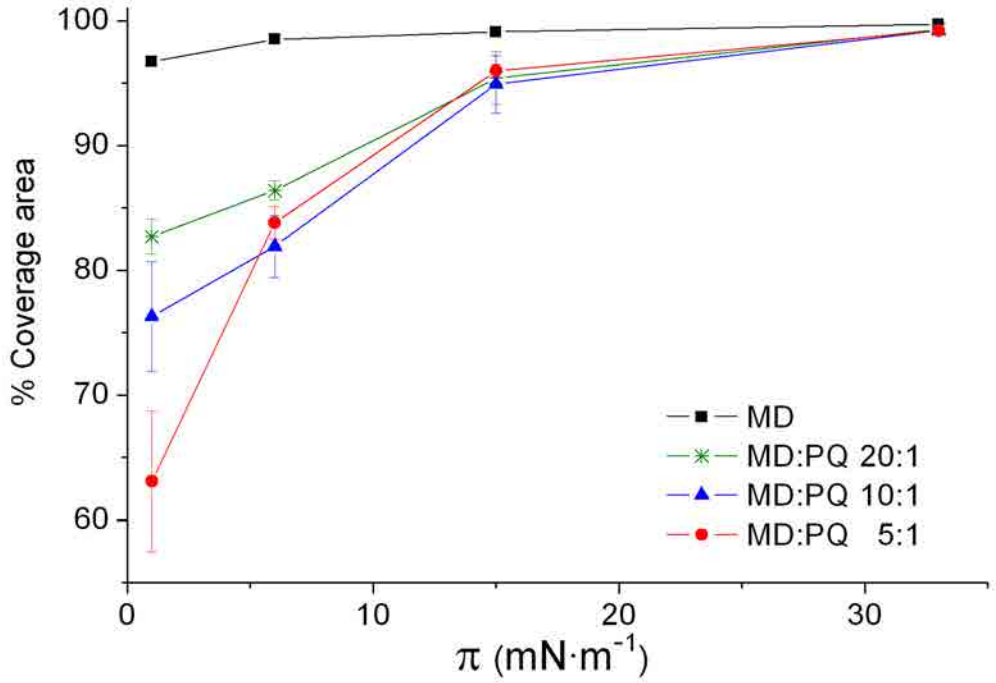

Figure 5.11.9. Monolayer coverage of the fair brown zones on the mica surface for the pure MD and the MD:PQ mixtures, calculated from AFM images.

The results obtained in Figure 5.11.9 for the MD:PQ systems show the expected trend of more surface covered by the compact state when decreasing the PQ content. Increasing the surface pressure, all the MD:PQ systems increases the presence of LC zones achieving at π = 15 $mN \cdot m^{-1}$ a nearly flat increase which is correlated with that the major content of PQ has been rejected from the lipid matrix. The MD:PQ 5:1 at π = 6 $mN \cdot m^{-1}$ is the unique exception for the explained trend, and the reason for that is the explained different effect of PQ in the MD matrix order at high PQ content. On the other hand, pure MD presents a

nearly flat increase of the area covered by the more compact phase when increasing the surface pressure. The explanation is the relatively quick transformation of the LE to LC state, which leads that the entire monolayer is in a high ordered state at 15 $mN \cdot m^{-1}$.

5.11.4 Electrochemical behaviour

In this section, the electrochemical behaviour of the ITO-MD:PQ/electrolyte systems and its mathematical treatment are presented. On the other hand, the results and their corresponding discussion of the pure components MD and PQ are exposed in sections 5.6.3 and 5.2.3 respectively, so that, they will be only presented in this section in case it is necessary to compare with the mixtures results. In our experiments, three CVs are required to obtain the stationary state in the electrochemical response, presenting a good reproducibility from the third scan and at least 15 cycles.

Figure 5.11.10 presents the cyclic voltammograms at 10 $mV \cdot s^{-1}$ of the system ITO-MD and ITO-MD:PQ 5:1 at several surface pressures which, in part, are the same that were selected for topographic AFM imaging on mica. It must be considered that the topographic images observed for the MD:PQ system on mica are not directly correlated with the film deposited on ITO due to the differences between substrates in surface roughness and physico-chemical properties, although it can be extrapolated.

The ITO-MD:UQ/electrolyte 5:1 at π = 33 $mN \cdot m^{-1}$ shows two reduction and two oxidation peaks. At π = 15 $mN \cdot m^{-1}$ two oxidation peaks are also present but only one reduction peak is observed, which is explained by the early hydrogen evolution that occurs at this surface pressure. The redox processes have been labelled according to those observed for the ITO-PQ and ITO-DGDG:PQ systems (Section 5.2.3 and 5.10.5, respectively). The main difference between the DGDG:PQ and the MD:PQ systems is that both processes (I and II) of the MD:PQ 5:1 system presents similar relevance whereas the process II_O becomes quite more important than I_O in the DGDG:PQ 5:1 system when increasing the surface pressure. On the other hand, it is interesting to observe that the double layer capacity of the ITO-MD experiments is fitted in the capacitive current of the ITO-MD:PQ systems (See Blank line in Figures 5.11.10). Moreover, a wave at ≈ 0.40 V can also be seen in the cathodic scan for the voltammogram at π = 33 $mN \cdot m^{-1}$.

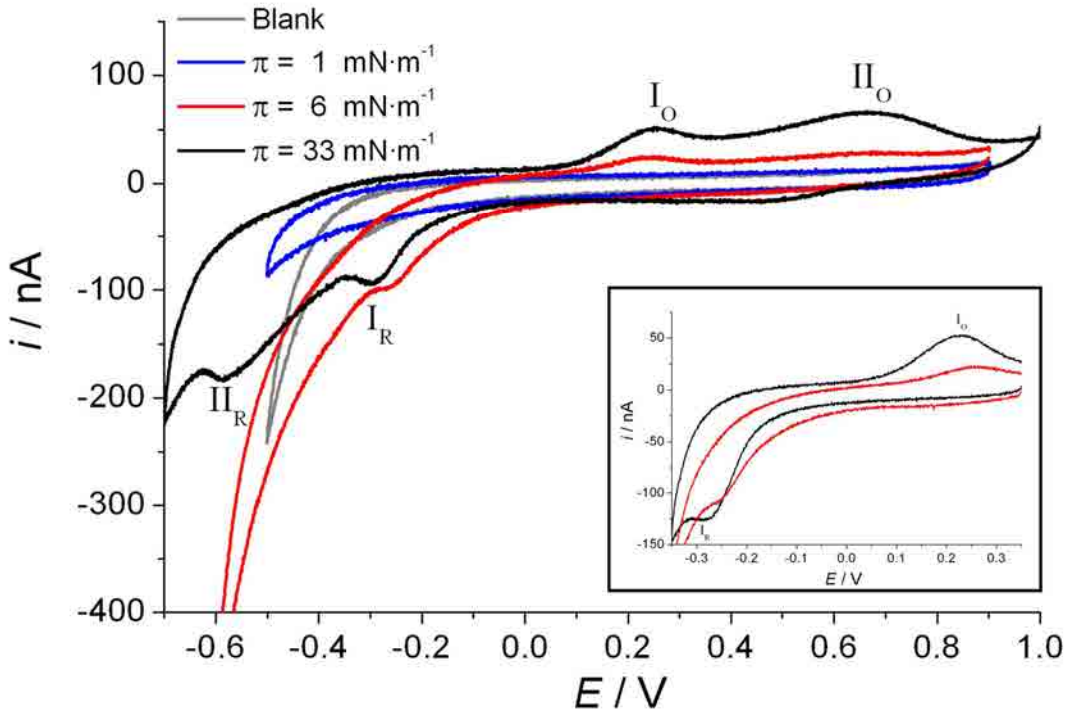

Figure 5.11.10. CV of ITO-MD:PQ 5:1 LB films transferred at several surface pressures. Blank line represents the CV of the ITO-MD electrode. Inset corresponds to the MD:PQ system at 5:1 ratio in short potential window transferred at π = 6 and 33 mN·m^{-1}. All CVs have been performed using 0.150 M of KCl electrochemical cell and a potassium phosphate buffered solution at pH 7.4, at a scan rate of 10 mV·s^{-1}.

Table 5.11.4. Redox peaks potentials and the formal potential that they represent for the ITO-MD:PQ 5:1/electrolyte system.

π (mN·m^{-1})	E_{pR} (I) (V)	E_{pO} (I) (V)	E_f (I) (V)	E_{pR} (II) (V)	E_{pO} (II) (V)	E_f (II) (V)
6	-0.27 ± 0.03	0.26 ± 0.02	-0.01 ± 0.02	-	0.68 ± 0.02	-
33	-0.29 ± 0.02	0.23 ± 0.02	-0.03 ± 0.02	-0.58 ± 0.02	0.67 ± 0.02	0.05 ± 0.02

Figure 5.11.11 presents the CVs for the ITO-MD:PQ 10:1 system at π = 33 mN·m^{-1} using several scan rates and the Figure 5.11.12 shows the CVs of the ITO-MD:PQ/electrolyte 5:1 and 10:1 systems at π = 33 mN·m^{-1} and the ITO-PQ/electrolyte system at π = 2 mN·m^{-1}, being all experiments scanned at 200 mV·s^{-1}. It is interesting to observe in Figure 5.11.12 that the cyclic voltammograms at 200 mV·s^{-1} of the ITO-MD:PQ 10:1 and 5:1 systems transferred at π = 33 mN·m^{-1}, presents the same redox peaks positions. However, the Figure 5.11.11 shows that when decreasing the scan rate, the shape of the cyclic voltammogram changes for the ITO-MD:PQ 10:1 system. In addition, the inset of Figure 5.11.11 represents

the CVs at 10 $mV \cdot s^{-1}$ of the ITO-MD:PQ/electrolyte 10:1 system at several surface pressures. The ITO-MD:PQ/electrolyte 10:1 system presents, at low scan rates, a capacitive current that involves a quite larger charge, as it can be observed in the inset of Figure 5.11.11.

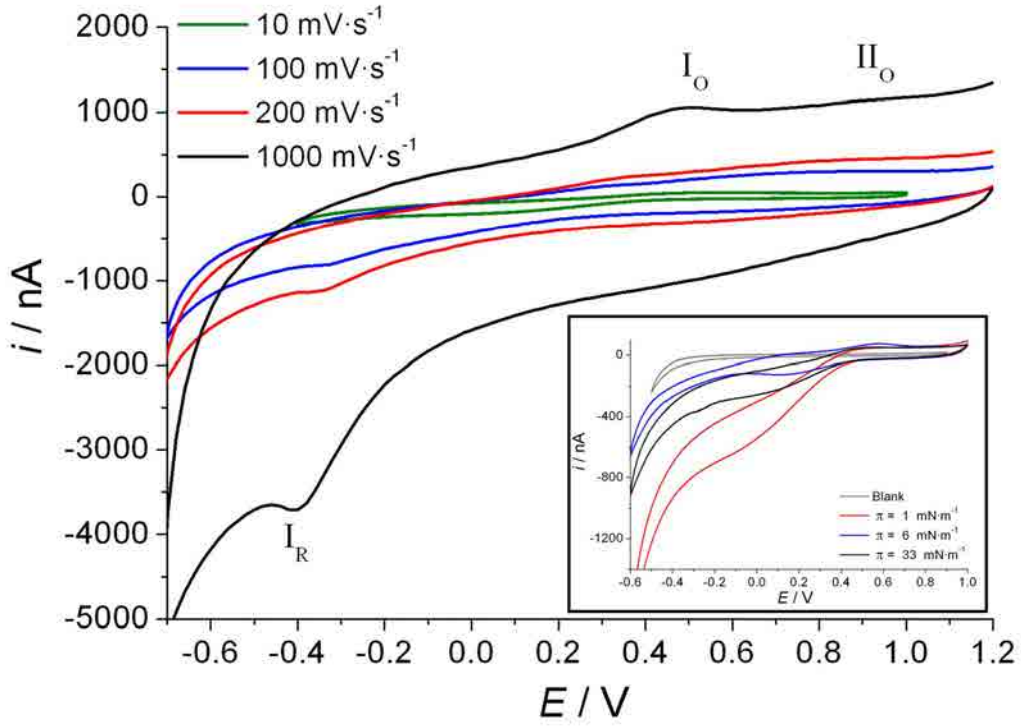

Figure 5.11.11. CVs for the ITO-MD:PQ 10:1 system transferred at π = 33 $mN \cdot m^{-1}$ using several scan rates. Inset corresponds to the CV of ITO-MD:PQ 10:1 LB films at several surface pressures. Blank line represents the CV of the ITO-MD electrode. All CVs have been performed using 0.150 M of KCl electrochemical cell, using potassium phosphate buffered solution at pH 7.4 and at a scan rate of 10 $mV \cdot s^{-1}$.

Although the global sight of this capacitive current is similar at the several surface pressures studied (Figure 5.11.11), the charge involved in it seems to have little relation with the surface pressure. We correlate this capacitive current with the polarization of the ITO-MD:PQ layer which induces structural changes on the monolayer and induces the penetration of a considerable quantity of hydrogen ions in the lipid matrix, being this process favoured at low scan rates. The relevance of this process on the total measured current seems to depend on the structure and compactness of the lipid layer that, in turn, depends on the surface pressure and the MD:PQ ratio. The magnitude of this capacitive current increases with the scan rate in a lower extent than the PQ faradaic redox peaks current, so only at high scan rates the redox peaks are seen, and, in consequence, the formal

potentials can not be elucidated for the ITO-MD:PQ/electrolyte 10:1 system. So that, only the peaks and formal potentials of redox processes I and II for the ITO-MD:PQ/electrolyte 5:1 system are summarized in Table 5.11.4. On the other hand, as it can be seen in the inset of Figure 5.11.12, the ITO-MD:PQ/electrolyte 5:1 system presents a process I with peaks position and formal potential very close to those of the ITO-PQ/electrolyte system (Section 5.2.3).

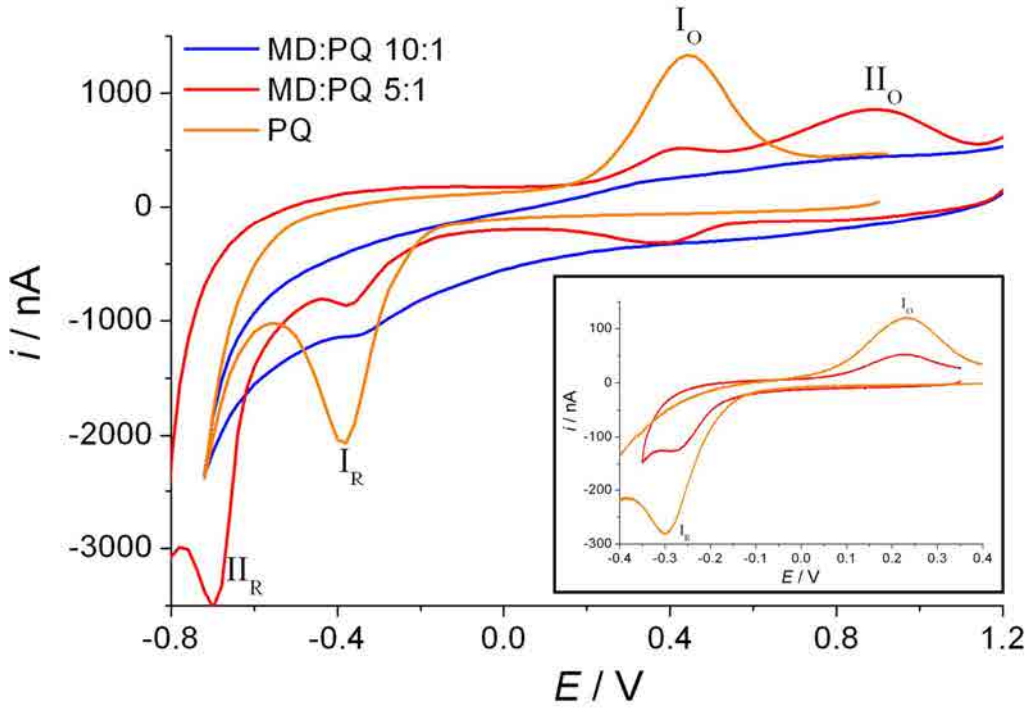

Figure 5.11.12. CVs of ITO-MD:PQ 5:1 and 10:1 transferred at π = 33 mN·m^{-1} and at 200 mV·s^{-1} and pure PQ transferred at π = 2 mN·m^{-1}. Inset presents the CVs of the same systems, except the ITO-MD:PQ 10:1, in a shorter potential window and at 10 mV·s^{-1}. All CVs have been performed using 0.150 M of KCl electrochemical cell using potassium phosphate buffered solution at pH 7.4.

Discussion of the electrochemical response of the ITO-MD:PQ/electrolyte system

We understand that the global reaction and the mechanism proposed for pure PQ in confined situation (Section 5.2.3) is the same for the PQ of the ITO-MD:PQ/electrolyte system. The shape of the voltammograms for the ITO-MD:PQ/electrolyte 5:1 system presents two important deviations respect to the theoretical models proposed in the literature to describe the cyclic voltammetric response of a surface confined reaction [29-31]. First, the peak shape, which is not symmetrical, presenting the reduction peak a sharper shape than the oxidation one, a similar situation that it was observed by Märtensson and

Agmo [32] and Hong and Park [22] studying UQ and hydroquinone respectively. Second, the redox peaks separation for process I or process II is larger than the expected for such systems. The ITO-MD:PQ/electrolyte 10:1 system presents a huge capacitance current that mask the redox peaks corresponding to the PQ/PQH_2 redox process, so only the electrochemical behaviour of the ITO-MD:PQ/electrolyte 5:1 system will be deeply explained in this section.

The different shape of reduction and oxidation peaks can be explained by the different hydrophilic character of the redox couple PQ/PQH_2, as it was pointed for the PQ-ITO system (Section 5.2.3). The larger polarity of PQH_2 compared with PQ leads the former to establish better attractive interactions by dipole-dipole or hydrogen bond between PQH_2 and MD headgroups and, in addition, the PQH_2-ITO, PQH_2-PQH_2 and PQH_2-water interactions are also enhanced [4,25-27,32-38,84,85,93] . During the oxidation scan PQH_2 is the reactant so the possibilities of hydrogen bonds are larger, increasing the stabilization of the PQH_2 molecule and making it more difficult to oxidise. These arguments are also valid for explaining the larger width of the oxidation peak compared with that of the reduction process.

The Figure 5.11.13 presents the redox peak potentials of processes I and II vs. the scan rate for the ITO-MD:PQ/electrolyte 5:1 system. The redox peaks separation for process II is larger than for process I indicating that process II is even more irreversible than process I. Moreover, the redox peaks separation for both processes is enhanced when increasing the scan rate. This separation makes both processes (I and II) more irreversible and it represents a similar trend to that it was observed by Marchal et al. [21] and by Laval and Majda [41]. This large separation for both processes aroused from the slow charge transfer rates at ITO-monolayer|electrolyte interface [32]. In addition, it can be also inferred from Figure 5.11.13 that the increase in the scan rate affects in a larger extent the oxidation peak potential than the reduction one, which produces that the midpoint potential for process I and II has scan rate dependence. On the other hand, it is interesting to observe that all the linear adjustments of the processes I and II reduction peaks for the ITO-MD:PQ/electrolyte 5:1 system (Figure 5.11.13) have a similar slope and similar trend is shown for the oxidation peaks of the same processes. In the ITO-MD:PQ/electrolyte 5:1 system, the y-intercept of the linear adjustment of each reduction peak is fixed regardless the surface pressure. The

absence of potential displacement when increasing the surface pressure indicates that in the MD:PQ system, the environment that PQ experiences is very similar at the studied surface pressures. Moreover, the figure has been separated in low and high scan rates because at low scan rates (< 20 $mV \cdot s^{-1}$) the linear adjustments of the reduction and oxidation peak potentials of processes I and II present a higher slope (Figure 5.11.13A) than at high scan rates (Figure 5.11.13B), which is explained by the hindrance increase of the electrochemical process when increasing the scan rate.

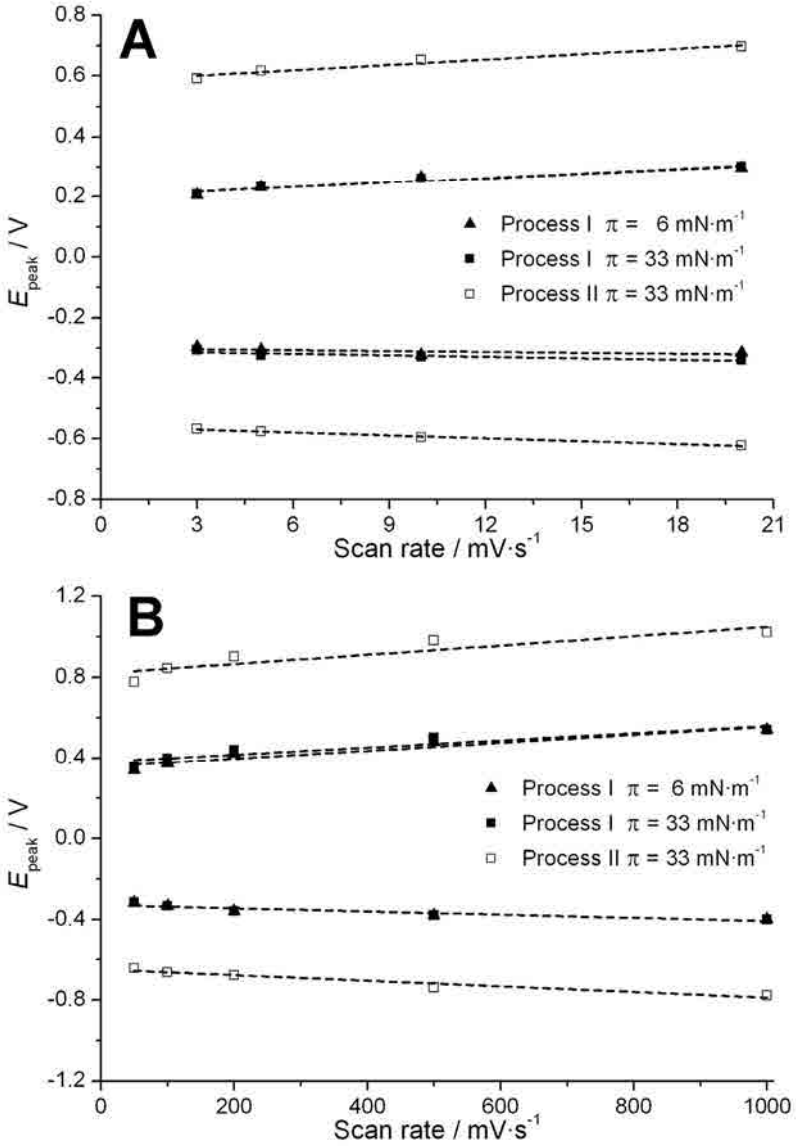

Figure 5.11.13. Peak potential vs. the scan rate for the ITO-MD:PQ 5:1/electrolyte system at π = 6 and 33 $mN \cdot m^{-1}$ at A) low scan rates and B) high scan rates.

Moreover, the current intensity of the redox peaks (i_{peak}) has been studied for the ITO-MD:PQ/electrolyte 5:1 system at several scan rates and it has been shown that the reduction

(not shown) and the oxidation current intensity are related by a linear dependence with the scan rate (Figure 5.11.14) so indicating that PQ molecules are surface confined in both processes [16,29] and that the electron transfer process is not diffusion controlled. Our results are in line with the observations of Märtensson and Agmo [32] for scan rates < 1 $V \cdot s^{-1}$, Gordillo and Schiffrin [28] and Li et al. [43] for monolayers containing UQ confined on the electrode surface.

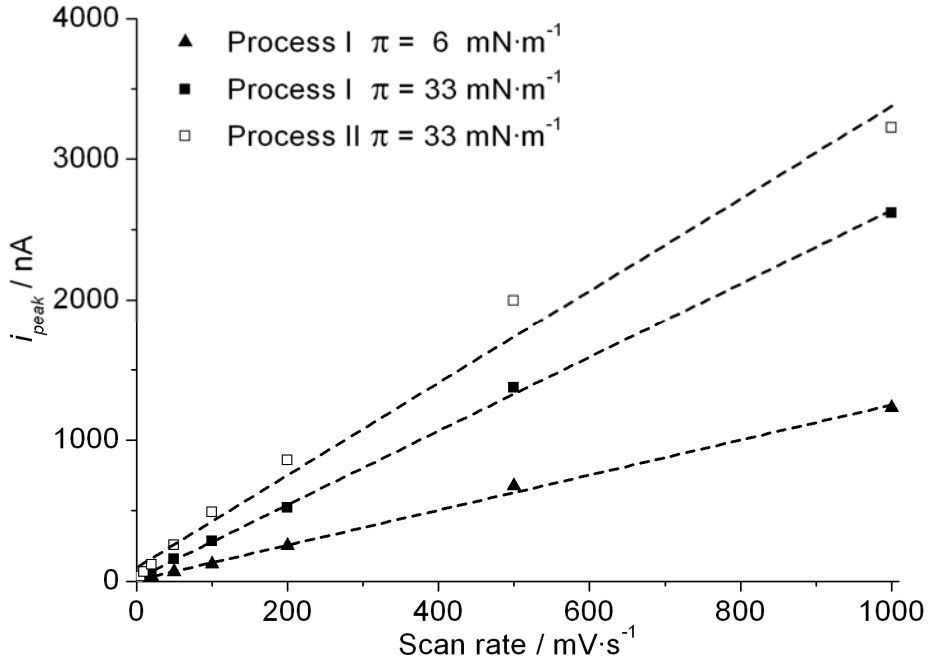

Figure 5.11.14. Oxidation peak intensity vs. the scan rate for the ITO-MD:PQ 5:1/electrolyte system at π = 6 and 33 $mN \cdot m^{-1}$.

The charge involved in the LB monolayer transferred at each surface pressure is obtained by integrating the area under the reduction or oxidation waves. The surface coverage (Γ) is obtained from the experimental values of charge and considering the global reaction for PQ in confined situation (Section 5.2.3). The Γ for the ITO-MD:PQ/electrolyte system is shown in Table 5.11.5 and compared with the expected value to obtain the electroactive fraction of PQ. The expected surface coverage (Γ_{expec}) values are calculated assuming that PQ and MD molecules are perfectly spread, accordingly to the corresponding ratio, on the ITO surface, being the resulting value corrected with the transfer ratio associated to it in the LB transfer process. We have chosen to show in Table 5.11.5 the oxidation surface coverage (Γ_O) of the redox processes, which are similar but lower than the results obtained for the reduction scan that have the undesirable contribution of hydrogen evolution.

Table 5.11.5. Expected and experimental total surface coverage, experimental surface coverage for process I and electroactive fraction involved in the whole redox process for ITO-MD:PQ 5:1/electrolyte system using 0.150 M of KCl electrochemical cell, using potassium phosphate buffered solution at pH 7.4 and at a scan rate of 10 $mV \cdot s^{-1}$.

π ($mN \cdot m^{-1}$)	Γ_{expec} (10^{-12} mol · cm^{-2})	$\Gamma_{O\ tot}$ (10^{-12} mol · cm^{-2})	$\Gamma_{O\ proc\ I}$ (10^{-12} mol · cm^{-2})	Electroactive fraction (%)
MD:PQ 5:1				
6	35.6	8.2	8.2	23.0
33	57.3	45.0	14.0	78.5

In our experiments the enough presence of available protons close to the PQ heads avoids the high local PQ concentration problem, so the electroactive fraction is enhanced when increasing the initial PQ content which is explained by the electron hopping effect (see Section 3.4.5). Moreover, the non-homogeneous electrode surface and the semiconductive properties of ITO induce it to behave different than metal surfaces like gold or mercury contributing with the different environments that PQ head experiences in the chain region [41] to reduce the electroactive fraction [9].

The explanations given in Section 5.8.5 when comparing our ITO-MGDG:UQ/electrolyte system with the literature, are also valid for the ITO-MD:PQ/electrolyte due to the high MGDG content in the MD mixture and the similarities between PQ and UQ, which induce a similar formal potential for processes I and II in our experimental conditions, as it has been shown in Sections 5.8.5 and 5.11.5. The slight differences observed between the literature for UQ and our results for PQ are related with the differences between both prenylquinones, the physicochemical properties of the substrate, the differences on the electrolyte solution and the differences in the distance prenylquinone head-substrate surface. All the formal potentials observed by previous authors for the quinone redox process are less thermodynamically favourable than that observed in this work, which is correlated with the higher availability of protons in our system. The process I observed in our experiments requires direct contact or short distance between ITO and the PQ head, which can be correlated with the exposed situations [21,23,41,86].

PQs are present in two main positions in natural cell membranes being PQ_A bounded to the PSII and PQ_B that can free move. The electron flow from PQ_A to PQ_B is possible thanks to

the higher redox potential for the latter due to the hydrogen bonds between the keto-oxygens and surrounding protein residues [130]. This natural behaviour can be compared with our biomimetic MD:PQ system in which the different positions "diving" and "swimming" has also different redox potential. The redox potential for the "swimming" PQ is ≈ 110 mV higher than that of the "diving" PQ, which, by chance, is in line with the ≈ 80 mV that PQ_A is higher than PQ_B [130]. The higher redox potential permit the electron flow from the diving position to the swimming position so favouring the electron hopping explained.

5.11.5 Global sight of the MD:PQ system transferred on ITO using the LB technique

In this section we explain the global behaviour of the MD:PQ system and the position of the PQ molecules in the monolayer studying the results obtained from the used techniques.

The lower C_s^{-1} values observed for the MD:PQ 5:1 mixture compared to the pure MD after the kink point indicate that the presence of remaining PQ molecules ("diving" position, see Section 3.4.2) reduce the compactness of the MD:PQ 5:1 mixture monolayer. However, the higher C_s^{-1} values observed for the MD:PQ 10:1 and 20:1 mixture compared to the pure MD after the kink point indicate that the presence of the remaining PQ molecules ("diving" position, see Section 3.4.2) influences the MD mixture obtaining a stabilization of the ternary mixture MGDG:DGDG:PQ (MD:PQ). Regardless the MD:PQ ratio of the mixture, the shape of their π-A isotherms, the shape of their C_s^{-1} curves and the shape of their kink points in the C_s^{-1} curves suggest that the system experiences a sudden PQ expulsion of most of the PQ content. However, it is important to indicate that this expulsion for the MD:PQ 10:1 and 20:1 is in a quite lower extent than that observed for the MGDG:PQ and DGDG:PQ systems (Section 5.9.1 and 5.10.1), which also points to the stabilization of the ternary mixture MGDG:DGDG:PQ at low initial PQ content. The expulsion of the PQ from the lipid heads region leads to the "diving" position without ITO-PQ contact and the "swimming" position, being this last position and the formation of aggregates favoured at large initial content of PQ and at ordered states, as it was previously observed for UQ [3,25,27,36]. So that, the expulsion of PQ is the way chosen by the MD:PQ mixture to

minimize its energy at the interface [49] and to minimize the low favourable interactions between PQ and the MD chains. The proportion of PQ at each position (diving [4,15, 36,88-95] or swimming [4,84,85,88,91-94,96-103,107]) is defined by the MD physical state and the initial PQ content.

A complete vision of the PQ positions in the MD:PQ monolayer can be obtained considering the thermodynamic description of the physical states, the AFM results of the MD:PQ 5:1 system on mica (Figure 5.11.8) and the CVs of Figures 5.11.10 and 5.11.12. The MD:PQ mixtures at low surface pressure, present less covered area by the LC state when increasing the PQ initial content (Figure 5.11.9). In addition, the height measured for the LC2 state of pure MD is higher than that of the MD:PQ mixtures These observations indicate that PQ is present in both physical states (LE and LC) of the MD:PQ mixtures. The CVs of Figures 5.11.10 and 5.11.12 show that the redox processes I and II are obtained presenting E_f (I) = -0.02 ± 0.02 V and E_f (II) = 0.05 ± 0.02 V. E_f (I) of the ITO-MD:PQ 5:1 system is close to that of process I for the ITO-PQ/electrolyte system (inset of Figure 5.11.12), which indicates that the local environment around each PQ is uniform in both situations [22]. So that, at low surface pressures regardless the MD:PQ domains are in LE or LC state (Figure 5.11.7A), we correlate the “diving” position with the PQ placed in the MD matrix and located in direct contact with the electrode surface. The compression of the explained monolayer induces two actions: First the compactness of the LC state, so favouring the rejection of part of the PQ in “diving” position. On the one hand, it can be vertically rejected to the diving position without ITO-PQ contact and, on the other hand, horizontally to the remaining LE zones so enriching them in PQ. Second, the phase change from LE to LC of the remaining LE zones (Figure 5.11.7B). Further compression results in smaller but more enriched LE zones and a more compact LC state as it is seen in Figure 5.11.7C and D. The non-observation of localized higher zones in Figure 5.11.7.C suggests that PQ molecules are present as single molecules or small pools of molecules in the LE state. These observations are different to that explained for the MGDG:UQ system (see Section 5.8.5) where filament protrusions were seen.

Moreover, the “diving” position present wide redox peaks that, based on the observations for the ITO-MGDG:PQ/electrolyte system (Section 5.9.5), comprises two redox processes I_α and I_β corresponding, respectively, to the PQ molecules in direct contact and the PQ

molecules close to the ITO surface. The difficult deconvolution of these peaks in the ITO-MD:PQ/electrolyte system, even at high scan rate, indicates that both peaks are close each other, suggesting slight changes in the environment that the PQ molecules experience at each position, being the process I_α favoured at low surface pressure. Both peaks of PQ molecules in "diving" position are not distinguished in the voltammograms because present similar formal potential. However, they can explain the slight dependency of formal potential with the surface pressure observed in Figure 5.11.13.

The presence of enriched domains is predictable based on the Van Dijck et al. [105] observations for saturated phospholipids with the same headgroup and others studies presented in the literature [27,35,36,41,93,95,98,106,107]. In addition, Figure 5.11.7C and D present small LE zones in circular shape, which is the shape adopted by the monolayers to minimize the surface tension of the nascent boundary when lipid reorientate in the layer boundaries [118]. They may indicate that the composition in and out the rounded shape is different. On the other hand, according to the values shown in Table 5.11.5, when increasing the surface pressure at which the LB film has been transferred, the charge under oxidation peak II is higher than that of oxidation peak I suggesting that, when changing from LE to LC, the vertical rejection is also favoured, placing part of the PQ molecules in the "swimming" position in the LC zones. The slow LE to LC physical state change permits that part of the PQ molecules to get the most stable position that is the "swimming position". According to the literature and considering the monolayer|air interface, the "swimming" position is more stable than the "diving" position due to the later disrupts the cooperative motions between the MD chains [102]. Moreover, above the MD chains, the medium is air whose hydrophobicity [104] added to the hydrophobicity of the end part of the MD chains stabilize the PQ [6] avoiding the distortion of being inserted between the MD chains. However, the "diving" position can be favoured thanks to a fast physical state change and/or part of the PQ molecules self-aggregate, forming head to head aggregates to withstand the hydrophobic environment of the lipid chain region, in accordance with Roche et al. [6]. It is important to consider that our experiments always present a higher PQ content than the minimum observed in the literature for UQ aggregation (0.5-2 mol%) [1,15,36].

Our results confirm that PQ is confined and the electron transfer takes place mainly by two mechanisms: First, by direct transfer and electron hopping between the PQ placed in "diving" position (process I), and second, by electron hopping through the lipid matrix (process II). The electron hopping favours the rate determining step (1_b) (Section 5.2.3) so favouring the electroreduction in the timescale used. At low surface pressure, the molecules are far enough each other to do not be affected by the electron hopping mechanism. Increasing the surface pressure the PQ headgroups are placed closer favouring the electron hopping redox process.

The differences observed between the CVs of the MD:PQ 5:1 system and the 10:1 could be anticipated by observing the marked different behaviour of their π-A isotherms, the C_s^{-1} curves and the AFM topographic images. The origin of the different capacitive current is unknown, although we propose that the MGDG:DGDG (MD) mixture and PQ at the 20:1 and 10:1 ratios establish strong interactions that stabilize the ternary mixture so forming the system MGDG:DGDG:PQ. At high PQ content, the large PQ presence avoids the ternary stability, so establishing the MGDG:DGDG system with the PQ molecules inserted, so that, producing little stabilization effect on the galactolipid mixture. On the other hand, for the ITO-MD:PQ 5:1 system, we correlate this little stabilization effect with the presence of the current wave at ≈ 0.40 V when scanning cathodically in Figures 5.11.10 and 5.11.12. This wave has no apparently correspondence at the anodic scan. However, our observations for the ITO-MD:PQ 10:1 system suggest that the oxidation correspondence of this wave is convoluted with I_O and II_O. This new wave seems to be favoured at low PQ content (10:1), but in order to clarify its origin, more studies must be performed, so with the results obtained, we can only confirm the presence of two different electrochemical behaviours depending on the PQ content in the MD mixture.

In order to clarify the position and organization of the MD and PQ molecules at each physical state, the Figure 5.11.15 represents the position of MD and PQ molecules of the MD:PQ 5:1 system at the surface pressures studied. This Figure 5.11.15 explains the different meaning of the fair and dark colours observed in the AFM images summarized in Table 5.11.3 and the PQ positions that origin the redox processes I_α, I_β and II.

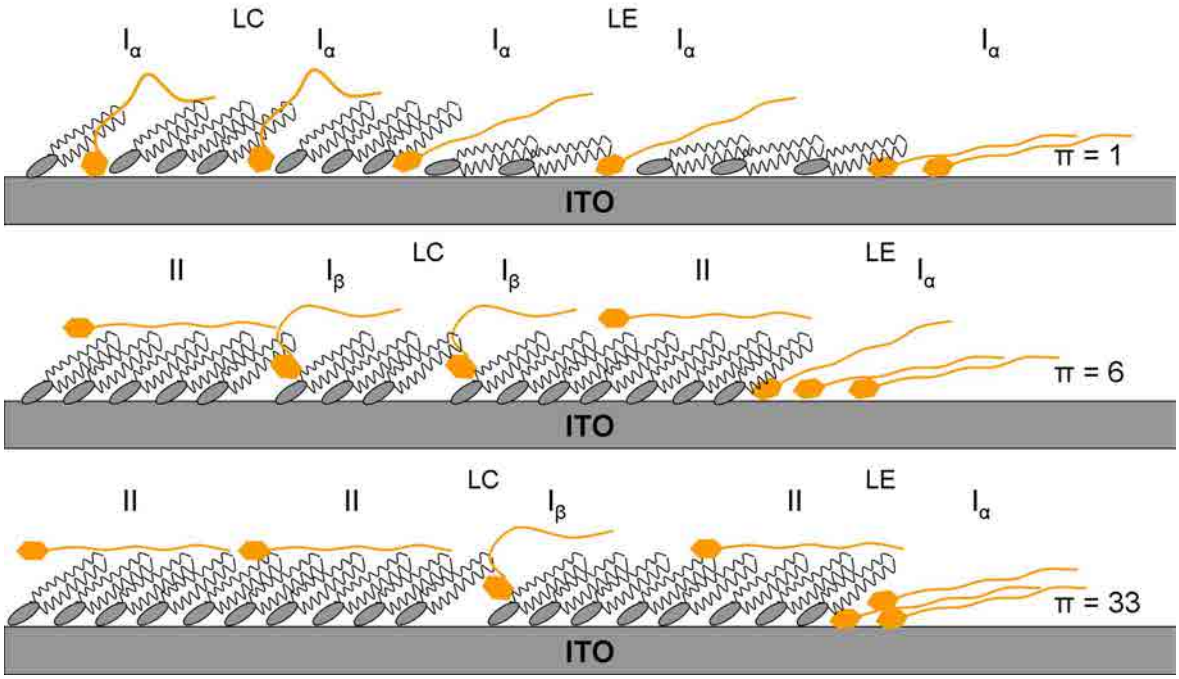

Figure 5.11.15. Scheme of the position of MD and PQ molecules of the MD:PQ 5:1 system at several surface pressures. The labels I_α, I_β and II indicate the PQ positions that origin the redox processes I_α, I_β and II.

5.12 Global sight of the galactolipid and galactolipid:quinone systems

In this section, the global sight extracted from the results of the galactolipids (Sections 5.3-5.6), quinones (Sections 5.1-5.2) and their mixtures (Sections 5.7-5.11) are exposed. On the other hand, we want to remark that the processes labelled as I_α and I_β in the galactolipid:quinone systems are correlated with the redox processes I and I' respectively shown for the DPPC:UQ system. The different nomenclature is based on that, in the case of galactolipid:quinone systems, the redox peaks and the formal potential of processes I_α and I_β are so close each other that they can rarely be deconvoluted, so we consider them as the convoluted process I. However, the processes I and I' present different redox peaks position and different formal potential. This fact points that both processes indicate quite different environment, which may be correlated with the different hydrophilicity, shape and size of the headgroup between galactolipids and DPPC that leads to a different quinone head-ITO distance.

The Figure 5.12.1 shows the π-A isotherms and C_s^{-1} curves (inset) of MGDG and DGDG pure components and the MD (MGDG:DGDG 2:1). The π-A isotherms in Figure 5.12.1 show that the three galactolipids present similar lift-off area. On the other hand, MD presents a lower limiting area than the pure components (See also Tables 5.4.1, 5.5.1 and 5.5.12). Moreover, MD also presents lower collapse pressure than the pure components (Figure 5.12.1). Both observations are explained by the larger formation of collapse structures (rounded white structures) for MD compared with the pure components, which induces that part of the monolayer molecules to be expulsed from the galactolipid|water interface, so reducing the number of molecules and their stability at this region. The $C_{s\ \max}^{-1}$ values (inset of Figure 5.12.1) indicate that MGDG presents LC phase at low surface pressure which undergoes S state at high surface pressure, whereas MD presents mostly LC during the entire isotherm. On the other hand, DGDG presents LE and LC at low and high surface pressure respectively. These results indicate that DGDG presents more fluid states than MGDG, which also affects the MD in which the presence of DGDG hindrances the formation of the S state despite of the high MGDG content.

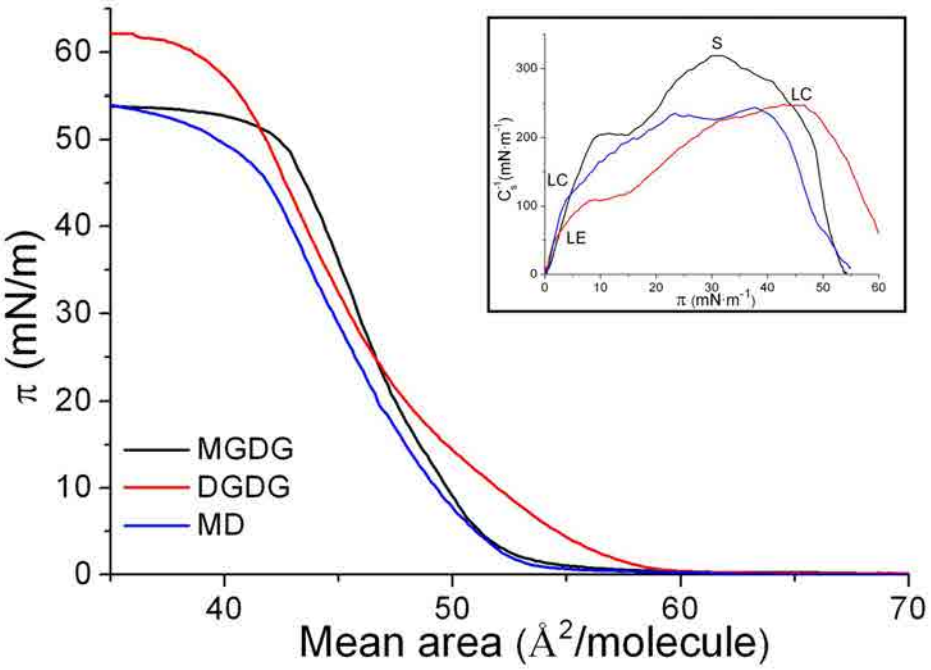

Figure 5.12.1 π-A isotherms for MGDG, DGDG and MGDG:DGDG mixtures at 21 ± 0.5 ºC on water subphase. Inset: Inverse of the compressibility modulus vs. surface pressure for the same systems.

The π-A isotherms and C_s^{-1} curves of UQ and PQ (Figure 5.1 and 5.2) show that both quinones collapse at low surface pressure, 11 mN·m^{-1} and 0.3 mN·m^{-1} respectively, presenting both LE phase at the most compact state. On the other hand, the galactolipid-quinone mixtures present π-A isotherms and C_s^{-1} curves (Figure 5.8.1, 5.8.2, 5.9.1, 5.9.2, 5.10.1, 5.10.2, 5.11.1 and 5.11.2) after the main quinone expulsion, with a global shape close to that of the pure galactolipid, which is the major component. However, at surface pressures before the main quinone expulsion, the surface pressure at which appears the kink point and the extent of the quinone expulsion is accorded to the quinone initial content in the mixture. The surface pressure of this kink point is higher when reducing the quinone content, which is correlated with that quinone is better retained in monolayers when it is present at low concentrations due to it affects in a lower extent the formation and shape of the ordered phases.

The Figure 5.12.2 presents the C_s^{-1} curves of all these studied systems only for the 5:1 ratio, based on the similarities explained for the different galactolipid:quinone ratios. The kink point (the first kink point in the MGDG:UQ system) is placed in all the systems, at a

surface pressure slightly higher than the collapse pressure for the pure quinone present at each system (UQ ≈ 11 mN·m^{-1} and PQ ≈ 0.3 mN·m^{-1}). This fact indicates that the quinone present in the mixtures determines the beginning of the LE to LC phase change of the galactolipid:quinone mixture. On the other hand, comparing different galactolipid:PQ mixtures it is clear that MGDG:PQ and MD:PQ presents the kink point at similar surface pressure whereas the DGDG:PQ shows it at higher surface pressure due to the more fluid physical state of pure DGDG.

All the galactolipid:quinone mixtures present the LC state after the kink point, showing also a similar $C_s^{-1}{}_{max}$ value with the exception of the MGDG:PQ system that presents a higher $C_s^{-1}{}_{max}$. This higher compactness of the MGDG:PQ system is explained by the high order conferred by the MGDG and the PQ expulsion at very low surface pressure, which permits the monolayer to behave closer to the pure MGDG. On the other hand, the phase rule has pointed the quinone expulsion for the galactolipid:quinone mixtures and the number of coexistent states that the mixtures present.

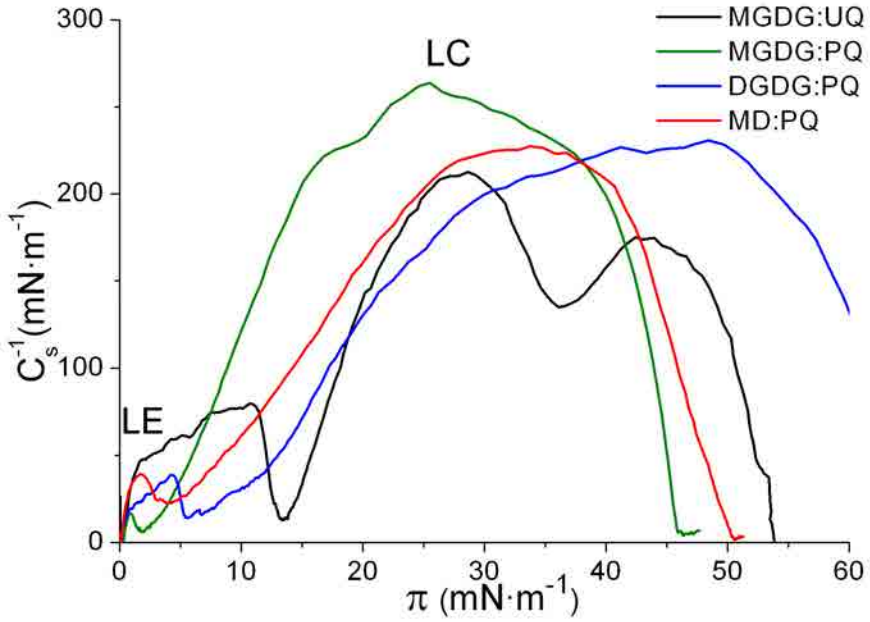

Figure 5.12.2. Inverse of the compressibility modulus vs. surface pressure for MGDG:UQ, MGDG:PQ, DGDG:PQ and MD:PQ mixtures with a 5:1 ratio on water subphase at 21 ± 0.5 ºC.

The thermodynamic studies for galactolipid:quinone mixtures show that galactolipid:quinone systems (Section 5.8.2, 5.9.2, 5.10.2 and 5.11.2) form non-ideal mixtures with positive deviation at low surface pressures (before the corresponding to the

quinone expulsion), which indicates that the interactions between the two components are weaker than the interactions between pure components. In addition the negative values observed at low surface pressures for ΔG_{mix} indicate that the mixed monolayers of galactolipid:quinone are more stable than pure components, although the low ΔG_{mix} values corroborate the low stability of the mixture.

The formation of non-ideal mixtures between quinones and galactolipids is explained by the difference in the chain length between both components which permits a free rotation of the quinone part that protrudes over the galactolipid producing also a motion of the galactolipid molecules, which induces an increase of the molecular area.

The Figure 5.12.3 presents the AFM topographic images for the pure galactolipid systems (A-C) and their corresponding 5:1 mixtures with PQ (D-F) all at π = 15 $mN \cdot m^{-1}$. The images show two main different tonalities of brown (fair and dark) and both correspond to the galactolipid or galactolipid:PQ monolayer, being each tonality correlated with a different physical state of the system monolayer.

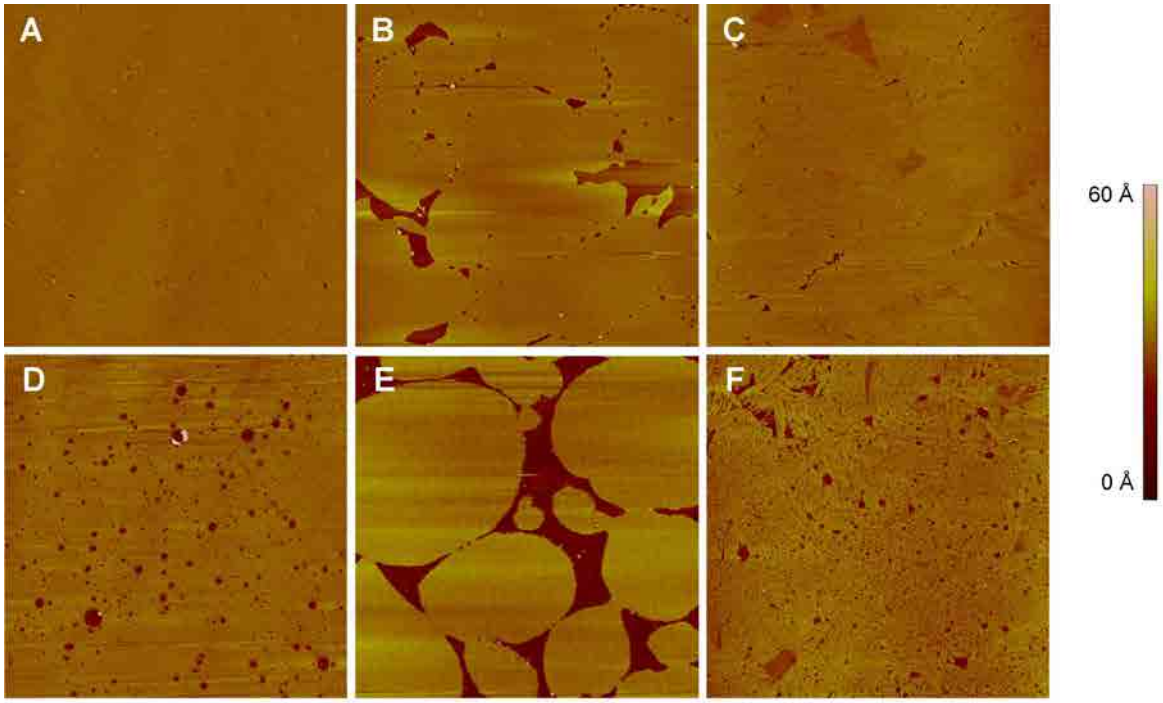

Figure 5.12.3 presents the AFM topographic images (10μm x 10μm) at 15 $mN \cdot m^{-1}$ for the pure systems: A) MGDG, B) DGDG, C) MD and their 5:1 corresponding mixture with PQ: D) MGDG:PQ, E) DGDG:PQ, F) MD:PQ.

Comparing the pure galactolipids (Figure 5.12.3 A-C), it can be observed that MGDG and DGDG differs substantially due to DGDG presents larger fluid zones than MGDG. Moreover, the MD at this surface pressure presents similar topographic images to pure MGDG. On the other hand, looking at the galactolipid:PQ 5:1 mixtures, it is also evident that MGDG:PQ and MD:PQ present similar topographic images and both different to that corresponding to the DGDG:PQ system, which present the LC phase in circular domains forming islands. These images confirms the trend observed using the π-A isotherms and C_s^{-1} curves (Figure 5.12.1) at which at low-medium surface pressure, MGDG leads the compactness of the MD (MGDG:DGDG 2:1) and MD:PQ systems. On the other hand, the compression of the galactolipid:PQ achieve at π = 33 $mN \cdot m^{-1}$ practically the entire monolayer in compact state remaining only small rounded LE zones.

The absolute phase heights obtained for the pure galactolipids and galactolipid:quinone 5:1 mixtures are presented in Table 5.12.1 and the physical state corresponding to each brown tonality at π = 15 $mN \cdot m^{-1}$ is exposed in Table 5.12.2. The absolute height of each physical state of pure galactolipids is similar each other. However, despite of the galactolipid:quinone 5:1 systems present practically the same physical states, the absolute height of each physical state of the galactolipid:quinone 5:1 systems present small differences which is explained by the different galactolipid-quinone interactions that can occur depending on the mixture components. On the other hand, the galactolipid:quinone systems follows the expected trend of more surface covered by a compact state (LC or S) when decreasing the quinone content, achieving a nearly flat increase when the major content of quinone has been rejected from the lipid matrix (See Figures 5.8.9, 5.9.9, 5.10.9, 5.11.9). The reason for this behaviour is that the reduced presence of quinone enhances the ordering of the galactolipid molecules.

Table 5.12.1. Height of each physical state for the LB monolayers of pure galactolipids and galactolipid:quinone 5:1 mixtures on mica. *Estimated value (more information in the text).

	LE	LC1	LC2	S			LE	LC1	LC2
					MGDG:UQ	5:1	6 ± 2		24 ± 1
MGDG	6 ± 2 *	21 ± 1	25 ± 1	27 ± 1	MGDG:PQ	5:1	6 ± 2	24 ± 1	26 ± 1
DGDG	6 ± 2 *	21 ± 1	24 ± 1		DGDG:PQ	5:1	6 ± 2 *	21 ± 1	23 ± 1
MD	6 ± 2 *	21 ± 1	25 ± 1		MD:PQ	5:1	6 ± 2 *	22 ± 1	24 ± 1

Table 5.12.2. Physical states of each zone (dark and fair brown) corresponding to pure galactolipids and galactolipid:quinone 5:1 mixtures at π = 15 mN·m^{-1}.

	Dark	Fair			Dark	Fair
			MGDG:UQ	5:1	LE	LC2
MGDG	LC2	S	MGDG:PQ	5:1	LE	LC2
DGDG	LC1	LC2	DGDG:PQ	5:1	LE	LC1
MD	LE	LC2	MD:PQ	5:1	LE	LC1

The AFM topographic images performed with galactolipid:quinone 10:1 and 20:1 systems present a behaviour comprised between the pure galactolipid and the galactolipid:quinone 5:1 systems, increasing the area occupied by the more compact domains when decreasing the quinone content, except the explained MD:PQ 20:1 and 10:1 (See Section 5.11.3). On the other hand, the BAM images (Figure 5.8.3, 5.9.3, 5.10.3) confirm that no segregation is observed at the micrometric scale, in opposition to the results observed at the nanometric scale using AFM.

The Figure 5.12.4 presents the cyclic voltammograms at 10 mV·s^{-1} of the systems ITO-PQ transferred on the collapse and ITO-galactolipid:PQ 5:1 transferred at π = 33 mN·m^{-1}. Moreover, inset of Figure 5.12.4 presents the ITO:UQ and the ITO-MGDG:UQ systems at the same conditions. These surface pressures have been chosen because each system presents the highest total charge involved in the redox processes.

Pure UQ presents two redox processes whereas PQ only presents one because PQ is incapable of forming ordered phases. So that, once transferred onto ITO, all the PQ molecules are placed in contact with the substrate surface. The ITO-galactolipid:quinone/electrolyte 5:1 systems at π = 33 mN·m^{-1}, show two reduction and two oxidation peaks, involving peak I the processes I_α and I_β. However, at surface pressures

below that value, the systems may present one (I_α) or two (I_α and I_β) redox processes. The exception for this trend is the ITO-MGDG:PQ/electrolyte 5:1 at π = 33 mN·m^{-1} which presents only I_α and I_β. On the other hand, the ITO-galactolipid:quinone/electrolyte 10:1 system (Figure 5.8.11, 5.9.11 and 5.11.11) present generally only one (I_α) or two (I_α and I_β) redox processes. The exception of this trend is the DGDG:PQ system (5.10.11 and 5.10.12) which, scanned at high scan rate, also shows the process II. The explanation for the exceptions is the sharp change LE to LC state, which favours the entrapment of the quinone molecules in the galactolipid matrix. The presence of two redox processes at π < 33 mN·m^{-1} seems to be related with a high initial quinone content, the presence of a medium-high compactness of the LC state and the formation of circular LE domains. On the other hand, the hydrogen evolution partially masks the reduction peak of process II, especially at medium-low surface pressures or at low initial quinone content. It has also been observed that when a high proportion of LC state is achieved at low surface pressure and at low quinone content, the hydrogen evolution takes place at more anodic values.

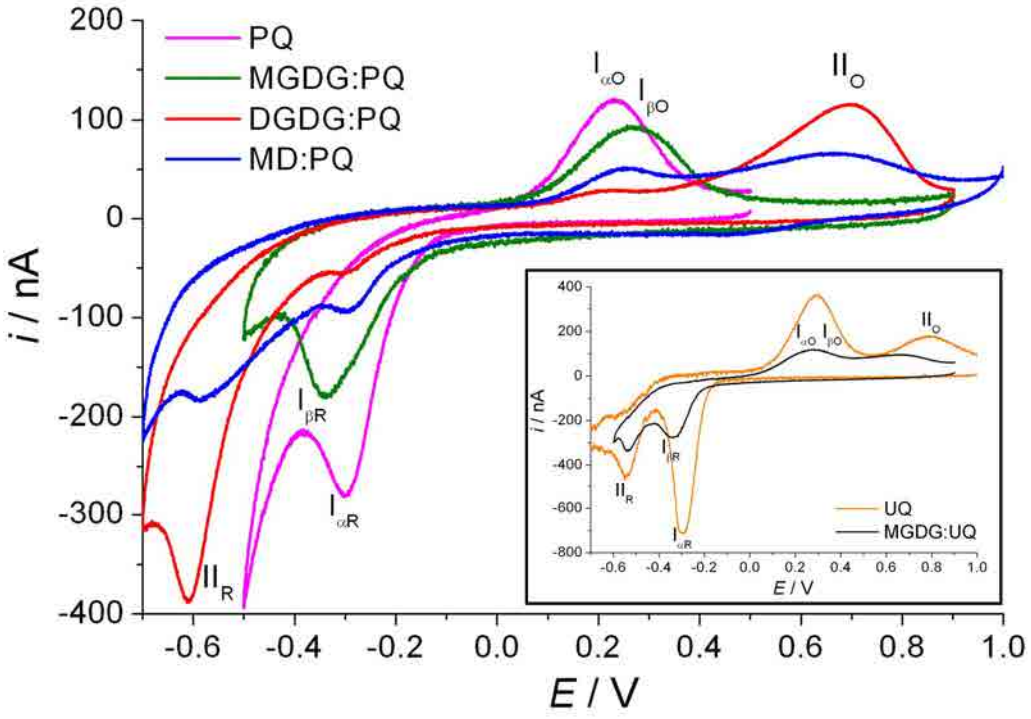

Figure 5.12.4. CVs of the ITO-PQ LB film transferred on the collapse and ITO-galactolipid:PQ 5:1 LB films transferred at π = 33 mN·m^{-1}. Inset, CVs of ITO-UQ LB films transferred on the collapse and ITO-lipid:UQ 5:1 LB films transferred at π = 33 mN·m^{-1}. All CVs have been performed using 0.150 M of KCl electrochemical cell and a potassium phosphate buffered solution at pH 7.4 , at a scan rate of 10 mV·s^{-1}.

It is also interesting to observe the CVs corresponding to the ITO-MGDG:PQ/electrolyte, ITO-DGDG:PQ/electrolyte and ITO-MD:PQ/electrolyte (Figure 5.12.4). The MD:PQ (MGDG:DGDG:PQ) system present a behaviour comprised between the MGDG:PQ and the DGDG:PQ. The charge involved at the redox peak of process I is the largest for the MGDG:PQ, followed by the MD:PQ and finally the DGDG:PQ that presents a very little charge value. On the other hand, the charge involved in process II is null for the MGDG:PQ, followed by the MD:PQ that presents a low charge and finally, the DGDG:PQ that practically the total charge corresponds to process II.

In all the CVs, the double layer capacity of the ITO-galactolipid experiment is fitted in the capacitive current of the galactolipid:quinone system which indicates that the galactolipid voltammetric response is the same both alone and in the galactolipid:quinone mixture, so producing non-effect on the quinone faradaic current of the mixture systems. The exception for this trend is observed for the MD:PQ 20:1 and 10:1 systems (See Section 5.11.6). On the other hand, the capacitive current of the ITO-galactolipid:quinone/electrolyte system can overlap the redox response, especially at low quinone initial content or at low surface pressure.

The redox process that it is observed in all systems (process I) presents a E_{pR} (I) = -0.31 ± 0.03 V and E_{pO} (I) = 0.24 ± 0.04 V values that determine a formal potential of E_f (I) = -0.04 ± 0.02 V and process II presents a E_{pR} (II) = -0.58 ± 0.04 V and E_{pO} (II) = 0.70 ± 0.03 V values that determine a formal potential of E_f (I) = 0.06 ± 0.02 V. It is evident that regardless being pure quinone or galactolipid-quinone system, all of them present a similar redox peaks and formal potentials for each redox process.

The electrochemical experiments for the ITO-MGDG:PQ/electrolyte system (Section 5.9.5) indicate that two different redox peaks (I_α and I_β) are involved in the redox wave that we label as peak I in all the ITO-galactolipid:quinone/electrolyte systems. The two processes correspond to the quinones in “diving” position with direct quinone head-ITO surface contact (I_α) and quinones in “diving” position with no contact (I_β), being favoured the I_β wave at high surface pressures. The no influence of these two processes in the formal potential is due to both have similar formal potential.

The global reaction and the mechanism proposed for pure quinone in confined situation (Section 5.1.3 and 5.2.3) seems to be the same also for the quinone of the galactolipid:quinone systems, being the main difference between processes I and II the position of the quinone in the monolayer not the mechanism (Chapter 5). The shape of the voltammograms for both pure quinone and the galactolipid:quinone systems present two important deviations respect to the theoretical models proposed in literature to describe the cyclic voltammetric response of a surface confined reaction. First, the redox peaks separation for process I or process II is larger than the expected for such systems. Second, the peak shape which is not symmetrical, present the reduction peaks a sharper shape than the oxidation ones, which is explained by the different hydrophilic character of the redox couple Q/QH_2. In addition, the larger polarity of QH_2 compared with Q leads the former to establish more attractive interactions, which explains the larger width of the oxidation peaks.

Both the ITO-quinone/electrolyte and the ITO-galactolipid:quinone/electrolyte systems present the redox peaks separation for process II larger than for process I, indicating that process II is even more irreversible than process I (Figure 5.8.13, 5.9.13, 5.10.13 and 5.11.13). Moreover, the redox peaks separation for both processes I and II is enhanced when increasing the scan rate making the process more irreversible. This large separation aroused from the slow charge transfer rates at ITO-monolayer|electrolyte interface. In addition, the increase in the scan rate affects in a larger extent the oxidation peak potential than the reduction one, which produces that the midpoint potential for process I and II has scan rate dependence. On the other hand, at low scan rates (< 20 $mV \cdot s^{-1}$) the linear adjustments of the reduction and oxidation peak potentials of processes I and II present a higher slope than at high scan rates, which is explained by the hindrance increase of the electrochemical process when increasing the scan rate.

The current intensity of the redox peaks (i_{peak}) of all the ITO-quinone or ITO-galactolipid:quinone systems is related by a linear dependence with the scan rate (Figure 5.1.5, 5.2.5, 5.8.14, 5.9.14, 5.10.14 and 5.11.14) so indicating that the quinone molecules are surface confined in both processes. The electron transfer takes place mainly by two mechanisms: First, by direct transfer and electron hopping between the quinones placed in “diving” position (process I), and second, by electron hopping through the lipid matrix (process II).

The ITO-galactolipid:quinone/electrolyte systems present a higher electroactive fraction when increasing the initial quinone content (Table 5.8.5, 5.9.5, 5.10.5, 5.11.5), which is explained both by the enough presence of available protons close to the quinone heads that avoids the high local quinone concentration problem and by the electron hopping effect (See Section 3.4.5). Moreover, the non-homogeneous electrode surface and the semiconductive properties of ITO induce it to behave different to metal surfaces like gold or mercury. The surface coverage corresponding to process I presents two different behaviours. On the one hand, the DGDG:quinone and MD:quinone, which tends to a saturation value for this process and, on the other hand, the MGDG:quinone mixtures which does not saturate. This different behaviour is related with the fast change from LE to LC state observed for the MGDG:quinone system.

The global vision of the galactolipid:quinone monolayers is that when increasing the surface pressure, the expulsion of the quinone from the lipid heads zone is produced inducing two actions. On the one hand, it can be vertically rejected to the “diving” position without ITO-quinone contact or to the “swimming” position being this last position and the formation of aggregates favoured at large initial content of quinone and at ordered states. On the other hand, it can be horizontally rejected to the remaining LE zones so enriching them in quinone. The presence of enriched small LE zones in circular shape may indicate that the composition in and out the rounded shape is different. On the other hand, the sharp change LE to LC state that it is produced in the MGDG:quinone systems entraps the quinone in “diving” position favouring the position I_{β}, although it is thermodynamically less favourable than the “swimming” position.

PQs are present in two main positions in natural cell membranes, being PQ_A bounded to the PSII and PQ_B that can free move. The electron flow from PQ_A to PQ_B is possible thanks to the higher redox potential for the latter due to the hydrogen bonds between the ketooxygens and surrounding protein residues. This natural behaviour can be compared with our system in which the different positions “diving” and “swimming” have also different redox potential. The redox potential for the “swimming” PQ is ≈ 100 mV higher than that of the “diving” PQ, which, by chance, is in line with the ≈ 80 mV that the redox potential of PQ_A is higher than PQ_B. The higher redox potential permit the electron flow from the “diving” position to the “swimming” position [130], so favouring the electron hopping mechanism.

5.13 References of Chapter 5

[1] Bilewicz, R.; Majda, M. Monomolecular Langmuir-Blodgett films at electrodes. Formation of passivating monolayers and incorporation of electroactive reagents. Langmuir, 1991, 7, 2794–2802.

[2] Bilewicz, R.; Sawaguchi, T.; Chamberlain, R.V.; Majda, M. Monomolecular Langmuir-Blodgett Films at Electrodes. Electrochemistry at Single Molecule “Gate Sites”. Langmuir 1995,11, 2256-2266.

[3] Bilewicz, R. Voltammetric Probing of Multicomponent Langmuir - Blodgett Monolayers Part I - Monolayers Containing Ubiquinone (Q10). Pol. J. Chem. 1993, 67,1695-1704.

[4] Quinn, P.J.; Esfahani, M.A. Ubiquinones have surface-active properties suited to transport electrons and protons across membranes. Biochem. J. 1980, 185, 715–722.

[5] Grzybek, M.; Stebelska, K.; Wyrozumska, P.; Grieb, P.; Langner, M.; Jaszewski, A.; Jezierski, A.; Sikorski, A.F. ESR and monolayer study of the localization of coenzyme Q10 in artificial membranes. Gen. Physiol. Biophys. 2005, 24, 449-460.

[6] Roche, Y.; Peretti, P.; Bernard, S. Influence of the chain length of ubiquinones on their interaction with DPPC in mixed monolayers. Biochim Biophys Acta. 2006, 1758, 468-478.

[7] Vitovič, P.; Nikolelis, D.P.; Hianik, T. Study of calix [4] resorcinarene–dopamine complexation in mixed phospholipid monolayers formed at the air|water interface. Biochim. Biophys. Acta 2006, 1758, 1852-1861.

[8] Jemiota-Rzemińska, M.; Latowski, D.; Strzałka, K. Incorporation of plastoquinone and ubiquinone into liposome membranes studied by HPLC analysis. The effect of side chain length and redox state of quinone. Chem. Phys. Lipids 2001, 110, 85-94.

[9] Hoyo, J.; Guaus, E.; Torrent-Burgues, J.; Sanz, F. Electrochemical behaviour of mixed LB films of ubiquinone – DPPC. J. Electroanal. Chem. 2012, 669, 6-13.

[10] Hillebrandt, H.; Wiegand, G.; Tanaka, M.; Sackmann, E. High Electric Resistance Polymer/Lipid Composite Films on Indium-Tin-Oxide Electrodes. Langmuir 1999, 15, 8451-8459.

[11] García-Esparza, S.; Blanco, L.M.; Bernès, S. Application of the Double Pulse Potential Chronoamperometry Technique to Modify the ITO Electrode Surface. Portugaliae Electrochim. Acta , 2008, 26, 517-525.

[12] Hoyo, J.; Guaus, E.; Oncins, G.; Torrent-Burgués, J.; Sanz, F. Incorporation of Ubiquinone in Supported Lipid Bilayers on ITO. J. Phys. Chem. B, 2013, 117 , 7498–7506

[13] Yeh, S-Y.; Wang, C-M. Anthraquinone-modified electrodes, preparations and characterizations. J. Electroanal. Chem. 2006, 592, 131–138.

[14] Petrova, S.A.; Kolodyazhny, M.V.; Ksenzhek, O.S. Electrochemical properties of some naturally occurring quinones. J. Electroanal.Chem. 1990, 277, 189–196.

[15] Moncelli, M.R.; Becucci, L.; Nelson, A.; Guidelli R. Electrochemical modeling of electron and proton transfer to ubiquinone-10 in a self-assembled phospholipid monolayer. Biophys J. 1996, 70, 2716-2726.

[16] Becucci, L.; Scaletti, F.; Guidelli, R. Gel-phase microdomains and lipid rafts in monolayers affect the redox properties of ubiquinone-10. Biophys J. 2011, 101, 134-143.

[17] Petrangolini, P.; Alessandrini, A.; Berti, L.; Facci, P. An Electrochemical Scanning Tunneling Microscopy Study of 2-(6-Mercaptoalkyl)hydroquinone Molecules on Au(111). J. Am. Chem. Soc. 2010, 132, 7445–7453.

[18] Sek, S.; Bilewicz, R. Voltammetric Probing of Molecular Assemblies of Ubiquinone-10 at the Air–Water Interfaces. J. Inclusion Phenom. Macrocyc. Chem. 1999, 35, 55-62.

[19] Moncelli, M.R.; Herrero, R.; Becucci, L.; Guidelli, R. Kinetics of electron and proton transfer to ubiquinone-10 and from ubiquinol-10 in a self-assembled phosphatidylcholine monolayer. Biochim. Biophys. Acta 1998, 1364, 373-384.

[20] Ohnishi, T.; Trumpower, B. L. Differential effects of antimycin on ubisemiquinone bound in different environments in isolated succinate-cytochrome c reductase complex. J.Biol. Chem. 1980, 255, 3278-3284.

[21] Marchal, D.; Boireau, W.; Laval, J.M.; Moiroux, J.; Bourdillon, C. An electrochemical approach of the redox behavior of water insoluble ubiquinones or plastoquinones incorporated in supported phospholipid layers. Biophys. J. 1997, 72, 2679-2687.

[22] Hong, H. G.; Park, W. Electrochemical characteristics of hydroquinone-terminated self-assembled monolayers on gold. Langmuir 2001, 17, 2485–2492.

[23] Marchal, D.; Boireau, W.; Laval, J.M.; Bourdillon, C.; Moiroux, J. Kinetics of redox conversion at a gold electrode of water-insoluble ubiquinone (UQ(10)) and plastoquinone (PQ(9)) incorporated in supported phospholipid layers. J. Electroanal. Chem. 1998, 451, 139-144.

[24] Ma, W.; Zhou, H.; Ying, Y.L.; Li, D-W.; Chen, G-R.; Long, Y-T.; Chen, H-Y. In situ spectroeletrochemistry and cytotoxic activities of natural ubiquinone analogues. Tetrahedron, 2011, 67, 5990-6000.

[25] Jemioła-Rzemińska, M.; Myśliwa-Kurdziel, B.; Strzałka, K. The influence of structure and redox state of prenylquinones on thermotropic phase behaviour of phospholipids in model membranes. Chem Phys Lipids 2002, 114, 169-180.

[26] Fiorini, R.; Ragni, L.; Ambrosi, S.; Littarru, G.P.; Gratton, E.; Hazlett, T. Fluorescence studies of the interactions of ubiquinol-10 with liposomes. Photochem. Photobiol. 2008, 84, 209–214.

[27] Ausili, A.; Torrecillas, A.; Aranda, F.; Godos, A.D.; Sánchez-Bautista, S.; Corbalán-García, S.; Gómez-Fernández, J.C. Redox state of coenzyme Q10 determines its membrane localization, J. Phys. Chem. B 2008, 112, 12696–12702.

[28] Gordillo, G.J.; Schiffrin, D.J. Redox properties of ubiquinon (UQ10) adsorbed on a mercury electrode. J. Chem. Soc., Faraday Trans., 1994, 90, 1913-1922.

[29] Bard, A.J.; Faulkner, L.R. Electrochemical Methods. Fundamentals and Applications, John Wiley & Sons, New York, 2001.

[30] Laviron, E. General expression of the linear potential sweep voltammogram in the case of diffusionless electrochemical systems. J. Electroanal. Chem. 1979, 101, 19-28.

[31] Daifuku, H.; Aoki, K.; Tokuda, K.; Matsuda, H. Electrode kinetics of surfactant polypyridine osmium and ruthenium complexes confined to tin oxide electrodes in a monomolecular layer by the Langmuir-Blodgett method. J. Electroanal. Chem. 1985, 183, 1-26.

[32] Mårtensson, C.; Agmo Hernández, V. Ubiquinone-10 in gold-immobilized lipid membrane structures acts as a sensor for acetylcholine and other tetraalkylammonium cations. Bioelectrochemistry 2012, 88, 171-80.

[33] Kruk, J. Charge-transfer complexes of plastoquinone and α-tocopherol quinone in vitro. Biophys. Chem. 1988, 30, 143–149.

[34] Aranda, F.J.; Gómez-Fernández, J.C. Influence of membrane fluidity on transport mediated by ubiquinones through phospholipid vesicles. Archives of Biochemistry and Biophysics 1982, 218, 525–530.

[35] Skowronek, M.; Jemioła-Rzemińska, M.; Kruk, J.; Strzałka, K. Influence of the redox state of ubiquinones and plastoquinones on the order of lipid bilayers studied by

fluorescence anisotropy of diphenylhexatriene and trimethylammonium diphenylhexatriene. Biochim. Biophys. Acta 1996, 1280, 115-119.

[36] Jemiola-Rzeminska, M.; Kruk, J.; Skowronek, M.; Strzalka, K. Location of ubiquinone homologues in liposome membranes studied by fluorescence anisotropy of diphenyl-hexatriene and trimethylammonium-diphenyl-hexatriene. Chem. Phys. Lipids 1996, 79, 55-63.

[37] Bilewicz, R.; Sek S.; Zawisza, I. Electron transport through composite monolayers. Russ. J. Electrochem. 2002, 38, 29-38.

[38] Kruk, J.; Strzałka, K.; Leblanc, R.M. Monolayer study of plastoquinones, alpha-tocopherol quinone, their hydroquinone forms and their interaction with monogalacto-syldiacylglycerol. Charge-transfer complexes in a mixed monolayer. Biochim. Biophys. Acta 1992, 1112, 19-26.

[39] Kruk, J., Strzałka, K. Charge–transfer complexes of plastoquinone and –tocopherol quinone in lecithin and octadecane. Chem. Phys. Lipids 1994, 70, 199–204.

[40] Kruk, J.; Strzałka, K.; Leblanc, R.M. Fourier transform infrared studies on charge-transfer interactions of plastoquinones and α-tocopherol quinone with their hydroquinone forms and MGDG. Biophys. Chem. 1993, 45, 235–244.

[41] Laval, J.M.; Majda, M. Electrochemical investigations of the structure and electron transfer properties of phospholipid bilayers incorporating ubiquinone. Thin Solid Films. 1994, 244, 836–840.

[42] Cheng, Y.; Cunnane V.J.; Kontturi, A-K.; Kontturi, K.; Schiffrin, D.J. Potential Dependence of Transmembrane Electron Transfer across Phospholipid Bilayers Mediated by Ubiquinone 10. J. Phys. Chem., 1996, 100, 15470–15477.

[43] Li, Y.; Shi, L.; Ma, W.; Li, D.W.; Kraatz, H.B.; Long, Y.T. 6-Vinyl coenzyme Q0: Electropolymerization and electrocatalysis of NADH oxidation exploiting poly-p-quinone-modified electrode surfaces. Bioelectrochemistry 2011, 80, 128-131.

[44] Ma, W.; Ying, Y.L.; Qin, L.X.; Gu, Z.; Zhou, H.; Li, D.W.; Sutherland, T.C.; Chen, H.Y.; Long, Y.T. Investigating electron-transfer processes using a biomimetic hybrid bilayer membrane system. Nat. Protoc. 2013, 3, 439-450.

[45] Ma, W.; Li, D-W.; Sutherland, T.C.; Li, Y.; Long, Y-T; Chen, H-Y. Reversible Redox of NADH and NAD+ at a Hybrid Lipid Bilayer Membrane Using Ubiquinone. J. Am. Chem. Soc. 2011, 133, 12366–12369

[46] Soriaga, M. P.; Hubbard, A. T. Determination of the Orientation of Adsorbed Molecules at Solid-Liquid Interfaces by Thin-Layer Electrochemistry:Aromatic Compounds at Platinum Electrodes. J. Am. Chem. Soc. 1982, 104, 2735-2742.

[47] Quan, M.; Sanchez, D.; Wasylkiw, M.F.; Smith, D.K. Voltammetry of quinones in unbuffered aqueous solution: reassessing the roles of proton transfer and hydrogen bonding in the aqueous electrochemistry of quinones. J. Am. Chem. Soc. 2007, 129, 12847-12856.

[48] Park, H.; Park, J-S.; Shim; Y-B. Redox reaction of benzoquinone on a lipid coated glassy carbon electrode. J. Electroanal. Chem. 1997, 438, 113-119.

[49] Guay, D.; Leblanc, R. M. Excess free energies of interaction of chlorophyll a with α-tocophelquinone and plastoquinone 3 and 9. A mixed-monolayer study. Langmuir, 1987, 3, 575–580.

[50] Es-Sounni, A.; Leblanc, R.M. Mixed monolayer studies of chlorophyll a and plastoquinone 9 at the nitrogen-water interface. Langmuir, 1992, 8, 1578–1581.

[51] Kruk, J.; Strzałka, K.; Leblanc, R.M. Linear dichroism and molecular orientation in Langmuir-Blodgett films of plastoquinones and alpha-tocopherol quinone. Biochim. Biophys. Acta. 1993, 1142, 6-10.

[52] Gordillo, G.J.; Schiffrin, D.J. The electrochemistry of ubiquinone-10 in a phospholipid model membrane. Faraday Discuss. 2000, 116, 89–107.

[53] Toimil, P.; Prieto, G.; Miñones, J. Jr.; Sarmiento, F. A comparative study of F-DPPC/DPPC mixed monolayers. Influence of subphase temperature on F-DPPC and DPPC monolayers. Phys. Chem. Chem. Phys. 2010, 12, 13323-13332.

[54] Yun, H.; Choi, Y-W., Kim, N.J.; Sohn, D. Physicochemical Properties of Phosphatidylcholine (PC) Monolayers with Different Alkyl Chains, at the Air/Water Interface. Bull. Korean Chem. Soc. 2003, 24, 377-383.

[55] Foglia, F.; Barlow, D.J.; Szoka, F.C.; Huang, Z.; Rogers, S.E.; Lawrence, M.J. Structural studies of the monolayers and bilayers formed by a novel cholesterol-phospholipid chimera. Langmuir, 2011, 27, 8275-8281.

[56] Chu, B.S.; Gunning, A.P.; Rich, G.T.; Ridout, M.J.; Faulks, R.M.; Wickham, M.S.; Morris V.J.; Wilde, P.J. Adsorption of bile salts and pancreatic colipase and lipase onto digalactosyldiacylglycerol and dipalmitoylphosphatidylcholine monolayers. Langmuir 2010, 26, 9782-9793.

[57] Baoukina, S.; Monticelli, L.; Risselada, H.J.; Marrink, S.J.; Tieleman, D.P. The molecular mechanism of lipid monolayer collapse. Proc. Natl. Acad. Sci. U S A. 2008, 105, 10803–10808.

[58] Ridsdale, R.A.; Palaniyar, N.; Possmayer, F.; Harauz, G. Formation of folds and vesicles by dipalmitoylphosphatidylcholine monolayers spread in excess. J. Membr. Biol. 2001,180, 21-32.

[59] Ding, J.; Doudevski, I.; Warriner, H.E.; Alig, T.; Zasadzinski, J.A. Nanostructure Changes in Lung Surfactant Monolayers Induced by Interactions between Palmitoyloleoyl-phosphatidylglycerol and Surfactant Protein B. Langmuir 2003, 19, 1539–1550.

[60] Alig, T.F.; Warriner, H.E.; Lee, L.; Zasadzinski, J.A. Electrostatic Barrier to Recovery of Dipalmitoylphosphatidylglycerol Monolayers after Collapse. Biophys J. 2004, 86, 897–904.

[61] Li, M.; Chen, M.; Sheepwash, E.; Brosseau, C.L.; Li, H.; Pettinger,B.; Gruler, H.; Lipkowski, J. AFM studies of solid-supported lipid bilayers formed at a Au(111) electrode surface using vesicle fusion and a combination of Langmuir-Blodgett and Langmuir-Schaefer techniques. Langmuir 2008, 24, 10313-10323.

[62] Aloisi, G.; Becucci, L.; Dolfi, A.; Moncelli, M.R.; Tadini-Buoninsegni, F.; Guidelli, R. Interfacial bioelectrochemistry: assessment and trends. J. Electroanal. Chem. 2001, 504, 1-28.

[63] Yang, J.; Kleijn J. M. Order in phospholipid Langmuir-Blodgett layers and the effect of the electrical potential of the substrate. Biophys J. 1999, 76, 323–332.

[64] Bishop, D.G.; Kenrick, J.R.; Bayston, J.H.; Macpherson, A.S.; Johns, S.R. Monolayer properties of chloroplast lipids. Biochim. Biophys. Acta. 1980, 602, 248-259.

[65] Schneider, J.; Dufrêne, Y.F.; Barger, W.R. Jr, Lee, G.U. Atomic force microscope image contrast mechanisms on supported lipid bilayers. Biophys. J. 2000, 79, 1107-1118.

[66] Tomoaia-Cotişel, M.; Zsakó, J.; Chifu, E.; Quinn, P.J. Influence of electrolytes on the monolayer properties of saturated galactolipids at the air-water interface. Chemistry and Physics of Lipids 1983, 34, 55–64.

[67] Tomoaia-Cotişel, M.; Zsako, J.; Chifu, E; Quinn, P.J. Hysteresis in compression-expansion cycles of distearoylmonogalactosylglycerol monolayers. Chem. Phys. Lipids, 1989, 50, 127–133.

[68] Gzyl-Malcher, B.; Filek, M.; Makyła, K.; Paluch, M. Differences in surface behaviour of galactolipids originating from different kind of wheat tissue cultivated in vitro. Chem Phys Lipids 2008, 155, 24-30.

[69] Filek, M.; Gzyl, B.; Laggner, P.; Kriechbaum, M. Effect of indole-3-acetic acid on surface properties of the wheat plastid lipids. J. Plant. Physiol. 2005,162, 245-252.

[70] Gzyl, B.; Filek, M.; Makyła, K. Langmuir monolayers of chloroplast membrane lipids. Thin Solid Films. 2008, 516, 8844–8847.

[71] Tazi, A.; Boussaad, S.; Leblanc, R.M. Atomic force microscopy study of cytochrome f (Cyt f) and mixed monogalactosyldiacylglycerol (MGDG)/Cyt f Langmuir-Blodgett films. Thin Solid Films, 1999, 353, 233-238.

[72] Georgiev, G.A.; Ivanova, S.; Jordanota, A.; Tsanova, A.; Getov, V.; Dimitrov, M.; Lalchev, Z. Interaction of monogalactosyldiacylglycerol with cytochrome b6f complex in surface films. Biochem. Biophys. Res. Commun. 2012, 419, 648-651.

[73] Bottier, C.; Géan, J.; Artzner, F.; Desbat, B.; Pézolet, M.; Renault, A.; Marion, D.; Vié, V. Galactosyl headgroup interactions control the molecular packing of wheat lipids in Langmuir films and in hydrated liquid-crystalline mesophases. Biochim Biophys Acta 2007, 1768, 1526-1540.

[74] Shao, L.; Konka, V. V.; Leblanc, R.M. Surface Chemistry Studies of Photosystem II. J. Colloid Interface Sci. 1999, 215, 92-98.

[75] Cain, R.G., Page, N.W., Biggs, S. Force calibration in lateral force microscopy, J.Colloid Interface Sci. 2000, 227, 55-65.

[76] Foley, A.A.; Brain, A.P.R.; Quinn, P.J.; Harwood, J.L. Permeability of liposomes composed of binary mixtures of monogalactosyldiacylglycerol and digalactosyldiacyl-glycerol. Biochim. Biophys. Acta 1988, 939, 430–440.

[77] Gzyl-Malcher, B.; Zembala, M.; Filek, M. Effect of tocopherol on surface properties of plastid lipids originating from wheat calli cultivated in cadmium presence. Chem. Phys. Lipids 2010, 163, 74-81.

[78] Castro, V.; Dvinskikh, S.V.; Widmalm, G.; Sandström, D.; Maliniak, A. NMR studies of membranes composed of glycolipids and phospholipids. Biochim. Biophys. Acta 2007, 1768, 2432-2437.

[79] Zaitsev, S.Y.; Kalabina, N.A.; Herrmann, B.; Schaefer, C.; Zubov, V.P. A comparative study of the photosystem II membrane proteins with natural lipids in monolayers. Mater. Sci. Eng., C. 1999, 8, 519–522.

[80] Hoyo, J.; Guaus, E.; Torrent-Burgues, J. Biomimetic monolayer films of monogalactosyldiacylglycerol incorporating ubiquinone. J. Colloid Interface Sci. 2012, 384, 189 − 197.

[81] Brezesinski, G.; Müller, H.J.; Toca-Herrera, J.L.; Krustev, R. X-ray diffraction and foam film investigations of PC head group interaction in water/ethanol mixtures. Chem. Phys. Lipids. 2001, 110, 183-194.

[82] Zhao, L.; Feng, S-S. Effects of lipid chain length on molecular interactions between paclitaxel and phospholipid within model biomembranes. J. Colloid and Interface Sci. 2004, 274, 55–68.

[83] Sanchez, J.; Badia, A. Atomic force microscopy studies of lateral phase separation in mixed monolayers of dipalmitoylphosphatidylcholine and dilauroylphosphatidylcholine. Thin Solid Films 2003, 440, 223–239.

[84] Roche, Y.; Peretti, P.; Bernard, S. The redox state influences the interaction of ubiquinones with phospholipid bilayers. J. Therm. Anal. Calorim. 2007, 89, 867-873.

[85] Kingsley, P.B.; Feigenson, G.W. 1H-NMR study of the location and motion of ubiquinones in perdeuterated phosphatidylcholine bilayers. Biochim Biophys Acta 1981, 635, 602–618.

[86] Jeuken, L.J.C.; Bushby, R.J.D.; Evans, S.D. Proton transport into a tethered bilayer lipid membrane. Electrochem. Commun. 2007, 9, 610–614.

[87] Gao, H.; Luo, G.A.; Feng, J.; Ottova, A.L.; Tien, H.T. Fabrication and photoelectric properties of self-assembled bilayer lipid membranes on conducting glass. J Photochem Photobiol B. 2000, 59, 87-91.

[88] Lenaz, G. ; Samori, B.; Fato, R.; Battino, M.; Parenti Castelli, G.; Domini, I. Localization and preferred orientations of ubiquinone homologs in model bilayers, Biochem. Cell. Biol. 1992, 70, 504–514.

[89] Afri, M.; Ehrenberg, B.; Talmon, Y.; Schmidt, J.; Cohen, Y.; Frimer, A.A. Active oxygen chemistry within the liposomal bilayer: Part III. Locating vitamin E, ubiquinol and ubiquinone and their derivatives in the lipid bilayer, Chem. Phys. Lipids 2004, 131, 107–121.

[90] Katsikas, H.; Quinn, P.J. Fluorescence probe studies of the distribution of ubiquinone homologues in bilayers of dipalmitoylglycerophosphocholine. Eur. J. Biochem. 1983, 131, 607– 612.

[91] Ondarroa, M.; Quinn, P.J. A difference infrared-spectroscopic study of the interaction of ubiquinone-10 with phospholipid bilayers. Biochem. J. 1986, 240, 325– 331.

[92] Samori, B.; Lenaz, G.; Battino, M.; Marconi, G.; Domini, I. On coenzyme Q orientation in membranes: a linear dichroism study of ubiquinones in a model bilayer, J. Membr. Biol. 1992, 128, 193– 203.

[93] Aranda, F.J.; Gomez-Fernandez, J.C. The interaction of ubiquinone-10 and ubiquinol-10 with phospholipid bilayers. A study using differential scanning calorimetry and turbidity measurements. Biochim. Biophys. Acta 1985, 820, 19–26.

[94] Katsikas, H.; Quinn, P.J. The polyisoprenoid chain length influences the interaction of ubiquinones with phospholipid bilayers, Biochim. Biophys. Acta 1982, 689, 363–369.

[95] Stidham, M.A.; McIntosh, T.J.; Siedow, J.N. On the localization of ubiquinone in phosphatidylcholine bilayers. Biochim. Biophys. Acta 1984, 767, 423– 431.

[96] Salgado, J.; Villalain, J.; Gomez Fernandez, J.C. Magic angle spinning 13C-NMR spin-lattice relaxion study of the location and effects of alphatocopherol, ubiquinone-10 and ubiquinol-10 in unsonicated model membranes. Eur. Biophys. J. 1993, 22, 151– 155.

[97] Katsikas, H.; Quinn, P.J. The distribution of ubiquinone-10 in phospholipid bilayers. A study using differential scanning calorimetry. Eur. J. Biochem. 1982, 124, 165– 169.

[98] Ulrich, E.L.; Girvin, M.E.; Cramer, W.A.; Markley, J.L. Location and Mobility of Ubiquinones of Different Chain Length in Artificial Membrane Vesicles. Biochemistry 1985, 24, 2501-2508.

[99] Ondarroa, M.; Quinn, P. J. Proton magnetic resonance spectroscopic studies of the interaction of ubiquinone-10 with phospholipid model membranes. Eur. J. Biochem. 1986, 155, 353-361.

[100] Fato, R.; Battino, M.; Degli Esposti, M.; Parenti Castelli, G.; Lenaz, G. Determination of partition and lateral diffusion coefficients of ubiquinones by fluorescence quenching of n-(9-anthroyloxy)stearic acids in phospholipid vesicles and mitochondrial membranes. Biochemistry 1986, 25, 3378-3390.

[101] Marchal, D.; Boireau, W.; Laval, J.M.; Moiroux, J.; Bourdillon, C. Electrochemical measurement of lateral diffusion coefficients of ubiquinones and plastoquinones of various isoprenoid chain lengths incorporated in model bilayers. Biophys. J. 1998, 74, 1937-1948.

[102] Hauss, T.; Dante, S.; Haines, T.H.; Dencher, N.A. Localization of coenzyme Q10 in the center of a deuterated lipid membrane by neutron diffraction. Biochim Biophys Acta. 2005, 1710, 57-62.

[103] Metz, G.; Howard, K.P.; van Liemt, W.B.S.; Prestegard, J. H.; Lugtenburg, J.; Smith, S.O. NMR Studies of Ubiquinone Location in Oriented Model Membranes: Evidence for a Single Motionally-Averaged Population. J. Am. Chem. Soc. 1995, 117, 564–565.

[104] Oncins, G.; Picas, L.; Hernández-Borrell, J.; Garcia-Manyes, S.; Sanz, F. Thermal Response of Langmuir-Blodgett Films of Dipalmitoylphosphatidylcholine Studied by Atomic Force Microscopy and Force Spectroscopy. Biophys J. 2007, 93, 2713–2725.

[105] Van Dijck, P.W.; Kaper, A.J.; Oonk, H.A.; de Gier, J. Miscibility properties of binary phosphatidylcholine mixtures. A calorimetric study. Biochim Biophys Acta. 1977, 470, 58-69.

[106] Mansourian, A.R.; Brain, A.P.R.; Quinn, P.J. Intermolecular mixing of saturated and unsaturated galactolipids. Biochem. Soc. Transactions 1986, 14, 738–739.

[107] Cornell, B.A.; Keniry, M.A.; Post, A.; Robertson, R.N.; Weir, L.E.; Westerman, P.W. Location and activity of ubiquinone 10 and ubiquinone analogues in model and biological membranes, Biochemistry 1987, 26, 7702– 7707.

[108] Ge, C.; Orosz, K.S.; Armstrong, N.R.; Saavedra, S.S. Poly(aniline) nanowires in sol-gel coated ITO: a pH-responsive substrate for planar supported lipid bilayers. ACS Appl Mater Interfaces 2011, 7, 2677-2685.

[109] Leonenko, Z.V.; Finot, E.; Ma, H.; Dahms, T.E.S.; Cramb, D.T. Investigation of Temperature-Induced Phase Transitions in DOPC and DPPC Phospholipid Bilayers Using Temperature-Controlled Scanning Force Microscopy. Biophys J. 2004, 86, 3783–3793.

[110] Nussio, M.R.; Oncins, G.; Ridelis, I.; Szili, E.; Shapter, J.G.; Sanz, F.; Voelcker, N.H. Nanomechanical characterization of phospholipid bilayer islands on flat and porous substrates: a force spectroscopy study. J. Phys. Chem. B 2009, 113, 10339-10347.

[111] Popovich, N.D.; Wong, S.S.; Yen, B.K.; Yeom, H.Y.; Paine, D.C. Influence of microstructure on the electrochemical performance of tin-doped indium oxide film electrodes. Anal Chem. 2002, 74, 3127-3133.

[112] Mou, J.; Yang, J.; Huang, C.; Shao, Z. Alcohol induces interdigitated domains in unilamellar phosphatidylcholine bilayers. Biochemistry 1994, 33, 9981-9985.

[113] Leonenko, Z.V.; Cramb D.T. Revisiting Lipid-General Anesthetic Interactions (I): Thinned Domain Formation In Supported Planar Bilayers Induced by Halothane and Ethanol. Can. J. Chem. 2004, 82, 1128–1138.

[114] Morandat, S.; El Kirat, K. Cytochrome c provokes the weakening of zwitterionic membranes as measured by force spectroscopy. Colloids Surf. B 2011, 82, 111−117.

[115] Koubi, L.; Tarek, M.; Klein, M.L.; Scharf, D. Distribution of halothane in a dipalmitoylphosphatidylcholine bilayer from molecular dynamics calculations. Biophys J. 2000, 78, 800-811.

[116] Berti, D.; Caminatia, G.; Baglioni, P. Functional liposomes and supported lipid bilayers: towards the complexity of biological archetypes. Phys. Chem. Chem. Phys. 2011, 13, 8769–8782.

[117] Castellana, E.T.; Cremer P.S. Solid supported lipid bilayers: From biophysical studies to sensor design. Surface Science Reports 2006, 61, 429–444.

[118] Leonenko, Z.V.; Carnini, A.; Cramb, D.T. Supported planar bilayer formation by vesicle fusion: the interaction of phospholipid vesicles with surfaces and the effect of gramicidin on bilayer properties using atomic force microscopy. Biochim. Biophys. Acta 2000, 1509, 131-147.

[119] Garcia-Manyes, S.; Oncins, G.; Sanz, F. Effect of temperature on the nanomechanics of lipid bilayers studied by force spectroscopy. Biophys J. 2005, 89, 4261-4274.

[120] Redondo-Morata, L.; Oncins, G.; Sanz, F. Force spectroscopy reveals the effect of different ions in the nanomechanical behavior of phospholipid model membranes: the case of potassium cation. Biophys. J. 2012, 102, 66-74.

[121] Zawisza, I.; Lachenwitzer, A.; Zamlynny, V.; Horswell, S.L.; Goddard, J.D.; Lipkowski, J. Electrochemical and photon polarization modulation infrared reflection absorption spectroscopy study of the electric field driven transformations of a phospholipid bilayer supported at a gold electrode surface. Biophys J. 2003, 85, 4055-4075.

[122] Zawisza, I.; Bin, X.; Lipkowski, J. Spectroelectrochemical studies of bilayers of phospholipids in gel and liquid state on Au(111) electrode surface. Bioelectrochemistry. 2004, 63, 137-147.

[123] Lipkowski, J. Building biomimetic membrane at a gold electrode surface. Phys. Chem. Chem. Phys. 2010, 12, 13874-13887.

[124] Daskalakis, N.N.; Müller, A.; Evans, S.D.; Jeuken, L.J.C. Driving bioenergetic processes with electrodes. Soft Matter, 2011, 7, 49-52.

[125] Wiegand, G.; Arribas-Layton, N.; Hillebrandt, H.; Sackmann, E.; Wagner, P. Electrical Properties of Supported Lipid Bilayer Membranes. J. Phys. Chem. B 2002, 106, 4245-4254.

[126] Bordi, F.; Cametti, C.; Gliozzi, A. Impedance measurements of self-assembled lipid bilayer membranes on the tip of an electrode. Bioelectrochemistry 2002, 57, 39-46.

[127] Shiba, H.; Maeda, K.; Ichieda, N.; Kasuno, M.; Yoshida, Y.; Shirai, O.; Kihara, S. Voltammetric study on the electron transport through a bilayer lipid membrane containing neutral or ionic redox molecules. J. Electroanal. Chem. 2003, 556, 1-11.

[128] Demel, R.A.; Geurts van Kessel, W.S.; Zwaal, R.F.; Roelofsen, B.; van Deenen, L.L. Relation between various phospholipase actions on human red cell membranes and the interfacial phospholipid pressure in monolayers. Biochim. Biophys. Acta 1975, 406, 97–107.

[129] Nowicka, B.; Kruk, J. Occurrence, biosynthesis and function of isoprenoid quinones. Biochim. Biophys. Acta 2010, 1797, 1587-1605.

[130] Glöckner, C. The donor and acceptor side of photosystem II: Structural and functional investigations. Ph.D. thesis, Technische Universität Berlin, Berlin, 2013.

Chapter 6

Conclusions

The characterization of the films prepared on solid substrates using, respectively, the LB and vesicle fusion technique show that the LB technique is more reproducible and it permits a better control on the film properties.

DPPC and DPPC:UQ bilayers on ITO using the vesicle fusion

- The AFM images of SPBs of DPPC:UQ on ITO formed using the vesicle fusion technique show no topographically significant visual differences according to the DPPC:UQ ratio. However, the SPB height increases for the DPPC:UQ 5:1 system and the force curves performed on top of the SPBs reveal a decrease of the breakthrough force values when increasing the UQ content in the mixture. Both observations can be explained by the formation of UQ pools or aggregates in the bilayer.
- The cyclic voltammetry of the DPPC:UQ SPBs on ITO shows two different irreversible redox processes, which, in addition to the force spectroscopy results, are correlated with the “diving” (I) and “swimming” (II) position, being the latter position favoured when increasing the UQ content.

The formation of monolayers using the Langmuir technique

- The results obtained indicate that UQ and PQ form monolayers at the air|water interface, showing LE state at the most compact state and, after the collapse, it

forms multilayers. On the other hand, DPPC, MGDG and DGDG present the coexistence of two different physical states, whereas MD presents mostly LC state. The coexistence of two phases, and the compactness of each of them, depend on the characteristics of the lipid headgroup.

- The lower collapse pressure and the larger lift-off and limiting area observed in the literature for unsaturated galactolipid compared with our saturated galactolipid is explained by the presence of unsaturations in the lipid chains, which hindrances the hydrogen bond formation and the tighter packing for both the heads and the tails.
- The different shape of the C_s^{-1} curves and the lower C_s^{-1} values observed at surface pressures below the main quinone expulsion (kink point) for the lipid:quinone mixtures, compared to the corresponding pure lipid, indicate the presence of quinone molecules in the lipid matrix, which leads to less ordered physical states.
- The shape of the π-A isotherms, the shape of the C_s^{-1} curves and the shape of the kink point in the C_s^{-1} curves give qualitative information about the expulsion. In addition, the surface pressure of this kink point is higher when reducing the quinone content, which is correlated with that quinone is better retained in monolayers when it is present at low concentrations due to it affects in a lower extent the formation and shape of the ordered phases.

AFM study of monolayers transferred on mica

- The deposition of quinone on mica shows that, after the collapse, quinone forms monolayers with some patches over it, which are correlated with quinone molecules expulsed from the monolayer and established in pools.
- The monolayers of galactolipids, once transferred to the mica surface, present zones with different height, which is correlated with a different tilting of the galactolipid molecules that indicate a different physical state.
- The lower height and lower proportion of the compact state generally observed for the lipid:quinone mixtures, compared with the corresponding lipid and the higher affinity of the quinone molecules for the LE state, indicate that quinone molecules are present in the lipid matrix in both physical states (LE and LC).

Cyclic voltammetric study of monolayers transferred on ITO

- The ITO-lipid electrode presents a slightly higher C_d values to that it has been reported for high quality lipid monolayers, so indicating that our monolayer is not completely homogeneous and it presents few defects.
- The electrochemical response shows for UQ one redox process (I) at low surface pressure, and it also appears a second redox process (II) when increasing the surface pressure. On the other hand, PQ shows only one redox process (I) at several surface pressures.
- The shape of the voltammograms for both pure quinone and the lipid:quinone systems present important deviations respect to the theoretical models proposed in the literature to describe the cyclic voltammetric response of a surface confined reaction.
- The ITO-lipid:quinone systems at high quinone content can present from one to three irreversible redox processes (DPPC:UQ I, I', II or galactolipid:quinone I_α, I_β, II) depending on the surface pressure at which the LB film has been transferred. However, two processes may be convoluted in one redox peak. On the other hand, at low quinone content they can present one or two redox processes (DPPC:UQ I, I' or galactolipid:quinone I_α, I_β) except the DGDG:PQ system at high surface pressure that it presents also process II.
- The simultaneous presence of three redox processes seems to be related with a high initial quinone content, the presence of a medium-high compactness of the LC state and the formation of circular LE domains.
- The ITO-galactolipid:quinone/electrolyte systems present a higher electroactive fraction when increasing the initial quinone content or increasing the transfer surface pressure, providing better conditions for the electron hopping. Direct transfer and electron hopping are the main electron transfer processes in these systems.
- MD:PQ 5:1 and the MD:PQ at low PQ content (10:1 and 20:1) systems present, unexpectedly, marked different behaviour at all the used techniques. We propose that the MGDG:DGDG (MD) mixture and PQ at the 20:1 and 10:1 ratios establish strong interactions that stabilize the ternary mixture.

Quinone position in the lipid matrix

- The results obtained from the different used techniques and their interpretation allow us to assign the position of the quinone molecules in the lipid matrix.
- At low surface pressures, the quinone in “diving” position is placed in the lipid matrix and located in direct contact with the electrode surface (process I or I_α). Increasing the surface pressure of the monolayer two actions take place: First the compactness of the LC state, so favouring the rejection of part of the quinone in “diving” position. On the one hand, it can be vertically rejected to the “diving” position without contact to the substrate (process I´ or I_β) and, on the other hand, horizontally to the remaining LE zones so enriching them in quinone (process I, I_α). Second, the LE to LC phase change of the remaining LE zones.
- Further compression results in a more compact state that leads to a partial quinone expulsion of the lipid matrix (process II). The formation of protrusions in the lipid:UQ systems are related with the presence of UQ molecules in “swimming” position (process II) forming pools on top of the monolayer.
- The proportion of quinone at each position (“diving” or “swimming”) is defined by the lipid physical state and the initial quinone content.

Appendix A

Symbols and acronyms

A	Area per molecule
A_w	Electrode area
A^E	Excess area
AFM	Atomic Force Microscopy
AM-AFM	Amplitude modulation-AFM
APTES	Aminopropyltriethoxysilane
A_{rms}	Rms-amplitude of the driven cantilever
B	Measurement bandwidth
BAM	Brewster Angle Microscopy
BLM	Black lipid membrane
C_B	Number of components in the bulk
C_d	Differential capacitance of the double layer
c_0^*	Concentration of the specie O in the bulk
C_S	Number of components confined to the surface
C_s^{-1}	Inverse of the compressibility modulus
$C_{s\ max}^{-1}$	Maximum of the inverse of the compressibility modulus
CV	Cyclic voltammetry
CVC	Critical vesicular coverage
CVs	Cyclic voltammograms

d	Thickness of a bilayer
DGDG	Digalactosyldiacylglycerol
DLVO	Derjaguin–Landau–Verwey–Overbeek theory
DMPC	Dimyristoylphosphatidylcholine
D_O	Diffusion coefficient of O
DOPC	1,2-Dioleoyl-sn-glycero-3-Phosphatidylcholine
DPPC	Dipalmitoylphosphatidylcholine
DPPG	Dipalmitoylphosphatidylglycerol
DSC	Differential scanning calorimetry
DSPC	1,2-distearoyl-sn-glycero-3-phosphocholine
DSPE	1,2-distearoyl-sn-glycero-3-phosphoethanolamine
E	Potential
E_f	Formal potential
EIS	Electrochemical impedance spectroscopy
E_{pO}	Oxidation peak potental
E_{pR}	Reduction peak potental
ESP	Equilibrium spreading pressure
F	Degrees of freedom in phase rule or Faraday constant in the electrochemistry section.
F_d	Ferredoxin
FRAP	Fluorescence recovery after photobleaching
F_v	Vertical force
FvP	Penetration curve
F_y	Threshold force
F_z	Minimum detectable interaction force
G	Gas state
G^E	Excess free energy of mixing
GUV	Giant unilamellar vesicles
HDME	Hanging mercury drop electrode
H_{II}	Hexagonal II phase
HPT	Head plus part of the tail
I	Redox process I
I’	Redox process I’
i_c	Charging current

i_f	Faradaic current
II	Redox process II
i_p	Peak intensity
I_r	Reflected intensity
IRRAS	Infrared reflection absorption spectroscopy
ITO	Indium tin oxide
I_α	Redox process I_α
I_β	Redox process I_β
k^0	Rate constant of the redox reaction
k_b	Boltzmann constant
k_c	Cantilever constant
LB	Langmuir-Blodgett technique
LC	Liquid condensed state
L_c	Subgel or lamellar crystalline or crystal phase
LC1	Molecules at the beginning of the LC state
LC2	Molecules at the more ordered state of the LC state
LE	Liquid expanded state
LPT	Last part of the tail
LS	Langmuir-Schaefer technique
LSV	Linear sweep voltammetry
LUVs	Large unilamellar vesicles
L_α	Liquid-crystalline or fluid phase
L_β	Lamellar gel or solid phase
$L_{\beta I}$	Interdigitated L_β phase
MD	MGDG:DGDG (2:1)
MGDG	Monogalactosyldiacylglycerol
MLVs	Multilamellar vesicles
MS	Mass spectrometry
n	Number of electrons
N_A	Avogadro's number
$NADP^+$	Nicotinamide Adenine Dinucleotide Phosphate
n_f	Refractive index of the media
NHE	Normal hydrogen electrode

n_i	Amounts of all components
NMR	Neutron magnetic resonance
$_O$	Subindex that refers to the oxidized form
OCP	Open circuit potential
OM	Octadecanethiol monolayer
OTS	Octadecyltrichlorosilane
OWS	Optical waveguide spectroscopy
P	Pressure
PA	Phosphatidic acid
P_B	Number of bulk phases
PC	Phosphatidylcholine
PCn	Plastocyanin
P_d	Puncture deformation
PE	Phosphatidylethanolamine
PG	Phosphatidylglycerol
Ph	Pheophytin
POPG	1-palmitoyl-2-oleoyl-sn-glycero-3-phosphoglycerol
PQ	Plastoquinone-9
PQH·	Radical plastoquinol-9
PQH_2	Plastoquinol-9
P_S	Number of monolayer phases in equilibrium each other
PS	Phosphatidylserine
PSI	Photosystem I
PSII	Photosystem II
pzc	Potential of zero charge
P_β	Ripple phase
Q_f	Quality factor
Q	Quinone
QH_2	Quinol
R	Ideal gas constant ($J \cdot mol^{-1} \cdot K^{-1}$) or Resistance in the electrochemistry section.
$_R$	Subindex that refers to the reduced form
S	Solid state
SAMs	Self-assembled monolayers

SCE	Saturated calomel electrode
SPB	Supported planar bilayer
SPM	Scanning Probe Microscopy
SPR	Surface plasmon resonance
SQDG	Sulfoquinovosyldiacylglycerol
SSC	Silver-silver chloride
STM	Scanning tunneling microscopy
SUVs	Small unilamellar vesicles
S_v	Vertical sensitivity
T	Temperature
t-BLM	Tethered bilayer membranes
T_c	Transition temperature from the gel phase to liquid crystalline phase
T_m	Melting temperature
TR	Transfer ratio of the monolayer
UQ	Ubiquinone-10
UQH·	Radical ubiquinol-10
UQH_2	Ubiquinol-10
UQ-n	Ubiquinone with alkyl chain of n units
v	Scan rate
V	Volume
W	Working electrode
α	Tilt angle of lipid molecules
α_p	Polarization of the incident light
α_t	Transfer coefficient
Γ	Surface concentration of the electroactive species
γ	Surface tension
Γ_{expec}	Expected total surface coverage
Γ_O	Oxidation surface coverage
Γ_{Otot}	Total oxidation surface coverage
ΔG_{mix}	Free energy of mixing
Δx	Photodetector signal variation
Δz	Vertical piezo displacement
θ	Angle of incidence

θ_B	Brewster's angle
π	Surface pressure
σ_M	Surface charge
ω_0	Free cantilever resonance frequency

Appendix B

Selected publications

Publications in Peer-review journals

- Hoyo, J.; Guaus, E.; Oncins, G.; Torrent-Burgués, J.; Sanz, F. Incorporation of ubiquinone in supported lipid bilayers on ITO. J. Phys. Chem. B 2013, 117, 7498−7506.
- Hoyo, J.; Guaus, E.; Torrent-Burgues, J. Biomimetic monolayer films of monogalactosyl-diacylglycerol incorporating ubiquinone. J. Colloid Interface Sci. 2012, 384, 189 − 197.
- Hoyo, J.; Guaus, E.; Torrent-Burgues, J.; Sanz, F. Electrochemical behaviour of mixed LB films of ubiquinone−DPPC. J.Electroanal. Chem. 2012, 669, 6−13.

Publications in Books

- Javier Hoyo-Pérez, Joan Torrent-Burgués, Fausto Sanz-Carrasco, “AVANCES DE LA ELECTROQUÍMICA EN IBEROAMÉRICA, PORTUGAL Y ESPAÑA”, 2010, vol 1, pp. 883- 888, Servicio de Publicaciones Universidad de Alcalá. Alcalá de Henares (Spain).

Presentations in international scientific meetings

- J. Hoyo, G. Oncins, J. Torrent-Burgués, F. Sanz, “Characterization of biomimetic mixed films of DPPC and UQ”, Third IBEC simposium on bioengineering and nanomedicine, Barcelona (Spain), June 2010.

- Javier Hoyo-Pérez, Joan Torrent-Burgués, Fausto Sanz-Carrasco, “Quinones Redox behaviour in supported lipid planar bilayers”, SIBAE 2010, Alcalá De Henares (Spain), July 2010.
- Javier Hoyo, Juan Torrent-Burgués, Ester Guaus and Fausto Sanz-Carrasco, “Biomimetic films of DPPC with biological quinones”, Second International Soft Matter Conference, Granada (Spain), July 2010.
- J. Torrent-Burgués, J. Hoyo, E. Guaus, G. Oncins, F. Sanz, “Characterization and behavior of supported lipid films with natural quinones”. 24th Conference of the European Colloid and Interface Society (ECIS 2010), Praga (Czech Republic), September 2010.
- J. Hoyo, E. Guaus and J. Torrent-Burgués, “Biomimetic films of MGDG incorporating ubiquinone”, 12th European conference on organised films, Sheffield (UK), July 2011.
- J. Hoyo, J. Torrent-Burgués and E. Guaus, “Organization and REDOX behaviour of UQ in DPPC films”, 25th meeting of the European Colloid and Interface Society (ECIS 2011), Berlin (Germany), September 2011.
- E. Guaus, J. Hoyo and J. Torrent-Burgués, “Electrochemical behaviour of UQ-10 in DPPC monolayers on ITO”, XXXII Reunión del Grupo de Electroquímica de la Real Sociedad Española de Química, Murcia (Spain), September 2011.
- J. Torrent-Burgués, J. Hoyo, G. Oncins, F. Sanz, “Force Spectroscopy of monolayers and bilayers of polar lipids”, BCNano11. University, Industry, Future, Barcelona (Spain), September 2011.
- J. Hoyo, E. Guaus, J. Torrent-Burgués, “UQ behaviour in biomimetic membranes of DPPC and MGDG”, Global questions on advanced biology, Barcelona (Spain), July 2012.
- Javier Hoyo, Ester Guaus, Gerard Oncins, Juan Torrent-Burgués, Fausto Sanz, “Incorporation of ubiquinone in supported lipid bilayers on ITO”, Sixth IBEC simposium on bioengineering and nanomedicine, Barcelona (Spain), May 2013.
- Javier Hoyo, Ester Guaus, Juan Torrent-Burgués, Fausto Sanz, “Electrochemical behaviour of Ubiquinone in MGDG natural mimicking membranes”, XXXIV Reunión del Grupo Electroquímica de la RSEQ y XV Encontro Ibérico de Electroquímica, Valencia (Spain), July 2013.

Appendix C

Resum en català

La fotosíntesi és el procés mitjançant el qual les cèl·lules de les plantes i bactèries converteixen la matèria inorgànica en orgànica gràcies a la llum. Aquest procés consta de diferents etapes i una d'elles és el transport electrònic per part de la plastoquinona-9 (PQ) des del fotosistema II fins al citocrom. En aquesta tesi, preparem membranes que emulen les característiques de les membranes de les cèl·lules naturals i les caracteritzem amb diverses tècniques per tal d'obtenir la posició de les molècules de PQ en la membrana i estudiar el seu comportament electroquímic. Aquestes membranes es preparen utilitzant diferents lípids y les seves mescles amb PQ y ubiquinona-10 (UQ).

Tant els components purs com les mescles s'han estudiat fent servir isotermes pressió superficial-àrea per molècula, ja que dona informació de l'estabilitat de la pel·lícula de molècules (pel·licula Langmuir) a la interfase aire|aigua. El tractament matemàtic dels resultats d'aquestes isotermes permet obtenir el comportament termodinàmic de la mescla i el seu estat físic. A més, s'han estudiat els sistemes in situ fent servir la tècnica de Brewster Angle Microscopy per observar la possibilitat de segregació microscòpica. Per altra banda, la pel·lícula Langmuir ha estat transferida sobre mica formant una monocapa Langmuir – Blodgett (LB) que simula la capa inferior de les membranes naturals. Aquesta capa s'ha caracteritzat topogràficament utilitzant AFM, s'ha mesurat l'alçada i s'ha estudiat l'estat físic que presenta. A més, aquestes pel·lícules s'han transferit sobre ITO que és un substrat hidrofílic que té unes bones característiques òptiques i elèctriques i per tant, permet obtenir el comportament electroquímic d'aquests sistemes. En afegit, el sistema DPPC:UQ s'ha estudiat preparant supported planar bilayers (SPBs) utilitzant liposomes. Aquestes SPBs

s'han caracteritzat per espectroscòpia de força, a més de les tècniques prèviament exposades que li són aplicables.

Els resultats obtinguts per les quinones pures indiquen que formen monocapes de Langmuir en fase líquid expandit (LE) a pressions superficials inferiors al col·lapse. L'estudi per voltametria cíclica (CV) de LB de quinones transferides sobre ITO mostra, en funció de la pressió superficial de transferència, un (I) o dos processos redox (processos I i II) amb els mateixos potencials formals per les dues quinones a pH biològic. Per altra banda, els lípids purs, en general, formen fases més compactes que els sistemes galactolípid:quinona. Els sistemes galactolípid:quinona indiquen que, a pressions baixes, es formen mescles no ideals, on estan afavorides les interaccions entre molècules iguals. A l'augmentar la pressió, el sistema pateix una transició de fase de LE a líquid compacte (LC) que provoca l'expulsió de la quinona de la zona dels caps dels lípids. L'estudi per CV indica que aquesta expulsió pot ser vertical, o horitzontal. Vertical, posicionant-se la quinona per sobre dels caps dels lípids, però encara dintre de la matriu lipídica, o fora de la matriu, posicionant-se perpendicularment a les cadenes lipídiques. L'expulsió horitzontal (de les zones LC) implica que la quinona va a parar a les zones LE, enriquint aquestes en quinona i formant-se "pools" de quinona. Les posicions descrites per la quinona en un sistema lípid:quinona es poden classificar en "diving" amb les quinones dintre de la matriu, ja sigui amb o sense contacte ITO-quinona, i la "swimming", que són quinones que estan a sobre de la matriu. Les posicions "diving" and "swimming" donen lloc a processos redox diferents i la càrrega que presenta cada procés, permet saber quina posició és dominant. Els dos processos redox són irreversibles donada la lenta transferència de càrrega en les interfases ITO-monocapa|electrolit. A més, aquest intercanvi d'electrons té lloc per transferència directa o per electron hopping.

Acknowledgements

Quiero agradecer a mis padres, Puri y Aurelio, su excepcional esfuerzo personal y económico por darme una educación y una formación académica de nivel. Han sido muy importantes para mi sus palabras y ejemplo en valores como la tenacidad, la lealtad, la proactividad en cualquier aspecto de la vida, el dar siempre el 100% en todo cuanto se hace y el no desfallecer incluso cuando las cosas van mal. Por todo esto y por todos los sacrificios que hemos hecho juntos, estamos hoy aquí.

Quiero agradecer a mi hermana, Cristina, su ayuda incondicional a mi sueño de dedicarme a la ciencia. Su gran implicación en tareas cotidianas y familiares me ha permitido reducir mi dedicación a dichas tareas lo que me ha posibilitado el poder concentrarme en mis estudios.

Vull agrair la Marta, la meva parella. Ella ha estat un suport importantíssim en tots els àmbits durant aquests anys de tesi doctoral. La seva comprensió i recolzament per la gran quantitat d'hores que he dedicat al doctorat dins i fora de casa és quelcom que mai oblidaré.

Per altra banda, vull agrair als meus supervisors de tesi, Prof. Joan Torrent i Dra. Ester Guaus, la seva dedicació i implicació. Al Joan, que ha estat amb mi des de que vaig començar la tesi doctoral perquè hem passat moltes hores discutint resultats, perquè ha hagut de suportar les meves teories i innovacions que sempre requerien una dosi menys alta d'optimisme. A l'Ester, qui sempre ha estat disposada a buscar un forat a la seva apretada agenda per discutir els resultats experimentals i pel seu esforç d'ampliar coneixements sobre alguna tècnica de caracterització que estava lluny de la seva formació. També vull agrair el Fausto, qui va ser el meu primer professor d'electroquímica, i que quan ens vam conèixer ja vam veure que la nostra relació no s'acabaria amb aquella assignatura. Ell va ser qui em va oferir fer un doctorat relacionat amb la fotosíntesi en col·laboració amb el grup d'investigació del Joan i l'Ester. A més, de permetre'ns fer servir els seus instruments de caracterització, Fausto ha estat un suport importantíssim en les discussions electroquímiques.

També vull agrair a la Universitat Politècnica de Catalunya la seva beca FPU que m'ha permés cursar aquesta tesi doctoral amb finançament econòmic.

Finalmente quiero acordarme de mis compañeros de laboratorio, muchos de ellos ya amigos, que han hecho el trabajo diario más ameno. Me acuerdo de mis primeros años de tesis en los que compartí laboratorio con Aleix, Lorena, Juanma, Marina, Anna A., Anna P., Felipe, Pau, Gerard, Jordi, Andrés, Michel, Chema y Marc. También tengo un recuerdo especial de aquellos con los que he compartido estos últimos años de tesis: Albert, Isma, Montse i Alex.

A todos vosotros y a aquellos que me he olvidado de poner en estas líneas, os doy las gracias.

Javi